Fluid Mechanics and Its Applications

Grazia Lamanna
Simona Tonini
Gianpietro Elvio Cossali
Bernhard Weigand *Editors*

Droplet Interactions and Spray Processes

Springer

Fluid Mechanics and Its Applications

Volume 121

The purpose of this series is to focus on subjects in which fluid mechanics plays a fundamental role. As well as the more traditional applications of aeronautics, hydraulics, heat and mass transfer etc., books will be published dealing with topics, which are currently in a state of rapid development, such as turbulence, suspensions and multiphase fluids, super and hypersonic flows and numerical modelling techniques. It is a widely held view that it is the interdisciplinary subjects that will receive intense scientific attention, bringing them to the forefront of technological advancement. Fluids have the ability to transport matter and its properties as well as transmit force, therefore fluid mechanics is a subject that is particulary open to cross fertilisation with other sciences and disciplines of engineering. The subject of fluid mechanics will be highly relevant in such domains as chemical, metallurgical, biological and ecological engineering. This series is particularly open to such new multidisciplinary domains. The median level of presentation is the first year graduate student. Some texts are monographs defining the current state of a field; others are accessible to final year undergraduates; but essentially the emphasis is on readability and clarity.

Springer and Professor Thess welcome book ideas from authors. Potential authors who wish to submit a book proposal should contact Dr. Mayra Castro, Senior Editor, Springer Heidelberg, e-mail: mayra.castro@springer.com

Indexed by SCOPUS, EBSCO Discovery Service, OCLC, ProQuest Summon, Google Scholar and SpringerLink

More information about this series at http://www.springer.com/series/5980

Grazia Lamanna · Simona Tonini ·
Gianpietro Elvio Cossali · Bernhard Weigand
Editors

Droplet Interactions and Spray Processes

Springer

Editors
Grazia Lamanna
Institute of Aerospace Thermodynamics
University of Stuttgart
Stuttgart, Baden-Württemberg, Germany

Gianpietro Elvio Cossali
Dipartimento di Ingegneria e
Scienze Applicate
Università degli Studi di Bergamo
Dalmine, Bergamo, Italy

Simona Tonini
Dipartimento di Ingegneria e
Scienze Applicate
Università degli Studi di Bergamo
Dalmine, Bergamo, Italy

Bernhard Weigand
Institute of Aerospace Thermodynamics
University of Stuttgart
Stuttgart, Baden-Württemberg, Germany

ISSN 0926-5112 ISSN 2215-0056 (electronic)
Fluid Mechanics and Its Applications
ISBN 978-3-030-33337-9 ISBN 978-3-030-33338-6 (eBook)
https://doi.org/10.1007/978-3-030-33338-6

This Springer imprint is published by the registered company Springer Nature Switzerland AG
The registered company address is: Gewerbestrasse 11, 6330 Cham, Switzerland

Foreword by the University Rectors (*Università degli Studi di Bergamo* and *Universität Stuttgart*-A Strategic Partnership)

The regions of Lombardy in Italy and Baden-Württemberg in Germany are tied by close economic relations for hundreds of years. Today, there are permanent commercial structures between privately owned companies on the one side and publicly owned undertakings on the other side as well as between the Chambers of Commerce and Industry (CCI) of regional locations in Bergamo and Stuttgart. In addition, the research universities of Bergamo (Università degli Studi di Bergamo) and Stuttgart (Universität Stuttgart) foster a deepened scientific and academic collaboration since many years. Both universities have declared this relationship as a **strategic partnership** and have installed this partnership in their internationalization strategies. The main goal of strategic partnership is a widespread integration, global networking, and teamwork on all levels:

- Jointly supporting young academics, particularly through cooperation in doctoral training and by integrating career path models
- Strengthening international research collaborations and benefitting from synergies with complementary university facilities
- Promoting cooperation in teaching, for example, in the development and implementation of double degree programs
- Diversifying and establishing mobility options for students, for example, by establishing joint summer schools
- Development and establishment of sustainable structured mobility models for researchers and administrative staff
- Specifically supporting researchers in the acquisition of third-party funding to promote joint research and teaching projects.

From the beginning, not only the research institutes have taken in the center stage, but also the academic exchange of students, libraries, language centers, members of both Rectorates, and administration people as far as academic orchestras and choirs. Every year several bilateral visits cultivate the scientific and cultural exchange and thus introduce an international profile and cultural choice to both universities, of which all university staff and university members can benefit from.

The International Research Training Group (IRTG) for Droplet Interaction Technologies (DROPIT), which has been established in October 2016 by the German Research Foundation (DFG), is an impressive example of the strategic partnership between the two universities. The IRTG brings researchers from Bergamo and Stuttgart together to work on droplet dynamics. DROPIT is a structured doctoral program, which leads the accepted doctoral students to graduation within three years. The doctoral program is supervised by professors of both universities. Under the management of Prof. Bernhard Weigand (Stuttgart) and Prof. Gianpietro Elvio Cossali (Bergamo), a close and successful research cooperation has been developed. Hereinafter, the scientific results of DROPIT will be presented.

Prof. Dr. Wolfram Ressel
Rector, Universität Stuttgart
Stuttgart, Germany

Prof. Dr. Remo Morzenti Pellegrini
Rector, Università degli Studi di Bergamo
Bergamo, Italy

Preface

Droplet interaction technologies find application in a large number of technological and industrial processes. These include spray cooling in the food and chemical industry, spray drying absorption for waste and pollutant treatment in process engineering, droplet collisions for the generation of powders and encapsulated material in the food and pharmaceutical industry, drop evaporation and droplet–wall interaction in internal combustion and aeronautical engines as well as in coating technologies. In all these applications, small-scale fluid dynamics may have a huge impact on the large-scale flow pattern, leading to drag reduction, heat transfer enhancement or depression, phase transition kinetics (e.g., drop condensation or nucleate boiling), acoustic impedance, and optical reflection.

To date, the consequences of the presence of different length scales on macroscopic properties and the associated amplification of surface transport have remained largely unexplored, being limited mainly to the formulation of empirical correlations based solely on macroscopic observations. On this basis, the International Research Training Group (IRTG) "Droplet Interaction Technologies - DROPIT" (GRK 2160/1) was established in October 2016 to focus on detailed droplet processes. The project is supported on the German side by the DFG (Deutsche Forschungsgemeinschaft), the German Science Foundation.

The objective of DROPIT is to identify the mechanisms through which small-scale interactions at the interface can couple with and influence large-scale features in the main flow. Here a systematic study is undertaken to investigate the interdependencies between small-scale and large-scale dynamics in the field of droplet interaction technologies. Due to the complexity of the problem, the analysis of such micro-/macro-interactions is not limited to a single aspect. Rather, an integrated approach is chosen that evolves along three parallel pathways, namely a numerical, experimental, and theoretical approach.

DROPIT is a joint initiative of the University of Stuttgart in Germany, the University of Bergamo, and the University of Trento in Italy. The project consists of 17 sub-projects, which are structured into three main research areas (drop–gas interaction, drop–wall interaction, and drop–liquid interaction). It involves researchers from a large number of different disciplines like mathematics, environmental engineering, aerospace and mechanical engineering, civil engineering, informatics and computer sciences and visualization. The project further consists of an extensive qualification program, which aims at fostering the education of young scientists and providing them the knowledge and skills to conduct independent research. More detailed information concerning the International Research Training Group GRK 2160/1 can be found online: www.project.uni-stuttgart.de/dropit/.

After three years of very successful work, selected current results of this project have been summarized in the present book.

In order to broaden the scope of this book, also two invited chapters have been included. These are written by Prof. Dr. S. S. Sazhin (University of Brighton) about "Classical and novel approaches to modelling droplet heating and evaporation" and by Prof. Dr.-Ing. G. Brenn (University of Graz) about "Droplet Shape Oscillations."

The DROPIT project is strongly linked with the international workshop on Droplet Impact Phenomena and Spray Investigations (DIPSI), which is held yearly in Bergamo. The DIPSI workshop, which is now at its thirteenth edition, represents an important opportunity to share recent knowledge on droplets and sprays in a variety of research fields and industrial applications. Thus, some selected contributions of the DIPSI workshop of 2019 have been added in order to enlarge the scope of this book towards additional practical applications on spray processes.

Many people helped us in all phases of the preparation of this book. We are very grateful for all the support in bringing this manuscript together. First of all, we would like to thank all doctoral students and Postdocs involved in DROPIT for their contributions to the book. In addition, we thank all principal investigators of the project for their support. Special thanks go to all reviewers of the book contributions for their support and very good comments, and to Prof. Sazhin and Prof. Brenn for their invited contributions to this book and to the whole project, through the seminars delivered to the doctoral students along the past three years.

In addition, we would like to thank Dr. Anne Geppert for her help during the preparation of this book.

All members of the DROPIT project are very thankful for the financial support from the Deutsche Forschungsgemeinschaft (German Science Foundation) and for the financial support from the University of Bergamo.

We kindly acknowledge the permission of Cambridge University Press and of AIP Publishing for reprinting some of the figures in this book.

Finally, we are very grateful that this book could be published in this series and thank Prof. André Thess for his help. In addition, we would like to acknowledge the very good cooperation with Springer Press during the preparation of this manuscript. Here we would like to thank in particular Mrs. Petra Jantzen, Mr. Arulmurugan Venkatasalam, and Dr. Jan-Philip Schmidt for their support.

Stuttgart, Germany — Grazia Lamanna
Bergamo, Italy — Simona Tonini
Bergamo, Italy — Gianpietro Elvio Cossali
Stuttgart, Germany — Bernhard Weigand
December 2019

Contents

Towards Sprays

Droplet–Gas Interaction

An Analytical Approach to Model the Effect of Evaporation on Oscillation Amplitude of Liquid Drops in Gaseous Environment

Gautham Varma Raja Kochanattu, Gianpietro Elvio Cossali and Simona Tonini

Abstract The combined effect of evaporation and oscillation of liquid drops in gaseous stagnant environment is analytically modelled. Mechanical energy and mass balances are used to derive the time evolution of drop size and amplitude of oscillation. Two approaches, based on different assumptions about the kinetic energy distribution inside the drop, are used to evaluate the energy loss due to evaporation. Conditions for oscillation damping by evaporation are derived. Application of the model to the case of water, acetone and n-dodecane drops evaporating in hot air shows a non neglectful decrease of drop lifetime, with respect to non-oscillating drops.

1 Introduction

Evaporation of liquid drops in a gaseous environment is a process widely studied and the available scientific literature on this subject is vast (see [1, 2] for a deep and recent literature review). This is due to the prominent interest on this phenomenon in a wide range of applications, from spray injection in automotive and aeronautics engines, to fire suppression, medical aerosol, etc. Mathematical modelling of the processes is very challenging due to the interaction of different phenomena (which comprise heat and mass transfer, drop/gas interaction, internal drop motion, etc.). When analytic approaches are chosen, mainly with the aim to develop simplified and CPU efficient analytical or semi-analytical models for implementation in CFD codes for dispersed flow prediction, the challenge becomes even more demanding. The analytical approach needs often drastic simplifications to yield manageable solutions,

G. Varma Raja Kochanattu (✉) · G. E. Cossali · S. Tonini
Department of Engineering and Applied Sciences, University of Bergamo, Bergamo, Italy
e-mail: g.varmarajakochan@studenti.unibg.it

G. E. Cossali
e-mail: gianpieTro.cossali@unibg.it

S. Tonini
e-mail: simona.Tonini@unibg.it

G. Lamanna et al. (eds.), *Droplet Interactions and Spray Processes*,
Fluid Mechanics and Its Applications 121,
https://doi.org/10.1007/978-3-030-33338-6_1

but from the first models that accounted for the effect of Stefan flow [3], many simplifying assumptions were relieved. Many researchers devoted considerable effort to better model the effect of external convection [4], the effect of high pressure [5], variability of gas properties [6–8], the presence of more than one component [9–11], the effect of non-sphericity [12–14], the effect of finite liquid conductivity and diffusivity [1, 15], the effect of drop shrinkage [16–19] to cite just a few of the available studies. Only recently the unsteady drop shape (oscillation) has been considered as a possible further phenomenon that may affect drop evaporation. The study of drop oscillation, after the first remarkable results on inviscid [20] and viscous [21] drops, has produced an extensive scientific literature to account for the many phenomena affecting the oscillation characteristics. The previously cited results were extended to predict the effect of host medium with non-negligible density [22], oscillation decay by viscous effects [23], effect of viscosity of the host medium [24], initial value effects [25], second order effects [26], internal circulation [27, 28], mode coupling in large amplitude oscillations [29, 30], non-Newtonian effects [31], to cite some of the most important achievements. Surprisingly, it is hard to find studies that consider the interaction between oscillation and evaporation. Almost all the available experimental observations are reported for low evaporation conditions (see for example [29, 32–34]), with few recent exceptions (see for example [35]). On the modelling side the papers [36, 37] were likely the first papers to report a phenomenological model for taking into account the effect of evaporation on oscillation, while recently an analytical attempt to model the effect of oscillation on evaporation rate was reported [38].

This lack of analytical studies on the problem of oscillating and evaporating drops motivates the present work, which represents an attempt to analytical modelling possible effects of interaction between the shape oscillation and the evaporation phenomena.

2 The Mathematical Model

Evaporation may affect the dynamics of an oscillating drop in different ways. It is well known that the frequency of a free drop oscillating in a non interacting environment, subject to surface tension as unique restoring force, is expressed, for the mode n, by the equation [20]:

$$\omega_n = \sqrt{\frac{\sigma}{R_d^3 \rho_L}} n(n-1)(n+2) \tag{1}$$

where R_d is the drop radius when the drop is in a spherical shape. The evaporation decreases the drop mass, and so R_d, thus increasing the oscillation frequency. Beside this, one can expect that evaporation may affect also the amplitude of oscillation and in the present section a simplified model to evaluate the effect of evaporation on the oscillation amplitude, and vice versa, is developed. Consider first an evaporating

non-oscillating (spherical) drop. Given a time step t_0, the evaporated mass Δm can be calculated as $\Delta m = \frac{1}{t_0}\int_0^{t_0} \dot{m}_{ev} dt$, where $\dot{m}_{ev}$ is the instantaneous evaporation rate. The loss of mechanical energy, under the form of surface energy since the drop kinetic energy is assumed to be constantly nil, is:

$$\Delta E_T = E_{\sigma,f} - E_{\sigma,i} = 4\pi\sigma\left(R_{d,f}^2 - R_{d,i}^2\right) \tag{2}$$

where suffixes i and f indicate the starting and ending of the time interval t_0, respectively. This loss of energy is the minimum loss, always present also when no kinetic energy can be lost or dissipated.

Considering now an oscillating drop, and excluding evaporation over the time interval t_0, which now is taken equal to the oscillating period, the sum of kinetic (E_k) and surface (E_σ) energy can be assumed constant when viscous dissipation is nil. It is known that the oscillating mode $n = 2$ is the one less affected by viscous dissipation [23] and it is then the one that may survive longer after the oscillation starts, as also reported by many experimental evidences [27–29]. The surface of the drop in this mode can be approximated by that of a spheroid oscillating between a prolate and an oblate shape, and this will be assumed in the following development. The starting point of the oscillation is quite arbitrary since it is a periodic phenomenon; usually it is taken as the point where the deformation is maximum and the kinetic energy is then minimum or even nil (see [25, 26]). In the present case, at the beginning of a cycle, the drop is assumed to be spherical, with minimum surface energy (equal to $E_{\sigma,i} = 4\pi\sigma R_{d,i}^2$) and maximum kinetic energy. The drop evolves deforming to an oblate shape, reaching a maximum deformation when the kinetic energy is assumed to be nil and the surface extension to be maximum, and then again toward a spherical shape and a prolate one (with again maximum surface energy and nil kinetic energy) recovering the spherical shape at the end of the cycle. In a non evaporating drop under inviscid flow approximation (no energy dissipation) the total (mechanical) energy balance is:

$$E_T = E_K(t) + E_\sigma(t) = \frac{1}{2}\rho_L \int_V u_L^2 dV + \sigma A(t) = const. \tag{3}$$

In this case, during drop deformation, surface energy $E_\sigma(t)$ transforms (ideally in a reversible way) to kinetic energy $E_k(t)$ and back, and the maximum surface extension reached in the oblate and prolate shapes must be the same, and the kinetic energy at the beginning and at the end of each cycle must be the same too.

In an evaporating drop this is not anymore true since loss of mass due to evaporation implies loss of energy. The oscillation period, using Eq. (1) with $n = 2$,

$$t_0 = \frac{2\pi}{\omega_2} = \frac{\pi}{4}\sqrt{\frac{R_d^3\rho_L}{\sigma}} \tag{4}$$

is of the order of $\sqrt{R_d^3 \rho_L / \sigma}$ and it is assumed to be always much shorter than the drop lifetime τ_{LT}, which can be estimated as the ratio of the initial drop mass and the evaporation rate, i.e. of the order of $R_d^2 \rho_L / \left(D_{10} \rho_g\right)$. For drops larger than few microns, under a wide range of ambient conditions, τ_{LT} is some orders of magnitude larger than t_0. The drop mass, oscillating frequency and total energy can then be considered constant over one oscillation period, and the mass and energy lost by evaporation are evaluated under a quasi-steady approximation. Thus, new mass, energy and frequency will be set up for the next period. The kinetic energy in the most deformed (oblate or prolate) state is assumed nil, then the total energy during a cycle can be calculated as

$$E_T = 4\pi R_d^2 \sigma \beta_{\max} \tag{5}$$

where $\beta_{\max}$ is the maximum value of the non-dimensional drop surface $\beta(t) = A(t) / \left(4\pi R_d^2\right)$. The variation of the surface energy after each cycle is still given by Eq. (2) while variation of the kinetic energy can be evaluated as:

$$\Delta E_K = E_{K,f} - E_{K,i} = \Delta m \, \bar{e}_K = \Delta m \frac{1}{t_0} \int_0^{t_0} e_K(t) dt \tag{6}$$

where $\bar{e}_K$ and $e_K(t)$ are the average kinetic energy over a cycle and the instantaneous kinetic energy per unit of mass abandoning the drop, respectively, while Δm is the drop mass variation in a cycle, that can be defined as:

$$\Delta m = \frac{4}{3} \pi \rho_L \left(R_{d,f}^3 - R_{d,i}^3\right). \tag{7}$$

The loss of mass can also be obtained, under quasi-steady approximation (see [38] for a discussion), integrating the instantaneous evaporation rate $\dot{m}_{ev}$ over a cycle:

$$\Delta m = -\int_0^{t_0} \dot{m}_{ev} dt = -\int_0^{t_0} \Gamma(t) \dot{m}_{ev}^{sphere} dt = -\dot{m}_{ev}^{sphere} t_0 \frac{1}{t_0} \int_0^{t_0} \Gamma(t) dt = -\dot{m}_{ev}^{sphere} t_0 \overline{\Gamma} \tag{8}$$

where $\dot{m}_{ev}^{sphere} = 4\pi R_d \rho_g D_{10} \ln(1 + B_M)$ is the evaporation rate of a spherical drop of radius R_d; the parameter Γ, given by:

$$\Gamma = \frac{\left|1 - \varepsilon^2\right|^{1/2}}{\varepsilon^{1/3}} \begin{cases} \dfrac{1}{\ln\left(\varepsilon + \sqrt{\varepsilon^2 - 1}\right)} & \text{prolate spheroidal} \\ \dfrac{1}{\pi - 2\arctan\left(\sqrt{\frac{1+\varepsilon}{1-\varepsilon}}\right)} & \text{oblate spheroidal} \end{cases} \tag{9}$$

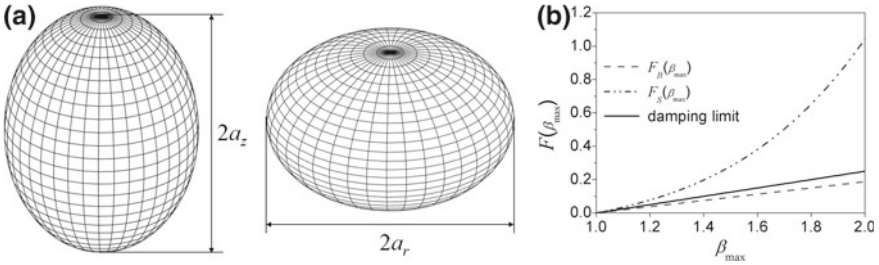

Fig. 1 **a** Prolate (left) and oblate (right) spheroids and definition of axial (a_z) and radial (a_r) spheroid half-axes. **b** $F(\beta_{\max})$ as predicted by the "bulk" and "surface" kinetic energy models and limit for drop oscillation damping

depends on the actual drop shape, which is defined by the drop aspect ratio $\varepsilon = a_z / a_r$ [13], where a_z and a_r are the half-axes of the spheroid (see Fig. 1a), and the quantity $\bar{\Gamma}$ is the time average of Γ over a cycle, which is shown (see appendix) to be a function only of the maximum value of β in the most deformed prolate and oblate shapes, $\beta_{\max}$, i.e. $\bar{\Gamma} = \bar{\Gamma}(\beta_{\max})$. The quantity $\bar{e}_K$ can be evaluated using different approaches, as it will be shown later, but all of them rely on the actual time-profile of the drop deformation, i.e. on the function $\beta = \beta(t)$. The minimum physical constraint on this profile is a consequence of the above discussed assumptions, i.e. the maximum value of β in the most deformed prolate and oblate shapes, $\beta_{\max}$, must be the same. A simple choice that satisfies these constraints is the following:

$$\beta = \frac{1 - \beta_{\max}}{2} \cos(2\omega_2 t) + \frac{1 + \beta_{\max}}{2}. \tag{10}$$

It should be noticed that the actual profile of $\beta(t)$ is then expected to be a critical element of the modelling. The evaluation of the kinetic energy of the mass that is lost by evaporation over a cycle may be based on two opposite assumptions that lead to different estimations of the kinetic energy loss.

2.1 Bulk Kinetic Energy Approach

It is assumed that the internal flow field produces an efficient mixing, then the average kinetic energy per unit of mass leaving the drop $e_K(t)$ is equal to the average kinetic energy over the whole drop, i.e.: $e_K(\mathrm{t}) = E_K(\mathrm{t})/m$. Since the total mechanical energy is assumed constant and equal to $4\pi\sigma R_d^2 \beta_{\max}$ over a cycle, the instantaneous drop kinetic energy $E_K(t)$ can be related to the instantaneous surface energy by Eq. (3), then:

$$\bar{e}_K = \frac{1}{m\, t_0} \int_0^{t_0} E_K(t)dt = \frac{3\sigma}{R_d \rho_L}\left(\beta_{\max} - \bar{\beta}\right) = R_d^2 \omega_2^2 \frac{3}{16}(\beta_{\max} - 1) \tag{11}$$

where $\bar{\beta} = (1 + \beta_{\max})/2$ is the average value of β over a cycle (see Eq. 10) and the oscillation frequency for the mode $n = 2$ was used (see Eq. 1).

2.2 Surface Kinetic Energy Approach

This approach assumes that the local kinetic energy is not uniform inside the drop. Then the kinetic energy associated to the evaporating mass, i.e. that close to the drop surface, may be used to evaluate $\bar{e}_K$. It is then necessary to introduce first the instantaneous value of the kinetic energy per unit of mass, $e_K(t)$, associated to the liquid mass close to the drop surface, which can be estimated as:

$$e_K(t) = \frac{1}{2} \frac{\int_A |v|^2 dA}{A} \tag{12}$$

where $|v|^2$ is the absolute value of the liquid velocity at the surface location, which can be set equal to the interface velocity since no mass flux is assumed to pass through the interface during a cycle. Then the average kinetic energy, per unit mass, which is associated to the evaporating mass, is calculated averaging Eq. (12) over a cycle.

2.2.1 Surface Velocity

Since the local surface velocity will be integrated over the ellipsoidal surface, it is necessary to evaluate it at any value of η, the angular coordinate in a spheroidal coordinate system:

$$\begin{array}{ll} x = a\sqrt{\zeta^2 - 1}\sqrt{1 - \eta^2}\cos\varphi & x = a\sqrt{\zeta^2 + 1}\sqrt{1 - \eta^2}\cos\varphi \\ y = a\sqrt{\zeta^2 - 1}\sqrt{1 - \eta^2}\sin\varphi & y = a\sqrt{\zeta^2 + 1}\sqrt{1 - \eta^2}\sin\varphi \\ z = a\zeta\eta & z = a\zeta\eta \\ \text{prolate spheroidal} & \text{oblate spheroidal} \end{array} . \tag{13}$$

In these systems, the spheroidal surface is given by the equation $\zeta = \zeta_0$. The condition of constant volume of the oscillating drop is $a_z a_r^2 = R_d^3$. Writing $a\sqrt{\zeta_0^2 \pm 1}$ in terms of R_d and $\varepsilon = a_z/a_r$, yields a parametrical equation of the spheroidal surface:

$$r = \sqrt{x^2 + z^2} = R_d \varepsilon^{-1/3}\sqrt{1 - \eta^2};\ z = R_d \varepsilon^{2/3}\eta \tag{14}$$

and the shape oscillation is then described by the variation of ε over time. Due to the assumed symmetry around the z-axis, the local surface value of $|v|^2$ is

$$|v|^2 = v_r^2 + v_z^2 = \left(\frac{\partial r}{\partial t}\right)_\eta^2 + \left(\frac{\partial z}{\partial t}\right)_\eta^2 = \frac{R_d^2 \dot{\varepsilon}^2}{9\varepsilon^{8/3}}\left[1 + \left(4\varepsilon^2 - 1\right)\eta^2\right] \tag{15}$$

and the integration of $|v|^2$ over the drop surface yields

$$e_K(t) = \frac{\int |v|^2 dA}{2A} = \frac{R_d^2}{36}\frac{\dot{\varepsilon}^2}{\beta(\varepsilon)\varepsilon^{10/3}} I(\varepsilon) \tag{16}$$

$$\begin{aligned} I(\varepsilon) =& A(\varepsilon) + B(\varepsilon)\begin{cases} \log\left(\frac{1+\sqrt{1-\varepsilon^3}}{1-\sqrt{1-\varepsilon^3}}\right)\Big/\sqrt{1-\varepsilon^2} & \varepsilon < 1 \\ 2\arctan\left(\sqrt{\varepsilon^2-1}\right)\Big/\sqrt{\varepsilon^2-1} & \varepsilon > 1 \end{cases}; \\ A(\varepsilon) =& \frac{\left(2+5\varepsilon^2-4\varepsilon^4\right)}{4\left(1-\varepsilon^2\right)} \\ B(\varepsilon) =& \frac{\varepsilon^2\left(4-3\varepsilon^2-4\varepsilon^4\right)}{8\left(1-\varepsilon^2\right)}. \end{aligned} \tag{17}$$

The average of $e_K(t)$ over an oscillation period can be written (see appendix) in a form that is similar to Eqs. (11), in fact both cases yield the relation:

$$\bar{e}_K = R_d^2 \omega_2^2 F(\beta_{\max}) \tag{18}$$

where $F(\beta_{\max})$ is a function only of $\beta_{\max}$ and equal to $F_B(\beta_{\max}) = 3(\beta_{\max} - 1)\big/16$ for the "bulk" model and to $F_S(\beta_{\max}) = \frac{1}{72\pi\omega_2}\int_0^{t_0} \frac{I(\varepsilon)}{\beta(\varepsilon)\varepsilon^{10/3}}\left(\frac{\dot{\beta}}{\beta'}\right)^2 dt$ for the "surface" model and the two functions are shown in Fig. 1b.

3 Model Implementation

In the previous section it was shown how the mass loss over a cycle and the kinetic energy associated to this mass can be estimated. From the mass loss Δm over a cycle, given by Eq. (8), the new drop equivalent radius $R_{d,f}$ is calculated as:

$$R_{d,f}^3 = R_{d,i}^3 - \frac{3}{4\pi\rho_L}\Delta m = R_{d,i}^3 - \frac{3}{4\pi\rho_L}\bar{\Gamma}\dot{m}_{ev}^{sphere} t_0 \tag{19}$$

and all quantities on the RHS are evaluated at the beginning of the cycle. The total mechanical energy variation is the sum of the variations of the kinetic and surface energy, then the new value of E_T is:

$$E_{T,f} = E_{T,i} + \Delta E_T = E_{T,i} + \Delta m \bar{e}_K + 4\pi\sigma\left(R_{d,f}^2 - R_{d,i}^2\right). \tag{20}$$

The values of the drop radius and mechanical energy at the beginning of the next cycle are then set equal to $R_{d,f}$ and $E_{T,f}$, respectively, a new value of ω_2 and t_0 can then be calculated for the next cycle, as well as the new value of $\beta_{\max}$:

$$\beta_{\max} = \frac{E_{T,f}}{4\pi R_{d,f}^2 \sigma}. \tag{21}$$

It can be observed that $\beta_{\max}$ can be interpreted as a non-dimensional form of the mechanical energy.

Beside the mechanical energy balance, a thermal energy balance could be set, which can be seen as a separated balance, as far as viscosity is assumed nil, and drop temperature would then enter into the model. Since the scope of the present work is to show the single effect of evaporation on oscillation, the drop temperature will be assumed to remain constant (isothermal process) and the thermal energy balance can be dismissed. It is worth to note that such a condition (isothermal process) can actually be observed in real processes, when a drop, after a first period of heating (or cooling), reaches the so called "plateau" temperature, i.e. a condition of very small temperature variation with time (refer to [1] for more details).

3.1 The Conditions for Oscillation Damping

It is known that viscous forces have a damping effect on the oscillation, since energy is dissipated. Also evaporation produces a loss of energy, but, since the amplitude of oscillation, $\beta_{\max}$, depends on the total energy and on the drop radius (see Eq. 21), and evaporation causes a decrease of both, then the variation of the maximum amplitude of oscillation with time depends on the relative variation of both energy and radius. Clearly for a non evaporating drop, a loss of energy results in a decrease of oscillation amplitude because the radius is constant. It can be observed that Eq. (20) implies $E_{T,f} < E_{T,i}$ and, from Eq. (5), this yields the inequality:

$$R_{d,i}^2 \beta_{\max,i} > R_{d,f}^2 \beta_{\max,f}. \tag{22}$$

The oscillation "damping" condition $\beta_{\max,f} < \beta_{\max,i}$ is not implied by Eq. (22), since $R_{d,i}^2 > R_{d,f}^2$. It is then of a certain importance to analyse when damping by evaporation may occur. Imposing the inequality $\beta_{\max,f} < \beta_{\max,i}$, then from Eq. (5):

$$\frac{E_{T,i}}{R_{d,i}^2} > \frac{E_{T,f}}{R_{d,f}^2}. \tag{23}$$

Using Eq. (20) to eliminate $E_{T,f}$ from Eqs. (23) and (5) to eliminate $E_{T,i}$ and Eq. (7) to evaluate Δm, yields the following inequality:

$$\bar{e}_K > \frac{3\sigma}{\rho_L} \frac{\left(R_{d,i} + R_{d,f}\right)}{\left(R_{d,i}^2 + R_{d,f} R_{d,i} + R_{d,f}^2\right)} (\beta_{\max} - 1) \tag{24}$$

which shows that there exists a minimum value of the average kinetic energy per unit mass, associated to the evaporated mass, which assures the decrease of oscillation amplitude. Equations (18) and (1) can be used to eliminate $\bar{e}_K$ and, observing that over a cycle the variation of drop radius is expected to be small (i.e. $R_{d,f} \simeq R_{d,i}$), the following condition for oscillation damping is found:

$$F(\beta_{\max}) > \frac{1}{4}(\beta_{\max} - 1). \tag{25}$$

In Fig. 1b this limit is reported and it can be seen that for the "bulk" kinetic energy model, the condition is never satisfied, and under these conditions the evaporation would enhance oscillation, that may also lead to drop break-up. When the "surface" kinetic energy model is used, instead, the condition is always satisfied and evaporation would damp oscillation.

4 Results and Discussion

The coupled effect of oscillation and evaporation of drops made of different liquids immersed in stagnant environment is analysed by applying the model above described. The drop temperature is assumed constant within the liquid. The gaseous mixture properties are calculated at reference temperature conditions, using the "1/3rd rule" [4], and different drop temperatures have been considered, with the aim to cover a wide-range of applicative test cases. As already stated, the drops are considered isothermal, a condition that is often reached, after the initial temperature variation, when a single component drop is evaporating in gaseous environment [1]. This assumption allows pointing out the single effect of drop oscillation on evaporation characteristics. Figure 2 shows the transient profiles of the drop size, non-dimensionalised with its initial value, for a water drop evaporating in stagnant air at 1000 K and at two liquid temperatures equal to 339.5 K and 370 K; three cases are analysed: (a) a non-oscillating spherical drop, (b) an oscillating drop when the "bulk kinetic energy" approach is used; (c) an oscillating drop when the "surface kinetic energy" approach is applied. The two drop temperatures correspond to the so-called 'plateau' temperature in a gaseous environment at 1000 K [8] and to conditions close to the boiling point. The maximum deformation has been imposed, for the oscillating test cases, setting $\beta_{\max} = 1.35$. Figure 2 also reports the transient profile of $\beta_{\max}$ as predicted by the three models (equal to 1 for the non-oscillating case). The results show the typical transient profiles of size reduction according to the well-known "D^2-law", which occurs when the evaporation is assumed isothermal, and this holds also for the oscillating drops. The drop oscillation, on the other

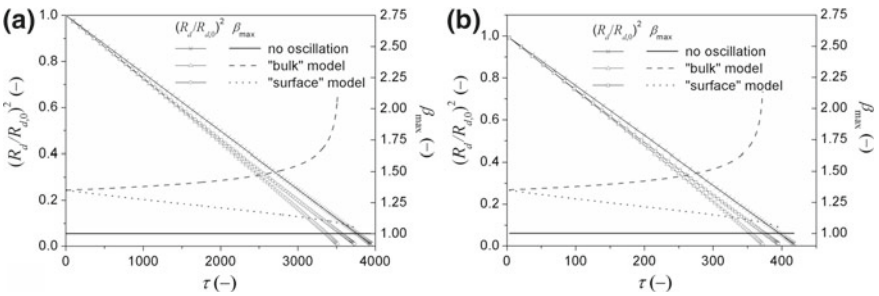

Fig. 2 Effect of drop oscillation on the transient profile of non-dimensional drop size as predicted by three models, for water drop with initial β_{max} equal to 1.35 and liquid temperature equal to (**a**) 339.5 K and (**b**) 370 K, vaporising in stagnant air at 1000 K

hand, noticeably accelerates the evaporation process, having a direct effect on the evaporation rate. The drop lifetime, which has been calculated when the drop volume reduces to 10^{-3} times the initial value, decreases to about 11%, compared to the non-oscillating case, when the loss of kinetic energy is calculated according to the "bulk" kinetic energy approach and to about 5% when the "surface" kinetic energy approach is used. The use of the non-dimensional time defined as $\tau = t D_v / \left(R_{d,0}\right)^2$ shows that the *relative* effect is independent of the liquid drop temperature, which has clearly an effect on the *absolute* drop lifetime.

As expected the "bulk" kinetic energy approach predicts an increase of the maximum surface excess area, i.e. of the oscillation amplitude, which has a steeper increase as the drop size reduces, while the "surface" kinetic energy approach predicts a reduction of the oscillation amplitude (see Sect. 3.1). These findings have been confirmed changing the drop initial size, temperature, surface excess area and varying the liquid species. The results are summarised in Fig. 3, which shows the effect of drop oscillation on the relative reduction of the drop lifetime (compared to the non-oscillating case) as predicted by the two models ("bulk" and "surface" kinetic energy approaches) as function of the initial value of β_{max}, for different fluids (water, n-dodecane, acetone), evaporating in stagnant air at 1000 K and with drop temperature varying from 300 K up to the boiling point of each species. The reduction of the drop lifetime due to oscillation, as predicted by the "bulk" kinetic energy approach, is almost linear as β_{max} increases, and it is practically independent of the liquid species and temperature. The "surface" kinetic energy approach predicts a lower reduction of the drop lifetime, again independently on the drop composition and temperature. The value of the gas temperature, here chosen to be 1000 K, affects the results through the value of the reference temperature at which the thermo-physical properties are calculated, then again it affects the absolute value of the drop lifetime, but not its relative reduction due to oscillation, in the limits of the simplifying assumptions above described. It is worth to notice that the results predicted by the two models may be seen as two extreme cases, and more detailed models, which may account for effects neglected by the present approaches (as viscous dissipation, temperature

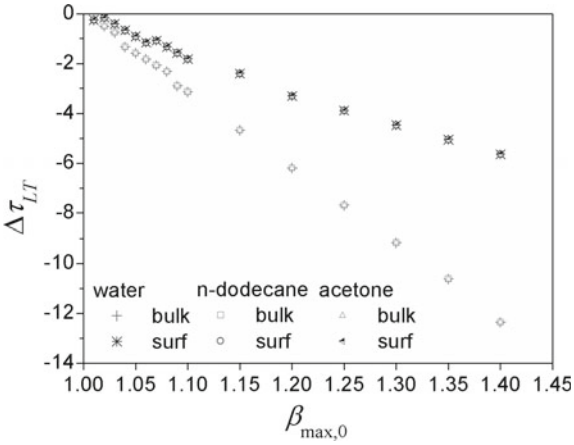

Fig. 3 Effect of drop oscillation on the drop lifetime as predicted by the two kinetic energy models, as function of the maximum drop initial deformation, for different drop species

variation, etc.), may predict a reduction of the drop lifetime that lays between the values above reported.

5 Conclusions

The transient evaporation of isothermal liquid drops in stagnant gas is analytically predicted, accounting for the oscillation between oblate and prolate shape. The loss of kinetic energy due to oscillation is calculated using two different assumptions: (a) perfect mixing, (b) stratified distribution of kinetic energy. The two approaches lead to different evolutions of the drop deformation: the first model predicts an increase of drop oscillation amplitude, while an oscillation damping due to evaporation is predicted by the second model. The effect of drop oscillation results in an almost linear reduction of the drop lifetime as a function of the initial drop deformation (first model), while the reduction is less than linear for the second energy model. These conclusions are found to be almost independent of the drop species and operating conditions, as confirmed by the reported parametrical analysis on water, acetone and n-dodecane drops under different evaporating conditions. The results predicted by the two models may be seen as two extreme cases and more detailed models, accounting for effects neglected by the present approach (non-isothermal conditions, effect of viscosity, etc.) may predict a reduction of the drop lifetime that lays between those above reported.

Appendix

The surface of a spheroid can be calculated as $A = 4\pi R_d^2 \beta$, where [13]

$$\beta = \frac{A}{4\pi R_d^2} = \frac{1}{2\varepsilon^{2/3}} \begin{cases} 1 + \frac{\varepsilon^2}{\sqrt{1-\varepsilon^2}} \frac{1}{2} \log\left(\frac{1+\sqrt{1-\varepsilon^2}}{1-\sqrt{1-\varepsilon^2}}\right) & \text{oblate } (\varepsilon < 1) \\ 1 + \frac{\varepsilon^2}{\sqrt{\varepsilon^2-1}} \arctan\left(\sqrt{\varepsilon^2-1}\right) & \text{prolate } (\varepsilon > 1) \end{cases} . \tag{A1}$$

When evaluating the time-integrals over a cycle, it is convenient to observe first that, given any function of $\beta(t)$, the integral can be broken into the sum of two integrals, over the two half-periods where the drop is in a prolate and oblate shape, respectively. Each of these integrals can in turn be split into the integral from the spherical shape ($\beta = 1$) to the maximum deformation ($\beta = \beta_{\max}$) and back. Changing the variable of integration from t to β, the integrals over time can be transformed into integral over β, from 1 to $\beta_{\max}$, for the two cases (oblate and prolate):

$$\int_0^{t_0} f(\beta) dt = 2 \int_{\substack{1 \\ prolate}}^{\beta_{\max}} \frac{f(\beta)}{|\dot{\beta}|} d\beta + 2 \int_{\substack{1 \\ oblate}}^{\beta_{\max}} \frac{f(\beta)}{|\dot{\beta}|} d\beta \tag{A2}$$

with $\dot{\beta} = \frac{d\beta}{dt}$. If the integral contains explicitly ε, equation (A1) can be used to substitute ε by $\varepsilon(\beta)$ and, if $\dot{\varepsilon}$ appears explicitly, then the variable transformation

$$\dot{\varepsilon} = \frac{d\varepsilon}{dt} = \frac{d\varepsilon}{d\beta}\frac{d\beta}{dt} = \frac{\dot{\beta}}{\beta'} \tag{A3}$$

where $\beta' = \frac{d\beta}{d\varepsilon}$, allows to eliminate it in favour of β and β'. From Eqs. (A1) and (10), the derivatives $\dot{\beta}$ and β' can be written as function of β:

$$\dot{\beta} = \frac{d\beta}{dt} = \omega_2 f(\beta, \beta_{\max}); \quad \begin{matrix} \beta' = \pm \frac{3+\varepsilon^{2/3}\beta(\varepsilon^2-4)}{3\varepsilon^{5/3}(1-\varepsilon^2)} . \\ -\text{oblate}, + \text{prolate} \end{matrix} \tag{A4}$$

To calculate the integral $\bar{\Gamma} = \frac{1}{t_0} \int_0^{t_0} \Gamma(t) dt$, first apply the transformation (A2) and then from Eqs. (A4) and (4) one obtains:

$$\bar{\Gamma} = \frac{1}{\pi} \left[\int_{\substack{1 \\ prolate}}^{\beta_{\max}} \frac{\Gamma(\beta)}{|f(\beta, \beta_{\max})|} d\beta + \int_{\substack{1 \\ oblate}}^{\beta_{\max}} \frac{\Gamma(\beta)}{|f(\beta, \beta_{\max})|} d\beta \right] \tag{A5}$$

where the symbol $\Gamma(\beta)$ is used for $\Gamma[\varepsilon(\beta)]$, showing that $\bar{\Gamma}$ is only a function of $\beta_{\max}$ and it is independent of the oscillation frequency. To calculate the integral $\bar{e}_K = \frac{1}{t_0}\int_0^{t_0} e_K(t)dt$, where $e_K(t)$ is given by Eq. (16), the integrand can be transformed, using Eq. (A3), (A4) and (A1), to a function of β; then, applying again transformation (A2) and using Eq. (4):

$$\bar{e}_K = \frac{R_d^2\omega_2^2}{36\pi}\left[\int_{1\,prolate}^{\beta_{\max}} \frac{I(\beta)}{\beta\varepsilon^{10/3}(\beta)}\frac{f(\beta,\beta_{\max})}{\beta'^2}d\beta + \int_{1\,oblate}^{\beta_{\max}} \frac{I(\beta)}{\beta\varepsilon^{10/3}(\beta)}\frac{f(\beta,\beta_{\max})}{\beta'^2}d\beta\right] \tag{A6}$$

where $I(\varepsilon)$ was transformed in a function of β using again equation (A1). Again the term in square brackets is a function of $\beta_{\max}$ only and

$$\bar{e}_K = R_d^2\omega_2^2 F_s(\beta_{\max}). \tag{A7}$$

References

1. Sazhin, S.S.: Droplets and Sprays. Springer, London (2014)
2. Sazhin, S.S.: Modelling fuel droplet heating and evaporation: recent results and unsolved problems. Fuel **196**, 69–101 (2017)
3. Fuchs, N.A.: Vaporisation and droplet growth in gaseous media. Pergamon Press, London (1959)
4. Abramzon, B., Sirignano, W.A.: Droplet vaporization model for spray combustion calculations. Int. J. Heat Mass Transfer **32**(9), 1605–1618 (1989)
5. Aggarwal, S.K., Mongia, H.C.: Multicomponent and high-pressure effects on droplet vaporization. J. Eng. Gas Turbines Power **24**, 248–255 (2002)
6. Tonini, S., Cossali, G.E.: A novel vaporisation model for a single-component drop in high temperature air streams. Int. J. Therm. Sci. **75**, 194–203 (2014)
7. Sobac, B., Talbot, P., Haut, B., Rednikov, A., Colinet, P.: A comprehensive analysis of the evaporation of a liquid spherical drop. J. Colloid Interface Sci. **438**, 306–317 (2015)
8. Cossali, G.E., Tonini, S.: An analytical model of heat and mass transfer from liquid drops with temperature dependence of gas thermo-physical properties. Int. J. Heat Mass Transfer **138**, 1166–1177 (2019)
9. Tong, A.Y., Sirignano, W.A.: Multicomponent transient droplet vaporization with internal circulation: integral equation formulation. Numerical Heat Transfer **10**, 253–278 (1986)
10. Zeng, Y., Lee, Y.C.F.: Multicomponent-fuel film-vaporization model for multidimensional computations. J. Propulsion Power **16**, 964–973 (2000)
11. Al Qubeissi, M., Sazhin, S.S., Crua, C., Turner, J., Heikal, M.R.: Modelling of biodiesel fuel droplet heating and evaporation: effects of fuel composition. Fuel **154**, 308–318 (2015)
12. Li, J., Zhang, J.: A theoretical study of the spheroidal droplet evaporation in forced convection. Phys. Lett. A **378**(47), 3537–3543 (2014)
13. Tonini, S., Cossali, G.E.: One-dimensional analytical approach to modelling evaporation and heating of deformed drops. Int. J. Heat Mass Transfer **97**, 301–307 (2016)

14. Zubkov, V.S., Cossali, G.E., Tonini, S., Rybdylova, O., Crua, C., Heikal, M., Sazhin, S.S.: Mathematical modelling of heating and evaporation of a spheroidal droplet. Int. J. Heat Mass Transfer **108**, 2181–2190 (2017)
15. Sirignano, W.A.: Fluid Dynamics and Transport of Droplets and Sprays. 2nd edn, Cambridge University Press (2010)
16. Gusev, I.G., Krutitskii, P.A., Sazhin, S.S., Elwardany, A.E.: New solutions to the species diffusion equation inside droplets in the presence of the moving boundary. Int. J. Heat Mass Transfer **55**(7), 2014–2021 (2012)
17. Sazhin, S.S., Krutitskii, P.A., Gusev, I.G., Heikal, M.R.: Transient heating of an evaporating droplet. Int. J. Heat Mass Transfer **53**(13), 2826–2836 (2010)
18. Sazhin, S.S., Krutitskii, P.A., Gusev, I.G., Heikal, M.R.: Transient heating of an evaporating droplet with presumed time evolution of its radius. Int. J. Heat Mass Transfer **54**(5), 1278–1288 (2011)
19. Tonini, S., Cossali, G.E.: Modelling liquid drop heating and evaporation: the effect of drop shrinking. Comp. Therm. Sci **10**(3), 273–283 (2018)
20. Rayleigh, L.: On the capillary phenomena of jets. Proc. R. Soc. Lond. A **29**, 71–97 (1879)
21. Lamb, H.: On the oscillations of a viscous spheroid. Proc. Lond. Math. Soc. **13**, 51–66 (1881)
22. Lamb, H.: Hydrodynamics, 6th edn. Cambridge University Press, United Kingdom (1932)
23. Chandrasekhar, S.: The oscillations of a viscous liquid globe. Proc. London Math. Soc. **9**, 141–149 (1959)
24. Miller, C., Scriven, L.: The oscillations of a fluid droplet immersed in another fluid. J. Fluid Mech. **32**, 417–435 (1968)
25. Prosperetti, A.: Free oscillations of drops and bubbles: the initial-value problem. J. Fluid Mech. **100**(2), 333–347 (1980)
26. Tsamopoulos, J.A., Brown, R.A.: Nonlinear oscillations of inviscid drops and bubbles. J. Fluid Mech. **127**, 519–537 (1983)
27. Trinh, E.H., Zwern, A., Wang, T.G.: An experimental study of small-amplitude drop oscillations in immiscible liquid systems. J. Fluid Mech. **115**, 453–474 (1982)
28. Trinh, E.H., Wang, T.G.: Large-amplitude free and driven drop-shape oscillations: experimental observations. J. Fluid Mech. **122**, 315–338 (1982)
29. Becker, E., Hiller, W., Kowalewski, T.: Experimental and theoretical investigation of large-amplitude oscillations of liquid droplets. J. Fluid Mech. **231**, 189–210 (1981)
30. Becker, E., Hiller, W., Kowalewski, T.: Nonlinear dynamics of viscous droplets. J. Fluid Mech. **258**, 191–216 (1994)
31. Brenn, G., Teichtmeister, S.J.: Linear shape oscillations and polymeric time scales of viscoelastic drops. J. Fluid Mech. **733**, 504–527 (2013)
32. Trinh, E.H., Thiessen, D.B., Holt, R.G.: Driven and freely decaying nonlinear shape oscillations of drops and bubbles immersed in a liquid: experimental results. J. Fluid Mech. **364**, 253–272 (1998)
33. Wang, T.G., Anilkumar, A.V., Lee, C.P.: Oscillations of liquid drops: results from USML-1 experiments in Space. J. Fluid Mech. **308**, 1–14 (1996)
34. Azuma, H., Yoshihara, S.: Three-dimensional large-amplitude drop oscillations: experiments and theoretical analysis. J. Fluid Mech. **393**, 309–332 (1999)
35. Al Zaitone, B.: Oblate spheroidal drop evaporation in an acoustic levitator. Int. J. Heat Mass Transfer **126**, 164–172 (2018)
36. Mashayek, F.: Dynamics of evaporating drops, Part I: formulation and evaporation model. Int. J. Heat Mass Transf. **44**(8), 1517–1526 (2001)
37. Mashayek, F.: Dynamics of evaporating drops, Part II: free oscillations. Int. J. Heat Mass Transf. **44**(8), 1527–1541 (2001)
38. Tonini, S., Cossali, G.E.: An evaporation model for oscillating spheroidal drops. Int. Comm. Heat Mass Transf. **51**, 18–24 (2014)

Improvement of the Level-Set Ghost-Fluid Method for the Compressible Euler Equations

Christoph Müller, Timon Hitz, Steven Jöns, Jonas Zeifang, Simone Chiocchetti and Claus-Dieter Munz

Abstract This paper describes improvements of a level-set ghost-fluid algorithm in the scope of sharp interface multi-phase flow simulations. The method is used to simulate drop-drop and shock-drop interactions. Both, the level-set and the bulk phases are discretized by a high order discontinuous Galerkin spectral element method. The multi-phase interface and shocks are captured with a finite volume sub-cell method. The first improvement, is the use of the finite-volume sub-cells to capture discontinuities in the level-set equation. This allows the simulation of merging droplets. The second improvement is the introduction of an increased polynomial degree for the level-set equation in comparison to the Euler equations. The goal of this modification is to reduce parasitic currents. Additionally, the whole method is validated against experimental results.

1 Introduction

The simulation of compressible multi-phase flow is a key challenge in scientific and industrial applications. There are two major concepts: sharp and diffuse interface methods. Among the former category both volume-of-fluid and level-set ghost-fluid method are popular. The latter was first introduced by Fedkiw et al. [6]. Several improvements were proposed over the years, e.g. Liu et al. [12, 13] and Wang et al. [22]. A variant, where a multi-phase Riemann problem is solved to obtain the ghost states at the interface was proposed by Merkle and Rohde [14]. Fechter et al. [3–5] extended the idea by using approximate multi-phase Riemann solvers and applied them within a high order level-set ghost-fluid framework. Thereby, both the level-set

C. Müller (✉) · T. Hitz · S. Jöns · J. Zeifang · C.-D. Munz
Institute of Aerodynamics and Gasdynamics, Pfaffenwaldring 21, 70569 Stuttgart, Germany
e-mail: christoph.mueller@iag.uni-stuttgart.de

S. Chiocchetti
Department of Civil Environmental and Mechanical Engineering, Laboratory of Applied Mathematics, Via Mesiano 77, 38123 Trento, Italy

G. Lamanna et al. (eds.), *Droplet Interactions and Spray Processes*,
Fluid Mechanics and Its Applications 121,
https://doi.org/10.1007/978-3-030-33338-6_2

and the bulk phases are discretized by a high order Discontinuous Galerkin Spectral Element Method (DGSEM) [8]. The multi-phase interface and shocks are captured with a finite volume sub-cell method [20].

Here, we introduce two improvements to the scheme of Fechter [3] First, finite-volume sub-cells are used to capture discontinuities in the level-set equation as well. This is required if two droplets approach each other and merge. Secondly, we introduce the possibility of an increased polynomial degree for the level-set equation, which allows a more accurate calculation of the level-set curvature.

In this work we restrict ourselves to the in-viscid case, so the Euler equations govern the bulk phases. An extension of the described sharp interface method to the viscid case is beyond the scope of this paper.

The paper is structured as follows: After introducing the governing equations in Sect. 2 we summarize the numerical framework and outline the two improvements in Sect. 3. Afterwards, in Sect. 4, we show the capability of the new scheme to handle merging droplets, investigate the benefits of a more accurate curvature calculation with respect to parasitic currents and conclude by presenting a comparison with experimental results for a complex shock-drop interaction.

2 Governing Equations

Both the liquid and the gaseous phase are modeled by the Euler equations

$$\frac{\partial \mathbf{q}}{\partial t} + \nabla \cdot \mathbf{F}(\mathbf{q}) = 0, \quad \text{with} \quad \mathbf{q} = \begin{pmatrix} \rho \\ \rho \mathbf{u} \\ \rho e \end{pmatrix} \quad \text{and} \quad \mathbf{F}(\mathbf{q}) = \begin{pmatrix} \rho \mathbf{u} \\ \rho \mathbf{u}\mathbf{u} + \underline{\mathbf{I}} p \\ (\rho e + p)\mathbf{u} \end{pmatrix}. \tag{1}$$

The density ρ, the momentum $\mathbf{m} = \rho \mathbf{u}$ with the velocity vector $\mathbf{u} = (u, v, w)^T$ and the total energy per unit volume $E = \rho e$ are conserved quantities and the equations above are conservation laws for mass, momentum and energy. The static pressure p and the unit tensor $\underline{\mathbf{I}}$ are the remaining quantities. The total energy of the system is the sum of the internal energy per unit volume $\rho\epsilon$ and the kinetic energy $\frac{1}{2}\rho \mathbf{u} \cdot \mathbf{u}$

$$E = \rho e = \rho \epsilon + \frac{1}{2} \rho \mathbf{u} \cdot \mathbf{u}. \tag{2}$$

In order to close the equation system we have to specify an equation of state (EOS) to link the pressure and the internal energy per unit mass ϵ:

$$p = p(\rho, \epsilon), \quad \epsilon = \epsilon(\rho, p). \tag{3}$$

Here, we use the algebraic stiffened gas EOS, see Saurel et al. [17], to approximate the equation of state for each phase. For more complex EOS the tabulation technique by Föll et al. [7] can be used.

In addition to the bulk phases we solve a level-set equation in conservative form

$$\frac{\partial \phi}{\partial t} + \nabla (\boldsymbol{s}\phi) = \phi \nabla \cdot \boldsymbol{s} \tag{4}$$

with the level-set velocity field $\boldsymbol{s}$. Equation (4) describes the transport of a signed distance function. Since this property is lost if the velocity field is non trivial the level-set equation has to be reinitialized by solving a Hamilton-Jacobi equation [21]

$$\frac{\partial \phi}{\partial \tau} + \mathrm{sgn}(\phi)\,(|\nabla \phi| - 1) = 0. \tag{5}$$

The re-establishment of the signed-distance property allows the calculation of the normal vector $\mathbf{n}_{LS}$ and the curvature κ as

$$\mathbf{n}_{LS} = \frac{\nabla \phi}{|\nabla \phi|}, \quad \kappa = -\frac{1}{2} \nabla \cdot (\mathbf{n}_{LS}), \tag{6}$$

by derivating the level-set field. Here, the level-set zero determines the position of the phase boundary between the liquid and the gaseous phase. The dynamics of the phases at this interface determine the velocity of the phase-boundary which is extrapolated into the volume by solving the Hamilton-Jacobi equations

$$\frac{\partial s^i}{\partial \tau} + \nabla s^i \cdot \mathbf{n}_{LS} = 0 \quad i = 1, 2, 3, \tag{7}$$

according to [1]. Hereby $\boldsymbol{s}$ denotes the extrapolated velocity field used for the level-set advection.

3 Numerics

In this section the building blocks of the level-set ghost-fluid framework are summarized.

3.1 The DGSEM Framework with Finite Volume Sub-cells

The DGSEM [8] with the shock-capturing based on finite-volume sub-cells [20] is used to discretize both the Euler equations in the bulk phases as well as the level-set equation. A novel aspect of our development is the use of the shock-capturing with the finite volume sub-cells also for the level-set equation. We come back to this point later.

The DGSE method is formulated on a hexahedral mesh. Each element is mapped to the unit cube, where the transformed equations are solved in the weak form. For this, the equations are multiplied by a test function and integrated in space. Both, the solution and the test functions are chosen from the same polynomial space, which is spanned by the tensor product of one-dimensional Lagrange polynomials. The integration is approximated by a quadrature rule. If the interpolation and integration points are the same one obtains the DGSE method. For the time integration low storage Runge-Kutta schemes [11] are used. Between the elements Riemann problems are solved to calculate numerical fluxes. The DGSEM scheme is efficient and accurate if the solution is smooth. However, high order schemes generate spurious oscillations at strong gradients. Therefore, we apply a sub-cell finite volume regularization following Sonntag and Munz [20]. Critical areas are identified by applying a modal smoothness indicator following Huerta et al. [9] and Persson et al. [15]. Another option is the use of geometrical information, for example the level-set function. In potentially unstable Discontinuous Galerkin (DG) cells we perform a conservative switch to a finite volume sub-cell representation, where each degree of freedom is represented by one finite volume sub-cell. On the sub-cells a first or second order finite-volume scheme is used. The coupling between DG and FV cells happens on element surfaces. The method of choice is to calculate the numerical fluxes in the finite volume representation and to project them onto the DG representation for the DG element.

The second new feature we present is the use of different polynomial degrees for the bulk phases and the level-set. The increased resolution of the latter allows a more accurate calculation of the level-set normals and curvature, which reduces errors known as parasitic currents. The main benefit is that the higher resolution is only added for the level-set, which helps to control the additional computational effort.

3.2 The Solution of the Hamilton-Jacobi Equations and the Derivatives of the Level-Set Field

The reinitialization as well as the velocity extrapolation require the solution of a Hamilton-Jacobi (HJ) equation. We use a 5th order WENO scheme [10] and combine it with a 3rd order low storage Runge-Kutta method with three stages [11]. This allows the efficient and stable solution of both equations. Following Fechter [3], another 5th order WENO scheme is used to calculate $\nabla\phi$ and $\nabla \cdot (\nabla\phi)$ and hence the normal vector of the level-set $\mathbf{n}_{LS}$ and its curvature κ.

3.3 The Level-Set Ghost-Fluid Method (LSGFM)

In this section we combine the previously described numerical methods and the level-set ghost-fluid framework. First, an overview over the interaction of the solvers

in one time-step is provided. Afterwards, a detailed account of the functionality of the ghost-fluid method is given including the decomposition of the domain and the determination of the phase boundary conditions. The six main steps of the level-set ghost-fluid algorithm are performed at the end of every time-step:

1. The level-set is reinitialized.
2. The domain decomposition into liquid and gaseous phase is updated based on the zero of the level-set function.
3. The DG-FV distribution is updated based on the modal smoothness indicator and geometrical information about the level-set zero.
4. The normal vector of the level-set and its curvature are calculated.
5. The boundary conditions at the surrogate phase boundary and its velocity are calculated.
6. The interface velocity is extrapolated into the volume to obtain a velocity field for the level-set transport.

Within the next time step the solution in the bulk phase and the advection of the level-set field can be calculated. The scheme is only first order in time. A higher order in time could be reached if all steps are performed after each Runge-Kutta stage. However, for the domain decomposition this is not possible. Within a Runge-Kutta time step the phase of each sub-cell has to remain constant to calculate a thermodynamically reasonable result.

All other steps could be performed in every stage, but we choose to update only the phase boundary conditions, since reinitialization and velocity extrapolation have a high computational effort. Next we explain both, the domain decomposition and the calculation of the phase boundary conditions at the surrogate surface. In Fig. 1 the domain decomposition into the two phases is demonstrated. The level-set zero marks the position of the actual phase boundary. The color jump indicates a surrogate phase interface. It is implicitly defined by determining the phase of each computational cell or sub-cell. The used metric is the sign of the level-set function at the cell's barycenter. As shown in the figure, we choose to swap all DG cells that touch the level-set zero to a finite volume representation. This allows a more detailed surrogate surface since

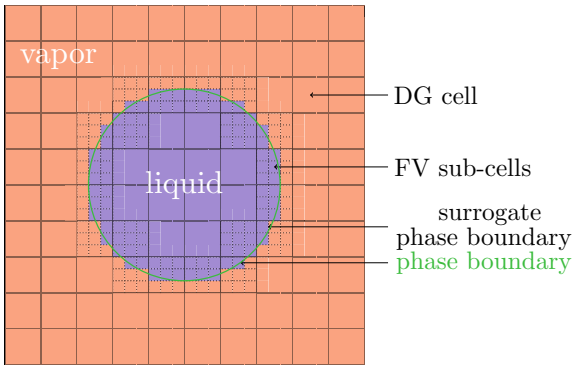

Fig. 1 Spatial decomposition with zero-level of the level-set function and the surrogate phase interface in the DG-FV method

the sub-cell approach mimics a grid refinement for this step. If the surrogate surface moved compared to the last time step, at least one finite volume sub-cell swapped its phase. Its state is determined by interpolating the states between the neighboring sub-cells of the same phase. This step violates the conservation laws. This is not avoidable and is inherent to ghost-fluid methods. The conservation is also violated by the final step, the calculation of the interface boundary conditions. The original ghost fluid method was described by Fedkiw et al. [6]. Several improvements were proposed over the years, e.g. Liu et al. [12, 13] and Wang et al. [22]. Here we use a variant, where a multi-phase Riemann problem is solved to obtain the ghost states at the interface (Merkle and Rohde [14]) and directly evaluate fluxes following the idea of e.g. Fechter et al. [4]. For the Euler equations there are two different options. We either solve the exact multi-phase Riemann problem iteratively in a fixed point formulation or we use an approximate solver, e.g. the HLLP Riemann solver [4, 18]. In both cases, complex equations of state can be used that distinguish between the two phases, and surface tension effects can be modeled by modifying the jump conditions across the contact discontinuity. The HLLP solver is an extension of the HLLC Riemann solver to the two-phase case. Its wave pattern is shown in Fig. 2. In the following we explain in more detail how the Riemann solver is incorporated into the framework. The multi-phase Riemann problem has to be solved normal to the level-set zero iso-surface to apply the surface tension effect correctly. In multi-dimensional problems the normal vector of the level-set and the curvature are interpolated linearly to the sub-cell sides. This happens on the finite volume sub-cell grid associated with polynomial degree N. Since the quantities are calculated on a grid associated with N_{LS}, the solution has to be projected first. The corresponding orthonormal coordinate system is obtained by applying a Gram-Schmidt orthonormalization to the interpolated normal vector. The initial data $\mathbf{U}_L$ and $\mathbf{U}_R$ are rotated and the Riemann problem is solved normal to the level-set zero iso-surface. We calculate the integral fluxes, one for each phase, and then rotate them back. The use of the integral fluxes is necessary within the HLLP framework since the intermediate states are not thermodynamically consistent. As mentioned before, the calculated boundary conditions do not satisfy the conservation laws in general. This is an inherent feature of ghost-fluid methods and is necessary to avoid oscillations. This problem arises since the mesh is aligned with the surrogate

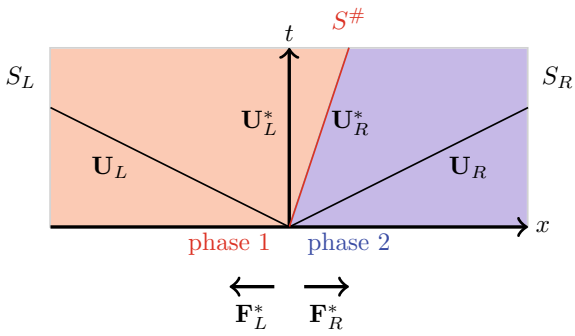

Fig. 2 Two-phase finite-volume sub-cell boundary with the structure of the HLLP two-phase Riemann solver

interface and not the exact level-set zero iso-surface. Additionally, we want to remark that the method is first order accurate in space directly at the surrogate surface, since the phase interface is a strong discontinuity that cannot be captured by higher order methods without oscillations.

4 Results

Three different problems are investigated. First, the parasitic currents around a stationary droplet are investigated to show the benefit of an increased resolution for the level-set field. Second, two droplets are merged to showcase this possibility due to finite volume sub-cells in the level-set operator. Finally, a comparison between experimental and simulation results is presented for a shock-droplet interaction at $\mathrm{Ma} = 2.4$.

4.1 Parasitic Currents Around a Stationary Droplet

Parasitic currents occur if the surface tension force is not modeled or calculated correctly. Detailed investigations have been made for incompressible flow, see e.g. [16]. A very common testcase is the investigation of parasitic currents around a stationary droplet. We follow the setup described in Albadawi et al. [2] and modify it for the compressible case. The setup is shown in Fig. 3a. The domain size is $[0.0, 0.05] \times [0.0, 0.05]$ and it is discretized by 55×55 DG cells. The polynomial degrees for the bulk phases and the level-set are $N = 1, 2, 3$ and $N_{LS} = 2, \ldots, 5$, respectively. The center of the drop is located at $[x, y] = [0.025, 0.025]$ with a radius of 0.005. Both phases are modeled with the stiffened gas law. The surface tension coefficient is $\sigma = 0.01$. The initial conditions and EOS parameters for the droplet and the surrounding atmosphere are

$$(\rho, u, v, p, \gamma, p_\infty)^T = \begin{cases} (1000, 0, 0, 3, 1.4, 0)^T & \text{droplet,} \\ (1, 0, 0, 1, 1.4, 0)^T & \text{gas.} \end{cases}$$

This is a numerical testcase, so dimensionless quantities are used. In particular the pressure level is only chosen this way to observe the parasitic currents properly. The simulation is run until $t = 0.1$. In contrast to the work of Albadawi et al. [2], we neglect viscous effects. The pressure level has a huge effect on the parasitic currents in the compressible case. Therefore, a direct comparison with incompressible results is meaningless. As a result we determine only trends in the following investigation. As a measure for the intensity of the parasitic currents we use the kinetic energy in the whole domain. The target value for a perfect scheme would be zero. In principle, we should approach this value to machine accuracy. However, in Table 1 we can

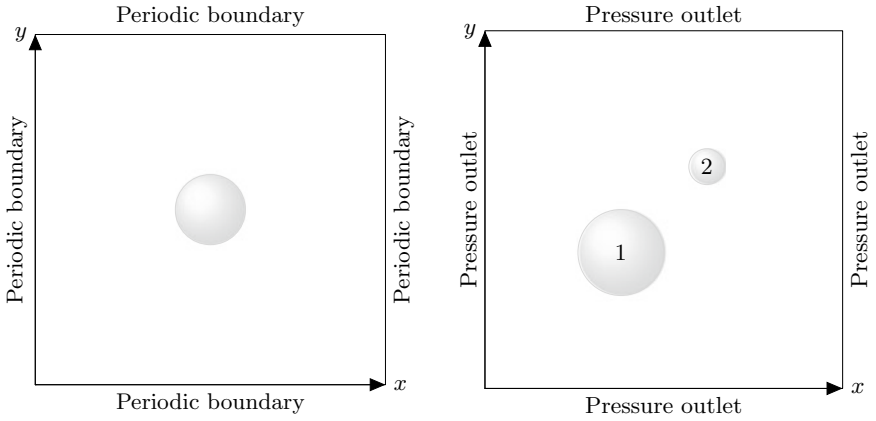

(a) parasitic currents (b) merging droplets

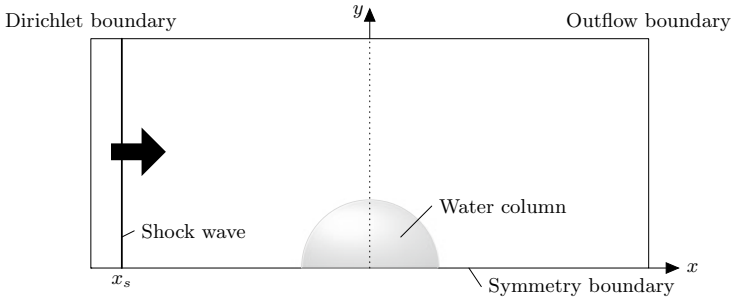

(c) shock-drop interaction

Fig. 3 Setups for the testcases

Table 1 Parasitic currents measure by the kinetic energy for different resolutions

	$N_{LS} = 2$	$N_{LS} = 3$	$N_{LS} = 4$	$N_{LS} = 5$
$N = 1$	0.128×10^{-11}	0.518×10^{-12}	0.445×10^{-12}	0.391×10^{-12}
$N = 2$	0.631×10^{-12}	0.275×10^{-12}	0.247×10^{-12}	0.243×10^{-12}
$N = 3$	–	0.109×10^{-12}	0.610×10^{-13}	0.571×10^{-13}

observe a different behavior. A higher polynomial degree for the level-set field leads to a reduction in the parasitic currents, though the decrease is quite slow. In addition, the effect of a higher polynomial degree for the fluid solution is more significant. The probable cause of this behavior is the interpolation of the curvature and level-set normal vector to the surrogate surface. This procedure is a one-dimensional linear interpolation on the finite-volume grid associated with polynomial degree N. Although we increase the accuracy of the calculation by increasing N_{LS}, we loose accuracy by the projection to the lower polynomial degree and the low order interpolation.

4.2 Merging Droplets Without Surface Tension

The merging of droplets is a major challenge in compressible level-set ghost-fluid methods. There are two major problems: First, the method must be able to capture the merging process. Second, the curvature has to be calculated correctly during the merge. Here, we target only the first problem and neglect the second since no surface tension is considered. The setup is shown in Fig. 3b. The domain size is $[0.0, 0.05] \times [0.0, 0.05]$ and it is discretized by 55×55 DG cells. The polynomial degrees for the bulk phases and the level-set are $N = 4$ and $N_{LS} = 4$, respectively. Drop 1 is located at $[x, y] = [0.019, 0.019]$ with a radius of 0.006 and drop 2 is located at $[x, y] = [0.031, 0.031]$ with a radius of 0.0025. Both phases are modeled with the stiffened gas EOS. The initial conditions and EOS parameters for the droplet and the surrounding atmosphere are

$$(\rho, u, v, p, \gamma, p_\infty)^T = \begin{cases} (1000, 0.2, 0.2, 10, 1.4, 1000)^T & \text{droplet 1,} \\ (1000, -0.5, -0.5, 10, 1.4, 1000)^T & \text{droplet 2,} \\ (4, 0, 0, 10, 1.4, 0)^T & \text{gas.} \end{cases}$$

Since this is only a numerical testcase, dimensionless quantities are used. The simulation is run until $t = 0.05$. In Fig. 4 the time frames $t = 0.01, 0.012, 0.014$ are shown. In the first row, results are shown for a DG-FV representation of the level-set field, whereas in the second row a DG representation for the level-set is used. In contrast to the second case, the droplets merge for the first case. As a result the velocities are much higher in the second row and the droplet surfaces oscillate if they are close to each other. In addition, the simulation does not run until the end but crashes. This testcase demonstrates very clearly that finite volume sub-cells for the level-set field allow the merging of droplets.

4.3 Shock-Droplet Interaction at Ma = 2.40

Finally, we compare the experimental data of Sembian et al. [19] with our simulation. The setup is shown in Fig. 3c. The domain size is $[-0.045\,\text{m}, 0.045\,\text{m}] \times [0.0\,\text{m}, 0.037\,\text{m}]$ and it is discretized by 150×61 DG cells. The polynomial degrees for the bulk phases and the level-set are $N = 5$ and $N_{LS} = 6$, respectively. The shock is located at $x_s = -0.040\,\text{m}$ and is defined by the conditions

$$(\rho_g, u, v, p)^T = \begin{cases} (580.7\,\frac{\text{kg}}{\text{m}^3}, 0\,\frac{\text{m}}{\text{s}}, 0\,\frac{\text{m}}{\text{s}}, 500\,\text{bar})^T & x \leq -0.04\,\text{m}, \\ (1.17\,\frac{\text{kg}}{\text{m}^3}, 0\,\frac{\text{m}}{\text{s}}, 0\,\frac{\text{m}}{\text{s}}, 1.01\,\text{bar})^T & x > -0.04\,\text{m}. \end{cases}$$

This results in a shock strength of $\text{Ma} = 2.4$ The center of the drop is located at $[x, y] = [0.0\,\text{m}, 0.0\,\text{m}]$ with a radius of $0.011\,\text{m}$ and its initial condition is

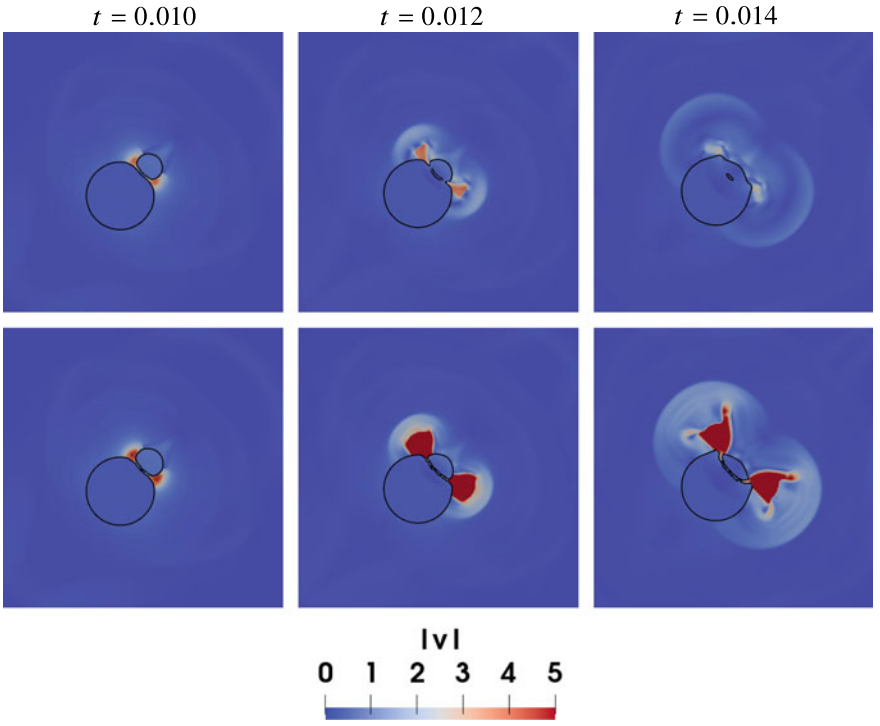

Fig. 4 |**v**| and droplet surface (black) for merging droplets in 2D without surface tension, top row: DG-FV representation for level-set, bottom row: DG representation for level-set

$(\rho_g, u, p)^T = (1000\,\frac{\text{kg}}{\text{m}^3}, 0\,\frac{\text{m}}{\text{s}}, 1.01\,\text{bar})^T$. The gas phase is modeled with a perfect gas law and the liquid phase with the stiffened gas EOS, which is identical to Tait's equation of state. The parameters are chosen identical to Sembian et al. [19]. The setup is shown in Fig. 3c. Note that surface tension effects are neglected due to the high Weber number of $\text{We} = 3.7966 \times 10^5$. A comparison between our highly resolved simulation and the experimental data of Sembian et al. [19] is shown in Fig. 5. The simulation data is post processed to generate the numerical Schlieren image. The time is taken from the simulation. The images are chosen to find a good match to the data of Sembian et al. [19] This is necessary since there is no information about the time in the experimental images.

In the early time instances we see an almost perfect agreement between simulation and experiment. For example at $t = 4.8 \times 10^{-5}$ s there is an agreement regarding the reflected and transmitted shock, as well as the Mach stem and the triple point. Both the wave structure and the locations of those phenomena are almost identical. At $t = 6.4 \times 10^{-5}$ s differences occur: the shock speed of the reflected shock is higher in the experiment and micromist occurs around the droplet. This in turn leads to a different attachment point for the shock wave after the drop. However, at $t = 9.4 \times 10^{-5}$ s we

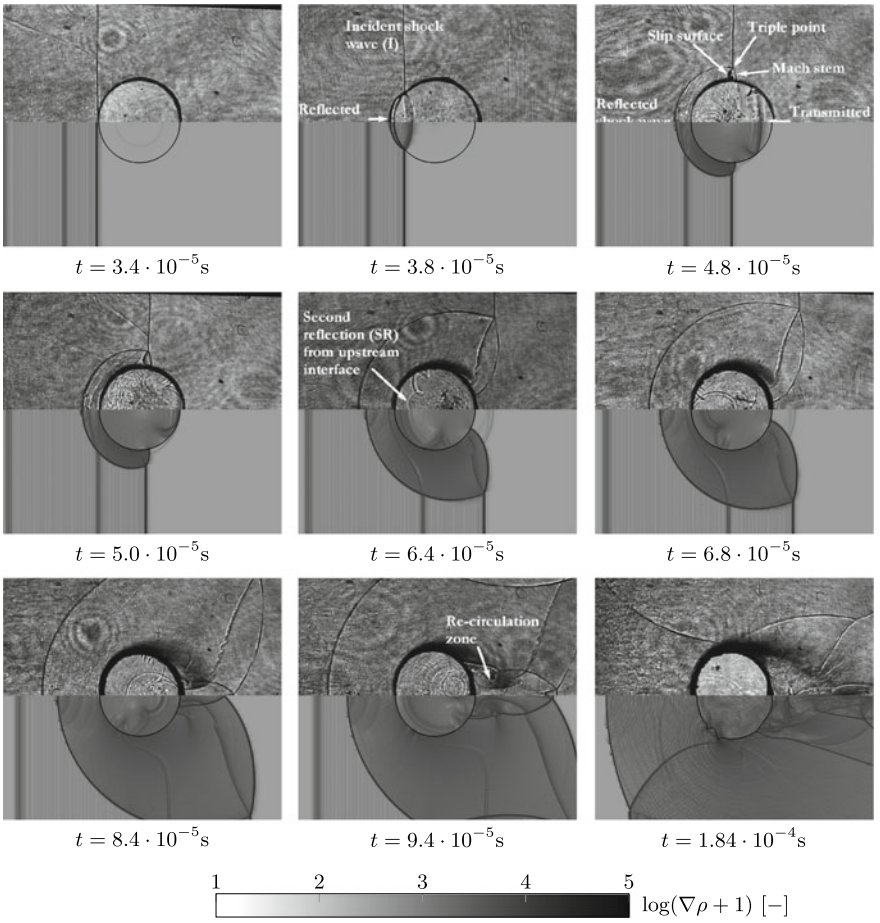

Fig. 5 Comparison of numerical Schlieren images (bottom) with experimental results (top) reproduced from Sembian et al. [19] (with permission of AIP Publishing)

see almost identical re-circulation zones. Finally, at $t = 1.84 \times 10^{-4}$ s the droplet shape starts to deform in the simulation, which is not observed in the experiment.

Overall the main physical features of the shock-droplet interaction are captured well by our numerical method. This supports the validity of the presented framework for simulations in the considered regime. The differences can be attributed to three main reasons: First, as we mentioned above Sembian et al. [19] did not provide the physical time to their image series, so the matching between experiment and simulation is not precise. Additionally, we run a 2D simulation. This means, the stripping of the water from the column wall is not possible in the simulation and so micromist cannot occur. The lack of this mist leads to different shock systems after the droplet due to different attachment points and might also explain the minor

differences in the re-circulation zone. Finally, the fluid behavior is approximated by a stiffened gas EOS. It is well known that this might lead to different sound speeds and hence is a possible explanation for the different shock speeds of the reflected shock. The interface deformation is not visible in the experiment since the area is clouded by micromist. If it is in fact not deformed, the lack of micromist in the simulation and the different EOS behavior might explain the differences.

5 Conclusion and Outlook

In this paper we provided an overview over a high order level-set ghost-fluid method based on the work of Fechter et al. [3–5]. Two improvements were introduced: finite volume sub-cells for the level-set field and different polynomial degrees for the solution of the level-set field and the Euler equations. Afterwards, we demonstrated that a higher polynomial degree of the level-set field leads to lower parasitic currents, although the effect is smaller than expected. This we attribute to the low order interpolation of the level-set normal and the curvature to the surrogate surface. An investigation into alternative interpolation methods is currently under way.

Afterwards, we showed that finite volume sub-cells are a possible solution of the discretization if merging droplets shall be simulated. A pure DG representation of the level-set field leads to a wrong behavior if two interfaces approach each other and ultimately to a crash of the simulation. The calculation of the curvature in this case remains unsolved for now but is a topic of future research. The main goal being droplet collisions with surface tension as well as drop wall interactions.

Ultimately, we demonstrated that our scheme is well designed to solve shock-drop interactions by showing a good agreement of our simulations with experimental results.

Acknowledgements C. Müller, J. Zeifang and S. Chiocchetti were supported by the German Research Foundation (DFG) though the project GRK 2160/1 “Droplet Interaction Technologies”. T. Hitz and S. Jöns were supported by the DFG through the project SFB-TRR 75 "Droplet Dynamics Under Extreme Ambient Conditions". The simulations were performed on the national supercomputer Cray XC40 (Hazel Hen) at the High Performance Computing Center Stuttgart (HLRS) under the grant number *hpcmphas/44084*.

References

1. Adalsteinsson, D., Sethian, J.: The fast construction of extension velocities in level set methods. J. Comput. Phys. **148**(1), 2–22 (1999). https://doi.org/10.1006/jcph.1998.6090
2. Albadawi, A., Donoghue, D., Robinson, A., Murray, D., Delauré, Y.: Influence of surface tension implementation in volume of fluid and coupled volume of fluid with level set methods for bubble growth and detachment. Int. J. Multiph. Flow **53**, 11–28 (2013). https://doi.org/10.1016/j.ijmultiphaseflow.2013.01.005

3. Fechter, S.: Compressible multi-phase simulation at extreme conditions using a discontinuous Galerkin scheme (2015). https://doi.org/10.18419/opus-3982
4. Fechter, S., Jaegle, F., Schleper, V.: Exact and approximate riemann solvers at phase boundaries. Comput. Fluids **75**, 112–126 (2013). https://doi.org/10.1016/j.compfluid.2013.01.024
5. Fechter, S., Munz, C.D.: A discontinuous galerkin-based sharp-interface method to simulate three-dimensional compressible two-phase flow. Int. J. Numer. Methods Fluids **78**(7), 413–435 (2015). https://doi.org/10.1002/fld.4022
6. Fedkiw, R.P., Aslam, T., Merriman, B., Osher, S.: A non-oscillatory eulerian approach to interfaces in multimaterial flows (the ghost fluid method). J. Comput. Phys. **152**(2), 457–492 (1999). https://doi.org/10.1006/jcph.1999.6236
7. Föll, F., Hitz, T., Müller, C., Munz, C.D., Dumbser, M.: On the use of tabulated equations of state for multi-phase simulations in the homogeneous equilibrium limit. Shock Waves (2019). https://doi.org/10.1007/s00193-019-00896-1
8. Hindenlang, F., Gassner, G.J., Altmann, C., Beck, A., Staudenmaier, M., Munz, C.D.: Explicit discontinuous Galerkin methods for unsteady problems. Comput. Fluids **61**, 86–93 (2012). https://doi.org/10.1016/j.compfluid.2012.03.006
9. Huerta, A., Casoni, E., Peraire, J.: A simple shock-capturing technique for high-order discontinuous Galerkin methods. Int. J. Numer. Methods Fluids **69**(10), 1614–1632 (2011). https://doi.org/10.1002/fld.2654
10. Jiang, G.S., Peng, D.: Weighted ENO schemes for Hamilton-Jacobi equations. SIAM J. Sci. Comput. **21**(6), 2126–2143 (2000). https://doi.org/10.1137/s106482759732455x
11. Kopriva, D.A.: Spectral element methods. In: Scientific Computation, pp. 293–354. Springer, The Netherlands (2009). https://doi.org/10.1007/978-90-481-2261-5_8
12. Liu, T., Khoo, B., Wang, C.: The ghost fluid method for compressible gas–water simulation. J. Comput. Phys. **204**(1), 193–221 (2005). https://doi.org/10.1016/j.jcp.2004.10.012
13. Liu, T., Khoo, B., Xie, W.: The modified ghost fluid method as applied to extreme fluid-structure interaction in the presence of cavitation. Commun. Comput. Phys. **1**(5), 898–919 (2006)
14. Merkle, C., Rohde, C.: The sharp-interface approach for fluids with phase change: Riemann problems and ghost fluid techniques. ESAIM: Mathe. Model. Numer. Anal. **41**(6), 1089–1123 (2007). https://doi.org/10.1051/m2an:2007048
15. Persson, P.O., Peraire, J.: Sub-cell shock capturing for discontinuous Galerkin methods. In: 44th AIAA Aerospace Sciences Meeting and Exhibit. American Institute of Aeronautics and Astronautics (2006). https://doi.org/10.2514/6.2006-112
16. Popinet, S.: An accurate adaptive solver for surface-tension-driven interfacial flows. J. Comput. Phys. **228**(16), 5838–5866 (2009). https://doi.org/10.1016/j.jcp.2009.04.042
17. Saurel, R., Petitpas, F., Abgrall, R.: Modelling phase transition in metastable liquids: application to cavitating and flashing flows. J. Fluid Mech. **607**, (2008). https://doi.org/10.1017/s0022112008002061
18. Schleper, V.: A HLL-type Riemann solver for two-phase flow with surface forces and phase transitions. Appl. Numer. Math. **108**, 256–270 (2016). https://doi.org/10.1016/j.apnum.2015.12.010
19. Sembian, S., Liverts, M., Tillmark, N., Apazidis, N.: Plane shock wave interaction with a cylindrical water column. Phys. Fluids **28**(5), 056102 (2016). https://doi.org/10.1063/1.4948274
20. Sonntag, M., Munz, C.D.: Efficient parallelization of a shock capturing for discontinuous galerkin methods using finite volume sub-cells. J. Sci. Comput. **70**(3), 1262–1289 (2016). https://doi.org/10.1007/s10915-016-0287-5
21. Sussman, M., Smereka, P., Osher, S.: A level set approach for computing solutions to incompressible two-phase flow. J. Comput. Phys. **114**(1), 146–159 (1994). https://doi.org/10.1006/jcph.1994.1155
22. Wang, C.W., Liu, T.G., Khoo, B.C.: A real ghost fluid method for the simulation of multimedium compressible flow. SIAM J. Sci. Comput. **28**(1), 278–302 (2006). https://doi.org/10.1137/030601363

A Solver for Stiff Finite-Rate Relaxation in Baer–Nunziato Two-Phase Flow Models

Simone Chiocchetti and Christoph Müller

Abstract In this paper we present a technique for constructing robust solvers for stiff algebraic source terms, such as those typically used for modelling relaxation processes in hyperbolic systems of partial differential equations describing two-phase flows, namely models of the Baer–Nunziato family. The method is based on an exponential integrator which employs an approximate linearised source term operator that is constructed in such a way that one can compute solutions to the linearised equations avoiding any delicate matrix inversion operations.

1 Introduction

Stiff algebraic source terms, accounting for mechanical relaxation and phase transition in two-phase flow models of the Baer–Nunziato type [3, 12, 14], are one of the key difficulties in computing solutions to these systems of hyperbolic partial differential equations (PDE). Their accurate solution is relevant for the study of droplet dynamics with Baer–Nunziato models. These weakly compressible phenomena can be accurately described by the reduced models that assume instantaneous pressure and velocity equilibrium like the one forwarded by Kapila et al. [10]. Solving more general sets of equations like [3, 12, 14] in the stiff relaxation limit gives results that are similar to those obtained from the instantaneous equilibrium model, while allowing more modelling flexibility, since less physical assumptions have to be made.

A simple computational strategy for dealing with stiff sources is the *splitting* approach [15, 18]. The procedure consists of two steps: at each timestep, first one solves the homogeneous part of the PDE

S. Chiocchetti (✉)
Laboratory of Applied Mathematics, University of Trento, via Mesiano 77, 38123 Trento, Italy
e-mail: simone.chiocchetti@unitn.it

C. Müller
Institute of Aerodynamics and Gasdynamics, Pfaffenwaldrig 21, 70569 Stuttgart, Germany

G. Lamanna et al. (eds.), *Droplet Interactions and Spray Processes*,
Fluid Mechanics and Its Applications 121,
https://doi.org/10.1007/978-3-030-33338-6_3

$$\partial_t \mathbf{Q} + \nabla \cdot \mathbf{F}(\mathbf{Q}) + \mathbf{B}(\mathbf{Q}) \nabla \mathbf{Q} = \mathbf{S}(\mathbf{Q}), \tag{1}$$

for example with a path-conservative [5, 11] MUSCL–Hancock [17] method, obtaining a preliminary solution $\mathbf{Q}_{\mathrm{H}}$ and then one can use this state vector as initial condition for the Cauchy problem

$$\frac{\mathrm{d}\mathbf{Q}}{\mathrm{d}t} = \mathbf{S}(\mathbf{Q}), \quad \mathbf{Q}(t_n) = \mathbf{Q}_{\mathrm{H}}, \quad t \in (t_n,\ t_{n+1}), \tag{2}$$

of which the solution will then yield the updated quantities at the new time level t_{n+1}. This way, the problem is reduced to the integration of a system of ordinary differential equations (ODE), and general-purpose ODE solvers or more specialised tools can be employed for this task.

It is often the case that the time scales associated with relaxations sources are much shorter than those given by the stability condition of the PDE scheme, thus one must be able to deal with source terms that are potentially stiff. In order to integrate stiff ODEs with conventional explicit solvers, one has to impose very severe restrictions on the maximum timestep size, and for this reason implicit methods are commonly preferred [16]. Unfortunately implicit solvers, are, on a per-timestep basis, much more expensive than explicit integrators, and they still might require variable sub-timestepping in order to avoid under-resolving complex transients in the solution.

In this work, we will develop a technique for constructing a solver for stiff finite-rate mechanical relaxation sources, specifically those encountered in models of the Baer–Nunziato type.

The proposed method overcomes the issues typical of explicit solvers with three concurrent strategies: first, the update formula is based on exponential integration [6, 13], in order to mimic at the discrete level the behaviour of the differential equation; second, information at the new time level t_{n+1} is taken into account by iteratively updating a linearisation of the ODE system, this is achieved without resorting to a fully implicit method like those introduced in [4], and for which one would need to solve a system of nonlinear algebraic equations at each timestep t_n; third, the method incorporates a simple and effective adaptive timestepping criterion, which is crucial for capturing abrupt changes in the state variables and dealing with the different time scales that characterise the equations under investigation.

2 Model Equations

We are interested in the solution of two-phase flow models of the Baer–Nunziato family, which can be written in the general form (1), with a vector of conserved variables defined as

$$\mathbf{Q} = [\alpha_1 \rho_1,\ \alpha_2 \rho_2,\ \alpha_1 \rho_1 \mathbf{u}_1,\ \alpha_2 \rho_2 \mathbf{u}_2,\ \alpha_1 \rho_1 E_1,\ \alpha_2 \rho_2 E_2,\ \alpha_1]^{\mathsf{T}}, \tag{3}$$

a conservative flux $\mathbf{F}$ and a non-conservative term $\mathbf{B}\,\nabla\mathbf{Q}$ written as

$$\mathbf{F}(\mathbf{Q}) = \begin{bmatrix} \alpha_1\,\rho_1\,\mathbf{u}_1 \\ \alpha_2\,\rho_2\,\mathbf{u}_2 \\ \alpha_1\,(\rho_1\,\mathbf{u}_1 \otimes \mathbf{u}_1 + p_1\,\mathbf{I}) \\ \alpha_2\,(\rho_2\,\mathbf{u}_2 \otimes \mathbf{u}_2 + p_2\,\mathbf{I}) \\ \alpha_1\,(\rho_1\,E_1 + p_1)\,\mathbf{u}_1 \\ \alpha_2\,(\rho_2\,E_2 + p_2)\,\mathbf{u}_2 \\ 0 \end{bmatrix}, \quad \mathbf{B}(\mathbf{Q})\,\nabla\mathbf{Q} = \begin{bmatrix} 0 \\ 0 \\ -p_\mathrm{I}\,\nabla\alpha_1 \\ +p_\mathrm{I}\,\nabla\alpha_1 \\ -p_\mathrm{I}\,\mathbf{u}_\mathrm{I}\cdot\nabla\alpha_1 \\ +p_\mathrm{I}\,\mathbf{u}_\mathrm{I}\cdot\nabla\alpha_1 \\ \mathbf{u}_\mathrm{I}\cdot\nabla\alpha_1 \end{bmatrix}, \tag{4}$$

and a source term vector written as

$$\mathbf{S}(\mathbf{Q}) = \begin{bmatrix} 0 \\ 0 \\ \lambda\,(\mathbf{u}_2 - \mathbf{u}_1) \\ \lambda\,(\mathbf{u}_1 - \mathbf{u}_2) \\ \lambda\,(\mathbf{u}_2 - \mathbf{u}_1)\cdot\mathbf{u}_\mathrm{I} + \nu\,p_\mathrm{I}\,(p_2 - p_1) \\ \lambda\,(\mathbf{u}_1 - \mathbf{u}_2)\cdot\mathbf{u}_\mathrm{I} + \nu\,p_\mathrm{I}\,(p_1 - p_2) \\ \nu\,(p_1 - p_2) \end{bmatrix}. \tag{5}$$

Here we indicate with α_1 and α_2 the volume fractions of the first phase and of the second phase respectively, with ρ_1 and ρ_2 the phase densities, $\mathbf{u}_1 = [u_1,\ v_1,\ w_1]^\mathsf{T}$ and $\mathbf{u}_2 = [u_2,\ v_2,\ w_2]^\mathsf{T}$ indicate the velocity vectors, $\alpha_1\,\rho_1\,E_1$ and $\alpha_2\,\rho_2\,E_2$ are the partial energy densities. The pressure fields are denoted with p_1 and p_2, and the interface pressure and velocity are named p_I and $\mathbf{u}_\mathrm{I} = [u_\mathrm{I},\ v_\mathrm{I},\ w_\mathrm{I}]^\mathsf{T}$. Finally, the parameters λ and ν control the time scales for friction and pressure relaxation kinetics respectively.

In the following, we will study the system of ordinary differential equations arising from the source term (5) only, that is, the one constructed as given in equation (2) and specifically its one-dimensional simplification in terms of the primitive variables $\mathbf{V} = \left[u_1,\ u_2,\ p_1,\ p_2,\ \alpha_1\right]^\mathsf{T}$, with an initial condition $\mathbf{V}_0 = \left[u_1^0,\ u_2^0,\ p_1^0,\ p_2^0,\ \alpha_1^0\right]^\mathsf{T}$. Since no source is present in the mass conservation equations, they have a trivial solution, that is, $\alpha_1\,\rho_1$ and $\alpha_2\,\rho_2$ remain constant in time; for compactness, these quantities will be included in our analysis as constant parameters, rather than as variables of the ODE system.

The one-dimensional ODE system is written as

$$\frac{\mathrm{d}u_1}{\mathrm{d}t} = \frac{\lambda}{\alpha_1\,\rho_1}\,(u_2 - u_1), \tag{6}$$

$$\frac{\mathrm{d}u_2}{\mathrm{d}t} = \frac{\lambda}{\alpha_2\,\rho_2}\,(u_1 - u_2), \tag{7}$$

$$\frac{\mathrm{d}p_1}{\mathrm{d}t} = \frac{\nu\,(p_I + k_{1a}\,p_1 + k_{1b})}{\alpha_1\,k_{1a}}\,(p_2 - p_1) + \frac{\lambda\,(u_I - u_1)}{\alpha_1\,k_{1a}}\,(u_2 - u_1), \tag{8}$$

$$\frac{\mathrm{d}p_2}{\mathrm{d}t} = \frac{\nu\,(p_I + k_{2a}\,p_2 + k_{2b})}{\alpha_2\,k_{2a}}\,(p_1 - p_2) + \frac{\lambda\,(u_I - u_2)}{\alpha_2\,k_{2a}}\,(u_1 - u_2), \tag{9}$$

$$\frac{\mathrm{d}\alpha_1}{\mathrm{d}t} = \nu\,(p_1 - p_2). \tag{10}$$

The choices for interface pressure and velocity are $p_I = p_2$ and $u_I = u_1$. Finally, one can verify that, using the stiffened-gas equation of state for both phases, we have $k_{1a} = 1/(\gamma_1 - 1)$, $k_{2a} = 1/(\gamma_2 - 1)$, $k_{1b} = \gamma_1\,\Pi_1/(\gamma_1 - 1)$, and $k_{2b} = \gamma_2\,\Pi_2/(\gamma_2 - 1)$.

3 Description of the Numerical Method

The methodology is described in the following with reference to a generic nonlinear first order Cauchy problem

$$\frac{\mathrm{d}\mathbf{V}}{\mathrm{d}t} = \mathbf{S}(\mathbf{V},\ t), \qquad \mathbf{V}(t_n) = \mathbf{V}_n, \tag{11}$$

for which the ODE can be linearised about a given state $\mathbf{V}^*$ and time t^* as

$$\frac{\mathrm{d}\mathbf{V}}{\mathrm{d}t} = \mathbf{B}^* + \mathbf{J}^*(\mathbf{V}^*,\ t^*)\,(\mathbf{V} - \mathbf{V}^*). \tag{12}$$

Here we defined the Jacobian matrix of the source $\mathbf{J}^* = \mathbf{J}(\mathbf{V}^*,\ t^*)$ and analogously the source vector evaluated at the linearisation state is $\mathbf{B}^* = \mathbf{S}(\mathbf{V}^*,\ t^*)$. We then introduce the vector

$$\mathbf{C}^* = \mathbf{C}^*(\mathbf{B}^*,\ \mathbf{J}^*) = \mathbf{C}^*(\mathbf{V}^*,\ t^*) \tag{13}$$

which will be used as an indicator for the adaptive timestepping algorithm and may be constructed for example listing all of the components of the matrix $\mathbf{J}^*$ together with all the components of the vector $\mathbf{B}^*$ and the state $\mathbf{V}^*$, or only with a selection of these variables, or any other relevant combination of the listed variables, that is, any group indicative of changes in the nature or the magnitude of the linearised source operator.

It is then necessary to compute an accurate analytical solution of the non-homogeneous linear Cauchy problem

$$\frac{\mathrm{d}\mathbf{V}}{\mathrm{d}t} = \mathbf{S}^*(\mathbf{V};\ \mathbf{V}^*,\ t^*) = \mathbf{B}^* + \mathbf{J}^*(\mathbf{V}^*,\ t^*)\,(\mathbf{V} - \mathbf{V}^*), \quad \mathbf{V}(t_n) = \mathbf{V}_n. \tag{14}$$

We will denote the analytical solution of the IVP (14) as $\mathbf{V}_\mathrm{e}(t;\ \mathbf{S}^*,\ t_n,\ \mathbf{V}_n)$. As for $\mathbf{S}^*(\mathbf{V};\ \mathbf{V}^*,\ t^*)$, the semicolon separates the variable on which $\mathbf{V}_\mathrm{e}$ and $\mathbf{S}^*$ continuously depend (t or $\mathbf{V}$) from the parameters used in the construction of the operators. The state vector at a generic time level t_n is written as $\mathbf{V}_n$, the variable timestep size is $\Delta t^n = t_{n+1} - t_n$.

3.1 Timestepping

Marching from a start time t_0 to an end time t^{end} is carried out as follows. First, an initial timestep size Δt^0 is chosen, then, at each time iteration, the state $\mathbf{V}_{n+1}$ at the new time level t_{n+1} is computed by means of the iterative procedure described below. The iterative procedure will terminate by computing a value for $\mathbf{V}_{n+1}$, together with a new timestep size $\Delta t^{n+1} = t_{n+2} - t_{n+1}$ based on an estimator which is embedded in the iterative solution algorithm. There is also the possibility that, due to the timestep size Δt being too large, the value of $\mathbf{V}_{n+1}$ be flagged as not acceptable. In this case, the procedure will return a new shorter timestep size for the current timestep $\Delta t^n = t_{n+1} - t_n$ and a new attempt at the solution for $\mathbf{V}_{n+1}$ will be carried out. Specifically, in practice we choose the new timestep size to be half of the one used in the previous attempt.

3.2 Iterative Computation of the Timestep Solution

At each iteration (denoted by the superscript k) we define an average state vector $\mathbf{V}^{*k}_{n+1/2} = (\mathbf{V}_n + \mathbf{V}^{*k-1}_{n+1})/2$ to be formally associated with an intermediate time level $t_{n+1/2} = (t_n + t_{n+1})/2$. For the first iteration we need a guess value for $\mathbf{V}^{*k-1}_{n+1}$, with the simplest choice being $\mathbf{V}^{*k-1}_{n+1} = \mathbf{V}_n$. Then the coefficients $\mathbf{C}^{*k}_{n+1/2}$ are computed as

$$\mathbf{C}^{*k}_{n+1/2} = \mathbf{C}^{*k}_{n+1/2}(\mathbf{V}^{*k}_{n+1/2},\ t_{n+1/2}). \tag{15}$$

In a joint way, one can build the affine source operator

$$\mathbf{S}^{*k}_{n+1/2} = \mathbf{S}^{*k}_{n+1/2}(\mathbf{V};\ \mathbf{V}^{*k}_{n+1/2},\ t_{n+1/2}). \tag{16}$$

Then one can solve analytically

$$\frac{\mathrm{d}\mathbf{V}}{\mathrm{d}t} = \mathbf{S}^{*k}_{n+1/2}(\mathbf{V};\ \mathbf{V}^{*k}_{n+1/2},\ t_{n+1/2}), \qquad \mathbf{V}(t_n) = \mathbf{V}_n, \tag{17}$$

by computing

$$\mathbf{V}^{*k}_{n+1} = \mathbf{V}_{\mathrm{e}}\left(t_{n+1};\ \mathbf{S}^{*k}_{n+1/2},\ t_n,\ \mathbf{V}_n\right). \tag{18}$$

It is then checked that the state vector $\mathbf{V}^{*k}_{n+1}$ be physically admissible: in our case this means verifying that internal energy of each phase be positive and that the volume fraction be bounded between 0 and 1. Also one can check for absence of floating-point exceptions. Additionally, one must evaluate

$$\mathbf{C}^{*k}_{n+1} = \mathbf{C}^{*k}_{n+1}\left(\mathbf{V}^{*k}_{n+1},\ t_{n+1}\right). \tag{19}$$

This vector of coefficients will not be employed for the construction of an affine source operator $\mathbf{S}^{*k}_{n+1}$, but only for checking the validity of the solution obtained from the approximate problem (17) by comparing the coefficients vector $\mathbf{C}^{*k}_{n+1}$ to $\mathbf{C}^{*}_{n}$, as well as comparing the coefficients $\mathbf{C}^{*k}_{n+1/2}$ used in the middle-point affine operator for the initial coefficients $\mathbf{C}^{*}_{n}$. At the end of the iterative procedure, one will set $\mathbf{C}^{*}_{n+1} = \mathbf{C}^{*k}_{n+1}$, so that this will be the new reference vector of coefficients for the next timestep. The convergence criterion for stopping the iterations is implemented by computing

$$r = \max\left(\frac{\left| \mathbf{V}^{*k}_{n+1} - \mathbf{V}^{*k-1}_{n+1} \right|}{\left| \mathbf{V}^{*k}_{n+1} \right| + \left| \mathbf{V}^{*k-1}_{n+1} \right| + \epsilon_r} \right), \tag{20}$$

and checking if $r \leq r_{\max}$, with $r_{\max}$ and ϵ_r given tolerances, or if the iteration count k has reached a fixed maximum value $k_{\max}$. Note that in principle any norm may be used to compute the error metric given in Eq. (20), as this is just a measure of the degree to which $\mathbf{V}^{*k}_{n+1}$ was corrected in the current iteration. Moreover we found convenient to limit the maximum number of iterations allowed, and specifically here we set $k_{\max} = 8$, but stricter bounds can be used. For safety, we decide to flag the state vector $\mathbf{V}^{*k}_{n+1}$ as not admissible, as if a floating-point exception had been triggered, whenever the iterative procedure terminates by reaching the maximum iteration count.

After the convergence has been obtained, in order to test if the IVP (11) is well approximated by its linearised version (17), we compute

$$\delta_{n+1/2} = \max\left(\frac{\left| \mathbf{C}^{*}_{n+1/2} - \mathbf{C}^{*}_{n} \right|}{\left| \mathbf{C}^{*}_{n+1/2} \right| + \left| \mathbf{C}^{*}_{n} \right| + \epsilon_\delta} \right), \tag{21}$$

$$\delta_{n+1} = \max\left(\frac{\left| \mathbf{C}^{*}_{n+1} - \mathbf{C}^{*}_{n} \right|}{\left| \mathbf{C}^{*}_{n+1} \right| + \left| \mathbf{C}^{*}_{n} \right| + \epsilon_\delta} \right), \tag{22}$$

and we verify if $\delta = \max(\delta_{n+1/2},\ \delta_{n+1}) \leq \delta_{\max}$. The user should specify a tolerance $\delta_{\max}$ as well as the floor value ϵ_δ, which is used in order to prevent that excessive precision requirements be imposed in those situations when all the coefficients are so small than even large relative variations expressed by Eqs. (21) and (22) do not affect the solution in a significant manner. If $\delta \leq \delta_{\max}$ we confirm the state vector at the new time level to be $\mathbf{V}_{n+1} = \mathbf{V}^{*k}_{n+1}$ and a new timestep size is computed as

$$\Delta t_{n+1} = \lambda \frac{\delta_{\max}}{\delta + \epsilon}, \quad \text{with} \quad \lambda = 0.8, \quad \epsilon = 10^{-14}, \tag{23}$$

otherwise the solution of the IVP (17) is attempted again with a reduced timestep size, specifically one that is obtained by halving the timestep used in the current attempt. The same happens if at any time the admissibility test on $\mathbf{V}^{*k}_{n+1}$ fails.

3.3 Analytical Solution of the Linearised Problem

The general solution to an initial value problem like (17) can be written as

$$\mathbf{V}(t) = \exp\left(\mathbf{J}^* (t - t_n)\right) \left(\mathbf{V}(t_n) + \mathbf{J}^{*-1} \mathbf{B}^* - \mathbf{V}^*\right) - \mathbf{J}^{*-1} \mathbf{B}^* + \mathbf{V}^*. \tag{24}$$

Note that, in addition to evaluating the matrix exponential $\exp\left(\mathbf{J}^* (t - t_n)\right)$, one must also compute the inverse Jacobian matrix $\mathbf{J}^{*-1}$. Computation of matrix exponentials can be carried out rather robustly with the aid of the algorithms of Higham [9] and Al-Mohy and Higham [1, 2], while inversion of the Jacobian matrix can be an arbitrarily ill-conditioned problem.

For this reason we propose the following strategy for choosing a more suitable linearisation and computing analytical solutions of the linearised problem for the ODE system (6)–(10). First, it is easy to see that the velocity sub-system (equations for u_1 and u_2) can be fully decoupled from the other equations, as the partial densities $\alpha_1 \rho_1$ and $\alpha_2 \rho_2$ remain constant in the relaxation step.

Then the solution of the velocity sub-system can be immediately obtained as

$$u_1(t) = \frac{\lambda}{k} \left(\frac{u_1^0}{\alpha_2 \rho_2} + \frac{u_2^0}{\alpha_1 \rho_1} + \frac{u_1^0 - u_2^0}{\alpha_1 \rho_1} \exp\left(-k (t - t_n)\right) \right), \tag{25}$$

$$u_2(t) = \frac{\lambda}{k} \left(\frac{u_1^0}{\alpha_2 \rho_2} + \frac{u_2^0}{\alpha_1 \rho_1} + \frac{u_2^0 - u_1^0}{\alpha_2 \rho_2} \exp\left(-k (t - t_n)\right) \right), \tag{26}$$

with $k = 1/\alpha_1 \rho_1 + 1/\alpha_2 \rho_2$.

In a second step, the pressure sub-system (8)–(9) is linearised as

$$\frac{\mathrm{d}p_1}{\mathrm{d}t} = k_p (p_2 - p_1) + k_u (u_I - u_1)(u_2 - u_1), \tag{27}$$

$$\frac{\mathrm{d}p_2}{\mathrm{d}t} = k_p (p_1 - p_2) + k_u (u_I - u_2)(u_1 - u_2), \tag{28}$$

where k_p and k_u are constant coefficients directly obtained from Eqs. (8)–(9). This way, at the cost of suppressing the dependence on α_1 in the Jacobian of the pressure sub-system, the homogeneous part of Eqs. (27)–(28) has the same simple structure found in the velocity sub-system, with the addition of a non-homogeneous term, which is known, as $u_1(t)$ and $u_2(t)$ already have been computed. The solution can again be evaluated using standard scalar exponential functions, which are fast and robust, compared to matrix exponentials and especially so, because one no longer needs to perform the inversion of the Jacobian matrix of the full system.

Finally, the solution to Eq. (10) can be integrated analytically from the expressions of $p_1(t)$ and $p_2(t)$. Full coupling of the system is restored in the successive iterations by recomputing the constant coefficients k_p and k_u using an updated midpoint value

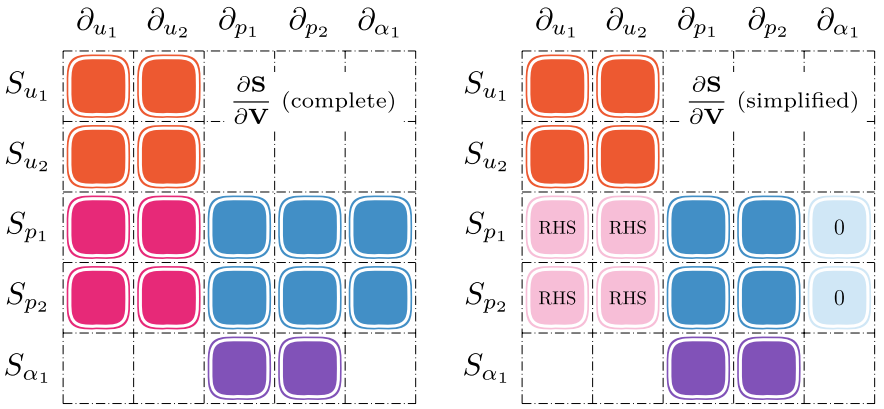

Fig. 1 Visual comparison between the structure of the complete Jacobian matrix for the ODE system (6)–(10) and the proposed three-step simplified structure. The RHS label indicates dependencies that are accounted for as non-homogeneous terms in the pressure sub-system, while the zeros mark dependencies that are suppressed entirely

for α_1. A visual representation of the approximate Jacobian matrix associated with the proposed solution method can be found in Fig. 1.

4 Test Problems

We provide validation of the proposed method first by computing solutions to the ODE system (6)–(10) and comparing the results with a reference solution obtained from a sixth order, fully implicit, Runge–Kutta–Gauss–Legendre method [4] (labeled RKGL3) employing adaptive timestepping (test problems A1 and A2, Figs. 2 and 3). Furthermore, test problem A1 is employed also for carrying out a convergence study of the scheme (Fig. 4), showing that second order convergence is easily achieved. The initial data for the ODE tests are, for test A1 (Fig. 5),

$$u_1^0 = -5\,\mathrm{m\,s^{-1}},\quad u_2^0 = 5\,\mathrm{m\,s^{-1}},\quad p_1^0 = 0.1\,\mathrm{Pa},\quad p_2^0 = 20\,\mathrm{Pa},\quad \alpha_1^0 = 0.9, \tag{29}$$

while for test A2,

$$u_1^0 = 0\,\mathrm{m\,s^{-1}},\quad u_2^0 = 0\,\mathrm{m\,s^{-1}},\quad p_1^0 = 2.0\times 10^8\,\mathrm{Pa},\quad p_2^0 = 1\,\mathrm{Pa},\quad \alpha_1^0 = 0.4. \tag{30}$$

The parametric data are, for test A1,

$$\begin{aligned} &\alpha_1\,\rho_1 = 1.0\,\mathrm{kg\,m^{-3}},\quad \alpha_2\,\rho_2 = 4.0\,\mathrm{kg\,m^{-3}},\quad \gamma_1 = 6,\quad \gamma_2 = 1.4,\\ &\Pi_1 = 0\,\mathrm{Pa},\quad \Pi_2 = 0\,\mathrm{Pa},\quad \lambda = 10^9\,\mathrm{kg\,m^{-1}\,s^{-1}},\quad \nu = 10\,\mathrm{Pa^{-1}\,s^{-1}}. \end{aligned} \tag{31}$$

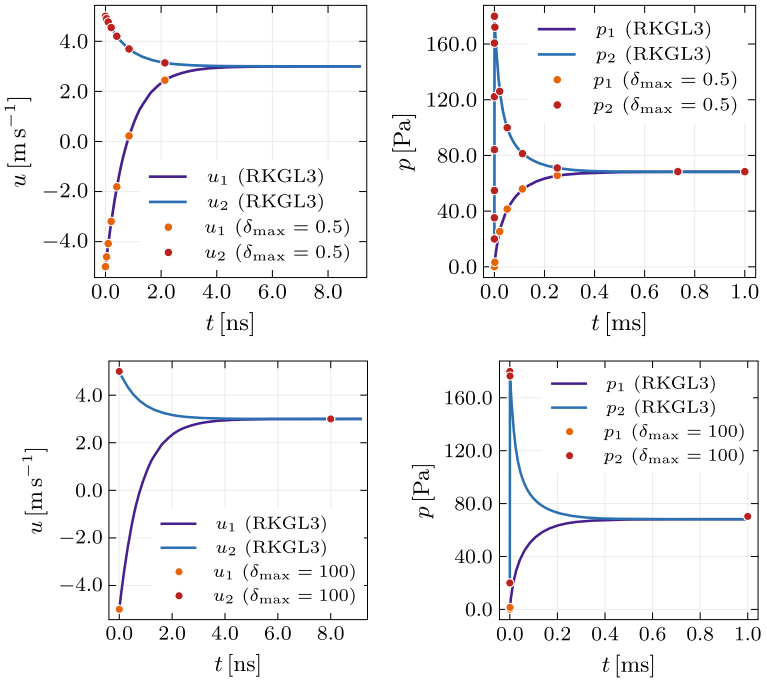

Fig. 2 Time evolution of velocities and pressures for test problem A1. In the top frames the linearisation tolerance parameter is set as $\delta_{\max} = 0.5$, employing 15 timesteps to reach the final time of 1.0 ms, while in the bottom frames we impose an extremely loose tolerance $\delta_{\max} = 100$, still showing good agreement with the reference solution but using only 4 timesteps for the full run

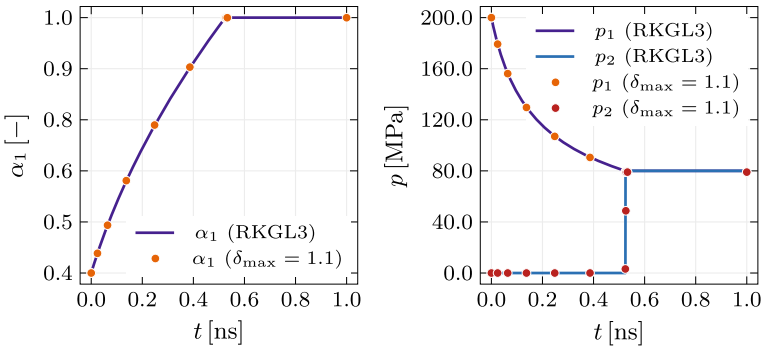

Fig. 3 Time evolution of volume fraction and pressure for test problem A2. The solution is well captured in 11 timesteps, using a linearisation tolerance $\delta_{\max} = 1.1$

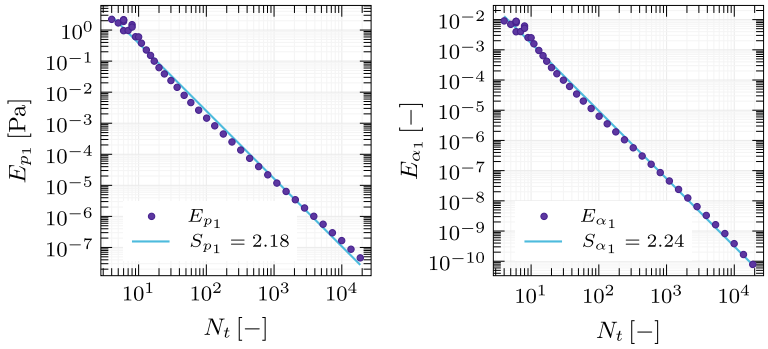

Fig. 4 Convergence results relative to 40 runs of test problem A1. On the bilogarithmic plane, the slopes of the regression lines are $S_{p_1} = 2.18$ and $S_{\alpha_1} = 2.24$ for the variables p_1 and α_1 respectively, indicating second order convergence

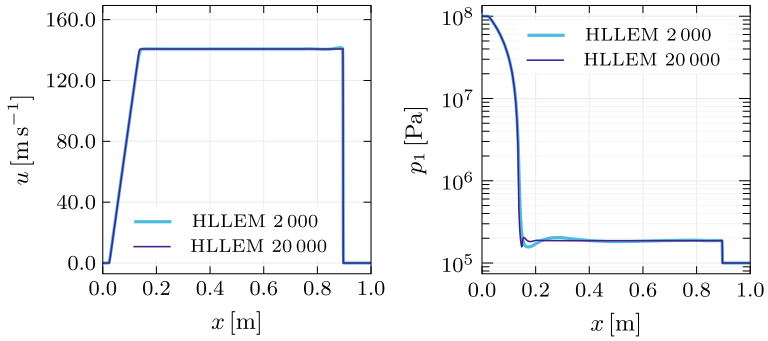

Fig. 5 Solution of test Problem RP1 on two uniform meshes of 2000 cells and 20,000 cells respectively, showing convergence with respect to mesh refinement

and for test A2,

$$\begin{aligned} &\alpha_1\,\rho_1 = 780.0\,\mathrm{kg\,m^{-3}},\quad \alpha_2\,\rho_2 = 0.22\,\mathrm{kg\,m^{-3}},\quad \gamma_1 = 6,\quad \gamma_2 = 1.4,\\ &\Pi_1 = 100\,\mathrm{Pa},\quad \Pi_2 = 0\,\mathrm{Pa},\quad \lambda = 10^9\,\mathrm{kg\,m^{-1}\,s^{-1}},\quad \nu = 10\,\mathrm{Pa^{-1}\,s^{-1}}. \end{aligned} \tag{32}$$

Then, we show an application of the method in the solution of the mixture-energy-consistent formulation of the six-equation reduced Baer–Nunziato model forwarded in [12], where the detailed description of the test cases can be found. For these simulations the interface pressure is computed as

$$p_I = \frac{Z_2\,p_1 + Z_1\,p_2}{Z_1 + Z_2},\quad \text{with}\quad Z_1 = \rho_1\,a_1 \text{ and } Z_2 = \rho_2\,a_2. \tag{33}$$

The first two shock-tube problems show that the method is able to deal with very stiff ($\nu = 10^{20}\,\mathrm{Pa^{-1}\,s^{-1}}$) sources, and in particular in Fig. 5 (RP1, featuring

a strong right-moving shockwave) we show mesh convergence of the solution by comparing two runs, both employing the HLLEM Riemann solver proposed in [7], on two different meshes consisting of 2000 uniform control volumes and 20,000 control volumes respectively. In Fig. 6 (RP2, two diverging rarefaction waves) we then show that, with very stiff relaxation ($\nu = 10^{20}\,\mathrm{Pa}^{-1}\,\mathrm{s}^{-1}$), the solution matches the one computed by solving directly the five-equation instantaneous equilibrium model [10], again using a mesh consisting of 2000 uniform cells for the six-equation model and a mesh of 20,000 uniform cells for the reference solution. All tests are run using a second order path-conservative MUSCL-Hancock scheme with $k_{\mathrm{CFL}} = 0.95$.

Finally, in Fig. 7 we show the behaviour of the solution of a third Riemann problem (RP3) with several different values of the pressure relaxation parameter ν (ranging from 10^{-8} to $10^{20}\,\mathrm{Pa}^{-1}\,\mathrm{s}^{-1}$), highlighting the vast range of solution structures that can be obtained not only with stiff relaxation (the pressure profiles p_1 and p_2 coincide) or in total absence of it, but also with finite values of the relaxation time scale. For RP3, the initial data on the left are

$$\begin{aligned} &\rho_1^{\mathrm{L}} = 1.0\,\mathrm{kg\,m^{-1}\,s^{-1}}, \quad \rho_2^{\mathrm{L}} = 0.2\,\mathrm{kg\,m^{-3}}, \quad u^{\mathrm{L}} = 0.0\,\mathrm{m\,s^{-1}}, \\ &p_1^{\mathrm{L}} = 1.0\,\mathrm{Pa}, \quad p_2^{\mathrm{L}} = 1.0\,\mathrm{Pa}, \quad \alpha_1^{\mathrm{L}} = 0.55, \end{aligned} \tag{34}$$

while on the right one has

$$\begin{aligned} &\rho_1^{\mathrm{R}} = 0.125\,\mathrm{kg\,m^{-3}}, \quad \rho_2^{\mathrm{R}} = 2.0\,\mathrm{kg\,m^{-3}}, \quad u^{\mathrm{R}} = 0.0\,\mathrm{m\,s^{-1}}, \\ &p_1^{\mathrm{R}} = 0.1\,\mathrm{Pa}, \quad p_2^{\mathrm{R}} = 0.1\,\mathrm{Pa}, \quad \alpha_1^{\mathrm{R}} = 0.45. \end{aligned} \tag{35}$$

The initial jump is located at $x = 0.6\,\mathrm{m}$, the domain is $x \in [0\,\mathrm{m},\ 1\,\mathrm{m}]$ and the final time is $t_{\mathrm{end}} = 0.15\,\mathrm{s}$. The parameters of the stiffened gas EOS are $\gamma_1 = 2.0$, $\gamma_2 = 1.4$, $\Pi_1 = 2.0\,\mathrm{Pa}$, $\Pi_2 = 0.0\,\mathrm{Pa}$.

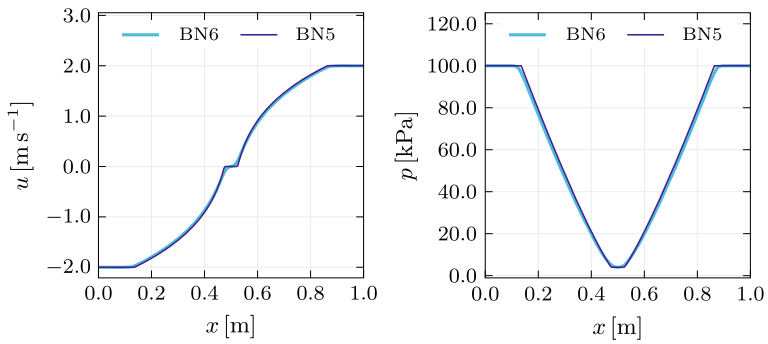

Fig. 6 Solution of test Problem RP2 computed from the six-equation Baer–Nunziato model (BN6) with stiff relaxation, compared with the five-equation Kapila model (BN5), showing convergence to the limit reduced model

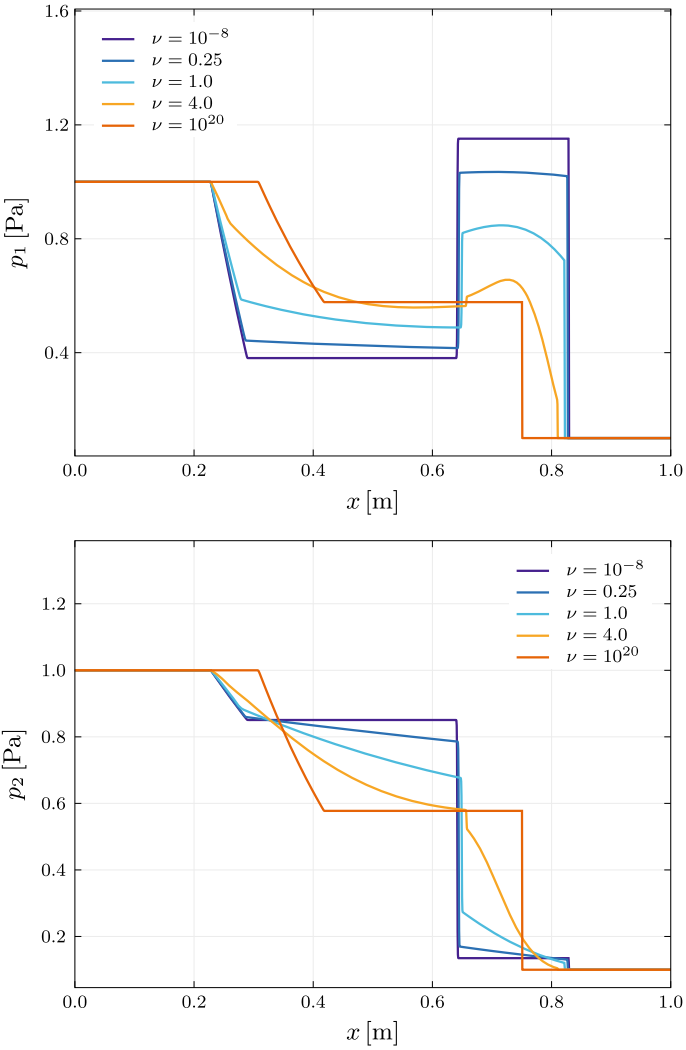

Fig. 7 Behaviour of the pressure variables in RP3 with several values of ν. It is clear that, in the stiff regime ($\nu = 10^{20}\,\mathrm{Pa}^{-1}\,\mathrm{s}^{-1}$), p_1 and p_2 converge to the same value, while they evolve in a completely distinct fashion if relaxation is set to act on longer timescales

5 Conclusions

We presented a technique for integrating ordinary differential equations associated with stiff relaxation sources and promising results have been shown for a set of test problems. The method can efficiently resolve very abrupt variations in the solution and adapt to multiple timescales. A key feature of the algorithm is that it can avoid delicate linear algebra operations entirely, thus improving the robustness of the scheme. Future applications will include liquid-gas and liquid-solid phase transition, strain relaxation for nonlinear elasticity [8] and the computation of material failure in elasto-plastic and brittle solids.

Acknowledgements The authors of this work were supported by the German Research Foundation (DFG) through the project GRK 2160/1 "Droplet Interaction Technologies".

References

1. Al-Mohy, A.H., Higham, N.J.: A new scaling and squaring algorithm for the matrix exponential. SIAM J. Matrix Anal. Appl. **31**(3), 970–989 (2009)
2. Al-Mohy, A.H., Higham, N.J.: Computing the action of the matrix exponential, with an application to exponential integrators. SIAM J. Sci. Comput. **33**(2), 488–511 (2011)
3. Baer, M.R., Nunziato, J.W.: A two-phase mixture theory for the deflagration-to-detonation transition (DDT) in reactive granular materials. Int. J. Multiph. Flow **12**(6), 861–889 (1986)
4. Butcher, J.C.: Implicit Runge-Kutta processes. Math. Comput. **18**(85), 50–64 (1964)
5. Castro, M., Gallardo, J.M., Parés, C.: High order finite volume schemes based on reconstruction of states for solving hyperbolic systems with nonconservative products. Applications to shallow-water systems. Math. Comput. **75**(255), 1103–1134 (2006)
6. Certaine, J.: The solution of ordinary differential equations with large time constants. In: Mathematical Methods for Digital Computers pp. 128–132 (1960)
7. Dumbser, M., Balsara, D.S.: A new efficient formulation of the HLLEM Riemann solver for general conservative and non-conservative hyperbolic systems. J. Comput. Phys. **304**(C), 275–319 (2016)
8. Dumbser, M., Peshkov, I., Romenski, E., Zanotti, O.: High order ader schemes for a unified first order hyperbolic formulation of continuum mechanics: viscous heat-conducting fluids and elastic solids. J. Comput. Phys. **314**, 824–862 (2016)
9. Higham, N.J.: The scaling and squaring method for the matrix exponential revisited. SIAM J. Matrix Anal. Appl. **26**(4), 1179–1193 (2005)
10. Kapila, A.K., Menikoff, R., Bdzil, J.B., Son, S.F., Stewart, D.S.: Two-phase modeling of deflagration-to-detonation transition in granular materials: reduced equations. Phys. Fluids **13**(10), 3002–3024 (2001)
11. Parès, C.: Numerical methods for nonconservative hyperbolic systems: a theoretical framework. SIAM J. Numer. Anal. **44**(1), 300–321 (2006)
12. Pelanti, M., Shyue, K.M.: A mixture-energy-consistent six-equation two-phase numerical model for fluids with interfaces, cavitation and evaporation waves. J. Comput. Phys. **259**, 331–357 (2014)
13. Pope, D.A.: An exponential method of numerical integration of ordinary differential equations. Commun. ACM **6**(8), 491–493 (1963)
14. Saurel, R., Petitpas, F., Berry, R.A.: Simple and efficient relaxation methods for interfaces separating compressible fluids, cavitating flows and shocks in multiphase mixtures. J. Comput. Phys. **228**(5), 1678–1712 (2009)

15. Strang, G.: On the construction and comparison of difference schemes. SIAM J. Numer. Anal. **5**, 506–517 (1968)
16. Toro, E.F.: Riemann Solvers and Numerical Methods for Fluid Dynamics. A Practical Introduction, Third edition. Springer, Berlin (2009)
17. van Leer, B.: Towards the ultimate conservative difference scheme. V. A second-order sequel to Godunov's method. J. Comput. Phys. **32**(1), 101–136 (1979)
18. Yanenko, N.N.: The Method of Fractional Steps. Springer (1971)

An Investigation of Different Splitting Techniques for the Isentropic Euler Equations

Jonas Zeifang, Klaus Kaiser, Jochen Schütz, Francesco Carlo Massa and Andrea Beck

Abstract For the accurate and efficient discretization of the low-Mach isentropic Euler equations, which can be used for the description of droplet dynamics, several IMEX splitting schemes have been introduced in literature. In this work, we cast multiple splittings into a common framework, which makes it possible to compare them numerically. Temporal discretization is done with IMEX Runge-Kutta methods, while for the spatial part, we rely on the discontinuous Galerkin spectral element method. It is shown that, while the influence of the splitting on accuracy is small, it has a large impact on efficiency.

1 Introduction

When considering weakly compressible droplet dynamics the physical phenomena often can be described by the isentropic Euler equations. For example in [15], they are used in a sharp interface ghost fluid method for the simulation of two-phase flows.

J. Zeifang (✉) · A. Beck
Institute of Aerodynamics and Gasdynamics, University of Stuttgart,
Pfaffenwaldring 21, 70569 Stuttgart, Germany
e-mail: jonas.zeifang@iag.uni-stuttgart.de

A. Beck
e-mail: andrea.beck@iag.uni-stuttgart.de

K. Kaiser
IGPM, RWTH Aachen University, Templergraben 55, 52062 Aachen, Germany
e-mail: kaiser@igpm.rwth-aachen.de

J. Schütz
Faculty of Sciences, Hasselt University, Agoralaan Gebouw D, 3590 Diepenbeek, Belgium
e-mail: jochen.schuetz@uhasselt.be

F. C. Massa
Department of Engineering and Applied Sciences, University of Bergamo, Viale Marconi 5,
24044 Dalmine, Italy
e-mail: francescocarlo.massa@unibg.it

G. Lamanna et al. (eds.), *Droplet Interactions and Spray Processes*,
Fluid Mechanics and Its Applications 121,
https://doi.org/10.1007/978-3-030-33338-6_4

This necessitates efficient schemes for the non-dimensionalized Euler equations at a low reference Mach number ε. Those equations are given by

$$\begin{aligned} \partial_t \rho + \nabla \cdot (\rho \mathbf{u}) &= 0, \\ \partial_t (\rho \mathbf{u}) + \nabla \cdot (\rho \mathbf{u} \otimes \mathbf{u}) + \frac{1}{\varepsilon^2} \nabla p &= 0, \end{aligned} \tag{1}$$

with the equation of state $p(\rho) := \kappa \rho^\gamma$ and $\kappa > 0$, $\gamma \geq 1$. ρ, $\mathbf{u}$ and p denote density, velocity vector and pressure, respectively. Considering so-called well-prepared initial data, see e.g. [5], one can show that there is a well-behaved limit as $\varepsilon \to 0$ [10]. This limit can be described by the incompressible Euler equations which are given by

$$\begin{aligned} \rho_{(0)} \equiv \text{const.} > 0, \quad \nabla \cdot \mathbf{u}_{(0)} &= 0, \\ \partial_t \mathbf{u}_{(0)} + \nabla \cdot (\mathbf{u}_{(0)} \otimes \mathbf{u}_{(0)}) + \frac{\nabla p_{(2)}}{\rho_{(0)}} &= 0, \end{aligned} \tag{2}$$

with $p_{(2)}$ denoting the hydrodynamic pressure.

In situations with small Mach numbers, the wave speeds of the different characteristics of the compressible equations differ tremendously, since the speed of sound tends to infinity for a vanishing Mach number. When using explicit numerical time integration methods, this requires the use of an impractically small time step $\Delta t = \mathcal{O}(\varepsilon)$ (or even smaller if the influence of overly diffusive schemes is considered [4]) due to the CFL condition.

Many attempts have been made to overcome this issue; for a recent overview see e.g. [2] and the references therein. One particular idea is to perform a flux splitting, see, e.g., [3–5, 9, 11, 14], where the flux is split into two parts: A flux related to the fast characteristics ('acoustic waves') treated IMplicitly and a part related to the slow parts ('material waves') treated EXplicitly, resulting in so-called IMEX schemes. One specific idea of a flux splitting, described in [8, 9, 16], is the so-called RS-IMEX splitting. Here, the splitting is based on a linearization around a given reference solution (RS) to obtain the implicitly treated flux.

The aim of this work is to compare the RS-IMEX splitting for the isentropic Euler equations with the splittings introduced in [4, 5] and to improve the efficiency of the RS-IMEX splitting by considering different possibilities of choosing the reference solution. The split equation system is discretized with a high order nodal discontinuous Galerkin scheme in space [6, 12] and a high order IMEX Runge-Kutta scheme in time [1, 13]; see [16] for more details on the implementation.

The paper is structured as follows: In Sect. 2 we introduce the different splittings. In Sect. 3 the numerical framework for the comparison is briefly summarized. Section 4 then shows numerical results for a variety of splittings including the comparison of performance. Finally, Sect. 5 offers conclusion and outlook.

2 A Generalized Splitting

In conservative form, the isentropic Euler equations, Eq. (1), can be written as

$$\partial_t \mathbf{w} + \nabla \cdot \mathbf{f}(\mathbf{w}) = 0,$$

with the state vector $\mathbf{w} := (\rho, \rho\mathbf{u})$. With a suitable identification of 'fast' and 'slow' parts, the flux can be split into a part $\widetilde{\mathbf{f}}$ that is treated implicitly and a part $\widehat{\mathbf{f}}$ that is treated explicitly, i.e.,

$$\partial_t \mathbf{w} + \nabla \cdot \mathbf{f}(\mathbf{w}) = \partial_t \mathbf{w} + \nabla \cdot \left(\widetilde{\mathbf{f}}(\mathbf{w}) + \widehat{\mathbf{f}}(\mathbf{w})\right) = 0.$$

In [7], Kaiser introduced a generalized notation for splitting the isentropic Euler equations given by

$$\widetilde{\mathbf{f}} := \begin{pmatrix} (1-\mathcal{M})\rho\mathbf{u} \\ \mathcal{K}(\rho,\mathbf{u}) + \frac{\mathcal{H}(\rho)}{\varepsilon^2} Id \end{pmatrix} \quad \text{and} \quad \widehat{\mathbf{f}} := \begin{pmatrix} \mathcal{M}\rho\mathbf{u} \\ \rho\mathbf{u}\otimes\mathbf{u} - \mathcal{K}(\rho,\mathbf{u}) + \frac{p(\rho)-\mathcal{H}(\rho)}{\varepsilon^2} Id \end{pmatrix}, \quad (3)$$

with $\mathcal{M}, \mathcal{K}$ and $\mathcal{H}$ being chosen such that the explicit and implicit parts are hyperbolic. In [7] it has been shown that a splitting according to Eq. (3) with an IMEX Runge-Kutta discontinuous Galerkin discretization is asymptotic consistent under some restrictions on $\mathcal{M}$, $\mathcal{K}$ and $\mathcal{H}$. For more details the reader is referred to [7].

We can cast the splittings used in this work into the above-mentioned framework:

1. Splitting by Degond and Tang [4] (DeTa): Take

$$\mathcal{M} = 0, \qquad \mathcal{K} = 0 \qquad \text{and} \qquad \mathcal{H} = \left(1-\varepsilon^2\right) p(\rho).$$

2. Splitting by Haack et al. [5] (HJL): Take

$$\mathcal{M} = \varepsilon^2, \qquad \mathcal{K} = 0 \qquad \text{and} \qquad \mathcal{H} = a(t)\rho,$$

   where $a(t) := \min_{\mathbf{x}} p'(\rho(\mathbf{x}, t))$ with $p' = \partial p/\partial\rho$ evaluated explicitly, i.e., for the implicit flux we use $a(t)$ evaluated at the previous stage.
3. RS-IMEX splitting [9]: For a given, so-called reference solution $\mathbf{w}_{\text{ref}}$, the RS-IMEX splitting is defined by setting

$$\mathcal{M} = 0, \quad \mathcal{K} = -\rho\mathbf{u}_{\text{ref}}\otimes\mathbf{u}_{\text{ref}} + \rho\mathbf{u}\otimes\mathbf{u}_{\text{ref}} + \mathbf{u}_{\text{ref}}\otimes\rho\mathbf{u} \quad \text{and}$$
$$\mathcal{H} = p(\rho_{\text{ref}}) + p'(\rho_{\text{ref}})(\rho_{\text{ref}} - \rho).$$

   The idea behind this splitting is a linearization of the convective fluxes around the reference solution $\mathbf{w}_{\text{ref}}$ and taking the remainder as an explicit flux contribution. In previous works, the reference solution was chosen to be the solution of the incompressible equations, Eq. (2), computed with the same order of accuracy as done for the compressible equations. In this work, we also present other choices:

- RS-IMEX-$q_C q_I$: Here, the computation of the compressible solution is done with polynomial order q_C, while the incompressible solution is computed with polynomial order $q_I \leq q_C$ to reduce computational effort.
- RS-IMEX-min: The explicitly evaluated reference solution is defined by

$$\mathbf{w}_{\text{ref}} := \min_{\mathbf{x}} \mathbf{w}(\mathbf{x}, t).$$

- RS-IMEX-mean: With the initially given $\rho_{(0)}$, $\mathbf{w}_{\text{ref}} = (\rho_{\text{ref}}, \mathbf{u}_{\text{ref}})^T$ is defined by

$$\rho_{\text{ref}} := \rho_{(0)} \qquad \text{and} \qquad \mathbf{u}_{\text{ref}} := \frac{1}{|\Omega|} \int_{\Omega} \mathbf{u} \mathrm{d}x,$$

  with $\mathbf{u}_{\text{ref}}$ being evaluated explicitly on the domain Ω.

3 Numerical Method

3.1 Discretization

The spatial discretization is done by applying the discontinuous Galerkin spectral element discretization [12] to the split equation as done in [16]. This discretization is based on an approximation of the solution as the tensor-product of one-dimensional Lagrange polynomials. A detailed description of the present spatial discretization method can be found in [6].

Temporal discretization is performed using IMEX Runge-Kutta methods [1, 13], which are combinations of implicit and explicit Runge-Kutta schemes. Depending on the splitting, a (non-)linear system of equations has to be solved for every IMEX Runge-Kutta stage. For this, we use a matrix-free (Newton-)GMRES method. To gain computational efficiency, a block-Jacobian preconditioner is equipped. A more detailed description of the solution strategy can be found in [16].

3.2 Calculation of the RS-IMEX Reference Solution

The reference solution for RS-IMEX-$q_C q_I$ requires the solution of the incompressible system with a polynomial ansatz of degree q_I which can be different (smaller than) the degree q_C for the compressible solution. This introduces an algorithmic challenge in that two distinct discretization operators must exist in parallel during the computation (on the same grid) which are coupled uni-directionally via the reference solution. An elegant way of achieving this is running two instances of the framework, which communicate by message passing interfaces (MPI). Note that in the following, we limit the investigations to the coarsest case of $q_I = 1$. The reference solution is computed using the artificial compressibility-type incompressible solver described

in [16]. It is equipped with a fully implicit time discretization using the implicit part of the IMEX Runge-Kutta schemes. In the following we denote the RS-IMEX-$q_C q_I$ scheme with $q_C = q_I$ as RS-IMEX-standard. All other splittings and both parts of the RS-IMEX-$q_C q_I$ splitting are parallelized by distributing the elements evenly on the available processors.

3.3 Discretization of HJL and DeTa Splitting

It is worth noting that the splittings proposed by Haack et al. [5] and Degond and Tang [4] were originally not intended to be used directly in a straightforward IMEX setting. Instead, the authors derived elliptic equations on the semi-discrete level that they then solved. In this work, however, we cast the splittings into our generalized form and discretize them via IMEX Runge-Kutta DG.

4 Numerical Results

In this section, we evaluate the accuracy and efficiency of the different splitting techniques discussed in Sect. 2. Therefore, we consider two testcases: For the first example an exact solution is known and it can hence be used for the evaluation of accuracy and efficiency. The second testcase is more complex and no exact solution is known. Hence, it is employed only to indicate if a splitting is able to predict a complex three-dimensional behavior and to evaluate its efficiency. Based on these testcases, we aim to answer the following specific questions:

- Do the splitting schemes differ in terms of accuracy? Given the unified form of the splitting techniques derived in this work and the common discretization by an IMEX discontinuous Galerkin discretization, what can be deduced about their computational efficiency?
- For the novel RS-IMEX splitting scheme, what is the influence of choosing the reference solution as outlined in Sect. 2 on its properties?

4.1 Testcase 1: HOT-Vortex

The high order traveling vortex (HOT-vortex) has previously been used in [8, 16] to investigate the transport properties of the schemes. The exact solution of this testcase describes the convection of a smooth vortex.

4.1.1 Initialization and Discretization

The initial conditions of the vortex are periodic and given on domain $\Omega = [0, 1]^2$:

$$\rho(\mathbf{x}, t=0) = 2 + (500\varepsilon)^2 \begin{cases} \frac{1}{2} e^{\frac{2}{\Delta r}} \Delta r - \mathrm{Ei}\left(\frac{2}{\Delta r}\right) & r < \frac{1}{2} \\ 0 & \text{otherwise} \end{cases}$$
$$\mathbf{u}(\mathbf{x}, t=0) = \begin{pmatrix} 1/2 \\ 0 \end{pmatrix} + 500 \begin{pmatrix} \frac{1}{2} - \mathbf{x}_2 \\ \mathbf{x}_1 - \frac{1}{2} \end{pmatrix} \cdot \begin{cases} e^{\frac{1}{\Delta r}} & r < \frac{1}{2} \\ 0 & \text{otherwise} \end{cases}, \tag{4}$$

with $r := \sqrt{(\mathbf{x}_1 - \frac{1}{2})^2 + (\mathbf{x}_2 - \frac{1}{2})^2}$, $\Delta r := r^2 - \frac{1}{4}$ and $\mathrm{Ei}(x) := \int_{-\infty}^{x} \frac{e^t}{t} \mathrm{d}t$. The equation of state for pressure is defined by $p(\rho) = \frac{1}{2}\rho^2$. We obtain the initialization of the incompressible solver, required for the RS-IMEX-standard and the RS-IMEX-$q_C q_I$, by setting $\varepsilon = 0$ in Eq. 4 and $p_{(2)} = \kappa\gamma\rho_{(0)}^{\gamma-1}\rho_{(2)}$.

We consider this testcase on a grid with 16^2 elements for the Mach numbers $\varepsilon \in \{10^{-1}, 10^{-2}, 10^{-3}, 10^{-4}\}$ and compare the errors for the different splittings at $t = 2$. The abort criteria of the linear and non-linear solvers are given in the Appendix, Table 2. Note that the time step prescribed by the convective velocity is kept fixed for the different splittings. Here, we use a third and fourth order discretization in space and time ($q_C = 2$ with IMEX-ARS-443 [1], $q_C = 3$ with IMEX-ARK-4A2 [13]).

4.1.2 Evaluation of Accuracy

Table 1 shows that there are only very slight differences between the different splittings concerning their errors. Note that for the DeTa splitting with $\varepsilon = 10^{-4}$ no stable solution could be found as machine accuracy issues become dominant for the matrix-free implementation of the nonlinear scheme. Hence, we can determine the required computational time with these parameters as done in the next paragraph.

Table 1 Total L_2 error at $t = 2$ for 3rd (upper) and 4th (lower) order scheme for the different splittings defined in Sect. 2

Total L_2 error	RS-IMEX-standard	RS-IMEX-$q_C q_I$	RS-IMEX-mean	RS-IMEX-min	HJL	DeTa
$\varepsilon = 10^{-1}$	8.36E−3	8.48E−3	8.35E−3	8.32E−3	7.02E−3	8.36E−3
$\varepsilon = 10^{-2}$	8.39E−3	8.47E−3	8.39E−3	8.26E−3	6.99E−3	8.40E−3
$\varepsilon = 10^{-3}$	8.39E−3	8.47E−3	8.39E−3	8.26E−43	6.98E−3	8.39E−3
$\varepsilon = 10^{-4}$	8.39E−3	8.47E−3	8.39E−3	8.25E−3	6.98E−3	–
$\varepsilon = 10^{-1}$	5.65E−4	5.65E−4	5.69E−4	7.81E−4	6.95E−4	5.79E−4
$\varepsilon = 10^{-2}$	5.26E−4	5.27E−4	5.25E−4	7.19E−4	6.70E−4	5.22E−4
$\varepsilon = 10^{-3}$	5.22E−4	5.23E−4	5.22E−4	7.34E−4	6.76E−4	5.22E−4
$\varepsilon = 10^{-4}$	5.21E−4	5.22E−4	5.21E−4	7.29E−4	6.75E−4	–

4.1.3 Evaluation of Efficiency and RS-IMEX Reference Solution Variant

Figure 1 shows a qualitatively similar behavior for $q_C = 2$ and $q_C = 3$: All schemes have a qualitatively similar behavior, showing convergence to a limit in computational time for a decreasing Mach number. We see that the DeTa splitting, the HJL-splitting and the RS-IMEX-mean/min require almost the same computational resources. In case that the matrix-free implementation is able to find a solution to the DeTa splitting, it is slightly more efficient than the other approaches.

Regarding the differences between the RS-IMEX variants, we note from Table 1 that no perceivable differences for the selected reference solution versions occur in terms of accuracy. In terms of computational resources however (Fig. 1), the RS-IMEX-mean and RS-IMEX-min are very similar but cheaper than the RS-IMEX-$q_C q_I$ variants. Note that deviations of RS-IMEX-31 from the expected shape can be caused by the non optimized load balancing introduced by coupling the compressible and incompressible solver.

4.2 *Testcase 2: Taylor-Green-Vortex*

The Taylor-Green vortex for the Euler equations has been adopted to the non-dimensional isentropic Euler equations in [16]. For details on the initialization the reader is referred to [16]. This inviscid testcase is used as an indicator if the splittings are able to predict a complex three-dimensional behavior. Secondly, we use it to evaluate the computational costs.

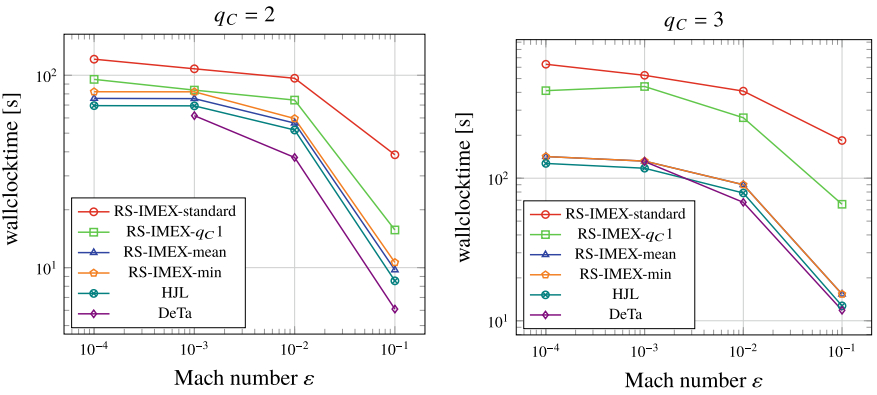

Fig. 1 Comparison of computational time on 24 cores of different splittings for HOT-vortex at different Mach numbers (left: 3rd order, right: 4th order). For $\varepsilon = 10^{-4}$, the DeTa splitting is not plotted due to machine accuracy issues

4.2.1 Evaluation of Solution Quality

We use a Cartesian box with 16^3 elements, a polynomial degree of $q_C = 3$ and the IMEX-ARS-443 scheme from [1]. The convergence criteria of the linear and nonlinear solvers are given in the appendix.

We consider the change of the scaled compressible kinetic energy as a measure for the dissipative properties of the schemes. For the chosen resolution it can be expected that the kinetic energy remains constant and starts decreasing after some time. Figure 2 illustrates that all considered splitting schemes have the same expected behavior. We have omitted the graphs for $\varepsilon \in \{10^{-2}, 10^{-3}, 10^{-4}\}$ as they show similar results as for $\varepsilon = 10^{-1}$. The results of the RS-IMEX-min are not displayed as large oscillations in the change rate of the kinetic energy are present. This instability can be cured by a smaller time step, indicating that for this more complex testcase, the choice of the reference solution could become more crucial than for the HOT-vortex. This issue warrants future study.

4.2.2 Evaluation of Efficiency and RS-IMEX Reference Solution Variant

Figure 2 shows that all linear schemes converge to a limit in computational time for a decreasing Mach number. The DeTa-splitting shows an increase in computational time for $\varepsilon = 10^{-4}$, possibly caused by machine accuracy issues. Here, the HJL-splitting and the RS-IMEX-mean are the most efficient schemes for all Mach numbers. It is obvious that modifying the standard RS-IMEX scheme results in large savings in computational time.

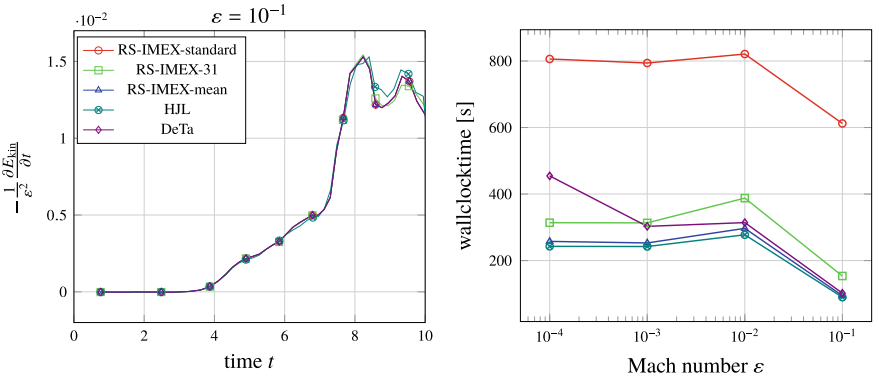

Fig. 2 Left: Scaled change rate of compressible kinetic energy for TGV with different splitting schemes (16^3 spatial elements, $q_C = 3$, IMEX-ARS-443) at $\varepsilon = 10^{-1}$. Symbols additionally visualize superposing curves. Right: Comparison of computational time with 144 cores

Comparing the RS-IMEX-standard with the RS-IMEX-31 scheme shows a nearly constant saving in computational costs, i.e., we see the savings calculating the incompressible solution on a lower polynomial degree, but do not see a Mach number dependent influence of a less accurate incompressible reference solution. The same results hold for the RS-IMEX-mean variant, which is slightly more efficient than the RS-IMEX-31 scheme.

5 Conclusion and Outlook

In the low Mach number limit, explicit time integration of the isentropic Euler equations becomes inefficient due to the prohibitively strict CFL condition. Established methods of overcoming this limitation are based on flux splittings which aim at separating fast and slow waves. A number of different formulations exist in literature, but the identification of the best approach is still elusive.

In this work, we have presented a contribution towards the goal of identifying and evaluating suitable splittings. A generalized form of a number of splittings has been introduced in [7]. Taking advantage of this form, we have established a numerical framework based on an IMEX Runge-Kutta discontinuous Galerkin discretization that allows a side-by-side comparison of the splitting methods. The considered testcases show that the particular choice of the splitting has hardly any influence on accuracy, but it can affect stability and efficiency. With the considered testcases, it is not possible to identify the most efficient scheme as it differs for the two testcases. It occurred that the splitting based on Degond and Tang (DeTa) [4] and the splitting based on Haack, Jin and Liu (HJL) [5] are most efficient but the RS-IMEX-mean scheme can compete in all cases. Nevertheless, the RS-IMEX-standard splitting scheme can be improved either using RS-IMEX-mean or RS-IMEX-$q_C q_I$. Especially if the calculation of the incompressible solution is computationally costly as for the Taylor-Green-Vortex, RS-IMEX-$q_C q_I$ can improve the standard RS-IMEX scheme significantly. Choosing the minimum as a reference solution (RS-IMEX-min) for this testcase results in a less stable scheme, while the - comparably simple - RS-IMEX-mean variant was successful.

Future research will include a more detailed view on the stability of the splittings. Moreover, testcases where both fast and slow characteristics have a significant influence on the solution and testcases related to droplet dynamics will be considered for the comparison. Furthermore the splittings will be compared against a fully explicit or implicit scheme.

Acknowledgements J. Zeifang has been supported by the German Research Foundation (DFG) through the International Research Training Group GRK 2160: Droplet Interaction Technologies. K. Kaiser has been partially supported by the German Research Foundation (DFG) through project No. 361/6-1; his study was supported by the Special Research Fund (BOF) of Hasselt University. F. Massa is supported by the Supporting Talented Researchers (STaRS) program of the University of Bergamo. We acknowledge the support and the computing time provided by the High Performance Computing Center Stuttgart (HLRS) through the *hpcdg* project.

Appendix

The relative convergence tolerances for the implicit method used in Sect. 4 are summarized in Table 2.

Table 2 Relative abort tolerances used by the implicit solver for HOT-vortex (left) and TGV (right). Note that *ic* denotes the tolerances for the incompressible solver

Tolerance	$\varepsilon_{\text{GMRES}}$	$\varepsilon_{\text{Newton}}$	$\varepsilon_{\text{GMRES,ic}}$	$\varepsilon_{\text{Newton,ic}}$	$\varepsilon_{\text{GMRES}}$	$\varepsilon_{\text{Newton}}$	$\varepsilon_{\text{GMRES,ic}}$	$\varepsilon_{\text{Newton,ic}}$
RS-IMEX-standard	10^{-6}	–	10^{-4}	10^{-3}	10^{-3}	–	10^{-3}	10^{-3}
RS-IMEX-$q_C q_I$	10^{-6}	–	10^{-4}	10^{-3}	10^{-3}	–	10^{-3}	10^{-3}
RS-IMEX-mean	10^{-6}	–	–	–	10^{-3}	–	–	–
RS-IMEX-min	10^{-6}	–	–	–	–	–	–	–
HJL	10^{-6}	–	–	–	10^{-3}	–	–	–
DeTa	10^{-2}	10^{-6}	–	–	10^{-1}	10^{-3}	–	–

References

1. Ascher, U.M., Ruuth, S., Spiteri, R.: Implicit-explicit Runge-Kutta methods for time-dependent partial differential equations. Appl. Numer. Math. **25**, 151–167 (1997)
2. Boscarino, S., Russo, G., Scandurra, L.: All Mach number second order semi-implicit scheme for the Euler equations of gasdynamics. J. Sci. Comput. **77**, 850–884 (2018)
3. Cordier, F., Degond, P., Kumbaro, A.: An asymptotic-preserving all-speed scheme for the Euler and Navier-Stokes equations. J. Comput. Phys. **231**, 5685–5704 (2012)
4. Degond, P., Tang, M.: All speed scheme for the low Mach number limit of the isentropic Euler equation. Commun. Comput. Phys. **10**, 1–31 (2011)
5. Haack, J., Jin, S., Liu, J.G.: An all-speed asymptotic-preserving method for the isentropic Euler and Navier-Stokes equations. Commun. Comput. Phys. **12**, 955–980 (2012)

6. Hindenlang, F., Gassner, G., Altmann, C., Beck, A., Staudenmaier, M., Munz, C.D.: Explicit discontinuous Galerkin methods for unsteady problems. Comput. Fluids **61**, 86–93 (2012)
7. Kaiser, K.: A high order discretization technique for singularly perturbed differential equations. Ph.D. thesis, RWTH Aachen University, Hasselt University (2018)
8. Kaiser, K., Schütz, J.: A high-order method for weakly compressible flows. Commun. Comput. Phys. **22**(4), 1150–1174 (2017)
9. Kaiser, K., Schütz, J., Schöbel, R., Noelle, S.: A new stable splitting for the isentropic Euler equations. J. Sci. Comput. **70**, 1390–1407 (2017)
10. Klainerman, S., Majda, A.: Singular limits of quasilinear hyperbolic systems with large parameters and the incompressible limit of compressible fluids. Commun. Pure Appl. Math. **34**, 481–524 (1981)
11. Klein, R.: Semi-implicit extension of a Godunov-type scheme based on low Mach number asymptotics I: One-dimensional flow. J. Comput. Phys. **121**, 213–237 (1995)
12. Kopriva, D.A.: Implementing Spectral Methods for Partial Differential Equations: Algorithms for Scientists and Engineers, 1st edn. Springer (2009)
13. Liu, H., Zou, J.: Some new additive Runge-Kutta methods and their applications. J. Comput. Appl. Math. **190**(1–2), 74–98 (2006)
14. Noelle, S., Bispen, G., Arun, K.R., Lukáčová-Medvid'ová, M., Munz, C.D.: A weakly asymptotic preserving low Mach number scheme for the Euler equations of gas dynamics. SIAM J. Sci. Comput. **36**, B989–B1024 (2014)
15. Schleper, V.: A HLL-type Riemann solver for two-phase flow with surface forces and phase transitions. Appl. Numer. Math. **108**, 256–270 (2016)
16. Zeifang, J., Kaiser, K., Beck, A., Schütz, J., Munz, C.D.: Efficient high-order discontinuous Galerkin computations of low Mach number flows. Commun. Appl. Math. Comput. Sci. **13**(2), 243–270 (2018)

Enabling Simulations of Droplets with the Direct Simulation Monte Carlo Method

Wladimir Reschke, Marcel Pfeiffer and Stefanos Fasoulas

Abstract The evaporation behaviour of droplets changes with their size. Most numerical tools to simulate evaporation phenomena of droplets solve macroscopic models such as the Navier-Stokes equations. These numerical tools have an advantage in computational effort compared to tools solving microscopic models such as the Boltzmann equation. However, macroscopic models lose physical validity for microscopic scales. One goal is therefore to estimate the necessary level of microscopic modelling for droplet evaporation. This requires a tool capable of solving a microscopic model, simulating evaporation of droplets, and which can be used on large computational domains. For this, the Direct Simulation Monte Carlo method is applied, which is capable of capturing microscopic effects on a larger domain. Two functionalities have been added to simulate droplets: a literature-based microscopic evaporation model and spherical moving bodies, which are independent of a body fitted mesh. With these functionalities, droplet size change resulting from evaporation and Brownian motion is simulated. This marks the first steps in order to compare results with macroscopic based simulation tools and estimate the necessary level of microscopic modelling.

1 Introduction

Droplet evaporation is an essential part in many technical applications such as combustion or spray injections. These applications often involve droplets of microscopic scale and the evaporation behaviour drastically changes with droplet size because of microscopic phenomena. Most numerical approaches for handling of

W. Reschke (✉) · M. Pfeiffer · S. Fasoulas
Institute of Space Systems, Pfaffenwaldring 29, 70569 Stuttgart, Germany
e-mail: reschke@irs.uni-stuttgart.de

M. Pfeiffer
e-mail: mpfeiffer@irs.uni-stuttgart.de

S. Fasoulas
e-mail: fasoulas@irs.uni-stuttgart.de

G. Lamanna et al. (eds.), *Droplet Interactions and Spray Processes*,
Fluid Mechanics and Its Applications 121,
https://doi.org/10.1007/978-3-030-33338-6_5

droplet evaporation are solving macroscopic models such as the Navier-Stokes equation. These models often assume local thermodynamic equilibrium which is not valid for microscopic scales. Microscopic based simulations that solve the Boltzmann equation have the advantage to capture the occurring physical processes but are limited to small scales because of the high computational effort.

Simulations of gas-liquid interactions solving microscopic models in literature are often limited to small scales and are conducted in order to understand and characterize evaporation processes [15, 17, 18]. Only a few researchers conducted microscopic-based simulations of droplet evaporation [9] and condensation growth [4] for larger scale problems. Up to date, the impact of microscopic models on macroscopic scales is of major interest, especially, when estimating the necessary level of detail that is required for the simulation of droplet-gas interactions.

Our goal is to investigate the necessity of microscopic modelling and its influences on macroscopic properties. Here, we show the first steps that enable micro-droplet simulations on a macroscopic scale using microscopic modelling. We use the particle simulation tool PICLas[1] [5] and extend the therein incorporated Direct Simulation Monte Carlo (DSMC) method [2]. The DSMC method approximately solves the Boltzmann equation

$$\frac{\partial f}{\partial t} + \mathbf{v} \cdot \nabla_{\mathbf{x}} f = \left.\frac{\partial f}{\partial t}\right|_{Coll}, \tag{1}$$

which describes the microscopic gas state and its changes, using the particle distribution function $f(\mathbf{x}, \mathbf{v}, t)$ that depends on the particles' position $\mathbf{x}$, velocity $\mathbf{v}$, time t, and $\frac{\partial f}{\partial t}|_{Coll}$, which represents the Boltzmann collision integral. The solution of the gas state is found by directly simulating particles and their interaction with one another. Herein, the particle distribution function $f(\mathbf{x}, \mathbf{v}, t)$ of the gas system is statistically approximated with N_p representative discrete particles distributed in space. Additionally, not all real molecules N_real are simulated but the simulation particles N_sim are weighted with $W_\mathrm{p} = N_\mathrm{real}/N_\mathrm{sim}$. Particle collisions are treated statistically and the appropriate probabilities are calculated with phenomenological models [3].

This paper summarises the new developments towards simulation of droplets with the DSMC method. The extensions include a model to treat liquid surfaces and an approach to simulate moving spherical droplets within a DSMC domain inside a body-fitted mesh. First, the implemented models for the treatment of liquid surface boundaries are introduced. Next, the implementation of macroscopic spheres that are required for the treatment of droplets and the necessary extensions of particle-tracking algorithms are explained. In the last section, results obtained from two simulations for testing the implementations are shown.

[1] https://github.com/piclas-framework/piclas.

2 Liquid Surface

The interaction of simulation particles with surfaces is described by scattering kernels [12, 19]. Here, particles are diffusively scattered on the surface by sampling the new velocities from probability distribution functions [20]. In tangential direction the velocities are sampled from a normal distribution F_N and the perpendicular velocity from a Rayleigh distribution F_R.

DSMC particles that collide with liquid surfaces are treated with a model introduced by Tsuruta [17] where the probability for a particle to condense and being removed from the gas domain is defined by the condensation coefficient

$$\sigma_c = \alpha \left[1 - \beta \exp\left(-\frac{m_p \, v_\perp^2}{2 \, k_B \, T_{liq}} \right) \right], \tag{2}$$

with the species specific condensation parameters α and β, the velocity perpendicular to the surface $v_\perp$, the Boltzmann constant k_B, the mass of the incident particle m_p, and the liquid temperature T_{liq}. Velocities perpendicular to the surface of reflected particles are sampled from a scaled Rayleigh distribution [18] given by:

$$F_{r,\perp} = \left(1 - \alpha + \alpha\beta \, \exp\left(\frac{-m_p \, v_\perp^2}{2 \, k_B \, T_{liq}} \right) \right) \left(1 - \alpha \, \frac{1-\beta}{2} \right)^{-1} F_R. \tag{3}$$

For the emission from liquid type surfaces, an appropriate number (N_{in}) of particles are created on the surface. The particle surface flux $\dot{n}$ that represents the evaporation flux is calculated using the Hertz Knudsen equation [7]. For a liquid surface area A_{liq} it is derived from the equilibrium distribution at a given temperature T_{liq} and effective saturation pressure $p_s^\star$, yielding

$$\dot{n} = \sigma_c \, A_{liq} \, \frac{p_s^\star}{\sqrt{2\pi \, m_p \, k_B \, T_{liq}}}. \tag{4}$$

The saturation pressure p_s for flat surfaces is calculated with the Antoine equation [1]

$$\log_{10}(p_s) = A - \frac{B}{C + T_{liq}}, \tag{5}$$

with the species specific parameters A, B, and C that are taken from the NIST database [11]. The effective saturation pressure is influenced by the surface curvature of the liquid interface, which can change drastically at microscopic droplet sizes. Consequently, it is calculated according to the Kelvin law [10]:

$$p_s^\star = p_s \left[\exp\left(\frac{\tau_s M}{\rho N_A k_B T_{liq}} \, \frac{2}{r} \right) \right], \tag{6}$$

with surface tension τ_s, molar mass M, Avogadro number N_A, the liquid density ρ, and the droplet radius r. Velocities of emitted particles in perpendicular direction to the surface are again sampled from a scaled Rayleigh distribution [18] given by:

$$F_{e,\perp} = \left(1 - \beta \exp\left(\frac{-m_p v_\perp^2}{2 k_B T_{liq}}\right)\right)\left(1 - \frac{\beta}{2}\right)^{-1} F_R. \tag{7}$$

3 Spheres Inside the DSMC Domain

PICLas uses body-fitted, hexahedral and unstructured computational meshes [8]. Consequently, it is necessary to track each particle in order to consider boundary interactions as well as to find the respective computational cell where it is located in or moves to. In PICLas, different tracking algorithms are implemented that differ by the representation of grid faces and the corresponding particle localization concept. The grid faces are either approximated with triangles and particles are traced in regard to these triangles [16], or the grid faces are described with (bi-)linear and curvilinear faces [13]. Depending on the chosen face representation, the respective algorithms are used.

Here, each particle is traced starting from the initial particle position $\mathbf{c}$ until its end position is reached and the appropriate element is found. Therefore, all faces of the respective elements it travels through, are checked for intersections. For this purpose, the particle position is described by its path

$$\mathbf{x} = \mathbf{c} + \alpha_1 \mathbf{t_1} \quad | \quad \alpha_1 \in [0, 1], \tag{8}$$

where $\mathbf{x}$ is the end position of the considered particle, $\mathbf{c}$ is the initial position, α_1 is the relative length of particle trajectory within a simulation time step, and $\mathbf{t_1}$ is the particle trajectory. In the case a considered particle intersects a face ($0 \leq \alpha_1 \leq 1$), the next adjacent element is checked or the corresponding boundary condition of this face is applied.

3.1 Extension of the Tracking Routines

The described tracking routines were extended to treat computational cells, which contain macroscopic spheres. These spheres are independent from the computational mesh, move freely inside the domain and interact with DSMC particles. Here, the considered macroscopic sized spheres with $\mathbf{r} = (r_x, r_y, r_z) : r_x = r_y = r_z$ are described by

$$|\boldsymbol{\chi} - (\boldsymbol{\zeta} + \alpha_2 \mathbf{t_2})|^2 = |\mathbf{r}|^2 \quad | \quad \alpha_2 \in [0, 1], \tag{9}$$

with the position of the sphere surface $\boldsymbol{\chi}$, the center position $\boldsymbol{\zeta}$, the radius $\mathbf{r}$, the relative length of the center trajectory α_2, and the center trajectory $\mathbf{t_2}$.

The first step to consider macroscopic spheres in a computational cell is the transformation of the DSMC particles' position to a relative position of the sphere center. Additionally, the particle trajectory is transformed relative to the sphere trajectory. This procedure is schematically shown in Fig. 1 and calculated according to

$$\mathbf{c}^\star = \mathbf{c} - \boldsymbol{\zeta}, \tag{10}$$

$$\mathbf{t}^\star = \mathbf{t_1} - \mathbf{t_2}. \tag{11}$$

This transformation reduces the problem to an intersection of a vector and a non-moving sphere. Subsequently, the solution of the quadratic equation

$$A\alpha_1^2 + B\alpha_1 + C = 0, \tag{12}$$

with the parameters

$$A = |\mathbf{t}^\star|^2,$$
$$B = \mathbf{c}^\star \cdot \mathbf{t}^\star,$$
$$C = |\mathbf{c}^\star|^2 - |\mathbf{r}|^2,$$

provides the solution for α_1 and the intersection position is calculated with Eq. (8). The position of the macroscopic sphere center $\boldsymbol{\zeta}$ is updated according to Eq. (9) after all DSMC particles were tracked.

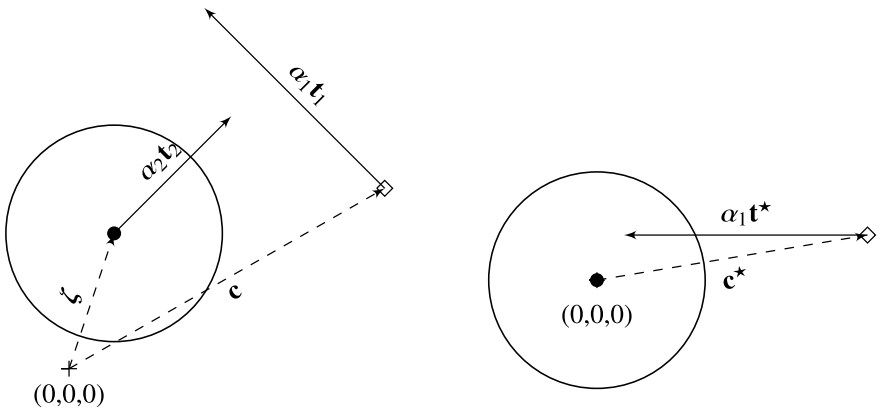

Fig. 1 Sketch showing the transformation of position and trajectory. The left sketch shows the position and trajectory in mesh reference coordinates. The left sketch visualizes the transformed position and trajectory in reference to the sphere center

3.2 Intersection with Spheres After Boundary Interactions

If a particle collides with a surface boundary during one time step before an intersection with a macroscopic sphere is calculated, additional conditions have to be considered. The particle trajectory changes ($\mathbf{t}_{1,0} \rightarrow \mathbf{t}_{1,1}$) and consequently the spheres' center position and trajectory length have to be adapted for the next intersection treatment.

Figure 2 shows a sketch of such a tracking trajectory alteration and the necessary adaptions during one time step. In this case, Eqs. (10) and (11) are extended to

$$\mathbf{c}^{\star} = \mathbf{c} - (\boldsymbol{\zeta} + \hat{\alpha}\mathbf{t_2}), \tag{13}$$

$$\mathbf{t}^{\star} = \mathbf{t_{1,i}} - (1 - \hat{\alpha})\mathbf{t_2}. \tag{14}$$

where $\hat{\alpha}$ represents the relative particle trajectory that the DSMC particle has already moved in the current time step. For each tracked particle, the relative trajectory is adapted after each boundary or sphere intersection according to

$$\hat{\alpha}_{\mathrm{n}} = \hat{\alpha}_{\mathrm{n}-1} + (1 - \hat{\alpha}_{\mathrm{n}-1})\alpha_1. \tag{15}$$

3.3 Influence of Collisions on Macroscopic Spheres

Each macroscopic sphere is described by a spin, momentum and internal energy that change due to collisions with DSMC particles. The transmitted momentum and spin rate are calculated according to

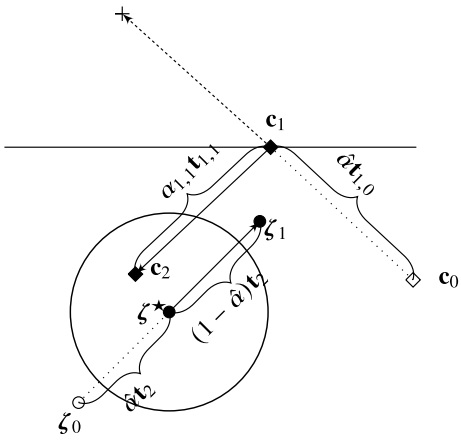

Fig. 2 Sketch showing the geometry, paths and transformation of a tracked DSMC particle after a boundary interaction for the purpose of calculating intersections with a sphere

$$\mathbf{F}_i = \frac{m_i \Delta \mathbf{v}_i}{\Delta t}, \qquad \mathbf{M}_i = \mathbf{r}_i \times \mathbf{F}_i, \tag{16}$$

where $\mathbf{F}_i$ is the transmitted force, $\mathbf{M}_i$ the corresponding angular momentum in regard to the intersection point $(\boldsymbol{\zeta} + \mathbf{r}_i)$, m_i a DSMC particles' mass and Δt the corresponding time step. The total force $\mathbf{F}$ and spin momentum $\mathbf{M}$ are calculated by summing over the number of collisions N_{coll}

$$\mathbf{F} = \sum_{i}^{N_{\text{coll}}} \mathbf{F}_i, \qquad \mathbf{M} = \sum_{i}^{N_{\text{coll}}} \mathbf{M}_i, \tag{17}$$

and are used to adjust the velocity $\mathbf{v}$ and spin $\boldsymbol{\omega}$ using the macroscopic sphere mass m_{MS} and moment of inertia Θ_{MS}

$$\Delta \mathbf{v} = m_{\text{MS}}^{-1} \cdot \mathbf{F} \Delta t, \qquad \Delta \boldsymbol{\omega} = \Theta_{\text{MS}}^{-1} \cdot \mathbf{M} \Delta t. \tag{18}$$

4 Simulations

The new DSMC-extensions of PICLas were tested using two simulation setups, which are presented here. In both setups, a resting sphere with a radius of $r = 2 \times 10^{-6}$ m, having a density of $\rho_{H_2O} = 997\,\text{kg}\,\text{m}^{-3}$ and temperature $T_{\text{liq}} = 300\,\text{K}$, is positioned at the center of the simulation domain. The domain consists of a cube of $10 \times 10 \times 10$ computational cells and a cube edge length of $x = 1 \times 10^{-5}$ m. The gas inside the simulation domain is initialized with two species (H_2O, O_2) using the parameters from Table 1. At the domain boundaries, a surface flux [6] is applied, which is comparable to a pressure condition leading to a constant temperature and density inside the domain. That means, particles that leave the domain are removed and additional particles are emitted into the domain using the parameters in Table 1.

Table 1 Selected simulation parameters (time step, end time, gas temperature, particle weighting factor, and molecule number density for H_2O and O_2). The same parameters are applied at the surface flux boundaries

Setup	Δt (s)	t_{end} (s)	T (K)	W_{p} (−)	$n_{H_2O,\text{vap}}$ (m^{-3})	n_{O_2} (m^{-3})
1	1×10^{-9}	1.0×10^{-5}	300–320	1×10^{4}	$0, 5 \times 10^{23}$	5, 8, 12×10^{23}
2	1×10^{-10}	1.5×10^{-5}	300	1×10^{3}	0	1×10^{25}

4.1 Droplet Evaporation

In the first setup, particles evaporate from a single spherical droplet and therefore, the sphere changes its size. Meanwhile, the sphere center remains stationary and the droplet temperature remains constant in each simulation. The simulation is repeated for different temperatures in the chosen temperature range. Additionally, different density cases are considered: first, two pure-vapour density cases without oxygen density ($n_{O_2} = 0$) and then three oxygen density cases without initial vapour density.

In every simulation the droplet radius decreases constantly ($\frac{\Delta r}{\Delta t} = \text{const.}$), because the sphere temperature remains constant, which is in a good agreement with the results published in Ref. [9]. Consequently, the decrease is described with the initial and the end state at $t = 10\mu s$ as depicted in Fig. 3.

Figure 4 shows the change of the radius at different temperatures and the corresponding densities. The solid black lines represent the radius decrease for $n_{H_2O,vap} = 0$ and $5 \times 10^{23} m^{-3}$ without oxygen background gas. The radius of the droplet decreases slower for higher vapour densities because of an increasing condensation rate. At the saturation density $n_{H_2O,vap} = n_{H_2O,sat}$ the droplet radius starts to

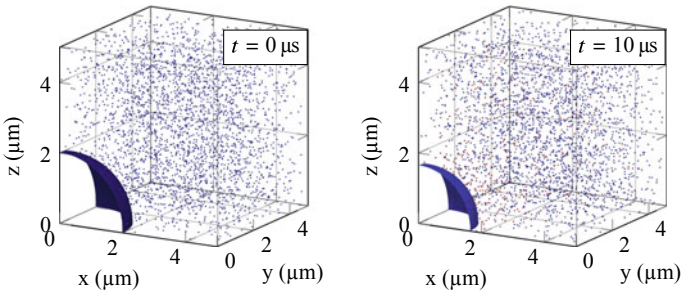

Fig. 3 Results for macroscopic sphere evaporation with $n_{H_2O,vap} = 0$, $n_{O_2} = 5 \times 10^{23} m^{-3}$ and $T = 300K$ at start (left) and end (right) of the simulation

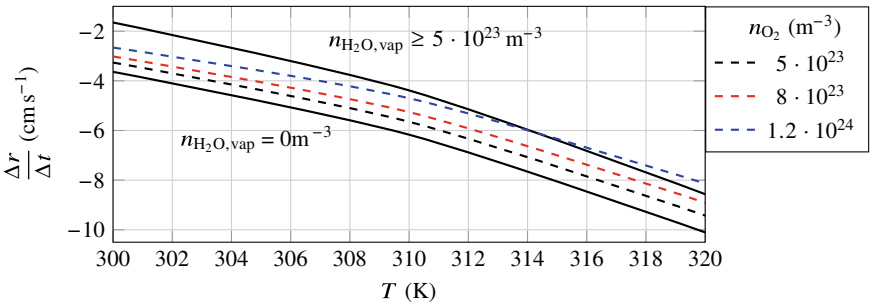

Fig. 4 Sphere radius decrease at different temperatures for various pure vapour (solid) and pure oxygen gas (dashed) densities

increase. For the temperatures 300, 310, and 320K, the corresponding saturation number densities are 8.53×10^{23}, 1.46×10^{24}, and 2.39×10^{24} m^{-3}.

Increasing the oxygen density without initial vapour density decelerates the evaporation because a vapour layer is formed around the droplet and the evaporation becomes diffusion driven. The density of the formed vapour layer can be estimated from Fig. 4 by comparing the dashed lines (oxygen background gas) with the solid lines (pure vapour simulations).

4.2 Brownian Motion

The momentum exchange is tested with the second simulation while evaporation processes at the sphere are disabled. The simulation is repeated three times with different random-number seeds. For each case, this leads to different initial velocities and spatial distribution of the DSMC particles.

The spheres display a random motion in the simulations and the path of the sphere centers is shown in Fig. 5. Each sphere starts to move because of the non-uniform pressure on the sphere surface resulting from the momentum exchange with DSMC particle collisions. This behaviour is similar to Brownian motion [14], which is observed in experiments.

5 Conclusion and Outlook

Understanding micro-droplet gas interactions is necessary for many industrial applications. Most common approaches neglect thermodynamic non-equilibrium effects for the simulation of droplets or are limited to quasi-steady conditions. In order to simulate micro-droplet gas interactions from a microscopic point of view, the DSMC module of the particle simulation tool PICLas has been extended.

The boundary modelling was extended by a literature-based model for the treatment of liquid interfaces. Here, condensation is treated by a description of a condensation coefficient and an appropriate particle flux is calculated for emission. Additionally, perpendicular velocities of reflected and emitted DSMC particles are sampled from a scaled Rayleigh distribution.

Simulations show a constant evaporation rate during each chosen case. The magnitude of the evaporation rate is dependent on temperature and vapour density. An increase in vapour density results in a decrease of evaporation rate. Similarly, an increase in non-vapour density results in the formation of a vapour layer around the droplet that leads to a decrease of evaporation rate.

The particle tracking algorithms in PICLas were extended with macroscopic sized spheres to account for droplets inside the gas domain that interact with DSMC particles. These interactions lead to momentum and energy exchange between the spheres and DSMC particles.

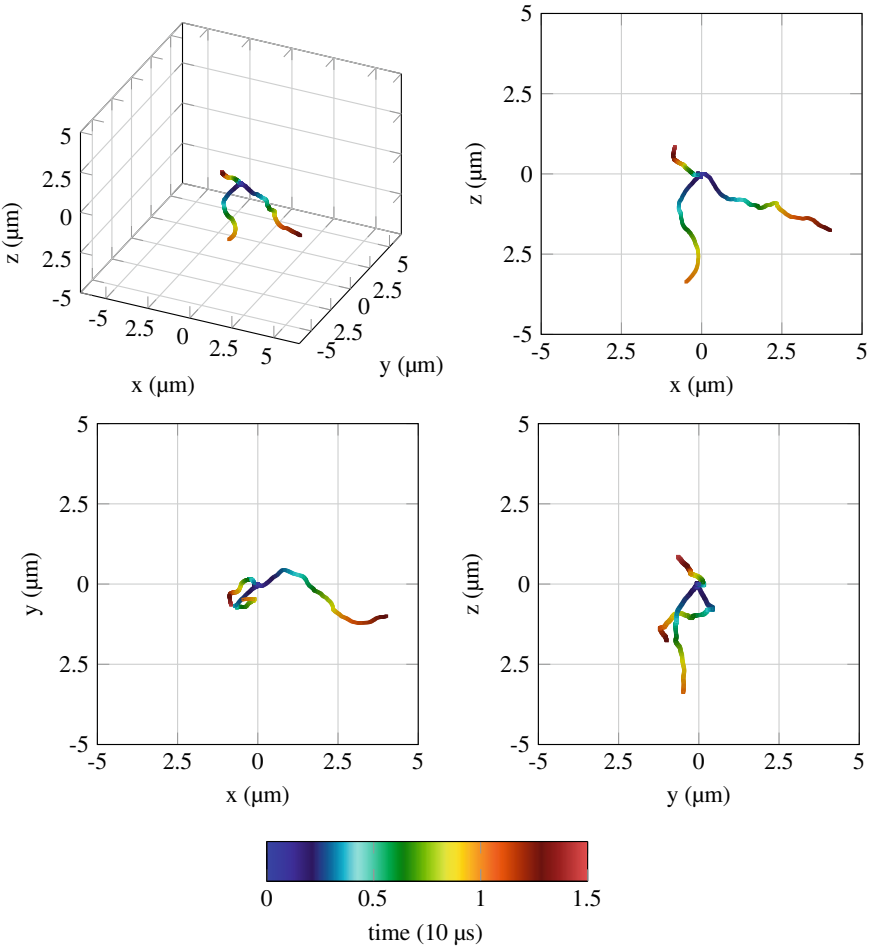

Fig. 5 Spatial evolution of macroscopic sphere center due to non-uniformly distributed collisions of DSMC particles on the sphere surface and momentum exchange

The tracking extensions allow for momentum and energy transfer on the macroscopic sphere, which lead to a random motion of the sphere. Enabling evaporation in addition to motion of the sphere might additionally influence this motion, and vice versa. In the evaporation simulations, the background density of a non-vapour gas reduced the evaporation rate because a vapour layer formed around the droplet. With Brownian motion, this vapour layer might be changed, which leads to an increase of the evaporation rate. However, further simulations and comparison with experiments are necessary.

The shown implementations and tests are a first step towards enabling simulations to evaluate the necessity of non-equilibrium assumptions on micro-droplet

gas interaction. Therefore, further simulations must be performed and compared to experiments as well as to simulations using equilibrium solvers.

Acknowledgements The authors thank the German Research Foundation (DFG, Deutsche Forschungsgemeinschaft) for funding this research within the project Droplet Interaction Technologies (DROPIT) of the International Research Training Groups (IRTG-2160).

References

1. Antoine, C.: Pressure calculation of various vapours. (Calcul des tensions de diverses vapeurs). Comptes rendus hebdomadaires des séances de l'Académie des Sciences **107**:778–780 (1888)
2. Bird, G.A.: Molecular Gas Dynamics and the Direct Simulation of Gas Flows. Clarendon, Oxford (1994)
3. Borgnakke, C., Larsen, P.S.: Statistical collision model for Monte Carlo simulation of polyatomic gas mixture. J. Comput. Phys. **18**(4), 405–420 (1975)
4. Carey, V., Oyumi, S., Ahmed, S.: Post-nucleation growth of water microdroplets in supersaturated gas mixtures: a molecular simulation study. Int. J. Heat Mass Transf. **40**(10), 2393–2406 (1997)
5. Fasoulas, S., Munz, C.-D., Pfeiffer, M., Beyer, J., Binder, T., Copplestone, S., Mirza, A., Nizenkov, P., Ortwein, P., Reschke, W.: Combining particle-in-cell and direct simulation Monte Carlo for the simulation of reactive plasma flows. Phys. Fluids **31**(7), 072006 (2019)
6. Garcia, A.L., Wagner, W.: Generation of the maxwellian inflow distribution. J. Comput. Phys. **217**, 693–708 (2006)
7. Hertz, H.: Ueber die Verdunstung der Flüssigkeiten, insbesondere des Quecksilbers, im luftleeren Raume. Ann. Phys. **253**(10), 177–193 (1882)
8. Hindenlang, F., Bolemann, T., Munz, C.-D.: Mesh curving techniques for high order discontinuous galerkin simulations. In: IDIHOM: Industrialization of High-Order Methods-A Top-Down Approach, pp. 133–152. Springer (2015) [Online; release V2.4]
9. Holyst, R., Litniewski, M., Jakubczyk, D.: Evaporation of liquid droplets of nano- and micrometer size as a function of molecular mass and intermolecular interactions: experiments and molecular dynamics simulations. Soft Matter **13**(35), 5858–5864 (2017)
10. Köhler, H.: The nucleus in and the growth of hygroscopic droplets. Trans. Faraday Soc. **32**, 1152–1161 (1936)
11. Linstrom, P.J., Mallard, W.G.: The NIST chemistry webbook: a chemical data resource on the internet. J. Chem. Eng. Data **46**(5), 1059–1063 (2001)
12. Maxwell, J.: On stresses in rarefied gases arising from inequalities of temperature (abstract) Phil. Mag **27**, 304 (1878)
13. Ortwein, P., Copplestone, S.M., Munz, C.-D., Binder, T., Reschke, W., Fasoulas, S.: A particle localization algorithm on unstructured curvilinear polynomial meshes. Comput. Phys. Commun. **235**, 63–74 (2019)
14. Pusey, P.N.: The study of Brownian motion by intensity fluctuation spectroscopy. Philos. Trans. R. Soc. London. Ser. A, Math. Phys. Sci. **293**(1402), 429–439 (1979)
15. Schlesinger, D., Sellberg, J.A., Nilsson, A., Pettersson, L.G.M.: Evaporative cooling of microscopic water droplets in vacuo: molecular dynamics simulations and kinetic gas theory. J. Chem. Phys. **144**(12), 124502 (2016)
16. Stindl, T.: Entwicklung und Untersuchung eines Partikelverfahrens zur Simulation elektromagnetischer Wechselwirkungen in verdünnten Plasmaströmungen. dissertation, Universität Stuttgart (2015)
17. Tsuruta, T.: Molecular boundary conditions and temperature jump at liquid-vapor interface. In: AIP Conference Proceedings, vol. 663. pp. 988–995. AIP (2003)

18. Tsuruta, T., Nagayama, G.: A microscopic formulation of condensation coefficient and interface transport phenomena. Energy **30**(6), 795–805 (2005)
19. Wadsworth, D.C., VanGilder, D.B., Dogra, V.K.: Gas-surface interaction model evaluation for DSMC applications. Technical report, DTIC Document (2002)
20. Walck, C.: Statistical Distributions for Experimentalists. Particle Physics Group (2007)

Droplet–Wall Interaction

Fabrication and Evaluation Methods of Micro-structured Surfaces for Droplet Impact Experiments

Patrick Foltyn, Markus Guttmann, Marc Schneider, Stephanie Fest-Santini, Dorthe Wildenschild and Bernhard Weigand

Abstract The continuously increasing importance of micro-structured surfaces in technical applications and research require further development and use of reliable manufacturing processes as well as investigation methods for quality assurance. An overview of possible reproduction processes will be given and a new fabrication route in combination of laser lithography and nickel electroplating to provide stable mold inserts is introduced. Three methods for inspecting the reproduction quality of the polymeric micro-structured surfaces are presented discussing the respective advantages and disadvantages as well as the limiting factors diminishing the resolving power. The replication quality of four micro-structured surfaces produced with the hot embossing method is investigated, and the results are compared using these three techniques. Additionally, the principle investigation strategy of a test rig for droplet impact experiments on micro-structured surfaces is going to be outlined. Finally, preliminary results of droplet impacts on a structured surface are shown and discussed.

P. Foltyn (✉) · B. Weigand
Institute of Aerospace Thermodynamics (ITLR), University of Stuttgart, Stuttgart, Germany
e-mail: patrick.foltyn@itlr.uni-stuttgart.de

M. Guttmann · M. Schneider
Institute of Microstructure Technology (IMT), Karlsruhe Institute of Technology, Karlsruhe, Germany

S. Fest-Santini
Department of Management, Information and Production Engineering, University of Bergamo, Dalmine (BG), Italy

D. Wildenschild
School of Chemical, Biological and Environmental Engineering, Oregon State University, Corvallis, USA

G. Lamanna et al. (eds.), *Droplet Interactions and Spray Processes*,
Fluid Mechanics and Its Applications 121,
https://doi.org/10.1007/978-3-030-33338-6_6

1 Introduction

The research on micro-structured surfaces over the last 25 years has tremendously increased, as the number of annual publications is indicating. The statistics show the number of publications per year searching for "micro-structured surfaces" and "microstructured surfaces" in Google Scholar. While there were only 1320 items published in the year 2000, the number of publications in 2010 quintupled to 6950. In 2018, this number almost doubled again with 12670 publications. This strong increase shows significantly the growing importance of research with micro-structured surfaces. This can be explained by the scientific progress but also by the further increasing capabilities of manufacturing and investigation techniques as well as a technical need of such surfaces.

Based on the classical works of Wenzel in 1936 [28] as well as Cassie and Baxter in 1944 [2], many researchers have investigated the interaction of droplets with smooth and structured surfaces. Droplet impacts have been systematically investigated by Rioboo et al. [20] and Marengo et al. [13] using different surfaces with varying structure and wettability. Courbin et al. [3] have focused on the dynamics of the spreading and imbibition process on surfaces with well-defined micro-patterns. Especially complex surface structures are used to modify the surface wettability used for technical applications like self-cleaning surfaces or improved coating quality. An increase in surface roughness will lead to an increase of the intrinsic wettability in case of hydrophilic surfaces and to a decrease of the intrinsic wettability in case of hydrophobic surfaces [14]. For structured surfaces with a well-defined pattern, deposited droplets on these surfaces will deviate from spherical caps. As a consequence, a variation of the contact angle and the projected distance of the opposite triple points can be observed, as reported in [1, 3, 5, 12, 14]. A deviation of the outcomes compared to perfectly smooth surfaces can not be seen only for static droplet-structure interactions but also for dynamic droplet impacts on structured walls. One type of deviation is e.g. the determination of preferential wetting directions, [11, 22, 25]. In conclusion, the shape and the size of the structure pattern are main parameter on which the wetting morphology depends on significantly.

Consequently, a proper manufacturing and evaluation of these surfaces are very crucial for any research in this topic as well as for the technical applications. What follows, is an overview of possible manufacturing processes of which the mold insert fabrication for the hot embossing process is further outlined. Possible evaluation methods with the respective advantages and disadvantages and first experimental results for droplet impacts on structured surfaces are also discussed.

2 Surface Reproduction and Experimental Methods

2.1 Reproduction of Micro-structured Surface Samples

A vast number of different micro-fabrication techniques are available, which can be chosen in considering the used material, the dimensions of the structure, the number of reproductions and the application of the produced micro-structures. Among them are lithographic processes, etching processes, sputtering, additive micro-fabrications, micro-milling, or molding processes which can be used for the micro-fabrication [21]. For the evaluation of droplet impacts on micro-structured surfaces, it is advantageous to vary the structure patterns and the materials for different wetting behaviors. In the framework of the International Research Training Group "**Drop**let **I**nteraction **T**echnologies" (GRK 2160/1: DROPIT), an investigation of droplet impacts onto structured walls from the top and lateral perspective but also from the bottom view is envisaged. This requires not only a proper micro-structure but also a transparent material whenever possible. Therefore, the surface materials Lexan® (PC), Plexiglas® (PMMA) and Teflon® (PTFE) have been selected.

The produced patterns are steep grooves and arrays of steep squared pillars at micrometric dimensions, as they are depicted in Fig. 1 and given in Table 1. The grooves with a height of 20 μm are due to manufacturing requirements specifically very long pillars with a width of 60 μm and a length of 500 μm. In the direction of the grooves, a gap between each pillar of 15 μm can be found. The spacing perpendicular to the grooves is also 60 μm, see Fig. 1a. The squared pillars with an edge length of 60 μm, 30 μm or 15 μm have also a height of 20 μm, see Fig. 1b and Table 1. The spacing between each pillar is the same size as the width of the respective pillar. In conclusion, the solid fraction remains the same for all structures while the Wenzel roughness factor is increasing with decreasing edge length, see [2, 28]. Acquired images of the surfaces using three different techniques can be found in Figs. 3, 4 and 5.

The polymeric surface samples were manufactured by the Karlsruhe Nano Micro Facility (KNMF) at the Karlsruhe Institute of Technology (KIT), Germany, using

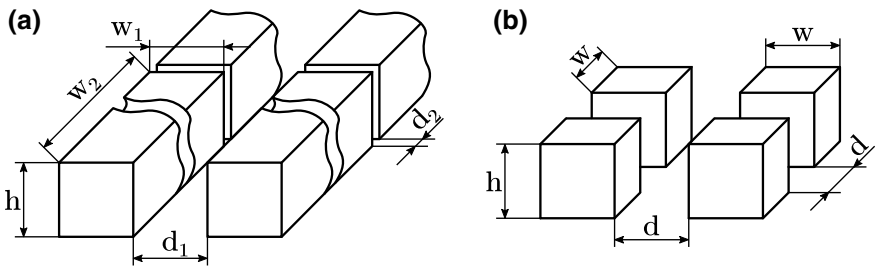

Fig. 1 Available structure patterns of **a** grooves and **b** pillars produced by the KNMF in Karlsruhe, Germany, with the given parameters in Table 1

Table 1 Dimensions of micro-structured surfaces. No. S1 corresponds to grooves, see Fig. 1a and no. S2-S4 are corresponding to pillars, see Fig. 1b

No.	Edge length	Distance	Height
S1	$w_1 = 60\,\mu m$, $w_2 = 500\,\mu m$	$d_1 = 60\,\mu m$, $d_2 = 15\,\mu m$	$h = 20\,\mu m$
S2	$w = 60\,\mu m$	$d = 60\,\mu m$	$h = 20\,\mu m$
S3	$w = 30\,\mu m$	$d = 30\,\mu m$	$h = 20\,\mu m$
S4	$w = 15\,\mu m$	$d = 15\,\mu m$	$h = 20\,\mu m$

Table 2 Process parameters for the hot embossing reproduction of polymeric micro-structured surfaces

Material		Temperature		Force (kN)
		Embossing (°C)	Demolding (°C)	
Lexan®	(PC)	165	105	200
Plexiglas®	(PMMA)	140	40	200
Teflon®	(PTFE)	200	100	175

the hot embossing technique. This technique allows a high replication rate of micro-structured surfaces in pressing a mold with high pressure and temperature into the respective polymeric blank, see Table 2. A broad description of the hot embossing technique can be found e.g. in the book of Worgull [29]. Due to the high efforts of the mold insert production, all four structured patterns were placed next to each other with a blank area in between, see Fig. 2. After the production, the differently structured surfaces are cut into single pieces for the individual experiments.

2.2 Mold Insert Fabrication

The combination of laser lithography and electroplating was used to create a highly pressure and temperature stable thick nickel mold insert for hot embossing experiments. For the master fabrication, first, a 200 nm thick layer of antireflective coating *AZ BAR-Li* (*Microchemicals GmbH, Ulm Germany*), which is also an adhesion promotor, was spin-coated onto a 2 mm thick 4" silicon wafer and then baked at 200 °C for 60 s. Second, a 20 µm thick resist layer *MR10* (*micro resist technologies GmbH, Berlin, Germany*) was spin-coated, followed by a baking step at 95 °C for 30 min.

The latterly four described structure patterns were written into the photoresist with the laser writer *DWL66fs* (*Heidelberg Instruments GmbH, Heidelberg, Germany*) using a 10 mm write head at a laser power of 125 mW. The laser writing allows the fabrication of steep resist structures at micrometric dimensions, as they are depicted in Fig. 1 and given in Table 1. The written structures were then subjected to a Post Exposure Bake (PEB) at 75 °C and subsequently developed in PGMEA for 90 min.

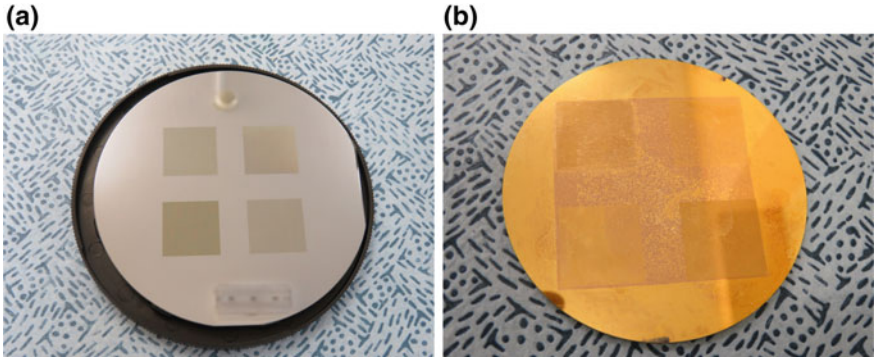

Fig. 2 **a** Silicon wafer with structured resist after laser lithography and **b** Nickel mold insert before removal of Cr/Au layer

A rinsing step in isopropanol and drying with air circulation at 30 °C terminates the fabrication of the structured master, see Fig. 2a. In order to transfer these polymeric structures into a stable metallic mold for the hot embossing process, thermal evaporation was used to prepare the resist structures for electroplating. 7 nm chromium acts as adhesive layer for a 50 nm gold layer as conducting plating base. Afterwards, a microscopic inspection of the resist structures was performed by means of SEM.

Nickel electroplating was carried out within a homemade boric acid containing nickel sulfamate electrolyte at a temperature of 52 °C (plating equipment with an electrolyte volume of 45 L from *Carl Dittmann GmbH & Co. KG, Karlsruhe, Germany*), a pH of 3.5 and a current density started at 0.1 A/dm^2 and increased up to 1.25 A/dm^2. To guarantee a good stability of the mold insert for the hot embossing experiments, the final thickness of the mold was chosen to 2.0 mm. To achieve this, galvanic deposition was carried out up to a height of approximately 2.8 mm (plating time ≈10 d). The desired height was realized using wire-EDM. To continue the mold fabrication, the thick silicon substrate was removed by wet-chemical etching with 30 w.−% KOH solution at 80 °C. The BAR-Li layer was removed by 15 min Reactive Ion Etching with O2 using *Etchlab 200–380* (*Sentech GmbH, Berlin, Germany*) and the resist was stripped using O2/CF4 Plasma Etching (*STP2020; R3T GmbH, Taufkirchen, Germany*) for 30 min at 1200 W and 22 °C. To generate the final outer dimensions of the mold with a diameter of 81 mm, see Fig. 2b, the structures were protected by AZ resist and a second wire-EDM step was performed. After chemical treatment with *AZ400K* (*Microchemicals GmbH*) and isopropanol, followed by the wet-chemical etching of the Cr/Au metallization layers, the SEM characterization of the microstructures concludes the mold insert fabrication. The SEM showed, that all structural elements have been transferred in detail and with sharp edges, what can be also seen by the finally reproduced structure patterns in Figs. 3, 4 and 5.

2.3 Evaluation Methods for Investigating Micro-structured Surfaces

For evaluating micro-structured polymeric surfaces, a compromise between accuracy, effort and gathered information has to be found. In the following, three different methods for surface evaluation are presented: the classical optical microscopy, the Scanning Electron Microscopy (SEM) and the micro Computed Tomography (microCT). The mentioned methods were exemplarily carried out on the Lexan® surfaces.

The non-intrusive inspections of surface patterns for major damages using a classical optical microscope working with transmitted light is very fast, economical and easy. However, the two-dimensional perspective allows only the inspection in the direction of transmittance. This is the reason why local damages might not be detected properly because tilted sides or partial ruptures of the pillar bases might be hidden. Also the interpretation of the projected defects can be very difficult. However, globally extended or severe damages, like rip-off, missing pillars or not fully embossed structures can be detected.

The resolving power of light microscopes is limited to approximately 0.3 μm due to light diffraction and interference and can be calculated by the Abbe criterion:

$$d_0 = 0.61\lambda/(n \sin \alpha) \tag{1}$$

where d_0 represents the minimum resolvable separation, λ the wavelength of the light, n the refractive index and α the half-angle of the aperture of the microscope objective. The numerical aperture, defined as $n \sin \alpha$ is usually indicated on the respective microscope objectives. The calculated distance d_0 is the half diameter of the "Airy disk" which is the distance between the first-order peak and first-order trough of the focused light dot [27, 30].

A Scanning Electron Microscope (SEM) can be used if a higher magnification than approximately 1000× of a classical optical microscope is needed. A well working electron optical system can create a beam diameter of 1 nm or finer, which will lead to a very high magnification. However, delocalization of imaging signals, constraints on beam size due to contrast and visibility considerations, mechanical stability of the setup and the vacuum, degradation of the sample and other influences can limit the resolving power. Nevertheless, for good experimental conditions a magnification of 100,000× or more can be reached [8, 30]. SEM is also a non-intrusive method, if no sputtering of the samples is needed. Two advantages of SEM, which are helpful for the interpretation of structures, are a tiltable specimen stage, allowing also inspections of the structure from a non-perpendicular position, as well as a spatial view.

Both methods, the classical optical microscope and the SEM, are only two-dimensional imaging techniques. MicroCT, instead, is reconstructing a three-dimensional shape from single X-Ray projections, which have been acquired at several angle steps with help of reconstruction algorithms [18, 26]. The reconstructed geometries can be exported and used for further analysis e.g. in CAD-systems or for

numerical simulations. The resolving power of the microCT is dependent amongst other influences on the focal spot size of the X-Ray source, the number of projections, the pixel resolution of the X-Ray detector and the detector aperture [9]. Advanced microCT systems can achieve a resolving power of about 1 µm/voxel. For high resolving power, the sample needs to be small enough to allow optimal projection onto the detector, and must also be mounted very close to the X-Ray source. At a resolution of about 3–4 µm, the micro-structured surface samples had to be cut into $4 \times 4\,mm^2$ sized pieces. Although the measurement principle itself is non-intrusive, this technique is intrusive for this application because of the need to cut samples down in size. Artifacts, e.g. due to non-optimal scan parameters (exposure time, energy levels, contrast challenges), a sample movement, degradation of the material by X-Rays and, if significant, X-Ray scattering can lead to lower reconstruction quality. Additionally, the low attenuation of thin polymeric structures can be a challenge for reconstruction.

2.4 Experimental Test Facility for Investigating Dynamic Droplet Impacts

The droplet impacts on micro-structured surfaces shall be investigated using three different perspectives. Two shadowgraphs, one from the top and one from the lateral perspective are captured simultaneously with one high-speed camera. This will help to determine the morphology of the droplet impact. The bottom view, captured by a second high-speed camera, is in a total-internal reflection configuration and allows to track the liquid spreading inside the structure and the imbibition into the structure. All three perspectives are acquired synchronously at 10 kHz and a resolution of 1 MPx. However, the results discussed in the following will be limited only to the lateral and the top view.

In future, the test rig shall be used to explore the occurring droplet impact phenomena on flat and structured surfaces for full-wetting cases but also for the complete range from wetting to non-wetting behavior.

3 Results and Discussion

3.1 Surface Evaluation

The acquired images with the optical largefield microscope *LEITZ Metalloplan* are shown in Fig. 3. The resolution of the images is 0.93 µm/Px and 0.24 µm/Px, respectively. The increasing magnification was necessary due to an easier investigation of the finer structure items. One drawback of the optical microscope is the bad recognition of the topology of three-dimensional structures. Only by knowing

the structure beforehand, it can be determined which areas are elevated and which areas are the channels of the structure. For simple structures, like presented, this is "straight forward". For more complex structures, it can be helpful to adjust the focal plane incrementally in order to recognize the topology. This multifocal plane approach is also used by modern light microscopes rastering the focal planes and combining the images to one image with fully focal depth over the height of rastering. This avoids then blurriness for out of focus areas. Further, it is important to notice, that the images in Fig. 3, taken by an *IDS UI-3080CP-M-GL Rev.2* with 5.04 MPx and a resolution of 0.24 µm/Px is at the limit of the resolving power of the optical microscope. A further increase of pixels of the camera will not lead to a significant improvement of image quality due to the optical limitations as described in Sect. 2.3 and the Abbe criterion in Eq. (1). For a higher camera resolution, the not perfectly distinct structures will be only smeared over more pixels compared to cameras with a lower resolution.

The SEM images are displayed in Fig. 4. With the help of the significantly higher magnification, a spatial view and the tiltable specimen stage, some ridges on the top of the structure can be detected and measured. In the optical microscope, the corresponding areas of these ridges can be only detected by some darker areas on the structures, e.g. the top and right sides of each pillar in Fig. 3c. Though, the proper interpretation of these areas would have been almost impossible without the SEM investigations. The output of the SEM are only two-dimensional pictures, as shown in Fig. 4. For measuring the dimension of the ridges or also the whole pillars, it is only possible to obtain the dimensions such as the height or the depth in considering the projection of the tilted structure onto the image plane. The tilt of the specimen stage for the shown images is set to 30°.

In contrast to this, the reconstructed microCT-scans, with a resolution of 3.3 µm/voxel in Fig. 5, can give much more information about the pillar shape. With the help of a specially developed routine for evaluating the ridge height, the shape of the pillars and height of the ridges can be determined, see also Fig. 6. However, in comparison to the SEM and the optical microscope, the resolving power of the microCT is usually significantly lower in part because of the very low X-Ray attenuation of the material. This means that features, which are in the size of two voxels and smaller, might not be resolved properly. But also for larger features, the resolving power might not be sufficiently high. The smallest pillars with an edge length of 15 µm (surface S4) are only represented by approximately 5 voxel for each spatial direction. This leads to a blurry and not well defined shape, so that often no orthogonal edges can be determined, see Fig. 5d. The challenge in the post-processing of reconstructed microCT-data is to transform the voxelized representation of surfaces into a smooth triangulated surface. This will make the surfaces usable for further investigations such as numerical simulations. There are several smoothing routines in commercial software packages like *Avizo* [24], but also in open-source software. For this post-processing step, a compromise between smoothing and shape conservation has to be found. In conclusion, a change of shape due to smoothing is acceptable if its magnitude is far lower than the resolution of the microCT scans. Under consideration of the limits in resolving power and the need of smoothing, the possibility

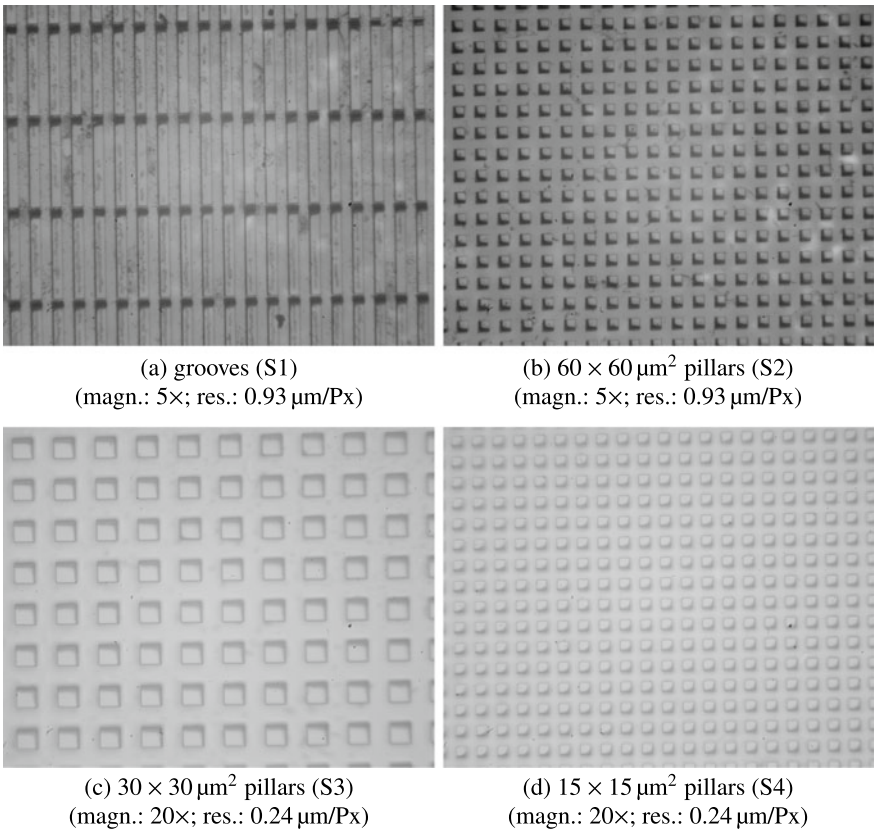

(a) grooves (S1)
(magn.: 5×; res.: 0.93 µm/Px)

(b) $60 \times 60\,\mu m^2$ pillars (S2)
(magn.: 5×; res.: 0.93 µm/Px)

(c) $30 \times 30\,\mu m^2$ pillars (S3)
(magn.: 20×; res.: 0.24 µm/Px)

(d) $15 \times 15\,\mu m^2$ pillars (S4)
(magn.: 20×; res.: 0.24 µm/Px)

Fig. 3 Micro-structured Lexan®-surfaces of different dimensions acquired with optical microscope using a combination of transmitted and reflected light. The magnification of each image is given at the respective image

of the surface export is, nevertheless, very powerful, since simulations can use the same surface patterns for droplet impacts as the experiment itself. The magnitude of deviations between real, exported surfaces and perfect, generic surfaces on the outcome of numerical simulations of droplet impacts will be investigated in the future. Here, also the influence of resolving power of the microCT on the numerical results need to be studied.

In the following, the dimension of one single but "defect" 60 µm pillar of the reconstructed microCT S2 surfaces is analyzed. For the detailed analysis, a separate microCT-scan was performed with a resolution of 2.7 µm/voxel and compared to SEM images. Due to sample preparation and availability of the measurement devices, the scanned surface samples were not identical so that not exactly the same pillar was measured with the SEM and microCT. The surface was reconstructed, exported and the profile along several slices of the pillar analyzed, as depicted in Fig. 6. The

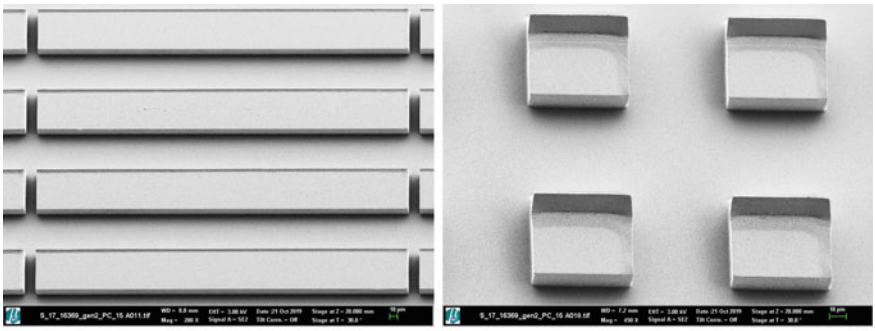

(a) grooves (S1, magn.: 99×) (b) 60 µm × 60 µm (S2, magn.: 400×)

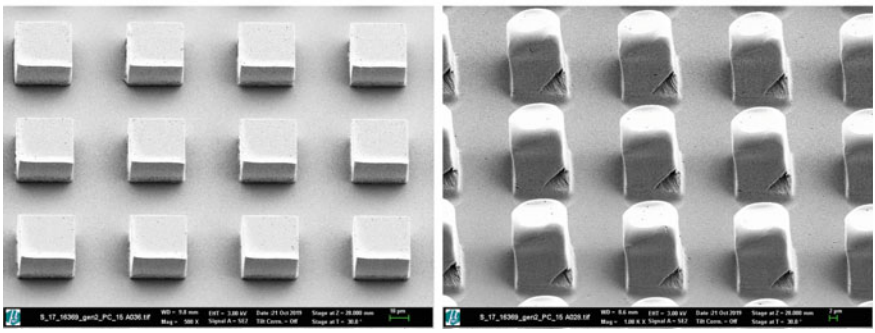

(c) 30 µm × 30 µm (S3, magn.: 300×) (d) 15 µm × 15 µm (S4, magn.: 500×)

Fig. 4 Micro-structured Lexan®-surfaces of different dimensions acquired with Scanning Electron Microscopy (SEM). The magnification of each image is given at the respective image. The specimen stage was tilted by 30°

elevation of the ridge measured by microCT was about 3 voxel or approximately 8 µm and matches very well to the SEM measurements. These findings were expected, since the production procedure can be considered as very reliable during the hot embossing process. The reason for the partially elevated rim might be a sticking nickel mold on the pillars side during the demolding phase of the hot embossing process. The resulting high local forces lead to the observed local deformations in case of large pillars or might elongate the whole pillar in case of smaller edge lengths. In general, the influence of non-perfectly shaped pillars are assumed to be neglectable since the magnitude as well as the number of defect pillars are not very high. However, a numerical simulation of droplets impacting on these exported surfaces might give further information in the future.

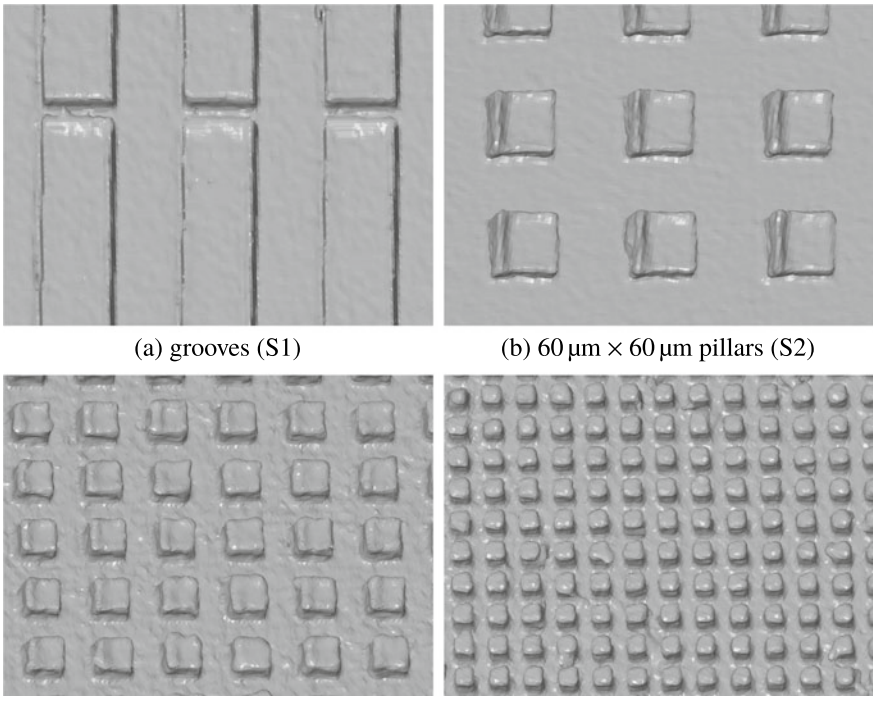

(a) grooves (S1) (b) 60 µm × 60 µm pillars (S2)

(c) 30 µm × 30 µm pillars (S3) (d) 15 µm × 15 µm pillars (S4)

Fig. 5 Micro-structured Lexan®-surfaces of different dimensions acquired with micro Computed Tomography (microCT), reconstructed and exported as stl.-surface. Resolution: 3.3 µm/voxel

3.2 Droplet Impact on Micro-structured Surfaces

Preliminary experiments on the previously mentioned test rig are used to determine the fundamental morphology of droplet impacts on such micro-structured surfaces. For the experiment presented in the following a blunt needle with 0.40 mm outer and 0.22 mm inner diameter was used as droplet generator. The produced droplets had always a reproducible diameter D in the range of (1.78 ± 0.03) mm and a reproducible velocity u_{imp} in the range of (1.22 ± 0.01) m/s. The Reynolds number Re, Weber number We, Capillary number Ca and Ohnesorge number Oh can be calculated as follows [19]:

$$Re = \frac{\rho D u_{\text{imp}}}{\mu}, \qquad We = \frac{\rho D u_{\text{imp}}^2}{\sigma}, \qquad Ca = \frac{u_{\text{imp}} \mu}{\sigma}, \qquad Oh = \frac{\mu}{\sqrt{\rho D \sigma}} \tag{2}$$

The dimensionless time τ for the droplet impact is defined as

$$\tau = t\frac{u_{\text{imp}}}{D} \tag{3}$$

In the following, a droplet impact of isopropanol (2-propanol) with a diameter of $D = 1.77\,\text{mm}$ and an impact velocity of $u_{\text{imp}} = 1.22\,\text{m/s}$ will be further discussed, see also Fig. 7. The density for isopropanol, the surface tension and the dynamic viscosity of $\rho = 785\,\text{kg/m}^3$, $\sigma = 23.0\,\text{mN/m}$ and $\mu = 2.43\,\text{mPa s}$ have been used [15, 23]. With Eqs. (2) the dimensionless parameters can be determined to: $Re = 699.3$, $We = 90.5$, $Ca = 0.129$ and $Oh = 0.0136$. The free surface energies for isopropanol, $\sigma_L^p = 3.5\,\text{mN/m}$ and $\sigma_L^d = 19.5\,\text{mN/m}$, [15], can predict a full-wetting behavior on flat PC surfaces using the OWRK-model [10, 16, 17]. Consequently, it can be expected that for all kind of structures on the PC-wafer a full-wetting behavior will occur. This can be confirmed by the experiments on $60 \times 60\,\mu\text{m}^2$ pillars of PC (surface S2).

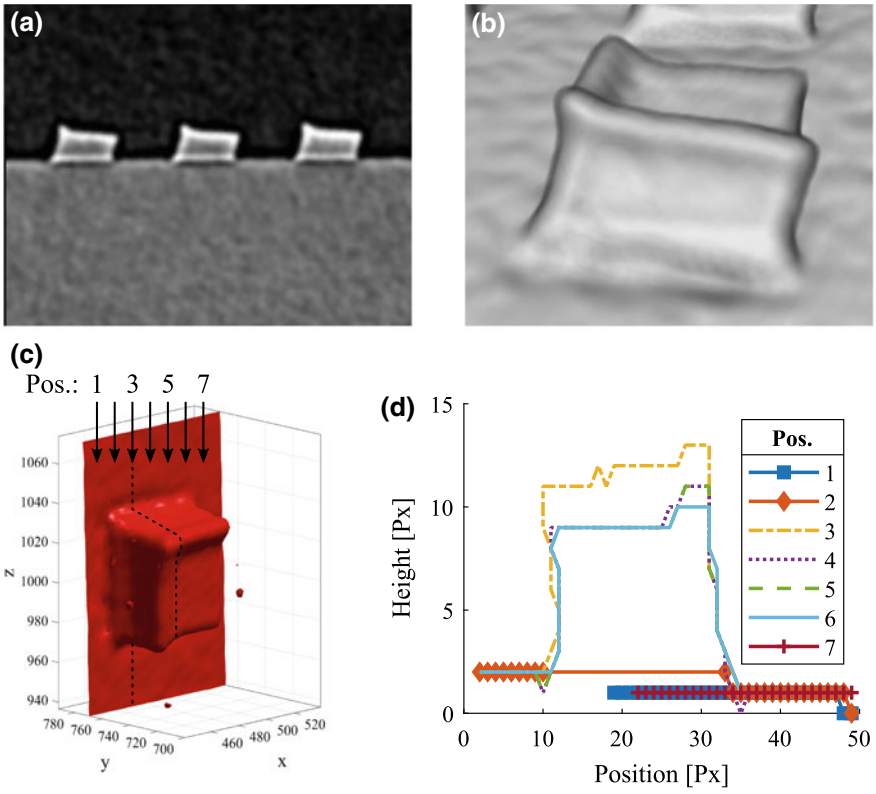

Fig. 6 Procedure for the evaluation of one single pillar with an edge length of 60 µm (surface S2) acquired by microCT with 2.7 µm/voxel: **a** single slice of reconstructed three-dimensional volume, **b** volume rendering of reconstructed three-dimensional volume, **c** exported single pillar with positions of sections, **d** height profile of each slice

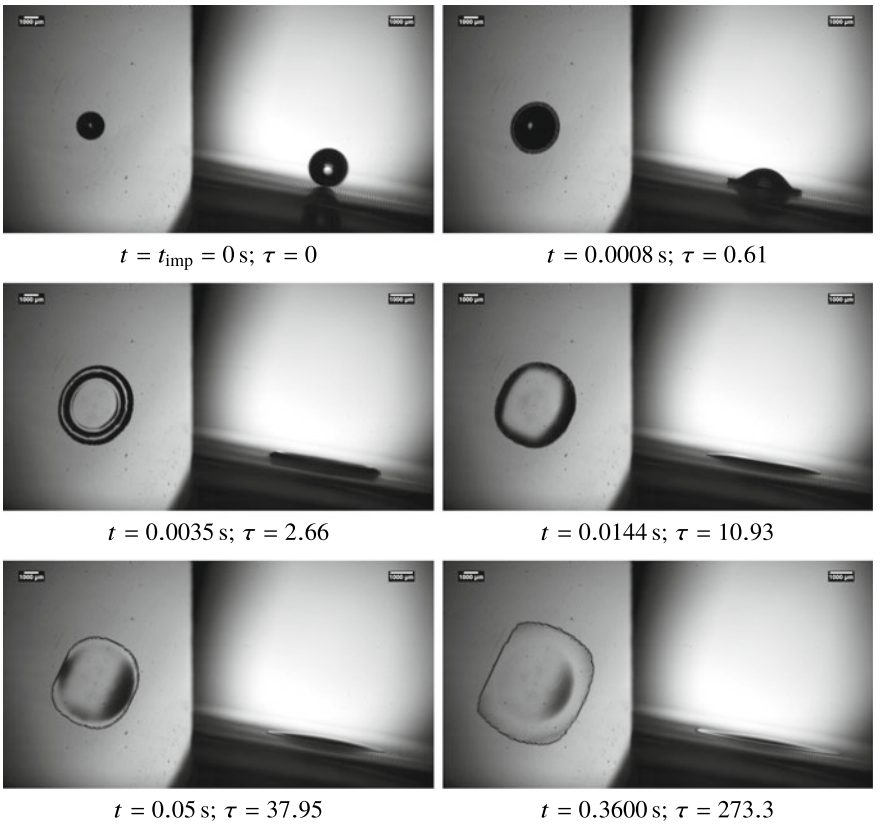

Fig. 7 Chronological sequence of a drop impact of isopropanol with a diameter of $D = 1.77$ mm and an impact velocity of $u_{imp} = 1.22$ m/s on a structured PC surface (S2) with $60 \times 60\,\mu m^2$ pillars at a $Re = 699.3$ and $We = 90.5$. Left image: top view, scale: 29.8 µm/pixel; right image: lateral view, scale: 19.2 µm/pixel

The overall morphology is following a deposition behavior and match the described splash/non-splash limits in [19], see Fig. 7. Two spreading regimes can be observed, the inertia driven spreading at the beginning of the droplet impact and the viscous spreading during the end of the impact. The inertia driven regime occurs at $\tau \lesssim 10.93$. The very slow spreading viscous regime at $\tau \gtrsim 10.93$ is mainly driven by capillary forces and follows the observations of [4]. The authors have observed a "zipping" of the liquid, which is the energetically favorable way of viscous imbibition into micro-structures. If one row of pillars is completely filled with liquid, the liquid will advance at a very limited area, mostly in between two pillars, to the next row. Afterwards, the liquid is "zipping" to the side filling the whole row inside the structure until the liquid will proceed to the next row of pillars.

3.3 Film Thickness Measurement of Droplet Lamella

During the droplet impact on smooth surfaces, the formation of a droplet lamella can be expected. Thickness measurements of droplet lamellas are very challenging due to the high dynamics of the impact and the large range of expected film thicknesses. The experimental test rig, will use the newly developed LASER Pattern Shift Method (LPSM) to measure the lamella thickness during the droplet impact. The method is evaluating the parallel shift of a laser pattern which is directly proportional to the film height, [6]. In using the Position Sensitive Detector (PSD) *1L30_SU2* of *SITEK Electro Optics*, the sampling rate can be increased to 500 kHz so that the temporal development of the lamella thickness can be captured [7].

The development of the LPSM will be continued, in order to measure the liquid film thickness inside the structure during the droplet impact. A three-dimensional profile of the film thickness as output will then give further information about the liquid distribution which can be used e.g. for validating detailed numerical simulations.

4 Conclusion

The influence of micro-structures on deposited droplets and droplet impacts can be determined by deviations from the spherical shape and preferential spreading directions. The dimensions of structure have a significant influence of the outcome. Therefore, a high reproduction quality and reliable inspection technique for such micro-structured surfaces are needed. Due to the requirements of dimensions and shape, the surfaces were produced with the hot embossing process. Also other reproduction possibilities for micro-structured surfaces were mentioned. As investigation methods for the surface structure the optical largefield microscope, the Scanning Electron Microscopy (SEM) and the micro Computed Tomography (microCT) have been used. While the Abbe criterion is mainly limiting the resolving power of the optical microscope the quality of SEM is limited by the electron beam quality. The resolving power of microCT is mainly influenced by focal spot size and the specimen size, and limited by X-Ray absorption, which is what produces image contrast. Choosing the right method is not easy, since it is always a compromise between availability of the technique, effort and information which can be extracted from the different techniques. The optical largefield microscope and SEM are two imaging methods, which can be used for measuring the dimensions from the images. However, the projection into the image plane needs to be considered for the determination of dimensions. Both techniques are either very economical or can provide a very high magnification of up to 100,000× or more. MicroCT, instead, has a lower resolving power, but can provide an export of the digitalized volumes of the scanned surfaces. These exported volumes can be then used e.g. for numerical simulations. The analyzed micro-structured surfaces show mainly a proper reproduction quality.

The influence of the deviation between experimental and generic surfaces onto the droplet impact outcomes needs to be numerically investigated in the future. Finally, preliminary results of a droplet impact on the structured surfaces have shown preferential spreading directions. Future investigations will then also focus on the effect of the flow inside the structure and on the heat transfer on micro-structured walls.

Acknowledgements The authors kindly acknowledge the financial support of this work by the Deutsche Forschungsgemeinschaft (DFG) in the frame of the International Research Training Group "Droplet Interaction Technologies" (GRK 2160/1: DROPIT). The mold fabrication and replication was carried out with the support of the Karlsruhe Nano Micro Facility (KNMF proposal 2016-017-016369, www.knmf.kit.edu), a Helmholtz Research Infrastructure at Karlsruhe Institute of Technology (KIT, www.kit.edu). The microCT imaging was conducted at the microCT facilities of the University of Bergamo and at the microCT facilities of the Oregon State University (microct.oregonstate.edu). The authors would like to thank all involved staff at the universities for their friendly support.

References

1. Bico, J., Tordeux, C., Quéré, D.: Rough wetting. Europhysics Letters (EPL) **55**(2), 214–220 (2001). https://doi.org/10.1209/epl/i2001-00402-x
2. Cassie, A.B.D., Baxter, S.: Wettability of porous surfaces. Trans. Faraday Soc. **40**, 546–551 (1944). https://doi.org/10.1039/TF9444000546
3. Courbin, L., Bird, J.C., Reyssat, M., Stone, H.A.: Dynamics of wetting: from inertial spreading to viscous imbibition. J. Phys.: Condens. Matter **21**(46), 464127 (2009). http://stacks.iop.org/0953-8984/21/i=46/a=464127
4. Courbin, L., Denieul, E., Dressaire, E., Roper, M., Ajdari, A., Stone, H.A.: Imbibition by polygonal spreading on microdecorated surfaces. Nat. Mater. **6**(9), 661–664 (2007). https://doi.org/10.1038/nmat1978
5. Foltyn, P., Restle, F., Weigand, B.: 360° evaluation of projected contact angles of static droplets on structured surfaces. In: Droplet Impact Phenomena & Spray Investigations (DIPSI), Bergamo, Italy (2019). https://doi.org/10.6092/DIPSI2019
6. Foltyn, P., Roth, N., Weigand, B.: Development and calibration of the laser pattern shift method for measuring the lamella topology during drop impact on walls. In: 29th European Conference on Liquid Atomization and Spray Systems, Paris, France (2019)
7. Foltyn, P., Roth, N., Weigand, B.: Verfahren zur Messung der Schichtdicke einer optisch transparenten Schicht, insbesondere einer Flüssigkeitsschicht. EP 19 192 074.3 application (2019)
8. Goldstein, J.I.V., Joy, D.C., Michael, J.R., Ritchie, N.W., Scott, J.H.J. (eds.): Scanning Electron Microscopy and X-Ray Microanalysis, 4th ed. 2018 edn. SpringerLink. Bücher. Springer, New York, NY (2018). https://doi.org/10.1007/978-1-4615-0215-9. Online-Ressource (XXIII, 550 p. 546 illus., 409 illus. in color, online resource)
9. Hsieh, J.V. (ed.): Computed Tomography: Principles, Design, Artifacts, and Recent Advances, 3rd ed. edn. SPIE Press monograph ; PM259. SPIE Press, Bellingham, Wash (2015). http://dx.doi.org/10.1117/3.2197756. Online-Ressource
10. Kaelble, D.H.: Dispersion-polar surface tension properties of organic solids. J. Adhes. **2**(2), 66–81 (1970). https://doi.org/10.1080/0021846708544582
11. Kim, S.J., Kim, J., Moon, M.W., Lee, K.R., Kim, H.Y.: Experimental study of drop spreading on textured superhydrophilic surfaces. Phys. Fluids **25**(9), 092110 (2013). https://doi.org/10.1063/1.4821985
12. Kim, D., Pugno, N.M., Ryu, S.: Wetting theory for small droplets on textured solid surfaces. Sci. Rep. **6**, 37813 (2016). https://doi.org/10.1038/srep37813

13. Marengo, M., Antonini, C., Roisman, I.V., Tropea, C.: Drop collisions with simple and complex surfaces. Curr. Opin. Colloid & Interface Sci. **16**(4), 292–302 (2011). https://doi.org/10.1016/j.cocis.2011.06.009. http://www.sciencedirect.com/science/article/pii/S1359029411000859
14. McHale, G., Shirtcliffe, N.J., Aqil, S., Perry, C.C., Newton, M.I.: Topography driven spreading. Phys. Rev. Lett. **93**, 036102 (2004). https://doi.org/10.1103/PhysRevLett.93.036102
15. Ohm, A., Lippold, B.: Charakterisierung der benetzbarkeit von arzneistoffpulvern mit hilfe der sessile-drop technik, teil 2: Kritische oberflächenspannung und randwinkel/oberflächenspannungskurven. Pharm. Ind. **48**(5), 508–513 (1986)
16. Owens, D.K., Wendt, R.C.: Estimation of the surface free energy of polymers. J. Appl. Polym. Sci. **13**(8), 1741–1747 (1969). https://doi.org/10.1002/app.1969.070130815
17. Rabel, W.: Einige Aspekte der Benetzungstheorie und ihre Anwendung auf die Untersuchung und Veränderung der Oberflächeneigenschaften von Polymeren. Farbe und Lacke **77**(10), 997–1005 (1971)
18. Radon, J.: über die bestimmung von funktionen durch ihre integralwerte längs gewisser mannigfaltigkeiten. In: Berichte über die Verhandlungen der Königlich-Sächsischen Akademie der Wissenschaften zu Leipzig, Mathematisch-Physische Klasse, vol. 69, pp. 262–277. Teubner, Leipzig (1917)
19. Rein, M., Delplanque, J.P.: The role of air entrainment on the outcome of drop impact on a solid surface. Acta Mechanica **201**(1), 105 (2008). https://doi.org/10.1007/s00707-008-0076-9
20. Rioboo, R., Tropea, C., Marengo, M.: Outcomes from a drop impact on solid surfaces. Atomization and Sprays **11**(2), (2001)
21. Silverio, V., Cardoso de Freitas, S.: Microfabrication techniques for microfluidic devices, Chap. 2, pp. 25–51. Springer International Publishing, Cham (2018). https://doi.org/10.1007/978-3-319-59593-1_2
22. Stapelbroek, B.B.J., Jansen, H.P., Kooij, E.S., Snoeijer, J.H., Eddi, A.: Universal spreading of water drops on complex surfaces. Soft Matter **10**, 2641–2648 (2014). https://doi.org/10.1039/C3SM52464G
23. Th.Geyer: Safety data sheet according to 1907/2006/ec, article 31. Tech. rep., Th. Geyer GmbH & Co. KG (2017). https://shop.thgeyer-lab.com/erp/zertifikate/searchSDB_or_COA.action?artikel=11646872&isDirectLink=true&searchSDB=true&hersteller=740
24. Thermo Fisher Scientific: User's Guide Avizo Software 2019 (2019). https://assets.thermofisher.com/TFS-Assets/MSD/Product-Guides/users-guide-avizo-software-2019.pdf
25. Vaikuntanathan, V., Sivakumar, D.: Maximum spreading of liquid drops impacting on groove-textured surfaces: Effect of surface texture. Langmuir **32**(10), 2399–2409 (2016). https://doi.org/10.1021/acs.langmuir.5b04639. PMID: 26885767
26. van Aarle, W., Palenstijn, W.J., Beenhouwer, J.D., Altantzis, T., Bals, S., Batenburg, K.J., Sijbers, J.: The astra toolbox: a platform for advanced algorithm development in electron tomography. Ultramicroscopy **157**, 35–47 (2015). https://doi.org/10.1016/j.ultramic.2015.05.002. http://www.sciencedirect.com/science/article/pii/S0304399115001060
27. Watt, I.M.V. (ed.): The Principles and Practice of Electron Microscopy, 2nd edn. Cambridge University Press, Cambridge [U.A.] (1997)
28. Wenzel, R.N.: Resistance of solid surfaces to wetting by water. Ind. Eng. Chem. **28**(8), 988–994 (1936). https://doi.org/10.1021/ie50320a024
29. Worgull, M.: Hot Embossing: Theory and Technology of Microreplication (Micro and Nano Technologies). Elsevier (2009). https://www.sciencedirect.com/book/9780815515791/hot-embossing
30. Zhou, W., Apkarian, R., Wang, Z.L., Joy, D.: Fundamentals of Scanning Electron Microscopy (SEM), pp. 1–40. Springer New York, New York, NY (2007). https://doi.org/10.1007/978-0-387-39620-0_1

Use of X-ray Micro Computed Tomography for the Investigation of Drying and Salt Precipitation in a Regular Glass Bead Structure

Robert Haide and Maurizio Santini

Abstract Micro computed tomography is a powerful tool for the inspection of porous media since it essentially provides the possibility to reconstruct a three dimensional volume of an object at micrometric spatial resolution. The technique is non-intrusive, while still being capable of dealing with matter that is opaque at the wavelengths of visible light. The processing of the obtained data such as segmentation and morphology characterization in multi-phase porous systems is a challenging research topic for the comprehension of countless physical problems in a variety of technical applications. This research project is dedicated to the investigation and optimization of all aspects along the process chain, starting from the preparation of adequate porous samples towards the acquisition of the computed tomographies and data processing until pore-scale fluid displacement processes in multi-phase systems can eventually be visualized and characterized. Presented here are the production process of a regular glass bead pack, the data acquisition and processing methods and the obtained results for tomographic experiments during which the pack is containing distilled water, doped with potassium iodide and air and is subjected to drying in ambient atmosphere. The sample design allows validation of values derived from tomographic data with analytically predictable values.

R. Haide (✉)
Department of Management, Information and Production Engineering, University of Bergamo, viale Marconi 5, 24044 Dalmine, Italy
e-mail: robert.haide@unibg.it

M. Santini
Department of Engineering and Applied Sciences, University of Bergamo, viale Marconi 5, 24044 Dalmine, Italy
e-mail: maurizio.santini@unibg.it

G. Lamanna et al. (eds.), *Droplet Interactions and Spray Processes*, Fluid Mechanics and Its Applications 121,
https://doi.org/10.1007/978-3-030-33338-6_7

1 Introduction

Systems of porous media containing two or more fluid phases are crucially relevant for applications such as oil and gas recovery, chemical separations, drying processes, catalysis, material manufacturing and a great variety of other engineering applications. The fluids distribute within the solid in a way to minimize system energy, while being strongly influenced by the system's wettability. Wetting fluids spread over the solid areas, whereas non-wetting fluids occupy the pore centers. The pore structure usually is microscopic and is, in general, orders of magnitude smaller than the characteristic scales governing the overall processes [1]. Evaporation from a porous medium, for example, is a typical multi-phase system, where the invading gaseous phase, usually wet air, replaces the evaporating liquid. The macroscopic measurable behavior of the system is the drying rate, which is affected by atmospheric conditions, pore morphology as well as transport properties such as thermal and hydraulic conductivities and vapor diffusion. These complex and highly dynamic interactions between the medium properties, transport processes and boundary conditions make the prediction of drying rates a challenging task.

Recently, an exponentially increasing amount of studies utilizes micro computed tomography in order to determine pore scale properties of materials and investigate their effect on parameters, such as mass transfer [2, 3] and capillary pressure to interfacial area to saturation relationships. Running experiments with glass beads as the solid porous matrix is a common practice [4, 5]. The properties of glass beads, such as a smooth surface and their X-ray attenuation coefficient, provide the optimal basis to develop robust experimental and post-processing routines. For a comprehensive overview of the principles of computed tomography see e.g. [6].

2 Materials and Methods

In the following, the tomography equipment and the sample production will be described. The choice of fluids will be elucidated, and an overview of the used data processing methods will be given.

2.1 Tomography Equipment

The tomography setup at the faculty laboratory is a prototype assembly of high-performance building blocks, that overcome a lot of the limitations of ready-made tomography systems that are currently on the market. It is based on an open-type X-ray source (160 kVp @ 200 µA), a high-precision air-bearing rotating stage and a flat panel X-ray detector. The detector is characterized by a custom-designed scintillator plate, a high dynamic range, full programmability and triggerability. It is based on

an amorphous silicon (a-Si) sensor array, acquiring 16-bit gray level images with a pixel matrix of 4096 by 4096, where each quadratic pixel has an edge length of 100 μm. For a more detailed description of the setup, refer to [7].

2.2 Materials

The solid structure of the porous medium is built up of precision glass beads, arranged in a regular manner. It was considered advantageous to choose a material that can be manufactured to high precision grades in millimetric and even micrometric dimensions, since a regular arrangement of the sample can provide a structure with easily predictable geometric parameters, which can in turn be used to validate the tomographic acquisition process. Preliminary experiments were additionally conducted with steel and ceramic beads, yet it was confirmed that glass is the most suitable material, due to its X-ray attenuation behavior. Eventually, high-precision glass beads with a diameter of 0.7 ± 0.01 mm (soda-lime glass) were chosen (SiLibeads® type P).

The fluid phases were chosen to be bi-distilled water, doped with potassium iodide (KI) and ambient air, as they can be considered immiscible once the air is saturated and are easily available. Potassium iodide serves as a contrast agent. It allows for a clear segmentation of the phases in the reconstructed volume. The initial mass ratio of KI to water was chosen to be 1:3. It was necessary to choose a fairly high amount of contrast agent in the presented experiments due to a large variation of the attenuation coefficient of the beads. This variation occurs as beads from different production batches are mixed. The unavoidable variation of components during glass production leads to the differing in attenuation values. During drying, the relative percentage of KI increases and when the sample has dried out by approximately 78%, the solution is fully saturated and salt precipitation occurs.

2.3 Sample Production and Filling

A sealable sample holder was custom-designed and manufactured in-house by fused deposition modeling 3D printing, using ABS (Acrylonitrile Butadiene Styrene). After printing, the container was treated in acetone fume, in order to seal the surface. A closing cap and a lid, to keep the upmost layer of beads in place were manufactured in the same way. The used material provides the necessary properties such as high transitivity to X-rays, low deterioration under X-ray radiation, chemical stability versus the used materials and a low thermal expansion coefficient around room temperature. The chosen spatial dimensions are a compromise between highest achievable scanning resolution and volume of the inner porosity-based representative elementary volume (REV). In order to minimize the influence of the container walls on the fluids contained in the REV a distance of at least one and a half bead diameters from the REV is deemed necessary. Furthermore, the whole sample holder assembly is

designed to allow for frictionless, air-tight sealing and opening, in order to not disturb the porous material and its content during those operations. This is achieved by adding a small basin at the bottom end of the container that is to be filled with butyl-rubber tape (Tacky Tape®). The closing cap then has to be put over the container, and its rim has to be submerged into the rubber.

Due to the precise shape of the container, it was possible to construct a regular, hexagonal close packing of the glass beads by placing them manually, while using a limited amount of nylon support structures to bolster the sides. Thereby, two sets of characteristical pore shapes are formed. They are called tetrahedral and octahedral pores. The beads were cleaned in acetone before they were packed. A hexagonal close packing exhibits, alongside the cubic close packing, the densest possible packing structure of equally sized spheres that is currently known [8]. The packing density η, which is defined as the relation of the volume of the beads contained in an REV to the total volume of the REV, is in this case

$$\eta = \frac{\pi}{3\sqrt{2}} \approx 0.74 \tag{1}$$

The complete packing consists of 755 glass beads, arranged in 9 layers with a layering structure of A-B-A-C-A-B-A-C-A [9] and 12 nylon support bars (see Fig. 1).

For the purpose of filling, a small hole was included by design into the bottom of the container, that can be connected to the tubing of a peristaltic pump (Ismatec® ISM596). This provides the possibility to infiltrate the porous medium from the bottom side at a slow rate of 53 µl/min, thus avoiding undesired enclosing of air in the pores. After filling, this hole is sealed.

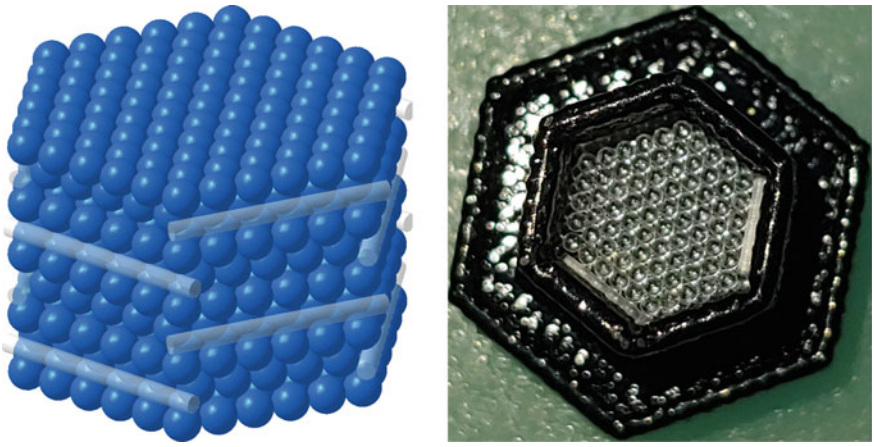

Fig. 1 CAD model of porous structure and top view of sample container with packed beads and nylon support bars; the nominal diameter of one glass bead is 0.7 mm

2.4 Scanning Parameters

The X-ray attenuation of materials is dependent on their density, their atomic number and their dimensions. The scanning parameters were carefully iterated, in order for the acquired data to provide the highest information content. A tube voltage of 90 kV and a target current of 14 μA were deemed optimal.

During preliminary experiments, it became clear that the X-ray beam has to be pre-filtered before passing through the object, in order to avoid beam hardening artifacts. Beam hardening is a common effect that occurs when X-rays from a poly-chromatic source pass through an object, and their lower-energy portion is filtered out. This induces difficulties for the reconstruction algorithm, that may result in artifacts. For elucidation of the beam hardening effect, see e.g. [10]. In the case at hand, the beam is filtered through 1.5 mm of glass directly after it is produced at the source.

The required exposure time per projection in this configuration in order to achieve sufficient contrast is 2.3 s. A maximum scanning resolution of roughly 5 μm is possible, considering the size of the porous sample. At such a high resolution, achieving high-quality reconstructions with conventional reconstruction algorithms requires a large amount of projections to be taken, resulting in acquisition times of up to two and a half hours. In Fig. 2, a single X-ray projection of the solid porous structure is depicted.

2.5 Reconstruction

Reconstructions of the obtained data are to this date done with the reconstruction module of the commercial software package VGSTUDIO MAX by Volume Graphics GmbH [11]. Here, the conventional and well-approved filtered back projection algorithm enhanced for cone beam tomography [12] is utilized. It provides reliable, high-quality reconstructions, and the software package has several functionalities implemented that allow for correction of minor misalignment of the components

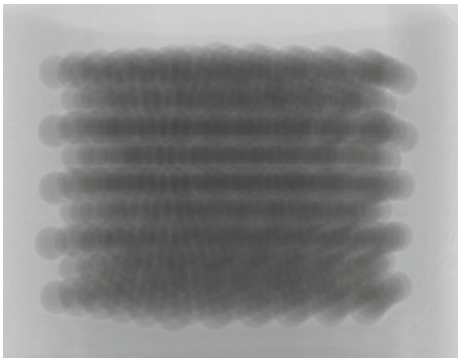

Fig. 2 Single X-ray projection of the sample at a resolution of 5 μm per pixel

of the tomography setup. The downside to this procedure is the necessity of fine sampling, resulting, as mentioned, in large acquisition times.

An effort is currently underway, to use powerful algebraic reconstruction algorithms, such as SIRT (Simultaneous Iterative Reconstruction Technique) [13] or DART (Discrete Algebraic Reconstruction Technique) [14] in the flexible, open source software framework ASTRA [15] for this project. Given the fact, that the sample only consists of a limited number of materials, the full potential of the discrete reconstruction technique could be attained. This could potentially result in a significant decrease of required projections and thereby a decrease of acquisition time.

2.6 Segmentation

Adequate segmentation of the phases poses one of the central challenges. The most promising method currently in use, is segmentation by k-means clustering [16]. It relys on adequate pre-processing of the reconstructed data. Here, non-local means filtering [17] with previous estimation of the noise standard deviation σ [18] is applied. The slice-wise image processing and segmentation strategy employed for the discussed data set is described in the Fig. 3.

The used input parameters for the non-local means filter are a 5 by 5 similarity neighborhood, a 13 by 13 search window and a filtering parameter of 10 σ.

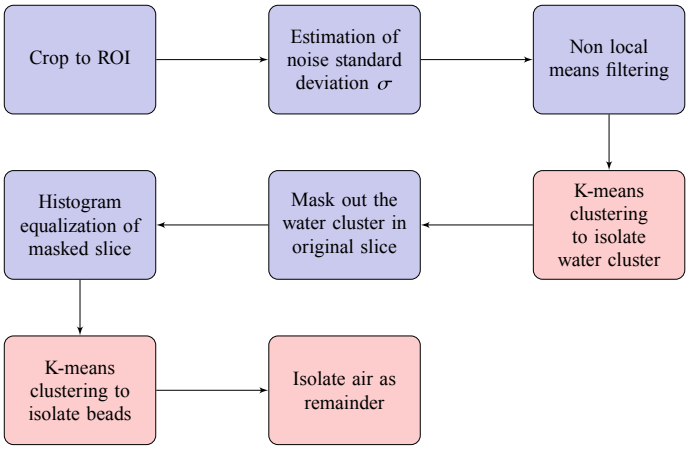

Fig. 3 Segmentation strategy

3 Results and Discussion

3.1 Preliminary Experiments

The applicability of the process chain was tested and validated through a set of preliminary experiments. The influence of reducing the resolution and the detector dynamic range was evaluated in order to ensure the robustness of the used methods. It was found, that the influence of the dynamic detector range on the quality of the tomographic data is not dominant for the configuration at hand. This implicates, that the utilized dynamic range could be restricted to 14 bits, resulting in faster scanning times. Considering the bead size and pore sizes of the medium, a resolution higher than 15 µm is necessary to adequately reproduce analytically calculated values for the global porosity from the tomographic data. The diameter tolerance of ±0.01 mm, indicated by the manufacturer, could be reproduced through overlaying fitting spheres on the reconstructed volume of the beads, using the software package GOM Inspect [19]. The analytical value for the global porosity in a regular pack is supposed to be 26%. The value measured from the tomographic data in the inner ROI (Region Of Interest) by voxel counting was 26.6%.

3.2 Evaporation Experiments

Drying curves, that have been logged for the regular pack containing two phases indicate, that the characteristic drying periods, described in literature, can be observed (see Fig. 4). An extended range of constant drying rate is present, that spans from the initial full saturation down to a saturation of approximately 10% before the typical

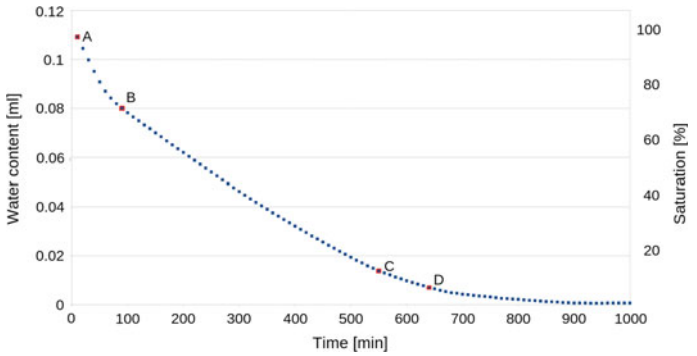

Fig. 4 Drying curve of regular bead pack; temperature during drying was 298 ± 0.5 K and relative humidity was 35 ± 5%

falling rate period sets in [20]. The drying curves were acquired in order to gain information on the necessary time steps between the tomographic experiments.

For the set of tomographic experiments, the regular pack was fully saturated with KI-doped water and then subjected to drying intervals with a water loss of between 5 and 15% each. The drying occurred in ambient atmosphere, while logging the temperature and the relative humidity of the surrounding laboratory space. After a drying interval was completed, the sample holder was sealed and a relaxation period of 10 hours was granted in order for the interfaces to redistribute and achieve a minimum of free surface energy. Then, a scan was taken respectively. In the following, the results of four time steps are presented. Two time steps during the initial period at liquid saturation states of 98 and 72% (positions A and B in Fig. 4), and two time steps at the conversion to the falling rate period, where the liquid saturation ranges between 15 and 8% (positions C, D in Fig. 4).

3.3 Pore Size Distribution

The obtained data was segmented, using the mentioned segmentation strategy. An exemplary depiction can be seen in Fig. 5. The pore size distribution is obtained by using the 'Separate Objects' module of the software package Avizo® by Thermo Fisher Scientific [21]. Here, the pores are separated, using the watershed algorithm [22]. A value of 1 is used for the seed marker extent and the operation is conducted in 3D with a neighborhood connectivity of 26. The pore sizes given in Fig. 6 correspond to the diameter of volume-equivalent spheres. The bi-modal pore size distribution of

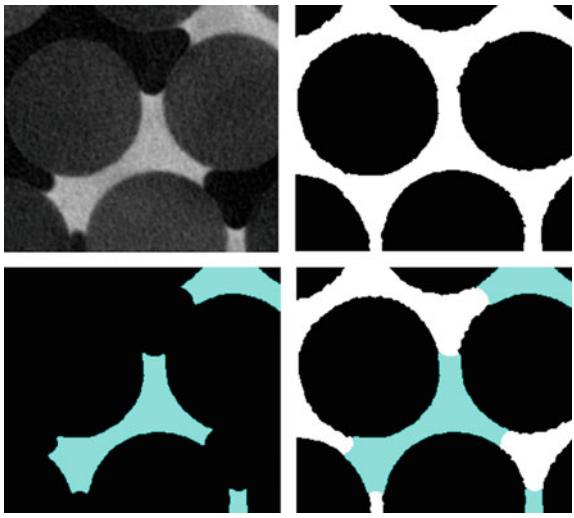

Fig. 5 Slice of the reconstructed volume (upper left) and segmentation; total pore space (upper right), water (lower left), combined (lower right)

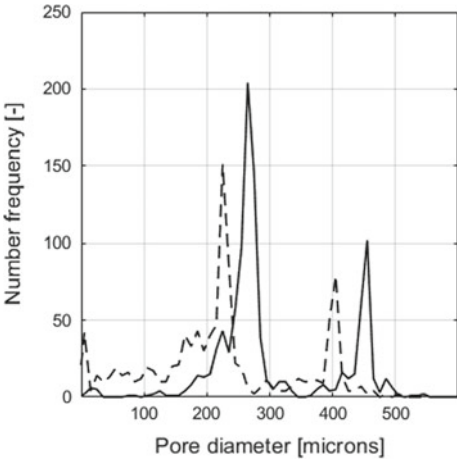

Fig. 6 Pore size distribution (continuous line) and distribution of air-filled pores at a saturation of 15% (dashed line)

the structure represents the two sets of pores that were created by regularly packing the beads. A minor amount of diverse-sized pores is present at the outer boundaries of the volume. The original pore size distribution (continuous line in Fig. 6) can be compared to the distribution of air-filled pores at an intermediate state of saturation (dashed line in Fig. 6). Here, the bi-modality of the pore size distribution is still represented, while the total number of pores has decreased due to the omitting of water-filled pores. The appearing smaller values reflect partially filled pores.

3.4 Distribution of the Fluid Clusters

The evolution of the respective clusters can be traced and visualized using Avizo®. Water films of a thickness down to approximately twice the scanning resolution are included (see Fig. 7).

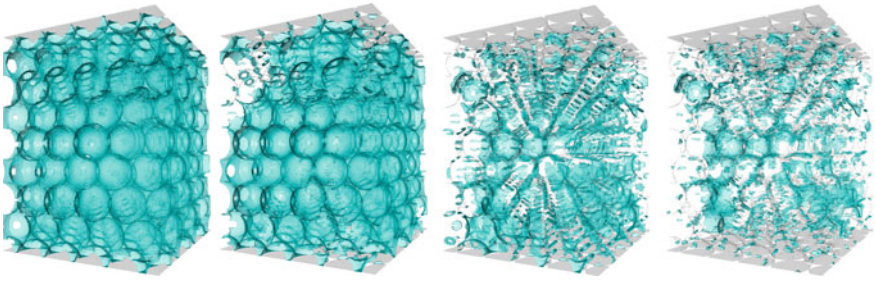

Fig. 7 Morphological change of a liquid cluster in the ROI; liquid saturation from the left: 98, 72, 15, 8%

During drying a main liquid cluster develops, which is connected through the sample from bottom to top. Through this cluster, liquid is fed to the drying front by capillary suction. The main cluster is maintained until the liquid saturation reaches roughly 10% and the second, mainly diffusion controlled drying period sets in [20]. Apart from the main cluster, several isolated clusters form that consist in general of pendular rings. Here, the liquid is trapped in the crevices that are formed between to touching beads due to the balance of interfacial forces [23]. In Fig. 8, pendular rings can be clearly distinguished from the main cluster. The number of isolated clusters increases and reaches its maximum at approximately 10% liquid saturation. After that the number of clusters decreases again, as individual clusters dry out completely. In Fig. 9 on the left side, the number of clusters for the four representative saturation states is given. The saturation profiles over the sample height (Fig. 9 right side) show a decrease of saturation towards the bottom end of the sample. This can be attributed to the fact that the air phase can also invade the ROI from the sides after the irregular pores close to the container wall are dried out. Figure 10 illustrates the relation of the total volume of the main cluster to the cumulative volume of the disconnected clusters.

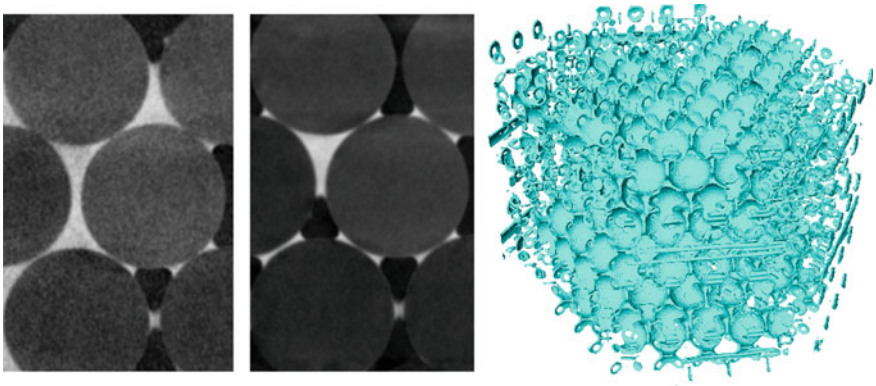

Fig. 8 Drying of the main cluster and formation of pendular rings; 3D visualization of the liquid cluster of the whole volume

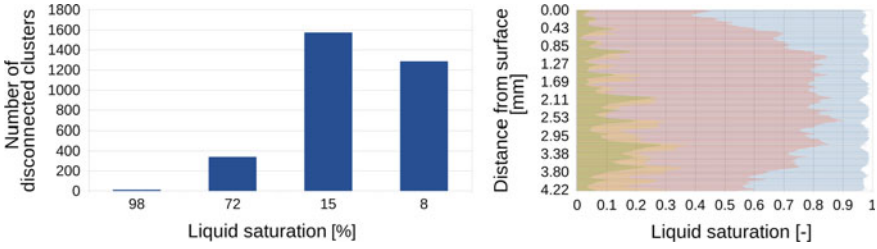

Fig. 9 Number of disconnected liquid clusters and saturation over sample height at the saturation states depicted in Fig. 6

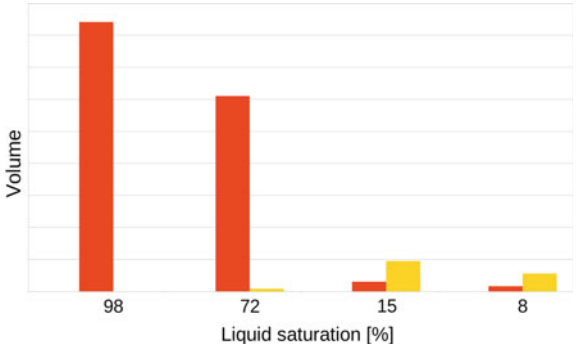

Fig. 10 Relation of the volume of the main cluster to the cumulative volume of the disconnected clusters; the red bars on the left correspond to the main cluster, i.e. the largest connected volume

3.5 Salt Precipitation

As soon as the water is saturated with salt, precipitation occurs. During the drying period that is controlled mainly by the connected liquid cluster, salt gets transported to the drying front. Thereby, the salt concentration is increased at the top of the sample, and the formation of a salt crust begins [24]. Only after the main cluster gets disconnected from the surface, crystallization happens within the porous medium. In the experiment presented here, 90% of the salt precipitates at the surface. This is consistent with the value of the Peclet number, which is in porous media defined as [25]

$$Pe = \frac{e\ h}{D_e\ \epsilon} \tag{2}$$

where e is the evaporation rate, h the sample height and D_e the effective diffusion coefficient of the dissolved salt. The effective diffusion coefficient incorporates the influence of the pore structure on diffusion. It is assumed here, that this influence is negligible in a first approximation, since the pores are well connected and several orders of magnitude larger than the solute particles. Assuming an effective diffusion coefficient of $D \approx 2 \cdot 10^{-9}\mathrm{m}^2/\mathrm{s}$ [26] and an average evaporation rate of $e \approx 1.5 \times 10^{-7}$ m/s, which is obtained by dividing sample height by the time it takes until a sample filled with pure water has dried out completely, the Peclet number is roughly 2.3 and thereby considerably greater than 1. This indicates a capillary-controlled precipitation behavior [25]. The formation of the crust has additional effects on the drying rate due to the creation of a new micro-porous structure [27]. Here, those effects are neglected, since they are not very pronounced and barely observable due to the fact that the crust forms late in the drying process and doesn't cover the sample surface completely. A slice comparison before crust formation and after the crust is fully developed at the end of the drying process and a 3D visualization of the crust, as well as the grid structure of the lid, are depicted in Fig. 11. It can be seen, that the salt crust is creeping upwards, through the grid of the lid.

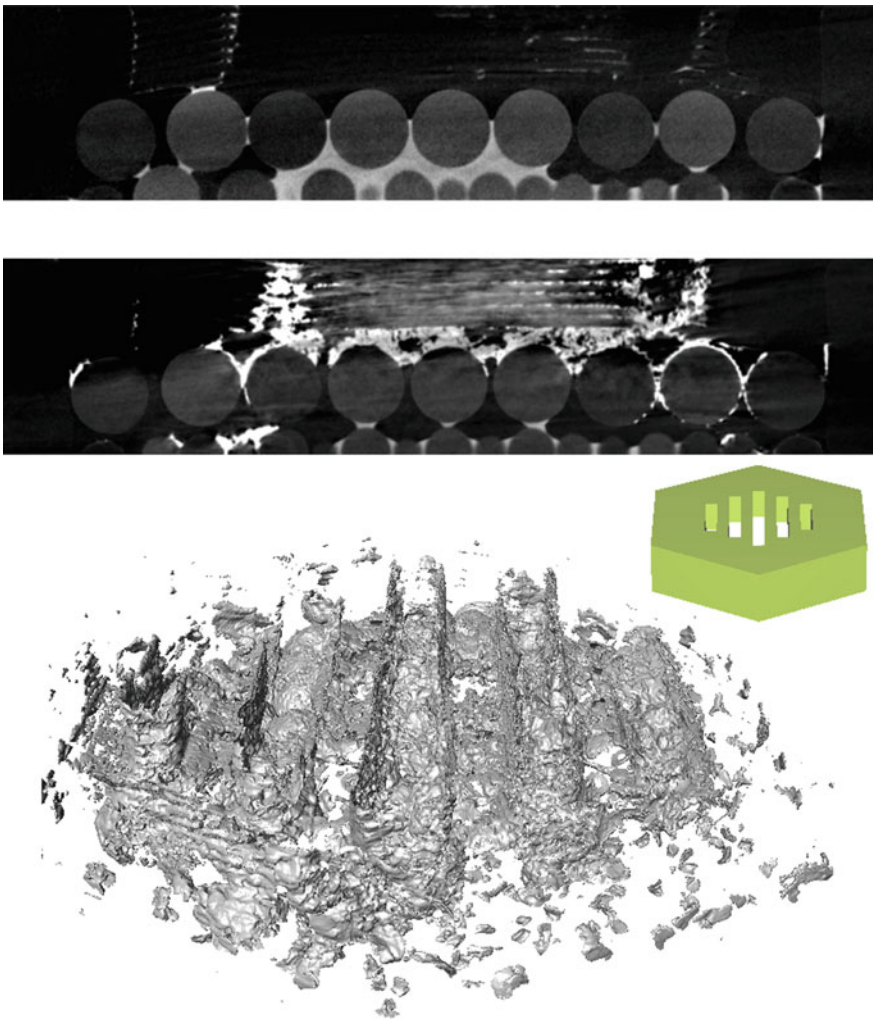

Fig. 11 Formation of the salt crust on the upmost bead layer and in the grid of the lid

4 Conclusions

In the presented work a regular glass bead sample was created in a precise manner, utilizing the flexibility offered by the fused deposition modeling 3D printing process. The structure is considered advantageous for the validation of tomographic multi-phase flow experiment through the comparison of analytically predictable and tomography-derived parameters. The conducted tomographic experiments provide the possibility to gain insight into drying and salt precipitation mechanisms in porous

media. Improved reconstruction and robust segmentation methods play a key role for the adequate evaluation and visualization of the acquired tomographic data.

In the next step of the project, more experimental sets will be conducted, including the introduction of n-dodecane as a second liquid phase. A reduction of the used contrast agent is aspired. Interfacial area and curvature measurements will be extracted from the tomographic data. It is envisaged to eventually couple fluid displacement processes that occur on the pore scale to larger scale flow models and to derive necessary parameters that can be fed into extended pore network model simulations.

Acknowledgements The authors acknowledge the help and guidance of Dr.-Ing. Stephanie Fest-Santini.

References

1. Wildenschild, D., Sheppard, A.P.: X-ray imaging and analysis techniques for quantifying pore-scale structure and processes in subsurface porous medium systems. Adv. Water Resour. **51**, 217–246 (2013)
2. Foerst, P., Melo de Carvalho, T., Lechner, M., Kovacevic, T., Kim, S., Kirse, C., Briesen, H.: Estimation of mass transfer rate and primary drying times during freeze-drying of frozen maltodextrin solutions based on X-ray μ-computed tomography measurements of pore size distributions. J. Food Eng. **260**, 50–57 (2019)
3. Warning, A., Verboven, P., Nicolaï, B., van Dalen, G., Datta, A.K.: Computation of mass transport properties of apple and rice from X-ray microtomography images. Innov. Food Sci. Emerg. Technol. **24**, 14–27 (2014)
4. Li, T., Schlüter, S., Dragila, M.I., Wildenschild, D.: An improved method for estimating capillary pressure from 3D microtomography images and its application to the study disconnected nonwetting phase. Adv. Water Resour. **114**, 249–260 (2018)
5. Gueven, I., Frijters, S., Harting, J., Luding, S., Steeb, H.: Hydraulic properties of porous sintered glass bead systems. Granul. Matter 19–28 (2017)
6. Kak, A.C., Slaney, M.: Principles of computerized tomographic imaging. Soc. Ind. Appl. Math. (2001)
7. Santini, M., Guilizzoni, M., Fest-Santini, S.: X-ray computed microtomography for drop shape analysis and contact angle measurement. J. Colloid Interface Sci. **409**, 204–210 (2013)
8. Conway, J.H., Sloane, N.J.A.: Sphere Packings, Lattices and Groups, 2nd edn. Grundlehren Der Mathematischen Wissenschaften (1993)
9. Krishna, P., Verma, A.R.: Closed packed structures. Int. Union Crystallogr. (1981)
10. Ketcham, R.A., Hanna, R.D.: Beam hardening correction for X-ray computed tomography of heterogeneous natural materials. Comput. Geosci. **67**, 49–61 (2014)
11. Volume Graphics GmbH. https://www.volumegraphics.com/en/products/vgstudio-max.html. Cited 25 Nov 2019
12. Feldkamp, L.A., Davis, L., Kress, J.: Practical cone-beam algorithm. J. Opt. Soc. Am. **1**, 612–619 (1984)
13. Gilbert, P.: Iterative methods for the reconstruction of three dimensional objects from their projections. J. Theor. Biol. **36**, 105–117 (1972)
14. Batenburg, K.J., Sijbers, J.: DART: a practical reconstruction algorithm for discrete tomography. IEEE Trans. Image Process. **20**(9), 2542–2553 (2011)
15. van Aarle, W., Palenstijn, W.J., Cant, J., Janssens, E., Bleichrodt, F., Dabravolski, A., de Beenhouwer, J., Batenburg, K.J., Sijbers, J.: Fast and flexible X-ray tomography using the ASTRA toolbox. Opt. Express **24**(22), 25129–25147 (2016)

16. Lloyd, S.P.: Least square quantization in PCM. Bell Telephone Laboratories Paper (1957)
17. Buades, A., Coll, B., Morel, J.M.: A non-local algorithm for image denoising. Comput. Soc. Conf. Comput. Vis. Pattern Recognit. **2**, 60–65 (2005)
18. Immerkær, J.: Fast noise variance estimation. Comput. Vis. Image Underst. **64**(2), 300–302 (1995)
19. GOM GmbH. https://www.gom.com/3d-software/gom-inspect.html. Cited 26 Nov 2019
20. Toei, R., Okazaki, M.: Drying mechanism of capillary-porous bodies. J. Eng. Phys. **19**(3), 1123–1131 (1970)
21. Thermo Fisher Scientific. https://www.fei.com/software/avizo/?LangType=1033. Cited 26 Nov 2019
22. Beucher, S., Meyer, F.: The morphological approach to segmentation: the watershed transformation. Math. Morphol. Image Process. 433–481 (1993)
23. Chapman, R.: Physics for Geologists, 2nd edn (2002)
24. Shokri, N., Lehmann, P., Or, D.: Liquid-phase continuity and solute concentration dynamics during evaporation from porous media: pore-scale processes near vaporization surface. Phys. Rev. E **81**, 046308 (2010)
25. Huinink, H.P., Pel, L., Michels, M.A.J.: How ions distribute in a drying porous medium: a simple model. Phys. Fluids **14**(4), 1389–1395 (2002)
26. Dunlop, P.J., Stokes, R.H.: The diffusion coefficients of sodium and potassium iodides in aqueous solution at 25°. J. Am. Chem. Soc. **73**(11), 5456–5457 (1951)
27. Nachson, U., Weisbrod, N., Dragila, M.I., Grader, A.: Combined evaporation and salt precipitation in homogeneous and heterogeneous porous media. Water Resour. Res. **47**, W03513 (2011)

Image Processing of Two-Phase Data for Drop-Surface Interaction Obtained by X-Ray Microtomography

Stephanie Fest-Santini

Abstract Easier access to X-ray microtomography facilities has provided new insight from high-resolution imaging for various problems in drop-surface interaction research. Surface characterisation with respect to functional properties usually requires several of the following conditions: (a) imagining with sufficient resolution, (b) segmentation of the intensity data into different classes (c) triangulation and (d) curvature estimation. Two different test volumes are examined: scientific sand for discussing topics (a) as well as (b) and their influence on the example of porosity and pore classifications; and size-calibrated spheres with certificated sphericity for (c) and (d).

1 Introduction

Understanding drop-surface interaction is of central importance to many natural and engineered processes. The micro-scale is the scale at which many physical and chemical phenomena are rooted. Large-scale processes are often governed by these small-scale phenomena and, thereby, require also an inspection on the micro-scale. Tomography is one of the non-destructive techniques that allows, combined with three-dimensional visualization and analysis, the most comprehensive internal and external characterization of materials and structures at both micro-and macro-scale.

The principle of X-ray microtomography (microCT) relies on the principle of irradiating a sample with an X-ray beam and the acquisition of absorption images at different angular steps. The acquired so-called projection images represent views of the sample, providing internal details due to the penetration of X-rays. Projections are used in a mathematical reconstruction process to generate a volumetric data set. The latter consists of volumetric pixels (voxels) featuring a certain brightness. At a certain beam energy, this brightness is related to the X-ray density of the

S. Fest-Santini (✉)
Department of Management, Information and Production Engineering, University of Bergamo, Bergamo, Dalmine (BG), Italy
e-mail: stephanie.fest-santini@unibg.it

G. Lamanna et al. (eds.), *Droplet Interactions and Spray Processes*,
Fluid Mechanics and Its Applications 121,
https://doi.org/10.1007/978-3-030-33338-6_8

material which depends on the physical density and the atomic mass. The microCT enables not only the visualization of inner and outer structures but also dimensional measurements and advanced 3D analysis, such as wettability and interfacial capillary pressure measurements [1–4]. Examples for dimensional measurements include morphological analysis like pore sizes of porous media or texture dimensions of structured surfaces. Instead, the principle idea behind advanced analysis is to discretize the interfaces within the volume and to define vectors that have a direction perpendicular to these surfaces.

The contact angle θ is, then, found from the dot product of the vectors describing the fluid-fluid interface $\boldsymbol{n}|_{z_1}$ and the solid surface $\boldsymbol{n}|_{z_2}$.

$$\theta = \pi - \cos^{-1}\left(\boldsymbol{n}|_{z_1} \cdot \boldsymbol{n}|_{z_2}\right) \tag{1}$$

The capillary pressure P_c can be written as

$$P_c = 2\sigma\, k_m \tag{2}$$

where σ is the interfacial tension between the wetting and the non-wetting phase and k_m the interfacial mean curvature. The latter is defined as the average of the two principle curvatures k_1 and k_2.

$$k_m = 0.5 \cdot (k_1 + k_2) \tag{3}$$

This paper addresses analysis and quantification of the commonly large tomographic datasets for drop-surface interaction. Image based analysis requires always the identification of different phases as function of the individual voxels' brightness and the segmentation in different classes. The article is organized as follows: in Sect. 2, the performance of different thresholding methods and the resolution effect are evaluated by means of a tomographic test data set free of noise and blur. Section 3 addresses surface triangulations and a sensitive analysis is given for a known geometry. Recommendations for best practise are summarized in Sect. 4.

2 Analysis and Quantification

2.1 Segmentation

Image segmentation is a crucial step in image processing and affects all subsequent analysis. In absorption contrast tomography the intensity value associated with each voxel is proportional to its X-ray attenuation, which is a function of density, atomic number and the energy of the incident X-ray. Thereby, a common approach for decomposing an object into segments is the global thresholding. Here, classes are assigned to voxels by histogram evaluation only, without considering how gray values

are spatially distributed in the corresponding microCT volume. Plenty of different thresholding methods exist and have been reviewed by several authors [5–8]. Four of them—*entropy*, *factorization*, *moments* and *minimum error* method—were chosen for their performance evaluation using unconsolidated sand as a microCT test set.

The classic approach of the *entropy* principle relies here on the Shannon entropy as a measure of information content of a signal. Two classes are defined in the intensity histogram, and a threshold value is searched by minimizing the total classes' entropy (refer to [9, 10]). The *factorization* method is based on the Otsu criterion (see [11] for details) and maximizes the between-class variance. The *moment* method uses the moment-preserving bi-level thresholding described by Tsai [12]. Instead, the *minimum error* approach assumes the histogram composed of normal distribution for each class [13], which usually overlap at certain gray values. Assigning those voxels to one class would lead to misclassification error. The threshold is set for minimizing that error.

To generate the here investigated test data set, lose scientific sand (ACCUSAND® ASTM 100 grade no. 50/70) was scanned at 90 kV @ 10 μA_{target} and an emission focal spot of about 1.5 µm. The integration time was adapted to use the full detector's dynamic range of 16 bits and amounts 1.9 s. The angle step between radiographies depends on the specific magnification and size of the projected object. Those values were chosen according to the Nyquist theorem and are equal to 0.075°. The effective microCT resolution of about 3.007 µm is obtained according to [14].

The unconsolidated sand, its rendered microCT volume is shown in Fig. 1a, is composed by 99.8% (weight) of silicon dioxide and contains 0.2% (weight) of a material with higher X-ray attenuation (compare Fig. 4). For segmentation the microCT volume in grain and void space, see Fig. 1b and 1c, respectively, the threshold is often chosen by hand. Even there is a universal agreement that automated methods should be preferred, since they save operator time and eliminating operator subjectivity and bias.

However, the application of automated segmentation method requires sufficiently clean images resulting in a clear global bimodal intensity histogram as shown in Fig. 2. The "true" optimum threshold can be estimated by the intersection points

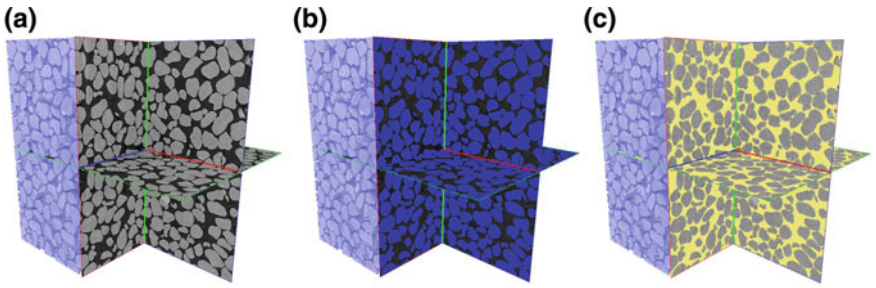

Fig. 1 **a** 3D render of microCT volume **b** highlighted solid matrix and **c** void space. Here, the *factorization* method was applied

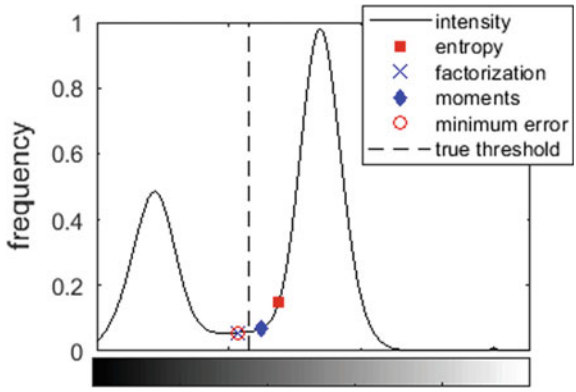

Fig. 2 Clear double-peaked (bimodal) histogram of the sand sample

of the individual gray value frequencies within each class and is shown as dashed line in Fig. 2. The tested automated segmentation methods are affected by bias in different directions. The *moments* approach bias towards the class with highest volume fraction, *minimum error* and *factorization* are shifted to lower thresholds. Instead, the entropy method fails completely in identifying a meaningful threshold.

The results of global segmentation methods are depicted in Fig. 3. The void space is shown white colour and the sold matrix in black colour. The *factorisation* and the *minimum error* approach exhibit smooth object boundaries. Misclassified voxel intensities applying the *entropy* and the *moments* method are highlighted by red frames.

One of the simpler measurements that can be made from tomographic images is the determination of the sample porosity (defined as fraction of the volume of voids over the total volume) which can be estimated by counting the number of voxels assigned to each class. Hence, a reliable segmentation is required. The obtained global porosities are summarized in Table 1. *Factorisation*, *moments* and *minimum error* methods lead to similar porosity values even if their bias directions of the threshold are different.

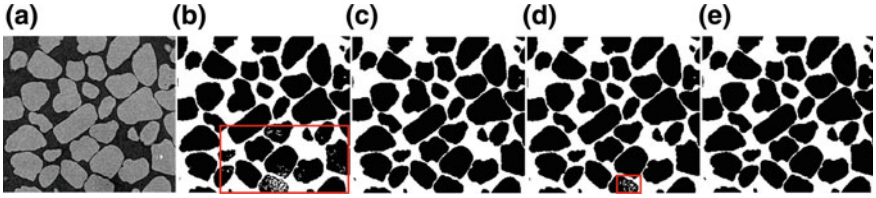

Fig. 3 Segmentation results for the four different segmentation methods. The void space is shown in white and grains in black: **a** original slice, **b** *entropy* method, **c** *factorisation* method, **d** *moments* method, **e** *minimum error* method. Coloured frames highlight failures for various methods

Table 1 Global porosities for the selected segmentation methods

Method	Porosity (%)
Entropy	39.4
Factorization	35.4
Moments	36.4
Minimum error	35.3

It can be concluded that for sufficiently high-quality images, e.g. clear bimodal distribution of the intensity histogram and smooth object boundaries, automated segmentation can work well (see also [15]). Threshold's position, obtained by automated methods, in the intensity histogram should be always verified.

2.2 Resolution

Usually, the goal of microCT is to image at a high enough resolution to capture the geometry of microscopic features. Often, their size is previously unknown, and a sufficient resolution is evaluated on the basis of an intensity histogram. The latter should feature a bimodal shape as shown in Fig. 4c. With decreasing resolution, the two peaks merge to one, and the resolution is insufficient to capture details on the micro-scale.

Instead for representing the pore-space distribution, the ability to image on a micro-scale resolution, i.e. distinguish precisely between individual grains, pores

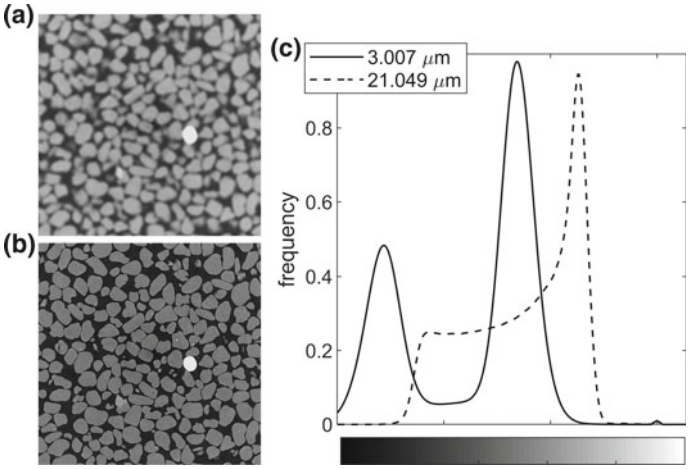

Fig. 4 **a** Slice of unconsolidated sand at 21.049 μm, with insufficient resolution to capture the geometry of features, **b** slices of the same region at 3.007 μm with sufficient resolution, **c** corresponding intensity histograms of single- and double-peaked distributions

and fluid phases, is required. In the following, the influence of the resolution on the pore size distribution is discussed. Herefor, the projections of the unconsolidated sand sample are binned and afterwards reconstructed obtaining microCT volumes twice, fourth and six times of the original resolution. Their intensity histograms have still the above discussed double-peak characteristic and would be evaluated as "sufficient" for micro-scale inspection. Segmentation, applying the *factorisation* approach, and subsequent counting of voxels assigned to the void spaces lead to global porosities. Their values are summarized in Table 2. With increasing micrometres-voxel scale (decreasing resolution), higher porosities are determined. However, the observed differences are smaller than those caused by the choice of an inadequate segmentation approach (compare to the *entropy* method in Table 1). It is necessary to highline that the accessed porosity does not increase with increasing resolution (decreasing voxel size) as may would be expected [16]. Note that, resolution effects are usually discussed on different field of views so that the dimension of the digitalized volume varies. Here, the field of view is kept constant.

The 3D void spaces are divided into single pores in the commercial program Avizo® [17] using a combination of watershed, distance transform und numerical reconstruction algorithm. Hereby, the marker extent factor was set to 1 and the connectivity to 26. From single pore volumes, sphere equivalent diameters are determined. The obtained volume-based cumulative pore size distributions Q_3 are depicted in Fig. 5. Distribution curves are shifted to larger pore sizes with decreasing resolu-

Table 2 Global porosities and mean pore diameters $d_{50,3}$ for different resolutions

Resolution (μm)	Porosity (%)	$d_{50,3}$ (μm)
3.007	35.4	189.9
6.014	35.6	230.4
12.028	36.2	300.4
18.042	38.0	360.7

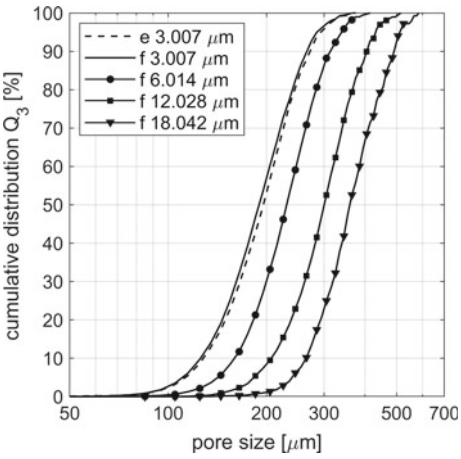

Fig. 5 Volume based cumulative pore size distribution for different resolutions. The abbreviation "e" denotes for the segmentation method *entropy* and "f" for *factorisation*

tion (increasing micrometres-voxel scale). Small details, like pore throats, cannot be detected so that pores appear connected and are interpreted as a unique larger pore. Consequently, the mean pore diameter $d_{50,3}$ is overestimated. In the specific test case, the mean pore diameter is estimated twice as large, when decreasing the resolution by a factor six. In consequence, only integral values of porosity or fluid saturation can be determined at resolution beyond the micro-scale. The preceding discussion shows that, for the accurate detection of pore-scale features, the evaluation of microCT data cannot be simply based on the intensity histogram, as commonly done.

In the following, it is discussed, which would be the best or what is an adequate resolution? Firstly, both low and high resolution microCT can generate misleading results of either less accurate or less representative values. For example, linking pore scale parameters to transport properties like diffusivity [18] or permeability [19]; diffusion will occur on both small and large pores while larger pores contribute predominantly to permeability over smaller pores. The resolution for diffusion analysis should be higher than that for permeability analysis and need to be adapted on the specific task and pore sample. The solution may lie in how to obtain representative (or larger) field of views while the accuracy remains constant. In Fig. 5, the pore size distribution of the data set with a resolution of 3.007 µm segmented with the *entropy* approach is also shown. The *entropy* method failed in predicting a global threshold and led to the highest calculated global porosity. Consequently, single pores are determined to be larger, and the cumulative curve in Fig. 5 is shifted to the right compared to the results obtained by the *factorisation* method for the same resolution. The mean pore diameter has an error of only 3% in comparison to the one obtained with the segmentation method *factorisation*. Hence, the bias caused by an inadequate segmentation method is much smaller than insufficient resolution for describing the pore size.

3 Surface Triangulations and Curvature Estimation

For complex measures in drop-solid interaction such as wetted surface area, fluid-fluid interfacial area and surface curvatures, simply counting of voxel faces results in an overestimation of the surface area. The latter cannot be corrected by a finer resolution. Therefore, surface mesh generating techniques in combination with smoothing algorithms should be applied in constructing triangulation of the surfaces. Widley used is e.g. the marching cubes algorithm [20]. Here, grayscale image data are segmented and from the resulting isosurfaces, the triangle mesh is computed. Herefor, linear interpolation is applied to identify surface patches. Another method is the Delaunay triangulation [21, 22].

The test data set for triangulations, according to ISO 3290 calibrated sphere of 1 mm in radius, was acquired scanning with 60 kV @ 15 μA_{target} and an emission focal spot of about 1.5 µm. The integration time amounts to 1.6 s and the step angle was 0.18°. The surface mesh is generated in Avizo® [17] based on the implemented marching cubes algorithm [23] and is rendered in Fig. 6a. A detail of the sphere is

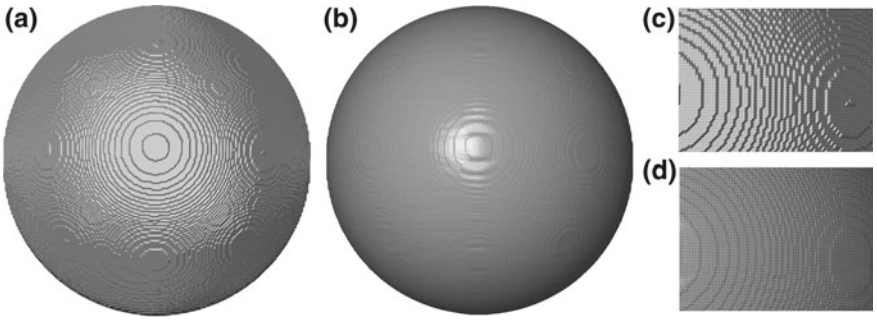

Fig. 6 Triangulated surface without surface smoothing (**a**) with surface smoothing (**b**) and respective detailed in (**c**) and (**d**)

depicted in Fig. 6c. Once a triangulated surface has been created, it is possible to directly measure the surface area by adding up the area of all triangles. Since the theoretical surface area and the volume of the calibrated sphere are known, their error can be determined. Both are overestimated, the surface by 8.6% and the volume by 0.09%. The inaccurate determination of the surface area from measured data arises from the fact that the triangles are only orientated parallel to the grid axis. As a consequence, the mesh is characterized by a staircase-like surface. Note that, imprecision eventually made during reconstruction, segmentation etc. are included in these errors. The application of the in Avizo® [17] implemented smoothing routine during surface generation can reduce the voxelized character of the boundary region. Here, the surface is smoothed using $7 \times 7 \times 7$ kernel size applying subvoxel weights such that the interface is naturally smoothed. By doing so, the labels are not modified. In general, smoothing should be applied with caution, and volume preserving needs to be always verified. In Fig. 6b, the smoothed surface mesh is depicted. The overestimating error of the surface area could be almost resolved and amounts to 0.12% keeping a constant volume. However, the close up in Fig. 6d shows that the mesh still features the voxelized character. The orientation of the triangles is limited to be parallel or at 45° inclined to the grid axis. This is a restriction of the marching cubes algorithm.

Since contact angle determination is based on the normal vectors to the surface, its calculation depends strongly on the orientation of the surface triangles, see Fig. 7. As described above, the margin cubes algorithm limits the normal vector direction so that an additionally volume-preserving Gaussian smoothing is recommend [3, 24], see the result in Fig. 7c. Here, normal and tangential smoothing filters were applied. The first reduces blocky voxel segmentation artefacts. Vertex displacement along the surface normal was restricted to half of the voxel size, and a total normal displacement was avoided applying a compensating shift in the vertex neighbours.

Instead, the curvature is a differential property and, thereby, extremely noise sensitive. The definition of mean and Gaussian curvature is shown in Eqs. (3) and (4), respectively.

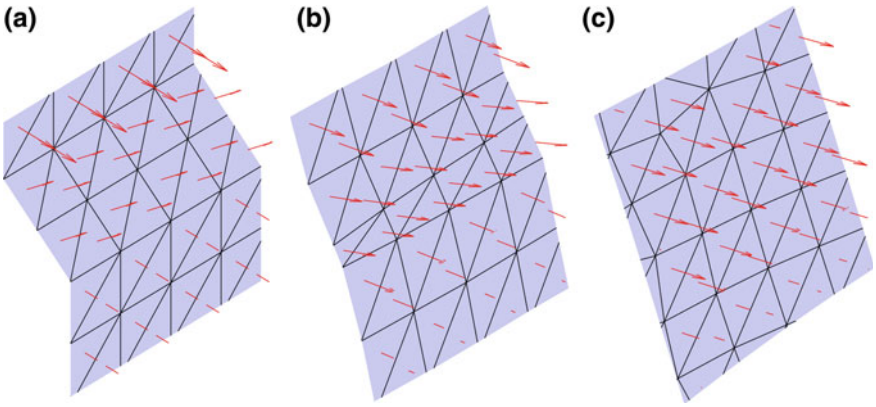

Fig. 7 Orientation of face normal vectors without surface smoothing (**a**) with surface smoothing (**b**) and additional tangential and vertical volume preserving Gaussian smoothing (**c**)

$$k_G = k_1 \cdot k_2 \tag{4}$$

Flynn and Jain [25] stated that the quality of curvature calculation is poor unless the mesh has been smoothed. Surface meshes based on tomographic data are affected by mesh resolution, regularity, valence and noise. A general overview can be found in the work from Gatzke and Grimm [26] comparing the sensitivity of different algorithms for estimating curvatures on triangular meshes. Local least-square approximation of the interface using quadric functions can improve significantly the curvature prediction [2, 13]. Here, a Monge patch [13] relative to the local tangent plane was used, so that the height function can be expressed by

$$f(x, y) = ax^2 + by^2 + cxy + dx + ey + f \tag{5}$$

The vertices were fitted to Eq. (5) considering the third-ring neighbourhood. Then, the eigenvectors and eigenvalues of the Hessian matrix were used to calculate the mean and Gaussian curvature. The averaged Gaussian curvature calculated for all vertexes, mesh quality depicted in Fig. 7c, could be precisely determined and correspond to the theoretical value of 1.00×10^{-6} $\mu m^2 \pm 0.13 \times 10^{-6}$ μm^2. The derivation of measured radius curvatures of each vertex for this dataset was found to be less than twice the voxel size and more accurate than comparative values specified in the literature [2].

4 Conclusions

The application of microcomputed tomography allows rather sophisticated analysis. Their interpretation and results are not anymore presented in a mere qualitative way.

Based on the data obtained and analysis performed on the two tomographic data, the following conclusions can be drawn:

- Bimodal intensity distributions are required for avoiding segmentation errors.
- Tomographic data featuring bimodal intensities distributions may not have micro-scale resolution.
- Insufficient resolution has larger impact on the morphological characterisation than an unproper chosen segmentation method.
- Advanced 3D analysis based on surface triangulations requires ad hoc volume preserving smoothing. Differential properties need an additional polygon fitting considering the vertexes' neighbourhood.

References

1. Scanziani, A., Singh, K., Blunt, M., Guadagnini, A.: Automatic method of in situ effective contact angle from X-ray micro tomography images of two-phase flow in porous media. J. Colloid Interface Sci. **496**, 51–59 (2017)
2. Armstrong, R.T., Porter, M.I., Wildenschild, D.: Linking pore-scale interfacial curvature to column-scale capillary pressure. Adv. Water Resour. **46**, 55–62 (2012)
3. AlRatrout, A., Raeini, A.Q., Bijeljic, B., Blunt, M.J.: Automatic measurement of contact angle in pore-space images. Adv. Water Resour. **109**, 158–169 (2017)
4. Santini, M., Guilizzoni, M., Fest-Santini, S., Lorenzi, M.: A novel technique for investigation of complete and partial anisotropic wetting on structured surface by X-ray microtomography. Rev. Sci. Instrum. **86**, 023708 (2015)
5. Shaoo, P., Soltani, S., Wong, A.: A survey of thresholding techniques. Comput. Vis. Graph. Image Process. **41**(11), 233–260 (1988)
6. Pal, N.R., Pal, S.K.: A review on image segmentation techniques. Pattern Recogn. **26**(9), 1277–1294 (1993)
7. Sezgin, M., Sankur, B.: Survey over image thresholding techniques and quantitative performance evaluation. J. Electron. Imaging **13**(1), 146–165 (2004)
8. Schlüter, S., Sheppard, A., Brown, K., Wildenschild, D.: Image processing of multiphase images obtained via X-ray microtomography: a review. Water Resour. Res. **50**, 3615–3639 (2014)
9. Pun, T.: Entropic thresholding: a new approach. Comput. Graph. Image Process. **16**, 210–239 (1981)
10. Kapur, J.N., Sahoo, P.K., Wong, A.K.C.: A new method for gray-level picture thresholding using entropy histogram. Comput. Vis. Graph. Image Process. **29**, 273–285 (1985)
11. Otsu, N.: A thresholding selection method from grayscale histogram. IEEE Trans. Syst. Man Cybern. **9**(1), 62–66 (1979)
12. Tsai, W.H.: Moment-preserving thresholding: a new approach. Comput. Vis. Graph. Image Process. **29**, 377–393 (1985)
13. Kittler, J., Illingworth, J.: Minimum error thresholding. Pattern Recogn. **19**(1), 41–47 (1986)
14. Santini, M., Fest-Santini, S., Foltyn, P.: On the local mass transfer rates around arbitrary shaped particles calculated by X-ray computed microtomography: prospective for a novel experimental technique. Int. Commun. Heat Mass Transfer **79**, 135–139 (2016)
15. Porter, M.I., Wildenschild, D.: Image analysis algorithm for estimating porous media multiphase flow variables from computational microtomography data: a validation study. Comput. Geosci. **14**(1), 15–30 (2010)
16. Peng, S., Hu, Q., Dultz, S., Zhang, M.: Using X-ray computed tomography in pore structure characterization for a Berea sandstone: resolution effect. J. Hydrol. **472–473**, 254–261 (2012)

17. Thermo Fisher Scientific: User's Guide Avizo Software 2019. https://assets.thermofisher.com/TFS-Assets/MSD/Product-Guides/users-guide-avizo-software-019.pdf (2019)
18. Zhang, Y., Xiao, L., Liao, G., Song, Y.-Q.: Direct correlation of diffusion and pore size distributions with low field NMR. J. Magn. Reson. **269**, 196–202 (2016)
19. Nickerson, S., Shu, Y., Zhong, D., Könke, C., Tandia, A.: Permeability of porous ceramics by X-ray CT image analysis. Acta Mater. **172**, 121–130 (2019)
20. Lorensen, W.E., Cline, H.E.: Marching cubes: a high resolution 3D surface construction algorithm. ACM SIGGRAPH Comput. Graph. **21**(4), 163–169 (1987)
21. Ruppert, J.: A Delaunay refinement algorithms for quality 2-dimensional mesh generation. J. Algorithms **18**, 548–585 (1995)
22. Shewchuk, J.R.: Delaunay refinement algorithms for triangular mesh generation. Comput. Geom. **22**(1–3), 21–74 (2002)
23. Hege, H.-C., Seebass, M., Stalling, D., Zockler, M.: A generalized marching cubes algorithm based on non-binary classifications. ZIB Preprint SC-97-05 (1997)
24. Garcia, D.: Robust smoothing of gridded data in one and higher dimensions with missing values. Comput. Stat. Data Anal. **54**(4), 1167–1178 (2010)
25. Flynn, P.J., Jain, A.K.: On reliable curvature estimation. IEEE Comput. Soc. Conf. Comput. Vis. Pattern Recogn. **88**, 5–9 (1989). (June 4–8 1989)
26. Gatzke, T.D., Grimm, C.M.: Estimating curvature on triangular meshes. Int J Shape Model **12**(1), 1–28 (2006)

A Phase Field Approach to Compressible Droplet Impingement

Lukas Ostrowski, Francesco Carlo Massa and Christian Rohde

Abstract We consider the impingement of a droplet onto a wall with high impact speed. To model this process we favour a diffuse-interface concept. Precisely, we suggest a compressible Navier–Stokes–Allen–Cahn model following [5]. Basic properties of the model are discussed. To cope with the fluid-wall interaction, we derive thermodynamically consistent boundary conditions that account for dynamic contact angles. We briefly discuss a discontinuous Galerkin scheme which approximates the energy dissipation of the system exactly and illustrate the results with a series of numerical simulations. Currently, these simulations are restricted to static contact angle boundary conditions.

1 Introduction

In many fluid dynamic scenarios the compressibility of a liquid is negligible. This allows for simplifications such that direct numerical simulations can rely on simpler incompressible models. In the context of droplet impingement incompressibility is only justified for small impact speeds. High impact speeds trigger compressibility effects of the liquid droplet, which can determine the flow dynamics significantly. Examples for high speed droplet impact scenarios can be found in many industrial applications such as liquid-fueled engines, spray cooling or spray cleaning. In [9] it has been shown that incompressible models are not adequate to describe high speed impacts, especially due to the fact that the jetting dynamics are influenced

L. Ostrowski (✉) · C. Rohde
Institute of Applied Analysis and Numerical Simulation, University of Stuttgart, Stuttgart, Germany
e-mail: Lukas.Ostrowski@ians.uni-stuttgart.de

C. Rohde
e-mail: Christian.Rohde@ians.uni-stuttgart.de

F. C. Massa
Department of Engineering and Applied Sciences, University of Bergamo, Bergamo, Italy
e-mail: francescocarlo.massa@unibg.it

G. Lamanna et al. (eds.), *Droplet Interactions and Spray Processes*,
Fluid Mechanics and Its Applications 121,
https://doi.org/10.1007/978-3-030-33338-6_9

by a developing shock wave in the liquid phase [8]. The time after the impact of the droplet until jetting is actually smaller than the predicted time of incompressible models due to the shock wave pattern. In [9] a compressible sharp-interface model is used for the simulations. However, sharp-interface models become intricate in the presence of changes in droplet topology and contact line motion. For this reason, we introduce a diffuse-interface model in this contribution, namely a compressible Navier–Stokes–Allen–Cahn phase field model which allows for complex interface morphologies and dynamic contact angles.

2 Phase Field Models

Phase field models form a special class of diffuse-interface models. In contrast to sharp-interface models, the interface has a (small) finite thickness and in the interfacial region the different fluids are allowed to mix. An additional variable, the *phase field*, is introduced which allows to distinguish the different phases. This concept has the advantage that only one system of partial differential equations on the entire considered domain needs to be solved, whereas for sharp-interface models bulk systems need to be solved, which are coupled across the interface by possibly complex conditions. Based on energy principles, phase field models can be derived in a thermodynamic framework, see [2, 6] for an overview. They fulfill the second law of thermodynamics, meaning that the Clausius–Duhem inequality [19] is fulfilled. In the case of isothermal models this is equivalent to an energy inequality. There are several (quasi-)incompressible [1, 12], compressible [3, 5, 20] and recently even incompressible–compressible phase field models [14, 18]. In this section we introduce a compressible Navier–Stokes–Allen–Cahn model.

2.1 A Compressible Navier–Stokes–Allen–Cahn System

We consider a viscous fluid at constant temperature. The fluid is assumed to exist in two phases, a liquid phase denoted by subscript L and a vapor phase denoted by subscript V. In each phase the fluid is thermodynamically described by the corresponding Helmholtz free energy density $\varrho f_{\mathrm{L/V}}(\varrho)$. The fluid occupies a domain $\Omega \subset \mathbb{R}^d$, $d \in \mathbb{N}$. Let $\varrho > 0$ be the density of the fluid, $\mathbf{v} \in \mathbb{R}^d$ the velocity and $\varphi \in [0, 1]$ the phase field. Following [5] we assume that the dynamics of the fluid is described by the isothermal compressible Navier–Stokes–Allen–Cahn system.

$$\partial_t \varrho + \operatorname{div}(\varrho \mathbf{v}) = 0, \tag{1}$$

$$\partial_t(\varrho \mathbf{v}) + \operatorname{div}(\varrho \mathbf{v} \otimes \mathbf{v} + p\mathbf{I}) = \operatorname{div}(\mathbf{S}) - \gamma \operatorname{div}(\nabla\varphi \otimes \nabla\varphi) \text{ in } \Omega \times (0, T), \tag{2}$$

$$\partial_t(\varrho\varphi) + \operatorname{div}(\varrho\varphi\mathbf{v}) = -\eta\mu. \tag{3}$$

The Helmholtz free energy density ϱf is defined as

$$\varrho f(\varrho, \varphi, \nabla\varphi) = h(\varphi)\varrho f_{\mathrm{L}}(\varrho) + (1 - h(\varphi))\varrho f_{\mathrm{V}}(\varrho) + \frac{1}{\gamma}W(\varphi) + \frac{\gamma}{2}|\nabla\varphi|^2 \tag{4}$$

$$=: \varrho\psi(\varphi, \varrho) + \frac{1}{\gamma}W(\varphi) + \frac{\gamma}{2}|\nabla\varphi|^2. \tag{5}$$

It consists of the interpolated free energy densities $\varrho f_{\mathrm{L/V}}$ of the pure liquid and vapor phases with the nonlinear interpolation function

$$h(\varphi) = 3\varphi^2 - 2\varphi^3, \tag{6}$$

and a mixing energy [4] using the double well potential $W(\varphi) = \varphi^2(1-\varphi)^2$.

The hydrodynamic pressure p is determined through the Helmholtz free energy ϱf by the thermodynamic relation

$$p = p(\varrho, \varphi) = -\varrho f(\varrho, \varphi) + \varrho\frac{\partial(\varrho f)}{\partial\varrho}(\varrho, \varphi). \tag{7}$$

We define the generalized chemical potential

$$\mu = \frac{1}{\gamma}W'(\varphi) + \frac{\partial(\varrho\psi)}{\partial\varphi} - \gamma\Delta\varphi, \tag{8}$$

which steers the phase field variable into equilibrium. Additionally, we denote by $\eta > 0$ the (artificial) mobility.

The dissipative viscous part of the stress tensor reads as $\mathbf{S} = \mathbf{S}(\varphi, \nabla\mathbf{v}) = \nu(\varphi)(\nabla\mathbf{v} + \nabla\mathbf{v}^\top - \mathrm{div}(\mathbf{v})\mathbf{I})$ with an interpolation of the viscosities $\nu_{\mathrm{L/V}}$ of the pure phases $\nu(\varphi) = h(\varphi)\nu_{\mathrm{L}} + (1 - h(\varphi))\nu_{\mathrm{V}} > 0$.

The energy of the system (1)–(3) at time t is defined as

$$\begin{aligned}\tilde{E}(t) &:= E_{\mathrm{free}}(t) + E_{\mathrm{kin}}(t)\\ &= \int_\Omega \varrho(\mathbf{x}, t) f(\varrho(\mathbf{x}, t), \varphi(\mathbf{x}, t), \nabla\varphi(\mathbf{x}, t)) + \frac{1}{2}\varrho(\mathbf{x}, t)|\mathbf{v}(\mathbf{x}, t)|^2 \,\mathrm{d}\mathbf{x}.\end{aligned} \tag{9}$$

Remark 1

1. The phase field φ is in general an artificial variable, however in this case it can be viewed as a mass fraction $\varphi = \frac{m_{\mathrm{V}}}{m}$, with the mass m_{V} of the vapor constituent and the total mass m of the fluid.
2. The special form of the nonlinear interpolation function h with $h'(0) = h'(1) \neq 0$ guarantees that (1)–(3) allows for physical meaningfull equilibria. This can be easily seen by considering a static single-phase equilibrium $\mathbf{v} = \mathbf{0}, \varphi \equiv 0$. If $h'(0) \neq 0$ then the right hand side of the phase field equation (3) does not vanish.

Assuming an impermeable wall, the velocity must satisfy the boundary condition

$$\mathbf{v} \cdot \mathbf{n} = 0 \quad \text{on } \partial\Omega. \tag{10}$$

Additionally, the system is endowed with initial conditions

$$\varrho = \varrho_0, \quad \mathbf{v} = \mathbf{v}_0, \quad \varphi = \varphi_0 \quad \text{on } \Omega \times \{0\}, \tag{11}$$

using suitable functions $(\varrho_0, \mathbf{v}_0, \varphi_0) \colon \Omega \to \mathbb{R}^+ \times \mathbb{R}^d \times [0, 1]$.

However, in order to close the system, Eq. (10) does not suffice. In the following section we derive a complete set of boundary conditions that allow for moving contact lines (MCL).

2.2 Boundary Conditions

The system (1)–(3) needs to be complemented with initial and boundary conditions. We are interested in MCL problems. With a sharp-interface point of view, the contact line is the intersection of the liquid-vapor interface with the solid wall. The requirement of a contact line moving along the wall renders the derivation of boundary conditions nontrivial. Figure 1 depicts a sketch of a compressible droplet impact scenario with the rebound shock wave dynamics and a moving contact line. We derive appropriate boundary conditions to handle MCL problems with the phase field system (1)–(3) in this section.

For the incompressible case, so called *general Navier boundary conditions* (GNBC) have been derived [16, 17]. Motivated by these works we extend GNBC to the compressible case.

Because phase field modelling goes well with energy principles we add a wall free energy term $\int_{\partial\Omega} g(\varphi)\ \mathrm{d}s$ to the energy $\tilde{E}$ from (9) and obtain

$$\begin{aligned} E(t) &= \tilde{E}(t) + E_{\text{wall}}(t) \\ &= \int_\Omega \varrho(t) f(\varrho(t), \varphi(t), \nabla\varphi(t)) + \frac{1}{2}\varrho(t)|\mathbf{v}(t)|^2 \ \mathrm{d}\mathbf{x} + \int_{\partial\Omega} g(\varphi(t)) \ \mathrm{d}s. \end{aligned} \tag{12}$$

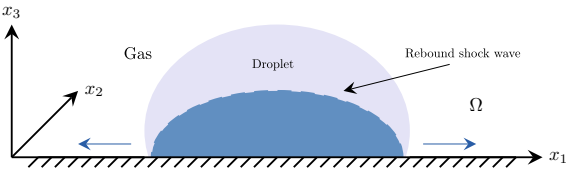

Fig. 1 Sketch of a compressible droplet impingement on a flat wall with moving contact line

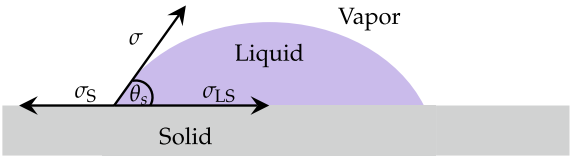

Fig. 2 Illustration of Young's equation $\sigma \cos(\theta_s) = \sigma_S - \sigma_{LS}$.

Here $g(\varphi)$ is the interfacial free energy per unit area at the fluid-solid boundary depending only on the local composition [17]. The specific choice for g is motivated by Young's equation. With a sharp-interface point of view we have

$$\sigma \cos(\theta_s) = \sigma_S - \sigma_{LS}, \tag{13}$$

with the surface free energy σ of the liquid, the static contact angle θ_s, surface free energy σ_S of the solid, and interfacial free energy σ_{LS} between liquid and solid, see Fig. 2. We prescribe the difference in energy for g, i.e.

$$\sigma_S - \sigma_{LS} = g(0) - g(1). \tag{14}$$

Then, we choose a smooth interpolation between the values $\pm\frac{\Delta g}{2} = \pm\frac{g(1)-g(0)}{2}$. However, it was shown in [16] that the choice of the kind interpolation has no large impact. Hence, for reasons of consistency we use h as interpolation function. With (13) we obtain

$$g(\varphi) := -\sigma \cos(\theta_s) \left(h(\varphi) - \frac{1}{2} \right). \tag{15}$$

A variation $\delta\varphi$ of φ leads to a variation δE of the energy (12), that is

$$\delta E = \int_\Omega \mu \delta\varphi \ \mathrm{d}\mathbf{x} - \int_{\partial\Omega} L(\varphi) \frac{\partial\varphi}{\partial_{\boldsymbol{\tau}}} \delta\varphi_{\boldsymbol{\tau}}.$$

Here,

$$L(\varphi) := \gamma \frac{\partial\varphi}{\partial\mathbf{n}} + g'(\varphi)$$

can be interpreted as uncompensated Young stress [16]. The boundary tangential vector is denoted by $\boldsymbol{\tau}$ and $\mathbf{n}$ denotes the outer normal. Thus, $L(\varphi) = 0$ is the Euler–Lagrange equation at the fluid-solid boundary for minimizing the energy (12) with respect to the phase field variable. We assume a boundary relaxation dynamics for φ given by

$$\partial_t \varphi + \mathbf{v} \cdot \nabla_{\boldsymbol{\tau}} \varphi = -\frac{\alpha}{\varrho} L(\varphi), \tag{16}$$

with a relaxation parameter $\alpha > 0$. Here $\nabla_{\boldsymbol{\tau}} := \nabla - (\mathbf{n} \cdot \nabla)\mathbf{n}$ is the gradient along the tangential direction. Since $\mathbf{v} \cdot \mathbf{n} = 0$, we have $\mathbf{v} \cdot \nabla_{\boldsymbol{\tau}} \varphi = v_{\boldsymbol{\tau}} \frac{\partial \varphi}{\partial \boldsymbol{\tau}}$, and finally we obtain

$$\partial_t \varphi + v_{\boldsymbol{\tau}} \frac{\partial \varphi}{\partial \boldsymbol{\tau}} = -\frac{\alpha}{\varrho} L(\varphi) \quad \text{on } \partial\Omega. \tag{17}$$

In order to complete the derivation of the GNBC we incorporate a slip velocity boundary condition. In single phase models, the slip velocity is often taken proportional to the tangential viscous stress. However, in our case we also have to take the uncompensated Young stress into account. In [16] it is shown from molecular dynamic simulations that the slip velocity should be taken proportional to the sum of the tangential viscous stress and the uncompensated Young stress. Hence, with the slip length $\beta > 0$ we prescribe the boundary condition

$$\beta v_{\boldsymbol{\tau}} + \nu(\varphi) \frac{\partial v_{\boldsymbol{\tau}}}{\partial \mathbf{n}} - L(\varphi) \frac{\partial \varphi}{\partial \boldsymbol{\tau}} = 0 \quad \text{on } \partial\Omega. \tag{18}$$

Away from the interface the last term in (18) drops out and we have the classical Navier-slip condition but in the interface region the additional term acts and allows for correct contact line movement.

In summary we obtain the following GNBC for the MCL problem

$$\mathbf{v} \cdot \mathbf{n} = 0, \tag{19}$$

$$\beta v_{\boldsymbol{\tau}} + \nu(\varphi) \frac{\partial v_{\boldsymbol{\tau}}}{\partial \mathbf{n}} - L(\varphi) \frac{\partial \varphi}{\partial \boldsymbol{\tau}} = 0, \qquad \text{on } \partial\Omega. \tag{20}$$

$$\partial_t \varphi + v_{\boldsymbol{\tau}} \frac{\partial \varphi}{\partial \boldsymbol{\tau}} = -\frac{\alpha}{\varrho} L(\varphi) \tag{21}$$

The GNBC (19), (20), (21) contain certain subcases. For $\alpha \to \infty$ we obtain the static contact angle boundary condition and with $\beta \to \infty$ we end up with no-slip boundary conditions.

Remark 2 Since currently our dynamic contact angle model is not yet implemented, we will adress a validation of the GNBC in future work. In [13] the analog to (19)–(21) for an incompressible phase field model is validated with numerical experiments.

2.3 Energy Inequality

For isothermal models thermodynamical consistency means to verify that solutions of the problem at hand admit an energy inequality. The energy introduced in (12) consists of the bulk and wall free energies and the kinetic energy. To describe the total energy the entropic part is missing. That means the entropy production of the system (1)–(3) is exactly $-\frac{\mathrm{d}}{\mathrm{d}t} E(t)$. Hence, by assuring that the energy E decreases

over time, we show increasing entropy and therefore thermodynamical consistency. For the system (1)–(3) we have the following result.

Theorem 1 (Energy inequality) *Let* $(\varrho, \mathbf{v}, \varphi)$ *with values in* $(0, \infty) \times \mathbb{R}^d \times [0, 1]$ *be a classical solution of* (1)–(3) *in* $(0, T) \times \Omega$ *satisfying the boundary conditions* (19)–(21) *on* $(0, T) \times \partial\Omega$. *Then for all* $t \in (0, T)$ *the following energy inequality holds:*

$$\begin{aligned}
&\frac{\mathrm{d}}{\mathrm{d}t} E(t) = \frac{\mathrm{d}}{\mathrm{d}t}(E_{\text{free}}(t) + E_{\text{kin}}(t) + E_{\text{wall}}(t)) \\
&= \frac{\mathrm{d}}{\mathrm{d}t}\left(\int_\Omega \varrho f(\varrho, \mathbf{v}, \varphi, \nabla\varphi) + \frac{1}{2}\varrho|\mathbf{v}|^2 \ \mathrm{d}\mathbf{x} + \int_{\partial\Omega} g(\varphi) \ \mathrm{d}s\right) \\
&= -\int_\Omega \frac{\eta}{\varrho}\mu^2 \ \mathrm{d}\mathbf{x} - \int_\Omega \mathbf{S} \colon \nabla\mathbf{v} \ \mathrm{d}\mathbf{x} - \int_{\partial\Omega} \beta|v_\tau|^2 \ \mathrm{d}s - \int_{\partial\Omega} \frac{\alpha}{\varrho}|L(\varphi)|^2 \ \mathrm{d}s \leq 0. \quad (22)
\end{aligned}$$

As expected, we have entropy production due to phase transition, viscosity, wall slip, and composition relaxation at the solid interface.

Proof In a straightforward way we compute:

$$\begin{aligned}
\frac{\mathrm{d}}{\mathrm{d}t} E(t) =& \frac{\mathrm{d}}{\mathrm{d}t}\left(\int_\Omega \varrho f(\varrho, \varphi, \nabla\varphi) + \frac{1}{2}\varrho|\mathbf{v}|^2 \ \mathrm{d}\mathbf{x} + \int_{\partial\Omega} g(\varphi) \ \mathrm{d}s\right) \\
=& \frac{\mathrm{d}}{\mathrm{d}t}\left(\int_\Omega \frac{1}{\gamma}W(\varphi) + \varrho\psi(\varrho, \varphi) + \frac{\gamma}{2}|\nabla\varphi|^2 + \frac{1}{2}\varrho|\mathbf{v}|^2 \ \mathrm{d}\mathbf{x} + \int_{\partial\Omega} g(\varphi) \ \mathrm{d}s\right) \\
=& \int_\Omega \varphi_t\left(\frac{1}{\gamma}W'(\varphi) + \frac{\partial(\varrho\psi)}{\partial\varphi} - \gamma\Delta\varphi\right) + \varrho_t\left(\frac{\partial(\varrho\psi)}{\partial\varrho} - \frac{1}{2}|\mathbf{v}|^2\right) + (\varrho\mathbf{v})_t \cdot \mathbf{v} \ \mathrm{d}\mathbf{x} \\
&+ \int_{\partial\Omega} \varphi_t(g'(\varphi) + \gamma\nabla\varphi \cdot \mathbf{n}) \ \mathrm{d}s.
\end{aligned}$$

Now we use (1)–(3) to replace the time derivatives in the volume integrals. Using (7) we obtain after basic algebraic manipulations

$$\begin{aligned}
\frac{\mathrm{d}}{\mathrm{d}t} E(t) =& -\int_\Omega \mathrm{div}(\varrho\mathbf{v})\left(\frac{\partial(\varrho\psi)}{\partial\varrho} - \frac{1}{2}|\mathbf{v}|^2\right) + \mathrm{div}(\varrho\mathbf{v}\otimes\mathbf{v}) \cdot \mathbf{v} \ \mathrm{d}\mathbf{x} - \int_\Omega \frac{\eta}{\varrho}\mu^2 \ \mathrm{d}\mathbf{x} \\
&- \int_\Omega \mathbf{v} \cdot \varrho\nabla\left(\frac{\partial(\varrho\psi)}{\partial\varrho}\right) - \mathrm{div}(\mathbf{S}) \cdot \mathbf{v} \ \mathrm{d}\mathbf{x} + \int_{\partial\Omega} \varphi_t L(\varphi) \ \mathrm{d}s.
\end{aligned}$$

We integrate by parts and have

$$\begin{aligned}
\frac{\mathrm{d}}{\mathrm{d}t} E(t) =& -\int_\Omega \frac{\eta}{\varrho}\mu^2 \ \mathrm{d}\mathbf{x} - \int_\Omega \mathbf{S} \colon \nabla\mathbf{v} \ \mathrm{d}\mathbf{x} + \int_{\partial\Omega} \varphi_t L(\varphi) \ \mathrm{d}s \\
&+ \int_{\partial\Omega} \mathbf{S}\mathbf{v} \cdot \mathbf{n} - \varrho\mathbf{v}\left(\frac{\partial(\varrho\psi)}{\partial\varrho} + \frac{1}{2}|\mathbf{v}|^2\right) \cdot \mathbf{n} \ \mathrm{d}s.
\end{aligned}$$

With the boundary conditions (19)–(21) we finally obtain

$$\frac{\mathrm{d}}{\mathrm{d}t}E(t) = -\int_\Omega \frac{\eta}{\varrho}\mu^2 \,\mathrm{d}\mathbf{x} - \int_\Omega \mathbf{S}\colon \nabla\mathbf{v} \,\mathrm{d}\mathbf{x} - \int_{\partial\Omega} \beta|v_\tau|^2 \,\mathrm{d}s - \int_{\partial\Omega} \frac{\alpha}{\varrho}|L(\varphi)|^2 \,\mathrm{d}s.$$

This concludes the proof. □

2.4 Surface Tension

There are different interpretations of surface tension. It can be either viewed as a force acting in tangential direction of the interface or as excess energy stored in the interface [10]. In line with our energy-based derivation we consider a planar equilibrium profile and integrate the excess free energy density over this profile. We assume that static equilibrium conditions hold, i.e. $\mathbf{v} = \mathbf{0}$. The planar profile is assumed to be parallel to the x-axis and density, velocity and phase field are independent from t, y, and z. Then the equilibrium is governed by the solution of the following boundary value problem on the real line.

Find $\varrho = \varrho(x)$, $\varphi = \varphi(x)$ such that

$$\left(-\varrho\psi - \frac{1}{\gamma}W(\varphi) - \frac{\gamma}{2}\varphi_x^2 + \varrho\frac{\partial(\varrho\psi)}{\partial\varrho}\right)_x = -\gamma(\varphi_x^2)_x, \tag{23}$$

$$\frac{1}{\gamma}W'(\varphi) + \frac{\partial(\varrho\psi)}{\partial\varphi} - \gamma\varphi_{xx} = 0, \tag{24}$$

and

$$\varrho(\pm\infty) = \varrho_{\mathrm{V/L}}, \quad \varphi(-\infty) = 0, \quad \varphi(\infty) = 1, \quad \varphi_x(\pm\infty) = 0. \tag{25}$$

Multiplying (24) with φ_x and subtracting from (23) yields

$$\frac{\partial(\varrho\psi)}{\partial\varrho} = const. \tag{26}$$

Multiplying (24) with φ_x, integrating from $-\infty$ to some $x \in \mathbb{R}$ using (23) and (25) leads to

$$\frac{1}{\gamma}W(\varphi(x)) + \varrho(x)\psi(\varrho(x), \varphi(x)) - \varrho_{\mathrm{V}}(x)\psi(\varrho_{\mathrm{V}}(x), 0) = \frac{\gamma}{2}\varphi_x^2(x). \tag{27}$$

From (27) we obtain for $x \to \infty$

$$\varrho_{\mathrm{L}}\psi(\varrho_{\mathrm{L}}, 1) = \varrho_{\mathrm{V}}\psi(\varrho_{\mathrm{V}}, 0) =: \overline{\varrho\psi}. \tag{28}$$

As mentioned before, surface tension can be defined by means of excess free energy. Roughly speaking an excess quantity is the difference of the quantity in the considered system and in a (sharp-interface) reference system where the bulk values are maintained up to a dividing interface. The interface position x_0 is determined by vanishing excess density.

In summary we define surface tension σ via the relationship

$$\begin{aligned}\sigma = &\int_{-\infty}^{x_0} \varrho f(\varrho, 0, \varphi, \varphi_x) - \varrho_{\mathrm{V}} \psi(\varrho_{\mathrm{V}}, 0) \ \mathrm{d}x \\ &+ \int_{x_0}^{\infty} \varrho f(\varrho, 0, \varphi, \varphi_x) - \varrho_{\mathrm{L}} \psi(\varrho_{\mathrm{L}}, 1) \ \mathrm{d}x,\end{aligned} \tag{29}$$

where (ϱ, φ) is a solution of (23)–(25). Using (27) we have

$$\sigma = \int_{-\infty}^{x_0} \gamma \varphi_x^2 \ \mathrm{d}x + \int_{x_0}^{\infty} \gamma \varphi_x^2 + (\varrho_{\mathrm{V}} \psi(\varrho_{\mathrm{V}}, 0) - \varrho_{\mathrm{L}} \psi(\varrho_{\mathrm{L}}, 1)) \ \mathrm{d}x. \tag{30}$$

With (28) it follows

$$\sigma = \int_{-\infty}^{\infty} \gamma \varphi_x^2 \ \mathrm{d}x = \sqrt{2} \int_{\varphi_{\mathrm{V}}}^{\varphi_{\mathrm{L}}} \sqrt{W(\varphi) + \gamma (\varrho \psi(\varrho(\varphi), \varphi) - \overline{\varrho \psi})} \ \mathrm{d}\varphi. \tag{31}$$

In the last step we used the transformation from x to φ integration. This is possible since ϱ can be written in dependence on φ: Assuming convex free energies $\varrho f_{\mathrm{L/V}}$ in (4), we have convex $\varrho \psi$ in ϱ and from (26) follows with the implicit function theorem $\varrho = \varrho(\varphi)$.

One can see that the surface tension is mainly dictated by the double well potential $W(\varphi)$. There is a contribution due to the equations of state of the different phases, however in the sharp-interface limit, i.e. $\gamma \to 0$ this contribution vanishes. This is a difference to (quasi-)incompressible models like [12]. There is no contribution due to the equation of states and the surface tension is purely determined by the double well function. Of course surface tension is a material parameter and given by physics depending on the fluids and walls considered. Therefore, in simulations the double well should be scaled accordingly to yield the correct surface tension. However, this can lead to numerical difficulties. To match typical surface tension values, W has to be scaled with very small parameters. This in turn demands an even smaller γ and therefore a high spatial resolution of the computational mesh. For that reason, we use a moderate scaling in our numerical experiments below.

3 Numerical Experiments

The phase field system (1)–(3) is of mixed hyperbolic-parabolic type. This complicates the derivation of discretization methods. An appropriate choice are discretizations based on discontinuous Galerkin methods. In fact even versions which reproduce the energy dissipation precisely are available [7, 11, 18]. The key idea behind those schemes is to achieve stabilization through the exact approximation of the energy, that means the energy inequality (22) should be fullfilled exactly on the discrete level without introducing numerical dissipation. This helps to prevent increase of energy and possibly associated spurious currents. Additionally, the schemes are designed such that they preserve the total mass. Motivated by [7, 11] we derived such a scheme for the system (1)-(3), for details we refer to [15]. In the following we present three numerical simulations using this scheme. We note that we present academic examples, i.e. chosen densities, velocity, and regimes of physical parameters do not match realistic fluids. The reason behind this is that for realistic equation of states and density values for current numerical schemes there is a slight mismatch between the density and phase field profile. This leads to a slightly too high percentage of liquid at very low density in the mixing zone and thus large negative pressures.

3.1 Choice of Parameters

For the equations of state in the bulk phases, we choose stiffened gas equations

$$\varrho f_{\mathrm{L/V}}(\varrho) = \alpha_{\mathrm{L/V}} \varrho \ln(\varrho) + (\beta_{\mathrm{L/V}} - \alpha_{\mathrm{L/V}})\varrho + \gamma_{\mathrm{L/V}},$$

with parameters $\alpha_{\mathrm{L/V}} > 0$, $\beta_{\mathrm{L/V}} \in \mathbb{R}$, $\gamma_{\mathrm{L/V}} \in \mathbb{R}$. In order to avoid preferring on of the phases, we choose the minima of the two free energies to be at the same height.

Due to surface tension the density inside a liquid droplet is slightly higher than the value which minimizes ϱf_{L}. The value of the surrounding vapor is slightly lower than the minimizer of ϱf_{V}. We choose the initial density profile accordingly. For the bulk viscosities we set $\nu_{\mathrm{L}} = 0.0125$ and $\nu_{\mathrm{V}} = 0.00125$. If not stated otherwise, the capillary parameter is taken $\gamma = 5 \cdot 10^{-4}$ and the mobility $\eta = 10$. The polynomial order of the DG polynomials is 2.

3.2 Merging Droplets

In order to illustrate that phase field models are able to handle topological changes, we consider the example of two merging droplets. Initially we have no velocity field, $\mathbf{v}_0 = \mathbf{0}$ and look at two kissing droplets. The computational domain is $[0, 1] \times [0, 1]$. The droplets are located at (0.39, 0.5) and (0.6, 0.5) with radii 0.08 and 0.12.

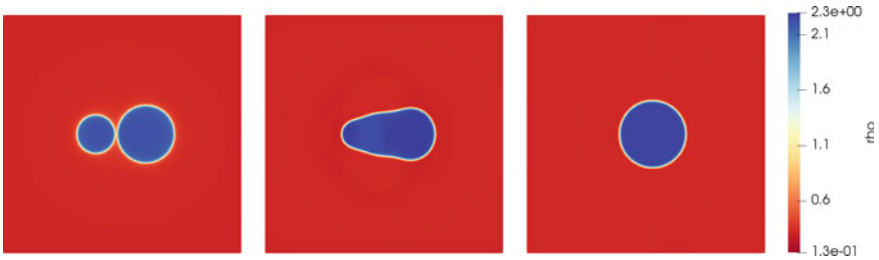

Fig. 3 Merging droplets. Density ϱ at times $t = 0$, $t = 0.2$, and $t = 2$ for $\eta = 10$.

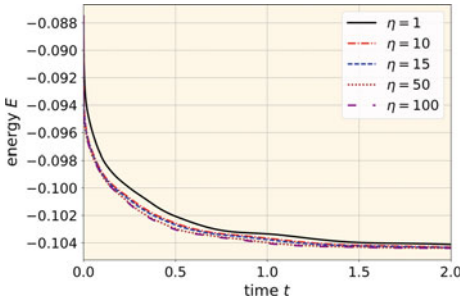

Fig. 4 Energy E over time for droplet merging simulation with different values for the mobility η

The parameters for the equations of states are $\alpha_L = 5$, $\beta_L = -4$, $\gamma_L = 11$, $\alpha_V = 1.5$, $\beta_V = 1.8$, $\gamma_V = 0.324$. The inital density profile is smeared out with value $\varrho_L = 2.23$ inside and $\varrho_V = 0.3$ outside the droplet. As expected the droplets merge into one larger droplet. This evolution with $\eta = 10$ is depicted in Fig. 3.

We can observe that the model handles topological changes easily. However, the dynamics of the phase field relaxation are determined by the mobility η which needs to be chosen according to the problem. This is illustrated in Fig. 4, where the energy over time for different values of the mobility η is plotted.

The numerical scheme is designed to mimic the energy inequality (22) on the discrete level. The discrete energy decreases, as expected from (22) the higher the value of η, the faster the energy dissipation.

3.3 Contact Angle

In this example we address droplet wall interactions. We consider the case of static contact angle. This means we let the relaxation parameter α in (17) tend to infinity. In the limit we obtain the static contact angle boundary conditions:

We set the static contact angle $\theta_s = 0.1\pi \approx 18°$. The computational domain, density values and EOS parameters are like in Sect. 3.2. As initial condition we use a droplet sitting on a flat surface with a contact angle of 90°. The droplet position is $(0.5, 0)$ with radius 0.2. Since the initial condition is far away from equilibrium we

Fig. 5 Wetting of smooth wall with (GNBC) boundary conditions for the static limit $\alpha \to \infty$ and contact angle $\theta_s = 0.1\pi$. Density ϱ at $t = 0$ and $t = 0.9$

have dynamics on the wall-boundary towards the equilibrium configuration. Thus, we can observe a wetting dynamic, see Fig. 5.

The wall contribution leads to a large force on the boundary, which renders the system stiff. Although we have an implicit scheme we increased the interface width to be able to handle the boundary terms. Hence, we chose in this simulation $\gamma = 10^{-2}$.

3.4 Droplet Impingement

With this example we consider droplet impingement. The computational domain is the same as in Sect. 3.2. As initial condition we use a droplet at $(0.5, 0.2)$ with radius 0.1. The parameters for the equations of states are $\alpha_\mathrm{L} = 5$, $\beta_\mathrm{L} = -0.8$, $\gamma_\mathrm{L} = 5.5$, $\alpha_\mathrm{V} = 1.5$, $\beta_\mathrm{V} = 1.8$, $\gamma_\mathrm{V} = 0.084$. The iniital density profile is smeared out with value $\varrho_\mathrm{L} = 1.2$ inside and $\varrho_\mathrm{V} = 0.3$ outside the droplet. The initial velocity inside the droplet is $v_y = -1$.

Sharp-interface models based on the Navier–Stokes equations in the bulk become ill-posed if no-slip conditions are imposed. However, solutions of phase field models come with contact line movement even if no-slip conditions are used. This is due to the fact that the contact line is regularized and the dynamics are driven by evolution in the phase field variable rather than advective transport. This can be seen in Fig. 6 where a droplet impact with no-slip conditions is simulated. This is a special case of the GNBC, with $\alpha \to \infty$ and $\beta \to \infty$.

It can be seen that the generalized chemical potential μ is low at the contact line which leads to fast dynamics in the phase field. This leads to a moving contact line. Additionally, especially in the Schlieren picture, we can see the (smeared out) shock waves in the vapor phase and also in the liquid phase where the shocks move faster due to a higher speed of sound in the liquid phase. In order to verify the compressibility of the droplet we plot the maximum of the local Mach number $M_{\rho f} = \bar{v}\sqrt{\frac{\bar{\rho}}{\rho_f}}$ in Fig. 7. We can observe a peak right after the impact.

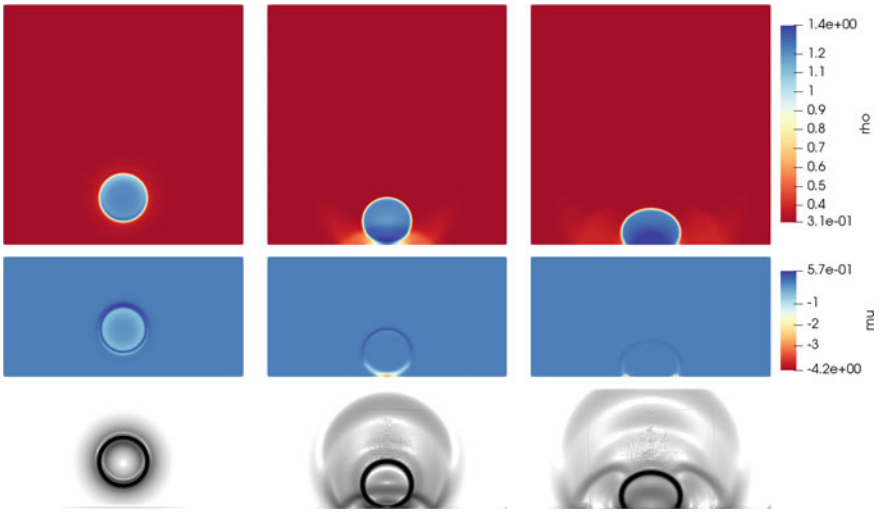

Fig. 6 Droplet impact simulation. Density ρ, chemical potential μ and Schlieren picture at times $t = 0.005$, $t = 0.13$, $t = 0.21$.

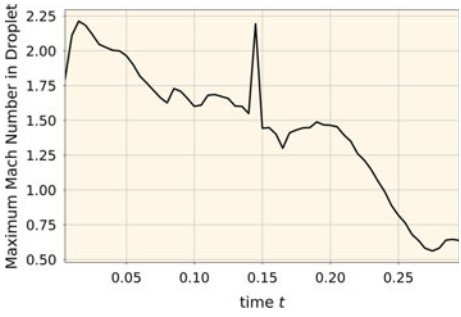

Fig. 7 Droplet impact simulation. Maximum of the local Mach number inside the liquid phase

4 Summary and Conclusions

In this work we presented a phase field approach to model and simulate compressible droplet impingement scenarios. To be precise, we introduced a compressible Navier–Stokes–Allen–Cahn model in Sect. 2.1. We discussed modelling aspects, with emphasis on the energy-based derivation. We highlighted the connection of thermodynamic consistency with an energy inequality. Further, we proved in Theorem 1 that solutions to the system fulfill this inequality. Surface tension can be interpreted as excess free energy. We quantified the amount of surface tension present in the model in Sect. 2.4. Moving contact line problems need special attention with respect to boundary conditions. Hence, physical relevant boundary conditions were derived as Generalized Navier Boundary Conditions in Sect. 2.2. In Sect. 3 numerical examples were given. In future work we implement the general, dynamic version of the GNBC to obtain jetting phenomena in the impact case.

References

1. Abels, H., Garcke, H., Grün, G.: Thermodynamically consistent, frame indifferent diffuse interface models for incompressible two-phase flows with different densities. Math. Models Methods Appl. Sci. **22**(3), 1150013, 40 (2012)
2. Anderson, D.M., McFadden, G.B., Wheeler, A.A.: Diffuse-interface methods in fluid mechanics. Annu. Rev. Fluid Mech. **30**(1), 139–165 (1998)
3. Blesgen, T.: A generalization of the Navier-Stokes equations to two-phase flows. J. Phys. D: Appl. Phys. **32**(10), 1119–1123 (1999)
4. Cahn, J.W., Hilliard, J.E.: Free energy of a nonuniform system. i. interfacial free energy. J. Chem. Phys. **28**(2), 258–267 (1958)
5. Dreyer, W., Giesselmann, J., Kraus, C.: A compressible mixture model with phase transition. Physica D **273–274**, 1–13 (2014)
6. Freistühler, H., Kotschote, M.: Phase-field and korteweg-type models for the time-dependent flow of compressible two-phase fluids. Arch. Rational Mech. Anal. **224**(1), 1–20 (2016)
7. Giesselmann, J., Pryer, T.: Energy consistent discontinuous Galerkin methods for a quasi-incompressible diffuse two phase flow model. M2AN Math. Model. Numer. Anal. **49(1)**, 275–301 (2015)
8. Haller, K.K., Ventikos, Y., Poulikakos, D.: Wave structure in the contact line region during high speed droplet impact on a surface: solution of the riemann problem for the stiffened gas equation of state. J. Appl. Phys. **93**(5), 3090–3097 (2003)
9. Haller, K.K., Ventikos, Y., Poulikakos, D., Monkewitz, P.: Computational study of high-speed liquid droplet impact. J. Appl. Phys. **92**(5), 2821–2828 (2002)
10. Jamet, D., Torres, D., Brackbill, J.: On the theory and computation of surface tension: the elimination of parasitic currents through energy conservation in the second-gradient method. J. Comput. Phys. **182**(1), 262–276 (2002)
11. Kränkel, M., Kröner, D.: A phase-field model for flows with phase transition. In: Theory, Numerics and Applications of Hyperbolic Problems II, pp. 243–254. Springer International Publishing, Cham (2018)
12. Lowengrub, J., Truskinovsky, L.: Quasi-incompressible Cahn-Hilliard fluids and topological transitions. Proc. R. Soc. A: Math. Phys. Eng. Sci. **454**(1978), 2617–2654 (1998)
13. Ma, L., Chen, R., Yang, X., Zhang, H.: Numerical approximations for allen-cahn type phase field model of two-phase incompressible fluids with moving contact lines. Commun. Comput. Phys. **21**(3), 867–889 (2017)
14. Ostrowski, L., Massa, F.: An incompressible–compressible approach for droplet impact. In: Cossali, G.E., Tonini, S. (eds.) Proceedings of the DIPSI Workshop 2019. Droplet Impact Phenomena & Spray Investigations (2019)
15. Ostrowski, L., Rohde, C.: Phase field modelling for compressible droplet impingement. In: Bressan, A., Lewicka, M., Wang, D., Zheng, Y. (eds.) Proceedings of the 17-th Conference on Hyperbolic Problems (2019)
16. Qian, T., Wang, X.P., Sheng, P.: Molecular scale contact line hydrodynamics of immiscible flows. Phys. Rev. E **68**, 016306 (2003)
17. Qian, T., Wang, X.P., Sheng, P.: A variational approach to moving contact line hydrodynamics. J. Fluid Mech. **564**, 333–360 (2006)
18. Repossi, E., Rosso, R., Verani, M.: A phase-field model for liquid-gas mixtures: mathematical modelling and discontinuous Galerkin discretization. Calcolo **54**(4), 1339–1377 (2017)
19. Truesdell, C.: The mechanical foundations of elasticity and fluid dynamics. J. Rational Mech. Anal. **1**, 125–300 (1952)
20. Witterstein, G.: Sharp interface limit of phase change flows. Adv. Math. Sci. Appl. **20**(2), 585–629 (2010)

Numerical Simulation for Drop Impact on Textured Surfaces

Martina Baggio and Bernhard Weigand

Abstract Superhydrophobic surfaces with small-scale features have recently gained interest, because impacting droplets may bounce-off faster with respect to a flat superhydrophobic surface. For such surfaces the correct numerical prediction of the impact phenomena is very difficult. Our goal is the numerical study of drop impact on such surfaces using Free Surface 3D (*FS3D*), our in-house code for the simulation of incompressible multi-phase flows. Until recently, *FS3D* was not able to represent the interaction of a droplet with a complex textured solid surface. In this work, we show how we added this feature to the code by implementing the representation of embedded arbitrary-shaped boundaries using a Cartesian grid. Two approaches were developed; a preliminary simplified approach and an ultimate, more rigorous one. We discuss both implementations and we show a comparison of the two approaches for a test case. The results show that the predictions for impact dynamics of the two approaches slightly differ. Although, the simplified approach shows only small errors in mass conservation, it is fundamentally not conservative. With the introduction of a new approach we were able to improve the conservativeness of our simulations.

1 Introduction

Superhydrophobic surfaces are of great technical interest because of their non-wetting behavior. Recently, it has been shown that superhydrophobic surfaces with macro-scale features with dimensions between 10^{-1} and 10^{0} mm can enhance water repellency by reducing the contact time between a water droplet and the solid surface. In particular, Bird et al. [1] have shown that the contact time for a droplet impacting on a superhydrophobic surface with a ridge was shorter than the contact time on a flat superhydrophobic surface because of the changed impact morphology. Gauthier et al. [2] found a relationship between contact time and number of liquid

M. Baggio (✉) · B. Weigand
Institute of Aerospace Thermodynamics, University of Stuttgart, Pfaffenwaldring 31, 70569 Stuttgart, DE, Germany
e-mail: martina.baggio@itlr.uni-stuttgart.de

G. Lamanna et al. (eds.), *Droplet Interactions and Spray Processes*,
Fluid Mechanics and Its Applications 121,
https://doi.org/10.1007/978-3-030-33338-6_10

sub-units formed during impact for droplet impacting on a superhydrophobic surface with a wire. The same trend between contact time and number of liquid sub-units was reproduced by Regulagadda et al. [3] for a drop impacting on the top and between superhydrophobic triangular ridges. The majority of literature dealing with contact time reduction on superhydrophobic surfaces with submillimetric- and millimetric-scale features consists of experimental studies. Chantelot et al. [4] performed both experiments and lattice Boltzmann simulations for drop impact on a superhydrophobic surface with a small spherical feature. Shen et al. [5] have presented experimental and numerical results for a drop bouncing on short cones. More numerical research exists for drop impact on superhydrophobic curved surfaces. Khojasteh et al. [6] have studied drop impact on hydrophobic and superhydrophobic spheres of different diameters. They used a Level-Set method for their simulations. Liu et al. [7] studied experimentally and numerically with a lattice Boltzmann method drop rebound on a cylindrical surface and analyzed the total momentum distribution in the directions parallel and perpendicular to the surface curvature. A numerical study on drop impact on hydrophobic and superhydrophobic cylinders at different wettabilites and impact velocities was also performed by Liu et al. [8]. It is apparent that only very few numerical research has dealt with drop impact on superhydrophobic surfaces with small scale features. This manuscript explain the method used in *Free Surface 3D (FS3D)* for predicting drop impact on textured surfaces. *FS3D* is a program for the Direct Numerical Simulation (DNS) of incompressible multi-phase flows, which was originally created at the Institute of Aerospace Thermodynamics at the University of Stuttgart and it is continuously being improved with new features. Up to now, *FS3D* has successfully been used for the prediction of various phenomena such as evaporation of oscillating droplets [9], drop collisions impact [10], jet break-up [11], ice formation [12] and sublimation [13]. Rauschenberger et al. [14] implemented a method to represent the motion of rigid particles immersed in a continuous fluid phase. However, until recently *FS3D* could not handle the motion of a fluid interface on a rigid body of arbitrary shape. Therefore, a prerequisite of our study was a method to represent arbitrary-shaped boundaries in a Cartesian grid. In this paper, after an illustration of *FS3D*'s numerical fundamentals, we will discuss two methods for the implementation of solid boundaries embedded in a Cartesian grid; a first approximate method and a second more rigorous method inspired by the work of Popinet [15]. With the first method, which was developed as a simplified approach, we introduced the necessary data structures and routines that later enabled us to develop the more rigorous method. After having illustrated the concepts on which the preliminary approach is based, we will discuss its problematics which led to the development of the second approach. After this, the second more rigorous method will be explained. Finally in Sect. 4 we compare results for a water drop impacting on a superhydrophobic surface with macro-ridges obtained with the two approaches.

2 Numerical Methods

In this section, the numerical fundamentals of *FS3D* are illustrated briefly; the work of Eisenschmidt et al. [16] provides a broader overview. Here we focus on the case of an incompressible Newtonian fluid of a single liquid phase immersed in a continuous gas phase. The flow is assumed to be isothermal without phase change. Thus, the energy equation does not need to be considered. The governing equations of the flow are then the conservation of mass:

$$\nabla \cdot \boldsymbol{u} = 0\,, \tag{1}$$

and momentum transport:

$$\frac{\partial(\rho \boldsymbol{u})}{\partial t} + \nabla \cdot (\rho \boldsymbol{u} \otimes \boldsymbol{u}) = -\nabla p + \nabla \cdot \mathbb{S} + \rho \boldsymbol{g} + \mathbf{f}_\sigma\,. \tag{2}$$

The $\mathbf{f}_\sigma$ term in Eq. (2) represents the surface tension force per unit volume which is different from zero only at the interface. This term is modeled with the Continuum Surface Stress (CSS) model of Lafaurie et al. [17]. A further equation is necessary for interface tracking. In *FS3D*, this equation is obtained with the Volume of Fluid (VOF) method of Hirt and Nichols [18]. The liquid disperse phase is represented by a colour function $\chi(\boldsymbol{x})$ defined as follows:

$$\chi(\boldsymbol{x}) = \begin{cases} 1 & \text{inside the liquid phase} \\ 0 & \text{outside the liquid phase} \end{cases}\,. \tag{3}$$

It is assumed that each material property of the flow ψ, as for example density ρ or dynamic viscosity μ, is constant within each phase and is given by

$$\psi(\boldsymbol{x}) = \psi_\mathrm{f}\chi(\boldsymbol{x}) + (1 - \chi(\boldsymbol{x}))\psi_\mathrm{g}\,, \tag{4}$$

where ψ_f and ψ_g are the material property constant values in the liquid and gas phase, respectively. The equation for interface tracking is obtained by considering the volume fraction $f = (1/\Omega)\int_\Omega \chi(\boldsymbol{x})d\boldsymbol{x}$, where Ω is an arbitrary control volume. The transport equation for f is:

$$\frac{\partial f}{\partial t} = -\nabla \cdot (f\boldsymbol{u})\,. \tag{5}$$

In a space discretized domain, f_i denotes the liquid volume fraction within the computational cell of index $\boldsymbol{i} = i\boldsymbol{e}_1 + j\boldsymbol{e}_2 + k\boldsymbol{e}_3$. The interface is then located by identifying those cells in which $0 < f_i < 1$ and reconstructed with the Piecewise Linear Interface Calculation (PLIC) scheme of Rider and Kothe [19]. Thus, in each interface cell

the interface is approximated by a plane of direction $-\hat{\boldsymbol{n}} = \nabla f / \|\nabla f\|$ and position determined analytically by the values of f.

2.1 FS3D's Advection Scheme

In *FS3D* two different methods are implemented for the numerical treatment of advection, a split and an unsplit scheme. Here the discussion is limited to the split scheme, since it was used for the presented results in this paper. Let us consider the advection equation for a generic scalar variable ϕ:

$$\frac{\partial \phi}{\partial t} + \boldsymbol{u} \cdot \nabla \phi = 0\,, \tag{6}$$

which can also be written as:

$$\frac{\partial \phi}{\partial t} = -\nabla \cdot (\phi \boldsymbol{u}) + \phi \nabla \cdot \boldsymbol{u}\,. \tag{7}$$

The variable ϕ can be the fluid volume fraction f or a component of momentum $\rho \boldsymbol{u} = \rho(u\boldsymbol{e}_1 + v\boldsymbol{e}_2 + w\boldsymbol{e}_3)$. The advection of ϕ is then carried out in each direction separately in three different steps (or sweeps) [19, 20]. Time integration of Eq. (7) is carried out subsequently for each sweep. For example, in $\boldsymbol{e}_1$ direction and for the first sweep one obtains:

$$\frac{\phi^* - \phi^n}{\Delta t} = -\frac{\partial(\phi u)}{\partial x} + [(1-\beta)\phi^n + \beta\phi^*]\frac{\partial u}{\partial x}\,, \tag{8}$$

where the superscript $*$ indicates an intermediate auxiliary time step. The second term on the right hand side is the divergence correction [19, 20], and $0 \leq \beta \leq 1$ a coefficient which indicates its implicit or explicit nature [20]. Space discretization of Eq. (7) leads to the discretized sweep equations. For example, in $\boldsymbol{e}_1$-direction:

$$\begin{aligned} \Omega \frac{\overline{\phi^*}_i - \overline{\phi^n}_i}{\Delta t} = -A_{\boldsymbol{e}_1} \Big\{ &\left(F_{\boldsymbol{i}+\frac{1}{2}\boldsymbol{e}_1}(\boldsymbol{u},\, \phi) - F_{\boldsymbol{i}-\frac{1}{2}\boldsymbol{e}_1}(\boldsymbol{u},\, \phi) \right) \\ &+ \left[(1-\beta)\overline{\phi^n}_{\boldsymbol{i}} + \beta \overline{\phi^*}_{\boldsymbol{i}} \right] \left(u_{\boldsymbol{i}+\frac{1}{2}\boldsymbol{e}_1} - u_{\boldsymbol{i}-\frac{1}{2}\boldsymbol{e}_1} \right) \Big\}\,, \end{aligned} \tag{9}$$

where $\Omega = (\Delta x \boldsymbol{e}_1 \times \Delta y \boldsymbol{e}_2) \cdot \Delta z \boldsymbol{e}_3 = \Delta x \Delta y \Delta z$ is a Cartesian control volume, $A_{\boldsymbol{e}_1} = \|\Delta y \boldsymbol{e}_2 \times \Delta z \boldsymbol{e}_3\| = \Delta y \Delta z$ its face perpendicular to $\boldsymbol{e}_1$. In Eq. (9), it was assumed that $\int_\Omega \phi \nabla \cdot \boldsymbol{u} d\boldsymbol{x} \approx \overline{\phi} \int_\Omega \nabla \cdot \boldsymbol{u} d\boldsymbol{x} = \overline{\phi}[\Delta y \Delta z (u_{\boldsymbol{i}+\frac{1}{2}\boldsymbol{e}_1} - u_{\boldsymbol{i}-\frac{1}{2}\boldsymbol{e}_1})\boldsymbol{e}_1 + \Delta z \Delta x (v_{\boldsymbol{i}+\frac{1}{2}\boldsymbol{e}_2} - v_{\boldsymbol{i}-\frac{1}{2}\boldsymbol{e}_2})\boldsymbol{e}_2 + \Delta x \Delta y (w_{\boldsymbol{i}+\frac{1}{2}\boldsymbol{e}_3} - w_{\boldsymbol{i}-\frac{1}{2}\boldsymbol{e}_3})\boldsymbol{e}_3]$. The terms $F_{\boldsymbol{i}\pm\frac{1}{2}\boldsymbol{e}_1}(\boldsymbol{u},\, \phi)$ in Eq. (9) denote the numerical fluxes. These are discretized with a second order Godunov scheme for the case of momentum components [20], whereas the geometrical procedure indicated by Rider and Kothe [19] is used to calculate the f-fluxes.

2.2 Solution of the Discretized Poisson Problem

Because the flow is incompressible, an equation for pressure is needed to solve Eq. (2). This equation is obtained by applying the divergence-free condition of the velocity field to the time-discretized Eq. (2). One obtains:

$$\frac{\nabla \cdot \tilde{\boldsymbol{u}}}{\Delta t} = \frac{\nabla^2 p}{\rho}, \tag{10}$$

where $\tilde{\boldsymbol{u}} = \tilde{u}\boldsymbol{e}_1 + \tilde{v}\boldsymbol{e}_2 + \tilde{w}\boldsymbol{e}_3$ is an auxiliary velocity field where all acceleration terms of Eq. (2) but the pressure gradient have been added. By integrating Eq. (10) over a control volume Ω and using of the Gauss theorem one obtains:

$$\int_{\partial\Omega} \frac{\tilde{\boldsymbol{u}} \cdot \hat{\boldsymbol{n}}}{\Delta t} d\boldsymbol{x} = \int_{\partial\Omega} \frac{\nabla p \cdot \hat{\boldsymbol{n}}}{\rho} d\boldsymbol{x}, \tag{11}$$

where $\hat{\boldsymbol{n}}$ denotes the normal vector to the surface $\partial\Omega$. Discretization of Eq. 11 leads to a system of equations of the form:

$$\mathbf{A}\overline{p} = \mathbf{b}, \tag{12}$$

where $\mathbf{A}$ is the system matrix with dimension $N_{cell} \times N_{cell}$, $\overline{p}$ and $\mathbf{b}$ are the vectors for the discrete p values and for the right hand side, respectively. Because the pressure gradient in Eq. (11) is discretized with central finite differences, on each line of the system corresponding to the control volume of index $\boldsymbol{i}$ all coefficients of $\mathbf{A}$ are zero but for the ones with positions $S_{\mathbf{A}} = \{0, \pm\boldsymbol{e}_1, \pm\boldsymbol{e}_2, \pm\boldsymbol{e}_3\}$ with respect to $\boldsymbol{i}$. $S_{\mathbf{A}}$ is called the structure of $\mathbf{A}$ [21]. Equation (12) is solved by a multigrid solver embedded into *FS3D* which is specialized to deal with matrices which have the structure $S_{\mathbf{A}} = \{0, \pm\boldsymbol{e}_1, \pm\boldsymbol{e}_2, \pm\boldsymbol{e}_3\}$ for each computational cell.

3 Treatment of Embedded Boundaries

3.1 The Simplified Approach

To represent embedded boundaries, an additional volume fraction variable f_b is introduced and the boundary surface is also approximated with the PLIC scheme. Embedded boundaries are then treated as rigid bodies of infinite density. This is obtained by setting to zero all coefficients of Eq. (12), which correspond to momentum control volumes in which $f_b > 0$. This is equivalent to solving Eq. (12) for the *stair-step* approximation of the boundary (see Fig. 1a). As a consequence however, the velocities on all faces of the vast majority of the boundary-cut cells are set to zero. One a-posteriori treatment of the velocity field is then necessary to advect the fluid volume fraction in these cells. Boundary-cut cells with zero velocities on all their

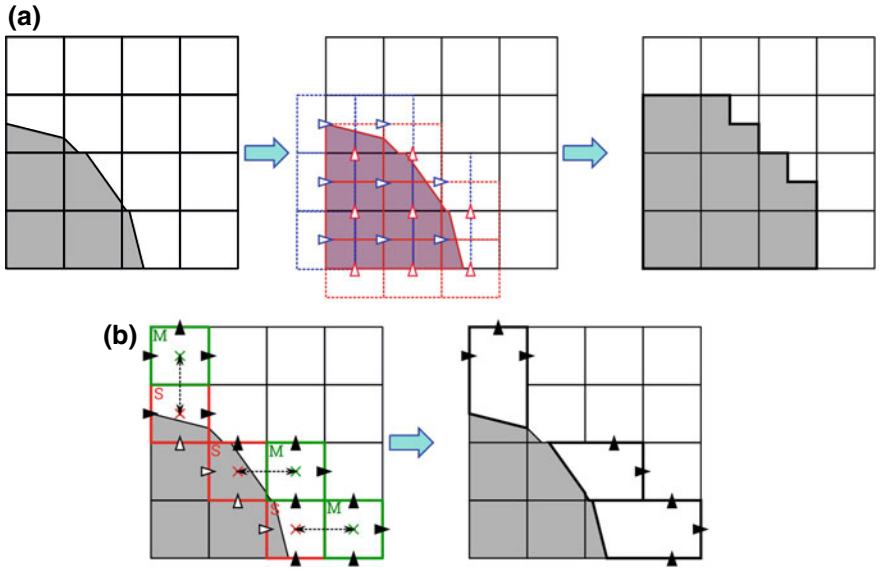

Fig. 1 The simplified approach to embed solid structures in a Cartesian grid. **a** Stair-step approximation of embedded boundaries. **b** Merging of critical cells with the neighbor in the direction of the largest normal component $\hat{\boldsymbol{n}}_b$.

faces are marked as *slaves* and linked to the neighbor in the direction of the largest component of $\hat{\boldsymbol{n}}_b$, which becomes their *master* (see Fig. 1b). This is made possible by the apposite structured data type *boundary cell*:

$$\texttt{boundary cell} \begin{cases} \texttt{type(boundary cell), pointer:} & \textit{master}, \textit{slave} \\ \texttt{integer(1:3):} & \boldsymbol{i} = i\boldsymbol{e}_1 + j\boldsymbol{e}_2 + k\boldsymbol{e}_3 \end{cases}$$

which is allocated in each boundary-cut cell and in its neighborhood. The advection of f is then carried out on the total volume of master-slave pairs using an averaged velocity field. The averaging of the velocity field after the solution of the Poisson equation causes an error in mass conservation. Even if those errors are very small in our simulations, this approach is fundamentally not conservative. With the purpose of improving conservativeness, we started the development of a new approach.

3.2 The New Approach

As in the simplified approach described in Sect. 3.1, embedded boundaries are represented by their volume fraction f_b and their surface is approximated with the PLIC scheme. However, instead of being treated as rigid bodies of infinite density, the boundaries are cut-off from the computational domain. Following the approach of

Popinet [15], the discretized equations for momentum transport (Eq. 2) and pressure (Eq. 10) are rewritten in terms of boundary-cut cell volume and faces. The same treatment is applied to the equations for interface transport (Eq. 5) and mass conservation (Eq. 1). Information about "free" volume and lateral "free" faces, as well as the orientation $\boldsymbol{n}_b$ and position l^* of the plane approximating the surface must then be stored for each boundary-cut control volume. The structured data type *boundary cell* is then modified as follows:

$$\textbf{boundary cell}\begin{cases}\texttt{real:} & l_b^*,\, f_b\\ \texttt{real(1:3):} & \hat{\boldsymbol{n}}_b\\ \texttt{real(1:3,1:2):} & a_{b\boldsymbol{i}}\\ \texttt{type(boundary cell), pointer:} & \textit{master},\ \textit{slave}\\ \texttt{integer(1:3):} & \boldsymbol{i}=i\boldsymbol{e}_1+j\boldsymbol{e}_2+k\boldsymbol{e}_3\end{cases}$$

where $a_{b\boldsymbol{i}}$ are the ratios of the lateral free to whole faces. For example:

$$a_{b\boldsymbol{i}}(1,1)\equiv a^-_{b\boldsymbol{e}_1}=\frac{A^-_{\boldsymbol{i}\boldsymbol{e}_1}}{A_{\boldsymbol{i}\boldsymbol{e}_1}}\,,\qquad a_{b\boldsymbol{i}}(1,2)\equiv a^+_{b\boldsymbol{e}_1}=\frac{A^+_{\boldsymbol{i}\boldsymbol{e}_1}}{A_{\boldsymbol{i}\boldsymbol{e}_1}}\,. \tag{13}$$

where $A^{\pm}_{\boldsymbol{i}\boldsymbol{e}_1}$ are the "free" lateral areas at positions $\boldsymbol{i}\pm\frac{1}{2}\boldsymbol{e}_1$. The *master* and *slave* pointer attribute are still needed to avoid problems caused by very small cut-cells, which we will address in Sect. 3.2.1. Since the grid is staggered, the structured data type *boundary cell* has to be allocated in staggered control volumes as well. Therefore, the new data type *boundary cell array*, is introduced:

$$\textbf{boundary cell array}\begin{cases}\texttt{type(boundary cell):} & bcell_c\\ \texttt{type(boundary cell):} & bcell_x\\ \texttt{type(boundary cell):} & bcell_y\\ \texttt{type(boundary cell):} & bcell_z\end{cases}$$

This data structure serves as container for *boundary cell* data types, one for each control volume associated with a position of index $\boldsymbol{i}$ of the computational domain (one scalar control volume and three staggered control volumes). The *boundary cell array* is allocated in each position of the computational domain, in which at least one of the associated control volumes is intercepted by the boundary surface and in its neighborhood. Since phase change is not considered here, the treatment of the advection term is the point of interest for interface tracking (Eq. 5). In the case of momentum transport (Eq. 2), apart for advection and pressure, other terms have to be considered: the viscous stresses $\nabla\cdot\mathbb{S}$, the body forces $\rho\boldsymbol{g}$, and the surface tension force $\mathbf{f}_\sigma$. For the surface tension force no special treatment is needed, since it only depends on the interface orientation $\hat{\boldsymbol{n}}$. Body forces and viscous stresses are calculated by using material properties calculated on boundary-cut cell volumes. That is

$$\psi_{\boldsymbol{i}} = \mathbf{min}\left(\left|\frac{f_{\boldsymbol{i}}}{1-f_{b,\boldsymbol{i}}}\right|, 1\right)\psi_l + \left(1 - \mathbf{min}\left(\left|\frac{f_{\boldsymbol{i}}}{1-f_{b,\boldsymbol{i}}}\right|, 1\right)\right)\psi_g, \tag{14}$$

where $0 < f_{b,\boldsymbol{i}} < 1$ and ψ is a material property as density ρ or viscosity μ. Apart for this, the usual *FS3D* schemes for calculating viscous terms and body forces are used. This is equivalent to consider computational nodes on whole cell centres instead of boundary-cut cell centres. Of course, this simplification comes at the cost of slightly reduced accuracy, but it spares the computational overhead of calculating the barycentres of boundary-cut cells and the distance between the barycentres to compute gradients and linear interpolations of needed variables.

3.2.1 Advection in Boundary-Cut Cells

The split advection scheme, illustrated in Sect. 2.1, is also used on boundary-cut cells. Here Eq. (9) takes the form:

$$\begin{aligned}\Omega(1-f_{b,\boldsymbol{i}})\tfrac{\overline{\phi^*}_{\boldsymbol{i}}-\overline{\phi^n}_{\boldsymbol{i}}}{\Delta t} = \\ -A_{\boldsymbol{e}_1}\left(a^+_{b\boldsymbol{e}_1}F_{\boldsymbol{i}+\frac{1}{2}\boldsymbol{e}_1}(\boldsymbol{u},\,\phi) - a^-_{b\boldsymbol{e}_1}F_{\boldsymbol{i}-\frac{1}{2}\boldsymbol{e}_1}(\boldsymbol{u},\,\phi)\right) \\ +\left[(1-\beta)\overline{\phi^n}_{\boldsymbol{i}} + \beta\overline{\phi^*}_{\boldsymbol{i}}\right]\left(V_{\boldsymbol{i}+\frac{1}{2}\boldsymbol{e}_1} - V_{\boldsymbol{i}-\frac{1}{2}\boldsymbol{e}_1}\right),\end{aligned} \tag{15}$$

where $a^{\pm}_{b\boldsymbol{e}_1}$ are the free to whole area ratio at positions $\boldsymbol{i} \pm \frac{1}{2}\boldsymbol{e}_1$ and V denotes an altered form of the divergence correction. For momentum advection, $V_{\boldsymbol{i}\pm\frac{1}{2}\boldsymbol{e}_1} = A_{\boldsymbol{e}_1}a^{\pm}\boldsymbol{u}_{\boldsymbol{i}\pm\frac{1}{2}\boldsymbol{e}_1}$, for f-advection, V is calculated geometrically and it corresponds to the ratio of the cut cell volume enclosed by $A_{\boldsymbol{e}_1}\boldsymbol{u}_{\boldsymbol{i}\pm\frac{1}{2}\boldsymbol{e}_1}\Delta t$ in upwind control volumes to the time step Δt. *FS3D*'s usual schemes are used to compute the numerical fluxes. As already mentioned in Sect. 3.2, this is equivalent to considering computational nodes on whole cell centres and, consequently, faces. In the case of f-advection, the volume of arbitrary polyhedra has to be calculated in order to compute the fluxes. For this, geometrical algorithms similar to these proposed by Pathak and Raessi [22] are used. The interface position is calculated iteratively until the volume of the polyhedron representing the liquid phase corresponds to the liquid volume fraction f. As reported by Popinet [15], the occurrence of very small cells leads to prohibitively small time steps in order to satisfy the Courant-Friedrichs-Lewy (CFL) condition. Small cells are then marked as slaves and merged to the neighbor in the direction of the largest normal component, which becomes their master. Advection is then carried out in the whole master-slave control volume.

3.2.2 Discretization of the Poisson Problem on Boundary-Cut Cells

Discretization of Eq. (10) on boundary-cut volumes leads to:

$$\sum_k \left(A a_b \frac{\nabla p}{\rho} \right)_k = \frac{1}{\Delta t} \sum_k (A a_b u)_k \tag{16}$$

where $k = \boldsymbol{i} \pm \frac{1}{2}\boldsymbol{e}_{1,2,3}$ are the positions of the faces of the considered scalar control volume. As already mentioned in Sects. 3.1 and 3.2.1, we consider computational nodes on whole face centres instead of boundary-cut cell centres. The pressure gradient $(\nabla p)_k$ can then be discretized by finite differences. Then, the formulation of Eq. (16) for each control volume leads to a system of equations analogously to Eq. (12). We observed that the use of whole-face centres may cause inaccurate values of the velocity field at very small boundary-cut cells. Better accuracy may be achieved by discretizing the pressure gradient differently, as indicated by Johansen and Colella [23]. However, this would change the structure of the system matrix $\mathbf{A}$, requiring a modification of the multigrid solver.

4 Results

In this section, a comparison of the two methods is shown for the case of a water drop impacting on the valley between two trapezoidal ribs at a Weber number $We = (\rho R U_0^2)/\sigma = 11.2$ (see Fig. 2). This setup is analogous to one of the cases studied by Regulagadda et al. [24]. Because of the symmetry of the problem, only a quarter of the computational domain was simulated with a total of $N_x \times N_y \times N_z = 192 \times 192 \times 192$ computational cells. The mesh was refined near the impact area.

In Fig. 3a comparison of the results obtained with the two methods is shown for different times during impact. It can be noted how the whole velocity field is affected by the choice of the method. Indeed, a difference is visible even before the drop touches the ribs. This is probably caused by the different treatment of the discretized elliptic Poisson equation. The impact occurs at a higher velocity in the new method, even if both simulations were initialized identically. Indeed, in Fig. 3b the droplet rim is thinner and faster and reaches a larger extension in the direction parallel to the ribs. The major differences however take place during the retraction phase. In both methods, the droplet assumes a three-lobed shape while retracting; in the approximate method however, these liquid sub-units merge just before take-off. The different

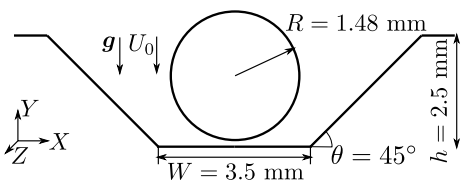

Fig. 2 Setup of the investigated case, which is analogous to one used in the experiments of Regulagadda et al. [24]

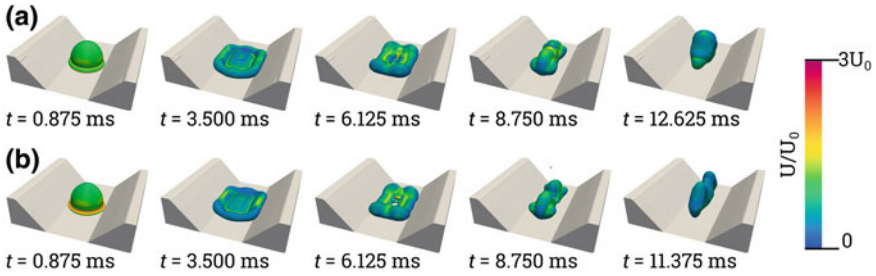

Fig. 3 Simulation results for drop impact on the valley between two trapezoidal ribs at $We = 11.2$. **a** Approximate approach. **b** New approach

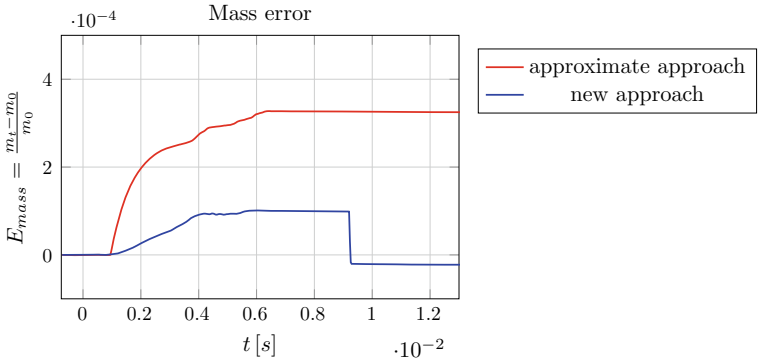

Fig. 4 Mass conservation error over time

impact morphology also explains the difference in contact time prediction. Indeed, according to Richard [25], the contact time t_0 on a flat superhydrophobic surface does not depend on impact velocity. Instead, it scales with the inertial-capillary time scale $\tau = \sqrt{\rho R^3/\sigma}$. For the case of a droplet impacting on a wire, Gauthier et al. [2] found that the contact time t_c was approximately $t_0/\sqrt{N_l}$, where N_l denotes the number of liquid sub-units formed during impact. The same trend was confirmed by Regulagadda et al. [3] for a drop impacting on the top and between triangular ribs. For the new approach, t_c/t_0 is closer to $1/\sqrt{(3)}$, as expected from the number of liquid sub-units. The formation of three lobes was also observed by Regulagadda et al. for impact on the valley between two triangular ribs at higher impact velocities. Both methods however underestimate the contact time for this case, which is close to $2\tau = 13.316$ ms, as can be seen from a further publication from the same authors [24]. For both cases, we observe an un-physical rupture of the lamella at $t \approx 6$ ms, which in the new approach comes together with the ejection of a very small secondary droplet. This occurs probably because the grid used for the comparison is too large to capture the thin film on the top of the solid surface. With the new method, a significant improvement in mass conservation was obtained. In Fig. 4 the

mass error $E_m = (m(t) - m_0)/m_0$ is shown for both simulations as a function of time. The sudden step in the mass error for the new approach at $t \approx 9.2$ ms is due to the ejection of the satellite droplet. It can be seen that the error in mass conservation could be reduced of about a factor of 3. We have indeed $E_{m,\infty,old} = \|(m(t) - m_0)/m_0\|_\infty = 3.27 \times 10^{-4}$ for the approximate approach and $E_{m,\infty,new} = 1.01 \times 10^{-4}$ for the new one. This is a remarkable achievement considering the fact that the contact time between liquid and ribs is short. Better performances are expected for cases in which the interaction between droplet and solid structures has a longer duration. Further investigation on the causes of the residual error in mass conservation is planned.

5 Conclusions

Two methods to embed boundaries of arbitrary shape in a Cartesian grid have been presented, one approximate and a more rigorous one. A comparison between the two approaches for the case of a droplet impacting between two trapezoidal ribs has shown a considerable difference in impact dynamics. The cause of this discrepancy still needs to be clarified, but we expect it to be due to the different treatment of the discretized Poisson problem. Even if the newer approach has shown a slightly larger discrepancy for the contact time prediction for the case under consideration, further research is needed to assess its accuracy for other surface geometries and impact velocities. On the other hand, a remarkable reduction of the mass conservation error was obtained. Small error in mass conservation are still present however, the cause of which will be addressed by further research.

Acknowledgements We thank the German Science Foundation (DFG) for the financial support of this research within the international research training group *Droplet Interaction Technologies, DROPIT*, GRK 2016/1.

References

1. Bird, J.C., Dhiman, R., Kwon, H., Varanasi, K.K.: Reducing the contact time of a bouncing drop. Nature **503**, 385–388 (2013)
2. Gauthier, A., Symon, S., Clanet, C., Quéré, D.: Water impacting on superhydrophobic macro-textures. Nat. Commun. **6**, 8001 (2015)
3. Regulagadda, K., Bakshi, S., Das, S.K.: Morphology of drop impact on a superhydrophobic surface with macro-structures. Phys. Fluids **29**, 082104 (2017)
4. Chantelot, P., Moqaddam, A.M., Gauthier, A., Chikatamaria, S.S., Clanet, C., Karlin, I.V., Quéré, D.: Water ring-bouncing on repellent singularities. Soft. Matter **14**(12), 2227–2233 (2018)
5. Shen, Y., Liu, S., Zhu, C., Tao, J., Chen, Z., Tao, H., Pan, L., Wang, G., Wang, T.: Bouncing dynamics of impact droplets on the convex superhydrophobic surfaces. Appl. Phys. Lett. **110**, 221601 (2017)

6. Khojasteh, D., Bordbar, A., Kamali, R., Marengo, M.: Curvature effect on droplet impacting onto hydrophobic and superhydrophobic spheres. Int. J. Comput. Fluid Dyn. **31**(6–8), 310–323 (2017)
7. Liu, Y., Andrew, M., Li, J., Yeomans, J.M., Wang, Z.: Symmetry breaking in drop bouncing on curved surfaces. Nat. Commun. **6**, 10034 (2015)
8. Liu, X., Zhao, Y., Chen, S., Shen, S., Zhao, X.: Numerical research on the dynamic characteristics of a droplet impacting a hydrophobic tube. Phys. Fluids **29**, 062105 (2017)
9. Schlottke, J., Dulger, E., Weigand, B.: A VOF-based 3D numerical investigation of evaporating, deformed droplets. Prog. Comput. Fluid Dyn. Int. J. **9**, 426–435 (2009)
10. Schlottke, J., Straub, W., Beheng, K.D., Gomaa, H., Weigand, B.: Numerical investigation of collision-induced breakup of raindrops. Part I: methodology 12 references and dependencies on collision energy and eccentricity. J. Atmos. Sci. **67**, 557–575 (2010)
11. Ertl, M., Weigand, B.: Analysis methods for direct numerical simulations of primary breakup of shear-thinning liquid jets. Atomization Sprays **27**(4), 303–317 (2017)
12. Reitzle, M., Kieffer-Roth, C., Garcke, H., Weigand, B.: A volume-of-fluid method for three-dimensional hexagonal solidification processes. J. Comput. Phys. **339**, 356–369 (2017)
13. Reitzle, M., Ruberto, S., Stierle, R., Gross, J., Tanzen, T., Weigand, B.: Direct numerical simulation of sublimating ice particles. Int. J. Thermal Sci. **145**, 105953 (2019)
14. Rauschenberger, P., Weigand, B.: Direct numerical simulation of rigid bodies in multiphase flow within an Eulerian framework. J. Comput. Phys. **291**, 238–253 (2015)
15. Popinet, S.: Gerris: a tree-based adaptive solver for the incompressible Euler equations in complex geometries. J. Comput. Phys. **190**(2), 572–600 (2003)
16. Eisenschmidt, K., Ertl, M., Gomaa, H., Kieffer-Roth, C., Meister, C., Rauschenberger, P., Reitzle, M., Schlottke, K., Weigand, B.: Direct numerical simulations for multiphase flows: an overview of the multiphase code FS3D. Appl. Math. Comput. **272**, 508–517 (2016)
17. Lafaurie, B., Nardone, C., Scardovelli, R., Zaleski, S., Zanetti, G.: Modelling merging and fragmentation in multiphase flows with SURFER. J. Comput. Phys. **113**(1), 134–147 (1994)
18. Hirt, C.W., Nichols, B.D.: Volume of fluid (VOF) method for the dynamics of free boundaries. J. Comput. Phys. **39**, 201–225 (1981)
19. Rider, W.J., Kothe, D.B.: Reconstructing volume tracking. J. Comput. Phys. **141**(2), 112–152 (1998)
20. Rieber, M.: Numerische Modellierung der Dynamik freier Grenzflächen in Zweiphasenströmungen, dissertation, University of Stuttgart (2004)
21. Wesseling, P.: An Introduction to Multigrid Methods. Wiley (1992)
22. Pathak, A., Raessi, M.: A three-dimensional volume-of-fluid method for reconstructing and advecting three-material interfaces forming contact lines. J. Comput. Phys. **307**, 550–573 (2016)
23. Johansen, H., Colella, P.: A Cartesian grid embedded boundary method for Poisson's equation on irregular domains. J. Comput. Phys. **147**(1), 60–85 (1998)
24. Regulagadda, K., Bakshi, S., Das, S.K.: Triggering of flow asymmetry by anisotropic deflection of lamella during the impact of a drop onto superhydrophobic surfaces. Phys. Fluids **30**, 072105 (2018)
25. Richard, D., Clanet, C., Quéré, D.: Contact time of a bouncing drop. Nature **417**, 811 (2002)

Upscaling of Coupled Free-Flow and Porous-Medium-Flow Processes

Sina Ackermann, Rainer Helmig and Stephanie Fest-Santini

Abstract The behavior of a coupled free-flow/porous-medium-flow system strongly depends on the pore-scale processes happening at the shared interface. Under certain conditions, drops form at this interface and affect the exchange of mass, momentum, and energy. The mutual influence of droplet-related pore-scale processes and the surrounding's macro-scale flow behavior poses a challenge for both the conceptual and the numerical model. The aim of this work is to develop a computationally efficient model concept, which takes the processes at both scales into account. We use a lower-dimensional interface domain to embed the drop dynamics into a coupled macro-scale model. In this domain, the droplet-related processes are modeled with separate balance equations. Coupling conditions take the fluxes from and to the macro-scale flow regimes into account. First results of a simple test case show that drop formation, growth, and detachment can be represented with this multi-scale three-domain approach.

1 Introduction

Drops at the interface between a porous medium and an adjacent free flow influence flow and transport processes in many technical applications and environmental scenarios. Fluxes across the common interface transfer mass, momentum, and energy between the two flow regimes. Pore-scale processes at the interface drive this

S. Ackermann (✉) · R. Helmig
Institute for Modelling Hydraulic and Environmental Systems, Pfaffenwaldring 61, 70569 Stuttgart, Germany
e-mail: sina.ackermann@iws.uni-stuttgart.de

R. Helmig
e-mail: rainer.helmig@iws.uni-stuttgart.de

S. Fest-Santini
Department of Management, Information and Production Engineering, Viale Marconi 5, 24044 Dalmine (BG), Italy
e-mail: stephanie.fest-santini@unibg.it

G. Lamanna et al. (eds.), *Droplet Interactions and Spray Processes*,
Fluid Mechanics and Its Applications 121,
https://doi.org/10.1007/978-3-030-33338-6_11

exchange and therefore influence the macroscopic flow behavior in both adjacent flow regimes. In a two-phase flow in a porous medium, the liquid phase reaches the interface to a gaseous single-phase free flow under certain conditions. Then, the liquid either evaporates immediately, or it forms interfacial drops. These drops reduce the available area for the gas exchange as well as the available cross-section for the free flow. In addition, they might accelerate the evaporation from the porous medium due to a larger liquid surface area. Besides formation and growth, processes such as spreading, merging, detaching or shrinking can impact the exchange processes and therefore the macroscopic flow behavior in the coupled system.

Modeling such systems is challenging due to the different temporal and spatial scales. REV-scale variables and balance equations are sufficiently accurate and computationally efficient to describe the macroscopic flow behavior in free flow and flow in porous media for real-life scenarios. However, droplet-related processes require a precise description on the pore-scale and a higher resolution in numerical simulations compared to the macroscopic flow regimes. The aim of this work is to develop a multi-scale, multi-physics model, which combines the advantages of model concepts on both scales to understand and predict the influence of droplet-related processes on the macroscopic behavior in a coupled free-flow/porous-medium-flow system. This model concept could help to design and improve technical applications, such as water management in fuel cells or heat management in turbines.

A two-domain approach to describe a coupled system with compositional flow under non-isothermal conditions is presented in [1]. The authors assume that all liquid that reaches the common interface evaporates immediately into the gaseous free flow. Based on this approach, a coupled macro-scale model, which includes the influence of interfacial drops is developed in [2]. The drop-dependent coupling concept is derived at the pore-scale. It extends the simple coupling concept by allowing the liquid phase to enter the thin interface region and form drops on the porous surface. This concept allows to model drop formation, growth and detachment depending on the conditions in the surrounding flow regimes. A simple homogenization concept transfers the pore-scale information to the REV-scale. A mortar method is applied to compute the drop volume in addition to the conventional primary variables. This approach limits the model's flexibility and does not allow to take lateral fluxes along the interface into account.

We extend the model concept presented in [2] by applying a three-domain approach to gain more flexibility in modeling drop dynamics. We compute all droplet-related processes in an additional lower-dimensional interface domain [3], which is plugged in between the free flow and the porous medium. This separate interface domain allows to take lateral fluxes along the porous surface into account. In addition, the infiltration of condensed drops into the porous medium can be represented. For a first analysis of the multi-scale model, only vertical fluxes across the interface are taken into account with the aim to obtain comparable results to the work in [2].

We present the model concepts for free flow (Sect. 2.1) and flow in porous media (Sect. 2.2) at the beginning of the following section. Then, we introduce our drop model concept (Sect. 2.3) and the adapted three-domain coupling concept (Sect. 2.4). In Sect. 3, we show the results of a simple test case. Section 4 contains a summary, conclusion and outlook.

2 Model and Coupling Concept

The focus of this investigation is on drops which form at the mutual interface under certain conditions. The underlying model concept is presented in the following. More details on the numerical aspects are given in [4].

Figure 1 shows an exemplary model domain Ω, which consists of the two non-overlapping sub-domains Ω_{ff} and Ω_{pm}. The sub-domains are separated by the interface Γ such that $\bar{\Omega} = \bar{\Omega}_{\mathrm{ff}} \cup \bar{\Omega}_{\mathrm{pm}}$, $\Omega_{\mathrm{ff}} \cap \Omega_{\mathrm{pm}} = \emptyset$ and $\bar{\Omega}_{\mathrm{ff}} \cap \bar{\Omega}_{\mathrm{pm}} = \Gamma$. The interface Γ is of one dimension less than Ω_{ff} and Ω_{pm}. The description of the droplet-related processes is derived in the full-dimensional interface domain Ω_{if} first. Then, a simple homogenization technique is applied to reduce the dimension such that the description can be used for the lower-dimensional interface domain Γ.

We assume a non-isothermal system. Each phase consists of the components water and air, which mix according to binary diffusion. Table 1 lists the common variables. Assumptions, balance equations and primary variables for the individual flow regimes are given in Sects. 2.1, 2.2 and 2.3. The coupling concept is presented in Sect. 2.4. An overview of the discretization techniques is given in Sect. 2.5.

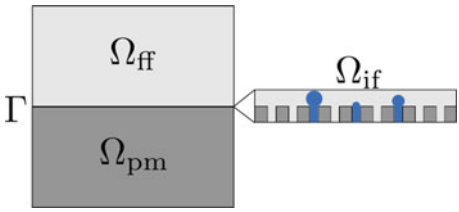

Fig. 1 The coupled three-domain system with the lower-dimensional interface Γ and the corresponding full-dimensional domain Ω_{if}

Table 1 List of symbols

γ	surface tension	Φ	porosity	$\mathbf{K}$	permeability tensor
θ	contact angle	c_s	solid heat capacity	k	relative permeability
λ	heat conductivity	D	diffusion coefficient	$\mathbf{n}$	unit outer normal vector
μ	dynamic viscosity	$\mathbf{g}$	gravity vector	S	saturation
ϱ	density	h	enthalpy	u	internal energy

2.1 Free Flow

We consider a single-phase gaseous free flow in Ω_{ff}. The gas is assumed to be a compressible Newtonian fluid, flowing under laminar conditions. The four balance equations given in Table 2 are solved to obtain the gas pressure p_g, the mass fraction of water in air $X_g^{\mathrm{H_2O}}$, the gas velocity $\mathbf{v}_g$ and the temperature T.

2.2 Flow in Porous Media

In the porous medium Ω_{pm}, a two-phase flow through a solid, rigid, homogeneous matrix is considered. In our case, the liquid phase is considered to be the non-wetting phase. Local thermodynamic equilibrium between all phases is assumed. We suppose slow flow velocities ($Re < 1$) and therefore apply Darcy's law for the momentum balance. For the mass transport, dispersion is neglected. Instead of resolving the porous medium on the pore-scale, we choose an REV-scale approach to model the flow and transport processes. The balance equations in Table 3 are solved for the gas pressure p_g, the mass fraction of water vapor in gas $X_g^{\mathrm{H_2O}}$ and the temperature T. Applying Darcy's law allows to compute the phase velocities as secondary variables and reduces the number of partial differential equations. The closure relations in Table 4 further reduce the number of unknowns to fit the number of equations.

Table 2 Balance equations for the free flow

Total mass	$\frac{\partial \varrho_g}{\partial t} + \nabla \cdot (\varrho_g \mathbf{v}_g) = q_g$
Momentum	$\frac{\partial (\varrho_g \mathbf{v}_g)}{\partial t} + \nabla \cdot \left(\varrho_g \mathbf{v}_g \mathbf{v}_g^{\mathrm{T}}\right) = -\nabla \cdot (p_g \mathbf{I}) + \nabla \cdot \left(\mu_g \left(\nabla \mathbf{v}_g + \nabla \mathbf{v}_g^{\mathrm{T}}\right)\right) + \varrho_g \mathbf{g}$
Water mass	$\frac{\partial (\varrho_g X_g^w)}{\partial t} + \nabla \cdot \left(\varrho_g \mathbf{v}_g X_g^w - D_g^w \varrho_g \nabla X_g^w\right) = q_g^w$
Energy	$\frac{\partial (\varrho_g u_g)}{\partial t} + \nabla \cdot \left(\varrho_g \mathbf{v}_g h_g - \lambda_g \nabla T\right) = q_T$

Table 3 Balance equations for flow in porous media

Mass	$\sum_{\alpha \in \{l,g\}} \Phi \frac{\partial (\varrho_\alpha S_\alpha)}{\partial t} + \nabla \cdot \left(\sum_{\alpha \in \{l,g\}} \varrho_\alpha \mathbf{v}_\alpha\right) = \sum_{\alpha \in \{l,g\}} q_\alpha$
Momentum	$\mathbf{v}_\alpha = -\mathbf{K} \frac{k_{r\alpha}}{\mu_\alpha} \left(\nabla p_\alpha - \varrho_g \mathbf{g}\right)$
Water mass	$\sum_{\alpha \in \{l,g\}} \Phi \frac{\partial (\varrho_\alpha X_\alpha^w S_\alpha)}{\partial t} + \nabla \cdot \left(\sum_{\alpha \in \{l,g\}} (\varrho_\alpha \mathbf{v}_\alpha X_\alpha^w - D_\alpha^{w,\mathrm{pm}} \varrho_\alpha \nabla X_\alpha^w)\right) = \sum_{\alpha \in \{l,g\}} q_\alpha^w$
Energy	$\sum_{\alpha \in \{l,g\}} \Phi \frac{\partial (\varrho_\alpha u_\alpha S_\alpha)}{\partial t} + (1-\Phi) \frac{\partial (\varrho_s c_s T)}{\partial t} + \nabla \cdot \left(\sum_{\alpha \in \{l,g\}} \varrho_\alpha \mathbf{v}_\alpha h_\alpha - \lambda_{\mathrm{pm}} \nabla T\right) = q_T$

Table 4 Closure relations for flow in porous media

Saturations	$S_g + S_l = 1$	Mole fractions	$x_l^a = \frac{p_g^a}{H_{gl}^a}$ (Henry's law)
Mass fractions	$X_\alpha^w + X_\alpha^a = x_\alpha^w + x_\alpha^a = 1$	Mole fractions	$x_g^w = \frac{p_{\text{sat, Kelvin}}^w}{p_g}$
Capillary pressure	$p_c = p_n - p_w$		

2.3 Interfacial Drops

Drops forming at the interface between a single-phase gaseous free flow and a two-phase flow in a porous medium pose a challenge to REV-scale coupling concepts. Due to a pressure gradient in the respective direction, the liquid phase might actually reach the common interface. If the liquid pressure in the porous medium is larger than the pore entry pressure and the gas pressure in the free flow, the liquid phase enters the surface pores:

$$p_l^{\text{pm}} \geq p_g^{\text{ff}} + \frac{2\gamma_{lg}\cos\theta}{r_{\text{pore}}} \,. \tag{1}$$

If the liquid phase is the non-wetting phase with respect to the porous medium, drops form on top of the interface in a region which is actually a part of the free flow. However, with the assumption of a single-phase gaseous free flow it is impossible to take liquid drops on the porous surface into account.

Therefore, we introduce an additional interface domain to the coupled model concept, where both phases can be present. Within this domain, all droplet-related processes are described with a separate set of equations. These equations take parameters into account which depend on the macroscopic flow regimes on both sides of the interface. In return, the behavior of the drops within the interface influences the macroscopic flow regimes through the exchange of mass, momentum, and energy.

In the following, a full-dimensional description of the droplet-related processes in Ω_{if} is presented. With the simple homogenization technique from [2], we obtain a lower-dimensional description of the interface which is then valid on the interface Γ as given in Fig. 1.

The full-dimensional interface domain consists of a thin layer of the porous medium and a thin layer of the free flow as depicted in Fig. 1. The pores are assumed to be vertical, parallel and constant in diameter. They are connected to the pores in the porous medium below. If the formation condition in (1) is fulfilled, the pore is assumed to be filled immediately, such that a liquid cap of half-spherical shape with the radius r_{pore} forms on the pore as shown in Fig. 2.

In this first approach, the drops are assumed to be non-deforming and symmetrical as illustrated in Fig. 3. They have a circular contact line and a constant contact angle towards the solid. Regardless of these simplifications, a drag force F_{drag} due to the free flowing fluid acts on the drops. This force is balanced by the retention force F_{ret}

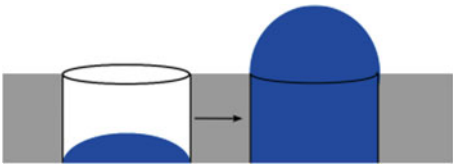

Fig. 2 If the drop formation condition in (1) is fulfilled, the pore is assumed to be liquid-filled and immediately occupied by a drop of $V_{\text{drop}} = \frac{2}{3}\pi r_{\text{pore}}^3$

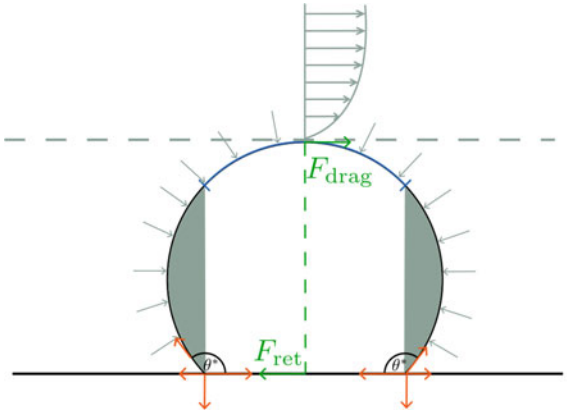

Fig. 3 Simplified spherical drops with constant contact angle. If the drag force $F_{\text{drag}} > F_{\text{ret}}$, the drop detaches

which depends on the drop's contact angle, radius and surface tension. If the drag force exceeds the retention force, the drop detaches and is carried away by the free flow. Both forces are computed as given in [2].

Instead of resolving all pores on the interface, a simple homogenization approach derived in [2] is applied. The interfacial pores are grouped in pore classes with a mean pore radius. In a homogeneous porous medium, the same pore size distribution holds in each control volume. All pores within a certain area Ω_{drop} are assumed to contribute to one global drop. Evaluating the drop formation condition (1) and summing up all of the resulting drop volumes leads to the global drop's initial volume. With geometrical relations as presented in [2], the drop-covered fraction a_{drop} of the drop domain Ω_{drop} can be determined. This area fraction is applied to the coupling fluxes as explained in Sect. 2.4.

A separate set of equations becomes necessary to describe the droplet-related processes within the interface domain. The toal mass balance is given as

$$\sum_{\alpha\in\{l,g\}} \Phi \frac{\partial(\varrho_\alpha S_\alpha)}{\partial t} + \nabla\cdot\left(\sum_{\alpha\in\{l,g\}} \varrho_\alpha \mathbf{v}_\alpha\right) = q^{\text{if,ff}} + q^{\text{if,pm}} + q^{\text{detach}} \,. \tag{2}$$

The first two source terms are equal to the coupling fluxes in (6) and (7) in the following section. The mass of the detached drops is represented in the source term

$$q^{\text{if,detached}} = \begin{cases} 0 & \text{drop has not detached} \\ \frac{\varrho_l V_{\text{drop}}}{\Delta t} & \text{drop has detached.} \end{cases} \tag{3}$$

For the two components $\kappa \in \{a, w\}$, the following component mass balance holds:

$$\sum_{\alpha\in\{l,g\}} \Phi \frac{\partial(\varrho_\alpha X_\alpha^\kappa S_\alpha)}{\partial t} + \nabla \cdot \left(\sum_{\alpha\in\{l,g\}} (\varrho_\alpha \mathbf{v}_\alpha X_\alpha^\kappa - D_\alpha^{\kappa,\text{pm}} \varrho_\alpha \nabla X_\alpha^\kappa) \right) = q^{\text{if,ff},\kappa} + q^{\text{if,pm},\kappa} + q^{\text{detach},\kappa} \,. \tag{4}$$

The source terms are defined corresponding to (3), (6) and (7). The same holds for the energy balance equation under the assumption of local thermodynamic equilibrium:

$$\sum_{\alpha\in\{l,g\}} \Phi \frac{\partial(\varrho_\alpha u_\alpha S_\alpha)}{\partial t} + (1-\Phi)\frac{\partial(\varrho_s c_s T)}{\partial t} + \nabla \cdot \left(\sum_{\alpha\in\{l,g\}} \varrho_\alpha \mathbf{v}_\alpha h_\alpha - \lambda_{\text{pm}} \nabla T \right) = q^{\text{if,ff},T} + q^{\text{if,pm},T} + q^{\text{detach},T} \,. \tag{5}$$

These equations are valid in the interface domain Γ. In a first step, we neglect horizontal flow along the interface for simplicity. Therefore, no fluxes occur across the boundaries of the lower-dimensional interface domain and the balance equations contain only storage and source terms.

2.4 Coupling Concept

The exchange of mass, momentum and energy between the free flow and the porous medium happens due to convective, diffusive and conductive fluxes across the common interface. These fluxes have been described in a simple coupling concept for compositional flows in [1, 5]. The simple coupling concept is valid for a two-domain approach with a single-phase gaseous free flow and a two-phase flow in a porous medium. The interface cannot store mass or energy, since it is devoid of thermodynamic properties. In the following, we extend the simple coupling concept for our three-domain approach and take the influence of surface drops into account.

For the three-domain approach, two sets of coupling conditions become necessary: one for the exchange between the free flow and the interface domain, and one for the porous medium and the interface domain. Due to the first simplification that only vertical fluxes occur, only an area of ΦA_Γ is available for exchange on both the upper and lower boundary of the interface domain. Between the interface domain and the porous medium, both gas and liquid fluxes can occur. Here, three cases need to be distinguished: gas flux through gas-filled pores, direct evaporation from liquid-filled pores and drop formation from liquid-filled pores. We neglect the second case for simplicity and therefore scale the gas fluxes with a_g and the liquid fluxes with a_{drop}.

Therefore, the total mass flux between the porous medium and the interface domain is multiplied by these fractions to account for the available interface area:

$$q^{\text{pm,if}} = [(\varrho_g \mathbf{v}_g) \cdot \mathbf{n}]^{\text{up}} a_g A_\Gamma + [(\varrho_l \mathbf{v}_l) \cdot \mathbf{n}]^{\text{up}} a_{\text{drop}} A_\Gamma \ , \tag{6}$$

where ϱ_α and $\mathbf{v}_\alpha$ are taken from the upstream domain up $\in$ {pm, if}. Between free flow and interface domain, only the gas phase can be exchanged across the area $\Phi A_\Gamma = (a_g + a_{\text{drop}}) A_\Gamma$:

$$q^{\text{ff,if}} = [(\varrho_g \mathbf{v}_g) \cdot \mathbf{n}]^{\text{up}} (a_g + a_{\text{drop}}) A_\Gamma \ , \tag{7}$$

with the upstream domain up $\in$ {ff, if}.
The same scaling applies to all other fluxes across the interface (see [1]). The set of equations for the local thermodynamic equilibrium holds in the three-domain as well and can be applied for the free-flow/interface and interface/porous-medium local thermodynamic equilibrium respectively. In contrast to the simple coupling concept, the interface can now store mass and energy within the drops.

2.5 Numerical Model

The three-domain approach is implemented in DuMu^x [6], a free and open-source simulator for flow and transport processes in porous media and free flow, by extending the available coupled two-domain model for free-flow/porous-medium-flow systems. A staggered grid discretization is applied for the free flow, while a cell-centered finite volume approach is chosen for both the interface and the porous medium. The temporal discretization is done with an implicit Euler method. The respective code to reproduce the following results is available under https://git.iws.uni-stuttgart.de/dumux-pub/Ackermann2019a.

3 Results and Discussion

The new interface concept is tested with a simple two-dimensional set-up as shown in Fig. 4. The free flow domain exceeds the porous medium domain to stabilize the flow field before interacting with the interface and porous medium. We set an inflow boundary condition on the left boundary and an outflow boundary condition on the right boundary. The upper boundary is a non-permeable wall. The porous medium's left and right boundaries are no-flow boundaries. On the lower boundary, a gas pressure that is slightly higher than the initial pressure within the porous medium is set to provoke a pressure gradient towards the interface.
Figure 4 shows the gas pressure in the whole model domain at $t = 15s$. In addition, the gas velocity in the free flow is depicted by gray arrows to indicate the flow field.

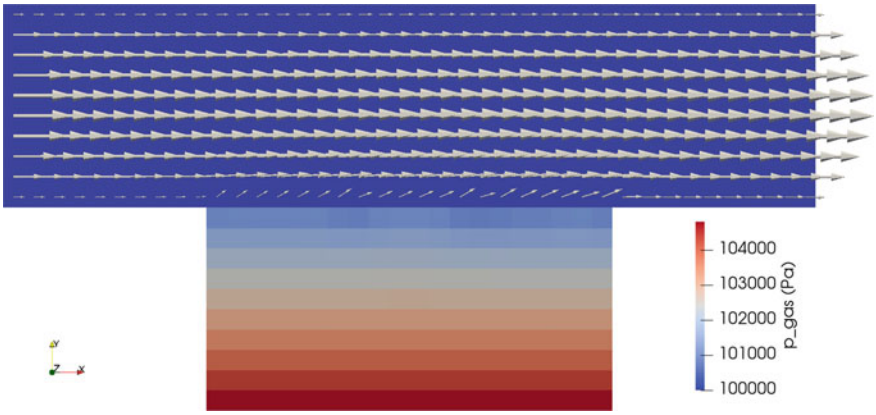

Fig. 4 Gas pressure in the free flow (upper half) and porous medium (lower half). The arrows indicate the gas velocity in the free flow

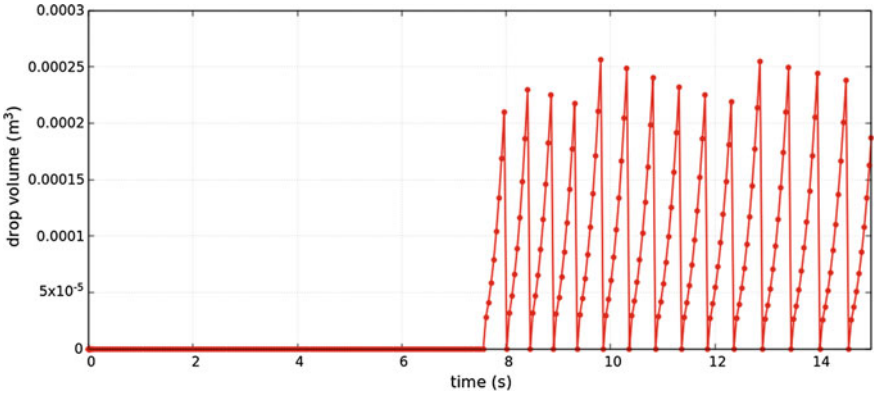

Fig. 5 Evolution of drop volume over time in one interface grid cell

The interface domain Γ cannot be seen here due to its lower-dimensional appearance. We analyse the interface processes by looking at the evolution of a drop over time. Figure 5 illustrates the drop volume in an interface grid cell in the center. Drop formation, growth and detachment for several drops can be observed.

As expected, the drops grow in several time steps as soon as the formation condition is fulfilled, and are detached when the drag force exceeds the retention force due to the increasing drop volume and radius. The results agree qualitatively with the findings in [2].

4 Conclusions

Including the influence of drops on the interface between a free flow and a flow in a porous medium poses a challenge for REV-scale model concepts. The three-domain approach developed in this work is able to represent simple drop dynamics such as formation, growth and detachment within a coupled macroscopic model.

Naturally, some pore-scale information is lost due to the upscaling and homogenization approach. However, the presented approach is computationally efficient while taking pore-scale processes into account.

The presented model is a first step towards a multi-scale approach to model the complex droplet-related processes at the interface between a free flow and a flow in a porous medium. With the assumption that only vertical fluxes take place, drop formation, growth and detachment can be taken into account. Dynamic processes such as spreading, merging, sliding, rolling and film flow along the porous surface are neglected. An extension to consider such lateral fluxes is conceptually developed and will be implemented. Additionally, a comparison with experiments to validate the concept is planned.

Acknowledgements We would like to thank the Deutsche Forschungsgemeinschaft (DFG) for the financial support for this work in the frame of the International Research Training Group "Droplet Interaction Technologies" (DROPIT).

References

1. Mosthaf, K., Baber, K., Flemisch, B., Helmig, R., Leijnse, A., Rybak, I., Wohlmuth, B.: A coupling concept for two-phase compositional porous-medium and single-phase compositional free flow. WRR **47**, W10522 (2011)
2. Baber, K., Flemisch, B., Helmig, R.: Modeling drop dynamics at the interface between free and porous-medium flow using the mortar method. Int. J. Heat Mass Transf. **99**, 660–671 (2016)
3. Gläser, D., Helmig, R., Flemisch, B., Class, H.: A discrete fracture model for two-phase flow in fractured porous media. Adv. Water Resour. **110**, 335–348 (2017)
4. Ackermann, S., Gläser, D., Flemisch, B., Helmig, R.: Multi-scale three domain approach for coupling free and porous media flow including drop interface processes. J. Comput. Phys. (Submitted) (2020)
5. Baber, K., Mosthaf, K., Flemisch, B., Helmig, R.: Numerical scheme for coupling two-phase compositional porous-media flow and one-phase compositional free flow. IMA J. Appl. Math. **77**, 887–909 (2012)
6. Koch, T., Gläser, D., Weishaupt, K., et al.: DuMu^x 3—an open-source simulator for solving multi-phase, component, scale, physics, domain, ... flow and transport problems in porous media with a focus on model coupling. Comput. Math. Appl. (Submitted) (2019)

A Locally-Refined Locally-Conservative Quadtree Finite-Volume Staggered-Grid Scheme

Melanie Lipp and Rainer Helmig

Abstract Simulating flow between porous media and adjacent free-flow regions in sufficient detail becomes computationally expensive when complex flow profiles develop. This is e.g. the case if a variety of strongly coupled physical processes is involved or if the surface between the two flow domains is rough. However, it is often sufficient to only use a fine grid resolution in regions of interest. Here, we present a locally-refined quadtree finite-volume staggered-grid scheme for the two-dimensional Navier-Stokes equations. Local mass and momentum conservation at lines, at which the sides of two finer control volumes touch the side of one coarser control volume, is ensured by defining the fluxes at the sides of coarser control volumes to be equal to the negative sum of fluxes at the two sides of finer control volumes. The method has been successfully applied to locally resolve the flow details in the vicinity of dividing streamlines in a fluid-flow test case. Being developed for the fully-coupled fully-implicit solution of the Navier-Stokes equations, this locally-refined grid scheme is a good basis for increasing the efficiency of simulations of free flow, which is strongly coupled to flow in adjacent domains.

1 Introduction

Flow and transport processes between porous media and adjacent free-flow regions are significant for a variety of industrial [9], environmental [13] and medical [6] applications. Multiple strongly coupled physical processes and non-flat surface geometries lead to a complex profile in such free flows, such that a small spatial resolution is required to capture the main flow features. The urgency of a small spatial resolution in the free-flow domain differs locally. In the following, three examples are given, in

M. Lipp (✉) · R. Helmig
Institute for Modelling Hydraulic and Environmental Systems, University of Stuttgart, Pfaffenwaldring 61, 70569 Stuttgart, Germany
e-mail: melanie.lipp@iws.uni-stuttgart.de

R. Helmig
e-mail: rainer.helmig@iws.uni-stuttgart.de

G. Lamanna et al. (eds.), *Droplet Interactions and Spray Processes*,
Fluid Mechanics and Its Applications 121,
https://doi.org/10.1007/978-3-030-33338-6_12

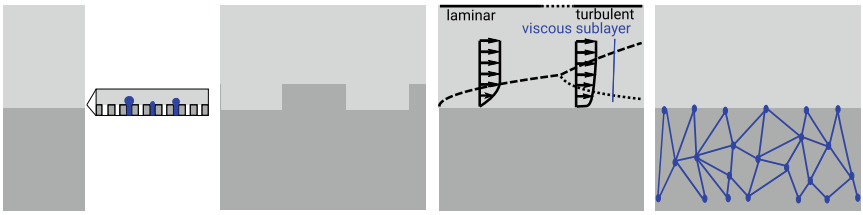

(a) Drops (blue) coming out of pores at an interface.

(b) Rough surface.

(c) Viscous sublayer. Dashes: boundary layer. Arrows: velocities.

(d) Pore-network model (blue).

Fig. 1 This figure illustrates situations in which local grid refinement is helpful within the context of porous-medium-flow free-flow coupling. The free-flow domain is represented in light grey, the porous-medium-flow domain in dark grey

which it is essential for fast and accurate simulations to locally refine the free-flow domain.

First, local refinement is required to capture large vortices developing after obstacles, in the context of flow over droplets developing at the free-flow porous-medium-flow interface (see Chap. of Sina Ackermann and Fig. 1a) and in the context of surface roughness (see Fig. 1b). Those vortices change the exchange processes across a porous-medium surface noticeably. Second, in the context of turbulent flow the viscous sublayer (see Fig. 1c) is extremely small. When using wall functions, it is required that the grid cells nearest to the wall are of small extension normal to the wall. For a rough wall, a grading of the grid is not sufficient to refine the interface region. Local refinement is required if overall refinement should be avoided. Additionally, for a flat wall, grading has the unfavorable effect of high-aspect-ratio grid cells. This can be avoided by local refinement. The viscous sublayer has a crucial effect on the local processes, e.g. evaporation processes, at a fluid-fluid-solid interface. Third, regions where thin pore throats of a pore network (see Fig. 1d) are in contact with a free flow should be locally resolved according to the pore size. Pore-network models are one way to describe the porous medium adjacent to a free-flow domain in detail [25].

To avoid oscillations of pressure and to ensure local conservation, the Navier-Stokes equations, which are used to model the free flow, are discretized using a finite-volume marker-and-cell (MAC) [11] approach, in which the control volumes for the mass balance and the control volumes for the components of the momentum balance build grids which are staggered with respect to each other, see Fig. 2a. The primary variable pressure p is situated on the cell centers (shown as black squares in Fig. 2), while the primary variable velocity $\boldsymbol{u} = (u, v)^\intercal$ is located on the cell faces (see arrows in Fig. 2). Within the finite-volume scheme, the mass balance is integrated over the grid cells (see red squares) and the x/y-component of the momentum balance is integrated over a control volumes shifted in x/y-direction with respect to the grid cells (see green/blue rectangles).

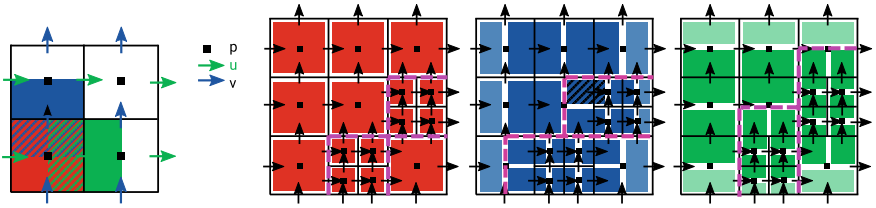

(a) Not refined. (b) Locally-refined example geometry.

Fig. 2 This sketch shows the control volumes and degrees of freedom in a not refined (left side) or refined (right side) non-graded staggered grid

One possibility to achieve local refinement of staggered grids is to use quadrilateral staggered grids as in [12]. However, this approach is less flexible than quadtree grids with hanging nodes. Another alternative is a generalization of the MAC scheme to non-rectangular meshes, as given for the Stokes equations in [4, 21]. The disadvantage of general meshes is their larger memory consumption when compared to quadtree data structures.

As to quadtree schemes, there are some approaches in the finite-difference context, e.g. [5, 10, 17, 20, 22] for staggered grids and [3] for hybrid staggered non-staggered grids, and in the finite-element context, e.g. [2]. However, they do not fulfill local mass conservation. In the finite-volume context, one approach is to use quadtree grids for the mass-balance control volumes, and define corresponding Voronoi meshes of non-rectangular momentum-balance control volumes [7]. A more commonly used approach, see e.g. [19, 23, 24], is to define corresponding rectangular momentum-balance control volumes, for which hanging nodes occur. In contrast to the approaches [19, 23, 24], which solve the Navier-Stokes equations by pressure-correction methods, this chapter presents a quadtree finite-volume staggered-grid scheme for a fully-coupled solution method of the Navier-Stokes equations. This is required for the intended application to free-flow porous-medium-flow coupling, in which realistic physical problems currently have to be solved by a monolithic approach.

Section 2 presents a locally-conservative discretization of the Navier-Stokes equations on a locally-refined quadtree grid. This discretization is applied to a stationary flow test case in Sect. 3, before conclusions are drawn in Sect. 4.

2 Methods

In this section, the numerical method is introduced, including details on stencils, interpolation factors and local conservation. The first subsection shows the equations which are solved within this work.

2.1 Governing Equations

The free flow is modeled by the Navier-Stokes equations for laminar, single (gaseous) phase, one-component, isothermal flow assuming a Newtonian fluid. The momentum balance reads

$$\frac{\partial \boldsymbol{u}}{\partial t} + \nabla \cdot (\boldsymbol{u}\boldsymbol{u}^{\mathsf{T}}) - \frac{\mu}{\varrho}\nabla \cdot (\nabla \boldsymbol{u} + \nabla \boldsymbol{u}^{\mathsf{T}}) + \frac{1}{\varrho}\nabla p - \boldsymbol{g} - \boldsymbol{q}_{\mathrm{u}} = 0 \tag{1}$$

with velocity $\boldsymbol{u}$, time t, dynamic viscosity μ, density ϱ, pressure p, gravity $\boldsymbol{g}$ and momentum sources/sinks $\boldsymbol{q}_u$. The mass balance is formulated as

$$\nabla \cdot \boldsymbol{u} - q_p = 0 \tag{2}$$

with mass sources/sinks q_p.

2.2 Discretization Concept

The equations are discretized on a staggered grid, see Fig. 2. The (possibly-graded) staggered grid is locally refined in this work by a quadtree structure with hanging nodes (h-refinement). In the unrefined case, one velocity degree of freedom is located on each face of the grid cells. In the refined case, coarse and fine cells touch, rising the question if velocity unknowns should exist in the center of the coarse face, see e.g. [24], or in the centers of the fine faces, see e.g. [3, 10]. The latter option is chosen. Furthermore, cells are divided into four equally-sized parts upon refinement.

A variety of geometries occur in locally-refined staggered grids. For instance, a coarse cell can be surrounded by zero, one, two, three or four refined cells. For simplicity, direct as well as diagonal neighbors are restricted to differ at most by one refinement level in this work. Grids from automatic refinement criteria (future work) have to be manipulated in order to fulfill the geometry rules. For this, the refined regions have to possibly be extended, the coarsened regions have to possibly be shrinked, as described e.g. in [18].

Control volumes In a refined grid, see Fig. 2b, three types of control volumes occur: coarse ones (big squares), fine ones (small squares) and transitional ones (rectangles).

In the case of Dirichlet boundary conditions for velocity, the velocities at the boundary are known, and for this reason they are no degree of freedom. The balance equations are only integrated over the fully-colored control volumes. For outflow boundary conditions (fixed pressures at the boundaries, zero velocity gradients normal to the boundaries), velocities are unknowns and balance equations are additionally integrated over the lightly colored control volumes:

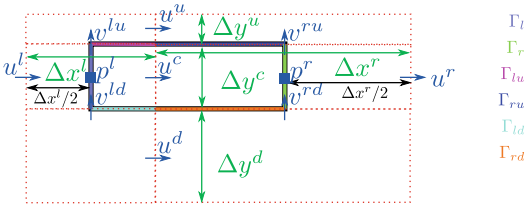

(a) Virtual stencil for the momentum balance control volume (solid line). Velocities u and v, distances Δx and Δy, pressures p and boundary segments Γ are defined at central (c), left (l), right (r), down (d) or up (u) or combined position. Red dotted lines represent ghost cells.

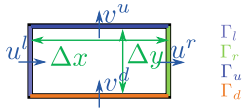

(b) Virtual mass balance stencil. Velocities u and v and boundary segments Γ are located at the left (l), right(r), down(d) and up (u). Distances Δx and Δy are defined.

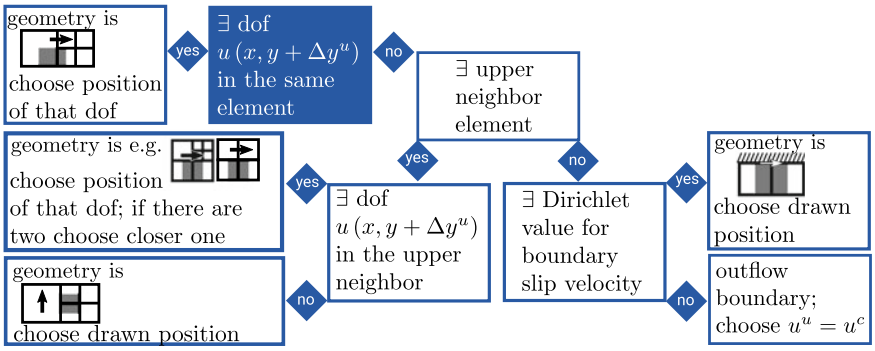

(c) Choice of the position of $u\,(x, y + (\Delta y_c + \Delta y_u)\,/2)$, depending on the surrounding degree of freedom (dof) positions. Any geometry should be considered representative up to reflection and rotation.

Fig. 3 Virtual stencils are defined for any control volume

Virtual stencils To ease the discretization of the Navier-Stokes equations, virtual stencils are introduced, see Fig. 3. They consist of real nodes, at which there exist degrees of freedom or boundary values, and virtual nodes, at which there exist neither degrees of freedom nor boundary values. For example, for the hatched control volumes in Fig. 2b, the nodes p^l, v^{ld} and u^l are virtual. In cases, in which the dotted rectangles in Fig. 3a are not grid cells, it is possible to interpret them as ghost cells.

The time derivative is discretized by a Backward Euler method, the advective terms are fully upwinded, and the diffusive terms are approximated by central differences. The spatial discretization of the x-component of the momentum balance is given by

$$I_\Omega + I_{\Gamma_l} + I_{\Gamma_r} + I_{\Gamma_{lu}} + I_{\Gamma_{ru}} + I_{\Gamma_{ld}} + I_{\Gamma_{rd}} = 0 \tag{3}$$

with the integrals

$$I_\Omega = \frac{\Delta x^l + \Delta x^r}{2} \Delta y^c \frac{\partial u^c}{\partial t} + \frac{\Delta x^l + \Delta x^r}{2} \Delta y^c \left(-g_x - q_{x,\mathrm{u}}\right) \tag{4}$$

$$I_{\Gamma_{l/r}} = \mathrm{sgn}(\boldsymbol{n}_{l/r}) \left(\Delta y^c \left(u^{l/r}, u^c\right)_{\mathrm{up}} \frac{u^{l/r} + u^c}{2} - 2\frac{\mu}{\varrho} \Delta y^c \frac{u^{c/r} - u^{l/c}}{\Delta x^{l/r}} + \frac{\Delta y^c}{\varrho} p^{l/r} \right) \tag{5}$$

$$I_{\Gamma_{lu/ru/ld/rd}} = \mathrm{sgn}(\boldsymbol{n}_{u/u/d/d}) \left(\frac{\Delta x^{l/r/l/r}}{2} \left(u^c, u^{u/u/d/d}\right)_{\mathrm{up}} v^{lu/ru/ld/rd} \right. \tag{6}$$

$$\left. - \frac{\mu}{\varrho} \frac{\Delta x^{l/r/l/r}}{2} \left(\frac{v^{ru/ru/rd/rd} - v^{lu/lu/ld/ld}}{\frac{\Delta x^l + \Delta x^r}{2}} + \frac{u^{u/u/c/c} - u^{c/c/d/d}}{\frac{\Delta y^c + \Delta y^{u/u/d/d}}{2}} \right) \right) \tag{7}$$

with

$$\mathrm{sgn}(\boldsymbol{n}_l) = -1,\ \mathrm{sgn}(\boldsymbol{n}_r) = 1,\ \mathrm{sgn}(\boldsymbol{n}_u) = 1,\ \mathrm{sgn}(\boldsymbol{n}_d) = -1 \tag{8}$$

over the area Ω and over the boundary segments $\Gamma_i,\ i = l, r, lu, ru, ld, rd$ of the control volume. In the compact notations, the slash is used to define several integrals simultaneously, e.g. to define I_{Γ_l} and I_{Γ_r} by $I_{\Gamma_{l/r}}$. The expressions $(\cdot)_{\mathrm{up}}$ denote an upwind decision, and the velocities and lengths are defined in Fig. 3a. Integrals for the y-component of the momentum balance are defined analogously. The discretization of the mass balance reads

$$I_\Omega + I_{\Gamma_l} + I_{\Gamma_r} + I_{\Gamma_u} + I_{\Gamma_d} = 0 \tag{9}$$

with

$$I_{\Gamma_{l/r}} = \mathrm{sgn}\left(\boldsymbol{n}_{l/r}\right) \Delta y u^{l/r},\ I_{\Gamma_{u/d}} = \mathrm{sgn}\left(\boldsymbol{n}_{u/d}\right) \Delta x u^{u/d},\ I_\Omega = -\Delta x \Delta y q_p \tag{10}$$

with virtual mass-balance-stencil components illustrated in Fig. 3b and signs as in Eq. (8).

The virtual stencil in Fig. 3a defines positions of (possibly virtual) velocities u^l, u^r, v^{lu}, v^{ru}, v^{ld}, v^{rd} in the surrounding of u^c. The positions of the parallel velocities $u^u = u\left(x, y + \left(\Delta y_c + \Delta y_u\right)/2\right)$ and $u^d = u\left(x, y - \left(\Delta y_c + \Delta y_d\right)/2\right)$ in the case of a control volume around $u(x, y)$, in contrast, depend on the surrounding geometry, as the distances Δy^u and Δy^d are not represented within the control volume. The algorithm, which is used to choose the positions of those parallel velocities, is explained exemplarily for $u\left(x, y + \left(\Delta y_c + \Delta y_u\right)/2\right)$ in Fig. 3c.

At boundaries, three special stencils occur, which are briefly discussed for control volumes around velocities u in the following. If there is a boundary with a Dirichlet velocity condition instead of an upper(u)/lower(d) neighboring cells, one sets $\Delta x^{u/d} = 0$ and $u^{u/d} = u^{\mathrm{boundary}}$. If there is a boundary with an outflow condition instead of an upper(u)/lower(d) neighboring cells, one sets $u^{u/d} = u^c$. For control volumes at outflow boundaries (at the right/left of the physical domain), which only extend to one side of the unknown boundary velocity u^c, one first sets $p^{l/r} = p^{\mathrm{boundary}}$, $v^{ld/rd} = v^{rd/ld}$, $v^{lu/ru} = v^{ru/lu}$ and $u^{l/r} = u^c$ and then $\Delta x^{l/r} = 0$. The variable p^{boundary} denotes the Dirichlet pressure value at the boundary.

Degrees of freedom contributing to virtual nodes Any velocity or pressure value at a virtual node is calculated from a bilinear interpolation from one to four values, as also e.g. in [19, 20, 24]. Figure 4 shows, for all possible geometries, which degrees of freedom are chosen

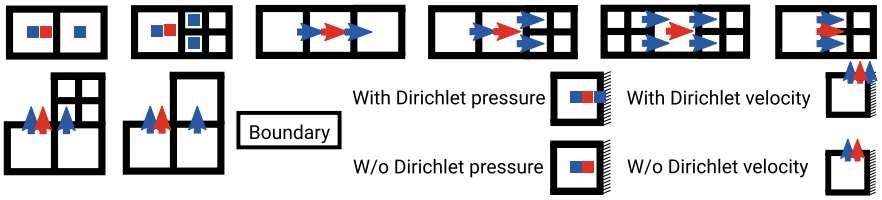

Fig. 4 Degrees of freedom (blue) contribute to the virtual nodes (red). Some geometries focus on cell centered primary variables (squares), some on face-centered ones (arrows)

to interpolate from. Any geometry should be considered representative up to reflection and rotation.

Interpolation factors Interpolations from one value are given the prefactor one. Otherwise, the interpolate $\Phi(x, y)$ is built from two to four values, which can either be located at two different x-values x_1 and x_2 and one to three y-values or at three different x-values and two different y-values y_1 and y_2 (see Fig. 4, considering reflection and rotation). In the former case, the interpolate is formulated as

$$\Phi(x, y) = \frac{(x_2 - x)}{(x_2 - x) - (x_1 - x)} \Phi(x_1, y) + \frac{(x_1 - x)}{(x_1 - x) - (x_2 - x)} \Phi(x_2, y) \tag{11}$$

with $\Phi(x_i, y),\ i = 1, 2$ either being degrees of freedom or being interpolates

$$\Phi(x_i, y) = \frac{(y_2 - y)}{(y_2 - y) - (y_1 - y)} \Phi(x_i, y_1) + \frac{(y_1 - y)}{(y_1 - y) - (y_2 - y)} \Phi(x_i, y_2) \tag{12}$$

from degrees of freedom $\Phi(x_i, y_1),\ \Phi(x_i, y_2)$. In the latter case, an interpolation (12) with $x_i = x$ is done, in which $\Phi(x, y_1)$ and $\Phi(x, y_2)$ are either degrees of freedom or interpolates of degrees of freedom according to Eq. (11) with $y = y_i,\ i = 1, 2$.

Local mass and momentum conservation To ensure local mass and momentum conservation, the discretization concept has to be modified. Fluxes I_Γ have to be continuous across the lines separating control volumes. With the unmodified scheme described above, fluxes are not yet continuous.

Consider, for example, the flow sketched in Fig. 5. It occurs between two plates with a parabolic inflow profile $u(0, y) = u_{\max} y\,(y_{\max} - y)$, no-flow no-slip conditions at the top and bottom and outflow conditions with fixed pressure p at the right. The stationary solution for this flow is $u(x, y) = u(y) = u(0, y)$. Of special interest is the region around an interface (red line) between coarse (C, blue) and transitional ($T1$, green and $T2$, red) control volumes for the x-component of the Navier-Stokes equation. The velocities represented by dotted arrows are interpolates from the velocities shown as solid arrows. Center (c), left (l), right (r), down (d) and up (u) positions are relevant, as are the surrounding control volumes (light blue). The flux contribution

$$F\left(\Delta y^c, u^{l/r}, u^c\right) = \mathrm{sgn}(\boldsymbol{n}_{l/r}) \Delta y^c \left(u^{l/r}, u^c\right)_{\mathrm{up}} \frac{u^{l/r} + u^c}{2} \tag{13}$$

from Eq. (5) along the marked line gives, considering interpolations, a flux

$$F_{C,r}\left(2\Delta y, \frac{u^c_{T_1} + u^c_{T_2}}{2}, u^c_C\right) \tag{14}$$

over the right side of the coarse control volume C. This is in general unequal to the negative of the sum

$$F_{T,l} = F_{T_1,l}\left(\Delta y, \frac{3u^c_C + u^u_C}{4}, u^c_{T_1}\right) + F_{T_2,l}\left(\Delta y, \frac{3u^c_C + u^d_C}{4}, u^c_{T_2}\right) \tag{15}$$

of the fluxes over the left sides of the transitional control volumes T_1 and T_2. In the example geometry Fig. 2b, such flux discontinuities occur along the pink dashed lines between the momentum control volumes. When the linear interpolations are replaced by higher-order interpolations, flux discontinuities additionally occur along the pink dashed line between the mass control volumes in Fig. 2b.

This need for a modified scheme does neither vanish when defining only one velocity degree of freedom at the coarse-fine grid-cell interface, nor when using more accurate interpolations for $u^{l/r}$, nor when using a higher-order method instead of the upwinding $\left(u^{l/r}, u^c\right)_{\text{up}}$. With one velocity degree of freedom at the interface, the coarse-transitional interface is simply shifted by one cell-in Fig. 5 that is to the right. For the remaining two aspects, consider the channel flow example in Fig. 5. Even for an exact interpolation, the flux $F_{C,r}\left(2\Delta y, u\left(3\Delta y\right), u\left(3\Delta y\right)\right)$ will be unequal to the negative of $F_{T,l} = F_{T_1,l}\left(\Delta y, u\left(3.5\Delta y\right), u\left(3.5\Delta y\right)\right) + F_{T_2,l}\left(\Delta y, u\left(2.5\Delta y\right), u\left(2.5\Delta y\right)\right)$. In a similar way, a higher-order method will use more (possibly interpolated) nodes at $y = 3\Delta y$ instead of $\left(u_{\text{interpolated}}\left(3\Delta y\right), u\left(3\Delta y\right)\right)_{\text{up}}$ for $F_{C,r}$, while it will use more (possibly interpolated) nodes at $y = 3.5\Delta y$ and $y = 2.5\Delta y$ for $F_{T_1,l}$ and $F_{T_2,l}$, not improving the flux continuity.

The scheme is modified in such a way, that coarse fluxes, in the above example $F_{C,r}$, are discarded and replaced by the negative of the respective fine fluxes, in the above example $F_{T_1,l} + F_{T_2,l}$.

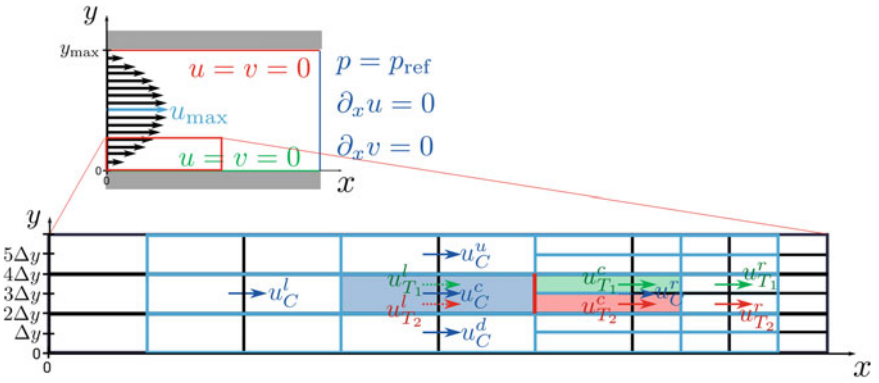

Fig. 5 This sketch shows an example setup of a flow between two plates to explain issues of local conservation

3 Numerical Test

The local refinement of the staggered grid has been implemented in the open-source numerical simulator DuMu$^{\mathrm{X}}$ [14, 15], with the grid data structure provided by ALUGrid [1]. A numerical example case introduced by Kovasznay [16] is presented. A stationary flow, the analytical solution of which is visualized by streamlines in Fig. 6(a), is simulated numerically. Dirichlet velocities coherent with the analytical solution

$$p = \frac{1}{2}\left(1 - \exp\left(2\lambda x\right)\right), \quad \boldsymbol{u} = \begin{pmatrix} 1 - \exp\left(\lambda x\right)\cos\left(2\pi y\right) \\ \frac{\lambda}{2\pi}\exp\left(\lambda x\right)\sin\left(2\pi y\right) \end{pmatrix}, \quad \lambda = \frac{1}{2\nu} - \sqrt{\frac{1}{4\nu^2} + 4\pi^2} \tag{16}$$

are set at all boundaries, pressures are fixed to analytical-solution values along the left boundary. The fluid has a kinematic viscosity of $\nu = 0.025$ and a density of $\varrho = 1$. Neither sources or sinks nor gravity are part of this example case. With refinement along dividing streamlines, the flow is simulated by solving Eqs. (1) and (2) using the Newton method and the direct linear solver UMFPACK [8]. The local refinement in Fig. 6d allows to, with slightly less grid cells, resolve the flow in the region of the diving streamlines in more detail than with the uniform grid in Fig. 6c.

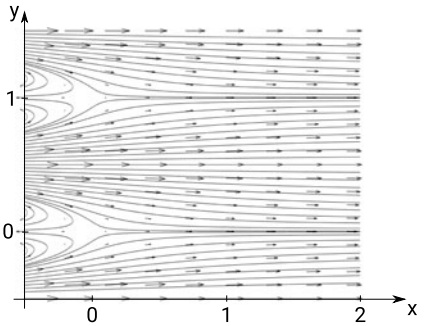

(a) Streamlines (lines) with velocities (scaled arrows).

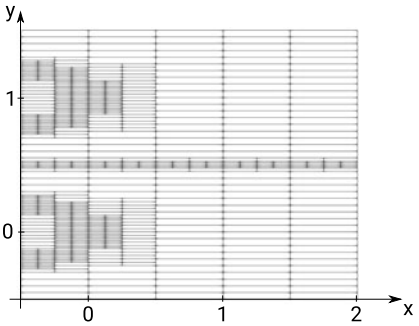

(b) Refined grid.

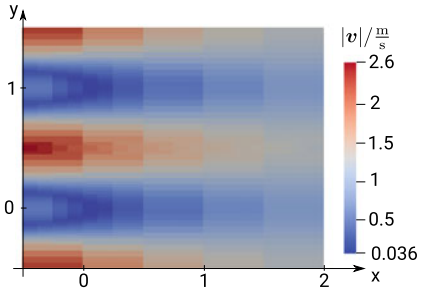

(c) Velocity magnitude, locally refined 5x40 grid with 662 grid cells.

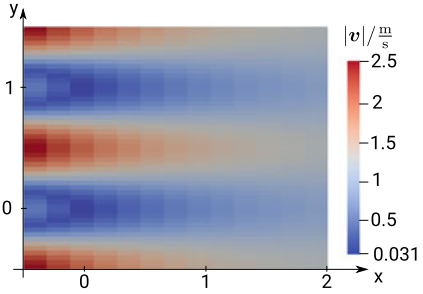

(d) Velocity magnitude, uniform 13x52 grid with 676 grid cells.

Fig. 6 As a numerical example case, a stationary flow with dividing streamlines is simulated

4 Conclusion

A locally-refined locally-conservative quadtree finite-volume staggered-grid scheme was developed for the Navier-Stokes equations in two dimensions. The discretization presented here has proven suitable to resolve local flow features in more detail, e.g. along dividing lines. In contrast to the pressure-correction methods used by similar approaches [19, 23, 24] to solve the Navier-Stokes equations, the proposed scheme is developed in the context of the fully-coupled fully-implicit solution of the Navier-Stokes equations. This allows to use the locally-refined grid for simulations of free flows which is strongly coupled to adjacent domains, this way contributing to more accurate and efficient simulations of e.g. evaporation processes. To show a gain in computational time, the current code has to be optimized. Without focus on performance, a local refinement of a finite-volume staggered-grid scheme has been implemented, while preserving local mass and momentum conservation.

Acknowledgements Melanie Lipp is supported by a scholarship of the Landesgraduiertenförderung Baden-Württemberg at the University of Stuttgart. We thank the Deutsche Forschungsgemeinschaft (DFG, German Research Foundation) for supporting this work by funding SFB 1313, Project Number 327154368. The code to produce the results of this chapter can be downloaded from https://git.iws.uni-stuttgart.de/dumux-pub/Lipp2019a.git.

References

1. Alkämper, M., Dedner, A., Klöfkorn, R., Nolte, M.: The dune-alugrid module. arXiv preprint arXiv:1407.6954 (2014)
2. Anderson, R.W., Pember, R.B., Elliott, N.S.: A dynamically adaptive arbitrary Lagrangian-Eulerian method for hydrodynamics. In: Computational Fluid and Solid Mechanics, pp. 1232–1236. Elsevier (2003)
3. Angelidis, D., Chawdhary, S., Sotiropoulos, F.: Unstructured cartesian refinement with sharp interface immersed boundary method for 3D unsteady incompressible flows. J. Comput. Phys. **325**, 272–300 (2016)
4. Beltman, R., Anthonissen, M.J.H., Koren, B.: Mimetic staggered discretization of incompressible Navier-Stokes for barycentric dual mesh. In: International Conference on Finite Volumes for Complex Applications, pp. 467–475. Springer, Heidelberg (2017)
5. Bennett, B.A.V., Smooke, M.D.: Local rectangular refinement with application to axisymmetric laminar flames. Combust. Theor. Model. **2**(3), 221–258 (1998)
6. Chauhan, V.P., Stylianopoulos, T., Boucher, Y., Jain, R.K.: Delivery of molecular and nanoscale medicine to tumors: transport barriers and strategies. Annu. Rev. Chem. Biomol. Eng. **2**, 281–298 (2011)
7. Chénier, E., Eymard, R., Herbin, R.: An extension of the mac scheme to some unstructured meshes. In: Fořt, J., Fürst, J., Halama, J., Herbin, R., Hubert, F. (eds.) Finite Volumes for Complex Applications VI Problems & Perspectives, pp. 253–261. Springer, Heidelberg (2011)
8. Davis, T.A.: Algorithm 832: Umfpack v4.3—an unsymmetric-pattern multifrontal method. ACM Trans. Math. Software **30**(2), 196–199 (2004)
9. Defraeye, T.: Advanced computational modelling for drying processes—a review. Appl. Energy **131**, 323–344 (2014)
10. Gerya, T.V., May, D.A., Duretz, T.: An adaptive staggered grid finite difference method for modeling geodynamic stokes flows with strongly variable viscosity. Geochem. Geophys. Geosyst. **14**(4), 1200–1225 (2013)

11. Harlow, F.H., Welch, J.E.: Numerical calculation of time-dependent viscous incompressible flow of fluid with free surface. Phys. Fluids **8**(12), 2182–2189 (1965)
12. Huang, Y.L., Liu, J.G., Wang, W.C.: A generalized mac scheme on curvilinear domains. SIAM J. Sci. Comput. **35**(5), B953–B986 (2013)
13. Jambhekar, V.A., Helmig, R., Schröder, N., Shokri, N.: Free-flow-porous-media coupling for evaporation-driven transport and precipitation of salt in soil. Transp. Porous Media **110**(2), 251–280 (2015)
14. Koch, T., Gläser, D., Weishaupt, K., Ackermann, S., Beck, M., Becker, B., Burbulla, S., Class, H., Coltman, E., Emmert, S., Fetzer, T., Grüninger, C., Heck, K., Hommel, J., Kurz, T., Lipp, M., Mohammadi, F., Scherrer, S., Schneider, M., Seitz, G., Stadler, L., Utz, M., Weinhardt, F., Flemisch, B.: Dumu^{x}3—An Open-source Simulator for Solving Flow and Transport Problems in Porous Media with a Focus on Model Coupling. arXiv:1909.05052 (2019)
15. Koch, T., Gläser, D., Weishaupt, K., Ackermann, S., Beck, M., Becker, B., Burbulla, S., Class, H., Coltman, E., Fetzer, T., Flemisch, B., Grüninger, C., Heck, K., Hommel, J., Kurz, T., Lipp, M., Mohammadi, F., Schneider, M., Seitz, G., Scholz, S., Weinhardt, F.: Dumux 3.0.0 (2018). https://doi.org/10.5281/zenodo.2479595
16. Kovasznay, L.I.G.: Laminar flow behind a two-dimensional grid. In: Mathematical Proceedings of the Cambridge Philosophical Society, vol. 44, pp. 58–62. Cambridge University Press (1948)
17. Kramer, R.M.J., Pantano, C., Pullin, D.I.: Nondissipative and energy-stable high-order finite-difference interface schemes for 2-d patch-refined grids. J. Comput. Phys. **228**(14), 5280–5297 (2009)
18. Löhner, R.: Applied Computational Fluid Dynamics Techniques: An Introduction Based on Finite Element Methods. Wiley (2008)
19. Manhart, M.: A zonal grid algorithm for dns of turbulent boundary layers. Comput. Fluids **33**(3), 435–461 (2004)
20. Minion, M.L.: A projection method for locally refined grids. J. Comput. Phys. **127**(1), 158–178 (1996)
21. Nicolaides, R.A.: Flow discretization by complementary volume techniques. In: 9th AIAA CFD Meeting, pp. 464–470. Buffalo, New York (1989)
22. Olshanskii, M.A., Terekhov, K.M., Vassilevski, Y.V.: An octree-based solver for the incompressible Navier-Stokes equations with enhanced stability and low dissipation. Comput. Fluids **84**, 231–246 (2013)
23. Papadakis, G., Bergeles, G.: A local grid refinement method for three-dimensional turbulent recirculating flows. Int. J. Numer. Methods Fluids **31**(7), 1157–1172 (1999)
24. Vittoz, L., Oger, G., Li, Z., De Leffe, M., Le Touzé, D.: A high-order finite volume solver on locally refined Cartesian meshes–benchmark session. In: International Conference on Finite Volumes for Complex Applications, pp. 73–89. Springer, Heidelberg (2017)
25. Weishaupt, K., Joekar-Niasar, V., Helmig, R.: An efficient coupling of free flow and porous media flow using the pore-network modeling approach. J. Comput. Phys. X **1**, 100011 (2019)

Droplet–Liquid Interaction

A New Perspective for the Characterization of Crown Rim Kinematics

Ronan Bernard, Visakh Vaikuntanathan, Grazia Lamanna and Bernhard Weigand

Abstract Droplet impact on wall-films are typical examples where 'splashing', the fragmentation of the crown rim during its expansion, takes place. The triggering instability mechanisms are directly linked to crown rim kinematics. This experimental study analyses which geometrical parameter is physically the most suited for studying crown rim kinematics during expansion. The problems associated with the classical geometrical parameters rim radius R_R and height H_R (often considered separately) are presented. First, the radial and axial rim expansions have different durations which prevents the definition of rim expansion in a unified way. Second, considering separately H_R and R_R leads to an incomplete picture of the impact process in terms of momentum transfer to the rim since the crown aspect ratio H_R/R_R varies strongly with the impact conditions. We show that considering the crown rim displacement instead solves these problems: a single peak during the impact process enables a clear definition of rim expansion (duration and magnitude). Furthermore, the temporal evolution of the rim displacement during expansion could systematically be fitted by a quadratic curve with high accuracy, which indicates a constant deceleration process. Thus, considering the rim displacement reveals important features of the crown rim kinematics.

1 Introduction to Rim Kinematics

The most common events, where the outcome of droplet impacting a wall-film can be seen, are during heavy rain falls: in the blink of an eye, a conical liquid structure of few millimeters forms and its upper part disintegrates, ejecting many tiny droplets. This phenomenon has been first studied by Worthington at the end of the nineteenth century [29]. From this point on, the interest for droplet impact on wall-films has not stopped growing since this phenomenon is encountered in many technical applications where droplets interact with a thin liquid layer: spray cooling, coating,

R. Bernard (✉) · V. Vaikuntanathan · G. Lamanna · B. Weigand
Institute of Aerospace Thermodynamics, Pfaffenwaldring 31, 70569 Stuttgart, Germany
e-mail: ronan.bernard@itlr.uni-stuttgart.de

G. Lamanna et al. (eds.), *Droplet Interactions and Spray Processes*,
Fluid Mechanics and Its Applications 121,
https://doi.org/10.1007/978-3-030-33338-6_13

extinguishing film fuelled fires, microfluidics in the pharmaceutical industry, fuel injection in combustion chamber with lubricating oil films... Besides, droplet impact on wall-films offers a synthesis of interesting phenomena of fluid mechanics among liquid/wall interaction in thin layers, short liquid/liquid interaction, strong flow redirection, and liquid sheet fragmentation. The latter is of particular interest since it involves liquid instabilities, which are encountered in even more natural and industrial processes. In the case of a droplet impact on a wall-film, liquid sheet fragmentation is associated with the so-called 'crown splashing' [3, 8, 18]. This impact outcome results from the destabilisation of the crown rim, the liquid torus at the top of the crown. A typical example of 'crown-type splashing' is given in Fig. 1 and is explained in detail in Sect. 1.1. In order to understand the processes leading to splashing, a deeper insight into the instability mechanisms occurring at the rim is necessary, the first step being the study of their main input parameters: the rim kinematics. In Sect. 2, the limitations of the geometrical parameters usually used to describe crown rim kinematics (rim height and radius) are presented. The corresponding problems are solved by considering the crown rim displacement from the impact point introduced in Sect. 3, revealing interesting kinematic features of the crown rim expansion.

1.1 Impact Process and Morphological Features

When a droplet impacts on a thin wall-film, the liquid of the droplet interacts strongly during few milliseconds with the wall-film liquid initially at rest. This results in a complex and fascinating liquid structure shown in Fig. 1.

Before the impact, the droplet of diameter D_d approaches the film with the velocity V_d orthogonally to the wall-film surface in our study. The wall-film liquid is at rest, and has a thickness h_f, which is usually non-dimensionalised by the droplet diameter, $\delta = {}^{h_f}/_{D_d}$. The characteristic "thin films" investigated here refers to wall-film thicknesses between 0.1 and 0.5 times the droplet diameter. The time at which the droplet touches the wall-film is taken as the beginning of impact, i.e. $t = 0$ ms in Fig. 1. As the droplet impacts the film, the liquids are deformed and a kinematic discontinuity is formed between the droplet with high momentum and the film at rest [30]. This leads to a liquid lamella expanding axially and radially, the so-called 'crown'. At the upper edge of the crown the 'rim', a liquid torus forms accumulating liquid from the crown-wall. Under certain impact conditions, the crown rim destabilises, forming a wavy structure. These instabilities may grow and develop into tiny liquid ligaments, 'the fingers', which then disintegrate into secondary droplets. The succession of all these events leading to the atomization of the crown during its expansion is referred to as "crown-type splashing". Investigating the instability mechanisms responsible for the number and growth of these fingers is necessary to understand how splashing is triggered. These instability mechanisms are still a highly discussed topic in the literature: most of the studies [5, 8, 21, 32] report a link to the Plateau-Rayleigh instability to explain the undulations on the crown rim considered

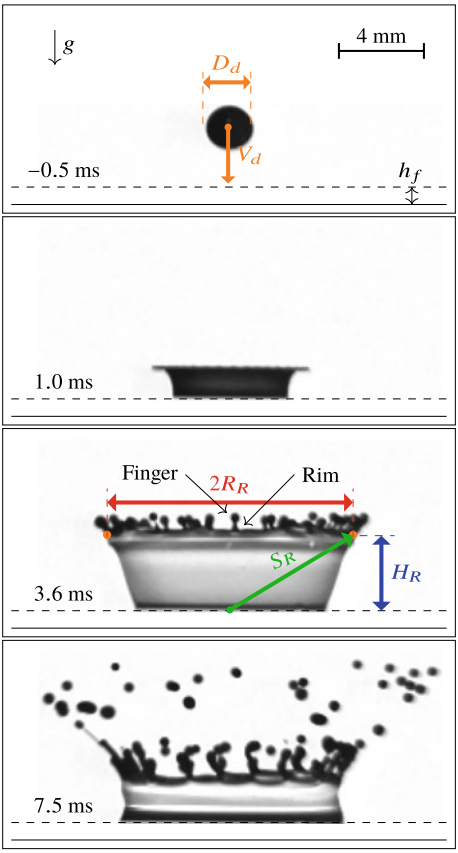

Fig. 1 Typical high-speed images of a crown formed during droplet impact on a wall-film (case of 'crown-type splashing'). The primary impact parameters (droplet diameter D_d, droplet impact velocity V_d, and wall-film thickness h_f), as well as the morphological features of interest (rim, fingers) are highlighted. The classical geometrical parameters of the crown rim (radius R_R and height H_R) of the crown are marked, as well as the crown rim displacement from the impact point S_R. Impact conditions: B10 droplet impacting on B5 wall-film (see liquid properties in Table 1), D_d = 2.02 mm, V_d = 2.99 m/s, δ = 0.10

as the liquid cylinder. Other studies [13, 15, 22] explained it by the Rayleigh-Taylor instability, or by its impulsive limit, the Richtmyer-Meshkov instability. An interplay of both Rayleigh-Taylor and Plateau-Rayleigh instabilities was also proposed [1]. However, to explain the diminution of splashing at low ambient pressure, the predominance of the Kelvin-Helmholtz instability was also suggested [31]. Although the mechanisms associated to these models are different, they all rely on the kinematic parameters of the crown rim as input parameter: the velocity difference with the air for the Kelvin-Helmholtz instability, and the crown rim acceleration for the Rayleigh-Taylor/Richtmyer-Meshkov instabilities. The Rayleigh-Plateau instability

is dependent on the rim thickness, which is in turn linked to rim acceleration according to a recent study on unsteady sheet fragmentation [28]. Thus, an extensive study on crown rim kinematics is needed to investigate the dominant instability mechanisms for different impact conditions. As a first step, the focus of this work is to find a relevant geometrical parameter representative of the rim motion during crown expansion.

1.2 Experimental Set-Up and Methodology

The experimental set-up for droplet impact on a wall-film consists of three main elements: a droplet generation system, a high-speed shadowgraphy imaging system and a thin pool. The droplet is dripping off by gravity from a needle of 0.8 mm diameter. The height of the needle is used to vary the droplet impact velocity V_d. Shortly before the impact, the single droplet goes through a laser barrier that triggers the high-speed camera (Photron FASTCAM SA1.1, 20,000 frames per second, shutter 1/92 ms). The thin pool, where the droplet impacts, is illuminated in backlit mode by two LEDs orthogonal to each other in the horizontal plane, the two light paths being directed with mirrors and lenses to the camera. Thus, a two-perspective shadowgraphy is obtained on a single frame of the high-speed camera. This allows a temporal resolution of 0.05 ms and a temporal resolution of 80 µm/pixel of the impact process. More details on the experimental set-up can be found in Geppert et al. [11] who developed it. The impact pool consists of a thin metallic ring (inner diameter 60 mm, height 0.6 or 1.2 mm) glued on a transparent plate. This transparent plate is made of sapphire providing a high refractive index compared to the liquids used to make the measurement of the wall-film thickness reliable with a confocal chromatic sensor (micro-Epsilon IFS2405-3) that enables a measurement error below 1% in the range of this study [11]. The thin pool is filled till the desired film thickness h_f prior to impact. The droplet diameter D_d and droplet velocity V_d are measured from the post-processed high-speed images shortly before impact ($\approx$1.5 ms) by using an in-house MATLAB® routine with a measurement error below 3% [11]. This routine also enables the extraction of the primary geometrical parameters of the rim; the rim height H_R and the rim radius R_R.

The liquids used for the droplet and the wall-film were different, i.e. a *binary* droplet/wall-film system. Besides the important technical applications of binary droplet/wall-film systems (e.g. Selective Catalytic Reduction with different urea-water concentration [26], or fuel/lubricant interaction in combustion engines [11]), it gives a deeper insight into the distinct role of the droplet and wall-film, especially of their respective viscosity [2]. In this work, different silicone oils combinations between droplet and wall-film were systematically investigated. The corresponding ranges of droplet diameter D_d and impact velocity V_d, wall-film thickness h_f, as well as their respective liquid properties are summarized in Table 1. The choice of these liquids allows a large variation of dynamic viscosities (2.70–96.3 mPa s), by keeping a small variability of density ($\pm$3.5%) and surface tension ($\pm$8%).

Table 1 Silicone oils used with their respective liquid properties, as well as the experimental range of the primary impact parameters (droplet diameter D_d and impact velocity V_d, and/or wall-film thickness h_f

Oil	μ (mPa s)[a]	ρ (kg/m^3)[a]	σ (mN/m)[a]	D_d (mm)[b]	V_d (m/s)[b]	h_f (μm)[c]
B3	2.70	900	18.0	1.93–2.02	1.80–4.29	198–1058
B5	4.60	920	19.2	–	–	199–1056
B10	9.45	945	20.2	1.96–2.07	1.93–4.35	200–1034
B20	19.1	955	20.6	–	–	199–1051
B50	48.0	960	20.8	1.95–2.18	2.31–4.37	199–1054
B100	96.3	963	20.9	–	–	200–1005

[a]Supplier data, [b]Measured from high-speed images, [c]Measured using confocal chromatic sensor

The normalized wall-film thickness δ varied between 0.1 and 0.5, which corresponds to a *thin* wall-film case. At a given δ and liquid combinations, the impact velocity is progressively increased till crown-type splashing is reached. Thus, the experimental database contains both deposition and splashing outcomes.

2 Classical Geometrical Parameters of Crown Rim and Associated Problems

There have been numerous experimental investigations [6, 7, 9–12, 16–19, 21, 24, 25, 27, 30] on the macroscopic crown properties such as crown rim height H_R and crown rim radius R_R. These two parameters, which are the first intuitive geometrical parameters related to the crown rim are very often studied separately in literature [18, 30]. Surprisingly, contradictory conclusions regarding the effect of impact conditions (e.g. wall-film thickness, droplet impact velocity, etc.) on both parameters taken independently can be found in the literature. While some studies [6] report a major dependency of Weber number (We) and Reynold number (Re) on the crown height H_R, others [7, 24, 25] found a significant increase of H_R with δ, or different trends depending on its values [12, 19] i.e. strong increase for small δ (smaller than 0.25) and diminuing influence at high wall-film thicknesses. For the rim radius R_R, most of the literature follows a theoretical square-root dependency of the form ${}^{R_R}/_{D_d} = C\,(\tau - \tau_0)^n$ [30], with $n = {}^1/_2$, and $\tau = {}^{tV_d}/_{D_d}$ the normalized inertial time and τ_0 its initial value at the moment of impact. Most of the discussion in literature focuses on the sensitivity of the parameter C to the impact parameters, again with contradictory conclusions. While some works [9] found a strong influence of the surface tension (and with it the Weber number), many studies [6, 10, 16, 17, 21, 27, 30], report only a weak dependence of Weber and Reynolds numbers with the parameter C being mostly driven by the wall-film thickness δ despite different conclusions on its influence. Further, a recent study [11] showed that the square-root dependency is only valid at the early stage of impact, other effects such as rim contraction and

crown inclination playing a significant role in the later times. All these contradictory conclusions suggest that considering separately H_R and R_R may not be suitable to study crown rim kinematics during expansion in a unified manner. Indeed, the relation between H_R and R_R is dependent on the impact parameters, their temporal behaviour (see Sect. 2.1) as well as in their magnitude (see Sect. 2.2). Thus, it is not possible to capture an overall picture of rim expansion process by considering separately H_R and R_R.

2.1 Radial and Axial Expansions of Crown Rim

Two typical temporal evolutions of crown rim radius R_R and height H_R are shown in Fig. 2 with red triangles and blue circles, respectively. The corresponding maxima of each geometrical parameter are highlighted with white circles. These maximum values are used to define the magnitude and duration of the corresponding expansions. In Fig. 2a, both maxima occur simultaneously which makes the definition of a rim expansion phase possible, corresponding to the time until the maxima are reached highlighted by a vertical dashed line. To the contrary in Fig. 2b, R_R and H_R have maxima at different times; R_R keeps increasing slowly while H_R recedes. A recent

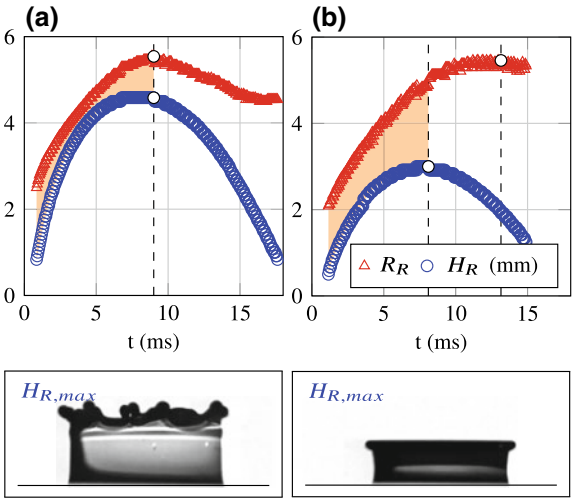

Fig. 2 Typical temporal evolutions of the classical geometrical parameter of crown rim, height H_R and radius R_R. The maxima corresponding to the end of radial (R_R) and axial (H_R) rim expansions are marked by white circles. The relative difference between them is highlighted with an orange shaded area. The corresponding difference in morphologies are shown with high-speed images corresponding to the time at which $H_{R,\max}$ is reached. Impact conditions: **a** B10 droplet on B5 wall-film (see Table 1), D_d = 2.03 mm, V_d = 2.99 m/s, δ = 0.298; **b** B10 droplet impacting on B3 wall-film (see Table 1), D_d = 2.05 mm, V_d = 2.15m/s, δ = 0.294

study investigating the scaling of crown rim radius [4] has shown that in these cases, the maximum value of R_R is not representative of the expansion phase. This continuous increase of R_R during the entire impact process is not an exception. The duration of the radial expansion (R_R) is, in most of the cases, longer than the axial expansion (H_R): in 70% of the experiments in our silicone oil database, the expansion duration of crown radius is 10% longer than that of crown height, and in averaged 33% longer for the entire database. In these cases where the radial and axial expansion durations are different, a unified definition of the crown rim expansion can not be provided in terms of either R_R of H_R.

2.2 Crown Aspect Ratio Dependent on Impact Parameters

The relative importance of H_R to R_R is significant in terms of momentum transfer to the rim in the radial and axial directions. Considering a single geometrical parameter (H_R or R_R) to describe rim kinematics and link it to the impact conditions is reliable only if they vary the same way with the impact parameters. In other words if the momentum repartition between axial and radial directions remains the same, regardless of the impact conditions. In Fig. 2, this relative importance is qualitatively highlighted with an orange shaded area up to $H_{R,\max}$. In Fig. 2a, only small differences between H_R and R_R can be observed, the temporal evolution of H_R and R_R are of similar magnitude, i.e. the momentum transferred to the rim is split quite equally in axial and radial directions. To the contrary in Fig. 2b, H_R is much smaller than R_R, the expansion is less pronounced in the axial direction than in the radial one. The high-speed images in Fig. 2 show how the crown is smaller for case (b) than in case (a), despite similar values of crown radius. These differences between R_R and H_R can be quantified by considering the crown aspect ratio $H_R/R_R(\%)$. Since this ratio varies over time as can be seen qualitatively in Fig. 2 from the orange shaded area, the aspect ratio is averaged over time during crown expansion as defined in Sect. 3 (i.e. based on crown rim displacement S_R). With this, an aspect ratio of 100% would mean that the crown height is as big as the crown rim radius in average during expansion. The corresponding value of aspect ratios for the cases presented in Fig. 2 are 81% in case (a) and 59% in case (b). The aspect ratios for the entire experimental database are plotted in Fig. 3 (each symbol corresponds to one experiment) in function of a modified impact parameter:

$$\kappa_{f,avg} = \mathrm{Re}_{avg}{}^{0.25}\mathrm{We}_{avg}{}^{0.5} = \frac{h_f{}^{0.75} V_d{}^{1.25} \left(\rho_d + \rho_f\right)^{0.75}}{2^{0.25} \left(\sigma_d + \sigma_f\right)^{0.5} \left(\mu_d \mu_f\right)^{0.125}} \tag{1}$$

The modified impact parameter $\kappa_{f,avg}$ represents the overall droplet/wall-film system by considering impact parameters such as the film-thickness h_f and droplet impact velocity V_d, and taking into account both droplet and wall-film liquid properties (density ρ, surface tension σ and dynamic viscosity μ). It is derived from a classical

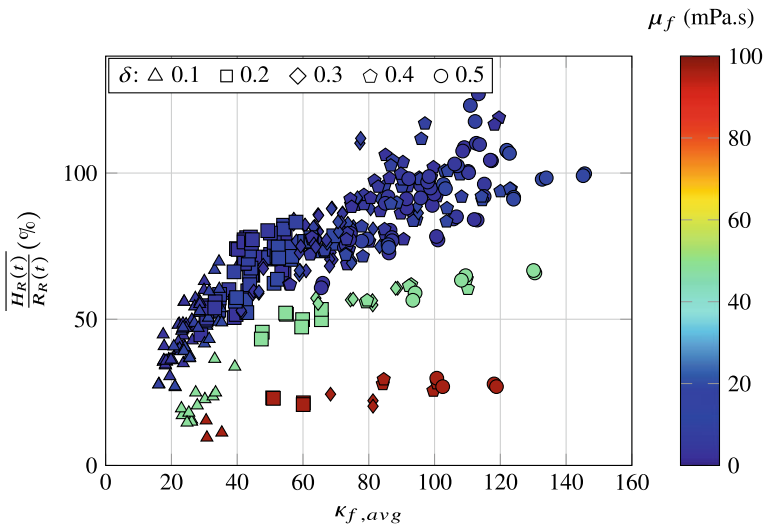

Fig. 3 Crown aspect ratio $\overline{H_R(t)/R_R(t)}$ averaged over time during rim expansion as a function of the impact parameter $\kappa_{f,avg}$ (Eq. 1). The crown aspect ratio gives an indication of the relative importance of momentum/energy transfer in radial and axial directions. Each symbol corresponds to a given dimensionless wall-film thickness δ

definition of the impact parameter $\kappa = \mathrm{Re}^{0.25}\mathrm{We}^{0.5}$ [20], which is widely used in the literature in this form or a similar one (see the review article of Liang and Mudawar [18]). However, the liquid properties used here in the classical Reynolds and Weber numbers are averaged between droplet and wall-film, and the length scale used is the wall-film thickness h_f and not the droplet diameter, i.e. $\mathrm{Re}_{avg} = {\rho_{avg} V_d h_f}/{\mu_{avg}}$ and $\mathrm{We}_{avg} = {\rho_{avg} {V_d}^2 h_f}/{\sigma_{avg}}$. The necessity of averaging droplet and wall-film properties has been already shown for binary droplet/wall-film [3]. However, the type of averaging to be used remains a challenging question. Based on previous attempts [3, 12, 14] and our observations from our silicone oil database, the averaged liquid properties between droplet and wall-film (subscript *avg*) are calculated as follows: $\rho_{avg} = {(\rho_d+\rho_f)}/{2}$, $\sigma_{avg} = {(\sigma_d+\sigma_f)}/{2}$, and $\mu_{avg} = \sqrt{\mu_d \mu_f}$.

In Fig. 3, the averaged aspect ratio is increasing with increasing $\kappa_{f,avg}$, but at different values depending on the wall-film viscosity. Here, it is interesting to note that the aspect ratio varies over a very large range, from around 10% for small $\kappa_{f,avg}$ and high wall-film viscosities to almost 140% for high $\kappa_{f,avg}$ and small wall-film viscosities. This large range of variations of the relative importance of H_R to R_R suggests that considering only H_R or R_R leads to an incomplete picture in terms of momentum repartition, necessary to understand rim kinematics during expansion.

3 Relevance of the Crown Rim Displacement from the Impact Point

In order to provide a more unified approach for all crown morphologies (i.e. for different aspect ratios), a geometrical parameter more suited to track the rim motion during expansion is necessary. The crown rim displacement from the impact point $S_R = \sqrt{{R_R}^2 + {H_R}^2}$ seems to be a good candidate since it combines both rim radius and height. The corresponding temporal variation of the rim displacement S_R is shown in Fig. 4 in green for the two cases already presented in Fig. 2. From these two examples, it is possible to see the advantages of considering S_R as described in Sects. 3.1 and 3.2.

3.1 Length Scale of Crown Rim Expansion

From the temporal evolution of S_R in the two cases of Fig. 4, a single peak during the impact process (marked with a white circle) can systematically be observed. Hence, this single peak enables the definition of the expansion phase of the rim corresponding to the phase before the receding of S_R. This defines a unique expansion duration

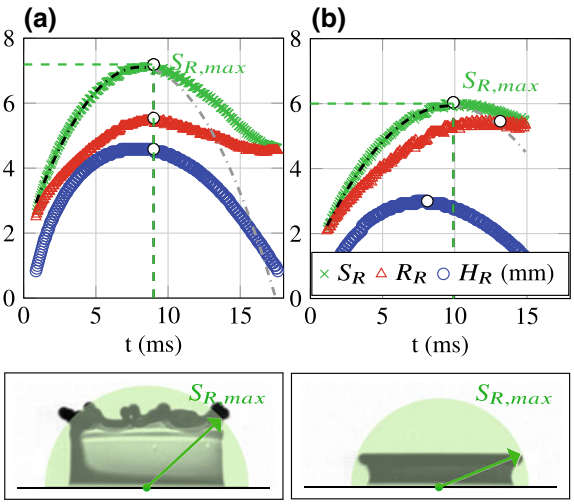

Fig. 4 Typical temporal evolution of the parameters crown rim height H_R and radius R_R, as well as the crown rim displacement S_R for the two cases presented in Fig. 2. The maxima of each geometrical parameters are marked with white circles. The end of the expansion phase, defined with the maximum value of crown rim displacement $S_{R,\max}$ is highlighted with a vertical dashed line. The high-speed images corresponding to the end of the expansion phase are given with a semicircle of radius $S_{R,\max}$ embedding the entire rim motion

and a unique expansion magnitude $S_{R,\max}$ (marked by vertical and horizontal green dashed lines in Fig. 4, respectively). The maximum rim expansion $S_{R,\max}$ can be seen as the radius of a hemispherical surface (represented in the high-speed images of Fig. 4 with green shaded area) embedding the entire rim motion. Thus, $S_{R,\max}$ is a good candidate as typical length scale of the expansion process valid for all crown morphologies. Furthermore, the rim motion during expansion mostly occurs along the rim displacement vector itself, the azimuthal angle of the rim displacement playing only a minor role in this phase. S_R alone gives then a more reliable picture of the rim expansion process than H_R or R_R alone. Focusing on the distancing from the impact point with S_R, a representative picture of the crown rim expansion kinematic can be achieved.

3.2 Quadratic Distancing from the Impact Point

Another interesting feature of S_R is that the temporal evolution during expansion could be fitted by a second degree polynomial. The resulting parabolic curve is shown in Fig. 4 for the two examples presented in Fig. 2. The choice of a parabolic curve comes from the existing theoretical models in literature [10, 23, 24] for which the equation of crown motion indicates a maximum possible degree of 2 in time for crown length scales. These parabolic fits revealed very good coefficients of determination R^2 for our entire experimental database with an average of 0.994. Hence, considering S_R enabled us to observe a quadratic distancing of the rim from the impact point with time. This is particularly interesting since it corresponds to a constant deceleration process, often assumed in the literature for such droplet impact phenomena as recently in a study on unsteady sheet fragmentation [28]. Considering S_R during the impact process shows that the assumption of a constant deceleration process can be reasonably used for droplet impact on wall-films. Furthermore, S_R, combining the radial and axial expansion, opens the possibility of a universal treatment of droplet impact kinematics on dry and wetted surfaces. The kinematic parameter, such as averaged velocity and acceleration, can be directly extracted from the fit coefficients. The plot of all constant decelerations is given in Fig. 5 as function of the impact parameter $\kappa_{f,avg}$ (defined in Sect. 2). The error of the acceleration measurements from the quadratic fits (confidence bounds of 95%) is of 7.5% in average for the entire database with a standard deviation of 6.0%. The wall-film thickness δ seen as the most influencing parameter is represented with different symbols in Fig. 5. All constant decelerations collapse in a single universal trend with $\kappa_{f,avg}$ since it gives a overall representation of the droplet/wall-film system. It is worth noting here that no particular separation in the trend between deposition and splashing outcomes can be observed when using an inertial non-dimensionalisation of the rim deceleration. This universal trend can now be very useful to input rim deceleration into the corresponding instability models (presented in Sect. 1) for a large range of impact conditions, and thus get a deeper insight into the underlying physical processes leading to splashing.

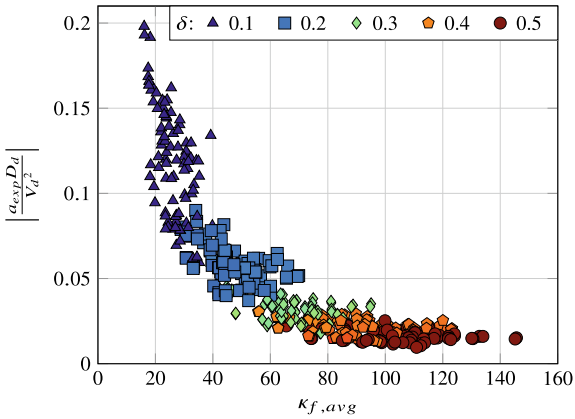

Fig. 5 Universal trend of non-dimensionalised deceleration of crown rim expansion in function of the modified impact factor $\kappa_{f,avg}$ (Eq. 1) representative of the droplet/wall-film system

4 Conclusion

This article focuses on the phenomena of droplet impact on wall-films. The morphological features and the temporal evolution of the liquid structures formed during the impact process have been presented: the crown rim can destabilise into fingers and then into secondary droplets, leading to 'splashing'. Looking into the crown rim kinematics in the expansion phase will help getting a better understanding of the underlying instability mechanisms. Thus, this study analyses which geometrical parameter is physically the most suited to get meaningful information on crown rim kinematics. A large experimental database of binary droplet/wall-film systems of different silicone oils (viscosities between 2.70–96.3 mPa s) is used. The wall-film thicknesses are varied between 0.1 and 0.5 times the droplet diameter. The difficulties to describe the crown expansion process with the classical geometrical parameters rim radius R_R and height H_R (often considered separately) are presented. First, radial and axial rim expansions have different durations, the radial expansion being more prolonged compared to the axial one of about 30% in average for our database. These different durations prevent the definition of the rim expansion phase in a unified way. Second, considering separately H_R and R_R leads to an incomplete picture of the impact process in terms of momentum transfer to the rim since the crown aspect ratio H_R/R_R varies strongly with the impact conditions (from 10 to almost 140% in averaged during expansion). This complex interdependency of H_R and R_R may explain the different—sometimes contradictory—conclusions on their sensitivity to impact conditions in literature. Thus, the crown rim displacement S_R is used instead of H_R or R_R. The temporal evolution of S_R systematically exhibits a single peak. Hence, a clear definition of the crown rim expansion (duration and magnitude) is possible for all crown morphologies. The maximum displacement $S_{R,\max}$ embeds the entire rim motion and, thus, can be seen as a typical length scale of expansion. Furthermore, the temporal evolution of the rim displacement during expansion could systematically be fitted by a quadratic curve with high accuracy. As often assumed in literature,

this corroborates a constant deceleration process of rim expansion for droplet impact on wall-film. All non-dimensionalised constant decelerations could be merged into a single universal trend with a modified impact parameter. Hence, the crown rim displacement S_R seems to be the correct length scale for describing the rim expansion. Thus, it provides a unified approach for all crown morphologies and offers the possibility of extracting the kinematic parameters and makes it a suited parameter to describe crown rim kinematics.

Acknowledgements The authors gratefully acknowledge the financial support of the Deutsche Forschungsgemeinschaft (DFG) within the frame of the international research training group "Droplet Interaction Technologies"—DROPIT (GRK2160/1).

References

1. Agbaglah, G., Josserand, C., Zaleski, S.: Longitudinal instability of a liquid rim. Phys. Fluids **25**(2), 022103 (2013)
2. Banks, D., Ajawara, C., Sanchez, R., Surti, H., Aguilar, G.: Effects of drop and film viscosity on drop impacts onto thin films. Atom. Sprays **23**(6), 525–540 (2013). https://doi.org/10.1615/AtomizSpr.2013007494
3. Bernard, R., Foltyn, P., Geppert, A., Lamanna, G., Weigand, B.: Generalized analysis of the deposition/splashing limit for one- and two-component droplet impacts upon thin films. ILASS-Europe (2017). https://doi.org/10.4995/ILASS2017.2017.4810
4. Bernard, R., Geppert, A., Vaikuntanathan, V., Lamanna, G., Weigand, B.: On the scaling of crown rim diameter during droplet impact on thin wall-films. In: ICLASS 2018 (2018)
5. Bremond, N., Villermaux, E.: Atomization by jet impact. J. Fluid Mech. **549**, 273–306 (2006)
6. Cossali, G., Marengo, M., Coghe, A., Zhdanov, S.: The role of time in single drop splash on thin film. Exp. Fluids **36**(6), 888–900 (2004)
7. Davidson, M.R.: Spreading of an inviscid drop impacting on a liquid film. Chem. Eng. Sci. **57**(17), 3639–3647 (2002)
8. Deegan, R., Brunet, P., Eggers, J.: Complexities of splashing. Nonlinearity **21**(1), C1 (2007)
9. Fujimoto, H., Ogino, T., Takuda, H., Hatta, N.: Collision of a droplet with a hemispherical static droplet on a solid. Int. J. Multiph. Flow **27**(7), 1227–1245 (2001)
10. Gao, X., Li, R.: Impact of a single drop on a flowing liquid film. Phys. Rev. E **92**, 053005 (2015). https://doi.org/10.1103/PhysRevE.92.053005
11. Geppert, A., Chatzianagnostou, D., Mesiter, C., Gomaa, H., Lamanna, G., Weigand, B.: Classification of impact morphology and splashing/deposition limit for n-hexadecane. Atom. Sprays **26**, 983–1007 (2016). https://doi.org/10.1615/AtomizSpr.2015013352
12. Geppert, A., Terzis, A., Lamanna, G., Marengo, M., Weigand, B.: A benchmark study for the crown-type splashing dynamics of one and two-component droplet wall-film interactions. Exp. Fluids **58**, 172(1–27) (2017). https://doi.org/10.1007/s00348-017-2447-2
13. Gueyffier, D., Zaleski, S.: Formation de digitations lors de l'impact d'une goutte sur un film liquide. Comptes Rendus de l'Académie des Sciences-Series IIB-Mechanics-Physics-Astronomy **326**(12), 839–844 (1998)
14. Kittel, H.M., Roisman, I.V., Tropea, C.: Splash of a drop impacting onto a solid substrate wetted by a thin film of another liquid. Phys. Rev. Fluids **3**, 073601(1–17) (2018). https://doi.org/10.1103/PhysRevFluids.3.073601
15. Krechetnikov, R., Homsy, G.M.: Crown-forming instability phenomena in the drop splash problem. J. Colloid Interface Sci. **331**, 555–559 (2009). https://doi.org/10.1016/j.jcis.2008.11.079

16. Lee, S.H., Hur, N., Kang, S.: A numerical analysis of drop impact on liquid film by using a level set method. J. Mech. Sci. Technol. **25**(10), 2567 (2011)
17. Liang, G., Guo, Y., Shen, S., Yang, Y.: Crown behavior and bubble entrainment during a drop impact on a liquid film. Theor. Comput. Fluid Dyn. **28**(2), 159–170 (2014)
18. Liang, G., Mudawar, I.: Review of mass and momentum interactions during drop impact on a liquid film. Int. J. Heat Mass Transf. **101**, 577–599 (2016). https://doi.org/10.1016/j.ijheatmasstransfer.2016.05.062
19. Mukherjee, S., Abraham, J.: Crown behavior in drop impact on wet walls. Phys. Fluids **19**(5), 052103 (2007)
20. Mundo, C., Sommerfeld, M., Tropea, C.: Droplet-wall collisions: experimental studies of the deformation and breakup process. Int. J. Multiph. Flow **21**(2), 151–173 (1995)
21. Rieber, M., Frohn, A.: A numerical study on the mechanism of splashing. Int. J. Heat Fluid Flow **20**, 455–461 (1999). https://doi.org/10.1016/S0142-727X(99)00033-8
22. Roisman, I.V.: On the instability of a free viscous rim. J. Fluid Mech. **661**, 206–228 (2010)
23. Roisman, I.V., van Hinsberg, N.P., Tropea, C.: Propagation of a kinematic instability in a liquid layer: capillary and gravity effects. Phys. Rev. E **77**, 046305 (2008). https://doi.org/10.1103/PhysRevE.77.046305
24. Roisman, I.V., Tropea, C.: Impact of a drop onto a wetted wall: description of crown formation and propagation. J. Fluid Mech. **472**, 373–397 (2002). https://doi.org/10.1017/S0022112002002434
25. Šikalo, Š., Ganić, E.: Phenomena of droplet-surface interactions. Exp. Thermal Fluid Sci. **31**(2), 97–110 (2006)
26. Terzis, A., Kirsch, M., Vaikuntanathan, V., Geppert, A., Lamanna, G., Weigand, B.: Splashing characteristics of diesel exhaust fluid (adblue) droplets impacting on urea-water solution films. Exp. Thermal Fluid Sci. **102**, 152–162 (2019). https://doi.org/10.1016/j.expthermflusci.2018.11.002
27. Trujillo, M., Lee, C.: Modeling crown formation due to the splashing of a droplet. Phys. Fluids **13**(9), 2503–2516 (2001)
28. Wang, Y., Dandekar, R., Bustos, N., Poulain, S., Bourouiba, L.: Universal rim thickness in unsteady sheet fragmentation. Phys. Rev. Lett. **120**, 204503(1–6) (2018). https://doi.org/10.1103/PhysRevLett.120.204503
29. Worthington, A.M., Cole, R.S.: Impact with a liquid surface, studied by the aid of instantaneous photography. Philosoph. Trans. R. Soc. Lond. Ser. A **189**, 137–148 (1897)
30. Yarin, A.L., Weiss, D.A.: Impact of drops on solid surfaces: self-similar capillary waves, and splashing as a new type of kinematic discontinuity. J. Fluid Mech. **283**, 141–173 (1995). https://doi.org/10.1017/S0022112095002266
31. Yoon, S.S., Jepsen, R.A., James, S.C., Liu, J., Aguilar, G.: Are drop-impact phenomena described by Rayleigh-Taylor or Kelvin-Helmholtz theory? Drying Technol. **27**, 316–321 (2009). https://doi.org/10.1080/07373930802682858
32. Zhang, L.V., Brunet, P., Eggers, J., Deegan, R.D.: Wavelength selection in the crown splash. Phys. Fluids **22**, 122105(1–9) (2010). https://doi.org/10.1063/1.3526743

Analytical Model for Crown Spreading During Drop Impact onto Wetted Walls: Effect of Liquids Viscosity on Momentum Transfer

Anne Geppert, Ronan Bernard, Bernhard Weigand and Grazia Lamanna

Abstract Drop impact onto wetted surfaces is of relevance to any spray coating application since the maximum spreading diameter and the residual film thickness of the applied liquid droplets affect the efficient distribution of the coating materials. In this paper, we propose a modification to existing models for crown propagation during single drop impact onto a wall-film based on the stagnation-point flow solution of Hiemenz. This offers two main advantages: a simple estimation of the film thickness decay rate, induced by the impulse transfer from impacting droplet to resting wall-film. Besides, the self-similarity of Hiemenz's solution allows a straightforward estimation of the momentum losses during radial liquid spreading along the wall. The incorporation of these estimations into existing inviscid models provides an excellent agreement with experiments over the entire crown elevation phase. Additionally, the effect of fluid viscosity and initial film thickness on the momentum transfer from droplet to wall-film is highlighted.

1 Introduction

Drop impact onto wetted walls is of relevance to many industrial applications as well as to natural science, such as soil erosion, pesticide spraying, icing on plane wings and spray coating applications, e.g. in robotic car painting or food processing. For spray coating applications, both the maximum spreading diameter and the residual thickness of the applied liquid films are of paramount importance for the efficient and uniform distribution of the coating material. Reducing the coating procedure to the basic phenomenon of a single droplet impacting onto a wetted surface, the impact process proceeds as follows: immediately after the impact the droplet diameter expands radially along the surface and may generate an upward growing crown,

A. Geppert (✉) · R. Bernard · B. Weigand · G. Lamanna
Institute of Aerospace Thermodynamics (ITLR), University of Stuttgart, Stuttgart, Germany
e-mail: anne.geppert@itlr.uni-stuttgart.de

G. Lamanna
e-mail: grazia.lamanna@itlr.uni-stuttgart.de

G. Lamanna et al. (eds.), *Droplet Interactions and Spray Processes*,
Fluid Mechanics and Its Applications 121,
https://doi.org/10.1007/978-3-030-33338-6_14

provided the impact kinetic energy is sufficiently high to overcome energy losses due to deformation and viscous effects (splashing regime). A detailed characterization of the impact outcomes and the splashing/deposition limit can be found in [8, 9, 19, 29]. For the onset of the splashing regime the non-dimensional parameter K represents the widely accepted choice. It can be expressed as a function of Weber ($We = \rho U_0^2 D_0/\sigma$) and Reynolds ($Re = U_0 D_0/\nu$) numbers as $K = We^{0.5} Re^{0.25}$. Here U_0 and D_0 are the impacting droplets velocity and diameter, and ν, ρ, and σ are the liquids kinematic viscosity, density, and surface tension, respectively. Several empirical correlations that express the threshold parameter K in terms of the non-dimensional film thickness $\delta = h/D_0$ are published [2, 6, 7, 14, 21, 26, 28, 30].

From a theoretical point of view, it is generally accepted to model the crown as a kinematic discontinuity, thereby neglecting any influence of viscous losses. This assumption dates back to the pioneering work of Yarin and Weiss [30], who proposed a square-root dependence for the crown base radius R_B upon the non-dimensional time $\tau = tU_0/D_0$: $R_B = C\sqrt{(\tau - \tau_0)}$. Here the value τ_0 corresponds to the initial value at the moment of impact. The non-dimensional constant C was determined empirically by fitting the experiments of Levin and Hobbs [17], according to $C = [2/(3\delta)]^{1/4}$. Thus, this modelling approach assumes a constant crown propagation speed equal to U_0. Several authors slightly modified the empirical parameter C of the square-root dependence to improve the agreement to their experimental results [1, 3–6, 10, 13, 18, 22, 23, 27, 30]. The dependence of the parameter C on the Weber and Reynolds numbers is a controversial issue. According to Refs. [1, 13, 18, 23], the crown radius is independent of both Weber and Reynolds number, while Fujimoto et al. [5] showed that surface tension indeed plays an important role on the evolution of the crown's radius. Gao and Li [6] recently clarified this controversy by introducing a correction factor $\lambda = u_\infty/U_0$ in the parameter $C = (2\lambda^2/3\delta)^{1/4}$. This factor takes into account momentum losses at the moment of drop impact due to deformation, viscous and inertial forces. The importance of energy losses during drop impact is corroborated by numerical simulations of Davidson [4], who showed that surface energy losses during drop impact can amount up to 10% of the total impact kinetic energy. Gao and Li [6] derived an empirical correlation for the energy loss factor from their experiments, which reads $\lambda = 0.26 Re^{0.05}/(We^{0.07}\delta^{0.34})$. The correlation shows that the dominating effect is provided by film inertia ($\delta^{0.34}$), while We and Re play only subordinate roles. Thus, the Gao-Li model still employs a constant crown propagation speed $u_\infty = \lambda U_0$, but it is significantly reduced due to the inclusion of energy losses compared to the crown propagation speed of the Yarin-Weiss model (U_0). Summarizing, classical inviscid modelling approaches assume the parameter C to be constant in time and mainly dependent upon the dimensionless film thickness δ. Furthermore, these models where validated with experimental data only up to $\tau \approx 3$.

A comparison over the entire duration of the impact process between experimental data for silicon oil B3 ($\nu = 3\,\mathrm{mm^2\,s^{-1}}$) and inviscid models [6, 30] is shown in Fig. 1. Except for the initial phase ($\tau \approx 3$) both inviscid models overestimate the spreading rate of the crown base radius and exhibit a reverse δ-dependence with respect to the experiments. The inviscid model's prediction of a slower spreading rate results from the increase in film inertia due to an increased initial film thickness

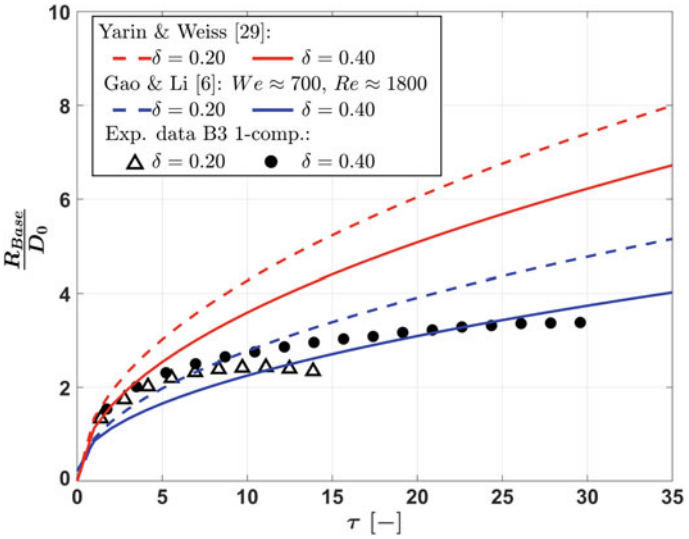

Fig. 1 Temporal evolution of the crown base radius: comparison between experiments and two inviscid models. Fluids: silicon oil B3 ($\nu = 3\,\mathrm{mm^2\,s^{-1}}$) for both droplet and wall film

δ. In the experiments, the opposite trend is observed. The decrease in film inertia is counterbalanced by the increased importance of viscous losses due to boundary layer effects. Boundary layer effects in general have been studied by several authors [20, 24, 27]. Marcotte et al. [20] demonstrated that the crown spreading consists of two distinct sheets, originating from the droplet and film, respectively. The sheets evolve on separate time scales and their merging time is mainly depending upon the viscosity ratio. Roisman [24] solved analytically the axisymmetric instationary viscous flow in a spreading film, generated by normal drop impact onto a rigid, planar, dry surface. He also provided an expression for the height of the residual film thickness. The existence of a residual film thickness has been confirmed experimentally by Kuhlmann et al. [15]. The authors measured the cavity film thickness for single droplet impact onto wetted walls in a range of $140 < We < 1000$ and $0.2 < \delta < 1.0$. They demonstrated the existence of a constant thickness region (sub-cavity) within the crown base area. Despite the noteworthy progress, none of the above studies led to the formulation of a model for the crown spreading rate that encompasses boundary layer effects.

These findings motivate the present work, where an alternative modelling approach for the temporal evolution of the crown base radius R_B is proposed, which explicitly incorporates momentum losses. It follows that the parameter C is no longer constant, but rather decreases in time with the decrease in the crown propagation speed induced by viscous losses. This requires an accurate estimation of the strain rate in the boundary layer, which not only depends on the fluid viscosity, but also on

the thinning rate of the initial wall-film [16]. The smooth transition from the inertia-driven to the viscous-controlled regime of crown propagation enables the accurate prediction of the crown base spreading rate over the entire crown elevation phase.

2 Modelling Approach

Our modelling strategy is based on the geometrical resemblance of the drop impact problem with the two-dimensional, orthogonal stagnation-point flow (SPF), as shown in Fig. 2a. This strategy offers two main advantages: simple estimation of the film height decay rate and a straightforward estimation of the momentum losses in the boundary layer because of the self-similarity of Hiemenz's solution for a plane stagnation point flow (SPF) [25]. This modelling approach divides the drop impact onto a wetted surface into two sub-processes [16], which are shown in Fig. 2. The first sub-process describes the momentum transfer during the drop's collision with the wall-film (phase a), which induces a decrease in wall-film thickness $h(t)$ with

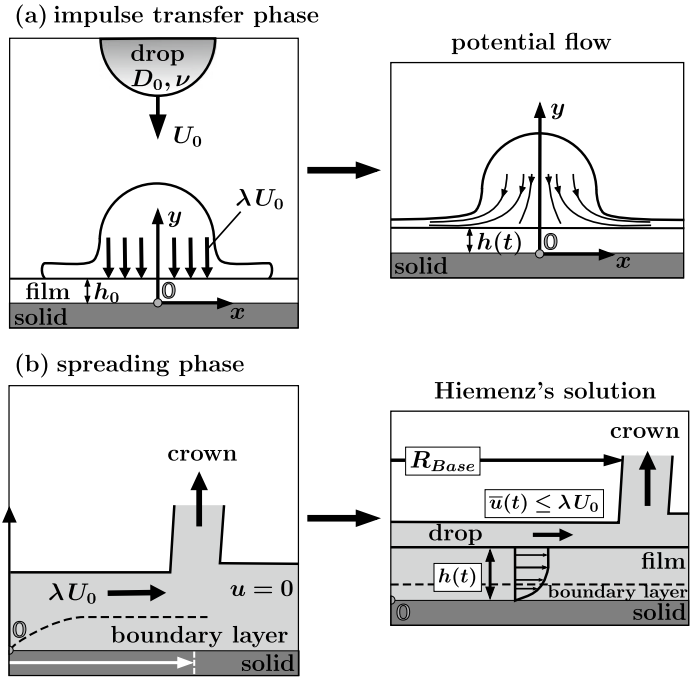

Fig. 2 Scheme of stagnation point flow (SPF) based modelling approach. Phase (**a**): impulse transfer from impacting drop to wall-film. Decay in film height modelled with potential theory. Phase (**b**): radial spreading along the surface with decreasing averaged velocity $\bar{u}(t)$, including momentum losses calculated by Hiemenz's solution

time. The impulse transfer, phase a, is modelled based on the assumption that, at the moment of impact and within a region close to the impact point, the flow inside the droplet resembles the potential flow of the stagnation point problem. The spreading phase b is modelled by assuming that droplet and wall-film liquids merge perfectly and start spreading radially outwards with an average velocity $\bar{u}(t)$. In contrast to inviscid models, this modification assumes a progressively decreasing speed of crown base propagation in time due to boundary layer effects.

2.1 Description of the Film Thickness Decay Rate

For the modelling of the film thickness decay rate we assume that the flow distribution within the impacting droplet is a frictionless potential flow. Additionally, sliding effects at the interface between droplet and liquid film are considered negligible. The x- and y-velocity components of the potential flow are expressed as $u_x = ax$ and $u_y = -ay$, where a is the strength of the potential flow. In the framework of the droplet impact problem, the constant a represents the momentum per unit length transmitted by the droplet to the wall-film at the moment of impact. Its value depends on the initial conditions of the impact process as $a = (\lambda U_0)/D_0$. The assumption of potential flow within the droplet is strictly valid only for an inviscid fluid. For viscous fluids it is necessary to include the effects of the boundary layer flow on the external potential flow. Hence, the concept of displacement thickness δ^* is introduced. It describes the displacement of the wall for an inviscid flow, in order to have the same mass transport as the viscous flow along the original wall [16]. Thus, the vertical velocity component of the external flow must be corrected for a viscous flow by δ^* [11, 12], yielding $u_y = -a(y - \delta^*)$. The displacement thickness for a plane stagnation-point flow is defined as $\delta^* = 0.6479\sqrt{\nu/a}$ in [11].

The decay rate of the wall-film thickness is expressed by $h(t) = h_0 - a(y - \delta^*)t$, where h_0 is the initial wall-film thickness. Being $h(t) = y$ at each time instant, the film thickness decay rate reads

$$h(t) = \frac{h_0 + 0.6479\sqrt{\nu a}\, t}{1 + at}. \tag{1}$$

Figure 3 depicts the film thickness decay rate for two selected experiments from Table I (see Sect. 3.2). The dashed lines represent the thickness of the flow boundary layer according to $h_{BL} = 2.4\sqrt{\nu/a}$ [25]. The intersection point between solid and dashed lines (same colour) marks the validity limit of the inviscid flow solution. As can be seen, for the B3-case (red) the inviscid solution is valid till $t \approx 3.2$ ms, which corresponds to $\tau \approx 4.5$, the time where the Gao-Li model starts deviating from the experimental data (see Fig. 1). For the B50-case applying the inviscid solution is not valid at all, since the initial wall-film thickness is already smaller than the boundary layer height, i.e. there is no intersection point between green solid and dashed lines in Fig. 3. Furthermore, an increase in liquid viscosity leads to a less steep curve

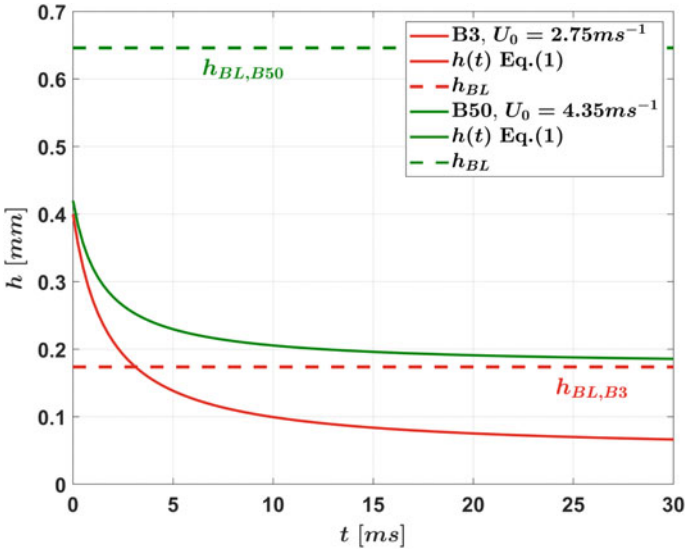

Fig. 3 Film thickness decay rate compared to boundary layer height [25] for silicon oils B3 ($\nu = 3\,\mathrm{mm^2\,s^{-1}}$) and B50 ($\nu = \mathrm{mm^2\,s^{-1}}$) at $\delta = 0.2$

progression of the film thickness decay rate. The increased viscous losses within the droplet itself reduce the momentum transfer to the wall-film and therefore inhibit the decay in wall-film thickness.

2.2 Momentum Loss Estimation

For the estimation of the momentum losses we will assume the following: before the wall-film thickness reaches the boundary layer height, the crown propagates at a constant average speed of $\bar{u}(t) = \lambda U_0$. Afterwards friction losses decrease the crown's propagation speed. Therefore, it is sufficient to determine the velocity profile within the boundary layer of a stagnation-point flow (SPF) to estimate the momentum losses. Following the methodology laid out by Hiemenz [25], the subsequent self-similar transformation leads to a reduction of the Navier-Stokes equations into an ordinary differential equation:

$$\eta = \sqrt{\frac{a}{\nu}}y, \qquad f(\eta) = \frac{\psi}{x\sqrt{\nu a}} \tag{2}$$

where ψ is the stream function. In the stagnation point region, the velocity components can be then expressed as $u_x = u_\infty(x) f'(\eta) = axf'(\eta)$ and $u_y = -\sqrt{\nu a}\, f(\eta)$. The transformed ordinary differential equation reads then as follows

$$f''' + ff'' + 1 - f'^2 = 0, \tag{3}$$

and is subject to the boundary conditions of no-slip and inviscid flow limit:

$$\eta = 0: \quad f = 0, \quad f' = 0; \qquad \eta \to \infty: \quad f' = 1. \tag{4}$$

Equation 3 is solved numerically with a shooting method to determine the non-dimensional velocity profiles $f'(\eta) = \bar{u}/u_\infty$. The momentum losses are then estimated by introducing a profile-averaged non-dimensional velocity according to:

$$\bar{f}' = \frac{1}{\eta_{\max}} \int_0^{\eta_{\max}} f' d\eta \tag{5}$$

where $\eta_{\max}$ coincides with the scaled height of the wall film, i.e. $\eta_{\max} = \sqrt{a/\nu}\, h(t)$. Since both functions $f'(\eta)$ and $f(\eta)$ cross the origin, the integration of Eq. (5) yields no integration constant [16, 25]. Hence, the non-dimensional profile-averaged velocity can be expressed as

$$\bar{f}' = \frac{\bar{u}}{u_\infty} = \frac{1}{\eta_{\max}} f(\eta_{\max}). \tag{6}$$

Even though the self-similar solution $f(\eta)$ itself does not change in time, the profile-averaged non-dimensional velocity $\bar{f}'$ will vary in time because $\eta_{\max}$ is a function of the time dependent film thickness $h(t)$.

The lamella's spreading velocity $\bar{u}(t)$ is estimated from the analytical solution. Therefore, the profile-averaged velocity $\bar{f}'$ needs to be transformed back to the physical coordinate system in agreement with

$$\frac{\bar{u}}{u_\infty} = \frac{1}{\sqrt{\frac{a}{\nu}} h(t)} f\left(\sqrt{\frac{a}{\nu}} h(t)\right). \tag{7}$$

The velocity outside the boundary layer, defined by potential theory, is herein denoted u_∞. It is assumed to be constant in the spreading phase (flow parallel to wall) and defined according to $u_\infty = \lambda U_0$, thus taking into account energy losses occurring during drop impact.

2.3 Implementation in Crown Base Evolution Model

This section describes the incorporation of the previously estimated time-dependent, average crown propagation speed $\bar{u}$ in the modelling approach of the crown base radius R_B. As introduced by Gao and Li [6], the crown speed is scaled with respect to the initial droplet impact velocity U_0. Hence, a modified correction factor λ_{AG} is proposed according to

$$\lambda_{AG} = \frac{\bar{u}}{U_0} = \frac{\lambda}{\sqrt{\frac{a}{\nu}}h(t)} f\left(\sqrt{\frac{a}{\nu}}h(t)\right). \tag{8}$$

Finally, the evolution of the crown's base radius is modelled as follows:

$$\frac{R_B}{D_0} = 0.5 + \left(\frac{2\lambda_{AG}^2}{3\delta}\right)^{1/4} \sqrt{\tau}. \tag{9}$$

There are three main difference between Eq. (9) and the Gao-Li model: the fundamental difference is the time-dependent factor λ_{AG}, which takes into account the decreasing spreading velocity of the lamella due to viscous losses. Second, the temporal offset parameter τ_0 is set to zero, since the moment of impact can be accurately determined in the present experiments. Third, the 0.5-shift results from the crown tracking in the experiments. It starts as soon as the droplet is no longer visible in the images, which occurs approximately when the crown radius equals the droplet radius.

3 Results and Discussion

The purpose of this section is two-fold: first, the effect of liquids viscosity and initial film thickness on the momentum transfer from the impacting droplet to the resting wall-film is discussed. Second, the effectiveness of the SPF-based modelling approach in reproducing the temporal evolution of the crown base radius R_B is demonstrated.

3.1 How Momentum Transfer is Affected by Fluids Viscosity and Initial Film Thickness

The effect of viscosity on the momentum transfer is apparent in three ways [16]: first of all, an increase in fluid viscosity leads to higher impact losses, which is captured by the empirical correlation of the energy loss factor $\lambda = 0.26Re^{0.05}/(We^{0.07}\delta^{0.34})$. Higher impact losses lead to a reduction of the available momentum that can be transferred to the wall-film, measured by λU_0. This causes the second effect of viscosity: if less momentum is transferred, the decay rate of the film thickness $h(t)$ is also reduced. This is shown in Fig. 3. As can be seen, the decay rate $h(t)$ of silicon oil B50 (green curve) is much slower compared to B3 (see also Eq. 1), even so the droplets impact velocity U_0 is much higher in the case of B50 (see legend of Fig. 3). Finally, the effect of viscosity on the lamella's spreading velocity $\bar{u}(t)$ is discussed. Therefore, Fig. 4 is consulted. For the low viscosity oil B3 (dashed red curve) lower impact losses result in a higher momentum transfer (higher starting value

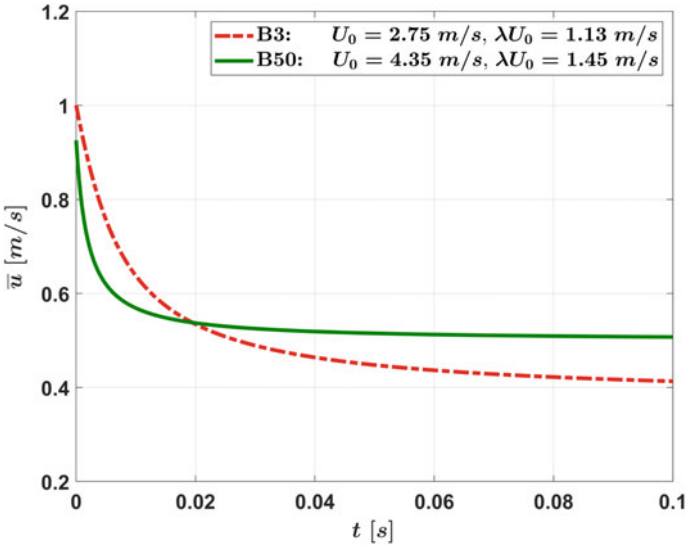

Fig. 4 Temporal evolution of the profile-averaged velocities for silicon oils B3 ($\nu = 3\,\mathrm{mm^2\,s^{-1}}$) and B50 ($\nu = 50\,\mathrm{mm^2\,s^{-1}}$) at $\delta = 0.2$

for $\bar{u}(t)$), but due to the higher spreading velocity also more momentum is dissipated. In contrast, for the high viscous oil B50 less momentum is available (higher impact losses), but also the momentum dissipation is lower because of the lower spreading velocity. Thus, towards the end of drop impact experiment (0.01–0.02 s) only small differences in the spreading velocity $\bar{u}(t)$ are observed in Fig. 4.

In addition, the wall film inertia, i.e. the initial film thickness δ, strongly influences the spreading velocity [16]. Recalling the definition of the constant $C(t) = (2\lambda_{AG}^2/3\delta)^{1/4}$, a reduced initial film thickness will result in lower inertial losses and therefore more momentum is transferred to the spreading lamella. This excess in momentum, however, is rapidly dissipated because viscous losses increase with decreasing film thickness δ. This corroborates the observation of only small differences in spreading velocity $\bar{u}(t)$ at the end of the drop impact process.

Regarding the evolution of the crown base radius R_B, the counterbalancing effects of inertial and viscous forces explain the similar curve progressions of the experimental data observed in Fig. 5. The SPF-model captures this interplay between viscous and inertial forces, which results in a very good prediction of the crown base radius evolution over the entire duration of the impact process.

Table 1 Listing of experimental parameters. All experimental details can be found in [9, 16]

Fluid	D_0	U_0	h_0	δ	λ	a	ρ	ν	σ
	mm	ms^{-1}	µm	–	–	s^{-1}	$kg\,m^{-3}$	$mm^2\,s^{-1}$	$mN\,m^{-1}$
B3	2.01	3.21	200	0.1	0.51	824	900	3.0	18.0
B3	1.98	2.75	400	0.2	0.41	572	900	3.0	18.0
B3	2.00	2.61	600	0.3	0.35	461	900	3.0	18.0
B3	1.98	2.73	800	0.4	0.32	447	900	3.0	18.0
B50	2.08	4.04	210	0.1	0.44	859	960	50.0	20.8
B50	2.11	4.35	420	0.2	0.33	690	960	50.0	20.8
B50	2.09	4.35	630	0.3	0.27	570	960	50.0	20.8

3.2 Effectiveness of SPF-Based Modelling Approach

The effectiveness of the SPF-based modelling approach is demonstrated in Fig. 5, where the temporal evolution of the crown base radius R_B obtained by experimental investigation is compared to predictions of the inviscid Gao-Li model as well as the SPF-based model. As can be seen, for both fluids the SPF-model's prediction agrees very well with the experimental data over the entire duration of the splashing event. The SPF-model therefore provides a significant improvement in comparison with the inviscid model of Gao and Li [6]. Furthermore, this new approach correctly captures the complex interplay among impact, inertial and viscous loss without the introduction of any empirical parameters.

But Fig. 5 also reveals the limitations of the SPF-modelling approach so far. Deviations from the experimental trend may be observed during the receding phase of the crown ($\tau > \tau(H_{cr,\max})$), where the flow is susceptible to capillary forces, which are not included in the SPF-model yet. For thicker wall-films and higher fluid viscosity (B50), the SPF-model's capability to reproduce the curvature of the experimental R_B-profile is also reduced because sliding effects at the interface between droplet and wall-film liquid as well as the formation of a cavity flow beneath the liquid surface are not considered.

4 Conclusion

A new approach for modelling the crown base propagation by employing the analytical stagnation point flow solution of Hiemenz is presented in this paper. The drop impact process on a wetted solid substrate is therefore divided into two subprocesses. The first sub-process, the impulse transfer from drop to wall-film, inducing a decrease in film thickness $h(t)$, is modelled based on the assumption that the flow inside the droplet resembles the potential flow of the stagnation point problem. The second sub-process, the spreading of the liquid lamella, is modelled by assuming perfectly mixed liquids that start spreading radially outwards with an average veloc-

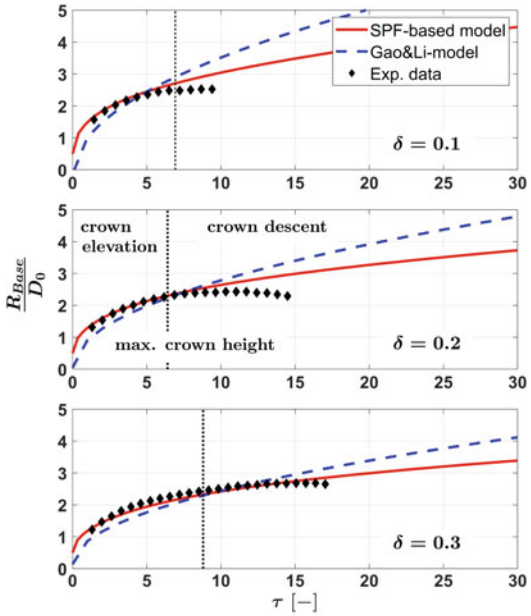

(a) Silicon oil: B3

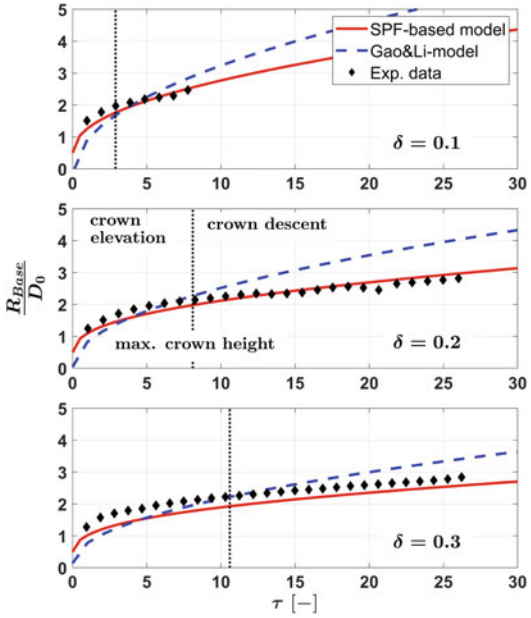

(b) Silicon oil: B50

Fig. 5 Temporal evolution of non-dimensional crown base radius R_B: comparison between experiments, Gao-Li model [6] and SPF-based modelling approach. Vertical lines mark the time when maximum crown height is reached and crown receding begins. Table 1 lists impact conditions

ity $\bar{u}(t)$. The average velocity $\bar{u}(t)$ decreases over time due to viscous losses, which are estimated from Hiemenz's solution for the boundary layer of a plane stagnation point flow. Introducing an adapted energy loss factor λ_{AG}, the time dependent velocity $\bar{u}(t)$ is integrated into the inviscid model of Gao and Li [6] for the crown base radius evolution $R_B(t)$. Thus, the new SPF-based modelling approach differs from inviscid theories because the assumption of a constant crown propagation speed is not retained. A comparison of the SPF-model predictions with experimental data for the crown base radius evolution R_B shows a very good agreement over the entire duration of the impact process. Therefore, the SPF-model provides a significant improvement with regard to inviscid modelling approaches. The momentum transfer from drop to wall-film and thereof also the evolution of the crown's base radius are affected by liquids viscosity and initial film thickness. A higher fluid viscosity leads to increased impact losses, which reduces the efficiency of the momentum transfer and slows down the film thickness decay rate. But since less momentum is available, the spreading velocity is lower and therefore the momentum dissipation is reduced. The higher amount of available momentum for low-viscous fluids leads to a higher spreading velocity and therefore to a higher momentum dissipation. The influence of the initial film thickness is similar: thinner initial film thicknesses result in lower inertial losses, but the excess momentum transferred to the spreading lamella is rapidly dissipated because viscous losses increase with decreasing film thickness. The SPF-model accurately captures this interplay between inertial and viscous forces, which is the reason for the model's excellent predictive capacity. But, the effectiveness of the SPF-modelling has also limitations because neither capillary forces during crown receding, sliding effects at the liquids interface or cavity flow are considered. Nevertheless, the SPF-modelling approach is a significant step towards fully understanding and predicting the crown propagation after drop impact onto wetted surfaces.

Acknowledgements The authors thank the Deutsche Forschungsgemeinschaft (DFG) for their financial support in the framework of the projects LA 2512/2-1, WE 2549/24-1 and GRK 2160/1 "Droplet Interaction Technologies" (DROPIT).

References

1. Agbaglah, G., Deegan, R.D.: Growth and instability of the liquid rim in the crown splash regime. J. Fluid Mech. **752**, 485–496 (2014). https://doi.org/10.1017/jfm.2014.240
2. Cossali, G.E., Coghe, A., Marengo, M.: The impact of a single drop on a wetted solid surface. Exp. Fluids **22**, 463–472 (1997). https://doi.org/10.1007/s003480050073
3. Cossali, G.E., Marengo, M., Coghe, A., Zhdanov, S.: The role of time in single drop splash on thin film. Exp. Fluids **36**(6), 888–900 (2004). https://doi.org/10.1007/s00348-003-0772-0
4. Davidson, M.R.: Spreading of an inviscid drop impacting on a liquid film. Chem. Eng. Sci. **57**, 3639–3647 (2002)
5. Fujimoto, H., Ogino, T., Takuda, H., Hatta, N.: Collision of a droplet with a hemispherical static droplet on a solid. Int. J. Multiph. Flow **27**, 1227–1245 (2001). https://doi.org/10.1016/S0301-9322(00)00075-6
6. Gao, X., Li, R.: Impact of a single drop on a flowing liquid film. Phys. Rev. E **92**(053005) (2015). https://doi.org/10.1103/PhysRevE.92.053005

7. Geppert, A., Chatzianagnostou, D., Meister, C., Gomaa, H., Lamanna, G., Weigand, B.: Classification of impact morphology and splashing/deposition limit for n-Hexadecane. Atom. Sprays **26**(10), 983–1007 (2016). https://doi.org/10.1615/AtomizSpr.2015013352
8. Geppert, A., Terzis, A., Lamanna, G., Marengo, M., Weigand, B.: A benchmark study for the crown-type splashing dynamics of one- and two-component droplet wall-film interactions. Exp. Fluids **58**(12), 1–27 (2017). https://doi.org/10.1007/s00348-017-2447-2
9. Geppert, A.K.: Experimental investigation of droplet wall-film interaction of binary systems. Ph.D. thesis, University of Stuttgart (2019)
10. Guo, Y., Wei, L., Liang, G., Shen, S.: Simulation of droplet impact on liquid film with CLSVOF. Int. Commun. Heat Mass **53**, 26–33 (2014). https://doi.org/10.1016/j.icheatmasstransfer.2014.02.006
11. Homann, F.: Der einfluss grosser zaehigkeit bei der stroemung um den zylinder und um die kugel. Z. Angew. Math. Mech. **16**(3), 153–164 (1936)
12. Joseph, D., Jing, J.D.D.F.T.W., Funada, T., Wang, J.: Potential Flows of Viscous and Viscoelastic Fluids. Cambridge Aerospace. Cambridge University Press (2014). https://books.google.de/books?id=MK3qjwEACAAJ
13. Josserand, C., Zaleski, S.: Droplet splashing on a thin liquid film. Phys. Fluids **15**(6), 1650–1657 (2003). https://doi.org/10.1063/1.1572815
14. Kittel, H.M., Roisman, I.V., Tropea, C.: Splash of a drop impacting onto a solid substrate wetted by a thin film of another liquid. Phys. Rev. Fluids **3**(073601) (2018). https://doi.org/10.1103/PhysRevFluids.3.073601
15. Kuhlmann, J.M., Hillen, N.L.: Droplet impact cavity film thickness measurements versus time after drop impact and cavity radius for thin static residual liquid layer thicknesses. Exp. Therm. Fluid Sci. **77**, 246–256 (2016). https://doi.org/10.1016/j.expthermflusci.2016.04.020
16. Lamanna, G., Geppert, A., Weigand, B.: On the effect of a thin liquid film on the crown propagation in drop impact studies. ILASS - Europe, 29th Conference on Liquid Atomization and Spray Systems. Paris, France (2019)
17. Levin, Z., Hobbs, P.V.: Splashing of water drops on solid and wetted surfaces: hydrodynamics and charge separation. Philos. Trans. A Math. Phys. Eng. Sci. **269**(1200), 555–585 (1971). https://doi.org/10.1098/rsta.1971.0052
18. Liang, G., Guo, Y., Shen, S., Yang, Y.: Crown behavior and bubble entrainment during a drop impact on a liquid film. Theor. Comp. Fluid Dyn. **28**(2), 159–170 (2014). https://doi.org/10.1007/s00162-013-0308-z
19. Liang, G., Mudawar, I.: Review of mass and momentum interactions during drop impact on a liquid film. Int. J. Heat Mass Transf. **101**, 577–599 (2016). https://doi.org/10.1016/j.ijheatmasstransfer.2016.05.062
20. Marcotte, F., Michon, G.J., Séon, T., Josserand, C.: Ejecta, corolla, and splashes from drop impacts on viscous fluids. Phys. Rev. Lett. **122**, 014501 (2019)
21. Okawa, T., Shiraishi, T., Mori, T.: Production of secondary drops during the single water drop impact onto a plane water surface. Exp. Fluids **41**, 965–974 (2006). https://doi.org/10.1007/s00348-006-0214-x
22. Philippi, J., Lagrée, P.Y., Antkowiak, A.: Drop impact on a solid surface: short-time self-similarity. J. Fluid Mech. **795**, 96–135 (2016)
23. Rieber, M., Frohn, A.: A numerical study on the mechanism of splashing. Int. J. Heat Fluid Flow **20**, 455–461 (1999). https://doi.org/10.1016/S0142-727X(99)00033-8
24. Roisman, I.V.: Inertia dominated drop collisions. II. An analytical solution of the Navier-Stokes equations for a spreading viscous film. Phys. Fluids (2009). https://doi.org/10.1063/1.3129283
25. Schlichting, H., Gersten, K.: Boundary-Layer Theory, 9th edn. Springer, Berlin, Heidelberg (2017)
26. Tropea, C., Marengo, M.: The impact of drops on walls and films. Multi. Sci. Tech. **11**, 19–36 (1999). https://doi.org/10.1615/MultScienTechn.v11.i1.20
27. Trujillo, M.F., Lee, C.F.: Modeling crown formation due to the splashing of a droplet. Phys. Fluids **13**(9), 2503–2516 (2001). https://doi.org/10.1063/1.1388541

28. Vander Wal, R.L., Berger, G.M., Mozes, S.D.: The combined influence of a rough surface and thin fluid film upon the splashing threshold and splash dynamics of a droplet impacting onto them. Exp. Fluids **40**(1), 23–32 (2006). https://doi.org/10.1007/s00348-005-0043-3
29. Yarin, A.L.: Drop impact dynamics: splashing, spreading, receding, bouncing.... Annu. Rev. Fluid Mech. **38**, 159–192 (2006). https://doi.org/10.1146/annurev.fluid.38.050304.092144
30. Yarin, A.L., Weiss, D.A.: Impact of drops on solid surfaces: self-similar capillary waves, and splashing as a new type of kinematic discontinuity. J. Fluid Mech. **283**, 1–33 (1995)

An Implicit High-Order Discontinuous Galerkin Approach for Variable Density Incompressible Flows

Francesco Carlo Massa, Francesco Bassi, Lorenzo Botti and Alessandro Colombo

Abstract In this work we present a high-order discontinuous Galerkin approach for the simulation of variable density incompressible (VDI) flows. Here, the density is treated as a purely advected property tracking possibly multiple (more than two) components, while the fluids interface is captured in a diffuse fashion by the high-degree polynomial solution thus not requiring any geometrical reconstruction. Specific care is devoted to deal with density over/undershoots, spurious oscillations at flows interfaces and Godunov numerical fluxes at inter-element boundaries. Time integration is performed with high-order implicit schemes thus preventing any time step restriction condition. Promising results with high-degree polynomial representation and relatively coarse meshes are achieved on numerical experiments involving high-density ratios (water–air) and the possible interaction of more than two components.

1 Introduction

Multi-component flows are peculiar of many industrial and technological processes, for instance the extraction and transport of hydrocarbons or the pollutants treatment. In the context of multi-component problems involving incompressible flows, the variable density incompressible (VDI) flow model shows interesting features. Indeed, the density is a purely advected property, which can be used to distinguish different components of different densities. The interface between components can be handled in a diffuse fashion as smooth variations of the density field. The main advantage

F. C. Massa (✉) · F. Bassi · L. Botti · A. Colombo
University of Bergamo, Bergamo, Italy
e-mail: francescocarlo.massa@unibg.it

F. Bassi
e-mail: francesco.bassi@unibg.it

L. Botti
e-mail: lorenzo.botti@unibg.it

A. Colombo
e-mail: alessandro.colombo@unibg.it

G. Lamanna et al. (eds.), *Droplet Interactions and Spray Processes*,
Fluid Mechanics and Its Applications 121,
https://doi.org/10.1007/978-3-030-33338-6_15

is that no reconstruction at the interface is required and, therefore, really complex three-dimensional interface topologies can be easily captured with no extra cost. However, an accurate representation of the interface is of fundamental importance in order to control the spreading and ensure meaningful results. The application of a high-order space discretization is thus very attractive since it can help in controlling the interface thickness by enhancing the accuracy of the solution approximation.

Discontinuous Galerkin (dG) methods are a class of high-order space discretization schemes, which approximates the problem solution with piecewise continuous polynomial functions inside mesh elements without imposing continuity constraints at inter-element boundaries. Favourable dispersion and dissipation properties and the ability to achieve a very high accuracy even on arbitrarily shaped mesh elements are peculiar features that make dG methods very appealing [1]. Nevertheless, several challenging numerical issues arise when applying high-order dG methods to VDI equations to deal with multi-component flow problems. In particular, specific care must be taken to formulate the inter-element inviscid Godunov fluxes, to ensure the positivity of the density and to control spurious oscillations of the density field arising at the interfaces.

Time integration of the discretised set of equations can be performed with temporal schemes. Among different types, the implicit schemes proved to be able to greatly enhance the computational efficiency of flow simulations [2]. Indeed, they can achieve very high orders of accuracy even in the context of differential algebraic equations, i.e., incompressible flows, and can be designed to have optimal stability properties. In particular, the linearly implicit Rosenbrock-type Runge-Kutta schemes, A-stable up to order five, have the appealing feature to be linearly implicit. Accordingly, they require to solve only linear systems and the Jacobian matrix must be assembled and factored only once per time-step, thus improving considerably the time integration efficiency.

The VDI flow model and the dG discretization are described in Sects. 2 and 3, respectively. Particular emphasis is given to the treatment of the above mentioned numerical issues: (i) Godunov fluxes, (ii) density positivity, (iii) Gibbs type phenomena. Section 4 reports two selected test cases of multi-component problem involving high density ratios. In Sect. 5 conclusions are given.

2 Variable Density Incompressible Flow Model

The model, which describes VDI flows in a d-dimensional space, comprises the divergence constraint, the momentum equation and the mass conservation equation

$$\begin{aligned} \frac{\partial u_j}{\partial x_j} &= 0, \\ \frac{\partial}{\partial t}(\rho u_i) + \frac{\partial}{\partial x_j}(\rho u_i u_j) &= -\frac{\partial p}{\partial x_i} + \frac{\partial \tau_{ij}}{\partial x_j} + \rho g_i, \\ \frac{\partial \rho}{\partial t} + \frac{\partial}{\partial x_j}(\rho u_j) &= 0, \end{aligned} \tag{1}$$

with $i, j = 1, \ldots, d$ and

$$\tau_{ij} = 2\mu \left[\frac{1}{2} \left(\frac{\partial u_i}{\partial x_j} + \frac{\partial u_j}{\partial x_i} \right) - \frac{1}{3} \frac{\partial u_k}{\partial x_k} \delta_{ij} \right]. \tag{2}$$

The dynamic viscosity can be defined as a suitable function of the density $\mu = \mu(\rho)$ while the body acceleration is typically set constant $|\mathbf{g}| = g$.

The distinguish feature of the model (1) lies in the simultaneous presence of the divergence free constraint and the continuity equation. As a consequence, the density is treated as a purely advected property, i.e., a property with null material derivative, that acts like a phase variable able to discriminate different components with different densities.

In the context of multi-component problems involving incompressible flows, the model (1) shows some advantages. Indeed, while different components are solely identified by different values of the density field, the interfaces between components are handled in a diffuse fashion as smooth (and possibly sharp) variations of the density variable.

3 The Discontinuous Galerkin Discretization

The model (1) can be written in the following compact form

$$\mathbf{D} \frac{\partial \mathbf{u}}{\partial t} + \nabla \cdot \mathbf{F}_c(\mathbf{u}) + \nabla \cdot \mathbf{F}_v(\mathbf{u}, \nabla \mathbf{u}) + \mathbf{s}(\mathbf{u}) = \mathbf{0}, \tag{3}$$

where $\mathbf{u} = \{p, u_i, \rho\} \in \mathbb{R}^m$ is the vector of the m conservative variables, $\mathbf{F}_c, \mathbf{F}_v \in \mathbb{R}^m \otimes \mathbb{R}^d$ are the convective and viscous flux functions, $\mathbf{s}$ is the source term and $\mathbf{D} \in \mathbb{R}^m \otimes \mathbb{R}^m$ is the difference between the identity and a single-entry matrices $\mathbf{D} = \mathbf{I} - \mathbf{J}^{11}$. The system (3) can be also formulated in terms of a generic set of variables $\mathbf{w}$ named working variables

$$\mathbf{D}\mathbf{P}(\mathbf{w}) \frac{\partial \mathbf{w}}{\partial t} + \nabla \cdot \mathbf{F}_c(\mathbf{w}) + \nabla \cdot \mathbf{F}_v(\mathbf{w}, \nabla \mathbf{w}) + \mathbf{s}(\mathbf{w}) = \mathbf{0}. \tag{4}$$

The matrix $\mathbf{P}(\mathbf{w})$ takes into account the transformation from conservative to working variables.

By multiplying Eq. (4) by an arbitrary smooth test function $\mathbf{v} = \{v_1, \ldots, v_m\}$, and integrating by parts, we obtain the weak formulation

$$\int_\Omega \mathbf{v} \cdot \left(\mathbf{DP}\left(\mathbf{w}\right) \frac{\partial \mathbf{w}}{\partial t} \right) d\mathbf{x} - \int_\Omega \nabla \mathbf{v} : \left[\mathbf{F}_c\left(\mathbf{w}\right) + \mathbf{F}_v\left(\mathbf{w}, \nabla \mathbf{w}\right) \right] d\mathbf{x} + \int_{\partial\Omega} \mathbf{v} \otimes \mathbf{n} : \left[\mathbf{F}_c\left(\mathbf{w}\right) + \mathbf{F}_v\left(\mathbf{w}, \nabla \mathbf{w}\right) \right] d\sigma + \int_\Omega \mathbf{v} \cdot \mathbf{s}(\mathbf{w}) d\mathbf{x} = 0, \quad (5)$$

where $\mathbf{n}$ is the unit vector normal to the boundary.

To discretize Eq. (5) by means of discontinuous Galerkin (dG) methods [1] we replace the solution $\mathbf{w}$ and the test function $\mathbf{v}$ with a finite element approximation $\mathbf{w}_h$ and a discrete test function $\mathbf{v}_h$, respectively, where $\mathbf{w}_h$ and $\mathbf{v}_h$ belong to the space of the polynomials of maximum degree k defined on each element K of the mesh $\mathcal{T}_h$ and the subscript h denote the mesh element dimension. Here, for each of the m equations of system (5) and for any mesh element K, we choose as the set of shape and test functions the set $\{\phi\}$ of orthogonal and hierachical basis functions in that element. With this choice each component $w_{h,j}$, $j = 1, \ldots, m$, of $\mathbf{w}_h$ can be expressed as $w_{h,j} = \phi_l W_{j,l}$, $l = 1, \ldots, N_{dof}^K$, $\forall K$, where $W_{j,l}$ are the components of the global vector $\mathbf{W}$ of the unknown degrees of freedom (DoFs). Therefore, the dG discretization of the governing equations consists in seeking, for $j = 1, \ldots, m$, the elements of $\mathbf{W}$ such that

$$\sum_{K\in\mathcal{T}_h} \int_K \phi_i D_{j,t} P_{t,k}\left(\mathbf{w}_h\right) \phi_l \frac{d W_{k,l}}{dt} d\mathbf{x} - \sum_{K\in\mathcal{T}_h} \int_K \frac{\partial \phi_i}{\partial x_n} \left[F_{c,j,n}\left(\mathbf{w}_h\right) + F_{v,j,n}\left(\mathbf{w}_h, \nabla_h \mathbf{w}_h + \mathbf{r}\left(\llbracket \mathbf{w}_h \rrbracket\right)\right) \right] d\mathbf{x} + \sum_{\partial K\in\mathcal{F}_h} \int_{\partial K} \llbracket \phi_i \rrbracket_n \left[\widehat{F}_{c,j,n}\left(\mathbf{w}_h^{\pm}\right) + \widehat{F}_{v,j,n}\left(\mathbf{w}_h^{\pm}, \left(\nabla_h \mathbf{w}_h + \eta_F \mathbf{r}_F\left(\llbracket \mathbf{w}_h \rrbracket\right)\right)^{\pm}\right) \right] d\sigma + \sum_{K\in\mathcal{T}_h} \int_K \phi_i s_j\left(\mathbf{w}_h\right) d\mathbf{x} = 0, \quad (6)$$

for $i = 1, \ldots, N_{dof}^K$. Repeated indices imply summation over ranges $k = 1, \ldots, m$, $l = 1, \ldots, N_{dof}^K$, $n = 1, \ldots, d$. $\mathcal{F}_h$ is the set of element boundaries and $\llbracket \cdot \rrbracket$ the jump operator. A further integration by parts of the equation (6) leads to the so called *strong* formulation [1]. In the current work the *strong* formulation is adopted for the convective flux contribute while the *weak* formulation is considered for the viscous flux treatment.

3.1 Numerical Fluxes

The dG discretization entails the definition of the numerical fluxes $\widehat{F}_c$ and $\widehat{F}_v$.

The numerical convective flux $\widehat{F}_c$ is here computed from the exact solution of local Riemann problems perturbed by means of the artificial compressibility. The approach takes inspiration from the work of Elsworth and Toro [3] and Bassi et al. [4]. The key idea is to add solely at the local problem level an artificial compressibility term, which allows to recover a tiny coupling between pressure and velocity. However, no pressure time derivative is added to the global divergence equation. A comprehensive analysis of three Riemann solvers for VDI flows and based on the artificial compressibility perturbation can be found in [5].

The numerical viscous flux $\widehat{F}_v$ is based on the BR2 scheme, proposed in [6] and theoretically analyzed in [7, 8]. Following this scheme, the viscous numerical flux is given by

$$\widehat{\mathbf{F}}_v\left(\mathbf{w}_h^{\pm}, \left(\nabla_h \mathbf{w}_h + \eta_F \mathbf{r}_F\left([\![\mathbf{w}_h]\!]\right)\right)^{\pm}\right) \stackrel{\text{def}}{=} \left\{\mathbf{F}_v\left(\mathbf{w}_h, \nabla_h \mathbf{w}_h + \eta_F \mathbf{r}_F\left([\![\mathbf{w}_h]\!]\right)\right)\right\} \tag{7}$$

where $\{\cdot\}$ is the average operator. The stability parameter η_F is defined according to [8].

3.2 Working Variables

Among different sets of working variables $\mathbf{w}$, e.g., conservatives and primitive ones, we want to use a set comprising the pressure, the velocity and a new variable named hereinafter *working density* $\widetilde{\rho}$. The density $\rho = \rho(\widetilde{\rho})$ is defined as a function of the new variable.

This choice wants to solve two main issues: (i) the density positivity, to be ensured at the discrete level; (ii) the control of density under/overshoots, deriving from the discretization of discontinuities inside density field, i.e., density interfaces, when dealing with multi-component flow problems. Indeed, both issues can be handled at the same time by means of a suitable definition of the function $\rho(\widetilde{\rho})$. In particular, here we impose that

$$\rho = \rho_+ \frac{r_\rho + 1 + \left(r_\rho + 1\right)\tanh(\sigma_s \widetilde{\rho})}{2 r_\rho}, \tag{8}$$

where ρ_+ (resp. ρ_-) is the user-defined maximum (resp. minimum) density field value, $r_\rho = \rho_+/\rho_-$ is the maximum density ratio and $\sigma_s \in \mathbb{R}\setminus\{0\}$ is a scaling factor.

It is an easy matter to see that the function (8) on one hand ensures the positivity of the density regardless the working density value, on the other hand limits the under/overshoots to the ρ_- value. The scaling factor σ_s is a free parameter that can be set in order to limit the initial range $\Delta\widetilde{\rho} = \widetilde{\rho}(\rho_+) - \widetilde{\rho}(\rho_-)$ of the working variable

$\widetilde{\rho}$ to the maximum value $\Delta_i \widetilde{\rho} = 1$

$$\sigma_s = \max \left[\frac{1}{\Delta_i \widetilde{\rho}} \ln \left(r_\rho \right) ; 1 \right]. \tag{9}$$

The set of working variables is thus

$$\mathbf{w} = [p, u_i, \widetilde{\rho}]^T, \tag{10}$$

and starting from conservative variables $\mathbf{u} = [p, \rho u_i, \rho]^T$, the transformation matrix reads

$$\mathbf{P}(\mathbf{w}) = \frac{\partial \mathbf{u}}{\partial \mathbf{w}} = \begin{bmatrix} 1 & 0 & 0 & 0 & 0 \\ 0 & \rho & 0 & 0 & \rho_{\widetilde{\rho}} u_1 \\ 0 & 0 & \rho & 0 & \rho_{\widetilde{\rho}} u_2 \\ 0 & 0 & 0 & \rho & \rho_{\widetilde{\rho}} u_3 \\ 0 & 0 & 0 & 0 & \rho_{\widetilde{\rho}} \end{bmatrix}, \tag{11}$$

where $\rho_{\widetilde{\rho}} = d\rho / d\widetilde{\rho}$.

3.3 Spurious Oscillations Control

The introduction of the variable $\widetilde{\rho}$ ensures the positivity of the density and limits its over/undershoots. However, Gibbs-type phenomena arising from high-order discretization of discontinuities, i.e., interfaces between different components, cannot be controlled with a simple change of a working variable. For this purpose we adopt an oscillation control approach which originates from the shock capturing strategies based on artificial viscosity [9, 10]. The key idea is to add to the original set of equations an additional diffusion term

$$\mathbf{DP}(\mathbf{w}) \frac{\partial \mathbf{w}}{\partial t} + \nabla \cdot (\mathbf{F}_c(\mathbf{w}) + \mathbf{F}_v(\mathbf{w})) + \mathbf{s}(\mathbf{w}) = \nabla \cdot (\nu_\epsilon \nabla \mathbf{u}(\mathbf{w})) . \tag{12}$$

The parameter ν_ϵ, named artificial viscosity, drives this diffusion and should be defined in such a way that its value is not null only where discontinuities occur.

The unique type of discontinuities in VDI flow problems is the contact discontinuity and only the density can change across it. Since we introduce and discretize the working density, we need to control $\widetilde{\rho}$ oscillations in order to control the density ones. The first step in such direction lies in the definition of a discontinuity detector, named also as smoothness sensor s. The adopted approach follows the algorithm proposed in [10] where for each element K the modal decay of the DoFs of the chosen variable, i.e., $\widetilde{\rho}$, is analysed. When the density field is smooth, the modal decay is quick and $s \gg 1$. Conversely, at contact discontinuities the DoFs decays slowly and $s \approx 1$. The artificial viscosity ν_ϵ is then defined according to [9] as

$$\nu_\epsilon = \begin{cases} \nu_{\epsilon 0} & \text{if} \quad s < s_0 - \Delta s \\ \dfrac{\nu_{\epsilon 0}}{2}\left[1 - \sin\left(\pi \dfrac{s_0 - s}{2\Delta s}\right)\right] & \text{if} \quad s_0 - \Delta s \leq s \leq s_0 + \Delta s \\ 0 & \text{otherwise,} \end{cases} \tag{13}$$

where $\nu_{\epsilon 0}$ is the maximum value of the artificial viscosity, s_0 is the user-defined threshold value of the smoothness sensor and $2\Delta s$ is the range of smoothness sensor values for which the viscosity assumes intermediate values between 0 and ν_ϵ. Furthermore, in [9] it is proposed to set $\nu_{\epsilon 0} \propto O(h/k)$, with h the mesh element size. This choice fits very well with dG approximation since it introduces a small quantity of viscosity which decreases with higher polynomial order allowing to capture discontinuities as thin layers with continuous sharp gradients inside a single mesh element. Here we consider $s_0 = 1$, $\Delta s = 0.75$ and $\nu_{\epsilon 0} = h/k$.

Since pressure and velocity gradients are not involved in density spurious oscillations at contact discontinuities, we can rewrite the additional diffusion term as

$$\nabla \cdot (\nu_\epsilon \nabla \mathbf{u}(\mathbf{w})) \rightarrow \nabla \cdot (\mathbf{b} \nu_\epsilon \nabla \rho)\,, \tag{14}$$

where $\mathbf{b} = \left\{0, u_{i=1,\ldots,d}, 1\right\}$. The dG discretization of (14) entails the treatment of viscous numerical fluxes. In order to avoid this issue we follow the idea proposed in [11] where the numerical flux contribute is neglected. Accordingly, the artificial viscous term acts like a conservative source term which spreads the density inside the single mesh element leaving untouched its mean value.

3.4 Time Integration

The numerical integration of the dG discretised set of equations by means of suitable Gauss quadrature rules leads to a system of nonlinear differential algebraic equations that can be summarised as

$$\mathbf{M_P}(\mathbf{W}) \frac{d\mathbf{W}}{dt} + \mathbf{R}(\mathbf{W}) = \mathbf{0}, \tag{15}$$

where $\mathbf{R}(\mathbf{W})$ is the vector of residuals and $\mathbf{M_P}(\mathbf{W})$ is the global block diagonal matrix arising from the discretization of the first term in Eq. (6). The time integration schemes adopted to solve the system (15) are the linearly implicit Rosenbrock-type Runge-Kutta (Rosenbrock) schemes [12] with optimal stability properties up to order five. The global time marching is adaptive [13].

Since linearly implicit, Rosenbrock schemes entail the solution of several linear systems of equations solved using the Generalized Minimal Residual (GMRES) method [14] with a preconditioning based on the Additive Schwarz Method (ASM) [15]. It is interesting to note that, thanks to the peculiar treatment of the convective numerical fluxes, the Jacobian matrix has non null pressure degrees of freedom.

Accordingly, the global matrix arising from the implicit time discretization is non singular. A comprehensive analysis of Rosenbrock schemes for a dG discretization can be found in [2].

4 Numerical Results

In this section the proposed dG appoach is tested on two selected cases: the Dry bed inviscid dambreak problem and the double dry bed inviscid dambreack problem.

4.1 Dry Bed Inviscid Dambreak Problem

The dambreak problem over a dry bed is a free surface problem that consists on a sudden collapse of a dam that separates water from air. The exact solution for shallow water (SW) equations has been derived by Ritter [16] in 1892.

As initial condition, the domain of dimension $[-50, 50] \times [0, 4]$ contains water in the region $[-50, 0] \times [0, 1.4618]$ and air elsewhere. The density ratio is $r_\rho = 800$. Null velocity, hydro-static pressure profile are imposed as initial condition. The gravity field is downward and the Froude number is $\mathrm{Fr} = 0.3193$. Transmissive condition is applied to the top boundary and slip wall condition is considered for remaining borders. Solutions are obtained using a sixth degree dG polynomial discretization on a coarse (260×8) and a fine (520×16) mesh. In particular, meshes are generated in order to ensure the exact projection of the initial working density field (see Fig. 1 for finer mesh). Time integration is performed with the fourth order Rosenbrock scheme RODASP [2].

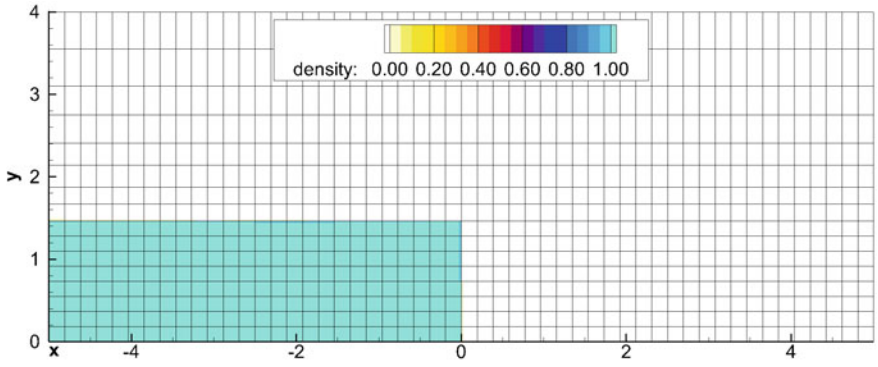

Fig. 1 Inviscid dambreak problem—initial density contour with the finer mesh

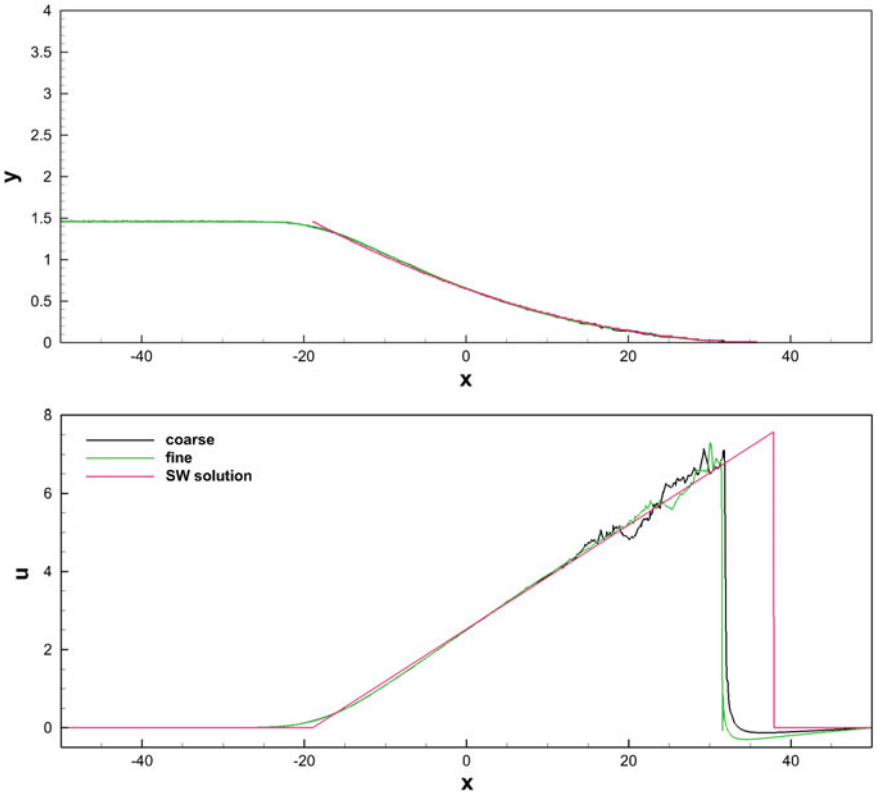

Fig. 2 Dambreak—comparison of coarse and fine mesh results with respect to the exact shallow water solution [16] at time $t = 5$. Free surface position and velocity profile at the bottom boundary are depicted on top and on bottom, respectively

In Fig. 2 results with both meshes are compared with the exact solution of the shallow water model at non-dimensional time $t = 5$, where the reference time is $t_0 = 1$ s. An excellent agreement is achieved except for the predicted position of the liquid front which is moved forward in the shallow water solution. This behaviour is well known for shallow water equations where no vertical accelerations are considered [17].

4.2 Dry Bed Inviscid Double-Dambreak Problem

In this section we formulate a new test case. The goal is to show the capabilities of the proposed dG variable density incompressible formulation to deal with more than two fluids. The test case is an inviscid problem with two dambreaks and three

components: two different liquids and one gas. The gas and the first liquid are again air and water while the second liquid, hereinafter named oil, has an intermediate density, i.e., the arithmetic mean value, between air and water. This test case is challenging since entails both high (water–air, oil–air) and low (water–oil) density ratio interactions.

The domain $[-5, 5] \times [0, 8]$ contains two liquid regions $[-5, -3.8] \times [0, 3.6]$ and $[3.8, 5] \times [0, 3.6]$ for water and oil, respectively, and is filled with air for the remaining part. Null velocity and hydrostatic pressure profile are imposed as initial conditions and slip wall condition is applied to all boundaries. The gravity field is downward and the Froude number is $\mathrm{Fr} = 0.3193$. Solutions are computed using a sixth degree dG polynomial approximation and the forth order RODASP scheme on a mesh of 50×40 quadrangular elements.

No references are available for this test case, therefore only the evolution in time of the multi-component problem is analysed. In Fig. 3 the density contours at non-dimensional times $t = 0.005$, 0.25, 0.50 and 0.75 are shown, where again the reference time is $t_0 = 1$ s. At early times the problem evolves as two single dambreak problems until liquid fronts collide ($t = 0.25$). After that, a wave of both water and oil rises ($t = 0.5$) and then collapses incorporating a small air bubble while the water front goes forward into the oil region ($t = 0.75$).

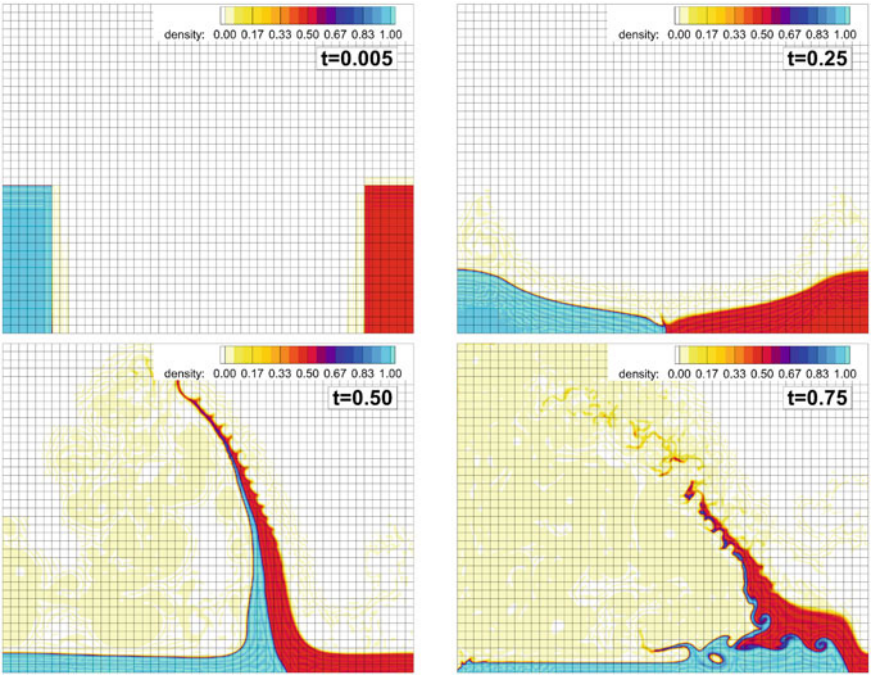

Fig. 3 Inviscid double-dambreak problem—density contour at different times. Blue is water (left) and red is oil (right)

5 Conclusions

An implicit high-order discontinuous Galerkin method for the simulation of variable density incompressible flows has been proposed. Godunov fluxes are treated by means of the exact solution of an artificial compressibility based Riemann solver. The introduction of a suitable change of variables and of an artificial viscosity shock capturing approach allows to deal with multi-component problems ensuring the density positivity and the control of Gibbs type phenomena at contact discontinuities. Thanks to the high order dG approximation promising results have been obtained despite the coarse meshes. In particular, the proposed method have shown the capability to deal with multi-component problems involving high density ratios and more than two fluids. However, no physical interaction between components at the material interface, e.g., surface tension, have been considered. This issue will be considered in future works.

Acknowledgements F. Massa is supported by the Supporting Talented Researchers (STaRS) programm of the University of Bergamo.

References

1. Hesthaven, J.S., Warburton, T.: Nodal Discontinuous Galerkin Methods. Springer, Berlin (2008)
2. Bassi, F., Botti, L., Colombo, A., Ghidoni, A., Massa, F.: Linearly implicit Rosenbrock-type Runge-Kutta schemes for the Discontinuous Galerkin solution of compressible and incompressible unsteady flows. Comput. Fluids (2015). https://doi.org/10.1016/j.compfluid.2015.06.007
3. Elsworth, D.T., Toro, E.F.: Riemann solvers for solving the incompressible Navier-Stokes equations using the artificial compressibility method. College of Aeronautics, Cranfield Institute of Technology, 9208 (1992)
4. Bassi, F., Crivellini, A., Di Pietro, D.A., Rebay, S.: An artificial compressibility flux for the discontinuous Galerkin solution of the incompressible Navier-Stokes equations. J. Comput. Phys. (2006). https://doi.org/10.1016/j.jcp.2006.03.006
5. Bassi, F., Massa, F., Botti, L., Colombo, A.: Artificial compressibility Godunov fluxes for variable density incompressible flows. Comput. Fluids (2018). https://doi.org/10.1016/j.compfluid.2017.09.010
6. Bassi, F., Rebay, S., Mariotti, G., Pedinotti, S., Savini, M.: A high-order accurate discontinuous finite element method for inviscid and viscous turbomachinery flows. In: Proceedings of 2nd European Conference on Turbomachinery Fluid Dynamics and Thermodynamics, pp. 99–108 (1997)
7. Brezzi, F., Manzini, G., Marini, D., Pietra, P., Russo, A.: Discontinuous Galerkin approximations for elliptic problems. Numer. Meth. Part. D. E. **16**, 365–378 (2000)
8. Arnold, D.N., Brezzi, F., Cockburn, B., Marini, L.D.: Unified analysis of discontinuous Galerkin methods for elliptic problems. SIAM J. Numer. Anal. **39**, 1749–1779 (2002)
9. Persson, P.-O., Peraire, J.: Sub-cell shock capturing for discontinuous Galerkin Methods. In: 44th AIAA Aerospace Sciences Meeting and Exhibit, Nevada (2006)
10. Klöckner, A., Warburton, T., Hesthaven, J.S.: Viscous shock capturing in a time-explicit discontinuous Galerkin Method. Math. Model. Nat. Phenom. (2011). https://doi.org/10.1051/mmnp/20116303

11. Jaffre, J., Johnson, C., Szepessy, A.: Convergence of the discontinuous Galerkin finite element method for hyperbolic conservation laws. Math. Models Methods Appl. Sci. **5**(3), 286–367 (1995)
12. Hairer, E., Wanner, G.: Solving Ordinary Differential Equations II. Springer, Berlin (2010)
13. Söderlind, G.: Digital filters in adaptive time-stepping. ACM Trans. Math. Softw. V 1–24 (2005)
14. Saad, Y., Shults, M.H.: A generalised minimal residual algorithm for solving nonsymmetric linear systems. SIAM J. Sci. Stat. Comput. **7**(3), 856–869 (1986)
15. Smith, B., Bjørstad, P., Gropp, W.: Domain Decomposition: Parallel Multilevel Methods for Elliptic Partial Differential Equations. Cambridge University Press, Cambridge (1996)
16. Ritter, A.: Die Fortpflanzung der Wasserwellen. Z. Ver. Deut. Ing **36**, 947–954 (1892)
17. Dressler, F.: Comparison of theories and experiments for the hydraulic dam-break wave. Proc. Int. Assoc. of Sci. Hydrol. Assemblée Générale **3**(38), 319–328 (1954)

Visualization Techniques for Droplet Interfaces and Multiphase Flow

Alexander Straub and Thomas Ertl

Abstract The analysis of large multiphase flow simulation data poses an interesting and complex research question, which can be addressed with interactive visualization techniques, as well as semi-automated analysis processes. In this project, the focus lies on the investigation of forces governing droplet evolution. Therefore, our proposed methods visualize and allow the analysis of droplet deformation and breakup, droplet behavior and evolution, and droplet-internal flow. By deriving quantities for interface stretching and bending, we visualize and analyze the influence of surface tension force on breakup dynamics, and forces induced by Marangoni convection. Using machine learning to train a simple model for the prediction of physical droplet properties, we provide a visual analysis framework that can be used to analyze large simulation data. Computing droplet-local velocity fields where every droplet is observed separately in its own frame of reference, we create local, interpretable visualizations of flow within droplets, allowing for the investigation of the influence of flow dynamics on droplet evolution.

1 Introduction

The simulation of multiphase flow is currently a very important topic, its applications covering a wide range in industry, from turbines and combustion engines in aerospace engineering to spray cooling in food processing. Here, droplets and their interaction with other liquids and solid objects come into play. Therefore, phenomena related to free surfaces, especially the influence of forces acting on the interface between fluids, have to be investigated. As simulation data is usually very large and complex, visualization lends itself well as a tool for analyzing the data. In our case, we want

A. Straub (✉) · T. Ertl
Institute for Visualization and Interactive Systems, Universitätsstr. 38,
70569 Stuttgart, Germany
e-mail: alexander.straub@vis.uni-stuttgart.de

T. Ertl
e-mail: thomas.ertl@vis.uni-stuttgart.de

G. Lamanna et al. (eds.), *Droplet Interactions and Spray Processes*,
Fluid Mechanics and Its Applications 121,
https://doi.org/10.1007/978-3-030-33338-6_16

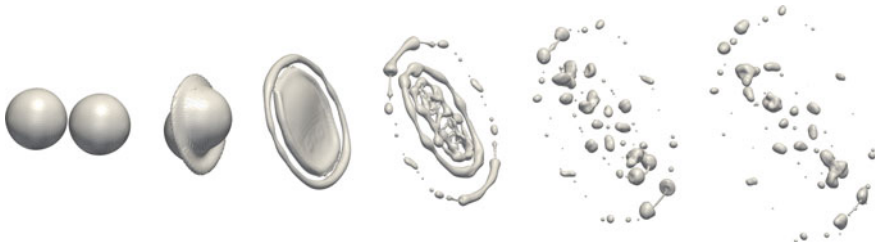

Fig. 1 Overview of the *Colliding Drops* dataset showing different time steps: from before impact to disintegration into small droplets

to visually analyze the effects of surface tension force and Marangoni convection on droplet deformation, the evolution of droplet properties, as well as droplet-internal flow.

The simulation data used in our work was obtained from direct numerical simulations (DNS), performed by the computational fluid dynamics (CFD) solver *Free Surface 3D* (FS3D) [3]. The data consists of a velocity field, as well as a volume of fluid (VOF) [12] field, which provides the information necessary to track the phases in the simulation, and which can be used for reconstructing the fluid interface. Like in the solver, we use piecewise linear interface calculation (PLIC) [30] for interface reconstruction and its visualization [14]. As a framework for visualizing and analyzing the data, we use ParaView [1], a tool which is also used by our cooperation partners and domain experts from the Institute of Aerospace Thermodynamics (ITLR) at the University of Stuttgart. The temporal evolution of an example dataset, which is used in the following, can be seen in Fig. 1. It shows the simulation of an off-center head-on collision of two water droplets, which after impact form a disc and eventually disintegrate into numerous smaller droplets.

This book chapter is based on the extended abstracts *Visual Analysis of Interface Deformation in Multiphase Flow* [25] and *Visualization and Visual Analysis for Multiphase Flow* [24], and as such contains figures from these publications.

2 Interface Deformation

As in multiphase flow the simulation of the free surfaces becomes of importance, so does the analysis of those forces involved in its physical description. Among others, surface tension force and forces induced by Marangoni convection influence the evolution of droplet interfaces, being in part responsible for the cohesion or breakup of droplets [20]. Thus, to help better understand this influence, we want to visualize interface deformation and show the correlation between deformation and topological changes. This work is based on the Master's thesis by Straub [23], and has been in part published in extended abstracts by Straub et al. [24, 25], as well as in an overview paper by Lamanna et al. [16].

2.1 Method

In order to visualize interface deformation of droplets in multiphase flow simulations, we derive two quantities from the velocity and volume of fluid fields, called metric and shape tensor. Their calculation is based on the two fundamental forms from differential geometry and are described by Floater and Hormann [5]. The results are two perpendicular vectors orthogonal to the interface normal, respectively. They are all visualized as tube glyphs indicating direction, and colored with respect to the magnitude of deformation.

The calculation of interface stretching is based on the first fundamental form from differential geometry, defined for the deformation rate of the fluid interface. This metric tensor has been previously described by Obermaier and Joy [21]. Note that we use the term *interface stretching* for a graphical and intuitive description and acknowledge that it is not a physically correct expression. Because the result of this calculation is a 2×2 symmetric matrix, we get two orthogonal eigenvectors and corresponding eigenvalues defined on the interface space, which, after transformation back into 3D space, represent the directions $\mathbf{v}_i$ and magnitudes λ_i of interface stretching. The values lie in the range $0 < \lambda_i < \infty$, with λ_i being the factor of stretching. This means, that values smaller than 1 show interface contraction, and values larger than 1 show interface stretching.

For the calculation of interface bending, we use the second fundamental form, which is called *shape tensor* in the following. This tensor, describing the change in curvature at a point on the fluid surface, can be defined based on the difference of two paraboloids, similar to Grinspun et al. [6]. The first paraboloid is fitted to the original interface, represented by a set of neighboring interface positions, using least squares, whereas the second paraboloid is fitted to the advected interface positions. This method of parabola fitting is also used in the solver FS3D and was described by Popinet [22]. After transforming both paraboloids into the same reference system $\langle r, s \rangle$, their difference in the form $a_0 r^2 + a_1 s^2 + a_2 rs$ can be used to define the shape tensor

$$S = \begin{pmatrix} 2a_0 & a_2 \\ a_2 & 2a_1 \end{pmatrix}.$$

From this tensor, both principal curvatures κ_i and their respective directions $\mathbf{k}_i$ can be computed and transformed back into 3D space. Here, the values are zero-centered, where positive values indicate an increase in concavity, and negative values an increase in convexity.

2.2 Results

Interface stretching is a useful quantity to find and analyze regions in which droplet breakup occurs, or interface-related forces lead to strong cohesion. An example for

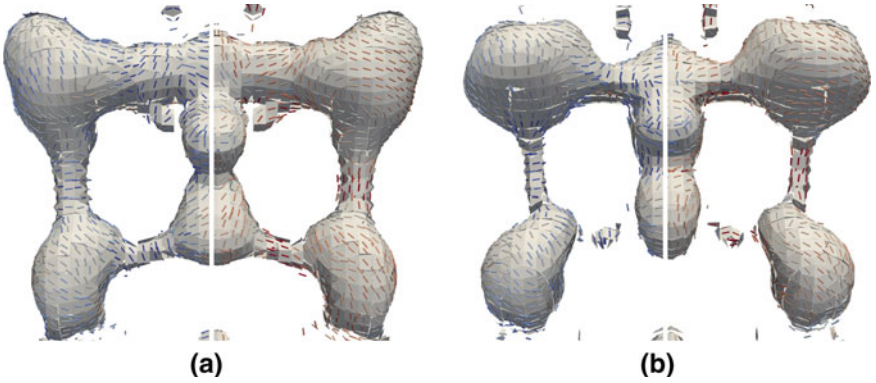

Fig. 2 Interface stretching and contraction for two time steps in the *Colliding Drops* dataset from left to right. Blue tube glyphs visualize smaller values indicating contraction on the left side of each image, large values are represented by red tube glyphs indicating stretching on the right side

the visualization of breakup dynamics in a dataset of two colliding water drops (see Fig. 1) can be seen in Fig. 2. Here, the ligaments connecting the larger droplets disintegrate over time. Looking at the values of stretching and contraction and their respective directions, this topological change can already be predicted from time steps before the actual breakup. In the first time step visualized in Fig. 2a, one can see smaller values represented by blue tube glyphs on the left side, indicating contraction along the curvature of the cylindrical structure. This contraction leads to a thinning of the ligaments. At the same time, stretching is visualized using red tube glyphs on the right side, acting in the directions towards the larger droplets. Looking at both stretching and contraction, this can be interpreted as fluid flow from the tunnels towards their endpoints, eventually leading to disintegration. In a subsequent time step, shown in Fig. 2b, the topological change of the lower horizontal tunnels can be observed.

On the other side, bending lends itself well to the analysis of simulations in which the change in curvature dominates the deformation process. As an example, a simulation of two drops of different species—left water and right ethanol—at the onset of coalescence is visualized for different time steps in Fig. 3. Both droplets have a diameter of 0.1495 cm. Due to a large difference of surface tension coefficients where the two drops meet, the Marangoni convection induces advection of the fluid from the ethanol drop, coating the surface of the water drop. Because of this advection along the surface, a capillary wave is formed, moving from where the drops are touching around the water drop on the left. This is an expected effect that was previously observed in experiments by Thoroddsen et al. [26], and can now be investigated further with our method. In Fig. 3a–c, the top row shows tube glyphs indicating an increase in convexity in front of the moving capillary wave, while in the bottom row one can see tube glyphs indicating an increase in concavity in the wake of the capillary wave.

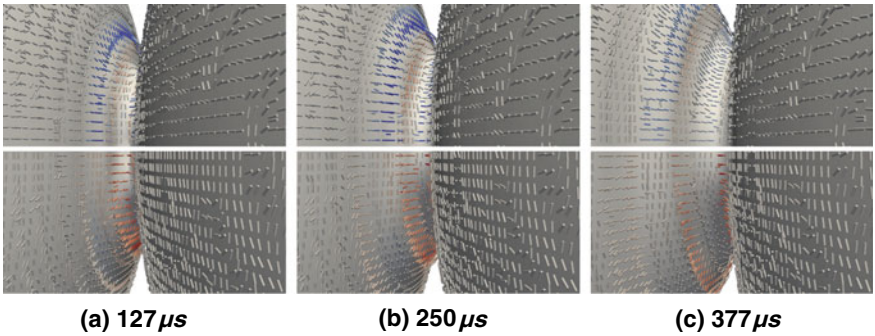

Fig. 3 Interface bending for a time series in the *Marangoni* dataset, where two initially static and barely touching droplets started to coalesce. In the top row, the negative values are depicted as blue tube glyphs indicating an increase in convexity. Red tube glyphs in the bottom row visualize positive values indicating an increase in concavity

3 Machine Learning for Droplet Behavior Prediction

While machine learning is already investigated for use in flow simulation solvers, e.g., for predicting regions of high uncertainty [17] or to speed up simulations [27], it can also be used in visualization. For visual analysis, an overview is given by Endert et al. [4].

The analysis of droplet behavior and droplet properties, especially due to the high dimensionality of the property space and the large number of different droplets, is not an easy task. Therefore, we want to use machine learning in order to predict droplet behavior, with respect to their properties, and to find droplets for which the learned model encounters a high prediction error. These droplets can be considered *interesting*, as they do not behave as predicted by the model and hence merit further investigation. This work is based on the Master's thesis by Heinemann [11].

3.1 Method

The method basically consists of three steps: segmentation of the simulation data into droplets and calculation of their characteristic properties for each time step, training a model using a deep neural network, and providing a visual analysis framework for the interactive visualization of the results.

As a first step, the simulation data has to be processed. This entails the segmentation into different droplets by analyzing the connectivity of non-empty cells in the volume of fluid field. While the segmentation is primarily done in order to be able to calculate droplet-specific properties, we also save the evolution of droplets in a graph, regarding topological changes due to collision and breakup. This graph is used later to define *traces* of droplets in subsequent time steps that can be used

for training. As properties, we aggregate many derived per-droplet quantities, such as the average velocity, rotational velocity, energies, surface-to-volume ratio, and so on.

For our machine learning approach, we train our model based solely on the input quantities, the input being one large vector storing all previously calculated properties per droplet. Our feed-forward neural network is then given k subsequent time steps of a droplet, as well as the following time step as result. Because droplet collision in multiphase flow is not influenced by the droplet's properties, we need to omit data which contains a collision. Here, we use our previously computed graph in order to filter out *traces* with collision events. Because one global trained model yields large prediction errors for certain properties, we train one separate model per property. In order to account for over-fitting, we use part of the data only for verification.

The resulting visualization framework allows us to analyze the trained results. In an overview, the total prediction error is visualized per droplet in a 3D view. Here, we can find and filter droplets based on prediction error or different properties. Then, a selected droplet can be analyzed further by visualizing the prediction error for each property, and comparing it to droplets with similar properties. Additionally, filtering, as well as brushing and linking allows the user to interactively analyze the data.

3.2 Results

All visualization steps are combined in a single visual analysis framework. Here, the simulation data, as well as all data generated by segmentation and training from machine learning, is visualized. An example is shown in Fig. 4. The window is split into sidebars where information about the selected droplet and the simulation data is shown and the user can apply filters. In the center, the simulation data and time series for similar droplets are shown in interactive 3D views.

The user is able to render a single time step or all time steps at once, and to filter for different properties. Additionally, color legends and the range of values can be adjusted, as well as different properties for visualization can be selected. All settings have an immediate effect on the rendered views, with rendering performed in real-time. To further analyze a droplet of interest, it can be selected by clicking on it. The views showing droplet properties are updated according to the selection. In the graphs, all relative errors for the droplet property predictions are visualized. Traces that show similar properties to the selected droplet are shown, with the top row showing the selected droplet's trace and the rows below showing the most similar traces, all visualized using the same color-coding. For further analysis of an *interesting* droplet found in our framework, external programs can be used, such as ParaView [1] for the example shown in Fig. 5.

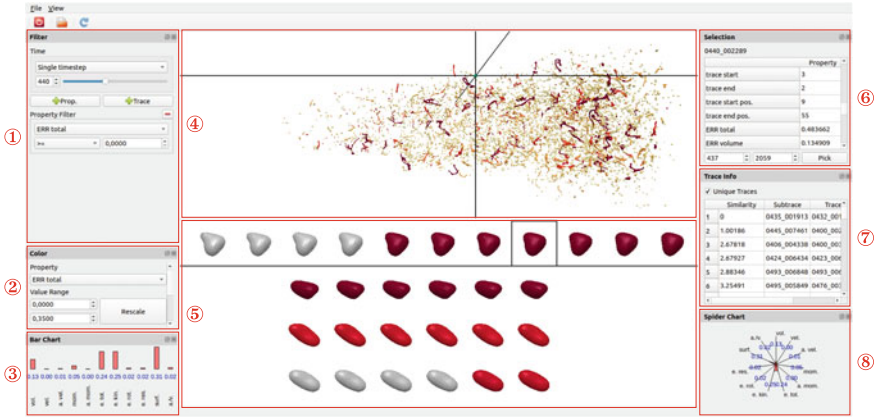

Fig. 4 Visual analysis framework for droplet behavior prediction. (1) Time step selection and filtering, here, filtering based on total error. (2) Color settings for visualized property. (3), (8) Bar and spider chart visualizing the relative error for different properties of the selected droplet. (4) 3D interactive overview showing the droplets of the jet dataset. (5) 3D interactive view of similar droplet traces. (6) Property view for the selected droplet. (7) Information about similar traces for the selected droplet

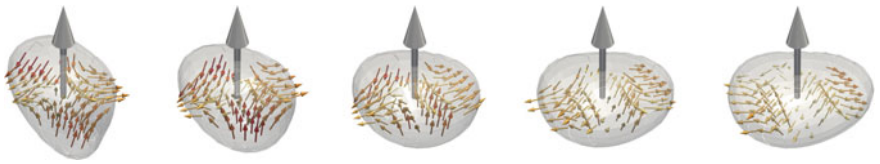

Fig. 5 Time series of a droplet deemed anomalous and found through the framework, indicating the general movement direction of the droplet, as well as visualizing the internal flow

4 Droplet-Local Flow

Topological changes and deformations are mostly influenced by the surface tension force [20]. However, fluid dynamics and thus interior flow of droplets are still of importance and impact droplet evolution. Therefore, to visualize the local flow of droplets, we propose modifications to streamlines, pathlines, and streaklines for the adaptation to 3D multiphase flow, as well as feature-based and droplet-local frames of reference. This work has been published in part by Straub et al. [24].

While streamlines, pathlines, and streaklines are well-established methods in flow visualization for 2D vector fields, they suffer from occlusion and visual clutter from overdraw in 3D. Therefore, different approaches have been developed in order to mitigate these problems. Popular techniques focus, e.g., on streamline seeding [18, 19] and opacity optimization [8, 9]. Our method's focus is on reducing occlusion and visual clutter by *removing* the translational and rotational velocity [13] of

droplets, essentially decomposing the input field [2]. This can be described as setting a frame of reference [7, 28]. Hence, it is even possible to combine our technique with seeding strategies and opacity optimization.

4.1 Method

Our method is composed of two steps. First, we have to compute the droplet-local velocity field by setting an individual frame of reference for each droplet. Then, streamlines, pathlines, or streaklines are drawn.

We calculate the translational velocity at the center of mass for each droplet, as well as the axis of rotation. In the following, we assume a cell-based grid where the velocity is defined at the cell center with a mass assigned to the whole cell. As the translational velocity $\mathbf{u}_c$ is simply the average velocity, it can be trivially described as the sum of all velocities $\mathbf{u}_i$, weighted by their respective masses $\mathbf{m}_i$. The axis of rotation $\boldsymbol{\omega}$ is calculated by minimizing the norm of the resulting velocities $\|\tilde{\mathbf{u}}_i\| = \left\|\mathbf{u}_i - \mathbf{u}_c - \boldsymbol{\omega} \times \mathbf{r}'_i\right\|$, with $\mathbf{r}'_i$ the positions relative to the center of mass. This minimization can be easily computed using least squares. The resulting droplet-local velocity field is defined by $\tilde{\mathbf{u}}_i = \mathbf{u}_i - \mathbf{u}_c - \boldsymbol{\omega} \times \mathbf{r}'_i$.

Similarly to the droplet-local velocity field, a feature-based velocity field can be computed. Here, the idea is to use line integration for the analysis of features, such as Lagrangian coherent structures (LCS) [10], e.g., finite time Lyapunov exponent (FTLE), or vortex core lines [15]. To this end, a velocity field is calculated, where the given structure, i.e., LCS or vortex core line, is fixed over time. This enables the user to analyze the flow relative to the given feature.

While there are no modifications needed for streamlines, some are needed for path- and streaklines. This is due to the fact that the *local* velocity field $\tilde{\mathbf{u}}(\mathbf{x}, t)$ is defined on the same domain as the original velocity field $\mathbf{u}(\mathbf{x}, t)$, hence it is not transformed. Therefore, the idea is to compute the original path- (or streak-) line and use its path $\mathbf{x}(t)$ for sampling at the correct position in the *local* velocity field. The *local* pathline is then defined by the initial value problem

$$\frac{\partial \tilde{\mathbf{x}}(t)}{\partial t} = T_{\omega}^{-1}\, \tilde{\mathbf{u}}(\mathbf{x}(t), t), \tag{1}$$

with initial position $\tilde{\mathbf{x}}(t_0) = \mathbf{x}(t_0) = \mathbf{x}_0$. Additionally, the velocities have to be transformed back into the droplet's original coordinate system at seeding time t_0, using the inverse rotation T_{ω}^{-1} given by integrating over all previous rotations $\boldsymbol{\omega}(t)$. The *local* streakline can be computed analogously, with the addition that the seed has to be moved, too. Those generalized streaklines have been previously introduced by Wiebel et al. [29]. Here, it is achieved by translating the seed with the translational velocity and rotating it around the axis of rotation.

Fig. 6 Original and local streamlines for the *Jet* dataset. Visualization of streamlines for the original vector field in the left image yields mostly straight lines. Interesting flow patterns can be observed in the local vector field on the right. The color indicates the flow direction from white to red

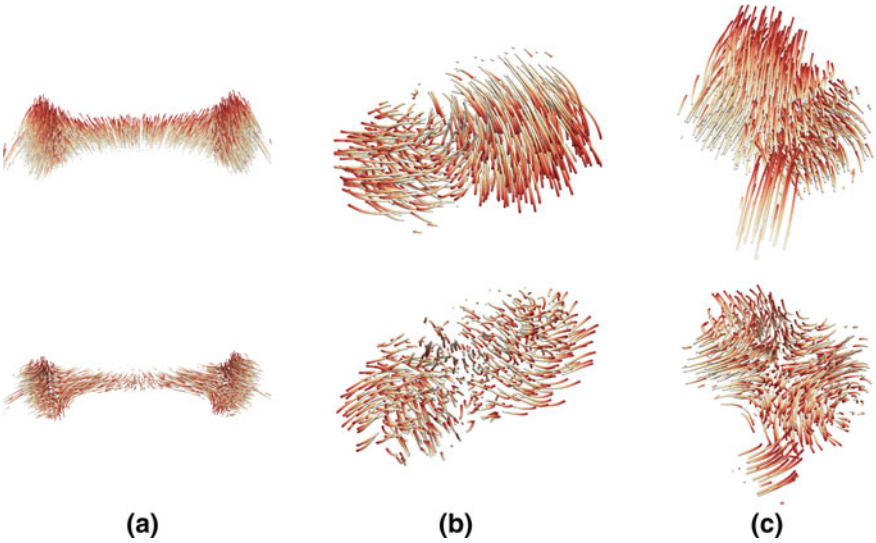

Fig. 7 Original and droplet-local pathlines for three examples in the *Colliding Drops* dataset. Pathlines for the original velocity field are shown in the top row, droplet-local pathlines in the bottom row. Again, the color indicates the flow direction from white to red

4.2 Results

A very trivial case, in which our method yields a better and more useful visualization, is for the *Jet* dataset depicted in Fig. 6. Here, the streamlines computed on the original field are mostly just straight lines due to the high translational velocity of the inflow. Hence, further analysis of the flow pattern is impossible. With our method, however, more detailed flow can be observed.

Some more complex cases can be observed in Fig. 7. In Fig. 7a, the pathlines for a ligament, which is moving upwards, is depicted. It is already observable from the original pathlines in the top image that the fluid is slightly moving towards the larger knobs at the side. In the visualization of the droplet-local pathlines, however, one can see that the relative movement of the particles within the ligament is directly towards those knobs, indicating that these will eventually form two separate droplets.

Figure 7b shows a droplet where in the visualization of the droplet-local pathlines two counter-rotating parts can be seen. In Fig. 7c one can observe a saddle structure in the droplet-local image in the bottom. However, this is not observable from the original pathlines in the top image.

5 Conclusion

Being driven by complex phenomena, free surfaces and flow dynamics have to be investigated. To this end, the presented work combines different approaches and methods for the visualization and analysis of droplets. Considering different aspects, the influences of different phenomena on droplet evolution, e.g., on breakup and deformation, are investigated in each of the projects using different visualization techniques:

- the influence of forces acting on the surface by visualizing shape changes,
- the influence of droplet and simulation properties using machine learning, and
- the influence of flow dynamics visualized as stream-, streak- and pathlines.

Acknowledgements This chapter was written by Alexander Straub and Thomas Ertl, but many more took part in the research for the herein presented projects (in alphabetical order): Sebastian Boblest, Steffen Frey, Moritz Heinemann, Grzegorz K. Karch, Filip Sadlo, Jonas Steigerwald, Gleb Tkachev, and Bernhard Weigand. This work was partially funded by Deutsche Forschungsgemeinschaft (DFG) as part of the Cluster of Excellence EXC 2075 "SimTech" (390740016), Transregional Collaborative Research Center SFB/Transregio 75 (84292822), and the International Research Training Group GRK 2160 "DROPIT" (270852890).

References

1. Ayachit, U.: The ParaView Guide: A Parallel Visualization Application. Kitware, Inc., New York (2015)
2. Bhatia, H., Pascucci, V., Bremer, P.: The natural Helmholtz-Hodge decomposition for open-boundary flow analysis. IEEE Trans. Vis. Comput. Graph. **20**(11), 1566–1578 (2014)
3. Eisenschmidt, K., Ertl, M., Gomaa, H., Kieffer-Roth, C., Meister, C., Rauschenberger, P., Reitzle, M., Schlottke, K., Weigand, B.: Direct numerical simulations for multiphase flows: an overview of the multiphase code FS3D. Appl. Math. Comput. **272**, 508–517 (2016)
4. Endert, A., Ribarsky, W., Turkay, C., Wong, B.L.W., Nabney, I.T., Blanco, I.D., Rossi, F.: The state of the art in integrating machine learning into visual analytics. Comput. Graph. Forum **36**(8), 458–486 (2017)
5. Floater, M.S., Hormann, K.: Surface parameterization: a tutorial and survey. In: Advances in Multiresolution for Geometric Modelling, pp. 157–186. Springer, Berlin (2005)
6. Grinspun, E., Hirani, A.N., Desbrun, M., Schröder, P.: Discrete shells. In: Proceedings of the 2003 ACM SIGGRAPH/Eurographics Symposium on Computer Animation, pp. 62–67. The Eurographics Association (2003)
7. Günther, T., Gross, M.H., Theisel, H.: Generic objective vortices for flow visualization. ACM Trans. Graph. **36**(4), 141:1–141:11 (2017)

8. Günther, T., Rössl, C., Theisel, H.: Hierarchical opacity optimization for sets of 3D line fields. Comput. Graph. Forum **33**(2), 507–516 (2014)
9. Günther, T., Theisel, H., Gross, M.H.: Decoupled opacity optimization for points, lines and surfaces. Comput. Graph. Forum **36**(2), 153–162 (2017)
10. Haller, G.: Lagrangian coherent structures. Ann. Rev. Fluid Mech. **47**(1), 137–162 (2015)
11. Heinemann, M.: ML-based visual analysis of droplet behaviour in multiphase flow simulations. Master's thesis, University of Stuttgart (2018)
12. Hirt, C.W., Nichols, B.D.: Volume of fluid (VOF) method for the dynamics of free boundaries. J. Comput. Phys. **39**(1), 201–225 (1981)
13. Karch, G.K., Beck, F., Ertl, M., Meister, C., Schulte, K., Weigand, B., Ertl, T., Sadlo, F.: Visual analysis of inclusion dynamics in two-phase flow. IEEE Trans. Vis. Comput. Graph. **24**(5), 1841–1855 (2018)
14. Karch, G.K., Sadlo, F., Meister, C., Rauschenberger, P., Eisenschmidt, K., Weigand, B., Ertl, T.: Visualization of piecewise linear interface calculation. In: IEEE Pacific Visualization Symposium (PacificVis 2013), pp. 121–128 (2013)
15. Kenwright, D.N., Haimes, R.: Vortex identification—applications in aerodynamics: a case study. In: IEEE Visualization '97, Proceedings, pp. 413–416. IEEE Computer Society and ACM (1997)
16. Lamanna, G., Tonini, S., Cossali, G.E., Weigand, B.: Selected results of the international research training group (GRK 2160/1) "droplet interaction technologies" (DROPIT). In: Proceedings of ICLASS 2018, 14th Triennial International Conference on Liquid Atomization and Spray Systems. ILASS (Institute for Liquid Atomization and Spray Systems) (2018)
17. Ling, J., Templeton, J.: Evaluation of machine learning algorithms for prediction of regions of high Reynolds averaged Navier Stokes uncertainty. Phys. Fluids **27**(8), 085103 (2015)
18. Marchesin, S., Chen, C., Ho, C., Ma, K.: View-dependent streamlines for 3D vector fields. IEEE Trans. Vis. Comput. Graph. **16**(6), 1578–1586 (2010)
19. McLoughlin, T., Jones, M.W., Laramee, R.S., Malki, R., Masters, I., Hansen, C.D.: Similarity measures for enhancing interactive streamline seeding. IEEE Trans. Vis. Comput. Graph. **19**(8), 1342–1353 (2013)
20. Myers, T.G.: Thin films with high surface tension. SIAM Rev. **40**(3), 441–462 (1998)
21. Obermaier, H., Joy, K.I.: Derived metric tensors for flow surface visualization. IEEE Trans. Vis. Comput. Graph. **18**(12), 2149–2158 (2012)
22. Popinet, S.: An accurate adaptive solver for surface-tension-driven interfacial flows. J. Comput. Phys. **228**(16), 5838–5866 (2009)
23. Straub, A.: Visualization of interface instabilities in two-phase flow. Master's thesis, University of Stuttgart (2016)
24. Straub, A., Heinemann, M., Ertl, T.: Visualization and visual analysis for multiphase flow. In: Proceedings of the DIPSI Workshop 2019. Droplet Impact Phenomena & Spray Investigations, pp. 25–27. Università degli studi di Bergamo (2019)
25. Straub, A., Karch, G.K., Boblest, S., Kaufmann, J., Sadlo, F., Weigand, B., Ertl, T.: Visual analysis of interface deformation in multiphase flow. In: Proceedings of the DIPSI Workshop 2018. Droplet Impact Phenomena & Spray Investigations, pp. 45–47. Università degli studi di Bergamo (2018)
26. Thoroddsen, S.T., Qian, B., Etoh, T.G., Takehara, K.: The initial coalescence of miscible drops. Phys. Fluids **19**(7), 072110 (2007)
27. Tompson, J., Schlachter, K., Sprechmann, P., Perlin, K.: Accelerating Eulerian fluid simulation with convolutional networks. In: Proceedings of the 34th International Conference on Machine Learning (ICML 2017), vol. 70, pp. 3424–3433. PMLR (2017)
28. Wiebel, A., Garth, C., Scheuermann, G.: Localized flow analysis of 2D and 3D vector fields. In: EuroVis05: Joint Eurographics—IEEE VGTC Symposium on Visualization, pp. 143–150. Eurographics Association (2005)

29. Wiebel, A., Tricoche, X., Schneider, D., Jänicke, H., Scheuermann, G.: Generalized streak lines: analysis and visualization of boundary induced vortices. IEEE Trans. Vis. Comput. Graph. **13**(6), 1735–1742 (2007)
30. Youngs, D.L.: An interface tracking method for a 3D Eulerian hydrodynamics code. Atomic Weapons Research Establishment (AWRE), Technical Report, 44(92) (1984)

On the Measurement of Velocity Field Within Wall-Film During Droplet Impact on It Using High-Speed Micro-PIV

Visakh Vaikuntanathan, Ronan Bernard, Grazia Lamanna, Gianpietro Elvio Cossali and Bernhard Weigand

Abstract The relationship between 'microscopic' velocity field and 'macroscopic' outcomes of liquid droplet impact on wall-films is not yet fully understood. This article reports a preliminary experimental investigation to measure the velocity field within wall-film when a droplet impacts on it, using micro-Particle Image Velocimetry (μ-PIV). The challenges associated with measuring the velocity field within the wall-film are outlined. In this context, the limitations of the traditional μ-PIV technique are discussed, leading to the adoption of high-speed μ-PIV as the suitable technique for measuring the spatio-temporal evolution of velocity within wall-film. The salient features of the high-speed μ-PIV set-up are discussed. Further, results from preliminary experimental investigations on water droplet impacting on water wall-film at moderate impact velocities are presented. It is seen that the current high-speed μ-PIV set-up can be used to obtain reliable measurements of in-plane radial velocity, V, at 'intermediate' values of radial, r, and temporal, t, coordinates. Within the measurement range of the current set-up, it is observed that V scales with r and t as $V \propto r/t$, which is similar to that reported in literature based on analytical considerations. The limitations of the current set-up, and the requirements for further experiments and validation are highlighted.

1 Introduction

The interaction of spray droplets with wall-films has been studied from a macroscopic perspective for quite some time [1]. However, the interaction of a liquid droplet with a wall-film made of a different liquid has not been explored in the same detail. Such

V. Vaikuntanathan (✉) · R. Bernard · G. Lamanna · B. Weigand
Institute of Aerospace Thermodynamics (ITLR), University of Stuttgart, Pfaffenwaldring 31, 70569 Stuttgart, Germany
e-mail: visakh.vaikuntanathan@itlr.uni-stuttgart.de

G. E. Cossali
Department of Engineering and Applied Sciences, University of Bergamo, Viale Marconi 5, 24044 Dalmine, Italy

G. Lamanna et al. (eds.), *Droplet Interactions and Spray Processes*,
Fluid Mechanics and Its Applications 121,
https://doi.org/10.1007/978-3-030-33338-6_17

droplet/wall-film interactions are commonly encountered in the form of fuel spray droplet impacting on lubricant wall-film in internal combustion engines [2] and spray droplets of aqueous urea solution impacting on wall-films of aqueous urea solution in automotive Selective Catalytic Reduction (SCR) systems [3–5]. Secondly, even though there have been numerous studies on the macroscopic outcome of a liquid droplet impacting on a wall-film of the same liquid (see the review article [1]), and a few recent studies with droplet and wall-film made of different liquids [2, 5–13], the microscopic velocity field within the wall-film responsible for the observed macroscopic outcomes is not known/studied to the same extent. These aspects set the broad motivation for the study presented in this chapter.

Macroscopically, when a liquid droplet impacts on a wall-film, a cylindrical crown-like structure is ejected radially outward and axially upward from the impact location. At some impact conditions, the rim of this crown destabilizes resulting in the formation of undulations on its surface, referred to as 'fingers'. When the growth rate of this rim instability is large enough, these fingers grow and undergo break-up to form secondary droplets—this outcome is commonly referred as 'crown splash'. When no such secondary droplets are formed, the outcome is referred as 'deposition'. The boundary between deposition and splash outcomes has been experimentally investigated from a macroscopic perspective, providing empirical correlations for the boundary in terms of non-dimensional parameters associated with impact such as Reynolds number, Ohnesorge number, and normalized wall-film thickness (see, for example, one of the earliest studies in [14] and the review article [1] for more details). However, the velocity and wall-film thickness fields responsible for the transition from deposition to crown splash are not yet understood. This sets the specific direction of the current study, that is, to understand the microscopic mechanisms leading to the macroscopic outcomes observed in liquid droplet impact on thin wall-films. More precisely, the study is directed towards understanding the velocity field within the wall-film responsible for the macroscopic outcomes of deposition and splashing (see Fig. 1). Additionally, finding the link between the velocity field within the wall-film and the crown angle at its base as well as the phenomenon of crown bottom breakdown [15] are of interest. For measuring the velocity field within the wall-film, the experimental approach based on μ-PIV is explored.

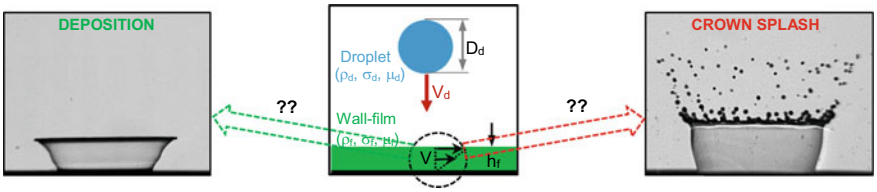

Fig. 1 Schematic illustration showing the phenomenon of droplet impact on wall-film, the associated parameters of interest, and macroscopic outcomes of deposition and crown splash

There are several challenges in using the traditional μ-PIV technique to study droplet impact on wall-films. The traditional μ-PIV technique, based on a double-pulsed low repetition rate laser and a high-resolution low frame rate camera, gives high temporal and spatial resolutions at a localized space-time coordinate in the flow field [16]. This is ideally suited for steady flows in micro-channels where it has been widely used [16]. The droplet impact phenomenon, on the other hand, is highly unsteady characterised by spatio-temporal changes in the velocity field within the wall-film as well as the wall-film thickness. Hence the traditional μ-PIV technique cannot be employed here to get an overall picture of velocity field within the wall-film. This is particularly true for droplet impacting on a wall-film made of a different liquid, since repetitive runs at shifted space and time coordinates would entail cleaning up the 'impure' wall-film and re-constructing the wall-film after each experimental run, out of hundreds of runs, at a given impact condition. Hence an alternative simpler strategy to this cumbersome experimentation process is needed.

This article reports the alternative set-up based on high-speed μ-PIV and its salient features in Sect. 2, followed by the results and discussion from a preliminary experimental investigation on distilled water droplet impacting on distilled water wall-film using this set-up in Sect. 3, and a summary of the main findings and recommendations for future work in Sect. 4. It should be noted here that even though the performance of the current set-up is demonstrated for distilled water droplet impacting on distilled water wall-film (details in Sects. 2 and 3), it could also be used for cases where the droplet and wall-film are made of different liquids.

2 Materials and Methods

In order to overcome the limitations of traditional μ-PIV technique, high-speed μ-PIV is employed. The entire set-up is shown in Fig. 2. A high-speed camera (FASTCAM SA-X2, Photron) together with a high intensity and high repetition rate light source (LED Constellation120E, Veritas) is used. A similar arrangement has been used for measuring velocity field inside droplets impacting on dry solid surfaces [17]. In the present case, the illumination is either in shadowgraph mode (as in Fig. 2) or from the bottom of the wall-film. The wall-film is formed on top of a sapphire glass plate of thickness $\approx$ 1 mm. Liquid droplet impact on this wall-film is imaged through the sapphire glass plate from its bottom with the help of microscope objectives (Carl Zeiss) giving overall magnifications from 12.5× to 400×. The image is projected onto the sensor of the high-speed camera giving spatial and temporal resolutions of $\approx$ 11 μm (at 12.5×) and $\approx$ 80 μs (at 12,500 fps), respectively. The wall-film is seeded with polystyrene (PS) tracer particles of diameter around 30 μm.

For this preliminary investigation, distilled water is used as the experimental liquid for both the droplet and the wall-film. Both the droplet and wall-film liquids are seeded with the PS tracer particles. Distilled water droplets of radius, R_d around 1.65 mm (±0.02 mm) could be repeatedly produced by pushing the liquid stored in a syringe (1 or 10 mL) through a blunt-tipped needle. The height of the needle tip

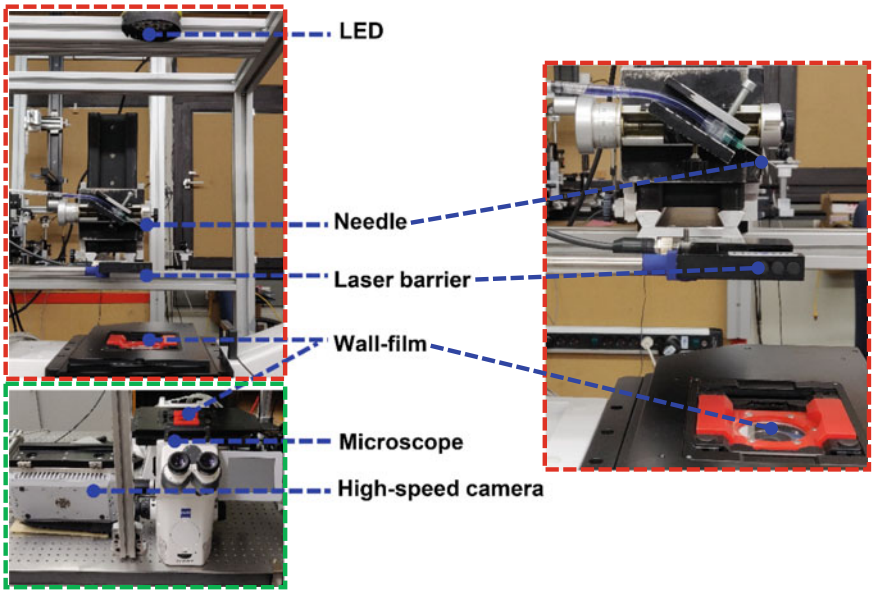

Fig. 2 The experimental set-up to perform high-speed μ-PIV, highlighting its salient components: Side view (red outline), magnified side view (right) showing the needle, laser barrier, and wall-film (red outline), and inclined front view (green outline)

from the surface of wall-film could be adjusted to simulate different droplet impact velocities. To create the wall-film of a desired thickness, the corresponding volume (knowing the diameter of the pool geometry) is taken in using a micro-pipette and gradually injected over the sapphire glass plate surface until a film is formed. All the data presented in this chapter correspond to a droplet impact velocity, V_d of around 2.66 m/s (±0.07 m/s) and wall-film thickness, h_f of around 0.5 mm (±0.05 mm). This corresponds to a non-dimensional wall-film thickness, $\delta = h_f/2R_d$ of around 0.15 (±0.02). Considering the properties of the droplet and wall-film (density, $\rho_d = \rho_f \approx 1000$ kg/m^3; dynamic viscosity, $\mu_d = \mu_f \approx 1$ mPa s; surface tension, $\sigma_d = \sigma_f \approx 72.8$ mN/m), the non-dimensional parameters corresponding to $V_d \approx 2.66$ m/s can be calculated as follows: $Re = 2\rho_d V_d R_d/\mu_d \approx 8778$; $We = 2\rho_d V_d^2 R_d/\sigma_d \approx 321$; and $\mathrm{Oh} = We^{0.5}/Re \approx 0.0020$.

3 Results and Discussion

Figure 3 shows typical high-speed microscopic shadowgraphy images of a water droplet impacting on water wall-film. One of the limitations of the shadowgraphy approach is the inability to observe the velocity field within the wall-film near the

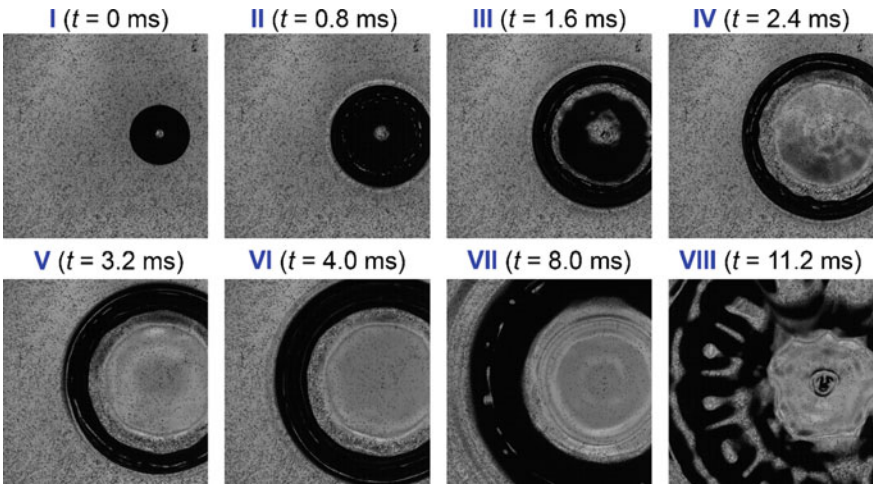

Fig. 3 Typical high-speed images captured using the high-speed μ-PIV set-up (Fig. 2). The time coordinate corresponding to each frame is indicated above the corresponding frame. Impact conditions: Droplet: distilled water; wall-film: distilled water; droplet radius, $R_d \approx 1.65$ mm; droplet impact velocity, $V_d \approx 2.66$ m/s; wall-film thickness, $h_f \approx 0.5$ mm. Both the droplet and wall-film are seeded with polystyrene tracer particles of diameter around 30 μm

neck region of the crown base (dark region in Fig. 3) and at the impact location during the early stages of impact. Another limitation of this technique is the inability to directly measure the out-of-plane velocity component, which is significant near the crown wall and at the impact location during the early stages of impact. Hence the current technique is ideally suited only for velocity field measurements at 'intermediate' values of the radial and time coordinates (r and t). Keeping these limitations and the measurement range of the set-up in mind, the results from the preliminary experimental investigations are presented and discussed below.

Figure 4 (*right*) shows the in-plane radial velocity, V, extracted from a typical high-speed image (Fig. 4 (*left*)), corresponding to a given time coordinate, t, using the open-source MATLAB application PIVlab [18]. The measurements are obtained at three typical radial coordinates (highlighted by circles marked as R1, R2, and R3 in Fig. 4 (*left*)). The variation of V with the azimuthal coordinate along each of these three circles is shown in Fig. 4 (*right*). The azimuthal coordinate along each of the circles is expressed in radians in X-axis, the radial velocity in Y-axis is expressed in pixels/frame, radial coordinates of the circles R1, R2, and R3 are indicated in pixels, and the scaling factors to convert pixels to metres and frames to seconds are given in Fig. 4 (*right*). Three main observations can be made from Fig. 4 (*right*):

(i) At a given radial location, V shows fluctuations along the azimuthal coordinate, with the corresponding average, V_{avg}, and the standard deviation of the fluctuations shown respectively by continuous and dashed horizontal lines of the same colour.

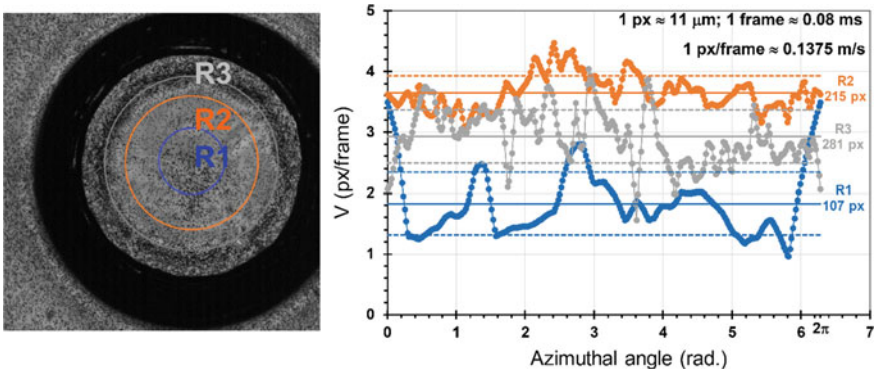

Fig. 4 (*Right*) Variation of in-plane radial velocity, V, (symbols connected by lines) with the azimuthal coordinate/angle measured along circles at three typical radial coordinates (R1, R2, and R3) as highlighted in a typical high-speed image at a given time coordinate t (*left*). The values of V measured at a given radial coordinate are averaged to get V_{avg} (continuous horizontal lines), and the corresponding upper and lower limits of V (dashed horizontal lines) are calculated as $V_{avg} + V_\sigma$ and $V_{avg} - V_\sigma$, V_σ being the standard deviation of V from V_{avg}

(ii) The average radial velocity, V_{avg}, increases with increase in radial coordinate from R1 to R2. This is in line with the scaling reported in literature based on analytical considerations [19].

(iii) The average radial velocity, V_{avg}, decreases with a further increase in radial coordinate from R2 to R3. It is clear from Fig. 4 (*left*) that in the vicinity of R3 there is an accumulation of particles as evidenced by a higher concentration of particles. This accumulation of particles is possibly due to a higher radial inflow compared to radial outflow of mass, and the difference in the mass flow may be re-directed normal to the plane of observation. This is highly plausible since the crown wall, where an intense out-of-plane re-direction of mass flow is expected, is in the vicinity of R3. Furthermore, the interface of droplet and wall-film, defined by a thick droplet rim, could be in the vicinity of R3, and hence the appearance of a 'bump-like' structure, where particles are accumulated due to an out-of-plane velocity component associated with the 'bump'. The decrease in V_{avg} from R2 to R3 could, hence, be due to an unaccounted out-of-plane velocity component, which is not directly measured using the current set-up.

Figure 5 shows the variation of V_{avg} with the radial coordinate at four typical times during the expansion of the crown base. During 'early' stages of the impact ($t \lesssim 3$ ms), V_{avg} increases with r, reaches a maximum, and then decreases with further increase in r. This non-monotonous trend of V_{avg} with r, as discussed with Fig. 4, could be due to the increase in out-of-plane velocity component with increasing r, associated with the flow re-direction into the crown wall. The effect of this flow re-direction becomes less important at 'later' stages ($t \gtrsim 3$ ms) as evidenced by the absence of a non-monotonous trend at $t = 3.36$ ms and $t = 4.24$ ms. At these later stages, V_{avg} increases with r and then remains constant after a certain radial

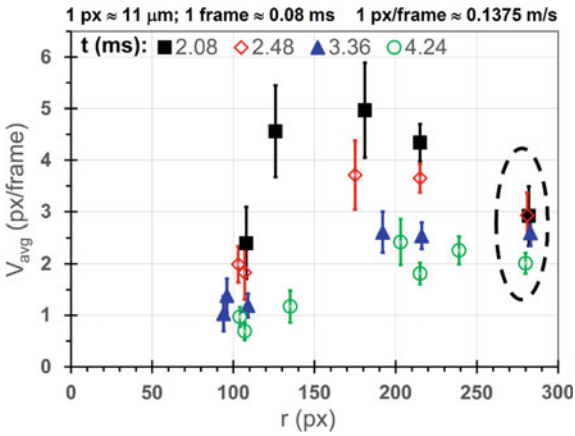

Fig. 5 Variation of azimuthally averaged radial velocity, V_{avg}, with radial coordinate at four typical time coordinates during the expansion of the crown base

coordinate (see the blue triangles and green circles in Fig. 5). Moreover, at a given radial coordinate, V_{avg} decreases with t, especially during the 'early' stages of impact. The velocity measurements in the vicinity of the 'bump-like' structure, where particle accumulation is seen, are marked by a dashed envelope in Fig. 5.

Figure 6 shows the azimuthally averaged radial velocity as a function of the similarity variable r/t. The data of V_{avg} in the vicinity of the 'bump-like' structure is not included in this plot. It is evident that there is a one-to-one correspondence between V_{avg} and r/t, suggesting a scaling between the two parameters; that is, $V_{avg} \propto r/t$. This is quite similar to the scaling for velocity within the film/lamella, V_l during droplet impact on wetted surfaces, $V_l = r/(t + \tau)$ reported, based on analytical considerations, in the literature (τ is a constant defined by initial conditions) [19].

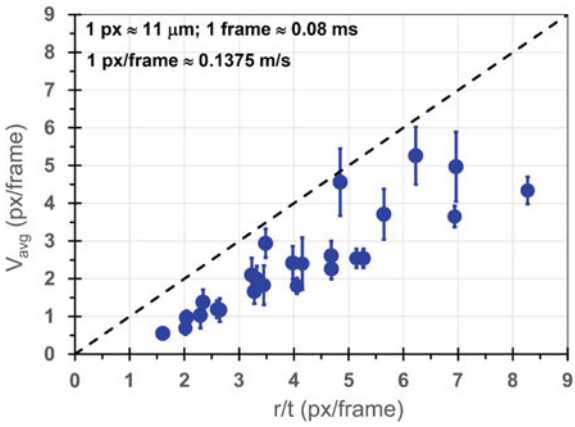

Fig. 6 Variation of azimuthally averaged radial velocity, V_{avg}, with the similarity coordinate, r/t. The error bars correspond to one standard deviation of the measurements from the average value. The dashed line plots the trend $V_{avg} = r/t$

4 Conclusions

An experimental investigation to measure the velocity field within a wall-film liquid when a liquid droplet impacts on it was reported. The challenges associated with the spatial and temporal scales associated with the droplet impact phenomenon, as well as the highly unsteady nature of the process were highlighted. The limitations associated with the application of traditional μ-PIV technique to this challenging problem were highlighted. Based on these, it was concluded that a high-speed μ-PIV technique is well-suited to measure the spatio-temporal variation of velocity within the wall-film when a droplet impacts on it.

The salient features of the high-speed μ-PIV set-up were detailed. Results from preliminary experimental investigations using the high-speed μ-PIV set-up were presented and discussed. At 'intermediate' values of radial, r and time, t coordinates, it was seen that the azimuthally averaged radial velocity, V_{avg} follows the scaling, $V_{avg} \propto r/t$. This is quite similar to the scaling reported in literature for droplet impact on dry and wet solid surfaces based on analytical considerations [19]. However, the current methodology based on high-speed shadowgraphy, relatively low magnification, and relatively large tracer particles restricts it from measuring z-resolved velocity field in the vicinity of crown wall and at very early stages in the vicinity of droplet impact location. In addition, the current methodology does not allow for the measurement of the out-of-plane velocity component responsible for the emergence of crown wall.

The ongoing experimental campaign uses a combination of shadowgraphy and bottom-lit illumination, and higher magnification with smaller tracer particles to measure z-resolved velocity field near the crown neck. Using smaller tracer particles is especially important when quantitatively comparing the experimental results with the predictions from analytical models, since the Stokes number, Stk, associated with the flow around the tracers should ideally be much less than 1 for an accurate measurement of the flow field. For PS particles (density, $\rho_p = 1050$ kg/m^3) of diameter, $d_p = 30$ μm used in this preliminary study with distilled water, $Stk \approx \rho_p V_d d_p / 18\mu_f \approx 4.7$ (with the velocity scale for flow around the particle approximated by V_d). However, with further studies on more viscous wall-films (such as silicone oils with $\mu_f \geq 5$ mPa.s), these PS particles in smaller size ($d_p = 10$ μm) could be more suitable. Incorporating macroscopic high-speed imaging in the current high-speed μ-PIV set-up is needed to relate one-to-one between the macroscopically observed outcomes and the microscopic velocity field measured within the wall-film. Furthermore, to measure out-of-plane velocity component in this region, astigmatism μ-PTV [20] and calculation using an additional measurement of the film thickness field will be explored. Tracer particles suitable for fuel droplets (say, diesel) and lubricant wall-films (say, silicone oil) will be used, to understand fuel-oil interactions in automotive engines.

Acknowledgements The authors gratefully acknowledge the financial support of the Deutsche Forschungs-gemeinschaft (DFG) within the framework of the international research training group "Droplet Interaction Technologies"—DROPIT (GRK2160/1).

References

1. Liang, G., Mudawar, I.: Review of mass and momentum interactions during drop impact on a liquid film. Int. J. Heat Mass Transf. **101**, 577–599 (2016)
2. Geppert, A., Chatzianagnostou, D., Meister, C., Gomaa, H., Lamanna, G., Weigand, B.: Classification of impact morphology and splashing/deposition limit for n-hexadecane. Atom. Sprays **26**, 983–1007 (2016)
3. Schweigert, D., Damson, B., Lüders, H., Börnhorst, M., Deutschmann, O.: Heat transfer during spray/wall interaction with urea water solution: an experimental parameter study. Int. J. Heat Fluid Flow **78**, 108432 (2019)
4. Weingarten, E., Bayer, T., Chaineux, M., Lüders, H., Bareiss, S.: Bosch AdBlue dosing technology for EU6-RDE and beyond. In: Tschöke, H., Marohn, R. (eds.) 11. Tagung Einspritzung und Kraftstoffe 2018. Proceedings, Springer Vieweg, Wiesbaden (2019)
5. Terzis, A., Kirsch, M., Vaikuntanathan, V., Geppert, A., Lamanna, G., Weigand, B.: Splashing characteristics of diesel exhaust fluid (AdBlue) droplets impacting on urea-water solution films. Exp. Therm. Fluid Sci. **102**, 152–162 (2019)
6. Thoroddsen, S.T., Etoh, T.G., Takehara, K.: Crown breakup by Marangoni instability. J. Fluid Mech. **557**, 63–72 (2006)
7. Banks, D., Ajawara, C., Sanchez, R., Surti, H., Aguilar, G.: Effects of drop and film viscosity on drop impacts onto thin films. Atom. Sprays **23**, 525–540 (2013)
8. Geppert, A., Terzis, A., Lamanna, G., Marengo, M., Weigand, B.: A benchmark study for the crown-type splashing dynamics of one- and two-component droplet wall-film interactions. Exp. Fluids **58**, 172(1–27) (2017)
9. Bernard, R., Foltyn, P., Geppert, A., Lamanna, G., Weigand, B.: Generalized analysis of the deposition/splashing limit for one- and two-component droplet impacts upon thin films. In: 28th European Conference on Liquid Atomization and Spray Systems, 6–8 Sept 2017
10. Chen, N., Chen, H., Amirfazli, A.: Drop impact onto a thin film: miscibility effect. Phys. Fluids **29**, 092106(1–7) (2017)
11. Aljedaani, A.B., Wang, C., Jetly, A., Thoroddsen, S.T.: Experiments on the breakup of drop-impact crowns by Marangoni holes. J. Fluid Mech. **844**, 162–186 (2018)
12. Kittel, H.M., Roisman, I.V., Tropea, C.: Splash of a drop impacting onto a solid substrate wetted by a thin film of another liquid. Phys. Rev. Fluids **3**, 073601(1–17) (2018)
13. Shaikh, S., Toyofuku, G., Hoang, R., Marston, J.O.: Immiscible impact dynamics of droplets onto millimetric films. Exp. Fluids **59**, 7(1–12) (2018)
14. Cossali, G.E., Coghe, A., Marengo, M.: The impact of a single drop on a wetted solid surface. Exp. Fluids **22**, 463–472 (1997)
15. Geppert, A., Terzis, A., Lamanna, G., Marengo, M., Weigand, B.: On the formation of secondary droplets from crown bottom breakdown during droplet impact on very thin films. In: 27th European Conference on Liquid Atomization and Spray Systems, 4–7 Sept 2016
16. Wereley, S.T., Meinhart, C.D.: Recent advances in micro-particle image velocimetry. Ann. Rev. Fluid Mech. **42**, 557–576 (2010)
17. Smith, M.I., Bertola, V.: Particle velocimetry inside Newtonian and non-Newtonian droplets impacting a hydrophobic surface. Exp. Fluids **50**, 1385–1391 (2011)
18. Thielicke, W., Stamhuis, E.: PIVlab—towards user-friendly, affordable and accurate digital particle image velocimetry in MATLAB. J. Open Res. Software **2**, e30 (2014)
19. Roisman, I.V., Tropea, C.: Impact of a drop onto a wetted wall: description of crown formation and propagation. J. Fluid Mech. **472**, 373–397 (2002)
20. Cierpka, C., Rossi, M., Segura, R., Mastrangelo, F., Kähler, C.J.: A comparative analysis of the uncertainty of astigmatism-μPTV, stereo-μPIV, and μPIV. Exp. Fluids **52**, 605–615 (2012)

Single-Camera 3D PTV Methods for Evaporation-Driven Liquid Flows in Sessile Droplets

Massimiliano Rossi and Alvaro Marin

Abstract The experimental characterization of liquid flows in sessile evaporating droplets is an important task for the fundamental understanding of the complex phenomena occurring in these apparently simple systems. The liquid flow induced by the droplet evaporation has a strong three-dimensional character and conventional visualization methods are typically difficult to apply. A more effective approach is to look inside the droplets from the substrate where the droplet lies and use single-camera 3D particle tracking velocimetry (PTV) methods to reconstruct the whole flow field. This paper discusses the implementation of an experimental setup for the quantitative characterization of the flow inside sessile evaporating droplets based on two single-camera 3D PTV methods: the Astigmatic Particle Tracking Velocimetry (APTV) and the General Defocusing Particle Tracking (GDPT). Exemplary results on different types of sessile evaporating droplets are reported and discussed. The presented approach is easy to implement, does not require special or costly equipment, and has the potential to become a standard tool for this type of experiments.

1 Introduction

The evaporation of droplets of water or other liquids is a ubiquitous phenomenon in nature and in many engineering and technological processes. The internal and superficial flows that spontaneously develop during the evaporation process are not trivial and depend on the droplet composition, substrate material, temperature and humidity of the surrounding, and other factors. The characterization and understanding of

M. Rossi (✉)
Department of Physics, Technical University of Denmark, DTU Physics Building 309, 2800 Kongens Lyngby, Denmark
e-mail: rossi@fysik.dtu.dk

A. Marin
Physics of Fluids Group, Max Planck Center for Complex Fluid Dynamics, University of Twente, Enschede, The Netherlands
e-mail: a.marin@utwente.nl

G. Lamanna et al. (eds.), *Droplet Interactions and Spray Processes*,
Fluid Mechanics and Its Applications 121,
https://doi.org/10.1007/978-3-030-33338-6_18

such flows is an active field of research and have important implications in many technological and biological processes, especially when the control or prediction of the shape and composition of the stain left at the end of the evaporation process is needed [1–3].

A classic example encountered in our everyday life is the ring-shaped stain observed when a spilled droplet of coffee dries out. Deegan et al. [4] in 1997 showed that particles are pushed to the ring-shaped stain due to a capillary flow that forces liquid (and the coffee particles dispersed in the liquid) toward the contact line to replenish the liquid lost during evaporation and maintain a minimal liquid-air surface (Fig. 1a). Additionally, the evaporation process cools down the liquid to a temperature lower than the one in the substrate, therefore temperature and surface tension gradients build up across the droplet and drive a Marangoni flow at the liquid-air surface [5]. In the case of water at room temperature, the thermal Marangoni flow is directed from the contact line toward the drop summit and has a strong influence on the final particle deposit (Fig. 1b).

The presence of surfactants, mineral salts or surface-active components dissolved in the liquid phase also has a huge impact on the internal and superficial flows [6, 7]. For example, chaotropic salts, such as NaCl, when dissolved in polar liquids as water increase the surface tension. In an evaporating water salty droplet, salt quickly concentrates at the drop corner where the liquid evaporation rate is stronger. This can reverse the direction of the Marangoni flow and the circulation of the internal flow, which must comply with the volume conservation (Fig. 1c). Surfactants lead to even more complex and unpredictable scenarios, due to the complexity of surfactant adsorption/desorption from the interface, micelle formation in the bulk, and the

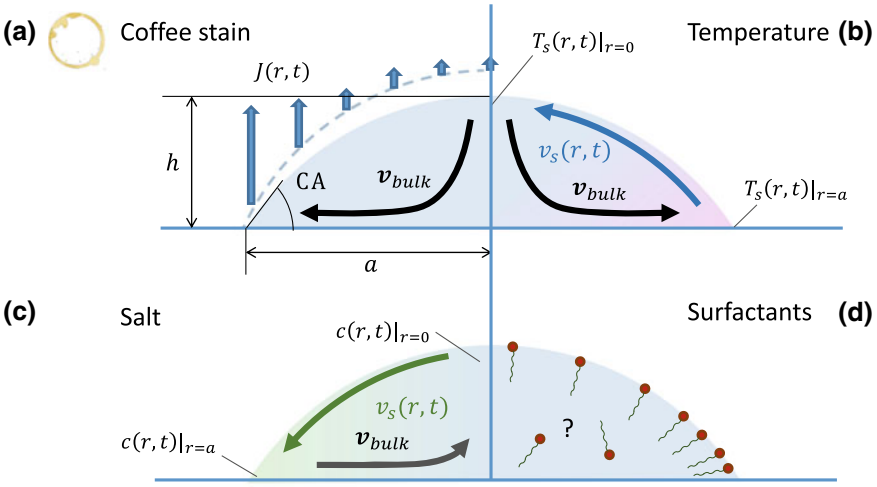

Fig. 1 Example of internal and superficial flows in sessile evaporating droplets: **a** Capillary flow, **b** thermal Marangoni flow, **c** concentration-driven Marangoni flow, **d** flow with surfactants

continuous decrease of liquid/air interface during the evaporation process [8, 9]. For this reason, very different liquid flow configurations can be observed depending on the nature of the surfactant and the stage of the droplet evaporation, as will be described below (Fig. 1d). Note that all cases discussed in the following chapters will use water as working liquid.

The experimental visualization or quantification of such flows is of paramount importance for the understanding of these phenomena and for the development and validation of numerical simulations or analytical models. Flow measurements inside evaporating droplets are, however, not an easy task, since conventional 2D or 3D visualization techniques fail when looking through a curved moving interface, as the drop interface. Another option is to look inside the drop from the bottom, but conventional methods will provide in this case a 2D projection of a complex 3D flow which is, in the best case scenario, difficult to interpret, but often gives a wrong picture of the flow field.

A solution is provided by the use of particle tracking methods based on a single-camera view, that allow to track the three-dimensional displacement of tracer particles dispersed in the fluid. In particular, methods based on defocusing have recently been used to characterize with unprecedented resolution the internal and superficial flow of different types of evaporating droplets [10–12]. In comparison with other methods such as confocal microscopy or holography, these methods do not need costly equipment and can be implemented using conventional inverted microscopes. Additionally, confocal microscopy and optical coherence tomography suffer of several constraints on both recording frame rates and total length of record, which can be easily avoided using single-camera 3D-PTV methods. In this work, we consider two methods, the Astigmatic Particle Tracking Velocimetry (APTV) and the General Defocusing Particle Tracking (GDPT), which have been successfully used to characterize the full flow field in evaporating droplets with excellent spatial and temporal resolution during the whole evaporation process [10–12]. In Sect. 2, the general guidelines to implement a suitable experimental setup are discussed as well as the basic principles of the methods. In Sect. 3, some examples of the results obtained with these methods on different types of sessile evaporating droplets are presented. Conclusions are provided in Sect. 4.

2 Materials and Methods

2.1 Experimental Setup

A schematic of a general experimental setup to perform single-camera 3D PTV measurements on sessile evaporating droplets is depicted in Fig. 2. The droplets are gently deposited on a transparent substrate (typically a microscope slide) and then placed inside a measurement chamber. The first purpose of the chamber is to protect the droplet from unwanted air flows, which can significantly disturb the superficial and

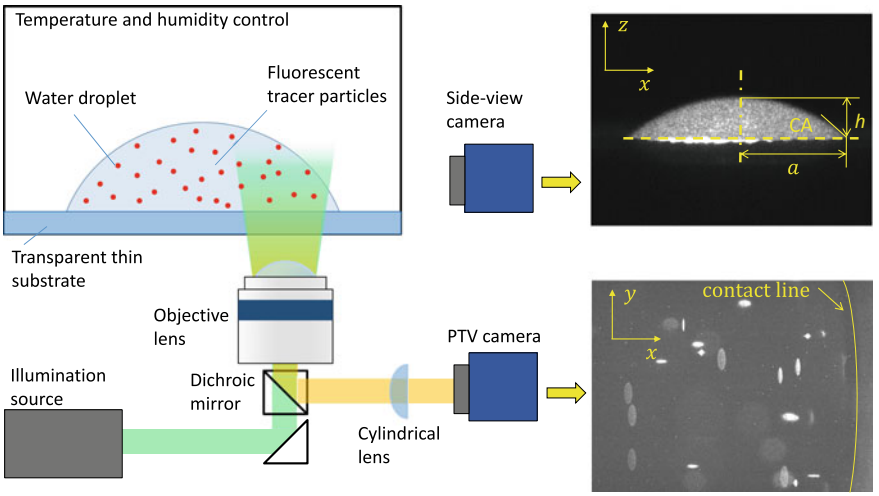

Fig. 2 Typical experimental setup to measure the internal flow of sessile evaporating droplets using the GDPT method including a side view camera to monitor the evaporation process

internal flows. For experiments where the active control of temperature or humidity is not required [11, 12], their values can be approximated to the ones measured in the laboratory. In this case, it is important that the chamber is not sealed otherwise the relative humidity inside will increase due to the evaporation process, changing continuously the boundary conditions. If active control of temperature and humidity is required, the chamber must be equipped with a suitable feedback-control system. The temperature control can be achieved using Peltier elements or microscope incubators [10]. The equipment for full humidity control is more complicated and expensive, however, for chambers relatively small (less than 0.2 l with droplet diameters of 1–10 mm), the vapour supply provided by the droplet is sufficient to rapidly saturate the chamber, therefore the humidity can be regulated simply by a controlled flow of dry air [10].

The global parameters to characterize the evaporation process, which are droplet radius, volume, and contact angle (CA), can be measured simultaneously from a side view of the droplet, as shown in Fig. 2. A teleobjective lens or a long-range microscope [10–12] are normally needed to achieve sufficient resolution. The drop radius, height, and CA can directly be measured after proper calibration from analysis of the side-view images, whereas the volume can be derived from these parameters considering that sessile water droplets always assume a spherical-cap geometry, as long as the radius/height of the droplet is below the liquid's capillary length.

To perform the flow velocity measurement with particle tracking, the liquid droplets need to be previously seeded with tracer particles. The particles in the fluid are observed from the bottom through the transparent substrate by means of an inverted microscope. The optical system is chosen in order to have particle images

with different shape depending on their depth position (as a consequence of defocusing or astigmatism, as described in the next section), therefore the full 3D displacement of each particle within a certain measurement volume can be determined. This approach allows to look at the internal flow of the droplets avoiding problems due to curved and moving surfaces, as it would be if the particles were observed from a top or side view.

As tracer particles, polystyrene spheres with a diameter of 1–2 μm functionalized with sulfate or carboxyl groups are typically used for measurements. The particle functionalization is specially important to disperse the polystyrene particles in polar liquids as water, which will be the liquid used for the cases discussed. Smaller particles would be strongly affected by the Brownian motion, whereas larger particles will tend to sediment within the time of a typical evaporation experiment (the polystyrene density $\rho_{PS} = 1050$ kg/m^3 is slightly larger than the one of water). To improve the image quality, the particles are commonly labelled with a fluorescent dye and observed with an epifluorescent system. In such system, the particles are illuminated with a monochromatic light (provided by a laser or high-power LED) at the excitation wavelength of the fluorescent dye, and a suitable dichroic mirror with longpass filter is used to acquire images only by collecting the light emitted by the particles. With this approach, most of the noise due to reflection or background patterns can be eliminated, and clear bright particle images on a dark background can be obtained (see example figure in Fig. 2).

2.2 Single-Camera 3D PTV Methods

The single-camera 3D PTV methods used to obtain the results presented in the following section rely on the fact that the tracer particles in the droplet are observed through an optical system with small depth of field (such as microscope objectives). In this case, the particle images are not in focus but have different degree of defocusing depending on their depth position. In general, the more a particle moves away from the focal plane of the objective lens, the larger will be the diameter of the corresponding particle image. This information can be used to obtain the depth position of the particle. A simple measurement of the particle image diameter, however, is not sufficient to determine whether the particle is behind or after the focal plane, due to symmetry reasons. Therefore, more sophisticated approaches are needed.

Astigmatic Particle Image Velocimetry (APTV). A clever approach to encode more efficiently the defocusing information is to induce an astigmatic aberration in the optical path using a cylindrical lens in front of the camera sensor [13]. In this way, there is no single focal plane and a particle image will be in focus in the horizontal direction in a different position than in the vertical direction, resulting in elliptical particle images. From the measurement of the length of major and minor axis of the particle images is then possible to measure the corresponding depth position of the particle (see Fig. 3a and Refs. [14, 15]).

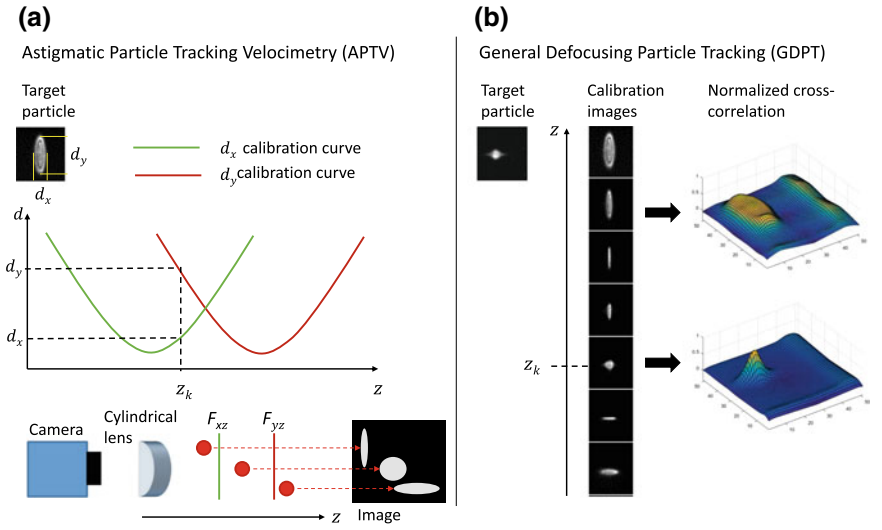

Fig. 3 Measurement methods for 3D particle tracking with a single camera. **a** Astigmatic Particle Tracking Velocimetry (APTV) [13–15]. **b** General Defocusing Particle Tracking (GDPT) [16, 17]

General Defocusing Particle Tracking (GDPT). A more general approach is to create a look-up table that maps the different particle images with their depth positions. Afterwards, a pattern recognition algorithm can be used to compare the recorded particle image with the ones in the look-up table and obtain the depth position [16]. In particular, we used here the peak value of the normalized cross-correlation between target and calibration images to rate their similarity (See Fig. 3b), with values from 0 to 1 (being 1 the perfect match). This approach has the advantage to be completely general and to rely only on the assumption that the particle images change in a systematic fashion with respect to their depth position. GDPT can work well with astigmatic optics but also with conventional optics that show a certain degree of spherical aberration (present in most conventional lenses). The spherical aberration introduces also an asymmetry in the particle image shape depending if it is behind or after the focal plane [18]. More information on this method and a freely-available software for GDPT analysis can be found in [17].

3 Results and Discussion

The results presented in this section have been obtained using the general experimental setup described in Sect. 2, and GDPT or APTV as single-camera PTV method. As tracer particles, polystyrene spheres with a diameter of 1 or 2 μm were used. For the liquids and evaporation conditions analysed, it has been demonstrated experimentally that this type of tracer particles follow faithfully the flow and the effect

of Brownian motion or sinking velocity is negligible [10]. For more details about experimental procedures and data processing, we refer to Refs. [10–12].

3.1 Ultrapure Water

In the simplest case of evaporation of sessile droplets of ultrapure water (UPW), the capillary flow described by Deegan et al. [4] is the dominant one, pushing the liquid in the bulk toward the contact line. Additionally, a weak but persistent temperature gradient develops across the droplet, since the liquid is cooled down by the evaporation process driving a heat flux from the substrate at larger temperature. The temperature gradient is extremely small, far below 1 K/mm, but sufficient to drive a thermal Marangoni flow on the surface.

Flow measurements performed with GDPT on a 2-mm-diameter sessile droplet of UPW are shown in Fig. 4a, for different CAs. Note that since CA decreases linearly in time, it is proportional to the *remaining evaporation time,* i.e. the time left before the end of the evaporation process. The measurements are originally three-dimensional but have been converted to cylindrical coordinates and plotted on the rz-plane on account of the axisymmetry of the system. The capillary flow is clearly visible, with the flow velocity increasing as it approaches the contact line, with velocities up to 4 μm/s. The thermal Marangoni flow is also present on the surface, directed toward the drop summit. A more detailed picture of the Marangoni flow is given in Fig. 4b, where the intensity of the superficial flow as a function of radial position and CA is shown. It can be seen as the larger magnitude of the Marangoni flow is observed close to the contact line ($r/a = 0.9$, with a being the droplet radius) with values around 2 μm/s, and it decreases as the droplet evaporates (i.e. for smaller CA).

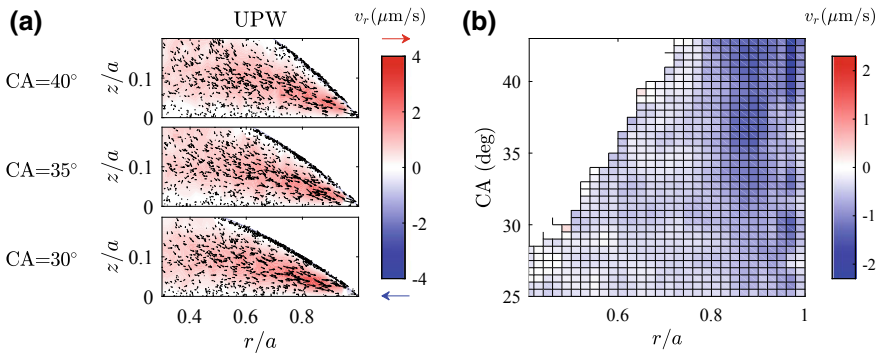

Fig. 4 **a** GDPT measurements of the flow field inside sessile evaporating droplets of UPW for different CA. **b** Magnitude of the thermal Marangoni flow as a function of radial position and CA [10]

3.2 *Mineral Water*

The measurements in Fig. 4 are in good qualitative agreement with numerical and analytical simulations, however they show values that are 2–3 orders of magnitude smaller than what predicted by the simulations [10, 19, 20]. The origin of this disagreement is still an open question and it is often suggested that it is due to the presence of insoluble surfactants. However, this assumption has never been proven experimentally, neither the nature of such insoluble surfactant contaminant identified. One strategy to check the effect of tiny amount of contaminants in the evaporation process is to look at different types of drinkable water and compare it with the results obtained with UPW.

In Fig. 5, the flow velocity fields measured for three types of commercially available mineral waters are reported. The velocity measurements are taken using GDPT and 1-μm-diameter polystyrene spheres as tracer particles [10]. The mineral waters, namely ViO, Vittel, and Gerolsteiner, have been chosen with an increasing content of dissolved mineral salts. When the content of mineral salts is low (ViO), the flow patterns and velocity magnitudes are very close to the ones of UPW droplets, suggesting that the superficial flow is still of thermocapillary nature and not affected by the small ionic contamination. For larger content of mineral salts (Vittel and Gerolsteiner), a recirculating flow, moving the fluid in the bottom toward the droplet center, appears. The superficial flow maintains the characteristics of a thermal Marangoni flow (moving from the contact line toward the drop summit), but it starts to slow down, probably because of the onset of the recirculating flow. These results suggest that the presence of tiny amount of contaminants cannot be the only reason for the discrepancy between experiments and simulations, and a more complex thermofluidic scenario must be considered.

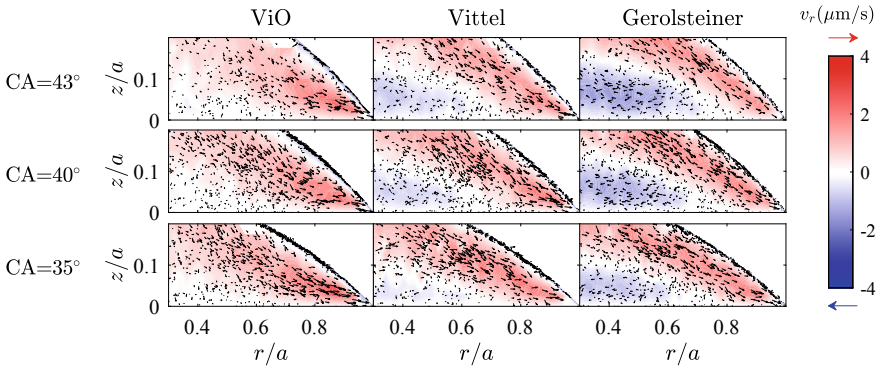

Fig. 5 GDPT measurements of the flow field inside sessile evaporating droplets of three different bottled mineral waters with increasing content of dissolved mineral salts: ViO, Vittel, Gerolosteiner [10]

3.3 Salty Solution

For a larger amount of salt in the water droplets, a reversal of the capillary flow is observed due to the strong solutal Marangoni flow generated by the accumulation of salt at the contact line. This local increase of salt generates a surface tension gradient and consequently a strong flow directed toward the contact line, which consequently drives the bulk flow toward the center of the droplet to comply with volume conservation. It has been shown that this flow can also lead to the formation of ring-shaped stains, however the stain morphology is radically different since the particles forming the stain arrive along the liquid-air surface, forming a monolayer of particles along the surface. 3D PTV measurements can be used to reveal this mechanism [11].

Measurements performed with APTV on a salty water droplet are shown in Fig. 6. The droplet had an initial volume of 0.8 μl, with initial CA of 40º and initial salt (NaCl) concentration of 100 mM. Figure 6a shows some exemplary measured particle trajectories: a reversed circulatory pattern is observed, with particles on the drop surface moving toward the contact line. The corresponding measured flow velocity profiles are shown in Fig. 6b.

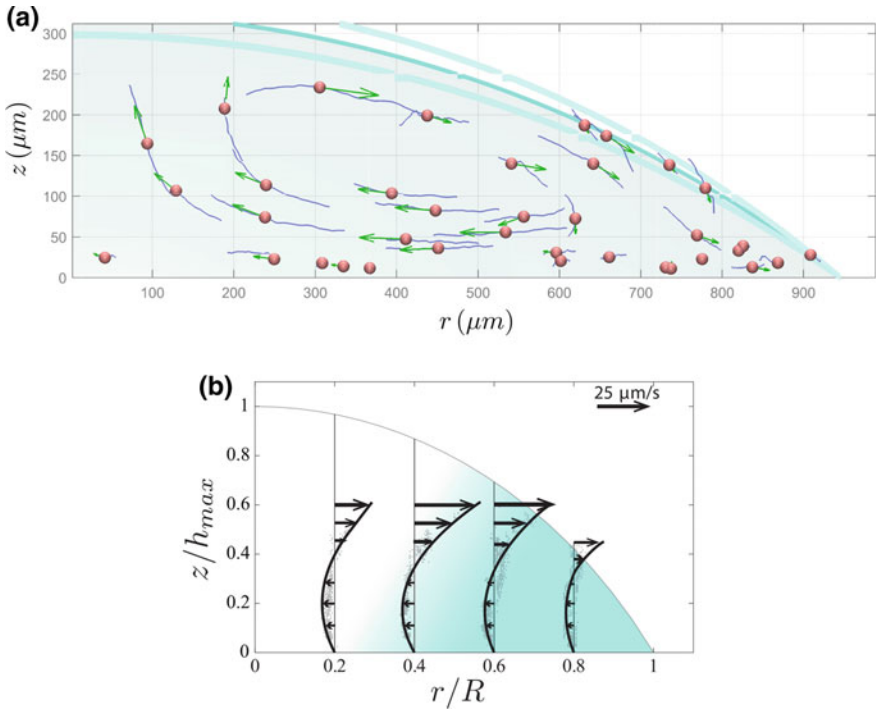

Fig. 6 APTV measurements of the flow field inside sessile evaporating droplets of salty water with an initial concentration of 100 mM NaCl [11]. **a** Particle trajectories and **b** velocity profiles

3.4 Surfactants

More complex scenarios can be observed in droplets with surfactants. The interfacial flows and the continuous droplet surface decrease influence critically the surfactant adsorption/desorption equilibrium at every instant of the evaporation process, giving rise to a very complex and dynamic liquid flow configuration that depends strongly on the surfactant nature. 3D PTV measurements are an indispensable tool to understand the effect of different surfactants at different concentrations. Velocity profiles calculated from APTV measurements on different types of droplets are shown in Fig. 7 [12]. In Fig. 7a, the reference experiment on UPW is shown, with the bulk capillary flow toward the contact line, and the thermal Marangoni flow toward the drop summit. Adding the surfactant Polysorbate 80 (P80) at its critical micelle concentration (CMC) changes dramatically this picture. As shown in Fig. 7b, P80 reduces the surface mobility, creating a rigid droplet surface that drastically reduces the bulk flow as a consequence of increased viscous dissipation. P80 is known to form fairly rigid and stable interfaces when the CMC is reached, which agrees with the results obtained from 3D PTV measurements. On the contrary, the ionic surfactant Sodium Dodecyl Sulfate (SDS) is known to generate very *elastic* and mobile interfaces. At 50 times the CMC it promotes strong flows inside the droplet with the establishment of two counter-rotating recirculating flows, as shown in Fig. 7c. These measurements

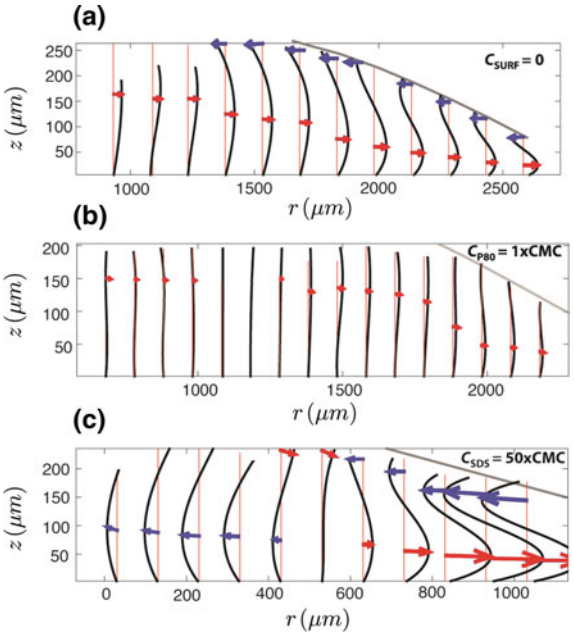

Fig. 7 APTV measurements in droplets with different surfactants [12]. **a** Reference case with UPW. **b** Droplet with surfactant P80 at 1 × CMC. **c** Droplet with surfactant SDS at 50 × CMC

provide a first quantitative picture of these complex phenomena, and provide the basis for the testing and improvement of numerical models and simulations.

4 Conclusions

We have presented an experimental approach for the quantitative characterization of the 3D flow inside sessile evaporating droplets based on single-camera 3D PTV methods. In particular, we applied two well-established 3D PTV methods based on defocusing: the Astigmatic Particle Tracking Velocimetry (APTV) and the General Defocusing Particle Tracking (GDPT). The effectiveness of this approach is demonstrated by presenting results obtained on different types of sessile droplets, at different experimental conditions. The presented experimental approach can be easily implemented on conventional inverted microscopes, and has the potential to become a standard procedure for these types of measurements.

Acknowledgements The authors acknowledge financial support by the Deutsche Forschungsgemeinschaft KA1808/22. MR acknowledges funding from the European Union's Horizon 2020 research and innovation programme under the Marie Sklodowska-Curie grant agreement no. 713683 (COFUNDfellowsDTU). AM acknowledges funding from the European Research Council (ERC-StG-2015 NanoPacks, grant agreement No. 678573).

References

1. Zheng, B., Roach, L.S., Ismagilov, R.F.: Screening of protein crystallization conditions on a microfluidic chip using nanoliter-size droplets. J. Am. Chem. Soc. **125**(37), 11170–11171 (2003)
2. Sempels, W., De Dier, R., Mizuno, H., Hofkens, J., Vermant, J.: Auto-production of biosurfactants reverses the coffee ring effect in a bacterial system. Nat. Commun. **4**, 1757 (2013)
3. Shahidzadeh-Bonn, N., Rafaı, S., Bonn, D., Wegdam, G.: Salt crystallization during evaporation: impact of interfacial properties. Langmuir **24**(16), 8599–8605 (2008)
4. Deegan, R.D., Bakajin, O., Dupont, T.F., Huber, G., Nagel, S.R., Witten, T.A.: Capillary flow as the cause of ring stains from dried liquid drops. Nature **389**(6653), 827 (1997)
5. Hu, H., Larson, R.G.: Marangoni effect reverses coffee-ring depositions. J. Phys. Chem. B **110**(14), 7090–7094 (2006)
6. Kim, H., Boulogne, F., Um, E., Jacobi, I., Button, E., Stone, H.A.: Controlled uniform coating from the interplay of Marangoni flows and surface-adsorbed macromolecules. Phys. Rev. Lett. **116**(12), 124501 (2016)
7. Conn, J.J., Duffy, B.R., Pritchard, D., Wilson, S.K., Halling, P.J., Sefiane, K.: Fluid-dynamical model for antisurfactants. Phys. Rev. E **93**(4), 043121 (2016)
8. Still, T., Yunker, P.J., Yodh, A.G.: Surfactant-induced Marangoni eddies alter the coffee-rings of evaporating colloidal drops. Langmuir **28**(11), 4984–4988 (2012)
9. Champougny, L., Scheid, B., Restagno, F., Vermant, J., Rio, E.: Surfactant-induced rigidity of interfaces: a unified approach to free and dip-coated films. Soft Matter **11**(14), 2758–2770 (2015)

10. Rossi, M., Marin, A., Kähler, C.J.: Interfacial flows in sessile evaporating droplets of mineral water. Phys. Rev. E **100**(3), 033103 (2019)
11. Marin, A., Karpitschka, S., Noguera-Marín, D., Cabrerizo-Vílchez, M.A., Rossi, M., Kähler, C.J., Valverde, M.A.R.: Solutal Marangoni flow as the cause of ring stains from drying salty colloidal drops. Phys. Rev. Fluids **4**(4), 041601 (2019)
12. Marin, A., Liepelt, R., Rossi, M., Kähler, C.J.: Surfactant-driven flow transitions in evaporating droplets. Soft Matter **12**(5), 1593–1600 (2016)
13. Cierpka, C., Segura, R., Hain, R., Kähler, C.J.: A simple single camera 3C3D velocity measurement technique without errors due to depth of correlation and spatial averaging for microfluidics. Meas. Sci. Technol. **21**(4), 045401 (2010)
14. Cierpka, C., Rossi, M., Segura, R., Kähler, C.J.: On the calibration of astigmatism particle tracking velocimetry for microflows. Meas. Sci. Technol. **22**(1), 015401 (2011)
15. Rossi, M., Kähler, C.J.: Optimization of astigmatic particle tracking velocimeters. Exp. Fluids **55**(9), 2014 (1809)
16. Barnkob, R., Kähler, C.J., Rossi, M.: General defocusing particle tracking. Lab Chip **15**(17), 3556–3560 (2015)
17. www.defocustracking.com
18. Rossi, M.: Synthetic image generator for defocusing and astigmatic PIV/PTV. Meas. Sci. Technol. **31**, 017003 (2020)
19. Hu, H., Larson, R.G.: Analysis of the effects of Marangoni stresses on the microflow in an evaporating sessile droplet. Langmuir **21**(9), 3972–3980 (2005)
20. Girard, F., Antoni, M., Sefiane, K.: On the effect of Marangoni flow on evaporation rates of heated water drops. Langmuir **24**(17), 9207–9210 (2008)

Towards Sprays

Drop Shape Oscillations

Günter Brenn

Abstract The present invited contribution to this book reviews the state of understanding and application of shape oscillations of liquid drops in a gaseous environment. The oscillations influence transport processes across the surface of spray drops, the drag as well as heat and mass transfer. The physical basics of linear and nonlinear oscillations are presented and discussed. For the linear case, the characteristic equation of the drop is derived, and the equations of motion are solved, accounting for the fact that the characteristic equation has pairs of complex conjugate solutions. The effects characterising the nonlinear case are reviewed and discussed. Shape oscillations of non-Newtonian, viscoelastic liquid drops exhibit interesting influences from time scales of the viscoelastic liquid relative to the oscillation period. The liquid elasticity may take over from surface tension as the restoring effect. Drop shape oscillations are used for measuring material properties of the drop liquid, such as dynamic viscosity and surface tension, as well as rheological and interfacial parameters. The most important measurement techniques and measured liquid properties are presented and discussed.

1 Introduction

Shape oscillations of drops have been of scientific and technical interest since more than a century. The oscillations change the shape and, for drops which are spherical in equilibrium, they increase the surface. The motion and increase of the drop surface may influence transport processes across the interface between the drop and the ambient medium. The effect on heat and mass transfer is more important for drops in a liquid than in a gaseous environment. The aerodynamic drag in a gas, however, may still be different for oscillating from non-oscillating drops. In the present context we review the state of knowledge on linear and nonlinear drop shape oscillations in

G. Brenn (✉)
Institute of Fluid Mechanics and Heat Transfer, Graz University of Technology, Graz, Austria
e-mail: guenter.brenn@tugraz.at

G. Lamanna et al. (eds.), *Droplet Interactions and Spray Processes*,
Fluid Mechanics and Its Applications 121,
https://doi.org/10.1007/978-3-030-33338-6_19

a gaseous environment, i.e., we restrict our discussion to spray drops. We aim to review the state of understanding of the drop shape oscillation physics, both linear and nonlinear, including non-Newtonian liquids. We also address the use of drop shape oscillations for the measurement of liquid and interfacial material properties.

2 The Physics of Drop Shape Oscillations

2.1 Linear Oscillations

The scientific analysis of drop shape oscillations started in the late 19th century by Rayleigh's work [1]. His paper treated the capillary instability of liquid jets, but included in its Appendix II an analysis of small-amplitude oscillations of a liquid mass around a spherical equilibrium shape. The analysis was carried out for an inviscid liquid drop in a dynamically inert environment (called a "vacuum"). The essential result was the angular frequency of oscillation of a drop with radius a, density ρ and surface tension σ for mode m, reading $\alpha_{m,0} = \sqrt{m(m-1)(m+2)}\sqrt{\sigma/\rho a^3}$. This corresponds to the eigenfrequency of an elastic system with spring constant σ and mass ρa^3. The mode m counts the number of lobes of the drop shape. The smallest possible number $m = 2$ corresponds to spheroidal deformations (with two lobes), while shapes with $m = 3$ and higher exhibit the corresponding higher numbers of lobes on the surface (Fig. 1). Rayleigh's result for the angular frequency says that, in the base mode $m = 2$, a water drop with a diameter of 5.1 cm vibrates at a frequency of 1 Hz [1].

Lamb [2, 3] generalised Rayleigh's result by accounting for the drop viscosity μ and the density of the ambient medium. The threshold Ohnesorge number $Oh = \mu/(\sigma a \rho)^{1/2}$ of the drop for the onset of aperiodic behaviour was predicted. A further generalisation of the analysis of linear drop shape oscillations was achieved in [4] by account for both the viscous and the inertial influences from the ambient medium hosting a viscous oscillating drop. A normal-mode analysis of shape oscillations of

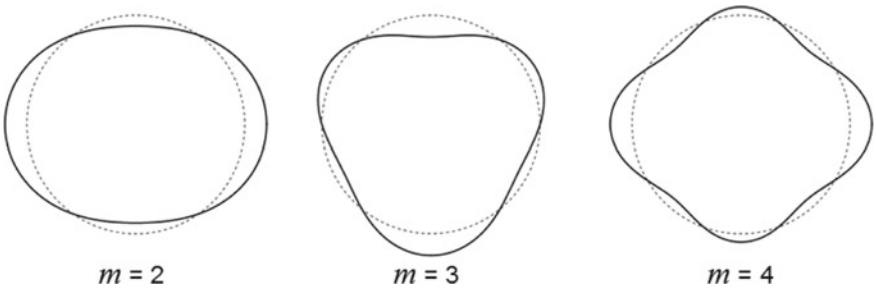

Fig. 1 Deformed drop shapes for modes $m = 2, 3, 4$. The dotted lines mark the spherical equilibrium shape

drops in an immiscible ambient fluid is due to Prosperetti [5, 6]. The important aspect of the onset of the oscillatory motion in a drop initially deformed and at rest, i.e. the initial-value problem, was analysed in [7]. Prosperetti showed that the analyses of linear drop oscillations by the normal-mode approach used in all investigations before may miss the fact that, in the range $0.5657 \leq Oh \leq 0.7665$ of the Ohnesorge number, oscillations starting out aperiodically may turn into periodic with ongoing time. The most important results of the here cited highlight papers are the angular frequency and damping rate of the oscillations, as well as the shapes of the deformed drops in linear motion.

2.1.1 Equations of Motion and Their Solutions

Linear oscillations of viscoelastic drops are analysed by solving the linearised equations of motion, following the normal-mode approach and using a linearised viscoelastic material law. The linearisation bases on small liquid velocities, so that products with their spatial derivatives are negligibly small.

The equations of motion are the equation of continuity and the linearised momentum equation without body force

$$\nabla \cdot \boldsymbol{v} = 0 \; ; \quad \rho \frac{\partial \boldsymbol{v}}{\partial t} = -\nabla p + \nabla \cdot \boldsymbol{\tau}. \tag{1}$$

The linearised viscoelastic material law is the Jeffreys model [8]. The time dependency of all the flow variables is given by an exponential function. In axisymmetric flow, the extra stress tensor $\boldsymbol{\tau}$ may therefore be written in the form

$$\boldsymbol{\tau} = \boldsymbol{T}(r, \theta) \cdot e^{-\alpha_m t} \tag{2}$$

where $T(r, \theta)$ is an amplitude function of the spatial coordinates and α_m is the complex angular frequency for mode m. The Jeffreys model then yields the stress tensor

$$\boldsymbol{\tau} = 2\eta_0 \frac{1 - \alpha_m \lambda_2}{1 - \alpha_m \lambda_1} \boldsymbol{D} = 2\eta(\alpha_m) \boldsymbol{D}, \tag{3}$$

where η_0 is the zero-shear viscosity of the fluid and $\boldsymbol{D} = (\nabla \boldsymbol{v} + \nabla \boldsymbol{v}^T)/2$ the rate-of-deformation tensor. This material law makes the structure of the momentum equation formally identical to that for a Newtonian fluid, except that the dynamic viscosity depends on the frequency of the deformation and on the two polymeric time scales stress relaxation time λ_1 and deformation retardation time λ_2.

The continuity and momentum equations are solved subject to the kinematic boundary condition that the rate of radial displacement of the drop surface $r_s(\theta, t)$ (Fig. 2) equals the radial velocity component at the location of the equilibrium drop radius a, and the dynamic boundary condition that the shear stress at the drop surface,

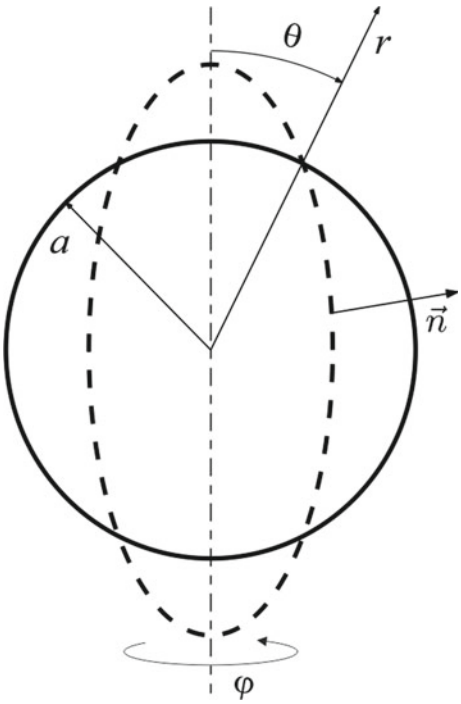

Fig. 2 Equilibrium and deformed drop shapes in the spherical coordinate system for mode $m = 2$. The deformed shape given by the dashed line may be represented as $r_s(\theta, t) = a + \epsilon_0 P_m(\cos\theta) e^{-\alpha_m t}$

evaluated at $r = a$, is negligibly small for a drop in a gas. The second dynamic boundary condition, stating that the (r, r) component of the total stress tensor vanishes at the drop surface, will reveal the characteristic equation of the system.

As a solution of the linear problem, the velocity components inside the drop in the radial and the polar angular directions may be preliminarily written as

$$v_r = -\left[C_{1m} r^{m-1} + C_{2m} q^2 \frac{j_m(qr)}{qr}\right] m(m+1) P_m(\cos\theta) e^{-\alpha_m t} \tag{4}$$

and

$$v_\theta = \left[C_{1m}(m+1) r^{m-1} + C_{2m} q^2 \left((m+1)\frac{j_m(qr)}{qr} - j_{m+1}\right)\right] \sin\theta P'_m(\cos\theta) e^{-\alpha_m t}, \tag{5}$$

respectively, where $q \equiv \sqrt{\alpha_m/\nu}$. The two integration constants C_{1m} and C_{2m} are determined by the kinematic and the zero shear stress boundary conditions. With the deformed drop shape in Fig. 2, the integration constants read

$$C_{1m} = \frac{\epsilon_0 \alpha_m}{m(m+1) a^{m-1}} \left[1 + \frac{2\left(m^2 - 1\right)}{2qaj_{m+1}(qa)/j_m(qa) - q^2 a^2}\right] \tag{6}$$

$$C_{2m} = -\frac{2(m-1)\epsilon_0 \alpha_m a}{mq[2qaj_{m+1}(qa) - q^2a^2 j_m(qa)]}. \tag{7}$$

This solution is formally identical with the results of [9] and [10].

The pressure field is readily obtained with the known velocity field by integration of the radial momentum equation and reads

$$p = -C_{1m}(m+1)\rho\alpha_m r^m P_m e^{-\alpha_m t}. \tag{8}$$

An integration "constant", which would be a function of θ and t, is zero in order that the zero normal stress boundary condition is satisfied.

2.1.2 The Characteristic Equation of the Drop and the Final Form of the Flow Field

The characteristic equation, allowing the complex angular frequency α_m to be determined, emerges from the zero normal stress boundary condition. Using the angular frequency of oscillation $\alpha_{m,0}$ of a nearly spherical inviscid body in a dynamically inert medium for mode m from Sect. 2.1, and the two integration constants (6) and (7), the characteristic equation of the drop reads

$$\frac{1}{\Omega_m^2} := \frac{\alpha_{m,0}^2}{\alpha_m^2} = \frac{2(m^2-1)}{q^2a^2 - 2qaj_{m+1}/j_m} - 1 + \frac{2m(m-1)}{q^2a^2}\left[1 + \frac{2(m+1)j_{m+1}/j_m}{2j_{m+1}/j_m - qa}\right] \tag{9}$$

Here, the spherical Bessel functions j_m and j_{m+1} are taken at the value qa of their arguments. The equation is identical to the results in [2] and [9]. Note that, for a viscoelastic liquid, the kinematic viscosity ν involved in the equation is a function of the complex oscillation frequency α_m. The oscillation frequency and damping rate for the special case of a Newtonian liquid drop are shown in Fig. 3 as func-

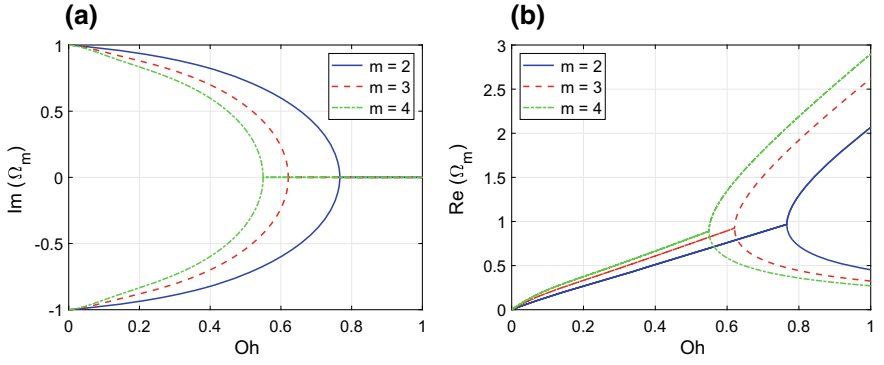

Fig. 3 **a** Angular frequency and **b** damping rate of shape oscillations of Newtonian drops with varying Ohnesorge number for modes $m = 2, 3, 4$

tions of the Ohnesorge number for the three modes $m = 2, 3, 4$. It is seen that the characteristic equation for a Newtonian liquid yields pairs of complex conjugate α_m. The imaginary part of α_2, i.e. the angular frequency for mode $m = 2$, vanishes for Ohnesorge numbers $Oh \geq 0.7665$ [7]. Initially deformed Newtonian drops with Ohnesorge numbers in that range return to the equilibrium shape in an aperiodic way, i.e., without oscillating.

Due to the complex conjugate solutions of the characteristic equation, α_m^+ and α_m^-, the flow field in the drop reads

$$v_r = -\left\{\left[C_{1m}^+ r^{m-1} + C_{2m}^+ q^{+2}\frac{j_m(q^+r)}{q^+r}\right]e^{-\alpha_m^+ t}\right. \tag{10}$$
$$\left. - \left[C_{1m}^- r^{m-1} + C_{2m}^- q^{-2}\frac{j_m(q^-r)}{q^-r}\right]e^{-\alpha_m^- t}\right\} m(m+1)P_m(\cos\theta)$$

$$v_\theta = \left\{\left[C_{1m}^+(m+1)r^{m-1} + C_{2m}^+ q^{+2}\left((m+1)\frac{j_m(q^+r)}{q^+r} - j_{m+1}\right)\right]e^{-\alpha_m^+ t}\right. \tag{11}$$
$$\left. + \left[C_{1m}^-(m+1)r^{m-1} + C_{2m}^- q^{-2}\left((m+1)\frac{j_m(q^-r)}{q^+r} - j_{m+1}\right)\right]e^{-\alpha_m^- t}\right\} \sin\theta P_m'(\cos\theta)$$

$$p = -C_{1m}^+(m+1)\rho\alpha_m^+ r^m P_m(\cos\theta)e^{-\alpha_m^+ t} - C_{1m}^-(m+1)\rho\alpha_m^- r^m P_m(\cos\theta)e^{-\alpha_m^- t} \tag{12}$$

Account for both solutions α_m^+ and α_m^- of the characteristic equation in the description of the flow field in the oscillating drop allows for two initial conditions to determine the amplitudes in the coefficients C_{1m} and C_{2m}.

2.2 Nonlinear Oscillations

Nonlinear shape oscillations of drops occur as a consequence of strong periodic surface forces from the environment or, in free oscillations, of strong initial surface deformation from the equilibrium shape. A theoretical description of this nonlinear motion was unavailable before 1983. The forced oscillations case was investigated experimentally by Trinh and co-workers in a neutrally buoyant immiscible liquid-liquid system [11]. Drops were levitated in the host liquid and acoustically driven to large-amplitude shape oscillations, ultimately leading to drop fission. Visualisation of the flow fields inside the drops at large oscillation amplitude showed circulation patterns not present at low amplitude. Free oscillations were studied extensively by the group of Kowalewski and co-workers in the 1990s [12, 13], leading to an equation for the damped oscillatory evolution of small deformation amplitudes with time and a theory of nonlinear drop shape oscillations. The authors investigated the oscillations of drops pinching off from disintegrating liquid jets in a state of strong deformation (Fig. 4). An investigation of the spectral composition of the drop surface shape from Legendre polynomials showed quantitatively the importance of the various deformation modes $m = 2, 3, 4, \ldots$ and their rates of damping. The

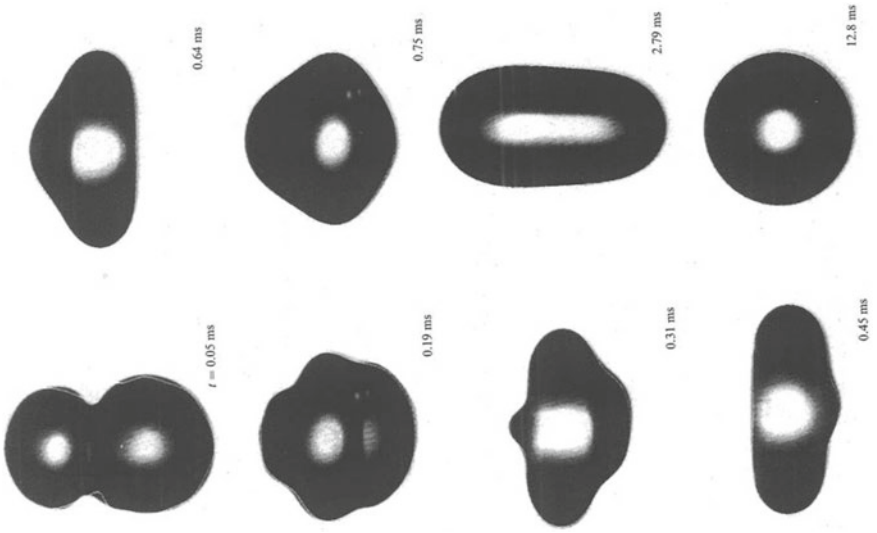

Fig. 4 Initially strongly deformed 0.4 mm ethanol drop (bottom left) oscillating after pinch-off from a jet. Time instants after breakoff from the jet, from bottom left to top right: 0.05 ms, 0.19, 0.31, 0.45, 0.64, 0.75, 2.79, 12.8 ms [12], reproduced with permission

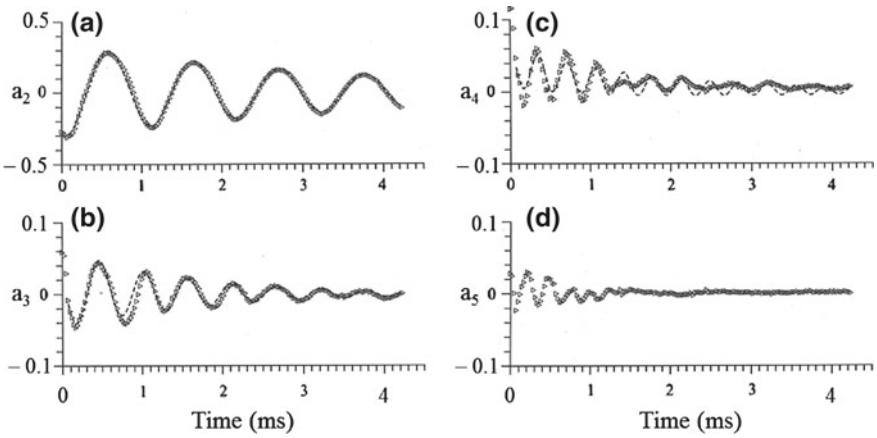

Fig. 5 Decay of non-dimensional modal deformations in a free damped shape oscillation of an ethanol drop. m = (**a**) 2, (**b**) 3, (**c**) 4, (**d**) 5 [12], reproduced with permission

higher modes contribute less to the deformation and are more strongly damped than the lower ones (Fig. 5).

First computational investigations of nonlinear drop shape oscillations with large amplitudes are due to [14]. Nonlinear oscillations of inviscid drops and bubbles were investigated theoretically in [15]. The authors found shapes deviating from the linear results, and angular frequencies decreasing with increasing oscillation amplitude (for

a maximum prolate aspect ratio of 1.4 by approx. 5% of $\alpha_{m,0}$). Their work showed that, as a consequence of the nonlinear flow dynamics, the drop spends a longer part of the oscillation period in the prolate than in the oblate state. The sinusoidal dependency of the shape on time is therefore lost with increasing oscillation amplitude. The theoretical results agree well with data from the computations by Foote [14].

The corresponding theoretical analysis of viscous drop shape oscillations using the weakly nonlinear approach is presently underway, following the preceding analysis [16] of weakly nonlinear liquid jet instability.

2.3 Shape Oscillations of Non-Newtonian Liquid Drops

Shape oscillations of drops from non-Newtonian, viscoelastic liquids were analysed linearly. In [17] it is shown for linear shape oscillations that the oscillation frequency depends on both the Ohnesorge number and the stress relaxation time λ_1 of the liquid, represented by the Deborah number $De_1 = \alpha_{m,0}\lambda_1$. For the ratio of the deformation retardation to stress relaxation times $\lambda_2/\lambda_1 = 1/10$ it is shown that, at $De_1 = 16$ and $Oh \approx 6$, angular oscillation frequencies up to 15% higher than the inviscid value are reached. Khismatullin and Nadim showed that, at small values $De_1 \approx 0.05$, the drop behaviour, which is aperiodic at Ohnesorge numbers greater than 0.72, turns into damped periodic at $Oh \approx 2.1$ again [10], as also found in [17]. At these relatively large Ohnesorge numbers, the physical origin for the elasticity enabling drop shape oscillations is liquid elasticity rather than surface tension.

3 Measuring Techniques Building on Drop Shape Oscillations

The dependency of linear drop shape oscillations on liquid material properties has been used since the 1980s for measuring those material properties. For moderate *Oh* numbers, the oscillation angular frequency depends on the liquid interfacial tension against its ambient medium and on its density. For drops of complex liquids, more liquid material properties, such as the surface extensional viscosity and bending modulus, as well as material time scales, influence the angular oscillation frequency [4, 10].

This "oscillating drop method" was first applied for measuring the surface tension of the drop liquid against the ambient air [18] and the interfacial tension between immiscible liquids [19]. The former authors determined the drop oscillation frequency from visualised drop images, the latter measured the resonance frequency to derive the interfacial tension, with the densities of the two liquids given.

The dynamic viscosity of aerodynamically levitated drops was measured in [20], making use of the resonance behaviour of the oscillating drop with account for the

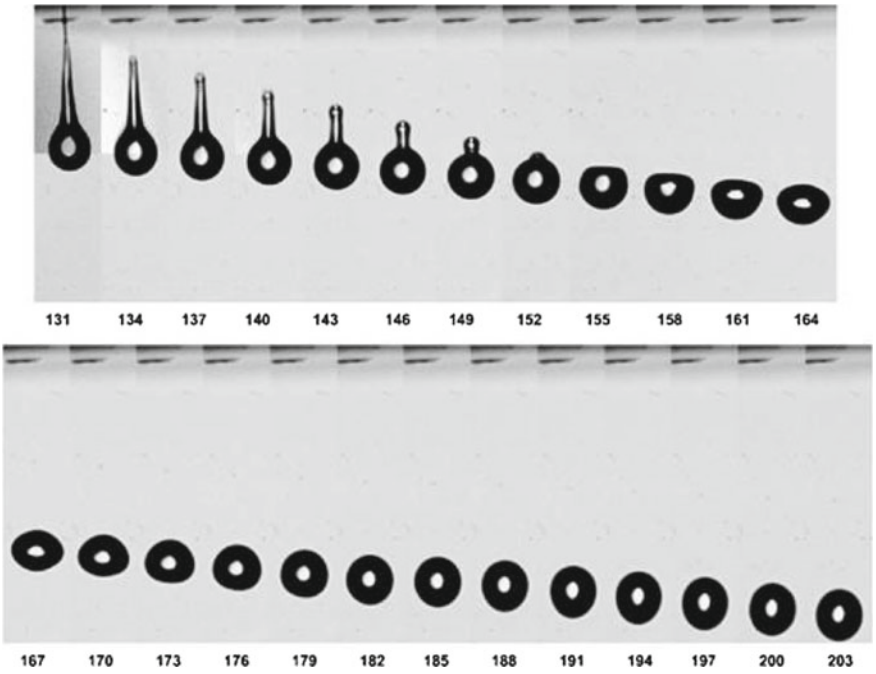

Fig. 6 Drop formation and shape oscillations in ink-jet printing. Numbers below the images are the times in μs after jet tip emergence from the nozzle [27]

spheroidal drop shape. The dynamic viscosity follows from a correlation with the width of the resonance peak, which the authors derive. The accurately measurable dynamic liquid viscosity ranges between 2 mPas and 150 mPas. The authors propose to apply the method to materials in the semisolid state [20]. Similarly, in [21] the damped oscillations of drops of the eutectic $Pd_{78}Cu_6Si_{16}$ were used for measuring the dynamic viscosity for varying temperature. The drops were observed in microgravity, so that an extra levitation technique was not needed. At the eutectic temperature of 1033 K, the measured dynamic viscosity was found to agree very well with results known from the literature.

For viscoelastic systems, the oscillating drop method was used for investigating rheological properties of the surface in [22, 23]. The materials were surfactant solutions, and the drops were levitated in the microgravity environment of the experiment. In the study [22], complementary effects of the bulk and the surface viscosities were found. Due to the coupling between the surface elastic and viscous effects, the surface viscosities can enhance or lower the damping rate of the drop. Experimental studies based on drop visualisation under microgravity conditions determined the frequency and damping rate of free drop oscillations excited by loudspeakers. The experiments quantified both bulk and surface viscoelastic properties of surfactant solutions with the aim of developing rational models of the behavior of the surfactants [23]. A study

with crude oil in water used the oscillating pendant drop method to determine the dilatational elasticity modulus and the dynamic interfacial tension of the oil [24]. The aim of that study was to quantify the absorption behaviour of crude oil surfactants at oil-water interfaces. A review of oscillating drop and bubble techniques is given in [25]. More recently, in [26] an oscillating drop method was developed for measuring the polymeric time scales λ_1 and λ_2 together with the zero-shear viscosity of semi-dilute and concentrated polymer solutions. For a given polymer-solvent system, the ratio λ_2/λ_1 turns out fairly constant over a wide range of concentrations, exhibiting a value $O(10^{-3})$, i.e. orders of magnitude smaller than, e.g., the value of $1/10$ used in many studies before. Successful oscillating-drop measurements of surface tension and viscosity of complex fluids in ink-jet printing (Fig. 6) are due to Hoath et al. [27].

4 Summary and Conclusions

Shape oscillations of liquid drops may affect transport processes across the drop surface due to influences on the velocity fields in both the drop and the ambient gas phase. The oscillations lead to a systematic increase of the drop surface over the spherical equilibrium shape. Small-amplitude oscillations may be treated linearly. Theoretical predictions of both their oscillation frequency and damping rate agree well with the experiment. Nonlinear oscillations may be driven by forces from the environment or may be due to strong initial deformations of the drops. The nonlinear motion reduces the oscillation frequency and enhances the damping rate. Furthermore, in the basic mode of deformation $m = 2$, during one period of oscillation the drop spends more time in the prolate than in the oblate shape. Non-Newtonian, viscoelastic drops may exhibit linear shape oscillations with frequencies greater than the corresponding inviscid drop. Furthermore, at a sufficiently high Ohnesorge number, the viscoelastic drop may exhibit damped oscillations, while the corresponding inelastic drop is aperiodic. The experimental *oscillating drop method* has been developed and applied since the 1980s for measuring liquid material properties, making use of drop shape oscillations. The method allows Newtonian and non-Newtonian, viscoelastic liquid as well as interfacial properties to be measured.

Acknowledgements Support from the Deutsche Forschungsgemeinschaft (DFG) and the Austrian Science Fund (FWF) through the joint project I-3326-N32 is gratefully acknowledged.

References

1. Rayleigh, Lord, J.W.S.: On the capillary phenomena of jets. Proc. R. Soc. London A **29**, 71–97 (1879)
2. Lamb, H.: On the oscillations of a viscous spheroid. Proc. London Math. Soc. **13**, 51–66 (1881)
3. Lamb, H.: Hydrodynamics, 6th edn. Cambridge University Press, Cambridge (1932)

4. Miller, C.A., Scriven, L.E.: The oscillations of a fluid drop immersed in another fluid. J. Fluid Mech. **32**, 417–435 (1968)
5. Prosperetti, A.: Viscous effects on perturbed spherical flows. Quart. Appl. Math. **35**, 339–352 (1977)
6. Prosperetti, A.: Normal-mode analysis for the oscillations of a viscous liquid drop in an immiscible liquid. J. Méc. **19**, 149–182 (1980)
7. Prosperetti, A.: Free oscillations of drops and bubbles: the initial-value problem. J. Fluid Mech. **100**, 333–347 (1980)
8. Bird, R.B., Armstrong, R.C., Hassager, O.: Dynamics of Polymeric Liquids. Wiley, New York (1987)
9. Chandrasekhar, S.: The oscillations of a viscous liquid globe. Proc. London Math. Soc. **9**, 141–149 (1959)
10. Khismatullin, D.B., Nadim, A.: Shape oscillations of a viscoelastic drop. Phys. Rev. E **63**, 061508 (2001)
11. Trinh, E., Wang, T.G.: Large-amplitude free and driven drop-shape oscillations: experimental observations. J. Fluid Mech. **122**, 315–338 (1982)
12. Becker, E., Hiller, W.J., Kowalewski, T.A.: Experimental and theoretical investigation of large-amplitude oscillations of liquid droplets. J. Fluid Mech. **231**, 189–210 (1991)
13. Becker, E., Hiller, W.J., Kowalewski, T.A.: Nonlinear dynamics of viscous droplets. J. Fluid Mech. **258**, 191–216 (1994)
14. Foote, G.B.: A numerical method for studying liquid drop behaviour: simple oscillation. J. Comp. Phys. **11**, 507–530 (1973)
15. Tsamopoulos, J.A., Brown, R.A.: Nonlinear oscillations of inviscid drops and bubbles. J. Fluid Mech. **127**, 519–537 (1983)
16. Renoult, M.-C., Brenn, G., Plohl, G., Mutabazi, I.: Weakly nonlinear instability of a newtonian liquid jet. J. Fluid Mech. **856**, 169–201 (2018)
17. Brenn, G., Teichtmeister, St.: Linear shape oscillations and polymeric time scales of viscoelastic drops. J. Fluid Mech. **733**, 504–527 (2013)
18. Hiller, W.J., Kowalewski, T.A.: Surface tension measurements by the oscillating droplet method. PCH PhysicoChemical Hydrodyn. **11**, 103–112 (1989)
19. Hsu, C.J., Apfel, R.E.: A technique for measuring interfacial tension by quadrupole oscillation of drops. J. Colloid Interface Sci. **107**, 467–476 (1985)
20. Perez, M., Salvo, L., Suéry, M., Bréchet, Y., Papoular, M.: Contactless viscosity measurement by oscillations of gas-levitated drops. Phys. Rev. E **61**, 2669–2675 (2000)
21. Egry, I., Lohöfer, G., Seyhan, I., Schneider, S., Feuerbacher, B.: Viscosity of the eutectic $Pd_{78}Cu_6Si_{16}$ measured by the oscillating drop technique in microgravity. Appl. Phys. Lett. **73**, 462–463 (1998)
22. Tian, Y.R., Holt, R.G., Apfel, R.E.: Investigations of liquid surface rheology of surfactant solutions by droplet shape oscillations: theory. Phys. Fluids **7**, 2938–2949 (1995)
23. Apfel, R.E., Tian, Y.R., Jankovsky, J., Shi, T., Chen, X., Holt, R.G., Trinh, E., Croonquist, A., Thornton, K.C., Sacco Jr., A., Coleman, C., Leslie, F.W., Matthiesen, D.H.: Free oscillations and surfactant studies of superdeformed drops in microgravity. Phys. Rev. Lett. **78**, 1912–1915 (1997)
24. Aske, N., Orr, R., Sjöblom, J.: Dilatational elasticity moduli of water-crude oil interfaces using the oscillating pendant drop. J. Dispersion Sci. Technol. **23**, 809–825 (2002)
25. Kovalchuk, V.I., Krägel, J., Aksenenko, E.V., Loglio, G., Liggieri, L.: Oscillating bubble and drop techniques. In: Möbius, D., Miller, R. (eds.) Novel Methods to Study Interfacial Layers, pp. 485–516. Elsevier, Amsterdam (2001)
26. Brenn, G., Plohl, G.: The oscillating drop method for measuring the deformation retardation time of viscoelastic liquids. J. Non-Newton. Fluid Mech. **223**, 88–97 (2015)
27. Hoath, S.D., Hsiao, W.-K., Martin, G.D., Jung, S.J., Butler, S.A., Morrison, N.F., Harlen, O.G., Yang, L.S., Bain, C.D., Hutchings, I.M.: Oscillations of aqueous PEDOT:PSS fluid droplets and the properties of complex fluids in drop-on-demand inkjet printing. J. Non-Newton. Fluid Mech. **223**, 28–36 (2015). https://doi.org/10.1016/j.jnnfm.2015.05.006, Creative Commons user license https://creativecommons.org/licenses/by/4.0/

Classical and Novel Approaches to Modelling Droplet Heating and Evaporation

Sergei Stepanovich Sazhin

Abstract Classical approaches to modelling the processes during droplet heating and evaporation are summarised. Novel approaches to modelling these processes are described. In these approaches, commonly used assumptions that the sum of vapour and air densities does not depend on the distance from the droplet surface, and that droplet thermal conductivity is infinitely high are relaxed. The most recent approaches to modelling these processes are briefly described.

1 Introduction

The importance of modelling droplet heating and evaporation has been widely discussed in the literature [1]. Key approaches to this modelling were derived more than half a century ago (e.g. [2]) and were summarised and further developed by Abramzon and Sirignano [3]. Formulae, originally derived in [2] and [3], have been widely used in various applications (see the discussion of this matter in [1]). On many occasions, the users of these formulae did not clearly understand how they were derived and what sort of additional assumptions were used during their derivation. Often they have ignored these assumptions and have used the formulae with sets of parameters to which they do not apply. More recent models without some of the restrictions used when deriving the original classical formulae have not attracted the attention of many researchers.

In this paper, the classical models of droplet heating and evaporation will be revisited paying particular attention to the assumptions used for the derivation of key formulae. The most important recent developments, in which some of these assumptions are relaxed, will be briefly summarised.

S. S. Sazhin (✉)
School of Computing, Engineering and Mathematics, Advanced Engineering Centre, University of Brighton, Brighton BN2 4GJ, UK
e-mail: S.Sazhin@brighton.ac.uk

G. Lamanna et al. (eds.), *Droplet Interactions and Spray Processes*,
Fluid Mechanics and Its Applications 121,
https://doi.org/10.1007/978-3-030-33338-6_20

2 Classical Approaches

All classical models of droplet heating and evaporation are based on several key assumptions which are not always clearly explained by the model developers and in some well known textbooks. Firstly, it is commonly assumed that vapour at the droplet surface is always saturated. In this case, the problem of droplet evaporation reduces to the problem of diffusion of vapour from the droplet surface to the ambient gas (air). The limitations of this assumption have been discussed since about one hundred years ago [4]. A more rigorous approach to this problem should take into account the kinetic effects in the immediate vicinity of the droplet surface. The discussion of these effects, however, is beyond the scope of this paper (see [1]).

Another assumption commonly used in classical models is that all processes are quasi-steady-state. This means that at each time step the parameters in the vicinity of the evaporating droplets depend on the position in space but not on time; they can change from one time step to another. In other words, it is assumed that the thermal and vapour boundary layers are instantaneously formed at the beginning of each time step. The limitation of this assumption is discussed at length in [1], where a fully transient solution to the problem of droplet heating (but not evaporation) is presented and discussed.

Finally, it is commonly assumed that liquid thermal conductivity is infinitely large which allows modellers to ignore all temperature gradients inside droplets. This assumption is justified by the fact that the thermal conductivity of liquid is indeed larger than that of gas. However, the formation of the liquid thermal boundary layer is controlled not by thermal conductivity but by thermal diffusivity. Due to the difference between liquid and gas densities, the thermal diffusivity of liquid is commonly about 2 orders of magnitude smaller than that of gas. This makes this assumption questionable.

In what follows, the derivation of some key classical equations describing droplet heating and evaporation is presented, using the above-mentioned assumptions. Additional assumptions used for the derivation of these equations are outlined.

Remembering the assumption that droplet evaporation is quasi-steady-state, the droplet evaporation rate is equal to the vapour mass rate through a sphere at any distance from the droplet centre. Taking into account that this mass rate is formed due to diffusion and convection (Stefan flow) processes, and making additional assumptions that the droplet is stationary and mono-component, we can present the vapour mass balance equation as:

$$\dot{m}_d = 4\pi R^2 \left(D_v \frac{\mathrm{d}\rho_v}{\mathrm{d}R} - \rho_v U \right) = 4\pi R^2 \left(D_v \frac{\mathrm{d}\rho_v}{\mathrm{d}R} - D_v \frac{\rho_v}{\rho_g} \frac{\mathrm{d}\rho_g}{\mathrm{d}R} \right), \qquad (1)$$

where D_v is the diffusion coefficient between the vapour and ambient gas (air), ρ_v (ρ_g) is vapour (gas) density, U is Stefan flow velocity, $R > R_d$ is the distance from the droplet centre, R_d is the droplet radius; note that $\dot{m}_d < 0$.

Equation (1) cannot be solved in the general case since we do not know the dependencies of ρ_v and ρ_g on R. The solution to this equation, however, becomes possible if following [2] and [3] we assume that $\rho_{\text{total}} = \rho_g + \rho_v = \text{const}$. In this case its integration from $R = R_d$ to $R = \infty$ (after some rearrangements) gives the following expression for $\dot{m}_d$ [1, 3]:

$$\dot{m}_d = -4\pi R_d D_v \rho_{\text{total}} \ln(1 + B_M), \tag{2}$$

where $B_M = (Y_{vs} - Y_{v\infty})/(1 - Y_{vs})$ is the Spalding mass transfer number, Y_{vs} ($Y_{v\infty}$) is the mass fraction of fuel vapour near the droplet surface (ambient gas). These mass fractions depend on temperature in the general case.

Equation (2) is the well known work horse for modelling droplet evaporation, although the assumptions based on which it was derived are often overlooked. The most important of these assumptions is $\rho_{\text{total}} = \rho_g + \rho_v = \text{const}$, which limits the range of its applicability because it introduces uncontrollable errors in modelling. This becomes particularly important when cold droplets are introduced to a very hot gas.

For constant droplet surface temperature, B_M is constant is well. In this case, Equation (2) leads to the statement $\mathrm{d}R_d^2/\mathrm{d}t$ is constant, leading to a well known D^2-law ($D = 2R_d$) [1].

An alternative approach to estimation of $\dot{m}_d$ can be based on the energy balance equation. Assuming, as in the case of Equation (1), that the droplet is stationary this equation can be presented as [1]:

$$4\pi R^2 k_g \frac{\mathrm{d}T}{\mathrm{d}R} = -\dot{m}_d c_{pv}(T - T_s) - \dot{m}_d L(T_s) + |\dot{q}_d|, \tag{3}$$

where k_g is gas thermal conductivity, $T(T_s)$ is gas (surface) temperature, L is specific heat of evaporation, c_{pv} is specific vapour heat capacity at constant pressure, $|\dot{q}_d|$ is heat spent on raising droplet temperature.

In contrast to Eqs. (1), (3) could be integrated if the temperature dependencies of k_g and c_{pv} were known. In most commonly used approaches to the solution of Eq. (3), however, both these parameters are assumed to be constant. In this case, its rearrangement and integration gives [1, 3]:

$$\dot{m}_d = -\frac{4\pi k_g R_d}{c_{pv}} \ln(1 + B_T), \tag{4}$$

where

$$B_T = \frac{c_{pv}(T_g - T_s)}{L(T_s) - (|\dot{q}_d|/\dot{m}_d)} \tag{5}$$

is the Spalding heat transfer number. Note that in some papers c_{pv} was replaced by c_p, and the latter was implicitly identified with the heat capacity of the ambient gas (see [1] for the details).

Since the left hand sides of Eqs. (1) and (4) are the same, a relation between B_T and B_M can be obtained [1, 3]. Possible generalisations of Eqs. (1) and (4), leading to the well known Abramzon and Sirignano model, are discussed in [1, 3].

Equations (1) and (4) are not closed as they contain an external parameter T_s which cannot be inferred from the gas phase model. To obtain the value of this parameter the gas phase model needs to be supplemented by the liquid phase model.

In the simplest case, the liquid phase model can be based on the assumption that the droplet temperature is homogeneous but is allowed to change with time. In that case, the rate of change of this temperature can be inferred from the energy balance equation [1]:

$$\frac{4}{3}\pi R_d^3 \rho_l c_l \frac{\mathrm{d}T_d}{\mathrm{d}t} = 4\pi R_d^2 h(T_g - T_d), \tag{6}$$

where h is the convection heat transfer coefficient, ρ_l and c_l are liquid density and specific heat capacity, respectively, T_d (T_g) is the droplet (ambient gas) temperature. Assuming that h, ρ_l and c_l are constant, the analytical solution to Eq. (6) becomes straightforward. This assumption is satisfied with confidence when Eq. (6) is applied within a short time step.

Note that h is closely linked with parameter $|\dot{q}_d|$ used in Eqs. (3) and (5). The details of calculating h for evaporating droplets are discussed in [1].

As mentioned earlier, the model described by the equations derived in this section is almost universally used by researchers focused on modelling droplet heating and evaporation and is implemented in most Computational Fluid Dynamics (CFD) codes known to us. More advanced models of these processes are discussed in the following sections.

3 The Tonini and Cossali Model

As mentioned in Sect. 2 the key limitation of Eq. (2) is that it is based on the assumption that $\rho_{\text{total}} = \rho_g + \rho_v = \text{const}$, the validity of which is questionable in many practical applications. The Tonini and Cossali [5] model was developed to relax this assumption and to provide a model which can be used for a much wider range of problems than the model based on Eq. (2). Their model is focused on the vapour phase. They assumed that there is no temperature gradient inside droplets, but their model could be linked with any other liquid phase model if necessary.

The analysis of [5] is based on steady-state mass, momentum and energy balance equations for the vapour and gas (air) mixture surrounding a liquid droplet:

$$\frac{\mathrm{d}}{\mathrm{d}R}\left(R^2 \rho_v U - R^2 D_v \rho_{\text{total}} \frac{\mathrm{d}Y_v}{\mathrm{d}R}\right) = 0, \tag{7}$$

$$\frac{\mathrm{d}}{\mathrm{d}R}\left(R^2 \rho_a U - R^2 D_v \rho_{\text{total}} \frac{\mathrm{d}Y_a}{\mathrm{d}R}\right) = 0, \tag{8}$$

$$\rho_{\text{total}} U \frac{\mathrm{d}U}{\mathrm{d}R} = \frac{\mathrm{d}p_{\text{total}}}{\mathrm{d}R} + \mu_{\text{mix}} \left(\frac{\mathrm{d}^2 U}{\mathrm{d}R^2} + \frac{2}{R} \frac{\mathrm{d}U}{\mathrm{d}R} \right), \tag{9}$$

$$\rho_{\text{total}} U c_{pv} \frac{\mathrm{d}T}{\mathrm{d}R} = k_{\text{mix}} \left(\frac{\mathrm{d}^2 T}{\mathrm{d}R^2} + \frac{2}{R} \frac{\mathrm{d}T}{\mathrm{d}R} \right), \tag{10}$$

where U is the Stefan flow velocity described earlier, transport and thermodynamic properties of the mixture of vapour (v) and air (a) are assumed to be constant. In contrast to the model described by Eq. (2), both ρ_{total} and T are allowed to depend on R. Partial (p_v and p_a) and total (p_{total}) pressures are inferred from the ideal gas and Dalton laws. See Appendix A of [10] for the derivation of (10).

These are the boundary conditions for System (7)–(10): $T(R = R_d) = T_s$, $T(R = \infty) = T_{a,\infty}$, $Y_v(R = \infty) = Y_{v,\infty}$, $p_v(R = R_d) = p_{vs}(T_s)$. Rearranging this system and assuming that

$$\frac{R_u T_{a,\infty} R_d^2}{M_v D_v^2} \gg 1 \tag{11}$$

allows us to obtain the following implicit equation for the normalised vapour mass flow rate:

$$\hat{m}_d + \left(\frac{\hat{m}_d}{1 - \exp\left(-\frac{\hat{m}_d}{\text{Le}}\right)} - \text{Le} \right) \left(\frac{T_s}{T_a} - 1 \right) = -\hat{p}_{v,\text{cr}} \ln \left[\frac{\hat{p}_{v,\text{cr}} - \hat{p}_{v,s}}{\hat{p}_{v,\text{cr}} - Y_{v,\infty}} \right], \tag{12}$$

where

$$\hat{p}_{v,\text{cr}} = 1 + \frac{\theta_{\text{TC}}}{1 - Y_{v,\infty}}, \quad \theta_{\text{TC}} = \frac{M_v - M_a}{M_a}, \quad \hat{p}_{v,s} = \frac{p_{v,s} M_v}{R_u T_{a,\infty} \rho_{a,\infty}},$$

$p_{v,s}$ is the saturation vapour pressure corresponding to T_s, R_u is the universal gas constant, M_v and M_a are molar masses of vapour and air,

$$\xi_{\text{TC}} = R_d / R, \quad G_{\text{TC}} = \ln(Y_a), \quad \hat{m}_d = -\tilde{\rho} \frac{\mathrm{d}G_{\text{TC}}}{\mathrm{d}\xi_{\text{TC}}}, \quad \tilde{\rho} = \rho_{\text{total}}(R) / \rho_{\text{total}}(R = \infty).$$

Equation (12) can be solved numerically. Once $\hat{m}_d$ has been obtained, the dimensional mass evaporation rate can be estimated from the following equation [5]:

$$\dot{m}_d = \hat{m}_d 4\pi D_v R_d \rho_{\text{total}}(R = \infty). \tag{13}$$

For the isothermal case and weak evaporation the solution to (12) coincides with Expression (2) in the limit when the contribution of convection (Stefan velocity) can be ignored. In this case Expression (2) reduces to the Maxwell equation [1]. An extension of this approach to non-spherical droplets is discussed in [6].

4 Modelling of the Liquid Phase

As mentioned in Sect. 2, the commonly used assumption that heat supplied to the surface of the droplet instantaneously spreads over the whole volume of the droplet leading to homogeneous temperature distribution within it is questionable. A more rigorous approach to the analysis of the processes in the liquid phase is based on the solution to the transient heat transfer equation inside the droplet:

$$\frac{\partial T}{\partial t} = \kappa \left(\frac{\partial^2 T}{\partial R^2} + \frac{2}{R} \frac{\partial T}{\partial R} \right), \tag{14}$$

where $\kappa = k_l/(c_l \rho_l)$, subject to the boundary condition at its surface

$$h(T_g - T_s) = k_l \left. \frac{\partial T}{\partial R} \right|_{R=R_d-0}, \tag{15}$$

$T_s = T_s(t)$ is the droplet's surface temperature, $T_g = T_g(t)$ is the ambient gas temperature (the effect of evaporation was ignored).

In most cases, Eq. (14), subject to the above-mentioned boundary and initial ($T(t=0) = T_{d0}(R)$) conditions, has been solved numerically. However, a series of papers summarised in [1] demonstrated a more efficient approach to this problem, based on the numerical solution to this equation at each time step and incorporation of this numerical solution into the general numerical scheme.

Assuming that $h = \text{const}$, the analytical solution to this equation subject to these boundary and initial conditions can be presented as:

$$T(R,t) = \frac{R_d}{R} \sum_{n=1}^{\infty} \left\{ q_n \exp\left[-\kappa_R \lambda_n^2 t\right] - \frac{\sin\lambda_n}{||\, v_n \,||^2\, \lambda_n^2} \mu_0(0) \exp\left[-\kappa_R \lambda_n^2 t\right] \right.$$
$$\left. - \frac{\sin\lambda_n}{||\, v_n \,||^2\, \lambda_n^2} \int_0^t \frac{\mathrm{d}\mu_0(\tau)}{\mathrm{d}\tau} \exp\left[-\kappa_R \lambda_n^2 (t-\tau)\right] \mathrm{d}\tau \right\} \sin\left[\lambda_n \left(\frac{R}{R_d}\right)\right] + T_g(t), \tag{16}$$

where λ_n are solutions to the equation:

$$\lambda \cos\lambda + h_0 \sin\lambda = 0, \tag{17}$$

$$||\, v_n \,||^2 = \frac{1}{2}\left(1 - \frac{\sin 2\lambda_n}{2\lambda_n}\right) = \frac{1}{2}\left(1 + \frac{h_0}{h_0^2 + \lambda_n^2}\right),$$

$$q_n = \frac{1}{R_d\, ||\, v_n \,||^2} \int_0^{R_d} \tilde{T}_0(R) \sin\left[\lambda_n \left(\frac{R}{R_d}\right)\right] \mathrm{d}R, \quad \kappa_R = \frac{k_l}{c_l \rho_l R_d^2}, \quad \mu_0(t) = \frac{h T_g(t) R_d}{k_l},$$

$h_0 = (h R_d/k_l) - 1$, $\tilde{T}_0(R) = R T_{d0}(R)/R_d$. The solution to Eq. (17) gives a set of positive eigenvalues λ_n numbered in ascending order ($n = 1, 2, \ldots$). In the limit, $k_l \to \infty$, solution (16) reduces to the solution to Eq. (6) as expected [1].

The effect of droplet evaporation in Solutions (16) can be taken into account by replacing gas temperature with the effective temperature:

$$T_{\text{eff}} = T_g + \frac{\rho_l L \mathrm{d}R_d/\mathrm{d}t}{h}. \tag{18}$$

The source term taking into account the volumetric absorption of external thermal radiation in the droplet can be incorporated into Eq. (14) and its Solution (16) [1]. The distribution of temperature inside the droplet, predicted by Solutions (16), allows us to obtain the heat rate supplied from a gas to the droplet and spent on raising droplet temperature from the following equation:

$$\dot{q}_d = 4\pi R_d^2 k_l \left.\frac{\partial T}{\partial R}\right|_{R=R_d-0}, \tag{19}$$

where $T(R)$ is determined by Expression (16). Substitution of (16) into (19) gives:

$$|\dot{q}_d| = 4\pi R_d k_l \sum_{n=1}^{\infty} \left\{ q_n \exp\left[-\kappa_R \lambda_n^2 t\right] - \frac{\sin\lambda_n}{||\ v_n\ ||^2\ \lambda_n^2} \mu_0(0) \exp\left[-\kappa_R \lambda_n^2 t\right] - \right.$$

$$\left. - \frac{\sin\lambda_n}{||\ v_n\ ||^2\ \lambda_n^2} \int_0^t \frac{\mathrm{d}\mu_0(\tau)}{\mathrm{d}\tau} \exp\left[-\kappa_R \lambda_n^2 (t-\tau)\right] \mathrm{d}\tau \right\} [-1 - h_0] \sin\lambda_n. \tag{20}$$

The authors of [7] (see also [8]) attempted to compare the predictions of the parameters of heated and evaporated droplets based on two models. In the first model, the values of $|\dot{q}_d|$ were inferred from the definition of the Spalding heat transfer number (Expression (5)). In the second model these values were taken directly from Expression (20). The predictions of these models were qualitatively similar, but the actual values of the rate of droplet evaporation and time evolution of temperature were visibly different. The reasons for this are not clear to us.

5 Recent Developments

The models discussed so far have focused on mono-component droplet heating and evaporation. In the case of multi-component droplets, evaporation of individual components leading to diffusion of species inside the droplets needs to be taken into account. The species diffusion equation can be written in a similar form to Equation (14), but with different boundary conditions, leading to a solution to this equation that differs from (16) [1]. A model based on the analytical solution to the species diffusion equation was developed, and the results are summarised in [1, 8]. For cases where droplets contain many components (one hundred or more) a modified version of this model, known as the multi-dimensional quasi-discrete model, was developed [9].

Another limitation of the models considered in the previous sections is that they are applicable only to spherical droplets. The generalisation of some of these models to the case of spheroidal droplets is discussed in [10]. The analysis in this paper was focused on mono-component droplets and spheroids with eccentricity close to 1. The analysis of strongly deformed multi-component droplets leading to a liquid film is presented in [11].

The third limitation of the models considered so far is that it was assumed that droplet heating and evaporation processes can be isolated from ignition and combustion processes. This assumption is particularly important in the case of fuel sprays (e.g. in internal combustion engines). Possible approaches to the modelling of spray heating, evaporation and ignition processes are discussed in [12, 13].

Acknowledgements This work was supported by the UK Engineering and Physical Science Research Council [grant EP/M002608/1] and the Royal Society [project 192007]. Dr. S. Tonini is gratefully acknowledged for helpful comments on the draft version of the paper.

References

1. Sazhin, S.S.: Droplets and Sprays. Springer, Heidelberg (2014)
2. Spalding, D.B.: Convective Mass Transfer—An Introduction. McGraw Hill (1963)
3. Abramzon, B., Sirignano, W.A.: Droplet vaporization model for spray combustion calculations. Int. J. Heat Mass Transfer **32**, 1605–1618 (1989)
4. Fuchs, N.A.: Evaporation and Droplet Growth in Gaseous Media. Pergamon Press, London (1959)
5. Tonini, S., Cossali, G.E.: An analytical model of liquid drop evaporation in gaseous environment. Int. J Therm. Sci. **57**, 45–53 (2012)
6. Cossali, G.E., Tonini, S.: An analytical model of heat and mass transfer from liquid drops with temperature dependence of gas thermo-physical properties. Int. J Heat Mass Transfer **138**, 1166–1177 (2019)
7. Sazhin, S.S., Al Qubeissi, M., Xie, J.-F.: Two approaches to modelling the heating of evaporating droplets. Int. Comm. Heat Mass Transfer **57**, 353–356 (2014)
8. Sazhin, S.S.: Modelling of fuel droplet heating and evaporation: recent results and unsolved problems. Fuel **196**, 69–101 (2017)
9. Sazhin, S.S., Al Qubeissi, M., Nasiri, R., Gun'ko, V.M., Elwardany, A.E., Lemoine, F., Grisch, F., Heikal, M.R.: A multi-dimensional quasi-discrete model for the analysis of diesel fuel droplet heating and evaporation. Fuel **129**, 238–266 (2014)
10. Zubkov, V.S., Cossali, G.E., Tonini, S., Rybdylova, O., Crua, C., Heikal, M., Sazhin, S.S.: Mathematical modelling of heating and evaporation of a spheroidal droplet. Int. J. Heat Mass Transfer **108**, 2181–2190 (2017)
11. Sazhin, S.S., Rybdylova, O., Crua, C.: A mathematical model for heating and evaporation of a multi-component liquid film. Int. J. Heat Mass Transfer **117**, 252–260 (2018)
12. Sazhin, S.S., Shchepakina, E., Sobolev, V.: Order reduction in models of spray ignition and combustion. Combust. Flame **187**, 122–128 (2018)
13. Sazhin, S.S., Shchepakina, E., Sobolev, V.: Parameterisations of slow invariant manifolds: application to a spray ignition and combustion model. J. Eng. Math. **114**(1), 1–17 (2019)

The Influence of Curvature on the Modelling of Droplet Evaporation at Different Scales

Grazia Lamanna, Gianpietro Elvio Cossali and Simona Tonini

Abstract The evaporation of liquid drops in stagnant gaseous environment is modelled, accounting for the effect of drop curvature and size at the macro- and microscopic scales. At the macro-scale level, the validity of the conjectured dependence of the local fluxes on the drop surface curvature is analysed. Analytical solutions to the gas-phase conservation equations for five drop shapes (sphere, oblate and prolate spheroids and inverse oblate and prolate spheroids), under uniform Dirichlet boundary conditions, are used to calculate the local vapour and heat fluxes. The analysis shows that in general non-dimensional fluxes do not solely depend on local curvature, but possibly the effect of the whole drop shape must be taken into account. At the micro-scale level, the equilibrium vapour pressure at a convex curved surface is higher than that at a flat surface, thus leading to a considerable enhancement of the evaporation rate for nanometre sized droplets. To model the increase in equilibrium vapour pressure, we consider the Kelvin correction. Our analysis shows that the Kelvin correction is strictly required for droplet radii below 20 Å, as typically encountered for modelling the growth of critical clusters in phase transition processes initiated by homogeneous nucleation. At these conditions, it is mandatory to consider also the repartition of molecules in the different phases, in order to prevent a significant overestimation of the equilibrium vapour pressure.

G. Lamanna (✉)
Institute of Aerospace Thermodynamics (ITLR), University of Stuttgart, Stuttgart, Germany
e-mail: grazia.lamanna@itlr.uni-stuttgart.de

G. E. Cossali · S. Tonini
Department of Engineering and Applied Sciences, University of Bergamo, Bergamo, Italy
e-mail: gianpietro.cossali@unibg.it

S. Tonini
e-mail: simona.tonini@unibg.it

G. Lamanna et al. (eds.), *Droplet Interactions and Spray Processes*,
Fluid Mechanics and Its Applications 121,
https://doi.org/10.1007/978-3-030-33338-6_21

1 Introduction

The phenomenon of drop evaporation has attracted the attention of the scientific community since decades for its wide range of industrial applications, like spray combustion, spray cooling, fire suppression, medical aerosols, to cite but a few.

The models of drop evaporation are classified into two main cathegories [1]: *hydrodynamic* and *kinetic* or *molecular dynamics* models. The *hydrodynamic* models assume that vapour in the vicinity of the drop surface is always saturated, then both the liquid and the gas phases can be treated as a continuum and the boundary conditions at the liquid/gas interface are function of the operating conditions (temperature, pressure and composition). The *kinetic* or *molecular dynamics* models account for the details of the detachment of molecules from the drop surface and they are based on the kinetic Boltzman equation (*kinetic* models, [2–4]) or molecular dynamics simulations (*molecular dynamics* models, [4–6]). In these models the assumption that both liquid and gas phases can be treated as a continuum is no longer valid and a much more complex dependence of the boundary conditions on the operating and geometry characteristics must be taken into account.

The first *hydrodynamic* model for drop evaporation is that of Maxwell [7], which assumes that steady-state evaporation from a spherical liquid drop suspended in stagnant air is driven by the diffusion of the vaporising species. Since then a huge amount of work was done on this subject, analysing the effect of drop composition, shape and temperature distribution, thermo-physical properties, equilibrium conditions at the liquid/gas interface, etc. (refer to [1, 8] for recent reviews on this subject). The majority of analytical models of drop evaporation assumes that the drop may be described as a perfect sphere (refer to [9] as the most common model of drop evaporation, usually implemented in CFD codes for spray applications). However, there exists experimental evidence (see for example [10]) that drops in spray applications are far from being spherical and drop deformation must be taken into account both locally, with a direct effect on the heat and mass fluxes, and globally, on the total heat and mass rates.

Since the early works on non-spherical drop evaporation modelling [11, 12], the effect of drop shape was considered through a direct influence of the surface curvature on the local fluxes. The cited work [12] evidenced, from the results of numerical simulations, using the Galerkin finite element method, the existence of a correlation for the rate of evaporation of deformed drop and showed that the mass flux varies along the surface of the deformed drop. The author proposed a correlation between the evaporation mass flux and the local surface curvature, based on a suggestion of Lian and Reitz, which in a work on the instability of evaporating liquid jets [13], postulated that the local evaporation flux, from a deformed surface, could be equated to that from a spherical drop having a mean curvature equal to the local mean curvature of the surface under consideration. More recently [14] it was shown, through an analytical solution of the species and energy conservation equation in spheroidal coordinates, that the local heat and mass flux on a spheroidal surface (either prolate or oblate) is proportional to the fourth root of the local Gaussian curvature. Later on it was shown that the same results holds also for triaxial ellipsoids [15].

On this account, it is important to point out that the effect of curvature on the evaporation and heat transfer from a droplet floating in a gaseous atmosphere can be analysed in different ways depending on the observation scale. When the scale is large enough so that the continuous assumption holds, i.e. the molecular constitution of the fluids can be disregarded, the effect of droplet shape can be separated from that of the boundary conditions [16, 17]. Under such assumption, the effect of droplet shape on the evaporation characteristics becomes a purely geometrical problem, and the local evaporation characteristics (vapour and heat fluxes) are usually linked to local shape characteristics, like surface curvature. On the other hand, when the observation scale becomes small enough, kinetic theory rather than continuous fluid mechanics must be used to model the phenomena. The appropriate non-dimensional number to identify the *kinetic regime* of droplet evaporation is the droplet Knudsen number $\mathrm{Kn}_d = \frac{\ell}{2r_d}$, where ℓ is the mean free path and r_d the droplet radius. When $\mathrm{Kn} \gg 1$, the rate of mass and energy transfer between the droplet and the surrounding ambient gas is described by the molecular fluxes towards the droplet surface and emanating from it. At this scale, boundary conditions may become dependent on the drop size, and possibly shape, through the local effect of the surface curvature on the balance between incoming and outcoming molecules. Specifically, the curvature of the vapor-liquid interface alters the equilibrium pressure in the vapour phase, as described first by the Kelvin equation [18] and later corrected by Gibbs [19–21]. The Kelvin equation is valid for a pure component, assuming an incompressible liquid and an ideal gas, and it yields

$$p^s_{v,r} = p^s_{v,\infty} \exp\left(\frac{2\sigma}{\rho_l R_v T_d r_d}\right) \tag{1}$$

where R_v is the gas constant, T_d denotes the droplet temperature, $p^s_{v,r}$ and $p^s_{v,\infty}$ represent the saturated pressure of the pure vapour for a curved and planar surface, respectively. As can be seen, the equilibrium vapor pressure at a convex curved surface is higher than that at a flat surface, thus leading to a considerable enhancement of the evaporation rate in the case of nanometre sized droplets. By taking the variation of the total thermodynamic Gibbs potential of the system of noninteracting droplets in equilibrium with the saturated vapor, Kuz [22] demonstrated that Eq. (1) is strictly valid until the molar interfacial volume can be neglected in relation with the molar liquid volume of the droplet. This condition is fulfilled for droplet size down to $r_d \approx 4\,\mathrm{nm}$ and limits the range of investigated sizes for the kinetically controlled regime of droplet evaporation. For modelling the growth of crystals or liquid clusters from homogeneous nucleation, instead, an improved relation should be employed that includes the mole number of each bulk phase and of the surface phase.

Based on the above considerations, the present paper discusses the influence of surface curvature on the droplet evaporation rate. The overall goal is to understand under which conditions curvature effects are no longer negligible for the accurate prediction of dropwise evaporation. In the process, an overview of macroscopic and kinetic modelling approaches is also provided.

2 Drop Evaporation Models at Different Scales

2.1 Effect of Surface Curvature at the Macroscopic Scale

The available analytical modelling of the evaporation from a liquid drop is based on the solution of the conservation equations for a continuous medium, accounting for the presence of interfaces. In such approach the interface is considered as a sufficiently smooth surface that separates two phases (liquid and gaseous), and evaporation is responsible for mass and energy flows across such interface. It has been observed [16] that the predicted heat and mass fluxes on this surface, under uniform Dirichlet boundary conditions, can be written in such a way that the properties of the gaseous mixture and the boundary conditions can be separated from the effects caused by the surface shape. In particular, the local heat and mass fluxes can be written under the form:

$$n_{v,n}^{(1)} = -f_m \nabla_n \Phi \tag{2}$$

$$q_n = -f_t \nabla_n \Phi \tag{3}$$

where the quantities f_m and f_t were analytically derived in [17] and found to depend only on the thermophysical properties of the gaseous phase and the boundary conditions (see [17] for all the details), while the function Φ is the solution of the Laplace problem:

$$\nabla^2 \Phi = 0 \tag{4a}$$

$$\Phi\,(\text{surface}) = 1;\ \ \Phi\,(\infty) = 0 \tag{4b}$$

and $\nabla_n \Phi$ is the component of the gradient of Φ normal to the surface.

It is then evident that, in this framework, the effect of the drop shape is fully contained in the form of the function Φ, and it is separated from the effect of boundary conditions and thermophysical properties.

As previously stated, in all the available analytical modelling of non-spherical drop evaporation, the local fluxes were considered directly influenced by the local surface curvature [12–15]. In particular, it was shown that for ellipsoidal (spheroidal and triaxial) drops the local heat and mass fluxes are proportional to the fourth root of the local Gaussian curvature. Although the extension of this result to the case of generally shaped smooth surfaces is tempting, it can be shown that it is not a general rule.

Given any smooth (twice differentiable) surface, the two principal curvatures κ_1, κ_2, can be related to mean, $\mathcal{C}$, and Gaussian, K_G, curvatures by the relations [23]:

$$\mathcal{C} = \kappa_1 + \kappa_2 \tag{5}$$

$$K_G = \kappa_1 \kappa_2 \tag{6}$$

The aim of the following analysis is to show that, contrary to what usually postulated and obtained for a special class of surfaces (ellipsoids), the values of these curvatures alone are not enough to define the local mass and heat fluxes from a non-spherical drop evaporating in a stagnant environment. To this end, it is sufficient to show that the mass flux (and consequently the heat flux) from surfaces of different shape having the same mean, $\mathcal{C}$, and Gaussian, K_G, curvatures at given points, is not the same.

Let search the solution of the problem (4) in different systems of coordinates in order to find the fluxes on the surface of a drop having the shape of one coordinate surface. Following [24], let consider the five curvilinear orthogonal coordinate systems: spherical, prolate and oblate spheroidal, inverse prolate and oblate spheroids, which can be defined in a unique form as:

$$x = aA(\zeta, \eta, \alpha)\cos(\varphi) \tag{7a}$$

$$y = aA(\zeta, \eta, \alpha)\sin(\varphi) \tag{7b}$$

$$z = aB(\zeta, \eta, \alpha) \tag{7c}$$

where $-1 \leq \eta \leq +1$,

$$A(\zeta, \eta, \alpha) = \frac{\sqrt{\zeta^2 + \alpha}}{\Theta(\zeta, \eta, \alpha)}\sqrt{1 - \eta^2};\ B(\zeta, \eta, \alpha) = \frac{\zeta \eta}{\Theta(\zeta, \eta, \alpha)} \tag{8}$$

and the range of the ζ-coordinate, the parameter α and the function $\Theta(\zeta, \eta, \alpha)$ are given in Table 1, while a is a size parameter (refer to [25] for details on these coordinate systems).

In these coordinate systems the surfaces defined by the parametric equation $\zeta = \zeta_0$ have typically the form reported in Fig. 1.

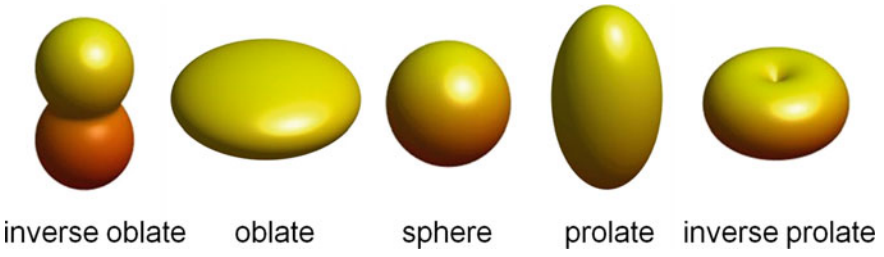

Fig. 1 Samples of inverse oblate, oblate, spherical, prolate and inverse prolate drop surface

Table 1 Non-dimensional mean and Gaussian curvatures for spherical, spheroidal and inverse spheroidal surfaces

Shape	α	Θ	Range of ζ	Ξ_n
Sphere	0	1	$0 \leq \zeta < 1$	ζ^{n+1}
Oblate	+1	1	$0 \leq \zeta < \infty$	$Q_n(i\zeta)$
Prolate	−1	1	$1 \leq \zeta < \infty$	$Q_n(\zeta)$
Inverse oblate	+1	$\zeta^2 + \alpha(1-\eta^2)$	$0 \leq \zeta < \infty$	$P_n(i\zeta)$
Inverse prolate	−1	$\zeta^2 + \alpha(1-\eta^2)$	$1 \leq \zeta < \infty$	$P_n(\zeta)$

These shapes can be observed in real experiments on oscillating drops (the oblate and prolate spheroids) and in binary drop collisions (inverse oblate and prolate drops) [26], then the following analysis has also an applicative value. It is worth to mention that the coordinates η and ζ and the parameter a have different meanings in different coordinate systems; for example for the spherical coordinate system, $\zeta = \frac{r}{r_d}$, $\eta = \cos\theta$, where r is the radial coordinate, θ is the polar (zenithal) angle and r_d is the radius of the droplet defined by the equation $\zeta = 1$, and in this case $a = r_d$. Assuming that the problem has rotational symmetry and observing that the scale functions in these coordinate systems are [25]:

$$h_\zeta = \frac{a}{\Theta}\sqrt{\frac{\left(\zeta^2+\alpha\eta^2\right)}{\left(\zeta^2+\alpha\right)}};\quad h_\eta = \frac{a}{\Theta}\sqrt{\frac{\left(\zeta^2+\alpha\eta^2\right)}{\left(1-\eta^2\right)}};\quad h_\varphi = \frac{a}{\Theta}\sqrt{\left(\zeta^2+\alpha\right)\left(1-\eta^2\right)} \tag{9}$$

the Laplace Eq. (4) can be written as (see [25]):

$$\frac{\partial}{\partial\zeta}\left[\frac{\left(\zeta^2+\alpha\right)}{\Theta}\frac{\partial\Phi}{\partial\zeta}\right] + \frac{\partial}{\partial\eta}\left[\frac{\left(1-\eta^2\right)}{\Theta}\frac{\partial\Phi}{\partial\eta}\right] = 0 \tag{10}$$

The solution of this equation can be written in a unified form as (see again [25] for each coordinate system):

$$\Phi = \Theta^{1/2}\sum_{n=0}^{\infty} g_n \frac{\Xi_n(\zeta)}{\Xi_n(\zeta_0)} P_n(\eta) \tag{11}$$

where the functions Ξ_n are reported in Table 1 for each coordinate system and the coefficients g_n are found by satisfying the Dirichlet condition $\Phi = 1$ on the surface $\zeta = \zeta_0$ and can be analytically calculated, thanks to the orthogonality of the Legendre polynomials, as:

$$g_n = \frac{2n+1}{2}\int_{-1}^{1}\frac{P_n(\eta)}{\Theta^{1/2}}d\eta \tag{12}$$

It can be easily observed that the spheroidal drop cases degenerate in a 1D solution, in fact in such cases $\Theta = 1$ and

$$g_n = \frac{2n+1}{2} \int_{-1}^{1} P_n(\eta)\, d\eta = \delta_{n0} \tag{13}$$

then

$$\Phi = \begin{cases} \frac{Q_0(i\zeta)}{Q_0(i\zeta_0)} = \frac{\arctan(\zeta)-\pi/2}{\arctan(\zeta_0)-\pi/2} & \text{oblate} \\ \frac{Q_0(\zeta)}{Q_0(\zeta_0)} = \frac{\log\left(\frac{\zeta+1}{\zeta-1}\right)}{\log\left(\frac{\zeta_0+1}{\zeta_0-1}\right)} & \text{prolate} \end{cases} \tag{14}$$

Having found Φ, the evaporation flux can be calculated from Eq. (2). To perform the wanted comparison we will assume that all the compared drops have the same volume, which can be obtained by properly choosing the size parameter a in relation to the equivalent drop diameter defined as $r_d = \left(\frac{3V}{4\pi}\right)^{1/3}$. This yields the following evaluation of a:

$$a = \frac{r_d}{f_r(\zeta_0)} \tag{15}$$

where

$$f_r(\zeta_0) = \begin{cases} \left(\zeta_0^2+\alpha\right)^{1/3} \zeta_0^{1/3} & \text{spheroidal} \\ \left\{ \frac{1}{8} \frac{\zeta_0}{\left(\zeta_0^2+\alpha\right)} \left[\frac{5\zeta_0^2+2\alpha}{\zeta_0^4} + \frac{I(\zeta_0)}{\left(\zeta_0^2+\alpha\right)^{1/2}} \right] \right\}^{1/3} & \text{inverse spheroidal} \end{cases} \tag{16}$$

and

$$I(\zeta_0) = \begin{cases} \frac{3}{2} \ln\left(\frac{\sqrt{\zeta_0^2+1}+1}{\sqrt{\zeta_0^2+1}-1} \right) & \text{inverse oblate} \\ 3 \arctan\left(\frac{1}{\sqrt{\zeta_0^2-1}} \right) & \text{inverse prolate} \end{cases} \tag{17}$$

while for the spherical case $f_r(\zeta_0) = 1$ (see also [15] for details).

2.1.1 Curvatures

Considering the rotationally symmetric surface parametrically defined by the equation $\zeta = \zeta_0$, the principal curvatures can be calculated as [27]:

$$\kappa_1 = \frac{A_{\eta\eta} B_\eta - A_\eta B_{\eta\eta}}{\left(A_\eta^2 + B_\eta^2\right)^{3/2}}; \qquad \kappa_2 = \frac{B_\eta}{|A| \left(A_\eta^2 + B_\eta^2\right)^{1/2}} \tag{18a}$$

and the following non-dimensional mean and Gaussian curvatures can be defined, using the equivalent drop radius, as:

$$\mathcal{C}^* = r_d\,(\kappa_1 + \kappa_2) \tag{19}$$

$$K_G^* = r_d^2\,\kappa_1\kappa_2 \tag{20}$$

where Table 2 reports their values for the drop shapes considered here.

The ranges of the coordinates ζ and η, reported in Table 1, limit the values of the mean and Gaussian curvatures. Figure 2a shows, on the $\mathcal{C}^* - K_G^*$ plane, the different regions for the different shapes.

From this map, it can be appreciated that there exists an overlapping among the regions corresponding to spheroids (oblate and prolate) and inverse spheroids (oblate and prolate). This must be interpreted as follows: chosen a point inside such region, say $\left(\mathcal{C}_1^*, K_{G1}^*\right)$, there exist an oblate spheroid, a prolate spheroid, an inverse oblate and an inverse prolate spheroid that, somewhere on their surfaces, have the same non-dimensional mean and Gaussian curvatures. If the evaporation flux depends only on the surface curvatures (either mean, Gaussian or both) then all these drops should have, at that given point on the surface, the same value of the non-dimensional evaporation flux, and this should happen for all the pairs $\left(\mathcal{C}^*, K_G^*\right)$ belonging to the common region above mentioned.

Table 2 Non-dimensional mean and Gaussian curvatures for spherical, spheroidal and inverse spheroidal surfaces

Shape	$\mathcal{C}^*$	K_G^*
Sphere	2	1
Spheroids	$\zeta_0^{4/3}\,\frac{2\zeta_0^2+\alpha(1+\eta^2)}{\left(\zeta_0^2+\alpha\eta^2\right)^{3/2}\left(\zeta_0^2+\alpha\right)^{1/6}}$	$\frac{\zeta_0^{8/3}\left(\zeta_0^2+\alpha\right)^{2/3}}{\left(\zeta_0^2+\alpha\eta^2\right)^2}$
Inv. spheroids	$\zeta_0\left[\frac{2\zeta_0^4+\alpha\zeta_0^2-1+\left[5\alpha\zeta_0^2+4\right]\eta^2+\eta^4}{\sqrt{\zeta_0^2+\alpha}\left(\zeta_0^2+\alpha\eta^2\right)^{3/2}}\right] f_r\left(\zeta_0\right)$	$\frac{\zeta_0^2\left(\zeta_0^2+\alpha(1+\eta^2)\right)\left(\zeta_0^2+\alpha(3\eta^2-1)\right)}{\left(\zeta_0^2+\alpha\eta^2\right)^2} f_r^2\left(\zeta_0\right)$

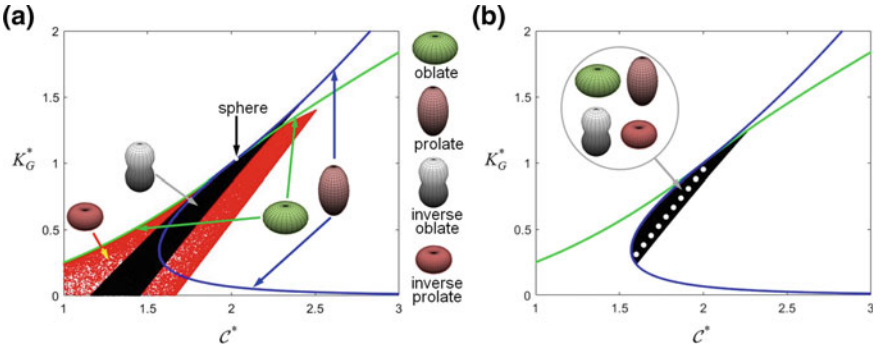

Fig. 2 **a** $\mathcal{C}^* - K_G^*$ regions for the selected drop shapes; **b** $\mathcal{C}^* - K_G^*$ overlapping region for the selected drop shapes (black) and selected points (white circles) for flux comparison (see Table 3)

2.1.2 Calculation of Fluxes and Curvatures

According to Eqs. (2) and (3) the heat and mass fluxes are function of the gradient of the function Φ, obtained by Eqs. (11) and (12).

The non-dimensionalisation of the fluxes can be obtained in two different ways. From Eqs. (2) and (3), a simple way to non-dimensionalise is:

$$n^*_{v,n} = \frac{n_{v,n}}{f_m r_d} = -r_d \nabla_n \Phi = \frac{q_n}{f_T r_d} = q^*_n \tag{21}$$

where the quantity $-r_d \nabla_n \Phi$ is a purely geometrical one and it can be explicitly defined as:

$$-r_d \nabla_n \Phi = -\frac{r_d}{h_\zeta\,(\zeta_0, \eta)} \left(\frac{\partial \Phi}{\partial \zeta}\right)_{\zeta=\zeta_0} \tag{22}$$

On the other hand, the following non-dimensionalisation was used in [14, 15]:

$$\hat{n}_{v,n} = \frac{n_{v,n} 4\pi r_d^2}{m_{ev}} \tag{23}$$

where the evaporation rate m_{ev} can be written as:

$$m_{ev} = \int_A n_{v,n} dA \tag{24}$$

and the the two non-dimensional forms can be related to each other by:

$$\hat{n}_{v,n} = \frac{n^*_{v,n} 4\pi r_d^2}{\int_A n^*_{v,n} dA} \tag{25}$$

It is interesting now to notice that for spheroids, the first way to non-dimensionalise the fluxes yields the explicit form:

$$n^*_{v,n} = \frac{\left(\zeta_0^2 + \alpha\right)^{-1/6} \zeta_0^{1/3}}{\sqrt{\left(\zeta^2 + \alpha\eta^2\right)}} \begin{cases} \frac{2}{(\pi - 2\arctan(\zeta_0))} & \text{oblate} \\ \frac{2}{\log\left(\frac{\zeta_0+1}{\zeta_0-1}\right)} & \text{prolate} \end{cases} \tag{26}$$

which can be related to the local Gaussian curvature by the relation:

$$n^*_{v,n} = \left(K^*_G\right)^{1/4} \frac{1}{\left(\zeta_0^2 + \alpha\right)^{1/3} \zeta_0^{1/3}} \begin{cases} \frac{2}{(\pi - 2\arctan(\zeta_0))} & \text{oblate} \\ \frac{2}{\log\left(\frac{\zeta_0+1}{\zeta_0-1}\right)} & \text{prolate} \end{cases} \tag{27}$$

where

$$\left(K_G^*\right)^{1/4} = \frac{\zeta_0^{2/3}\left(\zeta_0^2+\alpha\right)^{1/6}}{\sqrt{\left(\zeta_0^2+\alpha\eta^2\right)}} \tag{28}$$

Instead, for the second non-dimensionalisation method (23), since

$$\int_A n_{v,n}^* dA = \frac{8\pi r_d^2}{\left(\zeta_0^2+\alpha\right)^{1/3}\zeta_0^{1/3}} \begin{cases} \frac{1}{(\pi-2\arctan(\zeta_0))} & \text{oblate} \\ \frac{1}{\log\left(\frac{\zeta_0+1}{\zeta_0-1}\right)} & \text{prolate} \end{cases} \tag{29}$$

then

$$\hat{n}_{v,n} = \frac{n_{v,n}^* 4\pi R_d^2}{\int_A n_{v,n}^* dA} = \frac{\left(\zeta_0^2+\alpha\right)^{1/6}\zeta_0^{2/3}}{\sqrt{\left(\zeta^2+\alpha\eta^2\right)}} = \left(K_G^*\right)^{1/4} \tag{30}$$

Both non-dimensional forms yield a variation of the flux over the surface proportional to the fourth root of the Gauss curvature, which on the surface depends on the coordinate η; but the second one yields a form that is independent of the *shape*, i.e. it holds for both prolate and oblate. The use of the integral (29) seems to eliminate the dependence on the shape, maintaining only that on the local characteristics (the curvature).

2.1.3 Interdependence Between Fluxes and Local Curvature

To analyse the possible existence of a direct relationship between the non-dimensional fluxes (Eq. 23) and the local curvatures, the non-dimensional flux, $\hat{n}_{v,n}$, is calculated on points of the drop surfaces of differently shaped drops where both $\mathcal{C}^*$ and K_G^* (or equivalently κ_1 and κ_2) have specified values, and the results are then compared to each other. The set of values of $\mathcal{C}^*$ and K_G^* are chosen to belong to the above mentioned overlapping region in the $\mathcal{C}^* - K_G^*$ map and they are enlightened as white circles in Fig. 2b. These values of the mean and Gaussian curvatures can be found on some parts of the surface of spheroidal and inverse spheroidal drops; if the conjecture about the influence of curvatures on evaporation and heat fluxes were correct, the resulting values of $\hat{n}_{v,n}$ should coincide on those points of the surface of differently shaped drops having locally the same curvatures. Table 3 reports the values calculated from the solution (4) for the four cases of oblate/prolate spheroids and oblate/prolate inverse spheroids. It is evident that for the spheroids the non-dimensional flux is exactly equal to $\left(K_G^*\right)^{1/4}$, as reported in [14] and [15], while for the case of oblate and prolate inverse spheroids the non-dimensional flux assumes different values. This is enough to prove that the sole curvature of a surface (which is completely defined by $\mathcal{C}^*$ and K_G, or κ_1 and κ_2) does not define the evaporation and heat fluxes. Likely, there exists other geometrical parameters, possibly depending on the drop shape, that may completely define the geometrical effect on evaporation and heat fluxes, that at present are not yet evident.

Table 3 Non-dimensional fluxes for spheroids and inverse spheroids (oblate and prolate)

$\mathcal{C}^*$	K_G^*	$\hat{n}_{v,n}$		
		Spheroids	Inverse oblate	Inverse prolate
1.600	0.301	0.746	0.280	0.930
1.644	0.381	0.786	0.327	0.940
1.689	0.452	0.820	0.384	0.950
1.733	0.523	0.851	0.449	0.960
1.778	0.594	0.878	0.522	0.969
1.822	0.666	0.903	0.600	0.978
1.867	0.737	0.926	0.681	0.986
1.911	0.808	0.948	0.762	0.992
1.956	0.879	0.968	0.840	0.998
2.000	0.950	0.987	0.911	1.002

2.2 *Effect of Surface Curvature at the Microscopic Scale*

The objective of this section is to investigate the size range for which the Kelvin correction (see Eq. 1) induces a significant enhancement to the droplet vaporisation rate. For this purpose, two representative sizes are considered, namely $r_d = 600$ nm and $r_d = 6$ nm. For a physically accurate description of the mass and energy transfer between the droplet and the surrounding gas, a refinement to the classical diffusion-based evaporation theories must be considered. For this purpose, Langmuir [28] introduced the concept of a Knudsen layer, which is defined as a thin vapor layer surrounding the liquid droplet in the order of the molecular mean free path, where heat and mass transport are dominated by collision effects and have to be described by kinetic molecular theory [29]. The importance of the Knudsen layer correction is twofold. First, it is able to describe continuously the transition from a diffusion-controlled to a kinetic-controlled mechanism of mass and energy transfer in terms of the Knudsen number of the droplet Kn_d. If the droplet radius is much smaller than the molecular mean free path (i.e. $\mathrm{Kn}_d \gg 1$), then the Knudsen layer occupies a large volume around the droplet, with respect to the size of the droplet, and the heat and mass transfer are controlled by collisions of vapour molecules within the Knudsen layer. In contrast, if $\mathrm{Kn}_d \ll 1$, the Knudsen layer shrinks towards the droplet surface and the diffusion-controlled evaporation/condensation regime is recovered. Langmuir-type models, therefore, automatically assure that the correct description of the mass/energy transfer mechanism is adopted with increasing Kn_d (or equivalently decreasing droplet size). Second, it enables the inclusion of local non-equilibrium effects in the standard fluid dynamic equations for modelling droplet evaporation/condensation. The latter become dominant for large departure from the equilibrium state of the droplets and therefore are not considered here.

2.2.1 The Young Model

The Young model has been already extensively described and validated in literature [30–32]. Hence, only a short summary is presented hereafter. As can be seen in Fig. 3, the vapour-liquid interface is modelled as a sharp interface. Furthermore, vapour molecules leaving the droplet surface are assumed to have a Maxwellian velocity distribution function, corresponding to the temperature of the liquid, in agreement with recent findings from MD simulations [4, 33, 34]. In addition, saturated vapour density is assumed on the droplet surface, based on recent findings from Zhakhovsky et al. [4]. For the calculation of saturated properties, we included mixture and real gas thermodynamics. The equation of state and thermodynamic properties for the fluid mixtures are obtained from REFPROP [35] (®NIST). Curvature effects on the saturation pressure are also included, according to Eq. (1).

At the border of the Knudsen layer r_d, Young selected the Grad's distribution function, because it reproduces with high accuracy the (reverse) temperature jump predicted by analytical solutions of the Boltzman equation for large departure from the droplet equilibrium state [29, 36]. Note that the vapour properties at the Knudsen

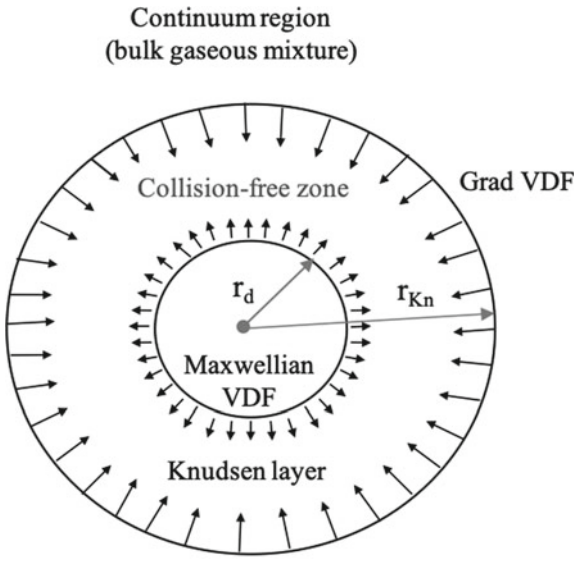

$$r_{Kn} = r_d + \beta\ell = r_d(1 + 2\beta Kn_d)$$

Liquid droplet	$0 < r < r_d$
Knudsen layer	$r_d < r < r_{Kn}$
Continuum region	$r_{Kn} < r < \infty$

Fig. 3 Schematic drawing of the Young model, based on Langmuir's Knudsen layer concept

border, e.g. T_v^{Kn} and p_v^{Kn}, are unknown and are calculated, at each time step, by employing a flux matching condition at r_{Kn}. Specifically, the net energy and mass flow rates are calculated independently both in the Knudsen layer ($\dot{E}^{\mathrm{fm}}$, $\dot{M}^{\mathrm{fm}}$) by employing gas kinetic theory and in the continuum region ($\dot{E}^{\mathrm{ct}}$, $\dot{M}^{\mathrm{ct}}$) by employing diffusion. Conservation of mass and energy across the Knudsen border (r_{Kn}) yields a system of equation in the unknowns T_v^{Kn} and p_v^{Kn}

$$\dot{E}^{\mathrm{fm}} = \dot{E}^{\mathrm{ct}} = \dot{E}\left(T_d, T^{\mathrm{amb}}, T_v^{\mathrm{Kn}}, p_v^{\mathrm{amb}}, p_{v,r}^{s}, p_v^{\mathrm{Kn}}, r_d, r_{\mathrm{Kn}}\right) \tag{31a}$$

$$\dot{M}^{\mathrm{fm}} = \dot{M}^{\mathrm{ct}} = \dot{M}\left(T_d, T^{\mathrm{amb}}, T_v^{\mathrm{Kn}}, p_v^{\mathrm{amb}}, p_{v,r}^{s}, p_v^{\mathrm{Kn}}, r_d, r_{\mathrm{Kn}}\right) \tag{31b}$$

Here the parameters T_{d}, r_{d} and r_{Kn} are inputs. As soon as the temperature and vapour pressure at the Knudsen border are known, the net mass and energy transfer ($\dot{M}$, $\dot{E}$) can be obtained from their respective free molecular or continuum expressions, subject to a new set of boundary conditions: $[T_d, p_{v,r}^{s}(T_d)]$ and $[T_v^{\mathrm{Kn}}, p_v^{\mathrm{Kn}}]$ for the free molecular regime and $[T_v^{\mathrm{Kn}}, p_v^{\mathrm{Kn}}]$ and $[T^{\mathrm{amb}}, p_v^{\mathrm{amb}}]$ for the continuum region. Hence, the effects of the Knudsen layer (i.e. the effects of the kinetic correction and of curvature) are felt on the continuum scale as a new set of boundary conditions. Note that the location of the Knudsen border is set at $r_{\mathrm{Kn}} = r_d + \beta\ell$, where β is an arbitrary constant in the range $0.5 < \beta < 1.5$. Young [30] proposed to use the value $\beta = 0.75$, since it gave a good agreement with kinetic studies of Chernyak [37] for pure monatomic vapours. In this work, we kept the same choice until further results from MD simulations will be available for polyatomic gases.

Finally, the temporal variation of the droplet temperature can be obtained by performing an energy balance at the droplet surface according to

$$m_d c_{p,l} \frac{dT_d}{dt} = -\dot{E} - \dot{M} L + \dot{M} h_v^{s} \tag{32}$$

where L is the latent heat, m_d the droplet mass, $c_{p,l}$ the heat capacity of the liquid and h_v^{s} the saturated specific enthalpy of the vapour molecules evaporating from the droplet surface. In Eq. (32), it is implicitly assumed that the energy and mass flow rates are positive when leaving the droplet. As can be seen, quasi-steady evaporation at constant wet-bulb temperature is not a prerequisite for the Young model. It is automatically reached when the net energy transfer from the gaseous phase is balanced by the energy losses due to evaporation.

2.2.2 The Effect of the Kelvin Correction

In order to understand the importance of curvature on the droplet evaporation rate, two representative droplet sizes are considered, namely $r_d = 600$ nm and $r_d = 6$ nm. All other properties are instead kept constant, specifically $T^{\mathrm{amb}} = 500$ K, $p^{\mathrm{amb}} = 10$ bar and $T_d = 363$ K. The result of this comparison is discussed below. As can be seen, for droplet diameters in the order of micrometers as shown Fig. 4, the effects

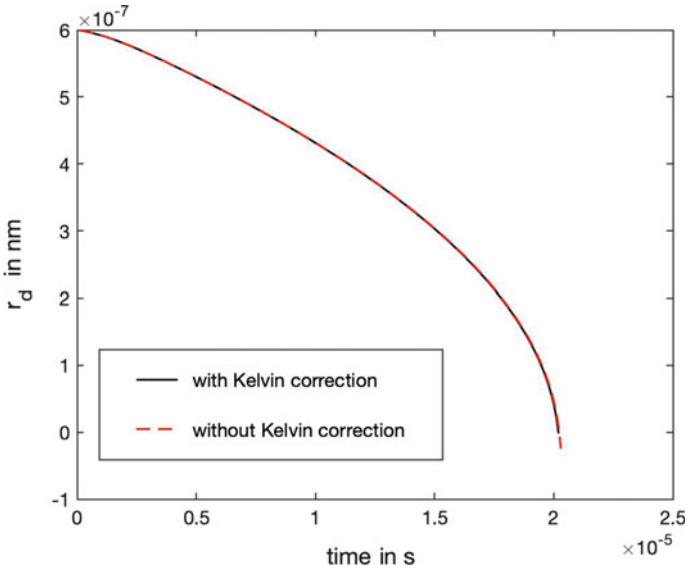

Fig. 4 Temporal evolution of the droplet radius. Initial conditions: $T^{\text{amb}} = 500$ K, $p^{\text{amb}} = 10$ bar and $T_d = 363$ K, $r_d = 600$ nm. Fluids: *n*-heptane in nitrogen

of curvature are basically negligible during the entire droplet evaporation process. This is because the Kelvin correction (see Eq. 1) is extremely sensitive to the droplet size and becomes relevant only for nanometer sized droplets, as shown in Fig. 5. The associated increase in the saturated vapour pressure due to the curvature correction is shown in Fig. 6, which explains the faster evaporation rate observed in Fig. 5 with the Kelvin correction.

At this point, it is important to revise critically the obtained results and recall the analysis on the validity of the Kelvin correction presented in Sect. 1. First of all, it is important to point out that the accuracy of the Young model predictions for nanometer-sized droplets at high-pressure was verified in [31, 32] and hence the presented results can be considered reliable. Second, for the modelling of droplet evaporation, the Kelvin effect on the saturation pressure can be safely neglected even in the nanometer-size range. Indeed, as can be deduced from Fig. 5, the error in the prediction of the droplet size stays below 1 nm during most of the droplet lifetime, which is well below the accuracy of any experimental measurement. Large deviations are observed only for droplet radii below 20 Å. The implication of this result is twofold. First, it shows that the Kelvin correction is strictly required only for the prediction of the critical cluster size in the modelling of phase transition processes initiated by homogeneous nucleation. Second, it corroborates the theoretical findings of Kuz [22], who proposed a correction to Eq. (1) to take into account the number of moles in the bulk and interfacial phases, according to

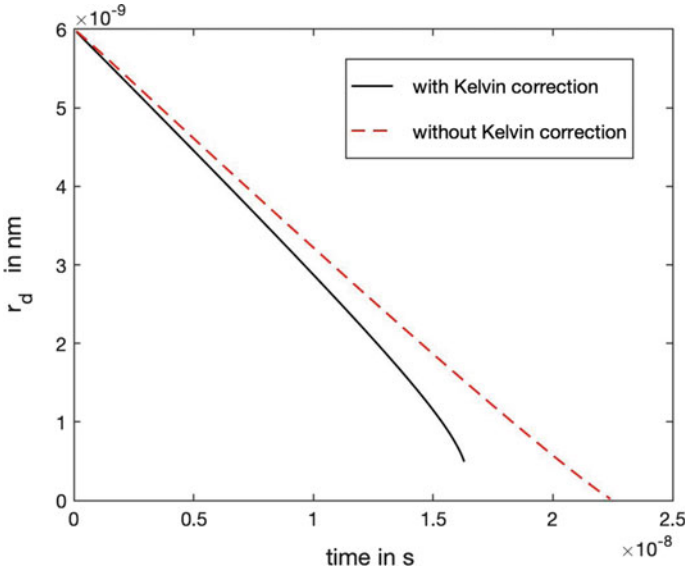

Fig. 5 Temporal evolution of the droplet radius. Initial conditions: $T^{\text{amb}} = 500$ K, $p^{\text{amb}} = 10$ bar and $T_d = 363$ K, $r_d = 6$ nm. Fluids: *n*-heptane in nitrogen

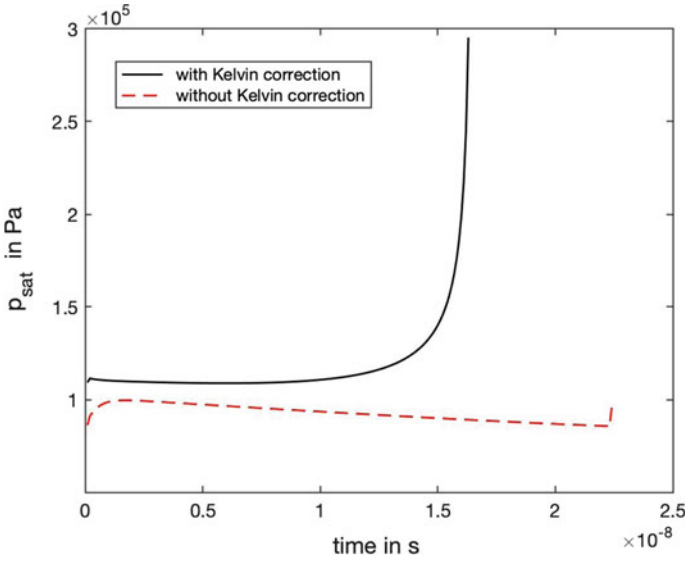

Fig. 6 Temporal evolution of the droplet radius. Initial conditions: $T^{\text{amb}} = 500$ K, $p^{\text{amb}} = 10$ bar and $T_d = 363$ K, $r_d = 6$ nm. Fluids: *n*-heptane in nitrogen

$$p^s_{v,r} = p^s_{v,\infty} \exp\left[\frac{1}{(1 + n^v/n^l + n^\sigma/n^l)} \frac{3\sigma}{\rho_l R_v T_d r_d}\right] \tag{33}$$

here n^v, n^l and n^σ represent the number of moles in the vapour, liquid and interfacial systems, respectively. By comparing Eqs. (1) and (33), it is clear that the classical Kelvin correction is recovered for any droplet size such that the interfacial volume is negligible in relation to the molar liquid volume of the droplet, namely $V^\sigma \ll V^l$ or equivalently $n^\sigma \ll n^l$. Under these circumstances, the following relation results between the number of moles in the liquid and vapour phase for the classical Kelvin correction to be valid: $n^v = 0.5n^l$. The exponential increase in the saturated vapour pressure observed in Fig. 6 for droplet radii below 20 Å is therefore not realistic and is due to the omission of the mole fraction correction in the estimation of the Kelvin factor.

3 Conclusions

The effect of drop shape and liquid-gas interface curvature on drop evaporation is investigated at the macro- and micro-scale levels, by applying hydro-dynamic and kinetic modelling, respectively. According to the macroscopic approach, the analytical solution of the conservation equations is obtained in the natural curvilinear coordinate systems for the selected five drop shapes: sphere, oblate and prolate spheroids and oblate and prolate inverse spheroids.

At the macroscopic scale, the effect of operating conditions (thermo-physical properties and boundary conditions) is fully separated from that of the drop geometry. For spherical and spheroidal drops the geometrical term of the non-dimensional local flux only depends on the surface local curvature (it is proportional to the forth root of the Gaussian curvature). However it is shown that for general drop shapes the fluxes cannot only depend on the surface local curvature, but possibly on other geometrical parameters describing the drop shape.

At the microscopic scale, boundary conditions may become dependent on the drop size and surface tension, in order to take into account the effect of local curvature. Specifically, the curvature of the vapour-liquid interface alters the equilibrium pressure in the vapour phase, thus leading to a significant enhancement of the evaporation rate. Our analysis shows that the Kelvin correction is strictly required only for the prediction of the critical cluster size in the modelling of phase transition processes initiated by homogeneous nucleation. At these conditions, it is mandatory to consider the repartition of molecules in the different phases, in order to prevent a significant overestimation of the equilibrium vapour pressure.

References

1. Sazhin, S.S.: Droplet and Sprays. Springer (2014)
2. Sazhin, S.S., Shishkova, I.N., Al Qubeissi, M.: A self-consistent kinetic model for droplet heating and evaporation. Int. J. Heat Mass Transf. **93**, 1206–1217 (2016)
3. Polikarpov, A.Ph., Graur, I.A., Gatapova, E.Ya., and Kabov, O.A.: Kinetic simulation of the non-equilibrium effects at the liquid-vapor interface. Int. J. Heat Mass Transfer **136**, 449–456 (2019)
4. Zhakhovsky, V.V., Kryukov, A.P., Levashov, V.Y., Shishkova, I.N., Anisimov, S.I.: Mass and heat transfer between evaporation and condensation surfaces: atomistic simulation and solution of Boltzmann kinetic equation. Proc. Natl. Acad. Sci. **116**(37), 18209–18217 (2018)
5. Chakraborty, S., Qiao, L.: Molecular investigation of sub-to-supercritical transition of hydrocarbon mixtures: multi-component effect. Int. J. Heat Mass Transf. **145**, 118629 (2019)
6. Xiao, G., Luo, K.H., Ma, X., Shuai, S.: A molecular dynamics study of fuel droplet evaporation in sub- and supercritical conditions. Proc. Combust. Inst. **37**(3), 3219–3227 (2019)
7. Maxwell, J.C.: Diffusion, 9th edn. Ency, Brit (1877)
8. Sazhin, S.S.: Modelling of fuel droplet heating and evaporation: recent results and unsolved problems. Fuel **196**, 69–101 (2017)
9. Abramzon, B., Sirignano, W.A.: Droplet vaporization model for spray combustion calculations. Int. J. Heat Mass Transf. **32**(9), 1605–1618 (1989)
10. Qian, J., Law, C.K.: Regimes of coalescence and separation in droplet collision. J. Fluid Mech. **331**, 59–80 (1997)
11. Jeng, S.M., Deng, Z.: Numerical simulation of deformed droplet dynamics and evaporation. Recent. Adv. Spray Combust.: Spray Combust. Meas. Model. Simul. **2**, 305–328 (1996)
12. Mashayek, F.: Dynamics of evaporating drops. Part I:formulation and evaporation model. Int. J. Heat Mass Transfer **44**, 1517–1526 (2001)
13. Lian, Z.W., Reitz, R.D.: The effect of vaporization and gas compressibility on liquid jet atomization. Atomization Sprays **3**(3), 249–264 (1993)
14. Tonini, S., Cossali, G.E.: An exact solution of the mass transport equations for spheroidal evaporating drops. Int. J. Heat Mass Transf. **60**, 236–240 (2013)
15. Tonini, S., Cossali, G.E.: One-dimensional analytical approach to modelling evaporation and heating of deformed drops. Int. J. Heat Mass Transfer **9**, 301–307 (2016)
16. Imaoka, R.T., Sirignano, W.A.: Transient vaporisation and burning in dense droplet spray. Int. J. Heat Mass Transf. **48**, 4354–4366 (2005)
17. Cossali, G.E., Tonini, S.: An analytical model of heat and mass transfer from liquid drops with temperature dependence of gas thermo-physical properties. Int. J. Heat Mass Transf. **138**, 1166–1177 (2019)
18. Thomson, W.: On the equilibrium of vapour at a curved surface of liquid. Philos. Mag. **4**, 448–452 (1871)
19. Gibbs, J.W.: The Scientific Papers of. J. Willard Gibbs, vol. 1, pp. 55–353. Woodbridge, Ox Bow (1993)
20. Elliott, J.A.W.: On the complete kelvin equation. Chem. Eng. Educ. **35**, 274–278 (2001)
21. Kaptay, G.: The gibbs equation versus the Kelvin and the Gibbs- Thomson equations to describe nucleation and equilibrium of nano-materials. J. Nanosci. Nanotechnol. **12**, 1–9 (2012)
22. Kuz, V.A.: A vapor pressure equation for droplets. Langmuir **9**, 3722–3723 (1993)
23. Nguyen-Schäfer, H., Schmidt, J.P.: Tensor Analysis and Elementary Differential Geometry for Physicists and Engineers. Springer (2014)
24. Tonini, S., Cossali, G.E.: Effect of local surface curvature on heating and evaporation of deformed droplets. In: DIPSI Workshop 2018-Droplet Impact Phenomena & Spray Investigations, Universit
25. Moon, P., Spencer, D.E.: Field Theory Handbook, 2nd edn. Springer-Verlag, Berlin (1988)
26. Quan, S., Lou, J., Schmidt, D.P.: Modeling merging and breakup in the moving mesh interface tracking method for multiphase flow simulations. J. Comput. Phys. **228**(7), 2660–2675 (2009)

27. Goldman, R.: Curvature formulas for implicit curves and surfaces. Comput. Aided Geom. Des. **22**, 632–658 (2005)
28. Langmuir, I.: The dissociation of hydrogen into atoms. Part II: calculation of the degree of dissociation and the heat of formation. J. Am. Chem. Soc. **37**, 417–458 (1915)
29. Sone, Y., Onishi, Y.: Kinetic theory of evaporation and condensation - Hydrodynamic equation and slip boundary condition. J. Phys. Soc. Jpn. **44**(6), 1981–1994 (1978)
30. Young, J.B.: The condensation and evaporation of liquid droplets at arbitrary Knudsen number in the presence of an inert gas. Int. J. Heat Mass Transf. **36**(11), 2941–2956 (1993)
31. Luijten, C.C.M.: Nucleation and Droplet Growth at High Pressure. Ph.D. Thesis, Technische Universiteit Eindhoven (1998)
32. Peeters, P., Pieterse, G., van Dongen, M.E.H.: Multi-component droplet growth. II. A Theoretical Model. Phys. Fluids **16**(7), 2575–2586 (2004)
33. Kobayashi, K., Kazumasa, H., Kon, M., Sasaki, K., Watanabe, M.: Molecular dynamics study on evaporation and reflection of monatomic molecules to construct kinetic boundary condition in vapor-liquid equilibria. Heat Mass Transf. **52**(9), 1851–1859 (2016)
34. Kobayashi, K., Kon, M., Watanabe, M.: Kinetic boundary condition in vapor-liquid two-phase system during unsteady net evaporation/condensation. Eur. J. Mech. B. Fluids **64**, 81–92 (2017)
35. Lemmon, E.W., Bell, I.H., Huber, M.L., McLinden, M.O.: NIST Standard Reference Database 23: Reference Fluid Thermodynamic and Transport Properties-REFPROP, Version 10.0. National Institute of Standards and Technology (2018)
36. Onishi, Y.: The spherical-droplet problem of evaporation and condensation in a vapour-gas mixture. J. Fluid Mech. **163**, 171–194 (1986)
37. Chernyak, V.G., Margilevskiy, A.Ye.: The kinetic theory of heat and mass transfer from a spherical particle in a rarefied gas. Int. J. Heat Mass Transfer **32**(11), 2127–2134 (1989)

On the Importance of Kinetic Effects in the Modelling of Droplet Evaporation at High Pressure and Temperature Conditions

Grazia Lamanna, Christoph Steinhausen and Bernhard Weigand

Abstract This work analyses whether the inclusion of interfacial temperature jumps is necessary in the modelling of droplet evaporation at high pressure. The analysis is divided into two parts. First, we revise the major findings from theoretical models and molecular dynamics simulations on the conditions leading to the inception of interfacial jumps and the main parameters affecting them. Second, an evaporation model is considered that includes a diffuse transition layer (Knudsen layer), in the order of a few mean free paths around the droplet, where transport processes are described by kinetic molecular theory. The analysis shows that discontinuities in temperature and chemical potential across the interface are important when molecular collisions control transport processes and result in large heat and mass fluxes. This may occur not only at low pressures, but also at high pressures and temperatures for conditions sufficiently far from global thermodynamic equilibrium and/or for sufficiently small droplets. On a macroscopic scale, the resulting correction to the boundary conditions for classical diffusion-controlled models may be significant at high evaporation rates.

1 Introduction

Understanding the simultaneous transfer of energy and mass through a liquid-vapour interface during evaporation is important both from a fundamental and technological point of view. The increasing progression of micro/nanofluidic devices has called for the inclusion of kinetic corrections in classical diffusion-controlled models of evaporation. The kinetic correction is required not only to take into account rarefaction effects induced by the downsizing of the devices, but also due to the increasing importance of local non-equilibrium effects at high evaporation rates. This occurs mainly for large departure from the droplet equilibrium state, measured in terms of temperature and chemical potential differences (or vapour pressure for measurable

G. Lamanna (✉) · C. Steinhausen · B. Weigand
Institute of Aerospace Thermodynamics (ITLR), University of Stuttgart, Stuttgart, Germany
e-mail: grazia.lamanna@itlr.uni-stuttgart.de

G. Lamanna et al. (eds.), *Droplet Interactions and Spray Processes*,
Fluid Mechanics and Its Applications 121,
https://doi.org/10.1007/978-3-030-33338-6_22

quantities) between the droplet surface and the ambient gas. Physically, it can be explained because vapour molecules, evaporating from the droplet surface, adapt to the ambient conditions through collisions with gas molecules. This process mainly takes place outside the "collision-free" zone, which extends typically over one or two mean free paths ℓ. From a theoretical standpoint, this requires the implementation of gas kinetic theory, which does not necessarily guarantee the continuity of temperature and vapour pressure across the interface. An elegant way to include local non-equilibrium effects in classical diffusion-based evaporation/condensation theories was proposed by Langmuir [18], who introduced the concept of a Knudsen layer. The latter can be regarded as as a diffuse, non-equilibrium transition layer in the order of a few mean free paths, where the transport of mass and energy in the vapour phase is described by molecular collisions, as shown schematically in Fig. 1.

Due to its relevance for the predictions of macroscopic temperature and vapour pressure jumps, we consider here the modelling of the rate of mass transfer from the droplet to the ambient gas mixture within the Knudsen layer. Specifically, it can be expressed as

$$\dot{M}^{fm} = \alpha_e \phi_I - (1 - \alpha_c)\phi_{II} + \phi_{II} = \alpha_e \phi_I + \alpha_c \phi_{II} \tag{1}$$

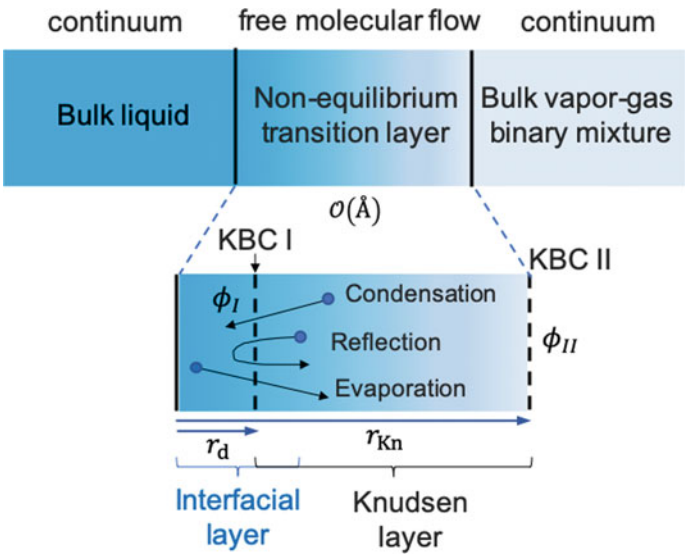

Fig. 1 Microscopic description of the liquid droplet—ambient gas system under unsteady evaporation conditions. Note that at the molecular length scale, both the vapour-liquid interface and the Knudsen layer interface are planar, even though they have a curvature in the macroscopic scale. The kinetic boundaries I and II represent the location of the sharp interface r_d and of the Knudsen layer border r_{Kn} in the macroscopic scale

where α_e and α_c are the evaporation and condensation coefficients, respectively. Their physical meaning is explained in Sect. 2. The kinetic boundary conditions (KBCs) ϕ_I and ϕ_{II} represent the molecular mass fluxes at the vapour-liquid sharp interface and at the Knudsen border, respectively. As can be deduced from Eq. (1), the mass transfer in the free-molecular region consists of three contributions, representing the mass flux from evaporated, reflected and incoming vapour molecules. Here carrier gas molecules do not contribute to the net mass flux, since they do not condensate nor evaporate. At the border of the Knudsen layer r_{Kn}, a flux matching condition is imposed to assure continuity of mass and energy transfer between the free-molecular and continuum regions.

Note that the kinetic expression for mass flux $\dot{M}^{fm}$ gains in importance with decreasing droplet size. This is controlled through the extent of the Knudsen layer, defined as $r_{\mathrm{Kn}} = r_d(1 + 2\,\beta\,\mathrm{Kn}_d)$ with $\mathrm{Kn}_d = \frac{\ell}{2r_d}$ and β a kinetic coefficient in the range $0.5 < \beta < 1.5$. Hence for $\mathrm{Kn}_d \gg 1$ the Knudsen layer occupies a large volume around the droplet and the energy and mass transfer are kinetically controlled. Alternatively, for $\mathrm{Kn}_d \ll 1$ the Knudsen layer basically merges with the droplet surface and the diffusion-controlled evaporation/condensation (continuum) regime is recovered. However, by solving the linearised Boltzmann equation for binary vapour-gas mixtures, Onishi [21] demonstrated that, for $\mathrm{Kn}_d \ll 1$ and simultaneously large departure from equilibrium, the influence of the kinetic correction is no longer negligible and leads to a significant increase in the predicted evaporation/condensation mass flux [15, 21]. Since macroscopic jumps in thermodynamic variables are directly proportional to the evaporating mass flux, it follows that they may become significant even in the continuum limit (i.e. for diffusion-controlled models of droplet evaporation).

Experimentally, temperature discontinuities at the liquid-vapour interface have been measured by different authors [1–3, 8, 9, 20, 24]. Recently, the validity and accuracy of these measurements has been recently questioned by several authors [3, 7, 10], reaching opposite conclusions on the existence of interfacial jumps. This controversy has been lately clarified by Polikarpov et al. [25]. The authors pointed out that, even under rarefied conditions, thermocouple measurements are always made too far from the upper boundary of the Knudsen layer. When these values are used as input in classical models, they result in a considerable overestimation of the evaporation rate. To overcome this limitation, Polikarpov et al. [25] suggested that kinetic theory should be employed to obtain the appropriate kinetic boundary conditions (KBCs) for evaporation models. In the following sections, we provide a brief overview of the main characteristics of KBC I and II, as derived by molecular dynamic simulations. Then we discuss how these findings can be incorporated into macroscopic models for droplet evaporation, suited for engineering applications. Finally, we investigate under which conditions macroscopic jumps in temperature may become significant even at high pressure conditions, where typically diffusion-controlled theories are employed for modelling droplet evaporation.

2 Review of Kinetic Boundary Conditions for Engineering Applications

With reference to Eq. (1), it is immediately clear that, for engineering applications, the complex description of transport processes in the non-equilibrium transition layer can be omitted by specifying kinetic boundary conditions (KBCs) at the entrance (I) and at the exit (II) of the Knudsen layer. Specifically, one needs to specify the molecular mass fluxes ϕ_I and ϕ_{II}. Macroscopically, the kinetic boundary is equivalent to impose the location of the sharp vapour-liquid interface r_d and the Knudsen layer interface r_{Kn}. For dropwise condensation/evaporation, r_{d} represents the droplet radius and r_{Kn} the upper border of the Knudsen layer, measured from the droplet centre. The molecular mass flux ϕ_{II} (KBC II) can be obtained analytically by solving the Boltzmann equation in the Knudsen layer with the boundary condition KBC I. For determining ϕ_I, instead, molecular dynamics (MD) simulations or mean-field kinetic theory have been employed [12, 14–16, 32]. Specifically, recent advances have shown that ϕ_I can be expressed as linear combination of reflection and condensation conditions according to

$$\phi_I = \rho_I \hat{f} = [\alpha_e \rho_v^{\mathrm{sat}}(T_d) + (1 - \alpha_c)\sigma]\hat{f}(T_d) \tag{2}$$

where $\hat{f}$ is the normalised Maxwellian distribution at the temperature of the liquid and σ has the units of density [12, 13]. The coefficients α_e and α_c are equal to one at equilibrium (i.e. $\rho_I = \rho_v^{\mathrm{sat}}$) and close to unity for pure vapours [32]. For binary mixtures, they decrease with increasing concentrations of dissolved carrier gas in the liquid [13], thus implying that the assumption of equilibrium vapour density at the droplet interface is no longer valid. A major drawback in the determination of α_e and α_c is that they strongly depend upon the position of the sharp interface r_d [12]. Due to this ambiguity, a new procedure was recently proposed to derive KBC I, based on the regression coefficients β_e and β_c yielding [12, 14–16],

$$\phi_I = [\beta_i(T_L)(\rho_v^{\mathrm{sat}} - \sigma) + \sigma]\hat{f}(T_L), \text{ with } i = e, c \tag{3}$$

Note that all parameters (β_i, ρ_v^{sat}, σ, $\hat{f}$) depend only upon the liquid temperature. This means that the evaporating molecules retain the VDF of the liquid (i.e. semi-Maxwellian), albeit not at the saturated density. In addition, it can be assured that, when Eq. (3) is used as KBC I, the correct values of mass and energy fluxes are obtained, irrespective of the position of the sharp interface [12]. The only drawback is that the regression coefficients β_i have been obtained only for monoatomic gases and therefore Eq. (3) cannot be employed for modelling evaporation/condensation problems in polyatomic gas mixtures. Ishiyama et al. [6] performed molecular dynamic simulations for determining KBC I at the interface between a polyatomic vapour and its condensed phase under steady evaporation conditions. The authors showed that KBC I is qualitatively similar to the kinetic conditions found for monoatomic vapours, thus confirming the appropriateness of assuming a Maxwellian distribu-

tion for the molecular velocity distribution function (VDF) of evaporating vapour molecules.

Based on the above results, Young [31] proposed a Langmuir-type evaporation/condensation model with two different VDFs as KBCs, namely a semi-Maxwellian VDF with equilibrium vapour density at the droplet interface and the Grad VDF at the border of the Knudsen layer. The model is valid for polyatomic vapour-gas mixtures at any concentration of inert gas and at arbitrary Knudsen number Kn_d. It is also not restricted to the *quasi-steady* regime of evaporation/condensation and can reproduce the (reversed) temperature jump within the Knudsen layer at high evaporation/condensation rates. In agreement with analytical solutions of the Boltzmann equation [21] and with more recent results from MD simulations [13], the Young model also predicts a decrease in macroscopic jumps with increasing inert gas concentration. Finally, the model is computationally efficient and has been validated for dropwise evaporation/condensation both at low [5, 29, 31] and high pressure conditions [19, 22, 23].

In the following section, we will therefore employ the Young model to investigate under which conditions the inception of temperature jumps may be observed also at high pressure and temperature conditions. To assess the plausibility of our analysis, the predictions from the Young's model are compared to results from non-equilibrium molecular dynamics (NEMD). The main advantage of NEMD simulations is that both thermodynamic and transport properties are obtained from intermolecular interactions with no additional assumptions on the equation of state or on the interface [4, 11, 27, 30] and its shape. In particular, we refer to the work of Qiao et al. [26], who employed NEMD to simulate dropwise evaporation at high pressure. Specifically, the authors studied the evaporation process of a nano-sized *n*-heptane droplet in a nitrogen atmosphere, at various ambient temperatures ($500 < T < 900$ K) and pressures ($1 < p < 20$ MPa). The simulations are used to corroborate our estimations of the temperature jump across the Knudsen layer and to address some of the limitations of the Young model.

3 Results

In order to investigate the importance of the Knudsen layer correction on the temperature jump, we follow closely the theoretical framework laid down by Onishi [21] and briefly summarised in Sect. 1. As a first step, we verify that for large droplets (i.e. droplet diameters of at least 1mm), the diffusion controlled regime is recovered, irrespectively of the temperature difference between the droplet and the ambient gas. For this purpose, we consider single droplet evaporation of *n*-alkanes into a nitrogen atmosphere with $T^{\mathrm{amb}} = 1300$ K and $p^{\mathrm{amb}} \in \{46\,\mathrm{bar}, 60\,\mathrm{bar}\}$, while the droplet temperature varies in the range $T_d = 0.5$–$0.98\ T_{\mathrm{crit}}$, where T_{crit} denotes the critical temperature of the *n*-alkanes. According to Onishi's analysis, under these conditions corresponding to $\mathrm{Kn}_d\ \mathcal{O}(10^{-6})$, the diffusion-controlled regime of droplet evaporation should be recovered. This verification has been presented in Lamanna et al. [17]

and therefore is not reproduced here. In addition, the temperature jump across the Knudsen layer should be always negligible under all conditions.

Figs. 2 and 3 show the temperature jumps at KBC I and II. For the jumps' estimations at the droplet interface (KBC I), we adopted the methodology presented in [17], based on the evaluation of the interfacial resistivities. As shown in [17], for the present conditions, all interfacial resistivities are in the order of $\mathcal{O}(10^{-7})$ (or even smaller) and result in negligible thermal losses across the vapour-liquid interface. This finding indirectly corroborates the assumption of local equilibrium at the droplet surface. This also implies that vapour molecules leave the droplet surface with a semi-Maxwellian VDF, corresponding to the temperature of the liquid droplet, as currently assumed by the Young model.

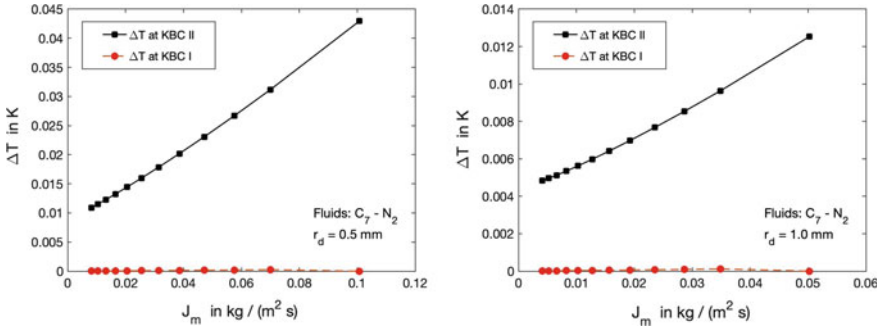

(a) Droplet radius: 0.5 mm (b) Droplet radius: 1 mm

Fig. 2 Comparison of temperature jumps ΔT at KBC I and II, respectively, for two characteristic droplet sizes. Fluids: *n*-heptane in nitrogen. Ambient conditions: $T^{\text{amb}} = 1300\,\text{K}$ and $p^{\text{amb}} = 60\,\text{bar}$. Each value represents one particular point in time of a dynamic simulation

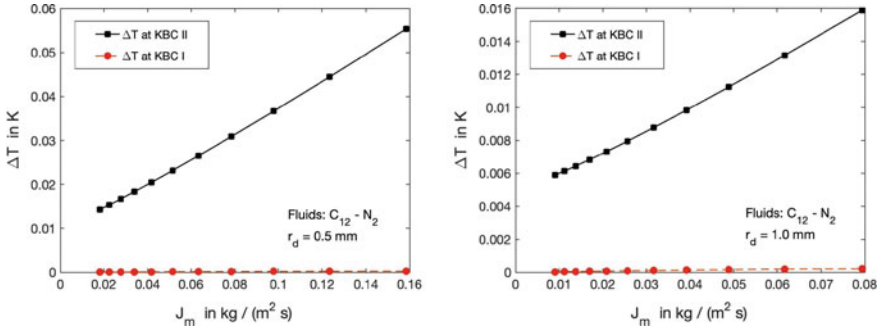

a) Droplet radius: 0.5 mm (b) Droplet radius: 1 mm

Fig. 3 Comparison of temperature jumps ΔT at KBC I and II, respectively, for two characteristic droplet sizes. Fluids: *n*-dodecane in nitrogen. Ambient conditions: $T^{\text{amb}} = 1300\,\text{K}$ and $p^{\text{amb}} = 46\,\text{bar}$. Each value represents one particular point in time of a dynamic simulation

The temperature jump predicted at Knudsen border (KBC II) is also insignificant for engineering applications. However, it remains one or two orders of magnitude larger than the temperature jumps at KBC I. In addition, while the jumps at KBC I do not vary with increasing droplet radius, the temperature jumps across the Knudsen layer decrease of roughly one order of magnitude when the droplet radius is increased from 0.5 to 1.0 mm. These differences can be easily explained by recalling that local non-equilibrium effects are implicitly included in the predictions of the Young model. This result is in agreement with the theoretical predictions of Onishi [21]. Onishi demonstrated that, for a given degree of departure from the droplet equilibrium state, the importance of the kinetic correction on the predicted evaporating/condensing mass flux increases with increasing Kn_d. For the present simulations, the Knudsen number increases from 4.1×10^{-6} to 8.3×10^{-6}, thus explaining the increase in the predicted temperature jump with the Young model.

As a second step, we systematically reduce the droplet size, while maintaining large temperature differences between the droplet and ambient gas. The associated increase in Kn_d implies that the "collision-free zone" (Knudsen layer) expands, thus retarding the temperature adaptation of vapour molecules to the ambient temperature. Under these conditions, the Young model [31] predicts a drastic increase in the Knudsen layer temperature jump, as shown in Table 1. As can be seen, significant temperature jumps across the Knudsen layer may exists even for $\mathrm{Kn}_d \ll 1$, in agreement with the findings by Onishi [21]. This theoretical result is also corroborated by experimental findings at medium vacuum [2, 9, 20, 28], where a direct correlation was found between the increase in the measured temperature jump and the associated mass flux. Instead, if the droplet radius is kept constant, the value of temperature jump/mass flux increases with increasing temperature difference $(T^{\mathrm{amb}} - T_d)$. This trend has been also confirmed experimentally in [3]. Finally, note that temperature jumps become relevant for $r_d < 6\,\mu\mathrm{m}$ which is characteristic for spray applications.

To validate the predictions from the Young model, Table 2 shows the comparison with NEMD results from Qiao et al. [26], who performed NEMD simulations for sub-critical droplet evaporation at high pressure conditions. As can be seen, also in the NEMD simulations, a temperature jump between the liquid phase and the surrounding vapour is observed. For $t = 3\mathrm{ns}$, the temperature gradient of the NEMD results extends over 1–2 mean free paths into the vapour phase (up to $r \approx 12\,\mathrm{nm}$). This approximately coincides with the Knudsen layer used in the Young model, extending up to $r_{\mathrm{Kn}} \approx 15\,\mathrm{nm}$. Despite the good agreement in the predicted temperature jumps, a deviation is observed in the predicted mass flux and hence in the resulting development of the droplet radius over time. Several factors may be responsible for this deviation. First, the exact location of KBC II of the Knudsen layer is not clearly defined, which has a direct influence on the predicted mass flux, as pointed out in [12, 13]. Second, the choice of the VDF at KBC II influences the flux of vapour molecules and should be confirmed by NEMD simulations. Third, in the present simulations, we assumed the evaporation α_e and condensation α_c coefficients to be unity, which directly affects the calculated mass flux. This assumption needs to be revised for

Table 1 Predicted temperature jumps across the Knudsen layer for droplets with various radii using the evaporation model of Young [31]. Test system: liquid n-heptane droplet in nitrogen at two representative ambient temperatures ($T^{\mathrm{amb}} = 500\,\mathrm{K}$ and $1200\,\mathrm{K}$), ambient pressure $p^{\mathrm{amb}} = 10\,\mathrm{bar}$ and droplet temperature $T_d = 363\,\mathrm{K}$. Mass and energy fluxes are also listed

r_d (nm)	Kn_d	$\Delta T^{\mathrm{Young}}$ (K)	J_m ($\mathrm{kg\,m^{-2}s^{-1}}$)	$\lvert J_e \rvert$ ($\mathrm{W\,m^{-2}}$)
$Case\ I : T^{\mathrm{amb}} = 500\,\mathrm{K}$				
6	$\mathcal{O}(1)$	84.5	199.8	4.08×10^{3}
60	$\mathcal{O}(10^{-1})$	18.4	53.2	1.96×10^{3}
600	$\mathcal{O}(10^{-2})$	2.1	3.36	240
6000	$\mathcal{O}(10^{-3})$	0.21	0.33	24.3
$Case\ II : T^{\mathrm{amb}} = 1200\,\mathrm{K}$				
6	$\mathcal{O}(10)$	646	1.46×10^{3}	1.09×10^{4}
60	$\mathcal{O}(1)$	248	1.06×10^{3}	2.26×10^{4}
600	$\mathcal{O}(10^{-2})$	35.1	6.80	1.30×10^{3}
6000	$\mathcal{O}(10^{-3})$	3.6	0.60	129.9

Table 2 Comparison of temperature jumps from NEMD results by Qiao et al. [26], and the model of Young [31] at a representative time $t = 3\,\mathrm{ns}$. Test system: liquid n-heptane droplet in nitrogen at ambient temperature $T^{\mathrm{amb}} = 500\,\mathrm{K}$, ambient pressure $p^{\mathrm{amb}} = 10\,\mathrm{bar}$ and droplet temperature $T_d = 363\,\mathrm{K}$

	ΔT_{jump} K	r_d nm	J_m $\mathrm{kg\,m^{-2}s^{-1}}$	$\lvert J_e \rvert$ $\mathrm{W\,m^{-2}}$
NEMD	85	≈ 2.5	≈ 500	–
Young	88	5.1	199	4.08×10^{3}

large concentrations of non-evaporating vapour components and polyatomic fluids. Results from NEMD simulations of evaporating droplets might help removing some of the above mentioned uncertainties.

4 Conclusion

This paper presented a detailed discussion on the need to include interfacial temperature jumps in the modelling of droplet evaporation. This topic is of particular relevance for engine applications, where micrometer-sized droplets are injected at high pressure and temperature conditions. For this purpose, the evaporation model by Young [31] that includes non-linear kinetic effects is employed to obtain the temperature discontinuity across the Knudsen layer. The analysis revealed that interfacial discontinuities in temperature and chemical potential become significant when mass and energy transfer are controlled by kinetic effects. This may occur not only at moderate vacuum conditions, but also at high pressures and temperatures in presence of

large perturbations to the droplet equilibrium state. The above findings indicate that consideration of temperature and chemical potential jumps becomes more important for decreasing droplet size and, therefore, should be considered in combustion applications including small droplets. The current approach is to assume a model in which heat and mass transfer are diffusion-controlled, after which empirical correlations are applied to enhance predicted transfer rates in order to match experimental data. As demonstrated in this paper, at high pressure and temperature conditions, assuming a diffusion-controlled model alone is not justified for small droplets (i.e. $r_d \leq 20\,\mu\mathrm{m}$), which would lead to significant underestimation of the droplet evaporation rate. Our analysis, however, also enabled us to highlight some of the limitations of the Young model. For example, both the positioning of the Knudsen layer and the modelling of the molecular mass flux at the droplet interface have an important influence on the predicted evaporation rate. To that end, a joint comparative study, based on the results from NEMD simulations at high pressures, would be highly desirable to reduce the above uncertainties for high temperatures and pressures.

Acknowledgements The authors thank the German Research Foundation (DFG) for financial support through the collaborative research center *Droplet Dynamics Under Extreme Ambient Conditions* (SFB-TRR 75, project number 84292822).

References

1. Badam, V.K., Kumar, V., Durst, F., Danov, K.: Experimental and theoretical investigations on interfacial temperature jumps during evaporation. Exp. Therm. Fluid Sci. **32**(1), 276–292 (2007)
2. Fang, G., Ward, C.A.: Temperature measured close to the interface of an evaporating liquid. Phys. Rev. E. **59**(1), 417–428 (1999)
3. Gatapova, E.Y., Graur, I.A., Kabov, O.A., Aniskin, V.M., Filipenko, M.A., Sharipov, F., Tadrist, L.: The temperature jump at water–air interface during evaporation. Int. J. Heat Mass Transfer **104**, 800–812 (2017)
4. Ge, J., Kjelstrup, S., Bedeaux, D., Simon, J.M., Rousseau, B.: Transfer coefficients for evaporation of a system with a Lennard-Jones long-range spline potential. Phys. Rev. E. **75**, 061604 (2007). https://doi.org/10.1103/PhysRevE.75.061604
5. Han, X., Han, Z., Zeng, W., Qian, J., Wang, Z.: Coupled model of heat and mass balance for droplet growth in wet steam non-equilibrium homogeneous condensation flow. Energies **10**, 2033 (2017)
6. Ishiyama, T., Takeru, Y., Fujikawa, S.: Molecular dynamics study of kinetic boundary condition at an interface between a polyatomic vapor and its condensed phase. Phys. Fluids **16**, 4713–4726 (2004)
7. Jafari, P., Amritkar, A., Ghasemi, H.: On temperature discontinuity at an evaporating water interface (2019)
8. James, R.A.: Onsager heat of transport at the liquid-vapour interface of glycerol-water solutions. Master's thesis, University of Canterbury (2007)
9. James, R.A., Phillips, L.F.: Onsager heat of transport for water vapour at the surface of glycerol-water mixtures. Chem. Phys. Lett. **425**, 49–52 (2006)
10. Kazemi, M.A., Nobes, D.S., Elliott, J.A.W.: Effect of the thermocouple on measuring the temperature discontinuity at a liquid-vapor interface. Langmuir **33**, 7169–7180 (2017)

11. Kjelstrup, S., Tsuruta, T., Bedeaux, D.: The inverted temperature profile across a vapor/liquid surface analyzed by molecular computer simulations. J. Colloid Interface Sci. **256**(2), 451–461 (2002). https://doi.org/10.1006/jcis.2002.8684
12. Kobayashi, K., Hori, K., Kon, M., Sasaki, K., Watanabe, M.: Molecular dynamics study on evaporation and reflection of monatomic molecules to construct kinetic boundary condition in vapor-liquid equilibria. Heat Mass Transfer **52**, 1851–1859 (2016)
13. Kobayashi, K., Sasaki, K., Kon, M., Fujii, H., Watanabe, M.: Kinetic boundary conditions for vapor-gas binary mixture. Microfluid. Nanofluid. **21**, 53 (2017)
14. Kon, M., Kobayashi, K., Watanabe, M.: Method of determining kinetic boundary conditions in net evaporation/condensation. Phys. Fluids **26**, 072003 (2014)
15. Kon, M., Kobayashi, K., Watanabe, M.: Liquid temperature dependence of kinetic boundary conditions in vapor-liquid interface. Int. J. Heat Mass Transfer **99**, 317–326 (2016)
16. Kon, M., Kobayashi, K., Watanabe, M.: Kinetic boundary conditions in vapor-liquid two-phase system during unsteady net evaporation/condensation. Eur. J. Mech. B/Fluids **64**, 81–92 (2017)
17. Lamanna, G., Steinhausen, C., Weigand, B., Preusche, A., Bork, B., Dreizler, A., Stierle, R., Groß, J.: On the importance of non-equilibrium models for describing the coupling of heat and mass transfer at high pressure. Int. Commun. Heat Mass Transfer **98**, 49–58 (2018). https://doi.org/10.1016/j.icheatmasstransfer.2018.07.012
18. Langmuir, I.: The dissociation of hydrogen into atoms. [Part II] calculation of the degree of dissociation and the heat of formation. J. Am. Chem. Soc. **37**, 417–458 (1915)
19. Luijten, C.C.M.: Nucleation and droplet growth at high pressure. Ph.D. thesis, Eindhoven University of Technology (1998)
20. Mills, C.T., Phillips, L.F.: Onsager heat of transport at the aniline-vapour interface. Chem. Phys. Lett. **366**, 279–283 (2002)
21. Onishi, Y.: The spherical-droplet problem of evaporation and condensation in a vapour-gas mixture. J. Fluid Mech. **163**, 171–194 (1986)
22. Peeters, P., Luijten, C.C.M., van Dongen, M.E.H.: Transitional droplet growth and diffusion coefficients. Int. J. Heat Mass Transfer **44**, 181–193 (2001)
23. Peeters, P., Luijten, C.C.M., Hruby, J., van Dongen, M.E.H.: Multi-component droplet growth. i. experiments with supersaturated n-nonane vapor and water vapor in methane. Phys. Fluids **16**, 2567 (2004)
24. Phillips, L.F.: Onsager heat of transport as a consequence of detailed balance at the gas-liquid interface. Chem. Phys. Lett. **396**, 350–352 (2004)
25. Polikarpov, A.P., Graur, I.A., Gatapova, E.Y., Kabov, O.A.: Kinetic simulation of the non-equilibrium effects at the liquid-vapor interface. Int. J. Heat Mass Transfer **136**, 449–456 (2019)
26. Qiao, L., Jain, S., Mo, G.: High Pressure Flows for Propulsion Applications, (to appear) Molecular Simulations to Research Supercritical Fuel Properties. Progress in Astronautics and Aeronautics. American Institute of Aeronautics and Astronautics (AIAA) (2019)
27. Simon, J.M., Kjelstrup, S., Bedeaux, D., Hafskjold, B.: Thermal flux through a surface of n-octane. A non-equilibrium molecular dynamics study. J. Phys. Chem. B **108**(22), 7186–7195 (2004). https://doi.org/10.1021/jp0375719
28. Ward, C.A., Fang, G.: Expression for predicting liquid evaporation flux: statistical rate theory approach. Phys. Rev. E. **59**(1), 429–440 (1999)
29. White, A., Young, J., Walters, P.: Experimental validation of condensing flow theory for a stationary cascade of steam turbine blades. Philos. Trans. R. Soc. Lond. **354**, 59–88 (1996)
30. Xu, J., Kjelstrup, S., Bedeaux, D., Røsjorde, A., Rekvig, L.: Verification of Onsager's reciprocal relations for evaporation and condensation using non-equilibrium molecular dynamics. J. Colloid Interface Sci. **299**(1), 452–463 (2006). https://doi.org/10.1016/j.jcis.2006.01.043. URL http://www.sciencedirect.com/science/article/pii/S0021979706000506
31. Young, J.B.: The condensation and evaporation of liquid droplets at arbitrary Knudsen number in the presence of an inert gas. Int. J. Heat Mass Transfer **36**, 2941–2956 (1993)
32. Zhakhovsky, V.V., Kryukov, A.P., Levashov, V.Y., Shishkova, I.N., Anisimov, S.I.: Mass and heat transfer between evaporation and condensation surfaces: atomistic simulation and solution of Boltzmann kinetic equation. Natl. Acad. Sci. (2018)

Direct Numerical Simulations of Evaporating Droplets at Higher Temperatures: Application of a Consistent Numerical Approach

Karin Schlottke, Jonathan Reutzsch, Corine Kieffer-Roth and Bernhard Weigand

Abstract A method for the numerical simulation of three-dimensional evaporation processes is applied to the evaporation process of isooctane droplets under slow inflow conditions and to the evaporation of a water droplet tandem in quiescent air. The method is a thermodynamically consistent numerical framework and was developed for the requirements of the evaporation of hot, liquid droplets. It is implemented into the in-house multi-phase code FS3D, which uses a Direct Numerical Simulation approach based on the Volume-of-Fluid method. Three different simulation cases are presented for the isooctane droplets and their results are in good agreement with literature correlations. The influence of the near drop neighbourhood can be observed in the simulation of the water droplet tandem.

1 Introduction

The numerical simulation of multi-phase flows is important to describe many processes in nature and engineering. In a lot of these applications, it is not only the coexistence of different phases which is of interest, but it is rather the heat and mass transfer including phase change between them where the focus of research is centred. The multi-phase code *Free Surface 3D* (FS3D) [2] has been especially developed to solve the Navier-Stokes equations and the energy equation for incom-

K. Schlottke (✉) · J. Reutzsch · C. Kieffer-Roth · B. Weigand
Institute of Aerospace Thermodynamics (ITLR), University of Stuttgart, Pfaffenwaldring 31, 70569 Stuttgart, Germany
e-mail: karin.schlottke@itlr.uni-stuttgart.de

J. Reutzsch
e-mail: jonathan.reutzsch@itlr.uni-stuttgart.de

C. Kieffer-Roth
e-mail: corine.kieffer-roth@itlr.uni-stuttgart.de

B. Weigand
e-mail: bernhard.weigand@itlr.uni-stuttgart.de

G. Lamanna et al. (eds.), *Droplet Interactions and Spray Processes*,
Fluid Mechanics and Its Applications 121,
https://doi.org/10.1007/978-3-030-33338-6_23

pressible flows with arbitrary free surfaces using the method of Direct Numerical Simulation (DNS).

The present paper summarizes the recently implemented new modelling of the evaporation process and shows its application to the simulation of both single evaporating isooctane droplets and an evaporating droplet tandem. A more elaborate description of the method including extensive derivations, a more detailed validation, and further DNS results can be found in [15]. The following Sect. 2 will give an overview of the mathematical formulation including the underlying assumptions, the conservation equations, and the jump conditions. Then, the numercial approach will be summed up briefly in Sect. 3. We will also explain here how the evaporation method works and how it is implemented and solved numerically. Section 4 will provide a comparison of simulation results with experimental and analytical literature data, and finally, Sect. 5 will draw overall conclusions.

2 Mathematical Formulation

This section provides a short description of the mathematical framework used in the software package FS3D for simulating evaporation processes. This includes the interface capturing method, the conservation equations and the corresponding jump conditions. Several assumptions are made a priori. First, the liquid phase is a pure substance. Second, the gaseous phase does not diffuse into the liquid phase. In general, all fluids are considered to be Newtonian and the flow is considered to be incompressible. At the interface, local thermal equilibrium is assumed. Both viscous dissipation and thermal radiation are neglected.

2.1 Interface Capturing and Material Properties

Hirt and Nichols [4] developed the Volume-of-Fluid (VOF) method in order to distinguish between different phases: An additional indicator variable, f_1, is introduced for the volume fraction of the liquid phase in each cell, where

$$f_1(\mathbf{x}, t) = \begin{cases} 1 & \text{in the dispersed phase,} \\ ]0, 1[& \text{for interfacial cells,} \\ 0 & \text{in the continuous phase.} \end{cases} \tag{1}$$

A second indicator variable f_2 can be introduced for the volume fraction of the vapour phase [3]. According to the used one-field formulation, the material properties are calculated using the VOF variables f_1 and f_2. The density ρ, for example, can be expressed throughout the whole domain as

$$\rho = \rho_l f_1 + \rho_v f_2 + (1 - f_1 - f_2)\rho_g, \tag{2}$$

where ρ_l, ρ_v, and ρ_g correspond to the densities of the liquid, vapour, and inert gas, respectively. An ideal mixture of vapour and inert gas is assumed in the gaseous phase (subscript $_{gp}$). Following [19], we calculate the local vapour mass fraction X_v by

$$X_v = \frac{f_2}{1 - f_1} \frac{\rho_v}{\rho_{gp}}. \tag{3}$$

2.2 Conservation Equations

The flow field is computed by solving the conservation equations for mass, momentum and energy. The conservation of mass is given by

$$\rho_t + \nabla \cdot (\rho \mathbf{u}) = 0. \tag{4}$$

Using the density of Eq. (2) and substituting it into the mass conservation Eq. (4), the transport equations of the VOF variables f_1 and f_2 then read

$$(f_1)_t + \nabla \cdot (f_1 \mathbf{u}_l) = -\frac{\dot{m}'''}{\rho_l} \tag{5}$$

and

$$(f_2)_t + \nabla \cdot \left(f_2 \mathbf{u}_{gp}\right) = \nabla \cdot (\mathscr{D}_{\text{bin}} \nabla f_2) + \frac{\dot{m}'''}{\rho_v}. \tag{6}$$

Here, we have the velocity vector $\mathbf{u}$, the volumetric vapour mass source $\dot{m}'''$, and the binary diffusion coefficient $\mathscr{D}_{\text{bin}}$. The differences between the velocities of the gaseous and the liquid phase, $\mathbf{u}_{gp}$ and $\mathbf{u}_l$, respectively, will be addressed in Sect. 3. The conservation of momentum is given by

$$(\rho \mathbf{u})_t + \nabla \cdot [(\rho \mathbf{u}) \otimes \mathbf{u}] = \nabla \cdot (\mathbf{S} - \mathbf{I}p) + \rho \mathbf{g} + \mathbf{f}_\gamma, \tag{7}$$

where p denotes the static pressure, $\mathbf{g}$ the volume forces such as gravity, and $\mathbf{f}_\gamma$ is a body force used to model surface tension at the phase interface. For Newtonian fluids, the viscous stress tensor $\mathbf{S}$ can be written as

$$\mathbf{S} = \mu \left[\nabla \mathbf{u} + (\nabla \mathbf{u})^T\right], \tag{8}$$

where μ denotes the dynamic viscosity.

Finally, the conservation of total energy is solved using the temperature form of the energy equation. Based on [18], a two-field approach is used. Here, each phase j is assigned a temperature field, T_l for the liquid phase and T_{gp} for the gasoues phase, respectively,

$$\left(\rho_j c_{p,j} T_j\right)_t + \nabla \cdot \left(\rho_j c_{p,j} T_j \mathbf{u}\right) = \nabla \cdot \left(k_j \nabla T_j\right) + \dot{q}_j'''. \tag{9}$$

We have the (isobaric) specific heat capacity c_p, the heat conductivity k_j, and the volumetric heat source $\dot{q}_j'''$ in interface cells. Especially at the interface, this method leads to a more precise temperature evolution compared to a one-field approach.

2.3 Jump Conditions

The conservation equations above are all given in differential form. They are only valid if the integrands are continuous. However, as this is not generally the case for multi-phase flows, additional constraints in the form of jump conditions are required. A detailed derivation of these jump conditions starting from the conservation equations in integral form can be found in [18].

With regards to the area specific mass flow rate $\dot{m}''$ across the interface, the jump condition for the conservation of mass at the interface reads

$$-\dot{m}'' = \rho_l \left(\mathbf{u}_l - \mathbf{V}\right) \cdot \mathbf{n} = \rho_{gp} \left(\mathbf{u}_{gp} - \mathbf{V}\right) \cdot \mathbf{n}, \quad \textit{at the interface.} \tag{10}$$

The vector $\mathbf{n}$ is the normal of the interface pointing from the liquid to the continuous phase, and $\mathbf{V}$ represents the total velocity of the interface.

From the mass jump condition we derive the local area specific evaporation rate as [5]

$$\dot{m}'' = \frac{\mathscr{D}_{\text{bin}} \rho_{gp}}{1 - X_v} \left(\nabla X_v\right)_n . \tag{11}$$

It should be noted that this term inherently includes the effect of the Stefan flow. The only remaining unknown is the vapour mass fraction X_v directly at the interface. Here, saturation is assumed locally. Hence, $X_v = X_{v,sat}$ at the surface can be calculated using the saturation pressure p_{sat}, which in turn is determined using the Wagner equation [8]. The binary diffusion coefficient $\mathscr{D}_{\text{bin}}$ is also taken from [8]. From the local area specific evaporation rate $\dot{m}''$, we can define an interfacial growth velocity due to the phase change as [12]

$$V_\Gamma = -\frac{\dot{m}''}{\rho_l}. \tag{12}$$

It is a relative velocity (between the liquid and the interface) solely caused by the phase change and does not include convection.

The jump condition of the energy equation can be expressed as

$$\dot{q}_l - \dot{q}_{gp} = \dot{m}'' \Delta H_v \tag{13}$$

following previous works, e.g. [18]. Here, $\dot{q}_l = \left(\nabla T_l\right)_n$, $\dot{q}_{gp} = \left(\nabla T_{gp}\right)_n$, and H_v represents the latent heat of vaporisation.

3 Numerical Approach

This section contains the numerical schemes involved in the calculation of the evaporation process used in FS3D. A detailed description of the general numerical framework and the results of the wide applicability of the FS3D code package can be found in literature [2, 3, 11, 13, 16, 17]. The following is a summary of the recently implemented framework for evaporation processes [15] which comprises the advection of the liquid and the gas phase followed by a consistent phase change loop.

3.1 Advection of Liquid and Gaseous Phase

The advection of both the liquid and the gaseous phase is uncoupled from the phase change loop and is executed before the latter. Due to the volume change at the interface, which is caused by the evaporation, the velocities of the gaseous and the liquid phase differ from each other in interfacial cells. This means, we need to extract two different velocities $\mathbf{u}_l$ and $\mathbf{u}_{gp}$ from the mass averaged velocity $\mathbf{u}$, which in turn is obtained from the solution of the momentum equation.

If we now combine the volume conservation and the momentum conservation Eq. (7), we obtain

$$\frac{\nabla \cdot \mathbf{u} - \nabla \cdot \tilde{\mathbf{u}}}{\Delta t} = \nabla \cdot \left[-\frac{1}{\rho\left(f_1, f_2\right)} \nabla p \right]. \tag{14}$$

This is the Poisson equation for pressure, where $\tilde{\mathbf{u}}$ is a preliminary velocity vector, which already accounts for all occurring forces except for the pressure. The resulting elliptical equation system has to be solved implicitly (e.g. by using a multigrid scheme).

In general, the velocity fields of both phases, $\mathbf{u}_{gp}$ and $\mathbf{u}_l$, need to be known for the determination of the volume source term $\nabla \cdot \mathbf{u}$ in the Poisson equation. However, they can only be obtained after the velocity field $\mathbf{u}$ has been calculated. This, in turn, requires again the knowledge of the velocities of the two phases. To escape this dilemma, a method was found to first calculate the volume source term from the evaporation rate and then determine the velocity fields of both phases. In contrast to previous methods, there is no need to distribute a velocity divergence error afterwards. The exact way how the velocities are extracted can be found in [15], along with a derivation of the volume source term. For the here presented study, the averaging method using the volume fractions was employed.

Now that the velocities of both phases, $\mathbf{u}_{gp}$ and $\mathbf{u}_l$, are known, the corresponding VOF variables can be advected. For the liquid phase, a *Godunov* type scheme is used, where each spatial direction can be treated independently from the others, and hence, three one-dimensional transport equations are solved successively. Through

proper permutation of the order of these transport equations (*Strang* splitting [21]), a second order temporal accuracy is achieved. After each step, a divergence correction is applied to all cells immerged in the liquid phase. As the velocity field in interfacial cells, however, is not divergence free, the divergence correction has to be revoked in these cells after the transport steps are completed. Otherwise, mass would not be conserved any more, as the divergence correction would lead to the loss or generation of mass in these non-divergence-free interfacial cells.

For the vapour phase advection, the calculation of geometrical fluxes is not necessary as the gaseous phase is assumed to be an ideal mixture of the vapour phase and the inert gas. Here, the fluxes are simply calculated using the wetting of the cell phases and the velocity field of the gaseous phase $\mathbf{u}_{gp}$. The temperature fields of the liquid and the gaseous phase, T_l and T_{gp}, respectively, are advected using the same fluxes as for the corresponding VOF variables, f_1 and f_2.

3.2 Phase Change Loop

The implemented phase change loop is based on the solution procedure for sublimating ice particles of [13]. It is adapted and considerably extended to fit the requirements of evaporation processes. This is crucial as the evaporation process is much faster than the sublimation and highly non-linear effects play a major role. A detailed description of the algorithm and an extensive discussion of theses issues can be found in [15]. The main idea is to consistently solve the coupling between the phase change, the diffusion of vapour, and the temperature distribution through the jump conditions. The coupling elements are the interface temperature T_{int} and the vapour mass fraction X_v.

All terms of the conservation equations are treated in a single consistent loop, except for the advective terms (cf. Sect. 3.1). The source term $\dot{m}'''$ in Eq. (5) is calculated using the growth velocity V_Γ, which means that the movement of the interface due to phase change is interpreted as a consequence of a flux rather than a mass source term. The interface is then advected with this velocity using a geometrical unsplit advection scheme. The source term in Eq. (6) is solved implicitly with the diffusion term as a Dirichlet boundary condition at the interface. We solve the heat conduction in a similar way for both phases by applying the heat fluxes at the interface. Convergence of the whole loop is achieved by relaxing the growth velocity V_Γ.

4 Results

The following sections show the application of the described consistent approach. First, a study of evaporating isooctane droplets is presented. The droplets are exposed to a slow inflow with two different temperature levels and two different vapour mass fractions. The results are then compared to experimental data and correlations from

literature. Additionally, an evaporating water droplet tandem is investigated. Here, the influence of the second droplet on the evaporation behaviour is of special interest. The result is compared to an analytical approach.

4.1 Single Isooctane Droplets

This section includes the results of applying the presented phase change loop to the simulation of isooctane droplets evaporating inside the combustion chamber of a gasoline engine. The results are then compared to literature data. The numerical setup is identical for all three simulations presented in the following. The 3D computational domain is of equal size in all three spatial directions and is resolved by 128 cells per dimension, as depicted in Fig. 1. The droplet is initialised in the centre of the domain with a diameter of $D = 11\,\mu\text{m}$ and an inital temperature of $T_{\text{drop}} = 380\,\text{K}$. It is resolved with 26 cells per diameter. A uniform inflow boundary condition is chosen on one side, where nitrogen is injected with a well defined vapour mass fraction, velocity, and temperature. On the outflow, a continuous boundary condition is used. On the lateral sides, a free-slip condition is imposed. The inflow velocity is set such that the resulting Weber number is $We = (u^2 D\rho_g)/\sigma = 1$ for all three cases (with σ being the surface tension). The overall pressure is set to $p = 600.0\,\text{hPa}$. Table 1 contains the values of the three varied parameters: the temperature of the nitrogen T_{gas} as well as the vapour mass fraction $X_{v,\text{inflow}}$ of the incoming flow, and the inflow velocity u_{inflow}. Additionally, this table also contains the resulting Reynolds numbers $Re = (\rho_g D\, u_{\text{inflow}})/\mu_g$ and Schmidt numbers $Sc = \mu_g/(\rho_g \mathscr{D}_{\text{bin}})$.

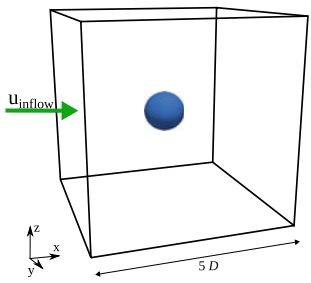

Fig. 1 Setup of numerical grid. Cubic domain with edge length of 5 D and a resolution of 128^3 cells

Table 1 Temperature T_{gas}, vapour mass fraction $X_{v,\text{inflow}}$, and velocity u_{inflow} of incoming nitrogen flow, as well as resulting Reynolds number Re and Schmidt Sc number of the droplet

Case	T_{gas}	$X_{v,\text{inflow}}$	u_{inflow}	Re	Sc
A	470 K	0.0	15.55 m/s	29.4	3.08
B	470 K	0.18	15.55 m/s	29.4	3.08
C	560 K	0.0	16.97 m/s	23.8	3.47

Material properties for isooctane and nitrogen were obtained from the NIST Standard Reference Database [7]. The binary diffusion coefficient was calculated according to the Chapman-Enskog theory [8] at the respective film temperature $T_{\text{film}} = (T_{\text{drop}} + T_{\text{gas}})/2$.

The simulations are evaluated after an initial development phase has been completed and a stationary Sherwood number has been reached,

$$Sh = \frac{\beta D}{\mathscr{D}_{\text{bin}}}. \tag{15}$$

Here, β denotes the local mass transfer coefficient. The Sherwood number for the evaporating droplet is calculated as an area average over the total droplet surface. Figure 2 shows the temperature distribution for case A in the xz-direction at the centre of the domain at the time the Sherwood number was evaluated. All three simulation cases are compared quantitatively to existing experiments and correlations from literature predicting the Sherwood number. A commonly used correlation is the one by Ranz and Marshall [9]

$$Sh = 2 + 0.6\, Re^{1/2} Sc^{1/3}, \tag{16}$$

which is based on their own experiments [10]. Additional, more recent experimental results by Schwarz and Smolik [20] lead Kulmala and Vesala to the following correlation [6]

$$Sh = 2.009 + 0.514\, Re^{1/2} Sc^{1/3}. \tag{17}$$

The comparison of the FS3D simulations with the mentioned experimental results [20] as well as the two correlations are shown in Fig. 3. Cases A and B basically result in the same Sherwood numbers and only vary slightly due to small

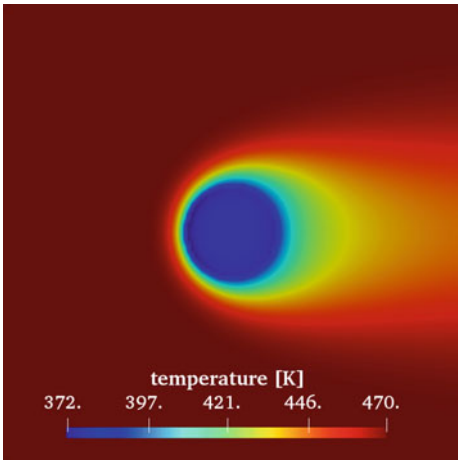

Fig. 2 Temperature distribution of case A in the xz-direction at the centre of the domain

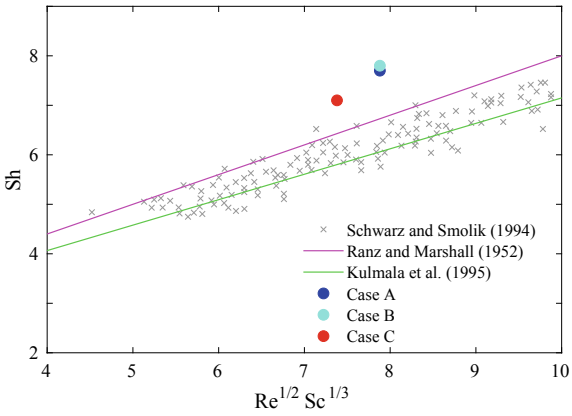

Fig. 3 Sherwood number: comparison of simulation results from FS3D with experimental results and correlations according to Eqs. (16) and (17)

numerical deviations. This behaviour is expected as the Sherwood number, i.e. the comprised local mass transfer coefficient, already takes into account the initial vapour mass fraction of the surrounding gas. As this parameter is the only difference between case A and case B, the Sherwood numbers should be equal. All three cases lie above the correlation by Ranz and Marshall [9]. This is due to the fairly high evaporation rates at the chosen conditions.

For increasing vapour mass rates, the influence of the Stefan flow on the boundary layer and, thus, on the Sherwood number, becomes more important. It is accounted for in the correlation

$$Sh(1 + B_M)^{0.7} = 2 + 0.87\, Re_m^{1/2} Sc_{\text{film}}^{1/3}. \tag{18}$$

proposed by Renksizbulut et al. [14] in the factor $(1 + B_M)^{0.7}$. The Spalding mass number B_M is defined as $B_M = (X_{v,\text{sat}} - X_{v,\infty})/(1 - X_{v,\text{sat}})$. The subscript $_{\text{film}}$ indicates that the material properties are evaluated at film conditions (i.e. at the film temperature T_{film}). The Reynolds number Re_m is calculated using mixed properties from both film and free stream conditions following [14], $Re_m = (\rho_g D\, u_{\text{inflow}})/\mu_{\text{film}}$. When the simulation results of the three cases are compared to this correlation, they lie below the predicted values as seen in Fig. 4. This behaviour indicates that the presented cases lie in the transition zone between low and high evaporating conditions.

4.2 Water Droplet Tandem

This section contains the simulation results of a water droplet tandem evaporating at a temperature of 293 K, which were already presented on the DIPSI workshop 2019. The temperature and vapour profiles in the near droplet neighbourhood are analysed and the evaporation rate is compared to the analytical model by [1]. The two droplets

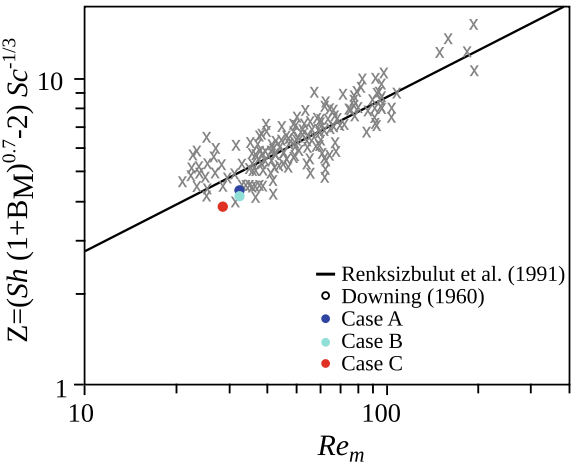

Fig. 4 Comparison of simulation results with the correlation according to Eq. (18). Data extracted from [14]

have a nondimensional distance of $\kappa = L/D = 2$, with L referring to the distance of the droplet centres. The surrounding gas is quiescent air. Both droplets have the same diameter of $D = 6 \times 10^{-4}$ m. The 3D computational domain is of equal size ($5D$) in all three spatial directions and is resolved by 128 cells per dimension. The contour plots of both the vapour volume fraction and the temperature distribution on a centre slice through the domain can be seen in Fig. 5. The figure also shows the expected symmetry of the problem. At the droplet surface, a temperature drop can be observed, even though the simulation is started in isotherm conditions (with the surrounding air also being at 293 K). This decrease is due to the latent heat of evaporation required for the phase change. Figure 6, which shows the distribution along the centre line, highlights this temperature drop as well.

The temperature and vapour profiles are significantly influenced by the existence of a second droplet. First, the total evaporation rate of the tandem is smaller compared to that of two single, isolated droplets. This is due to the fact that vapour accumulates between the droplets and cannot diffuse as easily to the surrounding. This causes a decrease in the gradient of the vapour volume fraction and therefore, to a lower evaporation rate. Second, the air between the droplets starts to cool down, which causes a further decrease of the evaporation rate.

The simulation results are then compared to an analytical solution using the so called screening factor. The latter compares the total evaporation rate of the tandem to the sum of the evaporation rates of two isolated droplets. It is defined as

$$\Phi = \frac{m_{\mathrm{ev},1} + m_{\mathrm{ev},2}}{m_{\mathrm{ev,is},1} + m_{\mathrm{ev,is},2}}. \tag{19}$$

From the DNS, we obtain a value of $\Phi_{\mathrm{DNS}} = 92.98\,\%$, wheras the analytical approach results in a value of $\Phi_{\mathrm{analytical}} = 80.48\,\%$. These values are in the same range, however, further investigations will give more insight why the simulations show a much weaker influence of the neighbouring droplet.

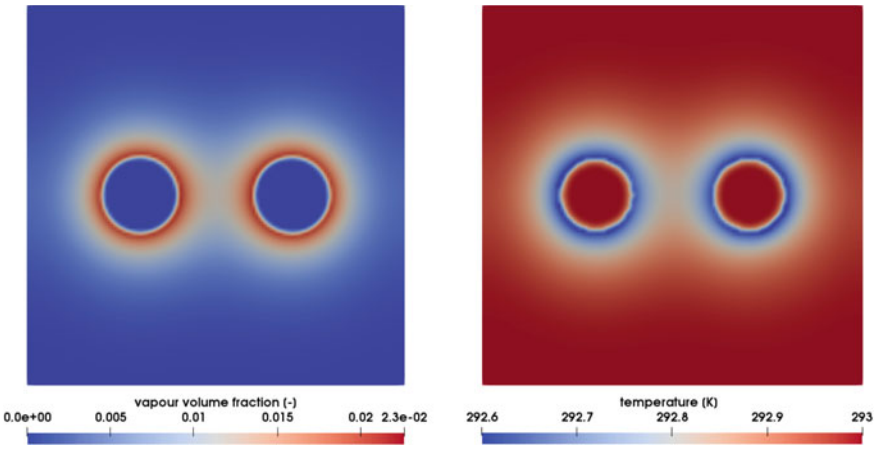

Fig. 5 Distribution of vapour volume fraction (left) and temperature (right) in the xz-direction at the centre of the domain

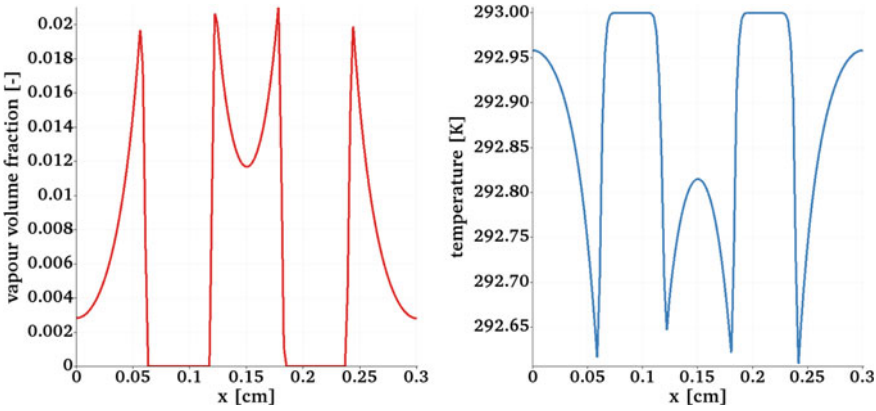

Fig. 6 Distribution of vapour volume fraction (left) and temperature (right) along centre line of the domain

5 Conclusion

A numerical framework was presented for the simluation of evaporation processes within a Finite Volume scheme using the VOF method. The used two-field formulation allows to set Dirichlet conditions on the sharp interface for the concentration of vapour and the temperature. The actual phase change is then solved in a consistent loop including the diffusive vapour transport and the energy equation. The framework is an extension of an already existing numerical scheme for the simulation of sublimating ice particles. It was adapted to fit the specific requirements when simulating the evaporation of hot, liquid droplets (as opposed to cold, rigid ice

particles). When simulating single evaporating isooctane droplets in hot nitrogen, a comparison with literature correlations shows that the chosen boundary conditions lead to evaporation rates in the transition zone between low and high evaporating conditions. The simulation of a water droplet tandem highlights the influence of the near droplet neighbourhood on the evaporation process.

Acknowledgements The research was carried out in the framework of the industrial collective research programme (IGF no. 19320 N/2). It was supported by the Federal Ministry for Economic Affairs and Energy (BMWi) through the AiF (German Federation of Industrial Research Associations eV) based on a decision taken by the German Bundestag. We thank the `High Performance Computing Centre Stuttgart` (HLRS) for support and supply of computational time on the Cray XC40 platform under Grant No. FS3D/11142.

References

1. Cossali, G., Tonini, S.: Variable gas density effects on transport from interacting evaporating spherical drops. Int. J. Heat Mass Transfer **127**, 485–496 (2018)
2. Eisenschmidt, K., Ertl, M., Gomaa, H., Kieffer-Roth, C., Meister, C., Rauschenberger, P., Reitzle, M., Schlottke, K., Weigand, B.: Direct numerical simulations for multiphase flows: an overview of the multiphase code FS3D. J. Appl. Math. Comput. **272**(2), 508–517 (2016)
3. Hase, M.: Numerische berechnung dreidimensionaler transportvorgänge an angeströmten, sich verformenden tropfen. Ph.D. thesis, Universität Stuttgart (2005)
4. Hirt, C.W., Nichols, B.D.: Volume of fluid (VOF) method for the dynamics of free boundaries. J. Comput. Phys. **39**(1), 201–225 (1981)
5. Kays, W., Crawford, M., Weigand, B.: Convective Heat and Mass Transfer, 4th edn. McGraw-Hill (2004)
6. Kulmala, M., Vesala, T., Schwarz, J., Smolik, J.: Mass-transfer from a drop 2. Theoretical-analysis of temperature-dependent mass flux correlation. Int. J. Heat Mass Transfer **38**(9), 1705–1708 (1995)
7. Lemmon, E.W., Bell, I., Huber, M.L., McLinden, M.O.: NIST Standard Reference Database 23: Reference Fluid Thermodynamic and Transport Properties—REFPROP, Version 10.0. National Institute of Standards and Technology (2018). https://doi.org/10.18434/T4JS3C
8. Poling, B.E., Prausnitz, J.M., O'Connell, J.P.: The Properties of Gases and Liquids, 5th edn. McGraw-Hill (2000)
9. Ranz, W.E., Marshall, W.R.: Evaporation from drops: Part 1. Chem. Eng. Prog. **48**(3), 141–146 (1952)
10. Ranz, W.E., Marshall, W.R.: Evaporation from drops: Part 2. Chem. Eng. Prog. **48**(4), 173–180 (1952)
11. Rauschenberger, P., Weigand, B.: Direct numerical simulation of rigid bodies in multiphase flow within an Eulerian framework. J. Comput. Phys. **291**, 238–253 (2015)
12. Reitzle, M., Kieffer-Roth, C., Garcke, H., Weigand, B.: A volume-of-fluid method for three-dimensional hexagonal solidification processes. J. Comput. Phys. **339**, 356–369 (2017)
13. Reitzle, M., Ruberto, S., Stierle, R., Gross, J., Janzen, T., Weigand, B.: Direct numerical simulation of sublimating ice particles. Int. J. Therm. Sci. **145**, (2019). https://doi.org/10.1016/j.ijthermalsci.2019.05.009
14. Renksizbulut, M., Nafziger, R., Li, X.G.: A mass-transfer correlation for droplet evaporation in high-temperature flows. Chem. Eng. Sci. **46**(9), 2351–2358 (1991)
15. Reutzsch, J., Kieffer-Roth, C., Weigand, B.: A consistent method for direct numerical simulation of droplet evaporation. J. Comput. Phys. (submitted)

16. Rieber, M.: Numerische Modellierung der Dynamik freier Grenzflächen in Zweiphasenströmungen. Dissertation, Universität Stuttgart (2004)
17. Schlottke, J.: Direkte Numerische Simulation von Mehrphasenströmumgen mit Phasenübergang. Ph.D. thesis, Universität Stuttgart (2010)
18. Schlottke, J., Rauschenberger, P., Weigand, B., Ma, C., Bothe, D.: Volume of fluid direct numerical simulation of heat and mass transfer using sharp temperature and concentration fields. In: ILASS - Europe 2011, 24th European Conference on Liquid Atomization and Spray Systems, Estoril, Portugal (2011). http://www.ilass.uci.edu/
19. Schlottke, J., Weigand, B.: Direct numerical simulation of evaporating droplets. J. Comput. Phys. **10**, 5215–5237 (2008)
20. Schwarz, J., Smolik, J.: Mass-transfer from a drop 1. Experimental-study and comparison with existing correlations. Int. J. Heat Mass Transfer **37**(14), 2139–2143 (1994)
21. Strang, G.: On the construction and comparison of difference schemes. SIAM J. Numer. Anal. **5**(3), 506–517 (1968)

Effects of Very High Injection Pressures on GDI Spray Structure

Alessandro Montanaro and Luigi Allocca

Abstract The flexibility in managing the air-fuel mixture formation in engines equipped with Gasoline Direct Injection (GDI) has demonstrated being an effective system to pursue the growing demand of energy efficiency and reduction of pollutant emissions. This injection modality improves the spray characteristics in terms of a better atomization of the fuel, finer droplet size and better distribution in the combustion chamber to enhance the combustion efficiency. Nowadays, it is known that very high-pressure injections are adopted in GDI systems to improve the spray atomization and, subsequently, the evaporation processes in the engine combustion chamber. In this study, the investigation of the influence of the pressure on gasoline spatial spread and thermo-dynamic status was carried out for different ambient densities (from 0.2 to 11.50 kg/m^3) and gas temperatures (from room to 200 °C) by a hybrid optical setup, shadowgraph and Mie scattering, to acquire in a cycle-resolved mode both the vapor and the liquid phases of the spray. The study was performed in a constant volume chamber (CVC) using a ten-hole GDI injector, 0.10 mm in diameter, with the injection pressure ranging from 40.0 to 100.0 MPa. The influences of the ambient and injection conditions on the characteristic parameters of the jets, such as tip penetration, cone-angle, and fuel spread, were extracted by a customized image-processing procedure developed in C#.

1 Introduction

The use of Gasoline Direct Injection (GDI) continuously increases due to the growing demand of efficiency and power output for i.c. engines. The optimization of the fuel injection process is essential to prepare an air-fuel mixture capable to promote efficient combustion, reduced fuel consumption and pollutant emissions. Good spray atomization facilitates fuel evaporation in i.c. engines thus contributing to the fuel economy and lowering the emissions. One of the key features of a multi-hole injector

A. Montanaro (✉) · L. Allocca
Istituto Motori-CNR, Naples, Italy
e-mail: a.montanaro@im.cnr.it

G. Lamanna et al. (eds.), *Droplet Interactions and Spray Processes*,
Fluid Mechanics and Its Applications 121,
https://doi.org/10.1007/978-3-030-33338-6_24

is to provide an optimal spray pattern in the combustion chamber and a good mixture homogenization considering the engine-specific characteristics such as fuel mass-flow rate, cylinder geometry, injector position and charge motion.

Different approaches allow pursuing the emission limit targets improving the combustion process inside the i.c. engines, through a progressive hybridization, more efforts in the transportation efficiency, and exploring advanced combustion strategies like gasoline compression ignition (GCI). The combustion by the GCI approach requires the fuel being injected at high pressures to reach the improvements in the thermal efficiency that several studies have demonstrated [1, 2].

In this context, the increase of the fuel injection pressure is believed to be a key feature to improve the fuel atomization degree and contribute to a fast and better vaporization of the mixture preparation [3–6]. Pressures up to 100 MPa and more are experienced for future market requirements, especially to meet the more and more stringent future emission legislation limits [7]. In particular, the increase of the injection pressure is considered a good way for particle number (PN) reduction due to improved spray atomization, faster evaporation and better mixture formation [8, 9].

Moreover, flash boiling phenomena is considered another relevant way to produce an optimal fuel spray with advantages in generating finer droplets, enhancing fuel/air mixture, improving the combustion, and reducing PN emissions [10–14]. Flash boiling, which features a two-phase flow that constantly generates vapor bubbles inside the liquid spray is ideal to achieve fast evaporation and combustion inside direct-injection (DI) gasoline engines. Many studies were implemented to understand the features and mechanisms of flash boiling sprays under conventional injection pressures (lower than 20.0 MPa) but few studies have been done to investigate how the spray structure varies at very-high injection pressure.

Within this context, this work aims to report the results of a complete campaign of investigation on the behaviour of gasoline injected by a high-pressure GDI injector in a constant volume vessel filled with gas (N_2) at diverse pressures and temperatures. Liquid and vapor phases of a GDI multi-hole spray were investigated to study mainly the effects of high injection pressure on spray morphology over a wide range of ambient and injection conditions. Moreover, the results will be able to provide a robust data set for combustion ambient design as well as for advanced CFD numerical models.

2 Materials and Methods

The study was performed by injecting commercial gasoline in a constant volume combustion vessel by a high-pressure GDI injector. The nozzle has ten identical holes with diameter (d0) of 100 μm and L/d = 7, having a static flow of 10.55 g/s @10.0 MPa. The fuel is supplied through a rail, heated by an electrical resistance and controlled in temperature (T_f) by a J-type thermocouple. The injector is allocated in a holder containing a jacket for fluxing a cooling liquid connected to a chiller for the

Table 1 Experimental conditions

p_{inj} [MPa]	40.0–55.0–70.0
t_{inj} [μs]	1000
T_{amb} [°C]	20–100–200
$\rho_g(N_2)$ [kg/m^3]	0.2–1.12–5.7–11.5
Fuel	Gasoline ($\rho = 720$ kg/m^3@15 °C)
$T_i - T_f$ [°C]	20–90

temperature control of the nozzle nose (T_i). The morphology of the fuel spray was depicted as function of the injection pressure (p_{inj}), ambient temperature (T_g), and gas density (ρ_g), keeping constant the energizing timing (t_{inj}) at 1000 μs. Nitrogen (N_2) was used to achieve the desired gas densities according with the different ambient temperatures, see Table 1. Ten consecutive sequences were acquired for each injection condition for an evaluation of the spray spread.

The spray morphology was investigated by two optical techniques, shadowgraph and Mie-scattering, acquiring the images along the same line-of-sight. This optical setup was arranged to visualize the liquid phase from Mie scattering images while the corresponding shadowgraph were employed to underline both liquid and vapor fraction of the spray. A pulsed LED was used as the shadowgraph light source while a high-intensity flash, synchronized with the injection event, provided the illumination for Mie-scattering. The spray images were collected by a high-speed C-Mos camera at a rate of 16,000 frames per second (fps) with an image window of 512 × 448 pixels. The camera was equipped with a 90 mm objective, f 1:2.8, resulting the spatial resolution 5.90 pixel/mm. The images acquired in the different operating conditions were analyzed by means of a post-processing software developed in C# environment. Shadowgraph and Mie-scattering images were processed by slight different procedures because presenting diverse intensity of the images. Procedure of background subtraction, gamma correction, morphology filtering and threshold filtering were applied on the shadowgraph and Mie-scattering spray images in order to better outline the contours of both vapor and liquid phase. The resulting spray images were then processed to compute the main macroscopic features of the spray, according to SAEJ2715 rule [15]. More details on optical setup as well as the adopted images processing procedure are reported in [16].

3 Results and Discussion

Figure 1 reports a shadowgraph spray image under evaporative conditions (T_{amb}: 200 °C) at 55.0 MPa and 5.7 kg/m^3 as injection pressure and ambient density, respectively. The shapes of the sprays appear structured into two lobes outlining the division of five jets per lobe with respect to the C-Mos camera line of sight. The spray image gives an immediate evidence of the vaporizing process occurring at high ambient temperature. The picture clearly show a dense liquid core (dark part), liquid portion,

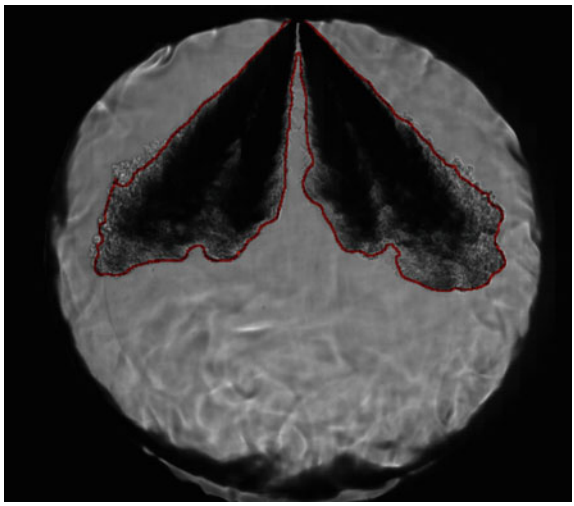

Fig. 1 Liquid and vapor portion at high ambient temperature (200 °C)

surrounded by a mixed area including ligaments, finely atomized droplets, and vapor phase. The noisy background is a consequence of the combined effect of both the high gas density and the high ambient temperature.

The influence of the ambient temperature on the liquid spray evolution at the gas density of 5.7 kg/m^3 is illustrated in Fig. 2 through spray evolution at different ambient temperatures and 40.0 MPa as injection pressure. Mie scattering spray images are reported at different time from the start of injection (SOI). The consequences of the temperature increase on the liquid part of the spray were well emphasized by the images collected by the Mie-scattering technique giving an immediate evidence of the vaporizing process. A strong reduction along of both the axial and the radial direction was registered because of the vaporization that mainly affects the jets periphery, where finely atomized particles are present. Under evaporative conditions, the spray forms and develops as follows: at the beginning, the liquid phase atomizes and progresses; in the meanwhile, enough heated gas is entrained to warm and vaporize the fuel; then, the liquid penetration slows down while the vapor phase still penetrates. At room temperature, the jets are bulky and longest penetrations are reached. Instead, the increase of the temperature causes the spray became skinny and the penetration shorter because of the evaporation process.

The corresponding liquid penetration profiles versus time are reported in Fig. 3. The spray penetration length is defined here as the maximum distance between the nozzle exit and farthest point of the spray tip along the spray axis. Each data point is an average of ten injection events for evaluating the cycle to cycle variation and the error bars are the standard deviation of the data. After an initial overlapping of the profiles, the general trend shows well-scaled penetrations versus. ambient temperatures with a strong inverse effect.

Figure 4 depicts the effects of the injection pressure on the spray evolution at room ambient temperature and gas densities of 1.12 (top) and 11.50 kg/m^3 (bottom).

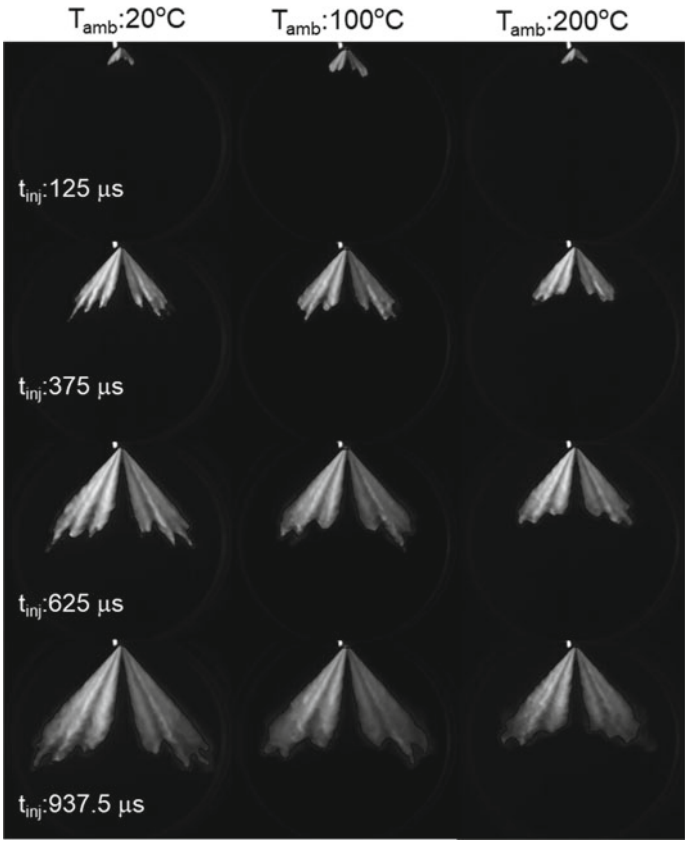

Fig. 2 Ambient temperature effect on liquid spray fraction, p_{inj}: 40 MPa and ρ_g: 5.7 kg/m^3

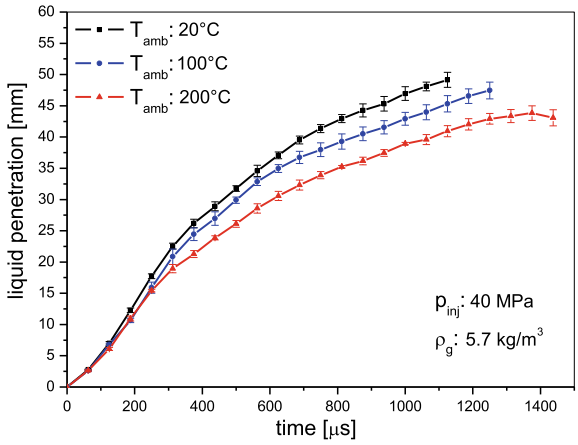

Fig. 3 Effect of ambient temperature on liquid penetration profiles

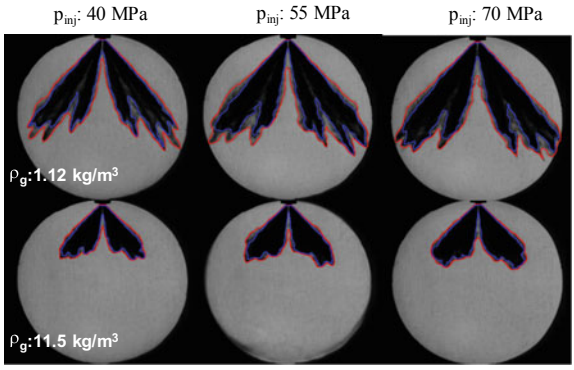

Fig. 4 Injection pressure effects on global spray structure

The pictures are shadowgraph frames that give evidence of the vapor phase (red color) and englobing the remaining liquid part (blue contour) extracted from Mie scattering images. The increase of the injection pressure produces a growth of the amount of injected fuel and thus of the momentum, since the injection duration was kept constant (1 ms). The increment of the injection pressure produces a better fuel atomization and a faster vaporization. The vaporized areas appear mainly confined at the front and on the periphery of the jets, where the fluidynamic interaction with the gas is strongest, the droplets are finely atomized and faster vaporize.

At atmospheric condition (top), the spray images show insignificant effects of the injection pressure on the spray penetration, whereas the spray plume width becomes wider when the injection pressure increases from 40 to 70.0 MPa. Vice versa, a slight tendency to increase the fuel penetration with growing the injection pressure can be noticed for the condition with 11.5 kg/m^3 as gas density. To confirm this, the global penetration lengths of the spray in Fig. 5 show differences of the fuel tip development versus time as function of the diverse injection pressures and ambient densities. In the

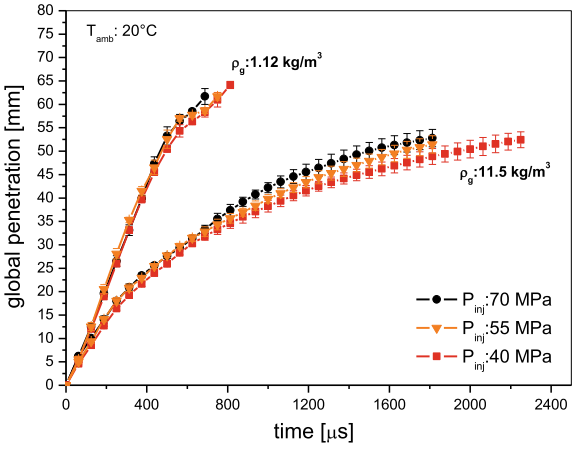

Fig. 5 Effect of the injection pressure on global spray penetration for two gas densities

figure, a negligible effect of the injection pressure at atmospheric condition is shown where the three profiles overlap all along the injection duration while little differences occur at the highest density of the ambient gas. These trends differ from the typical spray evolution under conventional injection pressure values (lower than 20.0 MPa) where the increasing of the injection pressure generates a significant increase of the spray penetration. The effect of the highest injection pressures produces a greatest momentum of the fuel and, at the same time, a strongest atomization of the droplet itself with a reduction in size. A balancing effect between the two process seems being highlighted in the penetration behavior.

In Fig. 6, the behavior of the fuel for different densities of the gas kept at the temperature of 200 °C is described. The temperature effects on the background gas are highlighted by the convective modes inside the sampling volume and figured by turbulences: their depictions are almost negligible at $\rho = 1.12$, light intense at 5.7 and very strong at 11.5 kg/m^3. Their effects are irrelevant for the purpose of the image processing because the characteristic evolution time of the convective modes are very slow with respect to the spray evolution; practically, they appear fixed. The spray images show a stronger sensitivity of the spray development to ambient pressure respect to the effect of the fuel injection pressure previously discussed.

At atmospheric condition of the gas (left) the evolution of the single plumes is still quasi-visible while, at the increasing of the gas density the jets become undistinguishable each other. An increase of the umbrella cone angle is registered and two main compact lobes appear. In addition to the brake effect due to the increased gas density, an additional reduction of the penetration is generated by the compression

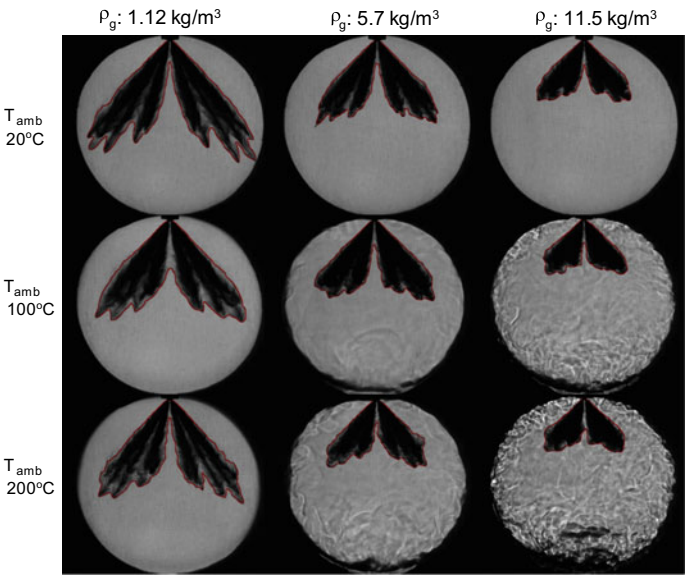

Fig. 6 Shadowgraph spray images for different gas densities; p_{inj}: 40 MPa and T_g: 200 °C

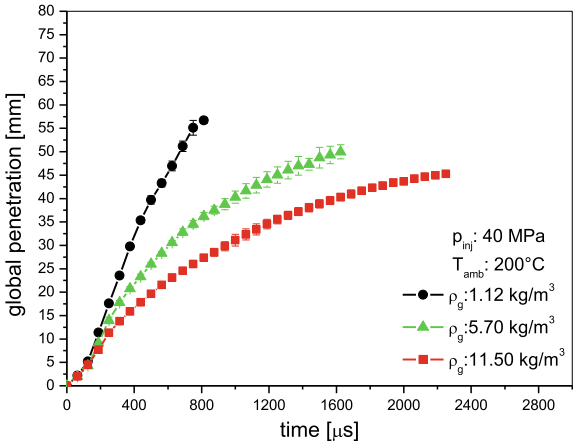

Fig. 7 Effect of gas density on global penetration; p_{inj}: 40 MPa, T_g: 200 °C

of the spray front, mainly constitute of vapor, easy to constrict. This effect appears more evident moving from 5.7 to 11.5 kg/m^3 of the gas density.

The corresponding measurements of the effects of the gas density on the tip penetration are described in Fig. 7. A scaling factor of the lengths vs. the gas density in the vessel appears clear: the higher is the density and the lower is the fuel penetration. This is strictly related to the brake effect of the gas in the chamber against the fuel propagation. At atmospheric density, the profile shows a quasi-linear trend for all the injection duration while a saturation of the penetration trend toward the highest densities is recorded in the propagation of the jet plumes. The short error bars per each density and all along the spray evolution confirm the stability of the spray shape repetitions. Similar behavior was observed also for the other investigated injection pressures (55.0 and 70.0 MPa) and ambient temperatures (20 and 100 °C) with well-scaled trends versus the ambient densities with a strong inverse effect.

The results discussed so far were obtained by keeping constant both fuel and nozzle temperature at room value. As known, the combined effect of the fuel temperature increase and the reduction of the ambient pressure is a common way to increase the fuel superheat degree and thereby increase the spray flash-boiling effect. In the last section of the work, we will discuss on flash boiling conditions under higher injection pressure. For multi-hole fuel injectors, a high level of flash boiling causes the plumes to merge into a single plume, usually better known as “spray collapse”. As consequence of this phenomenon, a thinner and longer spray is generally generated [16, 17]. Main portion of this effect is given by the fuel temperature but the huge contribution comes from the reduced backpressure on the spray blowing. It would increase the possibility of fuel-wall impingement in engines due to its longer spray penetration, which might result in a significantly increased amount of fuel adhered on the wall of the combustion chamber, and consequently cause the deposit, soot, and super-knock [18]. The increase of the injection pressure can be considered an option to suppress the plume-to-plume interaction of flash-boiling spray. The experimental results of the high injection pressure impact were summarized in Fig. 8, where

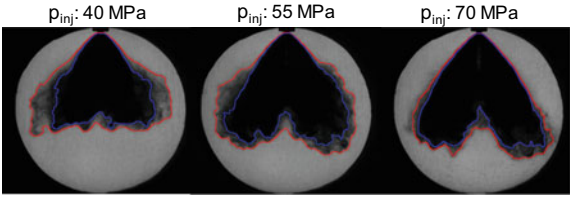

Fig. 8 Flash boiling conditions: effects of the high injection pressure on spray morphology

contours of the liquid and vapor phases of the spray, superimposed to the shadowgraph images are shown at the fixed time of 625 μs from SOI.

The inner (blue) contours were derived from the Mie scattering images and represent the liquid phase. The outer (red) contours were derived from the shadowgraph images and include the liquid core and vapor phase. The overlaying of the liquid phase contour onto the shadowgraph image allows the determination of the line-of-sight phase boundary. Both the fuel (T_f) and injector nozzle temperature (T_i) were fixed to 90 °C while the ambient pressure at 0.02 MPa realizing an ambient density of 0.23 kg/m^3 being the ambient temperature constant at room value. The spray images clearly show a different morphology with increasing of injection pressure under the same fuel temperature and ambient pressure, a strong reduction of the plume-to-plume interaction appears. At the lowest injection pressure (40.0 MPa), the spray plumes become fully collapsed to form a single body. Large vapor vortexes are visible at the bottom part of the spray and the individual plumes are no more identifiable. At increasing of the injection pressure (55.0 MPa), the characteristic spray collapse shape looks less evident: the vapor vortexes disappear, the spray cone angle increases and the global spray begins to separate into two main lobes. Finally, at further increasing of the injection pressure (70.0 MPa), the spray appears almost completely separated in two with a gap in the middle and the collapsed structure is not more evident. As a consequence, the phenomenon of collapse is usually depicted as that of adjacent plumes expanded by the flash boiling and connected in a way to form a ring shape, enclosing an empty region in the spray core. Hence, no gas can be trapped or transferred in the closed central region, generating a depression with a further fall of the plumes towards the spray core. This characteristic outcome of the spray, when flash boiling conditions occur, vanishes at higher injection pressures due to the increase of the spray velocity in the axial direction, as consequence of the momentum growing, became the dominant effect.

Figure 9 reports the global penetration profiles vs. time for different ambient conditions including the flashing one (green curve) at 70 MPa as injection pressure. After an initial overlapping of the curves at early stage, the spray develops in agreement with the diverse ambient conditions. The blue curve displays the penetration increase by moving from atmospheric (red curve) to sub-atmospheric (0.2 kg/m^3) ambient pressure due to the lower gas drag force. The combined effect of the sub-atmospheric conditions and high fuel temperature causes flash boiling conditions with consequent reduction of spray cone angle and spray penetration as shown in Fig. 9 (green curve).

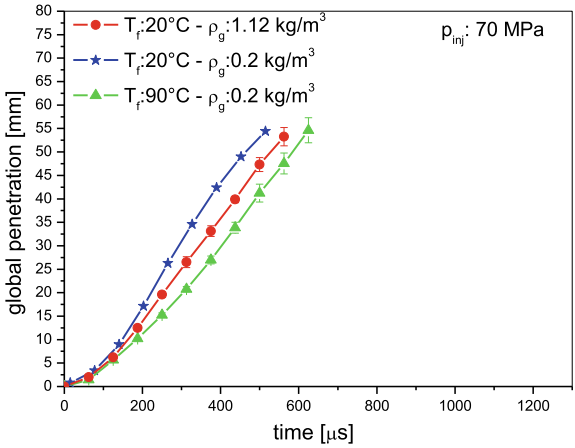

Fig. 9 Global penetration profiles for different ambient conditions

4 Conclusions

Liquid and vapor phases of a GDI multi-hole spray were investigated to study mainly the effects of very-high injection pressure on spray morphology under different ambient and injection conditions. The fuel spray was injected in a constant volume vessel and the change of the morphology was studied as function of the injection pressure, ambient temperature, and gas density in the vessel, representing different engine conditions.

The inverse proportionality of the penetrations to the gas densities indicates a stronger sensitivity of the spray development to ambient pressure. The increase of injection pressure produces a better fuel atomization and so an easier vaporization. The vaporized areas appear mainly confined at the front and on the periphery of the jets, where the fluidynamic interaction with the gas is strongest, the droplets are finely atomized and faster vaporize. The effect of the highest fuel momentum as consequence of the greatest injection pressures looks to be balanced by the effect of the strongest fuel atomization that produces the reduction of the droplet size and, therefore, of the spray development.

The characteristic outcome of the spray, at flash boiling conditions, weaken at higher injection pressures because of the increase in the spray velocity and the droplet momentum becomes the dominant effect.

Further investigations are planned to study the effects of the high injection pressure on spray morphology generated by injectors of the same family as the one investigated in this work but with different nozzles and L/D ratio.

Finally, the obtained results will provide useful data set for the CFD numerical models validation.

Acknowledgements The authors would like to acknowledge the Magneti Marelli S.p.A. Powertrain for the hardware supply and the technical support to the experimental work.

References

1. Kalghatgi, G.T., Risberg, P., Ångström, H.-E.: Partially pre-mixed auto-ignition of gasoline to attain low NOx at high load in a compression ignition engine and comparison with a diesel fuel. SAE Int. (2007). https://doi.org/10.4271/2007-01-0006
2. Manente, V., Johansson, B., Cannella, W.: Gasoline partially premixed combustion, the future of internal combustion engines? Int. J. Engine Res. **12**(3), 194–208 (2011). https://doi.org/10.1177/1468087411402441
3. Hoffmann, G., Befrui, B., Berndorfer, A., Piock, W., et al.: Fuel System pressure increase for enhanced performance of GDi multi-hole injection systems. SAE Int. J. Engines **7**(1), 519–527 (2014)
4. Postrioti, L., Cavicchi, A., Brizi, G., Berni, F., et al.: Experimental and numerical analysis of spray evolution, hydraulics and atomization for a 60 MPa injection pressure GDI System. SAE Technical Paper 2018-01-0271 (2018). https://doi.org/10.4271/2018-01-0271
5. Medina, M., Fatouraie, M., Wooldridge, M.: High-speed imaging studies of gasoline fuel sprays at fuel injection pressures from 300 to 1500 bar. SAE Technical Paper 2018-01-0294 (2018). https://doi.org/10.4271/2018-01-0294
6. Herweg, R., Haase, D., Dieler, T., Berndt, F., Rottenkolber, G.: Lean burn combustion for gasoline engines: potential of high frequency ignition and high pressure injection. In: 13th Stuttgart International Conference Automotive and Engine Technology (2013)
7. Commission Regulation (EU) No 459/2012 of 29 May 2012. https://eur-lex.europa.eu/legal-content/EN/TXT/?uri=celex%3A32012R0459
8. Klauer, N., Klüting, M., Schünemann, E., Schwarz, C., Steinparzer, F.: BMW TwinPower turbo gasoline engine technology—enabling compliance with worldwide exhaust gas emissions requirements. In: 34th Vienna Motor Symposium (2013)
9. Stadler, A., Brunner, R., Härtl, M., Wachtmeister, G., Sauerland, H.: Experimental investigations on high pressure gasoline injection up to 800 bar for different combustion modes. In: 27th Aachen Colloquium Automobile and Engine Technology, 1089 (2018)
10. Zeng, W., Xu, M., Zhang, Y., Wang, Z.: Laser sheet dropsizing of evaporating sprays using simultaneous LIEF/MIE techniques. Proc. Combust. Inst. **34**(1), 1677–1685 (2013)
11. Yang, J., Xu, M., Hung, D.L.S., Wu, Q., Dong, X.: Influence of swirl ratio on fuel distribution and cyclic variation under flash boiling conditions in a spark ignition direct injection gasoline engine. Energy Convers. Manag. **138**, 565–576 (2017)
12. Dong, X., Yang, J., Hung, D.L.S., Li, X., Xu, M.: Effects of flash boiling injection on in-cylinder spray, mixing and combustion of a spark-ignition direct-injection engine. Proc. Combust. Inst. (2018)
13. Senda, J., Wada, Y., Kawano, D., Fujimoto, H.: Improvement of combustion and emissions in diesel engines by means of enhanced mixture formation based on flash boiling of mixed fuel. Int. J. Engine Res. **9**(1), 15–27 (2008)
14. Yang, J., Dong, X., Wu, Q., Xu, M.: Influence of flash boiling spray on the combustion characteristics of a spark-ignition direct-injection optical engine under cold start. Combust. Flame **188**, 66–76 (2018)
15. Hung, D., Harrington, D., Gandhi, A., Markle, L., et al.: Gasoline fuel injector spray measurement and characterization—a new SAE J2715 recommended practice. SAE Int. J. Fuels Lubr. **1**(1), 534–548 (2009)
16. Allocca, L., Montanaro, A., Meccariello, G.: Effects of the ambient conditions on the spray structure and evaporation of the ECN spray G. SAE Technical Paper 2019-01-0283 (2019)
17. Montanaro, A., Allocca, L., Lazzaro, M.: Iso-Octane spray from a GDI multi-hole injector under non- and flash boiling conditions. SAE Technical Paper 2017-01-2319 (2017)
18. Guo, H., Ma, X., Li, Y., Liang, S., Wang, Z., Xu, H., Wang, J.: Effect of flash boiling on microscopic and macroscopic spray characteristics in optical GDI engine. Fuel **190**, 79–89 (2017)